MARTIN MARIETTA ENERGY SYSTEMS LIBRARIES

3 4456 0315961 3

ornl

ORNL/TM-11489

OAK RIDGE
NATIONAL
LABORATORY

MARTIN MARIETTA

CERAMIC TECHNOLOGY FOR ADVANCED HEAT ENGINES PROJECT SEMIANNUAL PROGRESS REPORT FOR APRIL 1989 THROUGH SEPTEMBER 1989

Prepared for
U.S. Department of Energy
Assistant Secretary for
Conservation and Renewable Energy
Office of Transportation Technologies
Advanced Materials Development Program

OAK RIDGE NATIONAL LABORATORY
CENTRAL RESEARCH LIBRARY
CIRCULATION SECTION
4500N ROOM 175
LIBRARY LOAN COPY
DO NOT TRANSFER TO ANOTHER PERSON
If you wish someone else to see this report, send in name with report and the library will arrange a loan.

CERAMIC TECHNOLOGY FOR ADVANCED HEAT ENGINES

CERAMIC TECHNOLOGY PROJECT
DOE/ORNL

OPERATED BY
MARTIN MARIETTA ENERGY SYSTEMS, INC.
FOR THE UNITED STATES
DEPARTMENT OF ENERGY

This report has been reproduced directly from the best available copy.

Available to DOE and DOE contractors from the Office of Scientific and Technical Information, P.O. Box 62, Oak Ridge, TN 37831; prices available from (615) 576-8401, FTS 626-8401.

Available to the public from the National Technical Information Service, U.S. Department of Commerce, 5285 Port Royal Rd., Springfield, VA 22161.

NTIS price codes — Printed Copy: A03; Microfiche: A01.

This report was prepared as an account of work sponsored by an agency of the United States Government. Neither the United States Government nor any agency thereof, nor any of their employees, makes any warranty, express or implied, or assumes any legal liability or responsibility for the accuracy, completeness, or usefulness of any information, apparatus, product, or process disclosed, or represents that its use would not infringe privately owned rights. Reference herein to any specific commercial product, process, or service by trade name, trademark, manufacturer, or otherwise, does not necessarily constitute or imply its endorsement, recommendation, or favoring by the United States Government or any agency thereof. The views and opinions of authors expressed herein do not necessarily state or reflect those of the United States Government or any agency thereof.

ORNL/TM-11489

Metals and Ceramics Division

CERAMIC TECHNOLOGY FOR ADVANCED HEAT ENGINES PROJECT SEMIANNUAL PROGRESS REPORT FOR APRIL 1989 THROUGH SEPTEMBER 1989

D. R. Johnson
Project Manager

Date Published: August 1990

NOTICE: This document contains information of a preliminary nature. It is subject to revision or correction and therefore does not represent a final report.

Prepared for
U.S. Department of Energy
Assistant Secretary for Conservation and Renewable Energy
Office of Transportation Technologies
Advanced Materials Development Program
EE 04 00 00 0

Prepared by the
OAK RIDGE NATIONAL LABORATORY
Oak Ridge, Tennessee 37831-6285
operated by
MARTIN MARIETTA ENERGY SYSTEMS, INC.
for the
U.S. DEPARTMENT OF ENERGY
under Contract DE-AC05-840R21400

MARTIN MARIETTA ENERGY SYSTEMS LIBRARIES

3 4456 0315961 3

REPORTS PREVIOUSLY ISSUED

ORNL/TM-9325	Period March 1983-September 1983
ORNL/TM-9466	Period October 1983-March 1984
ORNL/TM-9497	Period April 1984-September 1984
ORNL/TM-9673	Period October 1984-March 1985
ORNL/IM-9947	Period April 1985-September 1985
ORNL/TM-10079	Period October 1985-March 1986
ORNL/TM-10308	Period April 1986-September 1986
ORNL/TM-10469	Period October 1986-March 1987
ORNL/TM-10705	Period April 1987-September 1987
ORNL/TM-10838	Period October 1987-March 1988
ORNL/TM-11116	Period April 1988-September 1988
ORNL/TM-11239	Period October 1988-March 1989

Research sponsored by the U.S. Department of Energy, Assistant Secretary for Conservation and Renewable Energy, Office of Transportation Technologies, as part of the Ceramic Technology for Advanced Heat Engines Project of the Advanced Materials Development Program, under contract DE-AC05-840R21400 with Martin Marietta Energy Systems, Inc.

SUMMARY 1

0.0 PROJECT MANAGEMENT AND COORDINATION 3

1.0 MATERIALS AND PROCESSING 5

INTRODUCTION 5

1.1 MONOLITHICS 7

1.1.1 *Turbomilling of SiC Whiskers* (Southern Illinois University) 7

Reinforcements for High Temperature Ceramics (Keramont) 16

1.1.2 Silicon Nitride 26

Sintering of Silicon Nitride (AMTL) 26

Synthesis of High Purity Sinterable Si_3N_4 Powders (Ford) 32

Microwave Processing of Silicon Nitride (ORNL) 41

Silicon Nitride Milling Characterization (NIST) 49

1.1.4 Processing of Monolithics 52

Improved Processing (ORNL) 52

Improved Processing (Norton) 55

1.2 CERAMIC COMPOSITES 74

1.2.2 Silicon Nitride Matrix 74

SiC-Whisker-Toughened Silicon Nitride (Garrett) 74

Silicon Nitride-Metal Carbide Composites (GTE) 93

Development of Toughened Si_3N_4 Composites by Glass Encapsulated Hot Isotatic Pressure (Norton) 109

Fabrication of Si_3N_4/SiC Composites by Transient Liquid Phase Sintering (U. Michigan) 125

1.2.3 Oxide Matrix 136

Dispersion-Toughened Oxide Composites (ORNL) 136

Processing of Improved Transformation-Toughened Ceramics (Norton) 142

Processing and Characterization of Transformation-Toughened Ceramics with Strength Retention to Elevated Temperatures (Ceramatec) 160

1.2.4 Silicate Matrix 172

Low Expansion Ceramics for Diesel Engine Applications (VPI) 172

1.3 THERMAL AND WEAR COATINGS 196

1.3.1 ZrO_2 Base Coatings 196

Development of Adherent Ceramic Coatings to Reduce Contact Stress Damage of Ceramics (GTE) 196

Wear-Resistant Coatings (Caterpillar) 202

Development of Wear Resistant Ceramic Coatings for Diesel Engine Components (Cummins) 207

1.4 JOINING 227

1.4.1 Ceramic-Metal Joints 227

Joining of Ceramics for Heat Engine Applications (ORNL) 227

Analytical and Experimental Evaluation of Joining Silicon Nitride to Metal and Silicon Carbide to Metal for Advanced Heat Engine Applications (GTE) 232

Analytical and Experimental Evaluation of Joining Ceramic Oxides to Ceramic Oxides and Ceramic Oxides to Metal for Advanced Heat Engine Applications (BCL) 248

Analytical and Experimental Evaluation of Joining Silicon Carbide to Silicon Carbide and Silicon Nitride to Silicon Nitride for Advanced Heat Engine Applications (Norton) 268

2.0 MATERIALS DESIGN METHODOLOGY 275

INTRODUCTION 275

2.1 MODELING 277

2.1.1 Modeling 277

Microstructural Modeling of Cracks (UT) 277

2.2 CONTACT INTERFACES 279

2.2.1 Static Interfaces 279

Elastic Properties and Adherence of Thin Films and Coatings (UT) 279

2.2.2 Dynamic Interfaces 281

Studies of Dynamic Contact of Ceramics and Alloys for Advanced Heat Engines (Battelle) 281

2.3 NEW CONCEPTS 290

Advanced Statistical Concepts of Fracture in Brittle Materials (GE) 290

3.0 DATA BASE AND LIFE PREDICTION 301

INTRODUCTION 301

3.1 STRUCTURAL QUALIFICATION 303

Microstructural Analysis of Structural Ceramics (NIST) 303

Physical Properties of Structural Ceramics (ORNL) 306

Project Data Base (ORNL) 308

3.2 TIME-DEPENDENT BEHAVIOR 311

Characterization of Transformation-Toughened Ceramics (AMTL) 311

Fracture Behavior of Toughened Ceramics (ORNL) 319

Cyclic Fatigue of Toughened Ceramics (ORNL) 327

Rotor Data Base Generation (ORNL) 342

Toughened Ceramics Life Prediction (NASA-Lewis Research Center) 354

Life Prediction Methodology (Allison) 362

Life Prediction Methodology (GAPD) 370

3.3 ENVIRONMENTAL EFFECTS 379

Environmental Effects in Toughened Ceramics (U. Dayton) 379

Low Heat Rejection Diesel Coupon Tests (ORNL) 423

3.4 FRACTURE MECHANICS 433

Testing and Evaluation of Advanced Ceramics at High Temperature in Uniaxial Tension (North Carolina A&T State University) 433

Standard Tensile Test Development (NIST) 440

Fracture Toughness of Thin Coatings (Vanderbilt) 448

Effects of Impurities on the Adhesion of Thin Metallic Films to Ceramic Substrates (Vanderbilt) 450

3.5 NONDESTRUCTIVE EVALUATION DEVELOPMENT 453

Nondestructive Characterization (ORNL) 453

NDE Standards for Advanced Ceramics (ORNL) 459

Computed Tomography (ANL) 460

Nuclear Magnetic Resonance Imaging (ANL) 466

Powder Characterization (ORNL) 471

Power Characterization (Rutgers) 476

4.0 TECHNOLOGY TRANSFER 485

4.1 TECHNOLOGY TRANSFER 485

4.1.1 *Technology Transfer* (ORNL) 485

IEA Annex II Management (ORNL) 486

Standard Reference Materials (NIST) 490

CERAMIC TECHNOLOGY FOR ADVANCED HEAT ENGINES PROJECT SEMIANNUAL PROGRESS REPORT FOR APRIL 1989 THROUGH SEPTEMBER 1989

SUMMARY

The Ceramic Technology For Advanced Heat Engines Project was developed by the Department of Energy's Office of Transportation Systems (OTS) in Conservation and Renewable Energy. This project, part of the OTS's Advanced Materials Development Program, was developed to meet the ceramic technology requirements of the OTS's automotive technology programs.

Significant accomplishments in fabricating ceramic components for the Department of Energy (DOE), National Aeronautics and Space Administration (NASA), and Department of Defense (DoD) advanced heat engine programs have provided evidence that the operation of ceramic parts in high-temperature engine environments is feasible. However, these programs have also demonstrated that additional research is needed in materials and processing development, design methodology, and data base and life prediction before industry will have a sufficient technology base from which to produce reliable cost-effective ceramic engine components commercially.

An assessment of needs was completed, and a five year project plan was developed with extensive input from private industry. The objective of the project is to develop the industrial technology base required for reliable ceramics for application in advanced automotive heat engines. The project approach includes determining the mechanisms controlling reliability, improving processes for fabricating existing ceramics, developing new materials with increased reliability, and testing these materials in simulated engine environments to confirm reliability. Although this is a generic materials project, the focus is on structural ceramics for advanced gas turbine and diesel engines, ceramic bearings and attachments, and ceramic coatings for thermal barrier and wear applications in these engines. This advanced materials technology is being developed in parallel and close coordination with the ongoing DOE and industry proof-of-concept engine development programs. To facilitate the rapid transfer of this technology to U.S. industry, the major portion of the work is being done in the ceramic industry, with technological support from government laboratories, other industrial laboratories, and universities.

This project is managed by ORNL for the Office of Transportation Technologies, Office of Transportation Materials, and is closely coordinated with complementary ceramics tasks funded by other DOE offices, NASA, DoD, and industry. A joint DOE and NASA technical plan has been established, with DOE focus on automotive applications and NASA focus on aerospace applications. A common work breakdown structure (WBS) was developed to facilitate coordination. The work described in this report is organized according to the following WBS project elements:

0.0 Management and Coordination

1.0 Materials and Processing

- 1.1 Monolithics
- 1.2 Ceramic Composites
- 1.3 Thermal and Wear Coatings
- 1.4 Joining

2.1 Materials Design Methodology

- 2.1 Modeling
- 2.2 Contact Interfaces
- 2.3 New Concepts

3.0 Data Base and Life Prediction

- 3.1 Structural Qualification
- 3.2 Time-Dependent Behavior
- 3.3 Environmental Effects
- 3.4 Fracture Mechanics
- 3.5 NDE Development

4.0 Technology Transfer

This report includes contributions from all currently active project participants. The contributions are arranged according to the work breakdown structure outline.

0.0 PROJECT MANAGEMENT AND COORDINATION

D. R. Johnson
Oak Ridge National Laboratory

Objective/scope

This task includes the technical management of the project in accordance with the project plans and management plan approved by the Department of Energy (DOE) Oak Ridge Operations Office (ORO) and the Office of Transportation Technologies. This task includes preparation of annual field task proposals, initiation and management of subcontracts and interagency agreements, and management of ORNL technical tasks. Monthly management reports and bimonthly reports are provided to DOE; highlights and semiannual technical reports are provided to DOE and program participants. In addition. the program is coordinated with interfacing programs sponsored by other DOE offices and federal agencies, including the National Aeronautics and Space Administration (NASA) and the Department of Defense (DoD). This coordination is accomplished by participation in bimonthly DOE and NASA joint management meetings, annual interagency heat engine ceramics coordination meetings, DOE contractor coordination meetings, and DOE Energy Materials Coordinating Committee (EMaCC) meetings, as well as special coordination meetings.

1.0 MATERIALS AND PROCESSING

INTRODUCTION

This portion of the project is identified as project element 1.0 within the work breakdown structure (WBS). It contains four subelements: (1) Monolithics, (2) Ceramic Composites, (3) Thermal and Wear Coatings, and (4) Joining. Ceramic research conducted within the Monolithics subelement currently includes work activities on green state ceramic fabrication, characterization, and densification and on structural, mechanical, and physical properties of these ceramics. Research conducted within the Ceramic Composites subelement currently includes silicon carbide and oxide-based composites, which, in addition to the work activities cited for Monolithics, include fiber synthesis and characterization. Research conducted in the Thermal and Wear Coatings subelement is currently limited to oxide-base coatings and involves coating synthesis, characterization, and determination of the mechanical and physical properties of the coatings. Research conducted in the Joining subelement currently includes studies of processes to produce strong stable joints between zirconia ceramics and iron-base alloys.

A major objective of the research in the Materials and Processing project element is to systematically advance the understanding of the relationships between ceramic raw materials such as powders and reactant gases, the processing variables involved in producing the ceramic materials, and the resultant microstructures and physical and mechanical properties of the ceramic materials. Success in meeting this objective will provide U.S. companies with new or improved ways for producing economical, highly reliable ceramic components for advanced heat engines.

1.1 MONOLITHICS

1.1.1 Silicon Carbide

Turbomilling of SiC Whiskers and SiC Whisker-Ceramic Composites--
D. E. Wittmer (Associate Professor, Southern Illinois University at Carbondale, Carbondale, IL 62901)

Objective/Scope

The purpose of this work is to continue the investigation of the turbomilling process as a means of improved processing for SiC whisker-ceramic matrix composites and dispersion of matrix powders prior to composite processing.

Technical Progress

During this reporting period, contract negotiations for the initiation of Phase II of this contract were completed. Phase II is divided into 4 major tasks:

Task 1. Beneficiation of SiC whiskers.
Task 2. Development of aspect ratio reduction parameters.
Task 3. Improved dispersion of particulate matrices.
Task 4. Final Report

The turbomilling parameters investigated for Task 1 and 2 were:

MILLING MEDIA
--200 g of 3 mm Plastic (4200 beads)
--200 g of 3 mm PSZ (316 beads)

MILLING TIME
--120 min for Plastic Media
--60 min for PSZ Media
--Samples Pulled Every 15 min

MILLING SPEED--800 r.p.m. or 1200 r.p.m.

WHISKER LOADING LEVEL--200 g or 300 g

1 liter Distilled, Deionized Water

Task 1. Beneficiation of SiC Whiskers

During this phase of the project, American Matrix, Inc. (AMI) SiC whiskers (SiC_w) were processed in the turbomill to develop improved beneficiation techniques. In this task the influence of the density of the milling media on the beneficiation process and fracture behavior of the whiskers was studied. PSZ beads were used for high density media and nylon beads were used for the low density media.

Several small batches of AMI SiC_w were processed by turbomilling with the solids loading, fraction of milling media and turbomilling speed determined through the use of an experimental design matrix. Sedimentation techniques were then utilized to separate the fine whiskers from large whisker fragments and impurities and remove the soluble impurities.

The as-received SiC whiskers are presently being analyzed for free carbon, free Si, presence of unreacted silica, and chemical composition by standard analytical techniques to produce a baseline chemical composition. Selected products from the sedimentation process are also being analyzed, ie. the supernatant liquid for dissolved and ultra-fine saturated impurities, the resultant coarse whisker fraction and fine fraction chemical composition, surface area and particle sizes for coarse and fine fractions, and morphology. A portion of the beneficiated SiC_w will then be heat treated in vacuum or other appropriate atmosphere for comparison with the untreated virgin whiskers, and the untreated beneficiated whiskers. The information and products of this task will also be utilized in the development of future tasks.

Milling with either plastic media or PSZ media appears to solubilize Ca, Mg, Na, and K from the SiCW. The results of ICAP analyses are given in Table 1.

Table 1. Analyses of Supernatant From Turbomilled AMI SiC_W for 200 g. SiC_w and 1200 r.p.m.

Sample I.D.	Ca (ppm)	Mg (ppm)	Na (ppm)	K (ppm)
Deionized H_2O	< .01	< .01	< .01	.81
Plastic Media 60 min.	40.39	5.62	3.01	2.17
Plastic Media 120 min.	34.52	6.11	3.00	2.44
PSZ Media 60 min.	20.53	2.56	1.89	1.22

Task 2. Development of Aspect Ratio Reduction Parameters.

The SiC aspect ratio will be determined as a function of turbomilling parameters from the information generated during Task 1. During this task a model will be developed, based on the mathematical relationship between average surface area, average particle size and measured whisker diameters, to determine the average aspect ratio for the SiC_w products produced in Task 1. This calculated data will

then be compared to the aspect ratio as viewed by SEM and optical methods.

For AMI SiC_w the average diameter is approximately 1 um, therefore a close approximation of the aspect ratio can made from examination of the SiC_w lengths. SEM photomicrographs were prepared by dispersion of the SiC_w products of Task 1 in acetone, followed by evaporation of the SiC_w/acetone slurries on a warm Al SEM stub. Low magnification (50 and 100X) photomicrographs were then taken for each of the turbomilled products. Each individual whisker and particle was then measured. If the length was less than 4 um, then it was considered to be a particle. The whisker lengths (L) were then tabulated and grouped according to the ranges L<4 um, 4 um<L<8 um, 8 um<L<16 um and L>16 um. The summary of these results are shown in Figs. 1 through 4.

Figure 1 shows the comparison of SiC_w volume fraction for PSZ vs. plastic turbomilling media for 200 g batches of SiC_w turbomilled at 800 r.p.m. for 60 min. The PSZ media was much more effective in reducing the SiC_w aspect ratio into the 4 to 16 um size range than the plastic media. At 1200 r.p.m. (Fig. 2), keeping the other parameters the same, neither milling media appears to be that effective in reducing the aspect ratio for a major volume fraction of the SiC_w.

Figure 3 shows the comparison of the volume fraction of SiC_w produced as a function of milling speed, using the plastic media to turbomill 200 g batches of SiC_w for 120 min. These results demonstrate that turbomilling at 800 r.p.m. is somewhat more effective in reducing the SiC_w aspect ratio. For the PSZ media (Fig. 4), turbomilling at 800 r.p.m. for 60 min was much more effective than 1200 r.p.m. for 60 min in increasing the volume fraction of SiC_w between 4 and 16 um.

The conclusions that can be drawn from these results are:

1. The plastic media was effective in reducing the SiC_w aspect ratio without significantly increasing the volume of fine particulate.

2. The PSZ media, as expected, was more effective in reducing the aspect ratio even though the number of point-to-point contacts was significantly less than for the plastic media.

3. A turbomilling speed of 800 r.p.m. appears to be much more effective than 1200 r.p.m. in reducing the aspect ratio of the SiC_w for both plastic and PSZ milling media.

Work is continuing to determine the effects of turbomilling on the SiC_w aspect ratio during turbomilling and processing of whiskers/ceramic matrix composites. Whiskers developed as products of Task 1 will be dispersed in the matrix material selected by the Company. The whisker volume loading will be varied from 15 vol.% to 35 vol.% for the matrix material(s) to be specified later by the company. It is anticipated that silicon nitride will be one of the specified matrix materials. During turbomilling processing, samples will be pulled by syphon at selected time intervals and measured for particle size distribution, surface area and aspect ratio. The whisker aspect ratios will also be determined following consolidation of the composites. The results shall be monitored by density and fracture results for hot-pressed and/or HIPed and/or sintered samples.

Task 3. Improved Dispersion of Particulate Matrices.

In conjunction with Task 2, Task 3 will investigate the dispersion of the matrix material(s) specified by the Company by the turbomilling process, prior to the introduction of the SiC_w to the matrix. Slurry pH, solids loading, coarse:fine ratio, type and amount of dispersant and other turbomilling parameters will be adjusted and monitored to develop optimized conditions for dispersing the selected matrix material(s). Once these conditions have been identified, SiC_w from Task 1 at whisker loadings from 15 vol.% to 35 vol.% will be added, following the dispersion step. During this step it will be necessary to develop techniques to uniformly flocculate the resultant whisker/particulate dispersion to avoid separation upon mill discharge. The slurries produced in this task will then be vacuum assisted, pressure cast into disks for the preparation of test samples. Isopressing of the dry preforms may be required to enable densification. The results shall again be monitored by density and fracture results for hot-pressed and/or HIPed and/or sintered samples.

Status of Milestones

Phase II:

Task 1.	Beneficiation of SiC whiskers	Oct. '89 (Completed)
Task 2.	Development of aspect ratio reduction parameters.	Jan. '90
Task 3.	Improved dispersion of matrices	Aug. '90
Task 4.	Final Report	Sept.'90

Presentations and Publications

D. E. Wittmer and W. Trimble, "Aspect Ratio Reduction and Beneficiation of SiC Whiskers for Reinforcement of Ceramic Matrix Composites," The 91st Annual American Ceramic Society Meeting, Indianapolis, IN, April 23-27, 1989.

FIGURE 1

COMPARISON OF SiCw VOLUME FRACTION FOR PSZ VS. PLASTIC TURBOMILLING MEDIA

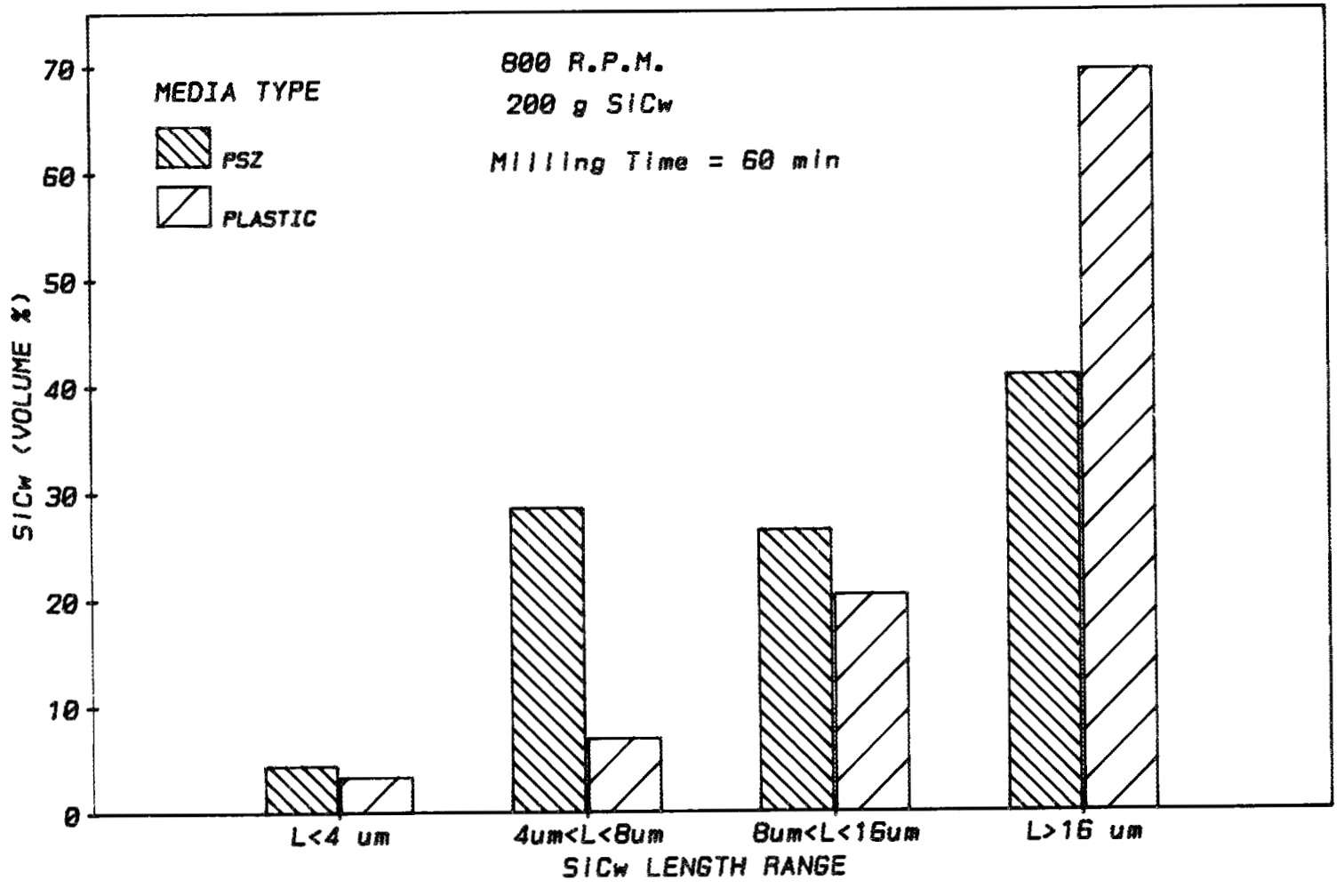

FIGURE 2

COMPARISON OF SiCw VOLUME FRACTION FOR PSZ VS. PLASTIC TURBOMILLING MEDIA

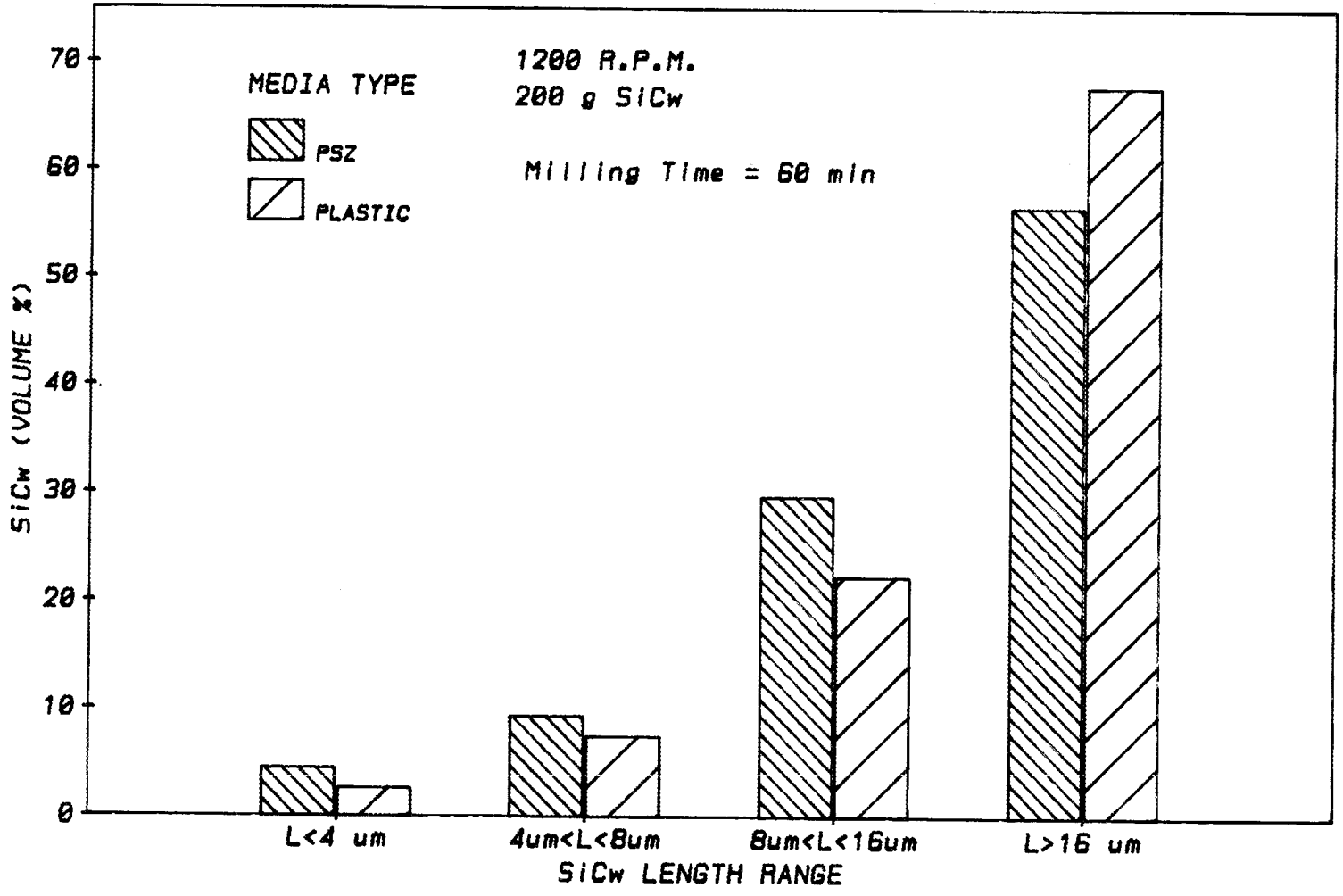

FIGURE 3

COMPARISON OF SiCw VOLUME FRACTION VS. TURBOMILLING SPEED USING PLASTIC MEDIA

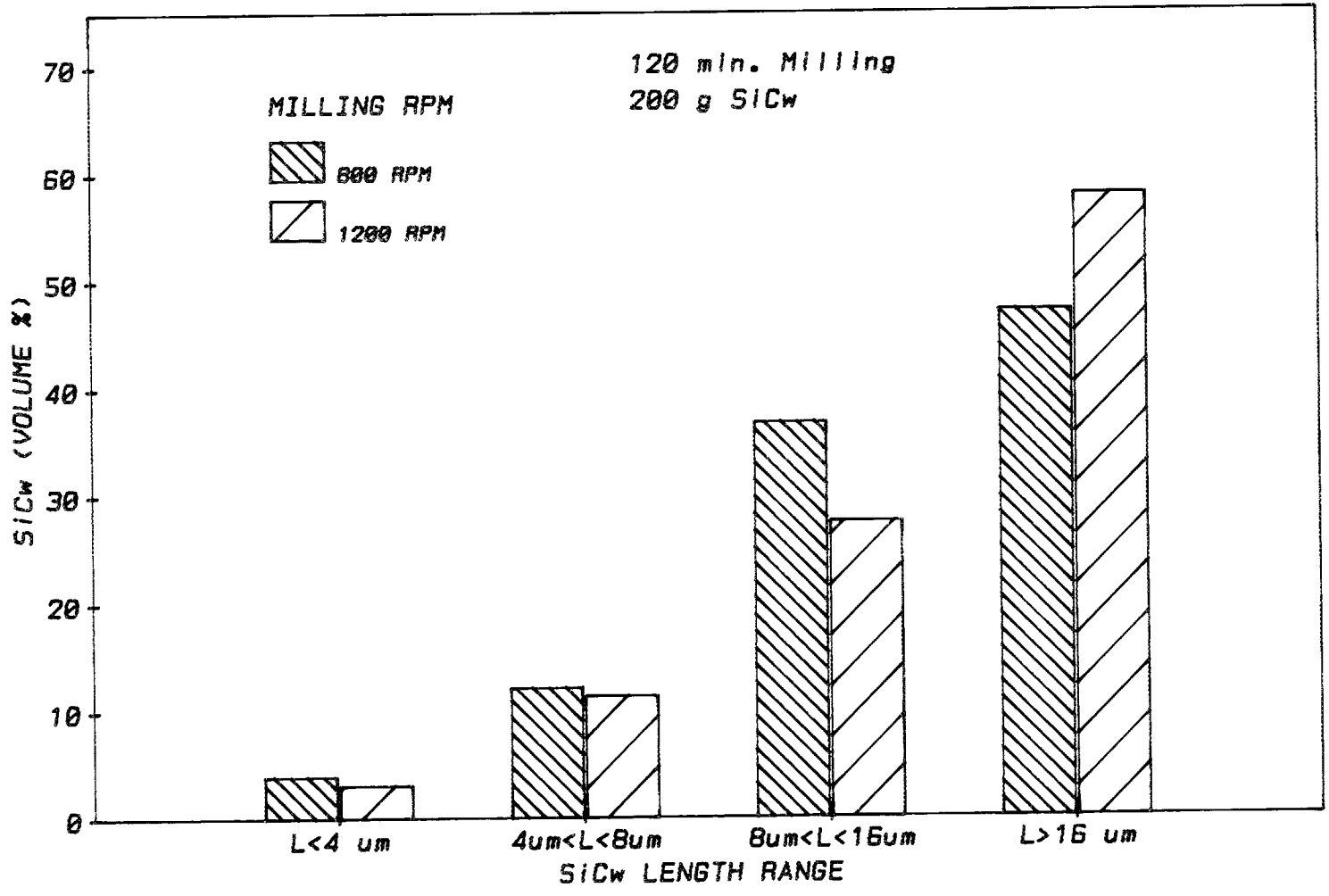

FIGURE 4

COMPARISON OF SiCw VOLUME FRACTION VS. TURBOMILLING SPEED USING PSZ MEDIA

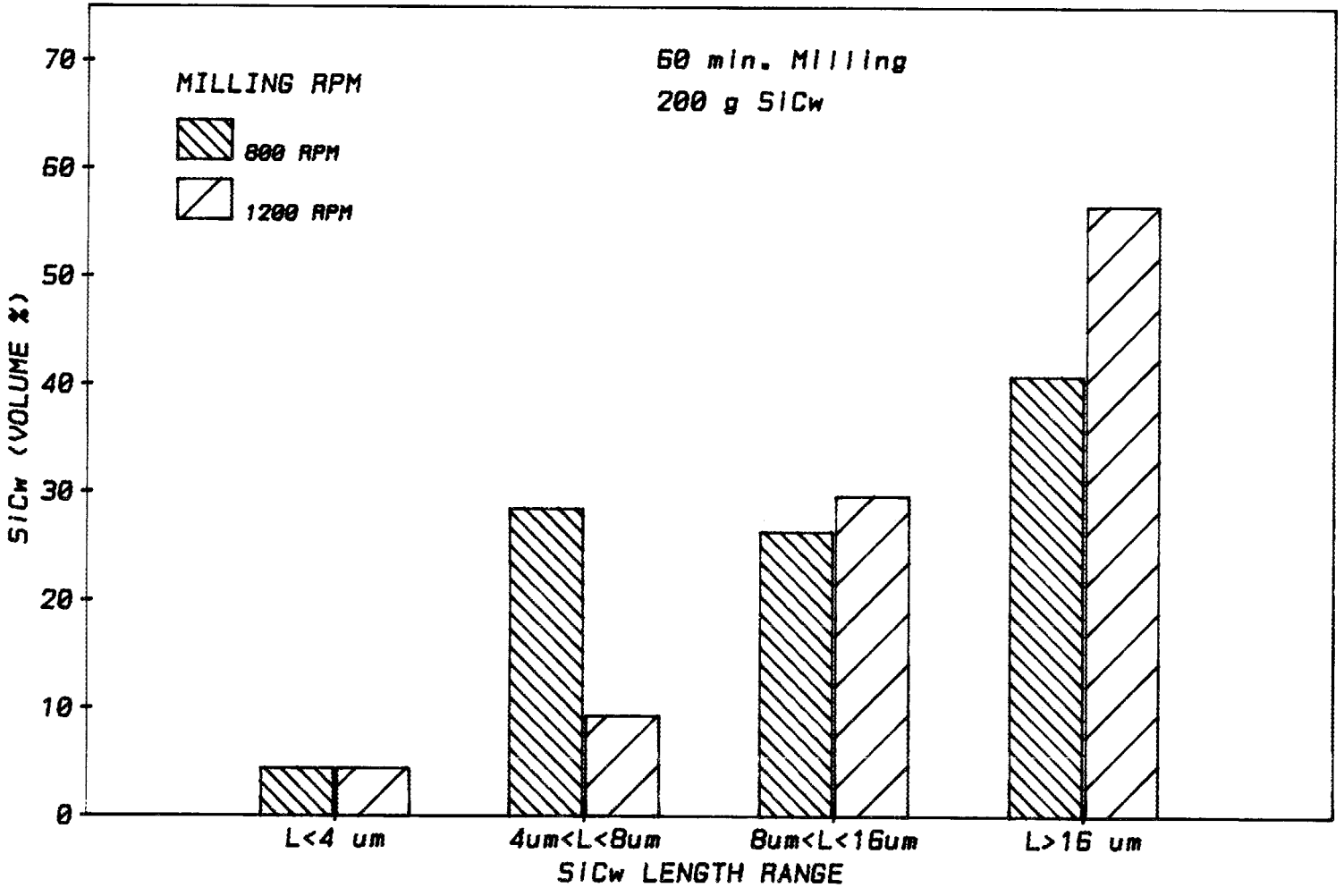

Reinforcements for High Temperature Ceramics - Christos I. Kyriacou, Juan L. Sepulveda, Mary A. Watson (Keramont Corporation)

Objective/scope

The production of TiB_2 whiskers; consolidation of composites of SiC matrix with TiB_2 whiskers, and testing of composites properties in air above 1200°C.

Technical progress

The growth and development of TiB_2 whiskers by the CVD-VLS mechanism has been investigated by the reaction:

$$TiCl_4(g) + 2BBr_3(g) + 5H_2(g) \xrightarrow[\text{catalyst}]{\sim 1150°C} TiB_2(w) + 6HBr(g) + 4HCl(g)$$

The reaction is carried out in a quartz tube 3 inches in diameter and 30 inches long. The precursor raw material of $TiCl_4$ and BBr_3 are in liquid form and are heated to a certain temperature to generate vapors which are transported to the reaction furnace by preheated helium gas. The catalyst is sprinkled on grafoil substrate and reacts with the gas to form TiB_2 whiskers. The overall experimental apparatus is shown in Figure 1.

I. Basic research

The research on the contract during the period of April to September of 1989, has focused on the development of a basic technology for the growth of TiB_2 whiskers. The parameters investigated were as follows:

i) Catalyst Type
ii) Substrate Type
iii) Reaction Temperature
iv) Gas Composition

The research performed for each parameter and the experimental results are discussed in the sections below. A summary of the results is also shown in Table 1.

i) Catalyst Type

A catalyst was identified based on thermodynamics and phase diagrams. The VLS growth of whiskers becomes possible by the presence of a catalyst. A TGA/DTA of the catalyst showed a melting point of about 950°C. At this temperature the catalyst melts and becomes a preferred site for the

deposition of TiB_2. TiB_2 then diffuses through the catalyst melt to the growing single crystal. The catalyst was found to be easily oxidized by exposure to air at temperatures above 400°C as was found by TGA.

The corrosion of the catalyst was found to be the most difficult problem in growing the TiB_2 whiskers. Accurate control of the gas composition and the reaction temperature were found to be necessary to minimize the corrosion of the catalyst.

The catalyst was found to result in the efficient growth of TiB_2 whiskers by the VLS mechanism. This was confirmed by the presence of catalyst spheres at the tip of the whiskers. SEM and EDAX analysis of the catalyst balls found a direct relation between the catalyst composition after growth and the diameter of the whiskers.

ii) Substrate Type

Three groups of substrates were tested for their effect on TiB_2 whiskers growth. The first group, consisted of oxide ceramics such as Al_2O_3 and SiO_2 and gave negative results. The second group consisted of metal substrates such as Fe, Ni and Ti. This group also gave negative results due to corrosion in the furnace environment. The third group consisted of covalent ceramics such as AlN and graphite. These gave positive results mainly due to their compatibility with the furnace environment, and their lack of reactivity with the catalyst.

iii) Reaction Temperature

The reaction temperature was varied from about 950°C which is the melting point of the catalyst, to 1200°C. The lower temperature range of <1000°C resulted in the formation of by-products associate with the corrosion of the catalyst. At temperatures between 1000 - 1100°C conical shape whiskers submicron in diameter, 10-20 micron long, were produced along with nodular structure coatings. The conical shape of the whiskers is believed to result by a simultaneous growth of the whiskers and corrosion of the catalyst. An SEM micrograph of the whiskers is shown in Figure 2.

At temperatures of 1100 - 1200°C cylindrical shape whiskers were grown with a diameter range of 1 - 5 microns and a length of 50 - 100 microns. These whiskers have a smooth surface morphology. SEM micrographs of this product are shown in Figure 3. A catalyst droplet appears to exist on the tip of the whiskers indicating the VLS growth mechanism. The fact that the corrosion of the catalyst is avoided results in higher growth density of the whiskers.

iv) Gas Composition

The composition of hydrogen was found to have a strong effect on the growth and morphology of the TiB_2 whiskers. At gas composition of $TiCl_4:BBr_3:H_2$ = 1:2:10 conical shape whiskers were produced. At gas composition of $TiCl_4:BBr_3:H_2$ = 1:2: $\geq$ 50 cylindrical shape whiskers were produced.

II. Process development

The basic conditions necessary for the growth of TiB_2 whiskers are shown in Table 2. These conditions were used to study other process parameters for the production of large quantities of whiskers. The parameters tested were:

i) Surface area
ii) Gas Flow Rate and Concentration
iii) Catalyst Concentration

The effect of each of these parameters is discussed below.

i) Surface Area

The surface area for the growth of the whiskers was increased by means of flexible Grafoil. The Grafoil was shaped in the form of a hollow tube inserted inside the quartz tube. However, not all the available area becomes effective in growing whiskers. The growth is higher on the area closer to the gas input ports and decreases sharply thereafter.

ii) Gas Flow Rate and Concentration

The total gas flow rate was increased by increasing the flow rate of the precursor saturation gas (He) and hydrogen to a total of 2.5 LPM. This resulted in increasing the effective area of growth further away from the input ports. The concentration of $TiCl_4$ and BBr_3 in the input gas stream was increased by increasing the saturation temperature of the precursor liquids.

iii) Catalyst Concentration

The amount of catalyst used to grow TiB_2 whiskers was varied from a monolayer of about 0.02 g/in^2 to about 0.2g/in^2. Catalyst concentration above 0.05 g/in^2 did not result in any increase in the growth density of the whiskers since growth primarily occurs on the surface of the catalyst layer. The growth of the whiskers on the surface only, resulted in limited whisker yield.

III. Characterization

The products and by-products of the reaction were characterized by SEM, EDAX, and XRD. Using SEM the morphology and size distribution of the whiskers were determined. By means of EDAX the composition of the catalyst balls and metallic impurities on the surface of the whiskers were detected. As produced whiskers on the grafoil surface were examined by X-ray diffraction. An XRD spectrum of the whiskers is shown in Figure 4, and is compared to a standard file for TiB_2 from JCPDS. Samples from our whiskers were sent to ORNL and to the Army Materials Technology Laboratory for analysis by TEM.

IV. Conclusions

Keramont has demonstrated a basic technology to produce TiB_2 whiskers by the VLS mechanism by means of a less expensive catalyst. The whiskers were observed to grow mostly on the surface of the catalyst layer and limited the production yield with the present installation available. It has been concluded that a new system for precursor gas mixing and distribution in the bulk volume of the catalyst layer will be necessary. A new furnace design with increased growth capacity would be necessary to grow large amounts of whiskers.

Status of milestones

Samples of TiB_2 whisker product have been delivered to ORNL and the Army Materials Technology Laboratory. A 5.0g sample of TiB_2 whiskers will be delivered to ORNL in the first week of November.

Composites of α-SiC/TiB_2 whiskers will be delayed to produce due to insufficient quantities of whiskers produced.

Publications

Our work on this contract has been presented at the annual DOE Automotive Technology Development Contractors' Coordination Meeting, October 23-26, 1989, Dearborn, Michigan.

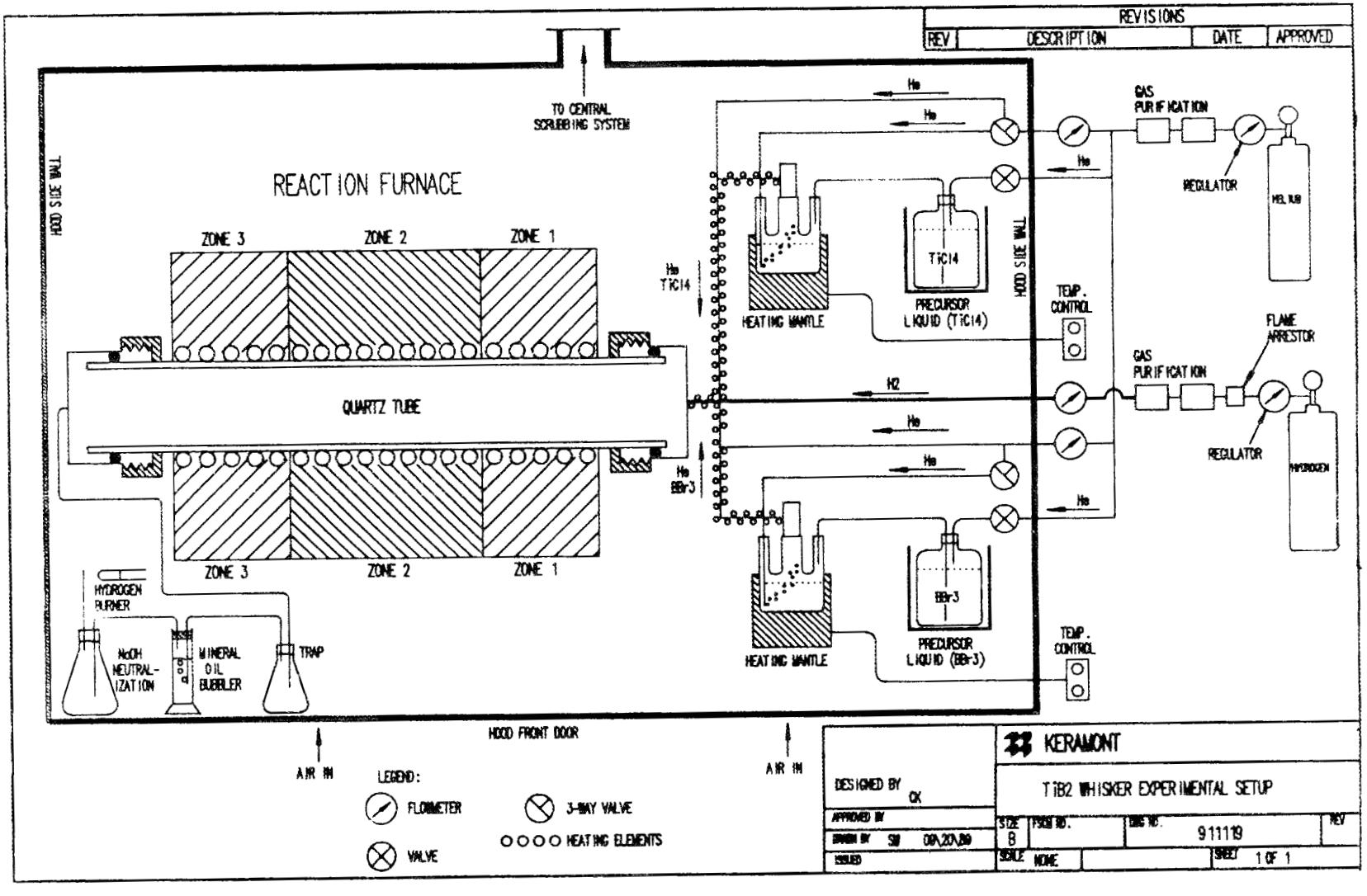

Figure 1. The experimental set-up for the growth of TiB_2 whiskers.

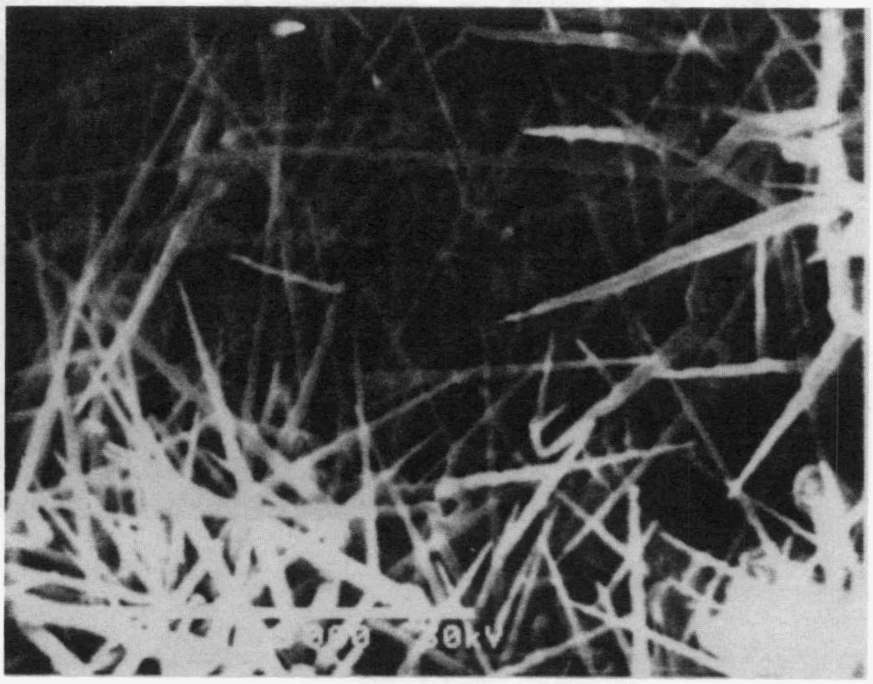

Figure 2. SEM Micrograph of conical shape VLS TiB_2 whiskers. Growth temperature 1000°C.

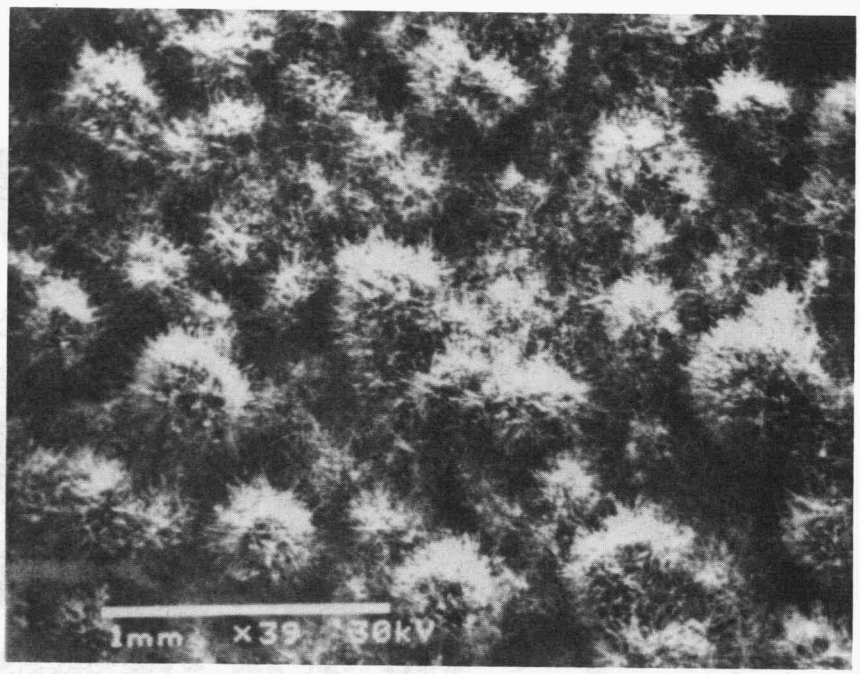

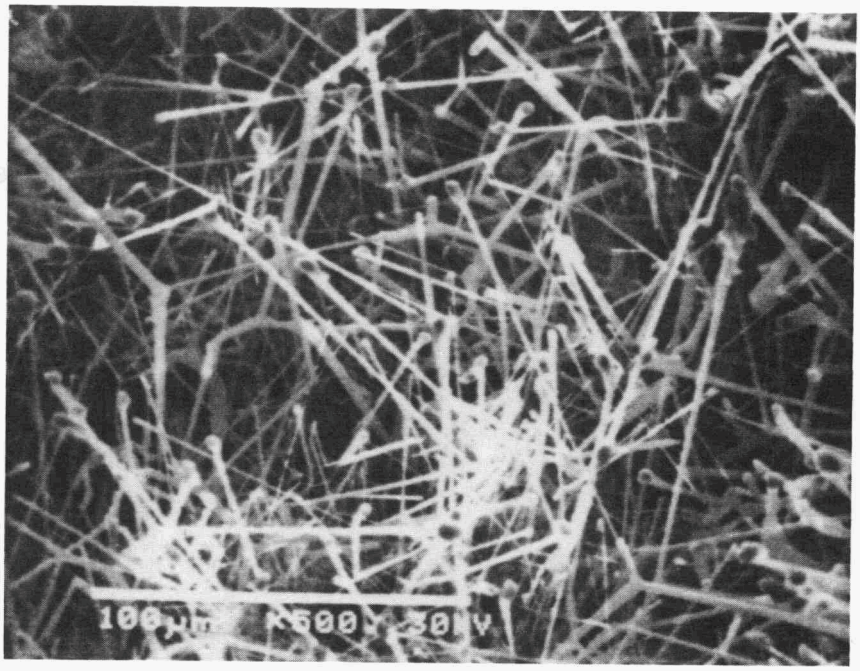

Figure 3. SEM Micrographs of VLS TiB_2 whiskers. Growth temperature 1150°C.

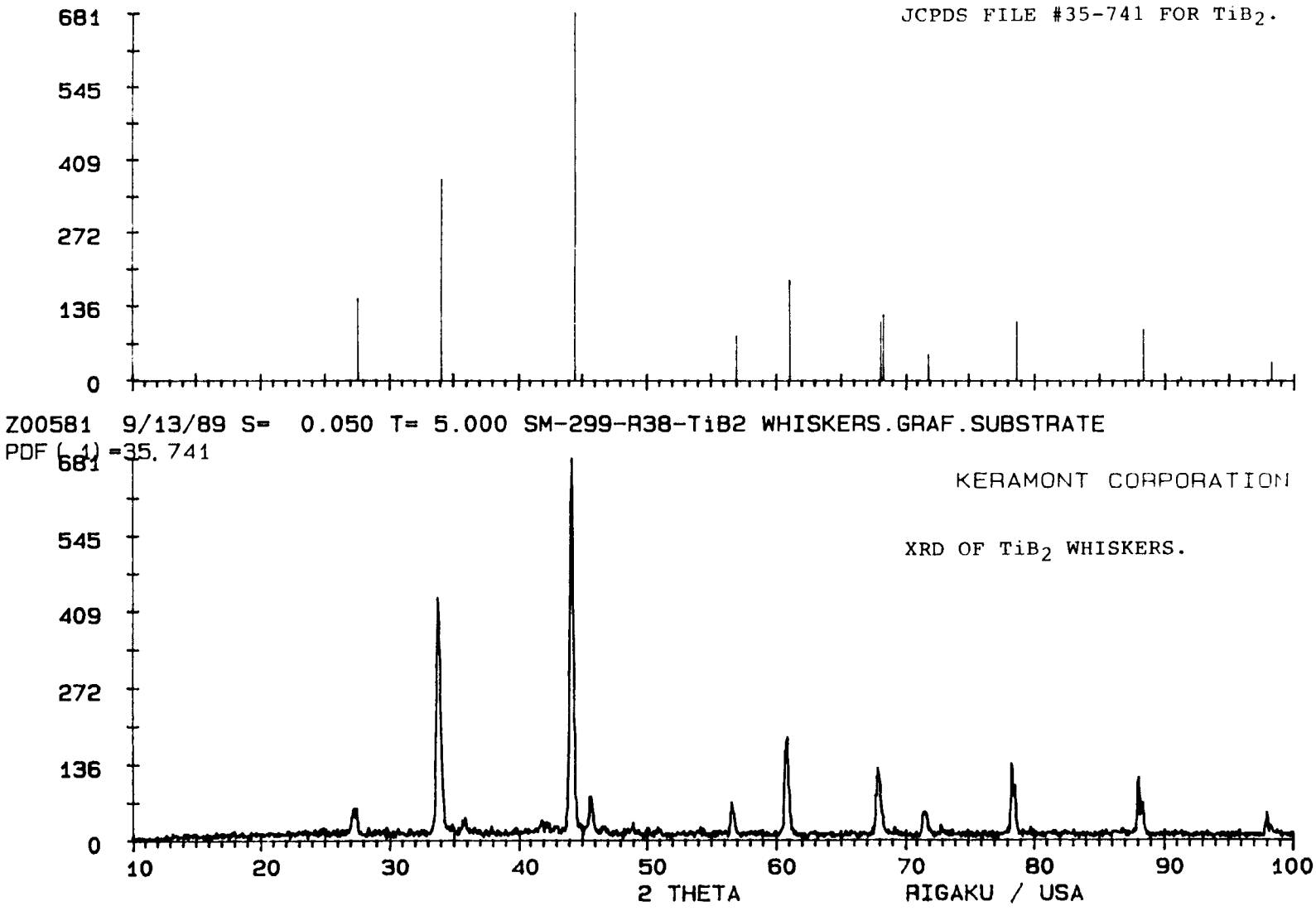

Figure 4. XRD for TiB_2 whiskers and reference JCPDS File #35-741.

Table 1. Summary of Experimental Results from Whisker Growth Development.

Catalyst

Eutectic Composition at ~950°C.
Catalyst Ball at Tip of Whiskers.
Very Efficient But Easily Corroded.

Substrates

Oxides (Al_2O_3, SiO_2): Negative
Metals: Negative (corrosion)
Covalent Ceramics (AlN, Grafoil): Positive

Temperature

<1000°C: No Whiskers, By-products.

<1100°C: Conical Shape Whiskers, Submicron Diameter 10-20 Microns Long, Rough Surface.

<1150°C: Cylindrical Whiskers, ~3 micron diameter 10-100 microns long, smooth surface.

Gas Composition

Low H_2 Concentration:	Catalyst corrosion, conical shape whiskers, low growth density.
High H_2 Concentration:	No catalyst corrosion, cylindrical shape whiskers, high growth density.
Precursor Gas Composition:	$TiCl_4/BBr_3$ - $1/\leq 2$

PRESENCE OF OXYGEN HINDERS WHISKER GROWTH

Table 2. Standard Conditions for Growth of TiB_2 Whiskers.

Temperature:	1150°C
Substrate:	Grafoil
Catalyst Concentration:	0.05 g/in^2
Gas Composition:	$TiCl_4$:BBr_3:H_2 = 1:2:50
Gas Flow Rate:	2.0 LPM
Reaction Time:	2 hrs

1.1.2 Silicon Nitride

Sintering of Silicon Nitride
G. W. Gazza (U. S. Army Materials Technology Laboratory)

Objective/Scope:

The program is concentrating on sintering compositions in the Si_3N_4-Y_2O_3-SiO_2 system using a two-step sintering method where the nitrogen gas pressure is raised to 7–8 MPa during the second step of the process. During the sintering, dissociation reactions are suppressed by the use of high nitrogen pressure and cover powder of suitable composition over the specimen. Variables in the program include the sintering process parameters, source of starting powders, milling media and time, and specimen composition. Resultant properties determined are room temperature modulus of rupture, high temperature stress-rupture, oxidation resistance, and fracture toughness. Successful densification of selected compositions with suitable properties will lead to densification of injected molded or slip cast components for engine testing.

Technical Progress

In order to produce the complex shapes required for engine testing of ceramic components, slip casting processes are being explored for selected compositions. A composition focused on at this point in the program for extensive evaluation is 85.8m/o Si_3N_4–4.73m/o Y_20_3–-9.47m/o SiO_2, designated as composition number 39. It was found previously that sintering could be promoted for the same compositions of interest if 1.0m/o of Mo_2C was added to the starting composition. Also, the Mo_2C particles were fine enough and well distributed, their presence as reacted MoxSiy particles in the body would not serve as fracture origins under fast fracture conditions at as found for coarser Fe-base impurity inclusions (1). The particles appear to be well distributed in the microstructure and analytical microscopy performed at MTL and ORNL (2) did not detect the presence of Mo in the $Y_2Si_2O_7$ grain boundary phase which was determined to be comprised of inter-connecting single crystals. Stress-rupture results obtained previously in this program demonstrated that the base composition shown above with 1m/o Mo_2C, lasted 750 hours under 300 MPa flexure stress at temperatures of 1200°C and 1250°C. Examination of the specimens after stress-rupture testing revealed some permanent strain in the bars. At 1250°C, after 750 hours, permanent strain readings ranged from 0.15–0.25%. STEM micrographs taken at ORNL (2) showed some cavitation in stress-rupture specimens at triple points and at a Mo_5Si_3 particle. In addition to grain boundary sliding at the grain/grain boundary interface, the softening and deformation of the pyrosilicate phase itself is suspected to significantly contribute to high temperature creep behavior.

Slip Casting Additive Stability:

During this period, investigation of slip casting techniques and additives continued for casting the 85.9m/o Si_3N_4–4.7m/o Y_2O_3–9.4m/o SiO_2 composition with and without 1 m/o Mo_2C additions. Several experiments were conducted to determine which slip casting additives would burn out cleanest and in which environmental condition should the burnout be performed, e.g., air, vacuum, or nitrogen. It was determined whether the additives vaporized or pyrolyzed requiring further removal of residual, typically carbon. After air firing the lignosol, however, some brownish-yellow residue remained. It is believed to be a

sulfur containing compound. Although some additives may play more than one role in the slip casting process, the additives studied were generally classified into four categories; defoamers/surfactants, binders, plasticizers, and deflocculants/dispersants. Table I identifies each additive and indicates its behavior when fired under different environmental conditions.

As observed in the Table, when fired in a nitrogen atmosphere, only the glycerol vaporized while the other additives investigated pyrolyzed to a black residue. Under vacuum, the glycerol, oleic acid, XUS 40303.00, and Triton DF-20 all vaporized while the others pyrolyzed. In air, a two cycle treatment was used. In the first step the additives were heated to 400°C for 2 hours and then examined to determine their condition. The glycerol had disappeared while the others had pyrolyzed to a black residue or for lignosol, a brownish-yellow residue. The temperature was then raised to 600°C and held for 24 hours. The residues of the oleic acid Darvan 821A, XUS 40303.00, methocel 20-214, and Triton DF-20 were oxidized away while some residue remained for the Antifoam Emulsion B, polyvinyl alcohol, and lignosol. Since the glycerol could be easily vaporized, it was mixed in a 1:1 ratio with some of the other additives to determine the behavior of the mixtures under different firing conditions. The results are shown in Table II. Under vacuum, at 600°C for 1 hour, the glycerol/Darvan 821A mixture and glycerol/polyvinyl alcohol mixtures both pyrolyzed while the glycerol/polyethylene glycol mixture vaporized. In air, the mixtures shown in Table II fired under this condition all pyrolyzed but could be oxidized away at 400°C for 60 hours.

Slip Casting

Various slurries were prepared using TOSOH TS-10*, Siconide M1152**, and a KBI*** manufactured silicon nitride powders. Although the primary powder used in this study is from TOSOH, the others were used for comparison because of their broader particle size distribution, differences in chemistry, and differences in method of manufacture. The compositions of the slurries are shown in Table III which include the particular Si_3N_4 powder used, Y_2O_3 and SiO_2 additives, and the various slip casting additives used to form the slurries. In every case except the Siconide S4 slurry, Darvan 821A was used as the dispersant. Darvan C was used in S4. The slurries were prepared by a milling and stir blending procedure to promote the uniform distribution of additives and the removal of entrapped air from the slurry. Solids loading ranged from 60–68% but most values were near 65%. Viscosity measurements were taken for each slurry in a Brookfied viscometer. In Figures 1a and 1b the slurry viscosity (Pa.s) is shown for different shear rates. Different spindles were used for data generation in Figure 1a vs 1b plots producing different shear rate levels. Thus far, only the TS2 slurry was used in both spindles. As seen in Figure 1a, the viscosities are lower for the TOSOH slurries than for the Siconde based slurries. This is not unexpected due to the much broader particle size distribution of the Siconide Si_3N_4 powder. Although each slurry has a somewhat different additive level, slurries TS1 and S3 are similar expect for the source of the Si_3N_4 powder. They are not compared directly on either 1a or 1b but can be compared indirectly from the TS2-S3 relationship in Figure 1b and the TS2-TS1 relationship in Figure 1a. The lower viscosities for S1 and S2 compared to the TS2 in Figure 1b may be due to the higher water content and lower XUS binder content of S1 and the higher Darvan content of S2. Subsequent to viscosity determinations, the remaining portion of each slurry was slip cast into a disc shape approximately 5cm in diameter × 1 cm thick. Although some cracking of the discs frequently occurred, "green" densities measured on pieces from the disc were in the 1.60–1.70 g/cc range. A series of

burnout and sintering studies are underway to determine burnout cycles and which combination of additives and concentration level will produce the densest sintered compact.

* TOSOH Corp., Tokyo, Japan
** KemaNord Ind., Stockholm, Sweden
*** Kawecki Berylco Industries, Inc., Boyertown, Pa. (not currently a Si_3N_4 supplier)

Unfortunately, progress is still being hindered by the unavailability of a 10 MPa overpressure sintering furnace requiring repair.

References

(1) Pasto, A. E., "Causes and Effects of Fe-Bearing Inclusions in Sintered Si_3N_4", Communications of the American Ceramics Society, Sept., 1984, C178–180.

(2) Allard, L., Ceramic Technolgy for Advanced Heat Engines Project Semiannual Progress Report for Oct. 1988–March 1989, pp. 19–20.

Status of Milestones

A. Evaluate slip casting methods for compositions of interest. Focus on pressure slip casting techniques. Slip cast specimens have been produced with "green" densities approximately 50% T.D. Various surfactant, dispersant, and binder additions are being evaluated.

B. Generate "green" bodies of silicon nitride with pyrosilicate grain boundary phases. Sinter specimens using high gas pressure, two-step, cladless sintering method.

C. Complete database of properties using sintered specimens from slip cast bodies. Complete microstructural examination of sintered material. Write final report. The 10 MPa gas pressure sintering furnace is unavailable and will not be ready for operation until early in 1990.

Table I. Effect of Heat Treating Environment on the Stability of Additives Used for the Slip Casting Process.

Additive	Environment		
	nitrogen	vacuum	air
glycerol	vaporized	vaporized	vapor.or oxid.
oleic acid	pyrolyzed	vaporized	pyrolyzed/oxid.
Darvan 821A	pyrolyzed	pyrolyzed	pyrolyzed/oxid.
XUS 40303.00	pyrolyzed	vaporized	pyrolyzed/oxid.
Antifoam Emulsion B	pyrolyzed	pyrolyzed	pyrolyzed
polyvinyl alcohol	pyrolyzed	pyrolyzed	pyrolyzed
methocel 20-214	pyrolyzed	pyrolyzed	pyrolyzed/oxid.
Triton DF-20	pyrolyzed	vaporized	pyrolyzed/oxid.
menhaden oil	--------	pyrolyzed	----------
lignosol	--------	pyrolyzed	pyrolyzed

(nitrogen and vacuum -- 600C/1 hr. air--400C/2 hr.;600C/24 hr.)

Table II. Effect of Heat Treating Environment on the Stability of Mixed Additives Used for the Slip Casting Process

Additive	Environment	
	vacuum	air
glycerol/Darvan C	--------	pyrolyzed/oxid.
glycerol/XUS 40303.00	--------	pyrolyzed/oxid.
glycerol/menhaden oil	--------	pyrolyzed/oxid.
glycerol/Darvan 821A	pyrolyzed	----------
glycerol/polyvinyl alc.	pyrolyzed	----------
glycerol/polyethylene glycol	vaporized	----------

(vacuum--600C/1 hr. air--400C/60 hrs.)

Table III. Slurry Compositions Using TOSOH TS-10, Siconide M1152, and KBI Silicon Nitride Powders (amounts in volume %).

	Slurry Designation							
Material	K1	TS1	TS2	S1	S2	S3	S4	S5
Si_3N_4	36.08	34.73	32.68	31.94	34.70	34.73	38.04	39.97
Y_2O_3	1.85	1.78	1.67	1.64	1.78	1.78	1.95	2.05
SiO_2	2.25	2.17	2.04	1.99	2.16	2.17	2.37	2.49
H_2O	56.75	57.44	59.92	61.72	57.38	57.44	53.33	52.45
glycerol	1.30	1.25	1.17	1.15	1.25	1.25	1.37	1.44
Darvan 821A	0.15	0.14	0.15	0.13	0.23	0.14	----	0.16
XUS 40303.00	1.62	2.50	2.35	1.44	2.49	2.50	2.74	1.44
Darvan C	----	----	----	----	----	----	0.21	----

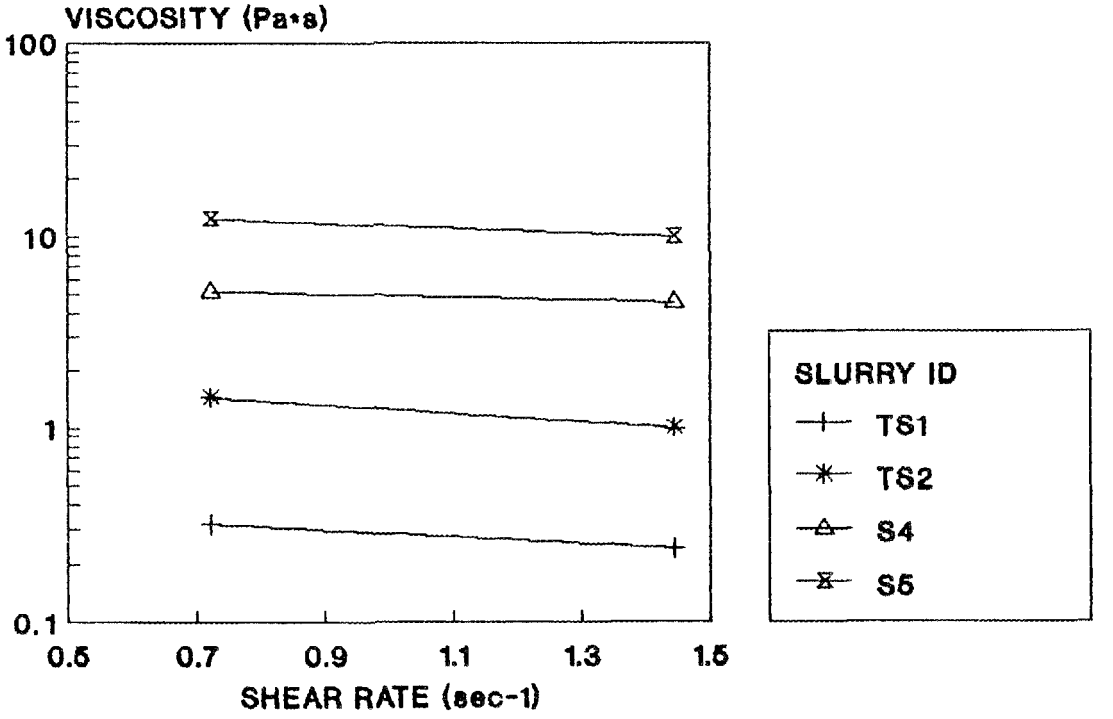

Figure 1a. Viscosity vs Shear rate for slurries prepared with TOSOH and Siconide Si3N4 powders.
(Brookfield Viscometer Spindle #7)

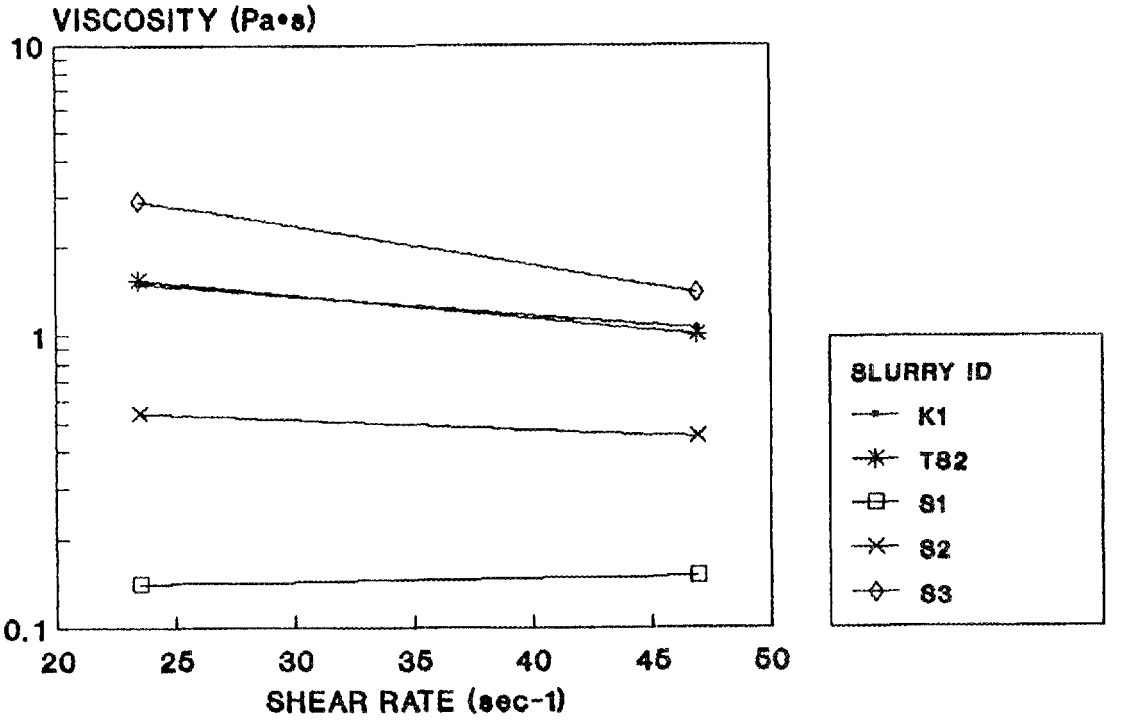

Figure 1b. Viscosity vs Shear rate for slurries prepared with TOSOH, Siconide,and KBI Si3N4 powders.
(Brookfield Viscometer Spindle #6)

Synthesis of High Purity Sinterable Si_3N_4 Powders

G. M. Crosbie, J. M. Nicholson, R. L. Predmesky, and E. L. Cartwright
(Research Staff, Ford Motor Company, Dearborn, Michigan)

Objective/scope

The goal of this task is to achieve major improvements in the quantitative understanding of how to produce sinterable Si_3N_4 powders having highly controlled particle size, shape, surface area, impurity content and phase content. Through the availability of improved powders, new ceramic materials are expected to be developed to provide reliable and cost-effective structural ceramics for application in advanced heat engines.

Of interest to the present powder needs is a silicon nitride powder of high cation and anion purity without carbon residue.

The process study is directed towards a modification of the low temperature reaction of $SiCl_4$ with liquid NH_3 which is characterized 1) by absence of organics (a source of carbon contamination), 2) by pressurization (for improved by-product extraction efficiency), and 3) by use of a non-reactive gas diluent for $SiCl_4$ (for reaction exotherm control).

In the "further development" phase begun October 1987, our goal is to test for unique properties of the ceramics sintered from the low carbon powders, before committing to a pilot plant of the 110 L scale designed. In view of powder quantities needed to allow tests of the ceramics, the major task is to design and implement a scaled-up version of the silicon nitride synthesis processing equipment to produce greater amounts of powders with high cation and anion purity and low carbon residue.

Technical progress

Introduction

Silicon nitride based ceramics are often considered to represent the toughest of the high-temperature (above 1000°C) monolithic ceramics intended for advanced heat engine use. Also, due to a desirable combination of lower temperature properties (wear resistance, low density, high hardness, and toughness), the nitride ceramics are already finding commercial applications in certain passenger vehicles.

Ceramic reliability and cost depend on powder qualities and subsequent processing. Because powders can limit the capability to achieve unique sintered properties and to fabricate complex shapes, the availability of appropriate powders is critical to advanced ceramics research. In the case of silicon nitride ceramics, the powder purity is especially important, since a low solubility in silicon nitride for many impurities leads to high concentrations of those impurities in grain boundary phases. Also, carbon residues (which are found in some otherwise high purity powders) are considered to be detrimental to second phase oxynitride development, thermal stability, and mechanical properties.

Previous work

Along with a 1989 publication,[1] the primary points of reference for the previous process work are the 1986 and 1987 Automotive Technology Development Contractors' Coordination Meeting proceedings papers[2,3] and the previous semiannual reports.[4,5,6]

In the previous lab demonstration work, we prepared a novel process flowsheet for preparation of Si_3N_4 with a block flow diagram and a

mathematical model of mass and heat balances for the "vapor chloride--liquid ammonia" process. We observed that the cooling from latent heat of vaporization of NH_3 more than offsets the heat of reaction at 0^oC and 75 psig.

Powder characteristics met or were approaching target values. Key results were achieved in the areas of phase and microstructure, and carbon purity. Si_3N_4 powder was produced with phase content, particle size and shape which are close to those characteristics considered desirable for pressureless sinterability.

Specifically, the powder derived by thermal decomposition of an intermediate imide product (from reaction of $SiCl_4$ with liquid NH_3 at 0^oC and 75 psig) was principally alpha silicon nitride (as determined by x-ray diffraction, which has little sensitivity to amorphous phases) with crystallite size of 0.2 to 0.3 micron and primarily equi-axed particle shape.

The process was identified to have features which are important for scale-up. Key features of near-neutral heat balance and liquid-like materials handling were demonstrated.

Also, improvements were achieved in yield, laboratory production rate, cation purity, and alpha/beta ratios.

In the extension period work, we prepared a pilot plant design for the "vapor-chloride - liquid ammonia" process, carried out additional process development including the "liquid chloride - liquid ammonia" direct reaction, campaigned runs to test process stability, carried out sintering tests, and reported on a new analytical method for discriminating amorphous and crystalline phases in silicon nitride powders.

Previous pre-pilot plant work

In the "further development" phase begun in the previous period, we increased reactor volume, took steps to improve quality of sealing of vessels and piping, and incorporated direct mechanical agitation while under pressure. By this means, we have equipment to produce 100 g lots of powder (by liquid-liquid and vapor-liquid routes) for sintering tests and characterization of the sintered materials.

Through joint work with an engineering firm, the 4 L scale skid-mounted imide reactor system was installed in a dynamometer test cell and pressure tested to 225 psig (1.65 MPa absolute) with nitrogen in March 1988.

We found evidence for rapid rinsing out of the chloride by-product with the use of agitation. We installed additional subsystems to the pre-pilot plant, found high oxygen contents in initial nitride powders produced, and extended transient flow modeling of the saturator.

With the liquid-chloride--liquid ammonia reaction, we obtained <0.1 um particle sizes and substantial content of fibrous morphology. Through He leak testing in the presence of liquid ammonia, changes were identified and made in O-ring fitting seals and the line to the condenser. Even with discounting of 5% for surface adsorbed oxygen, the powder had 4.5% oxygen contamination.

Summary of current period work

The first vapor-chloride--liquid ammonia runs were made. Equi-axed microstructures were obtained which were similar to those of the 1986 lab demonstration phase product. By use of the revised saturator-mixer

design, the vapor inlet stayed clear through multiple runs. Through improvements to the agitator seal and infrared handling, the intermediate product of the vapor reaction with liquid ammonia was shown to be the same imide as obtained by Billy, et al. (1975). Thermal decomposition led to a nitride without the Si_2N_2O phase previously seen. A pressureless sintered density of 88% of theoretical was obtained.

Pre-pilot operation

In this period, a notable improvement was made in particle morphology and size. These improvements are attributed to operation of the pre-pilot plant for the first time with the patented vapor-$SiCl_4$--liquid-ammonia process. The vapor-liquid process was developed in the preceding CTAHE subcontract. The pressurized liquid-SiCl4--liquid-ammonia process had been used in earlier pre-pilot periods.

In the scanning electron micrograph, Fig. 1, the powder is seen to be free of fibrous content which was seen in previous liq.-liq. reaction products. The equi-axed grains are submicron in size, but not so fine as to impede ceramic processing. An x-ray step-scan is shown in Fig. 2.

Aside from the product powder qualities, other important features observed in running the vapor-chloride--liquid-ammonia process were the absence of build-up in the $SiCl_4$ inlet tube, adequacy of the condenser chiller, a more uniform imide intermediate (facilitating slurry transfers), and an apparently higher Si_3N_4 product yield. Initial data were collected for testing of the saturator flow model, also.

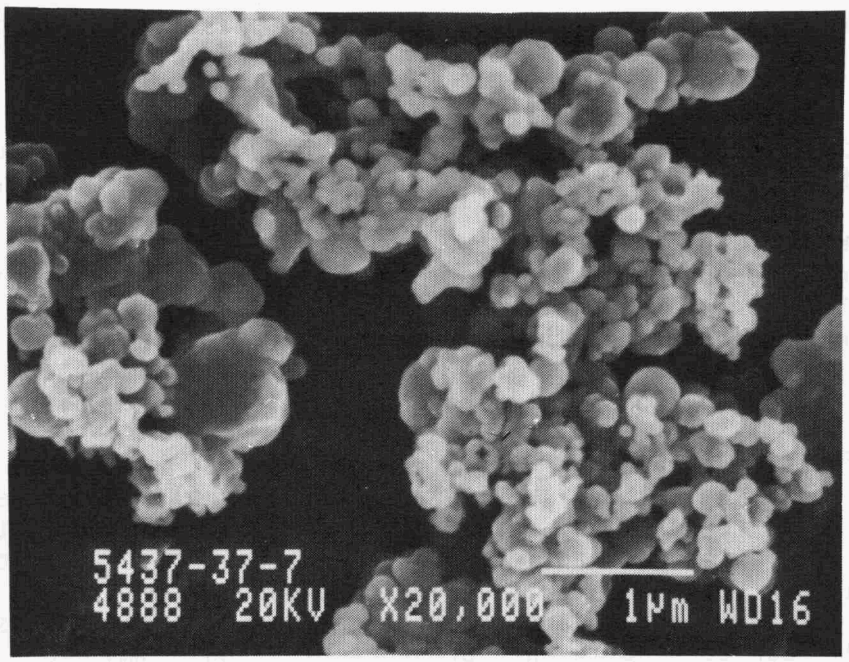

Figure 1. Scanning electron micrograph of Batch 5437-37. Equi-axed crystallites are present of a size less than 1 μm, but not finer than 0.2 μm. (Photography courtesy of W. T. Donlon.) The microstructure is as good or better than those of the smallest scale lab demonstration apparatus of the prior subcontract (in 1986).

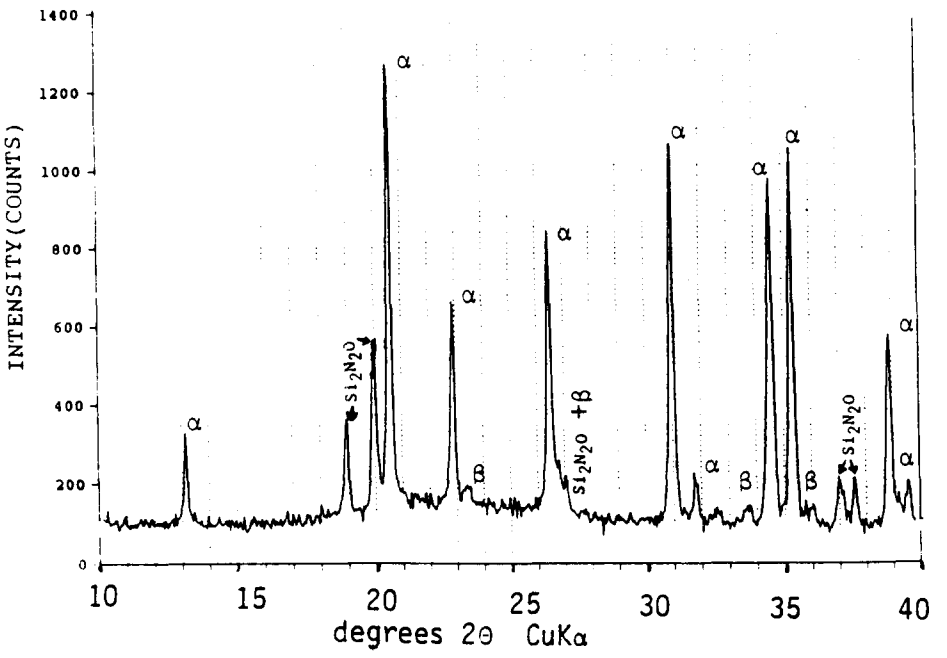

Figure 2. Step-scan x-ray diffraction scan of 5437-37. By peak integration, the Si_2N_2O content was determined to be 8%. (Courtesy of C. R. Peters.) Depending on preparation (dry or acetone dispersion), ratios of alpha/(alpha+beta) ranged from 84% to 90%. (The prior periods' method from peak height from a continuous trace gave alpha/(alpha+beta) of 96%.)

In the June-July 1989 period, six vapor-chloride--liquid-ammonia runs were made, including two in one week. These runs were used to initiate a parametric study of rinsing out of by-product NH_4Cl. Runs were made with six rinses, instead of the usual three. Another run was made with three rinses of 50 minute duration, instead of the usual 10 min. Alpha/(alpha+beta) ratios of the decomposition product ranged from 92% to 97% by the peak height method.[1]

Except for one case, the vapor chloride inlet to the reactor stayed clear. The exception was a case in which the gas at the reactor inlet was greatly supersaturated due to a deficiency in flow of gas bypassing the $SiCl_4$ saturator. In such a supersaturated vapor case, liquid $SiCl_4$ is expected to condense at the inlet, to react with NH_3, and to form a hard plug, as was observed in this one exceptional case.

Upgrades were made in the agitator seal and heat transfer items. A chip which was found in the ceramic rotating face probably led to seal leakage. Chiller lines which feed the vessel jackets were insulated against ambient heat. The heat transfer fluid in the system condenser was changed, with improvement in condenser cooling (and reduced loss of ammonia with the carrier gas flow).

---

[1] Peak height method attributed to H. D. Blair (Ford Research,1987):
%alpha/(%beta+%alpha) = 100% X 1.75 X alpha2 / (1.75 X alpha2 + beta2)
where alpha2 = average of I(alpha102) and I(alpha210)
34.51° (2.599 A) 35.24° (2.547 A)
beta2 = average of I(beta101) and I(beta210)
33.59° (2.668 A) 36.04° (2.492 A)

Because reactor gas tightness was decaying over many runs, steps were taken to improve the agitator mechanical seal. Efforts by the reactor manufacturer to repair the seal led twice to rapid failures upon NH_3 exposure. We machined a new shaft and installed it according to the intended sealing practice.

To answer the question of whether the seal repair was sufficient, an infrared analysis was made of the imide intermediate product (Fig. 3.) We made two trials of infrared spectrophotometry of imide intermediates produced in Runs 5437-53 and 5437-55 with the new sealing. Though a new glovebox was used in both cases, only in the case of complete anaerobic handling of the IR pellet (5437-55) was the spectrum of $Si(NH)_2$ found.

In Fig. 3, the experimental intermediate imide is compared with a reference $Si(NH)_2$ spectrum.[7] In the sister sample (5437-53) without as complete anaerobic handling (not shown), the major feature in this spectral range was a large Si-O absorption at 1045 cm^{-1}.

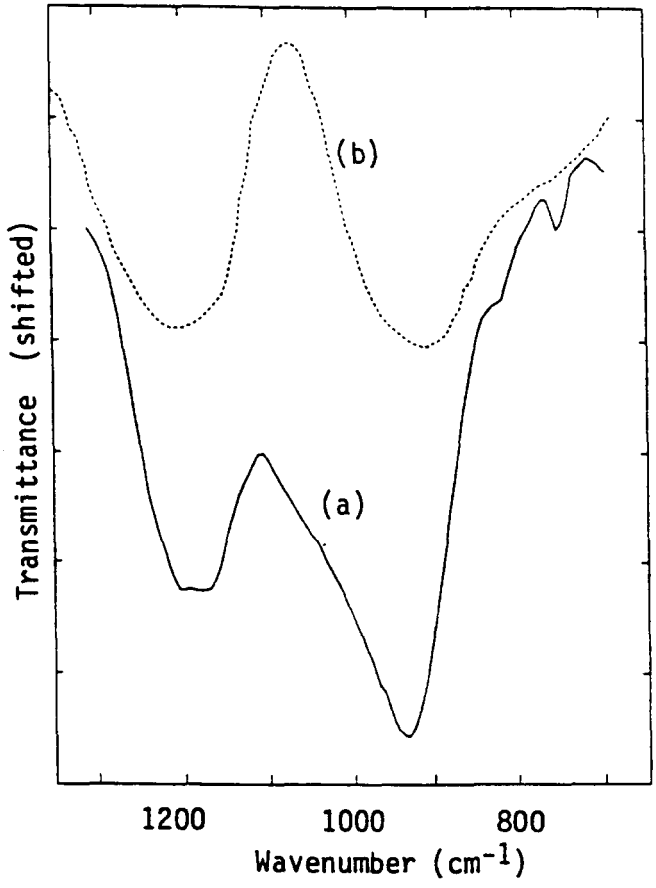

Figure 3. Comparison of infrared transmittance spectra: a) Experimental intermediate from Run 5437-55 (anaerobic method courtesy of C. K. Narula) and b) $Si(NH)_2$ adapted from M. Billy, et al. (1975).[7]

The necessary handling involved sealing the KBr-imide mixture in a pellet press in the glovebox, pressing under vacuum, and transferring the pellet to a KBr-window chamber for insertion into the spectrometer. (The sample handling equipment and direction for this preparation were provided by C. K. Narula, Ford Research.)

The good comparison to reference imide is evidence that the seal repair is sufficient to make a low-oxygen-contamination imide by the chloride-vapor--liquid-ammonia process under pressure. This, in turn, shows that the same compound can be formed as for Billy, et al.,[7] under the higher temperatures and pressures and the vapor process that we used.

Thermal decomposition of the intermediate (under a dilute nitrogen-ammonia gas mixture) led to a high alpha Si_3N_4 with little, if any, Si_2N_2O, by x-ray diffraction (Fig. 4). With reduced oxygen content so indicated, sintering tests were resumed. Following the procedure "D" of the baseline pressureless sintering study,[8] a ceramic density of 88% theoretical was obtained from the 5437-55 powder.

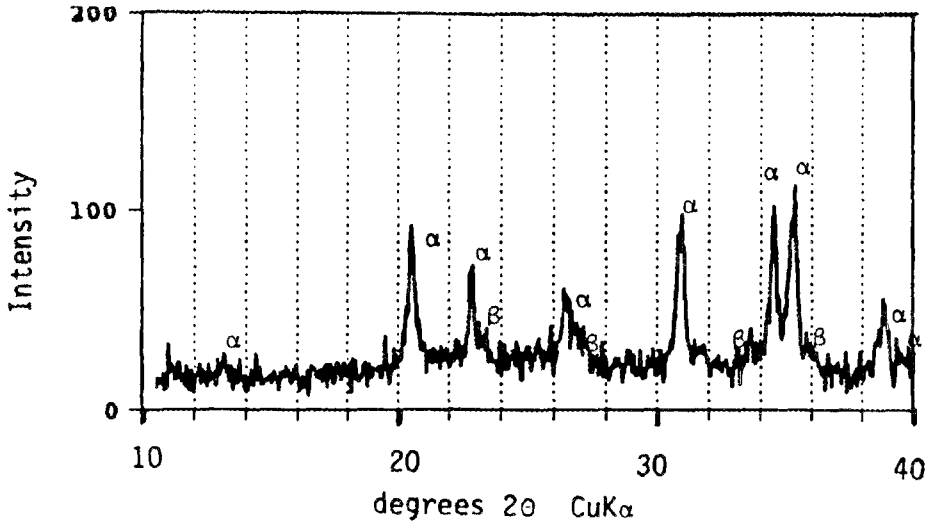

Figure 4. Step-scan x-ray diffraction scan of 5437-53 nitride. No peaks for Si_2N_2O are visible. (Courtesy of C. R. Peters, Ford Research.)

Pre-pilot plant yield

High process yields are important for credibility of cost estimates which have been made. With the care taken to avoid ambient exposure of the liquid precursors, it is not possible to simply weigh the $SiCl_4$ before and after a run is made. Through the use of records, estimates of input $SiCl_4$ vapor (and the Si_3N_4 equivalent) have been made. In spite of a steady carrier gas flow rate, the amount of vapor picked up in the saturator is a function of total pressure, which varies somewhat during a run. A plot of the estimate of equivalent instantaneous Si_3N_4 production rate for the first sub-run of run 5437-43 is then calculated, based on an assumption of pickup of 100% of the $SiCl_4$ vapor pressure at the saturator.

The curve for the complete run is numerically integrated to obtain a value of 36.5 g for the run. The amount of product recovered was 29.1 g, without adjustment for imide intermediate sampling and without compensation for some oxygen contamination. Thus, a yield value of 80% is calculated. This yield points to the reasonableness of the assumptions of complete reaction for the gas flow rates, turbine agitator speed, and vapor depth of introduction which were used.

Liquid-chloride--liquid-ammonia runs earlier in the April-Sept. 1989

Four of five liquid-liquid runs in this period were lost. In two cases (5437-33 and 5437-35), the intermediate product slurry would not flow out of the product holding tank to the thermal decomposition tube.

In two other cases (5437-27 and 5437-31), the thermal decomposition vessel perforated (and exposed the powder to air) after contact with the $LaCrO_3$ heater bars.

In run 5437-29, powder was produced with an alpha/(alpha+beta) ratio of 90% (by peak height). The nitrogen content was 35% (relative to stoichiometric Si_3N_4 at 40%) and the oxygen content was 9%, both by the Leco methods. The product amount of 8 g resulted from $SiCl_4$ sufficient for 120 g. (All input measures are subject to assuming metering vessels fill completely.)

Process comparison:

A comparison can be made between the pressurized liquid-liquid route and the pressurized vapor-liquid route to form Si_3N_4:

	Liq.$SiCl_4$-Liq.NH_3	Vap.$SiCl_4$-Liq.NH_3
Raw materials:		
$SiCl_4$	injected liquid	injected vapor
carrier gas	none (only purge)	yes
ammonia	liquid	liquid
Reaction:		
heat	exothermic (to 70°C)	endotherm (to -10°C)
reaction time	2 min	45 - 72 min
inlet residue	hard packed, crusty	soft, fluffy
Condenser:		
exhaust	clean	some packing
heat loading	always lagging	maintained temp.
Slurry transfer:		
ease of piping	sometimes no flow	yes
consistency	chunky, granular	milky
Dry intermediate:		
smoothness	non-uniform, crusty	uniform, fluffy
Si_3N_4 product:		
morphology	fibers and ultrafine	equi-axed
particle size	wide, including u'fine	submicron, not u'fine
yield	low e.g. 7%	high e.g. 80%

At the cost of recycling carrier gas and a longer reaction time, the vapor-liquid process leads to a powder feasible without fibers in a more desirable particle size range.

Continuous process flowsheet

Extended discussions were held regarding data required for conceptual design of a continuous reactor scheme, in lieu of the semi-continuous operation of the pre-pilot plant. Schemes for both the imide preparation and the high temperature decomposition were discussed with experienced outside personnel and possible additional economies identified.

Conclusions

With vapor-chloride--liquid-ammonia operation of the pre-pilot plant, we can obtain equi-axed morphology particles and yields of 80%. The intermediate formed by the vapor-liquid reaction is the same as that

obtained by Billy, et al.[7] at lower temperatures and pressures. The inlet flow design we have used has kept the vapor inlet clear. On thermal decomposition of the intermediate, alpha silicon nitride is formed, with no apparent Si_2N_2O. One sample tested sintered to 88% of theoretical density.

Status of Milestones

This two-year follow-on contract was initiated October 1, 1987 for the "Further Development of Synthesis of High-Purity Sinterable Silicon Nitride (Si_3N_4) Powders for Application in Ceramic Technology for Advanced Heat Engines Project."

In this period, the visits to the pre-pilot plant by potential licensees (previously designated as acceptable by the Government) furthered the intent of the milestone of initiating discussions which was met in the June-July 1989 period. Other milestones are on schedule.

Publications

G. M. Crosbie, R. L. Predmesky, J. M. Nicholson, and E. D. Stiles, "Prepilot Scale Synthesis of Silicon Nitride under Pressure," Bull. Am. Ceram. Soc., 68 [5] 1010-14 (1989).

G. M. Crosbie, R. L. Predmesky, and J. M. Nicholson, "Synthesis of High Purity Sinterable Silicon Nitride Powder," preprint of talk to be presented at the 27th Automotive Technology Development Contractors' Coordination Meeting, Dearborn, Michigan, Oct. 23-26, 1989.

"Si_3N_4 Powder Synthesis Process Licensing Available," Ceramic Technology Newsletter, No. 23, p. 8, April-June 1989.

K. R. Carduner, R. O. Carter III, M. J. Rokosz, C. R. Peters, G. M. Crosbie, and E. D. Stiles, "Silicon-29 Magic Angle Spinning Nuclear Magnetic Resonance of Sintered Silicon Nitride Ceramics," Chemistry of Materials, 1 [3] 302-07 (1989).

G. M. Crosbie, J. M. Nicholson, and E. D. Stiles, "Sintering Factors for a Dry-Milled Silicon Nitride-Yttria-Alumina Composition," Bull. Am. Ceram. Soc., 68 [6] 1202-6 (1989).

K. R. Carduner, C. S. Blackwell, W. B. Hammond, F. Reidinger, and G. R. Hatfield, "^{29}Si NMR Characterization of Alpha- and Beta-Si_3N_4," submitted to J. Am. Chem. Soc. for publication.

K. R. Carduner and G. R. Hatfield, "Solid State NMR: Applications in High Performance Ceramics," accepted for publication, J. Mater. Sci.

G. M. Crosbie, J. M. Nicholson, R. L. Predmesky, and E. D. Stiles, "Synthesis of Low-Carbon Si_3N_4: Pre-Pilot Study," presented at the 91st Annual Meeting of the American Ceramic Society, April 23-27, 1989, Indianapolis, Indiana.

References

1. G. M. Crosbie, R. L. Predmesky, J. M. Nicholson, and E. D. Stiles, "Prepilot Scale Synthesis of Silicon Nitride under Pressure," Bull. Am. Ceram. Soc., 68 [5] 1010-14 (1989).

2. G. M. Crosbie, "Silicon Nitride Powder Synthesis," pp.255-265 in: Proc. of the 24th Automotive Technology Development Contractors' Coordination Meeting, Soc. of Automotive Engineers, Warrendale, Pa., 1987. (P-197).

3. G. M. Crosbie, J. M. Nicholson, R. L. Predmesky, and E. D. Stiles, "Silicon Nitride Powder Synthesis Program," pp. 127-135 in: Proc. of the 25th Automotive Technology Development Contractors' Coordination Meeting, Soc. of Automotive Engineers, Warrendale, Pa., 1988. (P-209)

4. G. M. Crosbie, "Synthesis of High Purity Sinterable Si_3N_4 Powders," pp. 17-23 in Ceramic Technology for Advanced Heat Engines Project Semiannual Report for October 1986 Through March 1987, ORNL/TM-10469, Oak Ridge National Laboratory, Oak Ridge, Tenn., August 1987.

5. G. M. Crosbie, J. M. Nicholson, R. L. Predmesky, and E. D. Stiles, "Synthesis of High Purity Sinterable Si_3N_4 Powders," pp. 20-27 in Ceramic Technology for Advanced Heat Engines Project Semiannual Report for April Through September 1988, ORNL/TM-11116, Oak Ridge National Laboratory, Oak Ridge, Tenn., March 1989.

6. G. M. Crosbie, J. M. Nicholson, R. L. Predmesky, E. D. Stiles, and E. L. Cartwright, "Synthesis of High Purity Sinterable Si_3N_4 Powders," pp. 21-27 in Ceramic Technology for Advanced Heat Engines Project Semiannual Progress Report for October 1988 Through March 1989, ORNL/TM-11239, Oak Ridge National Laboratory, Oak Ridge, Tenn., August 1989.

7. M. Billy, M. Brossard, J. Desmaison, D. Giraud, and P. Goursat, "Synthesis of Si and Ge Nitrides and Si Oxynitride by Ammonolysis of Chlorides -- Comment on "Synthesis, Characterization, and Consolidation of Si_3N_4 Obtained from Ammonolysis of $SiCl_4$," J. Am. Ceram. Soc., 57 [5-6] 254 (1975).

8. G. M. Crosbie, J. M. Nicholson, and E. D. Stiles, "Sintering Factors for a Dry-Milled Silicon Nitride-Yttria-Alumina Composition," Bull. Am. Ceram. Soc., 68 [6] 1202-6 (1989).

Microwave Processing of Silicon Nitride

T. N. Tiegs, H. D. Kimrey, J. O. Kiggans, and E. C. Dickey (Oak Ridge National Laboratory)

Objective/scope

The objective of this research element is to identify those aspects of microwave processing of silicon nitride that might (1) accelerate densification, (2) permit sintering to high density with much lower levels of sintering aids, (3) lower the sintering temperature, or (4) produce unique microstructures. The investigation of microstructure development is being done on dense silicon nitride materials annealed in the microwave furnace. The sintering of silicon nitride involves two approaches. The first approach comprises heating of silicon nitride and sialon powder compositions in the 2.45- or 28-GHz units. The second approach deals with using reaction-bonded silicon nitride as the starting material and is done entirely in the 2.45-GHz microwave furnace.

Technical progress

Microstructure development. It has been established that microwave heating can accelerate or enhance diffusional processes, such as sintering and grain growth. This could be used to manipulate the microstructures of Si_3N_4 and sialon materials for improved properties. Potential benefits include (1) increased fracture toughness or inhibition to crack propagation by promoting acicular ß-grain growth, (2) improved high-temperature strength due to crystallization of glassy grain boundary phases that are normally present in these materials, and (3) higher hardness and high-temperature strength by being able to fabricate materials with lower than normal sintering aid contents and/or more-refractory sintering aids. Additional benefits of increasing the fracture toughness would be to reduce the variability and scatter in mechanical properties by reducing the flaw sensitivity of the materials. Also, by increasing the hardness of the materials, an improvement on the wear resistance should be observed. The sintering aids used in the Si_3N_4 and sialon materials influences the way in which the microstructure can be manipulated. To get a wide range of sintering aid levels, samples of Si_3N_4-4% Y_2O_3, Si_3N_4-6% Y_2O_3-2% Al_2O_3, Si_3N_4-12% Y_2O_3-4% Al_2O_3 and sialon-2% YAG were hot-pressed to full density and annealed both by microwave and conventional heating at 1200, 1400, and 1500°C for times of 10 and 20 h. The range of compositions was intended to give a wide range of glassy, grain-boundary phases to study the effects of crystallization and grain growth. The microwave annealing was done at 2.45 GHz.

The results on the changes in elastic modulus with annealing are given in Tables 1 through 5 for the various compositions. As shown, the microwaved samples generally had greater increases in the elastic modulus compared with conventionally annealed specimens. These relative changes in elastic modulus are indicative of greater crystallization of glassy, grain-boundary phases by the use of microwave annealing. This effect was more evident in the compositions with higher amounts of sintering aids.

X-ray diffraction was performed on specimens as-fabricated and those annealed at 1400°C for 10 h in the microwave and conventionally. Only minor differences were observed between the microwave- and conventionally annealed samples with the exception of the Si_3N_4-12% Y_2O_3-4% Al_2O_3 composition. These samples contained the greatest amounts of sintering aids, and the microwave-annealed sample showed an increased amount of sialon phases.

SEM examination of fracture surfaces was performed on the same samples used for the X-ray study. Essentially no differences in grain size or fracture behavior were observed for the Si_3N_4-4% Y_2O_3, Si_3N_4-6% Y_2O_3-2% Al_2O_3 and $Si_4Al_2O_2N_6$-2%$3Y_2O_3 \cdot 5Al_2O_3$ compositions. However, the fracture surfaces of the Si_3N_4-12% Y_2O_3-4% Al_2O_3 composition samples revealed that the microwave-annealed samples experienced enhanced grain growth along with the

composition samples had a less-glassy appearance and a more-crystalline fracture surface as shown in Fig. 2. No large differences in the grain size are obvious in those samples.

Table 1. Modulus results for hot-pressed Si_3N_4-4% Y_2O_3 after annealing by conventional and microwave heating

Type anneal	Temperature (°C)	Time (h)	Modulus as-fab.	Modulus post- anneal
Conventional	1200	10	294.8	295.3
Microwave	1200	10	312.9	308.8
Conventional	1200	20	294.8	295.1
Microwave	1200	20	312.5	313.0
Conventional	1400	10	309.2	310.3
Microwave	1400	10	308.0	312.4
Conventional	1400	20	309.2	306.1
Microwave	1400	20	308.0	307.8
Conventional	1500	10	312.6	308.5
Microwave	1500	10	312.5	308.1

Table 2. Modulus results for hot-pressed Si_3N_4-6% Y_2O_3-2% Al_2O_3 after annealing by conventional and microwave heating

Type anneal	Temperature (°C)	Time (h)	Modulus as-fab.	Modulus post-anneal
Conventional	1200	10	310.5	312.6
Microwave	1200	10	300.6	307.9
Conventional	1200	20	310.5	305.7
Microwave	1200	20	300.7	304.9
Conventional	1400	10	310.7	309.5
Microwave	1400	10	295.7	305.2
Conventional	1400	20	310.7	310.5
Microwave	1400	20	295.7	305.6
Conventional	1500	10	311.1	307.3
Microwave	1500	10	300.7	309.9

Table 3. Modulus results for hot-pressed Si_3N_4-12% Y_2O_3-4% Al_2O_3 after annealing by conventional and microwave heating

Type anneal	Temperature (°C)	Time (h)	Modulus as-fab.	Modulus post-anneal
Conventional	1200	10	298.6	306.7
Microwave	1200	10	287.6	N.D.
Conventional	1200	20	298.6	297.3
Microwave	1200	20	287.1	302.7
Conventional	1400	10	299.6	306.2
Microwave	1400	10	292.5	304.6
Conventional	1400	20	299.6	299.9
Microwave	1400	20	292.5	N. D.
Conventional	1500	10	298.2	294.2
Microwave	1500	10	287.1	N.D.

Table 4. Modulus results for hot-pressed $Si_4Al_2O_2N_6$-2% $3Y_2O_3{\cdot}5Al_2O_3$ after annealing by conventional and microwave heating

Type anneal	Temperature (°C)	Time (h)	Modulus as-fab.	Modulus post-anneal
Conventional	1200	10	252.8	250.7
Microwave	1200	10	254.6	255.2
Conventional	1200	20	252.8	249.3
Microwave	1200	20	257.9	271.1
Conventional	1400	10	252.8	254.4
Microwave	1400	10	254.7	253.7
Conventional	1400	20	252.8	254.4
Microwave	1400	20	254.7	266.7
Conventional	1500	10	252.0	253.1
Microwave	1500	10	257.9	267.9

Table 5. Modulus results for hot-pressed $Si_{4.5}Al_{1.5}O_{1.5}N_{6.5}$-2% $3Y_2O_3{\cdot}5Al_2O_3$ after annealing by conventional and microwave heating

Type anneal	Temperature (°C)	Time (h)	Modulus as-fab.	Modulus post-anneal
Conventional	1200	10	283.3	281.8
Microwave	1200	10	288.8	285.7
Conventional	1200	20	283.3	279.1
Microwave	1200	20	283.6	287.4
Conventional	1400	10	282.9	285.3
Microwave	1400	10	284.9	294.3
Conventional	1400	20	282.9	282.6
Microwave	1400	20	284.9	296.8
Conventional	1500	10	286.0	284.8
Microwave	1500	10	283.6	288.2

The results from the annealing study indicate an apparent enhancement of both grain growth and crystallization of glassy, grain-boundary phases in silicon nitride and sialon compositions with microwave annealing. Further examination of these processes will determine the effects of glass composition and the affect on mechanical properties.

Sintering of silicon nitride. It was reported previously that coupling to Si_3N_4-6% Y_2O_3-2% Al_2O_3 is very difficult in the 2.45-GHz microwave furnace. Additions of TiC, TiN, and SiC improved the coupling; however, field nonuniformities resulted in cracked parts. In addition, the results showed that the sintering temperatures required are similar to those used in conventional heating and that liquid phases must be present.

Additional samples of Si_3N_4-6 % Y_2O_3-2% Al_2O_3 (with and without the TiN, and SiC additions) and sialon were sintered in the 28-GHz microwave furnace. All of the samples coupled well, which was in contrast to the sintering attempts in the 2.45-GHz furnace. The results on the densification behavior are summarized in Table 6. As shown, the silicon nitride compositions did not achieve full density, while the sialon materials easily reached high density. Further tests will attempt to optimize the heating schedules for the silicon nitride compositions. The sialon samples sintered to full density in the 28-GHz furnace were tested for indent hardness and fracture toughness and compared with results from hot-pressed sialon material. Those results are summarized in Table 7. As indicated, the results show very little difference between hot-pressed and microwave-sintered sialon materials.

Table 6. Summary of results on sintering of silicon nitride in the 28-GHz microwave furnace

Sample composition	Sintering temperature (°C)	Sintered density (g/cm^3)	Fraction of theo. density
Si_3N_4[a]	1750	2.930	90
Si_3N_4[a]-2 w/o SiC	1750	3.042	93
Si_3N_4[a]-2 w/o TiN	1750	2.968	91
Sialon[b]	1650	3.120	98
Sialon[b]	1670	3.192	100

[a]Si_3N_4 with 6 wt % Y_2O_3 and 2 wt % Al_2O_3.
[b]Composition $Si_{4.5}Al_{1.5}O_{4.5}N_{6.5}$: Vesuvius Crucible, Grade AA Sinterable.

Table 7. Summary of results on indent hardness and fracture toughness of sialon materials[a] fabricated by hot-pressing and microwave sintering

Sample	Fabrication temperature (°C)	Indent hardness (GPa)	Indent fracture toughness ($MPa\sqrt{m}$)
Hot-pressed	1650	13.0	5.1
MW Sintered	1650	12.0	5.1
MW Sintered	1670	12.5	5.2

[a]Composition $Si_{4.5}Al_{1.5}O_{4.5}N_{6.5}$: Vesuvius Crucible, Grade AA Sinterable.

Reaction-bonded silicon nitride (RBSN). Reaction-bonded silicon nitride offers many advantages over sintered silicon nitride. Previous results showed enhanced reaction rates for

nitridation in the 2.45-GHz microwave furnace. Specimens of different Si powder purity and particle size were nitrided both in the microwave and in a conventional furnace. Those results are summarized in Fig. 3. It should be noted that the sample sizes were ~100 g for the microwave-heated and ~20 g for the conventionally-heated samples. The conventionally heated specimens were smaller because of furnace capacity in that particular furnace. In any event, the nitridation in the microwave appears to be increased by at least a factor of 3 compared with the conventionally nitrided specimens. Increased nitridation is observed with higher-Fe-content and smaller-particle-size Si powders for both the microwave- and the conventionally heated specimens. Nitridation is also enhanced by the use of Y_2O_3 and Al_2O_3 sintering aids. Thus, direct nitridation of high-purity Si followed by a sintering step may yield dense silicon nitride.

Further testing examined the effect of other sintering aids on the nitridation rates. The samples were approximately 100 g of high-purity Si powder (< 0.05% Fe) and were heated in a total cycle time of 23 h to 1400°C. These results are summarized in Table 8 and show not only the effect of the sintering aids but also of some processing variables. As shown, when the powders are wet milled in isopropanol, the nitridation rate is decreased. Similar effects have been observed by other researchers with methanol.[1] Increased nitridation with the use of Y_2O_3, MgO, or CeO_2 compared with the Y_2O_3-Al_2O_3 combination indicates that the Al_2O_3 may have an inhibiting effect on the nitridation reaction.

Table 8. Summary of results on effect of various sintering aids on the nitridation of silicon in the 2.45-GHz microwave furnace

Sintering aid content	Milling procedure	Silicon weight gain (%)	Nitridation reaction (%)
None	None	52.1	78
6% Y_2O_3-2% Al_2O_3	Dry	57.3	86
6% Y_2O_3-2% Al_2O_3	Wet[a]	50.2	76
6% Y_2O_3	Wet[a]	55.1	83
5% MgO	Wet[a]	55.9	84
8% CeO_2	Wet[a]	55.3	83

[a]Wet-milled in isopropanol.

References

1. B. W. Sheldon and J. S. Haggerty, "The Nitridation of High Purity, Laser-Synthesized Silicon Powder to Form Reaction Bonded Silicon Nitride," *Ceram. Eng. Sci. Proc.* 9[7-8], 1061-072 (1988)

Status of milestones

Milestone 112402 was not completed.

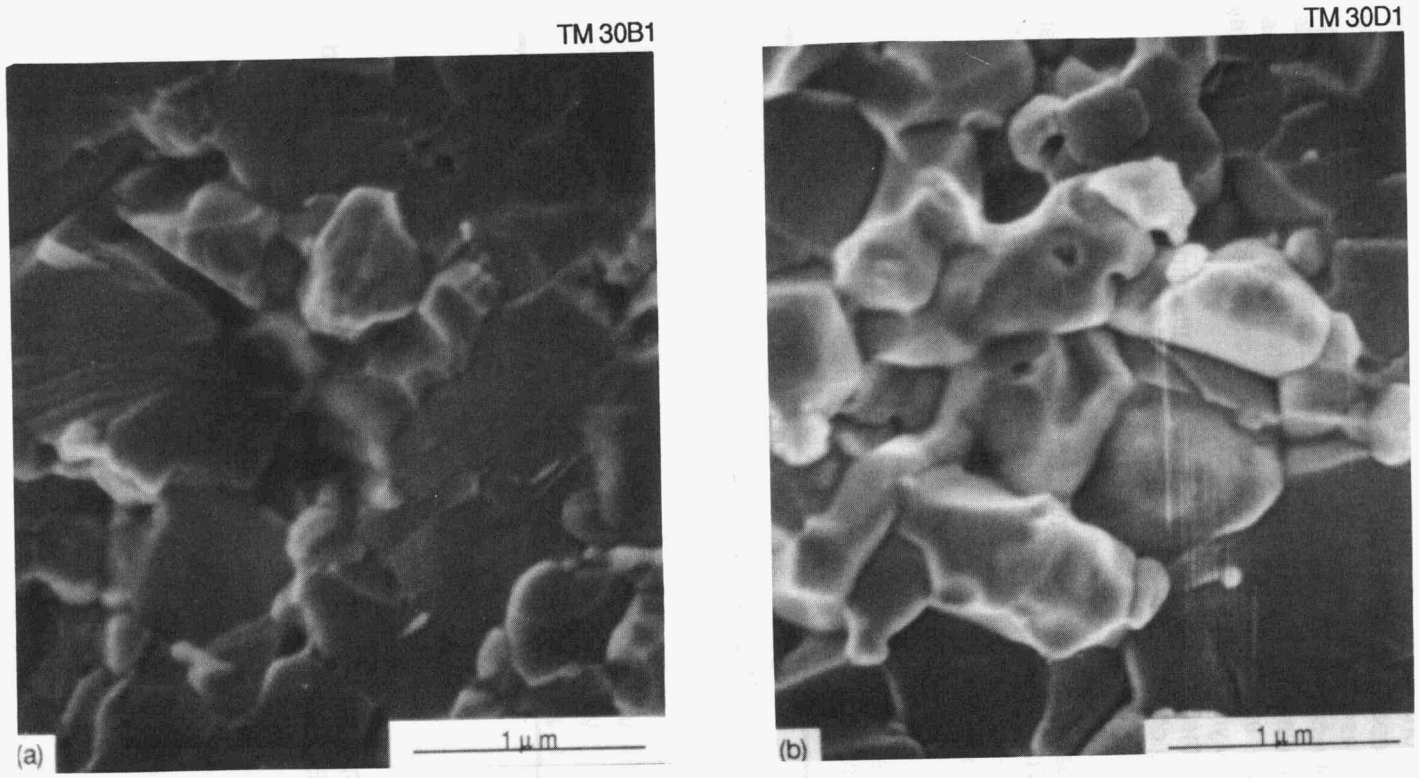

Fig. 1. Fracture surfaces of hot-pressed Si_3N_4-12% Y_2O_3-4% Al_2O_3 after annealing at 1400°C for 10 h with (*a*) conventional and (*b*) microwave heating.

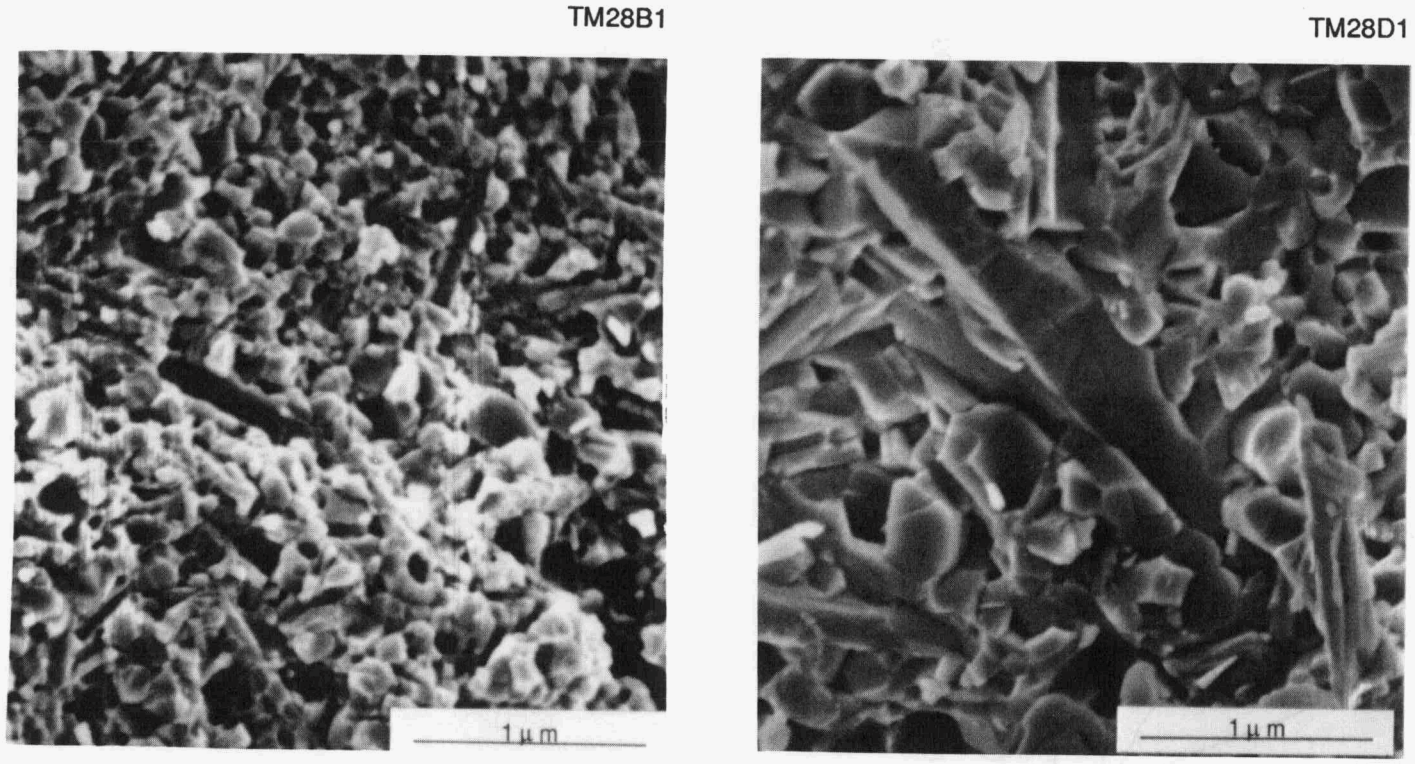

(*a*) (*b*)

Fig. 2. Fracture surfaces of hot-pressed $Si_{4.5}Al_{1.5}O_{1.5}N_{6.5}$ - 2% $3Y_2O_3 \cdot 5Al_2O_3$ after annealing at 1400°C for 10 h with (*a*) conventional and (*b*) microwave heating.

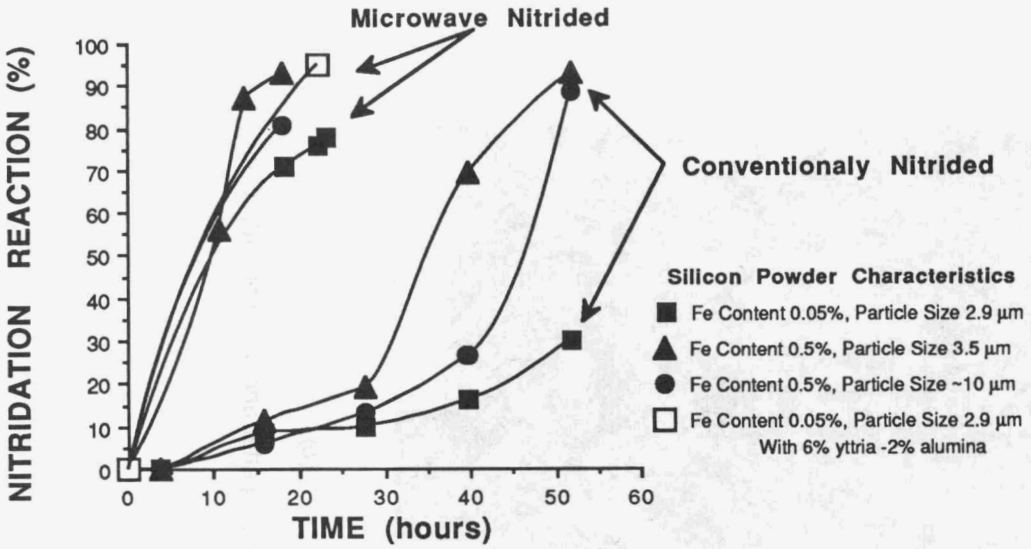

Fig. 3. Summary of results on nitridation of silicon with microwave and conventional heating.

Silicon Nitride Milling Characterization

S. G. Malghan, L. H. S. Lum and D. Minor
(National Institute of Standards and Technology)

Objective/Scope

Ceramics have been successfully employed in engines on a demonstration basis. The successful manufacture and use of ceramics in advanced engines depends on the development of reliable materials that will withstand high, rapidly varying thermal stress loads. Improvement in the starting ceramic powders is a critical factor in achieving reliable ceramic materials for engine applications. Milling of powders is an integral unit operation in the manufacture of silicon nitride components for advanced energy applications. The production and use of these powders require the use of efficient milling techniques and understanding of characteristics of the milled powders in a given environment. High energy attrition milling appears to offer significant advantages over conventional tumbling and attrition mills.

The objectives of this project are to: (1) develop fundamental understanding of surface chemical changes taking place when silicon nitride powder is attrition milled in aqueous environment, and (2) demonstrate the use of high energy attrition milling for silicon nitride powder processing, by developing measurement techniques and data on the effect of milling variables on the resulting powder. This study will provide data and models for effective application of high energy attrition milling to industrial processing of silicon nitride powder. It also will provide recommended procedures for physical and surface chemical characterization of powders and slurries involved in the milling process.

Technical Progress

The technical progress covered in this report includes characterization of powder, and installation of high energy attrition milling system.

Characterization of Starting Powder - The characterization study of starting powders for milling was extended to Ube's SNE-3 SNE-5 and SNE-10. Major emphasis was placed on obtaining basic surface chemical properties of the three powders. These data are useful in the interpretation of milling studies, especially when examining the effect of milling environment on the powder surface properties. The basic surface chemical properties (isoelectric point, IEP and zeta potential at a given pH) of aqueous suspensions of the as-received powders, aged powders, and anionic surfactant adsorbed powders were studied.

The basic surface properties of ceramic raw materials and properties such as zeta potential, surface charge density and isoelectric charge (IEP) are important for slurry processing of these raw materials. Typically these properties are determined by

electrophoresis or streaming potential techniques. In our experiments the Matec ESA system was used for measuring the electrokinetic properties of the silicon nitride powders in aqueous environment.

In this method an alternating electric field is applied to the suspension of powder in water. The electric field sets up relative motion between the particles and liquid, which generates a sound wave at the same frequency of the electric field. Each particle vibrating in the electric field generates sound waves which sum up to a coherent sound wave when many particles are involved. This effect is termed the "Electrokinetic Sonic Amplitude" (ESA). The ESA is the pressure amplitude per unit electric field generated by the particles (SI units pascals per volt per meter). The ESA is directly proportional to zeta potential, in dilute suspensions.

The as-received powders exhibited IEPs in the range of pH = 5.0 to 6.0. The IEPs increased as the fineness of the powder increased. This type of increase in IEP of the powders is most likely related to the extent of surface dissolution of the powders and parameters of the manufacturing process. Considering the degree of difference in fineness of the powders (SNE-3 to SNE-10 change of surface area is 3 to 10 m^2/g), the observed shift in IEP is considered to be minor. Based on these data, all three powders can be dispersed in aqueous environment in the pH ranges below 4 and above 7.

In the acidic pH range (4 and below) the ESA values (hence zeta potentials) increased as a function of powder fineness. The SNE-10, being the finest powder, has the highest ESA value. However, in the basic pH range above 7, the ESA values are slightly disordered with respect to their surface areas. The ESA values of SEN-3 are between those of SNE-5 and SNE-10. This type of behavior is attributed to presence of impurities at the surface of the SNE-3 powder.

All three powders were aged in aqueous environment containing a polyacrylate surfactant and their surface chemistry was examined after 4 and 72 hrs. aging. Several important surface chemical changes were observed:

- The presence of 10^{-3}M of the surfactant had the maximum effect on the SNE-10 powder, in which, the IEP shifted from a pH of 6.0 to 3.2, without aging.
- However, after aging for 4 hrs, all three powders attained the same type of surface, in which the IEPs ranged from pH = 3.0 to 3.2.
- If the quantity of surfactant was not sufficient, as in the case of 10^{-5}M, then the SNE-10 powder did not show a large shift in the IEP.
- At a concentration of approximately 10^{-3}M polyacrylic acid, all three powders can be dispersed at the natural pH of 8.5 - 8.9. The natural pH is defined as that pH of the suspension measured immediately after the suspension is prepared.

- Aging of the powder was found to destabilize the suspension even in the presence of 10^{-3}M concentration of the surfactant. The degree of destabilization was measured by decrease in ESA values before and after aging.

Additional studies on powder surface chemistry and data analysis are continuing.

High Energy Attrition Mill - The mill has been installed, related safety inspections are completed, and the mill is being prepared for trial runs. One of the major hurdles of obtaining small diameter (1 to 2 mm) silicon nitride media has been overcome. The 2 mm hot pressed silicon nitride media were obtained from a source in Netherlands.

Certain commercial equipment, instruments and materials may be identified in this report in order to adequately specify the experimental procedure. Such identification does not imply recommendation or endorsement by the National Institute of Standards and Technology, nor does it imply that the materials or equipment identifies are necessarily the best available for the purpose.

1.1.4 Processing of Monolithics

Improved Processing

R. L. Beatty, R. A. Strehlow, and O. O. Omatete (Oak Ridge National Laboratory)

Objective/scope

The objective of this research is to determine and develop the reliability of selected advanced ceramic processing methods. This program is to be conducted on a scale that will permit the potential for manufacturing use of candidate processes to be evaluated.

Technical progress

Gelcasting of silicon nitride. The first objective in the development of the gelcasting process for silicon nitride was preparation of a castable formulation at 50% or higher volumetric loading of solids. Work has been concluded on developing an initial formulation for gelcasting of silicon nitride specimens.

Numerous attempts were made to gelcast several silicon nitride powders, and a successful formulation was achieved using Starck Type S silicon nitride powder. This powder possesses a rather large nominal particle size and is not expected to sinter as readily as the finer powders. Nonetheless, because of the feasibility now demonstrated for casting it, we decided to use it as the formulation of choice for work in the near term as we continue efforts with a selection of finer powders.

The selected silicon nitride formulation includes aluminum and yttrium oxides as sintering aids. In order to minimize the solubility of yttrium (a potential contributor to flocculation) in the aqueous slurry, a compound with lower yttrium solubility, yttrium aluminate ($Y_3Al_5O_{12}$), was synthesized and used as sintering aid in this and several of the other preparations studied.

In dealing with aqueous concentrations of fine and active silicon nitride powders, the rate of hydrolysis is high and silica-containing gels form rapidly. We used three preparation approaches with dispersants selected on the basis of both literature reports and our tests using the scanning laser microscope particle-size analyzer.

Initially, we prepared UBE-SN-10 silicon nitride suspensions at volumetric concentrations of about 40% and then concentrated the resulting suspensions in vacuum. This led to parts with generally satisfactory appearance, which we believe to have contained agglomerates that formed during the concentration step. In the continuing work, no direct dispersion of this particular powder has been achieved in the concentration range near 50% using any of the dispersants we have studied. This powder appears to hydrolyze rapidly and to generate a suspension with thick gel-like appearance. In order to use this material, powder pretreatment may be required. Although we plan some additional dispersion studies on the as-received powder, the methods to be explored include both chemical and thermal treatments.

A second set of preparations followed the work of Hoffman et al.[1] In these preparations, a suspension containing 48 vol% was successfully prepared, mixed, and cast using Starck LC-12SX powder that had been oxidized in accordance with the reported work. Parts from this formulation showed cracks that developed following gelation. We believe, however, the cracking was due to our use of an improper mold-release agent and is not a serious problem.

A more important possible disadvantage of this method and formulation is the authors' requirement that the silicon nitride particles be oxidized. This poses problems of process control on scaling-up the process. The step also increases the oxygen content of the powder, which is not desirable for the optimal product properties. Oxygen analyses were obtained for two oxidation runs of 4 and 8 h at 600°C, with samples being taken from both the bottom and the top of the bed. The oxygen content for the as-received powder was 1.10 ± 0.08% and for all other samples the average was 2.09%, with a range of

1.83 to 2.33%. We plan further efforts with this method, but the oxygen content of the powder does not make it as attractive a choice for development in the near term as is the Type S powder.

The third approach referred to above used the larger-particle-size Type S powder. The method we developed involved ball-milling with dispersant at 50 vol %. We will explore the use of this formulation and continue to examine other powders, dispersants, dispersion methods, and powder pretreatments. Because of the strong scaleup advantages of an aqueous route for gelcasting silicon nitride, no work is presently planned on exploring possible nonaqueous alternatives.

Dispersion studies. Dispersion studies on alumina and silicon nitride powders were continued using the scanning laser microscope to observe changes in particle size distributions under various conditions. In addition to dispersion studies, we conducted a concentration-dependence study of the analyzer, attrition studies, and an examination of temperature-dependent effects. The dispersant studies were carried out on several powders and with several dispersants. Under the low-shear conditions used by the device, some dispersant activity could be measured. However, the approach of greatest utility involves the combined effects of dispersant and ultrasonication or milling by attritor, ball-mill, or turbo-mill.

Studies of the concentration dependence of the measured size distribution of alumina powder using this device were made for alumina at concentrations from 2 to 10 vol %. The size distribution was relatively insensitive to concentration, indicating the useful applicability of the method. However, the total particle count (particles counted in a 1 to 3 s sampling time) departed from linearity at concentrations of about 4 vol %, indicating that the data obtained at higher concentrations may not be appropriate or representative for quantitative use when applied to this material. The values at normal test dilutions are viewed as useful for the intended purpose of assessing the presence of large agglomerates at early slurry stages of processing.

Attrition studies were conducted using a small (0.5-L) attritor. A sample of yttrium aluminate that was synthesized during this period as a sintering aid was not successfully milled at times to 72 min. Ball milling, however, proved to be effective for this material. Two commercial silicon nitride powders, on the other hand, were tested using the attritor and were found to be effectively milled in water with either of the two polyacrylate dispersants tested so far.

In a third series of studies, the effect of temperature on the dynamic particle-size distribution, especially in the range of 19 to 23°C, was examined. This is the temperature range corresponding to the critical flocculation phenomenon, a well-known characteristic property of polymer systems. This was a test of the phenomenon for the particular polymeric dispersants we are using. By varying the temperature systematically over the range from 13 to 40°C, we found no effect that could be attributed to a coagulation or flocculation of the slurry at the concentration ranges of <10 vol %.

Some separate measurements on turbidity were conducted with the dispersant alone that did indicate the possible coalescence of the polymer in the expected temperature range of 19 to 23°C. However, this was in the absence of ceramic powder. We concluded that it is not necessary to specify and control temperature for this mixing-dispersion step.

Gelcasting of alumina. One of the features of the slurry gelcasting process is the apparent easy machinability of the dried castings before debindering. They are rugged and readily sawn or drilled without the use of special tools.

We are using alumina specimens to determine the range of machining operations that may be used and to develop the techniques required. We believe this work to be substantially independent of the ceramic powder that is used. A fine surface finish can be imparted by abrasive paper. Several of the test alumina specimens being prepared as part

of the development effort are being used to evaluate tool wear, surface quality, and other characteristics of interest. Specimens have been made using steel drills, a band saw, and hand files. A first attempt to machine a casting using lathe tools failed but will be repeated with a wider variety of specimens.

Industrial hygiene and environmental issues. Part of the advanced processing studies is associated with the issues of hygiene, safety, and environment. A literature search was conducted on acrylamide, a key ingredient of the process, and assistance was requested from the Industrial Hygiene Section of the Environmental Compliance Division. A survey of two staff members was carried out by that department over a 5-d period during normal operations. The results in every case showed no acrylamide at the detectable limit (15% of the maximum daily tolerance limit). This result is in accordance with our expectations based on measured air flows in the laboratory.

A waste-disposal procedure was developed and implemented, and a standard waste-disposal practice was written. After review by the Environmental and Health Protection Section of the Environmental Compliance Division, the suggestions received were incorporated into our standard operating procedures.

Drying studies. A drying cabinet design was tested using a glove box. Slow drying at room temperature is needed to avoid warpage and other evident strain. Relatively dry air is admitted to the cabinet periodically to maintain the set-point humidity as monitored by a meter. The satisfactory results of this test device permitted a design to be completed for a cabinet to hold sufficient samples for the full planned production rate. The cabinet was built and is being tested. For the tests, humidity was maintained by moisture from the test pieces, although a small water bath is used in the final design.

In supporting studies on drying, an automatic balance and an existing environmental chamber have been adapted for long-term studies. This should result in a fuller understanding of this centrally important stage of the process and permit optimal drying to be defined.

Grinding and specimen preparation. An automatic slicing machine to be used in cutting test specimens and performing surface-finishing operations was received and is being installed.

Status of milestones

A September 1989 milestone of choosing a silicon nitride formulation was met. A formulation decision has been made, and the first parts are now in process.

Publications

None.

References

1. M. J. Hoffman, A. Nagel, P. Greil, and G. Petzow, "Slip Casting of SiC-Whisker-Reinforced Si_3N_4," *J. Am. Ceram. Soc.* **72**(5), 765-769 (1989).

Improved Processing

Vimal K. Pujari* (Norton Company)

OBJECTIVE/SCOPE

The goals of this program** are to develop and demonstrate significant improvements in processing methods, process controls, and nondestructive evaluation (NDE) which can be commercially implemented to produce high-reliability silicon nitride components for advanced heat engine applications at temperatures to 1370°C. Achievement of this goal shall be sought by:

- The use of silicon nitride - 4% yttria composition which is consolidated by glass encapsulated HIPing.
- The generation of baseline data from an initial process route involving injection molding.
- Fabrication of tensile test bars by colloidal techniques - injection molding and colloidal consolidation.
- Identification of (critical) flaw populations through NDE and fractographic analysis.
- Correlation of measured tensile strength with flaw populations and process parameters.
- Minimization of these flaws through innovative improvements in process methods and controls.

*Other contributors are listed in the end of the text.

**"Research sponsored by the U.S. Department of Energy, Assistant Secretary for Conservation and Renewable Energy, Office of Transportation Systems, as part of the Ceramic Technology for Advanced Heat Engines Project of the Advanced Materials Development Program, under contract DE-AC05-840R21400 with Martin Marietta Energy Systems, Inc., Work Breakdown Subelement 1.1.4.1."

The quantitative program goals are: 1) mean RT tensile strength of 900 MPa and Weibull modulus of 20, 2) mean 1370°C fast fracture tensile strength of 500 MPa, and 3) mean 1230°C tensile stress rupture life of 100 hours at 350 MPa.

TECHNICAL PROGRESS

The technical progress against the major tasks, as described in the statement of work (SOW) is being described. The major tasks are: 1) Material Selection and Characterization; 2) Material Processing and Process Control; 3) Development and Application of NDE; 4) Property Testing and Microstructural Evaluation; 5) Reporting; 6) Quality Assurance.

In this period development efforts in the individual unit operations (sub tasks) leading to the total process are described. Where found suitable, fractional factorial design experiments based upon Taguchi method were conducted to optimize a particular unit operation No attempt was made at this stage to link various unit operations for the sake of total process optimization.

TASK 1

Material Selection and Characterization.
Material Selection A silicon nitride composition (with 4% yttria) is selected to perform the specified tasks and meet the required property goals. The silicon nitride powder to be used is derived from a diimide process such as that produced by Ube Ind.

Ube silicon nitride powder was chosen for its purity because it was observed that many of the carbothermally produced powders (Kemanord and Stark) contain significant amounts of iron impurities which lower the strength of the densified materials as flaws.

The above composition milled in alcohol has shown potential for meeting the targeted room and high temperature properties. In this program alcohol milled powder is chosen to develop the baseline Data employing injection molding as the Initial Process Route (IPR).

Subsequently, the 4% yttria silicon nitride composition for further process improvement will be processed in the aqueous medium and compared with the results obtained from alcohol milled powder.

Material Characterization Silicon nitride stock powders are analyzed for chemical composition, impurities, and particle size distributions. Phase analyses are carried out by x-ray diffraction.

Impurities are first assessed by emission spectrographic analysis. The cationic impurities are then determined by digestion of the powder, and analysis by AA, and ICP, and the anionic impurities are determined by ion chromatography. Surface area and particle size distributions are determined by BET, sedigraph, and light scattering techniques, to cover the range of fine particles.

Analyses are carried out at each unit operation leading to the total process, and the tests required at each step, as well as, the operational ranges, are defined by flowcharts such as depicted in Figure 1.

Verification and Validation

The results obtained from the above mentioned tests are verified as follows;

a) Samples sent for analysis, are separated into three sub-samples, and analyzed to obtain an estimate of the variation in the sampling procedure.

b) An additional sample is then sent to obtain verification of the results from the previous sample.
   * If the new sample lies in the range dictated by the previous results, an estimate of the actual average is then calculated and entered into the data base.
   * If the results from the new sample do not coincide with those obtained from previous analyses, step a) is repeated.

TASK 2

Material Processing and Process Control

The various sub tasks (unit operation) in this group are: i) Powder Processing; ii) Colloid Consolidation; iii) Injection Molding; iv) HIP densification; v) Machining and vi) Process Control.

i) Powder Processing

Effort in this unit operation includes comminution of powder blends and addition of yttria (4w%) in aqueous suspensions using solution precipitation technique. This unit operation is being developed in two concurrent stages. The procedure for aqueous milling and yttria precipitation technique is being developed using a small 500 gm batch milled in a closed loop vibratory mill. After drying, the powder

is cold isostatically pressed (CIP) into rectangular tiles and subsequently HIPed to achieve near theoretical density of 3.24gm/cc. MOR bars, 3mm x 4mm x 50mm, are being machined out of the tiles in order to evaluate the room and high temperature mechanical properties of this powder.

a) Technique Development

To silicon nitride powders milled in water with a surfactant, yttria was added from solution through a precipitation technique. Billets made from such powders with 4% Y_2O_3 were presintered and HIPed. The MOR bars made from such billets give flexure strength of 937 ± 83 MPa (for 15 bars) at room temperature and 599 ± 23 MPa (for 5 bars) at 1370°C. However, the stress rupture lives for 5 MOR bars were ≤ 40 hrs. at 1370°C at 300 MPa in air.

The causes of the low value of the stress rupture life is being investigated. The microstructure of the MOR bars is being examined and compared with that obtained from alcohol milled powder. The crystallinity of the grain boundary phase, and its composition, is also being examined. Also, the contribution of the metallic impurities from the surfactant to the powders are being evaluated.

The technique developed in the first stage is then applied to scale up the powder processing of milling and yttria addition.

b) Powder Processing Scale Up

The first 300kg lot of silicon nitride powder was procured. Of this, 100kg was alcohol milled with yttria powder to be used as a baseline comparison against water milling. A Class 10,000 hard-wall clean room has been constructed in which powder processing and colloidal consolidation will be performed. A Sweco vibratory mill was setup for both semicontinuous operation (8-30 kg) and batch operation (6-10kg). High purity silicon nitride milling media was specially fabricated for this program. The yttria precipitation technique has been scaled up.

The first batch cycle (6 kg) was made to "debug" the system and examine the effect of milling time in the large mill. The mill ran for 48 hrs. in a closed loop Sweco mode with no clogging. The particle size distribution of a 24 hr. sample was similar to t135HS weco. Other analysis is ongoing. Modifications to the yttria precipitation equipment were made based on results from this initial experiment, such as mixing technique and rate of base addition. The 24 hr. mill time will initially be used to generate powder and slurry for the forming operations of injection molding and colloidal consolidation, after which experimental design will begin to optimize chemistry and milling/precipitation parameters.

ii) Colloidal Consolidation

Two key steps in the colloidal consolidation development, i.e. slip formulation and tensile bar forming, are being developed simultaneously:

a) Slip Formulation
The objective of these experiments is to develop an aqueous suspension of silicon nitride containing 50-70 w/o solids for centrifugal/pressure casting of crack free NSF (Net Shape Formed) specimens. This requires development of suitable dispersant-binder system(s). As part of the initial screening process, various slips containing 60-70 w/o silicon nitride and combinations of binders (Bx) and dispersants (Dx) were prepared and pressure cast (into 76.2mm dia. x 12.7mm thick discs) at 0.2 MPa using colloid presses. Table 1 summarizes the lengths of time required for the green discs to develop visible cracks during drying in air under ambient conditions. From these screening tests a few potential slip formulations will be identified (see Table 1) for pressure/centrifugal casting of NSF bars.

b) Tensile Bar Casting
A centrifugal casting machine has been designed, built, and made operational. Initial operation of this machine led to several changes in design, primarily in the seals, to avoid leakage during the casting operation. Some changes in plaster mold design were also necessary for the same reason. Other mold materials have been

investigated including porous metal and plastic, and are currently being evaluated. Both centrifugal and pressure casting experiments are planned for the near future using the above mold materials and suitable slip formulation identified in section (a).

iii) Injection Molding (IM)

The three sub-steps in the injection molding (IM) process i.e. mold design, molding process optimization and dewaxing are being addressed concurrently. The IM process development was carried out using alcohol milled powder for which mechanical properties have already been established using four point bend MOR bars. As per SOW, the base line mechanical properties will be established using Initial Process Route (IPR) of injection molding employing alcohol milled powder.

a) Mold Design

In order to fabricate net shape tensile bars, three separate mold/gate designs were evaluated as shown in Figure 2. The double gated design 'G1' was made unbalanced to move the parting line away from the gage area. However, material flowed only from the larger of the two gates. At this point, therefore, the smaller gate was blocked and one gated design 'G2' was evaluated. Design G2 was evaluated with several different gate openings. With increasing gate size, better mold filling was observed which was further verified by microfocus x-ray (MFX) examination of as-molded tensile bars (see Task 3). It is obvious from the gate design G2 that the material has to flow a longer distance through converging and diverging flow paths. Therefore, an alternative gate design G3 (fan gate at the parting line) was evaluated. As expected, design G3 showed very different mold filling as compared to the design G2. Net shape tensile bars were, however, successfully molded using both the gate designs G2 and G3. These bars are presently being examined by MFX for soundness and dewaxability (see section (c) on dewaxing).

molding parameters. Molding batch A was used to evaluate gate designs G1 and G2 and conduct factorial design experiments. Molding batch B was used to evaluate the gate design G3. Molding results from batch A using gate design G2 and from batch B using gate design G3 are plotted in Figure 4. Batch A was molded under two different conditions. In each case after 10 moldings, bar weights seem to stabilize. Batch B, on the other-hand, was molded under a variety of conditions as evidenced by the plot to evaluate the mold filling and variations in the part-weight.

c) Dewaxing

Various combinations of environment, superimposed pressure and heating schedules were evaluated in the dewaxing of IM tensile bars. The heating schedules were designed based upon the TGA/DTA measurements on the binder and the powder/binder mixtures. Fixturing of tensile bars in the crucible both in the horizontal and the vertical orientations were also examined simultaneously. The results of these exploratory experiments are tabulated in Table 3. Orientation of the tensile bar in the crucible was found to have minimal effect. In vertical orientation, however, if the bars were not placed perfectly perpendicular to the base, minor buckling of the bar was observed. The dewaxing research, as is obvious from Table 3, is not yet complete. Nevertheless, net shape IM NSF bars have already been successfully dewaxed in whole in E_3 environment as shown in Figure 5. Further optimization of this dewax condition is on-going.

The dewaxed bars have also been degassed and are awaiting HIP densification.

iv) HIP Densification

For the purpose of evaluating net shape processing using the ASEA HIP process, ten CIPed and presintered rod blanks were submitted for green machining to near net shape prior to HIPing. An oversize part tolerance range of 0.010-0.040 inches was selected for evaluating warpage and reaction layer formation during HIPing. The seven rods which survived machining are being coated prior to HIPing to reduce reaction layer formation and HIP fixturing is being evaluated to reduce potential warpage problems during processing. These and injection molded samples will be HIPed shortly using a standard ASEA HIP cycle.

b) Molding Process Optimization
Experimental Design
Pre-iteration experiments have been carried out in injection molding in order to optimize machine settings that were thought to affect the characteristics of the molded NSF bars. These were done on a restricted scale using alcohol milled powder to generate baseline data. Formal linked designs will be carried out for process improvement in the second stage of the contract. The settings to be optimized over were; Barrel Temperature profile, Injection Speed Profile, Hold Pressure, Injection Pressure, and Mold Temperature. The quality of the molded piece was ascertained through the following characteristics; Molded Weight, and Voids detected by Microfocus x-ray. Based on the combined analysis of bar weight, and largest void size detectable by microfocus, machine settings (Table 2) were calculated, (and verified) which yielded the best results.

TABLE 2

Factor	Level
Injec. Speed Profile	**
Barrel Temp. Profile	**
Injec. Pressure Profile	+
Mold Temperature	+
Hold Pressure Profile	+

**highly significant *significant
+marginally significant

These settings, however, have been found to be highly sensitive to the starting conditions.

Figure 3 shows the correlation between the two key molding process variables and the optimum process regime.

Two large 8kg molding batches A and B were utilized to evaluate the mold/gate designs (as described in Section (a)) and optimize the

v) Machining

HIPed cylinder blanks were ordered to evaluate tensile bar geometries and procedures for mechanical testing. Some of these were machined at a local machine shop that has had experiences in this type of specimen. In addition, we performed machining trials to evaluate a new multi-axis CNC grinder at the machine builders shop. This unique grinding machine demonstrated the potential for significant reduction in machining time. Further testing will confirm whether tolerance and grinding damage is acceptable with this process. The Norton-Northboro machine shop is also machining some of the HIPed cylinders to standardize and evaluate their tensile bar grinding process.

vi) Process Control

a) Scheduling

Each step required in the manufacture of tensile bars has been broken into tasks and sub-tasks, down to individual operations. The availability of resources (furnaces/process equipment) and personnel operating them have been incorporated into a formal schedule. This allows for allocation of time on multi-user equipment to eliminate potential bottlenecks. This is a continuous process, and the schedule will be updated on a regular basis in order to include new operations and to keep track of current ones.

b) Database, Data Acquisition, Validation, and Analysis

A data acquisition/analysis scheme has been developed, which will simplify the process of data collection, validation and reporting. Data collection is being carried out through data-collection sheets filled by personnel involved in the various stages of the process. SPC charts, which will be used to flag deviations in the process, will be generated from data available in the database. This process will also serve as a data validation step, as all points outside specifications of SPC limits will be re-examined to ensure that no errors were made in transcription. Programs are currently being formulated to automate data entry and data reporting, so that the structure and identification and validation schemes will be transparent to the user.

TASK 3

Development and Application of NDE

A large number (>100) of injection molded tensile bars (from an experimental designed matrix for optimization of the process) were evaluated by microprojection film radiography. Voids appear to be the dominant type of defect existing in those samples; most of those voids are volume defects and exist mainly at the sample shoulder.

Using the x-ray data from these tensile bars a procedure has been devised to quantitatively report the flaw/defect population during various stages of processing for computerized material data base filing. The method briefly allows for storing pertinent flaw frequency and size distribution and location (surface versus volume) as obtained using microfocus radiography, ultrasonics and computer tomography.

Reference tensile samples with known seeded Fe inclusions have been prepared for use in quantitative NDE reliability of detection study. They were dry pressed, degassed, presintered and then HIPed. Size range of seeded Fe particles covers 20 to 200 um. The samples are presently being radiographed and will be used by subcontractors soon. Reference samples with simulated voids and density gradients are presently being made.

A number of HIPed and machined tensile Si_3N_4 samples, which are being tested as part of developing the tensile testing procedure using Cu/steel collets (avoiding the grip failure problem), were inspected before testing using microfocus radiography. The samples appear to be clean of defects except for very few inclusion particles which are <100 um in size. The objective is to be sure to isolate sample failure due to testing technique as opposed to those due to presence of defect.

TASK 4

Property Testing and Microstructural Evaluation

a) Tensile Testing: Design and Procedure

In light of recent problems in tensile testing (buttonhead failures) alternative specimen geometries and gripping fixtures have been considered. Originally stainless steel collets were used to test cylindrical specimens. Two sets (1 set = 6 split collets) of oxygen free copper collets have been ordered and received. Thirty

machined silicon nitride tensile rods have been ordered as have 30 as-hipped right cylinders. To date, thirteen right cylinders have been received.

The University of Dayton Research Institute has had success using the copper collets at both room and high temperatures. A brief outline of our proposed tensile testing procedure follows:

1. Align grips and specimen
2. Slowly load specimen to a predetermined load << the expected failure load and hold for a short (5 min.) duration
3. Fast load to failure

The slow load and soak allows the copper collet to conform to the buttonhead radius and potentially decrease the stress concentration on the buttonhead.

A fixture to be used for green and presintered tensile testing has been designed and ordered. The design employs a tapered rubber bushing for gripping the specimen.

REFERENCES

None

STATUS OF MILESTONES

All milestones are on schedule.

COMMUNICATIONS/VISITS/TRAVEL

o V. K. Pujari to New London, NH to attend Gordon Conference on "Novel Processing for Flaw Free Ceramics," August 14-18, 1989.

o V. K. Pujari, D. M. Tracey to ORNL, Oak Ridge, TN to discuss program plans and management issues, September 6, 1989.

o K. E. Amin, A. C. Stevens and J. A. Garwood to Precision Acoustic Devices (PAD), Freemont, CA to finalize NDE subcontracts, August 21-23, 1989.

o M. R. Foley visited UDRI, Dayton, OH to discuss tensile testing procedures, September 22, 1989.

PROBLEMS ENCOUNTERED

None

PUBLICATIONS

None

TECHNICAL CONTRIBUTORS

Vimal K. Pujari
Kamal E. Amin
Param H. Tewari
Craig A. Willkens
Norman I. Paille
Ajay K. Garg
R. Dennis Creehan
Michael R. Foley
Lenny C. Sales
Dennis M. Tracey
Stuart Tuffs
Stephen D. Hartline

TABLE 1

TIME REQUIRED FOR THE VARIOUS GREEN BODIES TO DEVELOP VISIBLE CRACKS DURING DRYING IN AIR UNDER AMBIENT CONDITIONS.

BINDER / DISPERSANT	NONE (Bo)	B1	B2	B3	B4	B5
D3	1 DAY	NO CRACKS	1 DAY	1 DAY	NO CRACKS	1 DAY
D4	10 DAYS	5 DAYS	<1 MIN	NO CRACKS	--	--

"NO CRACKS" MEANS THE GREEN BODY WAS CRACK FREE AFTER DRYING FOR 10 DAYS.

TABLE 3

DEWAXING PARAMETERS FOR INJECTION MOLDED TENSILE BARS

DEWAX ENVIRONMENT / HEATING SCHEDULE	E_1	E_2		E_3	
		LOW PRESSURE	HIGH PRESSURE	LOW PRESSURE	HIGH PRESSURE
SLOW HEATING RATE	BLISTERING BREAKAGE	BREAKAGE	BREAKAGE	BLISTER FREE BREAKAGE FREE	—
FAST HEATING RATE	BLISTERING BREAKAGE	—	BREAKAGE	—	—

BLISTERING - FAST EVOLUTION OF BINDER CAUSED BLISTERING AND BUBBLE FORMATION

BREAKAGE - BARS BREAK TRANSVERSELY AT TRANSITION POINTS AND IN THE MIDDLE OF THE GAGE AREA

Process Step	Estimated Duration Day/Hour/Min	Control Parameter	Measure Variable	Measure Technique
Receive alcohol milled powder from	Should be received as needed. X		Surface Area Particle Size Dist. Bulk Chem.: Oxygen Carbon Water Inclusion (size)	BET Single point Sedigraph LECO LECO Carl-Fisher Microfocus Radiog.
Coat with SURFACTANT #1 in P-K Blender.	X Hours	Time. Conc. of SURFACTANT		
Vacuum Dry	X Days X Hours	Time. vacuum Level. Temperature.	Amt. of SURFACTANT COATING	LOI Test
Dry Mill and Screen	X Days X Hours	Time. Mill rotation Speed. Screen size.	Surface Area. Particle Size Dist. Packing density. Contaminants	BET Single point Sedigraph Die-pressing Microfocus radiog.
Coat with SURFACTANT #2 in P-K Blender	X Hours	Time. Coating Concentrat.	Amt. of coating	LOI Test
Dry in Vacuum	X Days X Hours	Time. Temperature. Vacuum level	Coating existence Coating existence	IR IEP (PenKem)
Compounding	X Days	Binder Powder ratio Temperature. Time. Blender Speed.	Binder/Powder Ratio Iron Content Viscosity Inclusions	LOI test Emission Spectrosco Atomic Adsorption Capilliarometer Microfocus radiog.
De-airing and Pelletizing.	X Days (accum. 4 batches)	Temperature. Vacuum level. Pellet Size. Screw Speed.	Binder Distribution Binder/Powder Ratio Iron Content. Viscosity. Inclusions	NMRS LOI test Emission Spectrosco Atomic Adsorption Capilliarometer Microfocus Radiog.
Injection Molding.	X Days	Barrel Temperature. Nozzle Temperature. Hold Temperature. Injection Pressure. Hold Pressure.	Weight. Density Strength Dimensions Defect Character.: Voids Density Grad. Inclusions Cracks Voids Density Grad. Cracks Voids Density Grad. Inclusions Bindr/Powdr Xact	Scale Wax Break(MPa)+ Weib B Length meas. Microfocus Rad. (Film Digit.) Ultrasonics Computer Tomog. NMRS
De-Waxing and Air Burning.	X Days	Time. Temperature. Atmosphere. Heating Rate.	Shrinkage. Weight Loss. Carbon Content. Oxygen Content.	Length & Volume Scales LECO LECO
De-Gassing.	X Week	Time. Temperature. Atmosphere.	Strength. Carbon Content. Oxygen Content. Defect Characteriz. Voids Density Grad. Cracks Voids Density Grad. Porosity Inclusions Binder Removal	Break(MPa)+ Weib B LECO LECO Ultrasonics Computer Tomog. NMRI
HIPing.	X Days	Fixturing. Barrier Coating. Temperature Profile Hold Time. Pressure.	Density. Dimensional Change. Reaction Layer. Defect Characteriz.	Weight in water Length & Vol. Meas. SEM
Machining.	X Days	Rotational Speed. Feed Rate. Coolant.	Density. Surface Finish. Defect Character.: Surface flaws Voids Density Grad. Porosity Inclusions Cracks Voids Density Grad. Porosity Cracks Voids Density Grad. Porosity Inclusions	Weight in water Prophylometer Dye Penetrant Microfocus Rad. (Film Digit.) Ultrasonics Computer Tomog.
Testing.	X Days	Temperature. Loading rate.	Strength. Fractography Voids Inclusions Carbon Content. Oxygen Content.	Break(MPa)+ Weib B SEM Visual Exam LECO LECO

Figure 1. INITIAL PROCESS ROUTE FLOW DIAGRAM

(Alcohol Milled - Injection Molded - NSF)

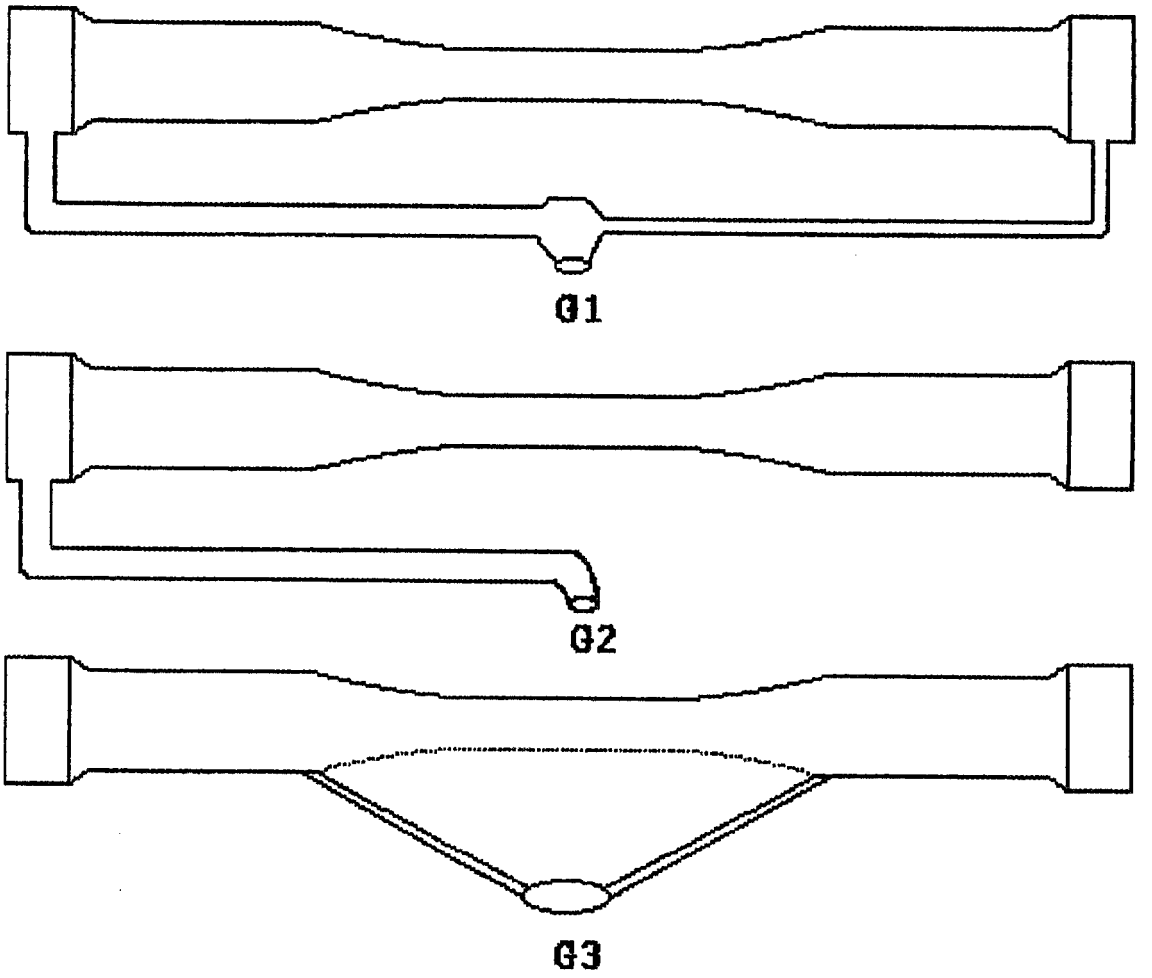

Figure 2. Gate Design for Tensile Bar Mold
(G1) Double Gate (G2) Single Gate (G3) Fan Gate

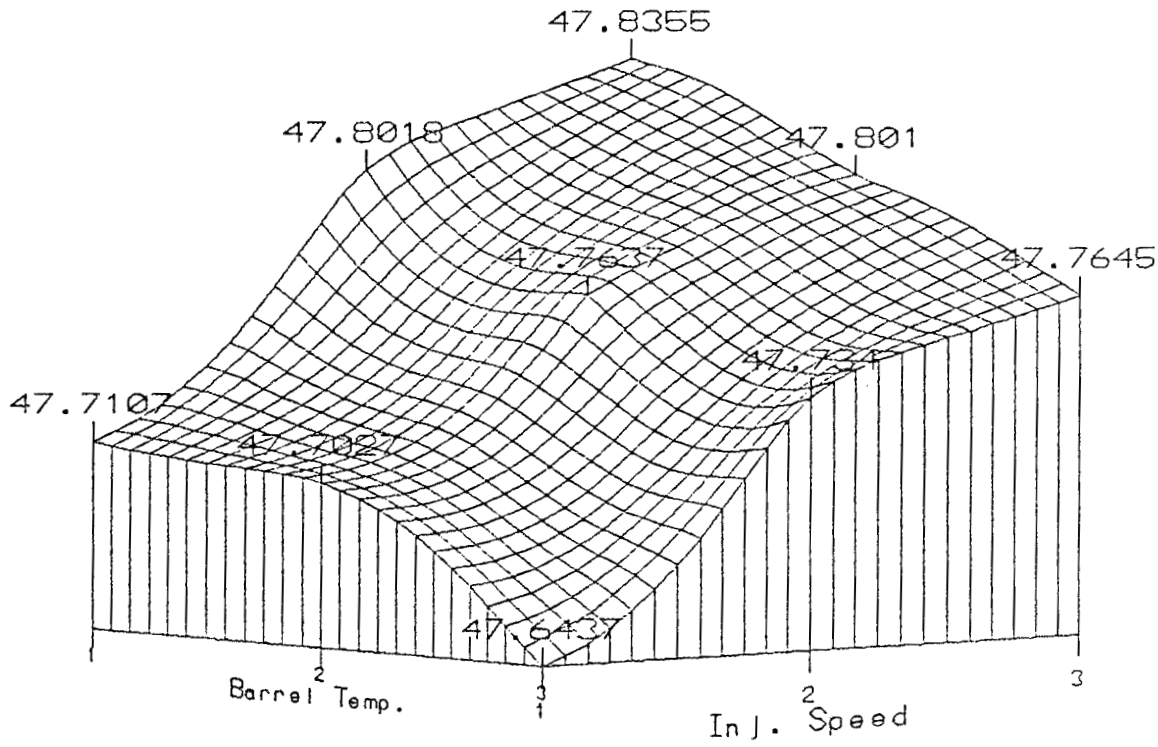

FIGURE 3 Weight of injection molded NSF bars as a function of Barrel Temperature and Injection Speed

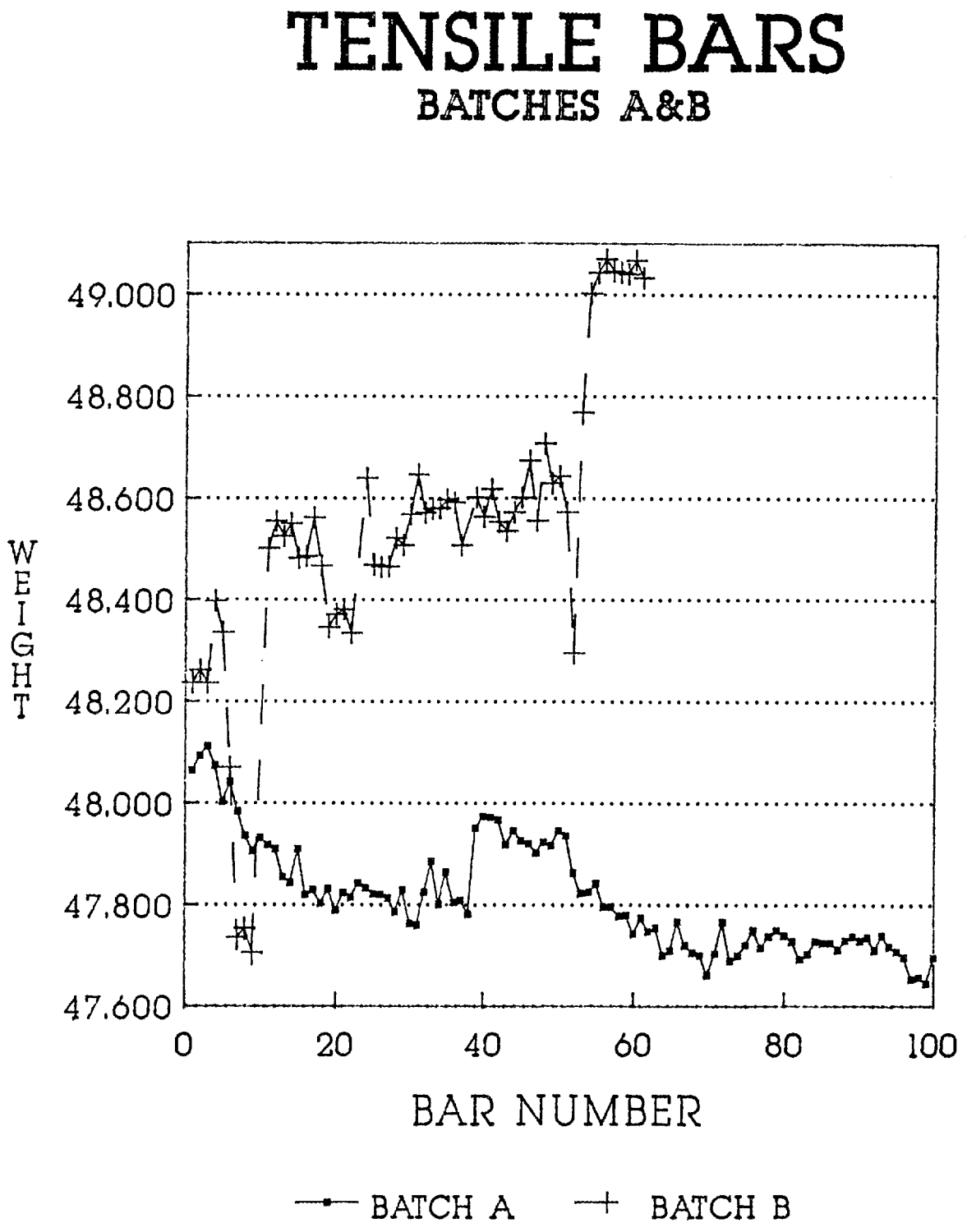

FIGURE 4 Weight (gm) of molded NSF bars as a function of molding time

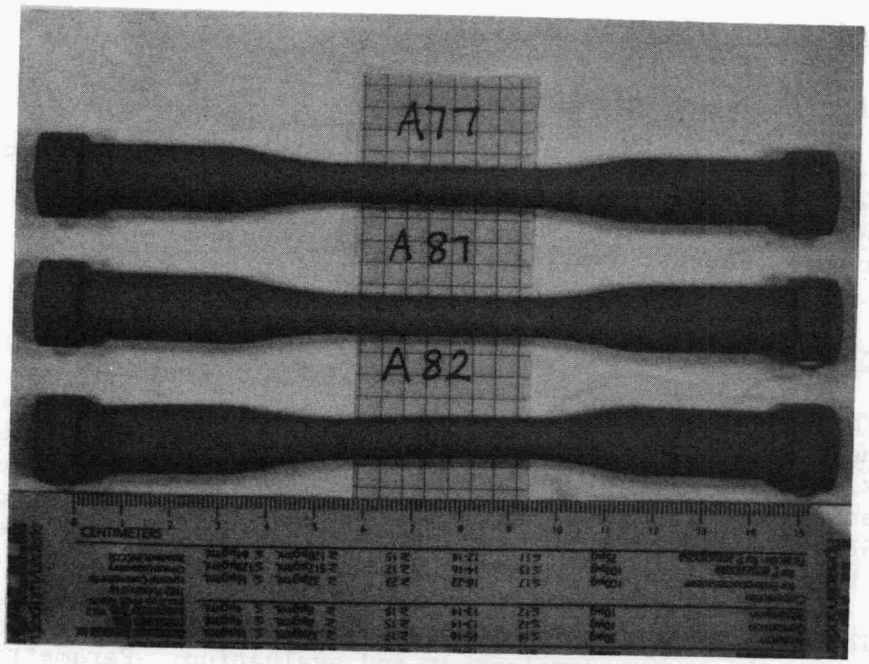

FIGURE 5 Injecion molded, dewaxed and presintered NSF bars

1.2 CERAMIC COMPOSITES

1.2.2 Silicon Nitride Matrix

SiC-Whisker-Toughened Silicon Nitride

H. Yeh, E. Solidum (Garrett Ceramic Components),
K. Karasek, G. Stranford and D. Yuhas (Allied-Signal Research and Technology),
S. Bradley (UOP Research Center), and
J. Schienle (Garrett Auxiliary Power Div.)

OBJECTIVE/SCOPE

The objective of this program (Phase II) is to maximize the toughness in a high strength, high temperature SiC whisker/Si_3N_4 matrix material system that can be formed to shape by slip casting and densified by a method amenable to complex shape mass production. The ASEA glass encapsulation hot isostatic pressing (HIP) technique shall be used for densification throughout the program.

The program is divided into seven technical tasks with multiple iterations of process development and evaluation. Parametric studies shall be conducted to optimize processing steps developed in the Phase I effort, guided by established analytical and NDE techniques. The seven technical tasks are: Task 1 -Selection of SiC whiskers, Task 2 - Baseline Casting Process, Task 3-Parametric Densification Study, Task 4 - Effect of Specimen Size and Shape, Task 5 - On-Going Evaluation of Alternate Whisker, Task 6 -Nanometer Deposition of Sintering Aids, and Task 7 - In Process Characterization and Process Control During Drying of Cast Ceramic Parts.

The technical effort was initiated in May 1988. Task 1 was completed in January 1989. Based on the results, HF-etched American Matrix Inc. SiC whiskers were selected for use for Tasks 2 -4. Task 2 was initiated in February 1989 and was completed in June 1989. Task 3 effort was initiated in July 1989.

Tasks 5, 6 and 7 were added onto this contract to supplement the mainline activities. These efforts were initiated during this reporting period.

TECHNICAL HIGHLIGHTS

TASK 1 - Selection of Whisker

All technical efforts have been completed and the results were summarized in Semi-Annual report October 1988 - March 1989. Based

on the results, HF-etched American Matrix SiC whiskers selected for use under Tasks 2-4.

TASK 2 - BASELINE CASTING PROCESS

The objective of this task is to develop a green forming process from powder preparation through slip casting, for composites containing 10, 20, 30 and 40 wt.% SiC whiskers. The matrix material is Garrett Ceramic Components' GN-10 Si_3N_4 formulation and the whisker are HF-etched American Matrix SiC. The optimized green composites shall be used for investigation under Task 3 Parametric Densification studies. Under this task, detailed characterizations shall be performed on the starting materials (matrix powders and whiskers), and in-process materials (slips, castings, etc.) by NDE and destructive techniques.

To maintain consistency in whisker properties a lot of 13-kg American Matrix SiC whiskers (designated as AM7 by Allied-Signal) has been purchased for this program. This lot of whiskers has been HF-etched and then Argon thermal treated to reduce the amount of surface SiO_2 layer (at American Matrix) as recommended by Task 1 results. A lot of 50 kg of Si_3N_4 powder was set aside for this program in order to minimize potential lot-to-lot variations in Si_3N_4 powders.

A) Characterization of Si_3N_4 Powder and SiC Whiskers

o Powder and Whisker Chemistry

The Denka 9S Si_3N_4 powder (Lot 91096) used was analyzed by induction coupled plasma emission spectroscopy (ICP) for impurities. Results follow in Table I.

Table I

Bulk Chemical Impurities in Denka 9S Si_3N_4 Powder

Element	Weight Percent
Ca	0.23
Fe	0.13
Al	0.15
Na	0.0023

Bulk carbon, nitrogen, and oxygen levels were obtained for the Denka 9S Si_3N_4 powder and the AM7 SiC whiskers. The C and N were measured by a fusion technique‡, and O content was determined by neutron activation analysis*. Results follow in Table II.

Table II

Bulk C, O, and N Contents

(Weight % +/- 0.1)

Element	Denka 9S Si_3N_4 Powder	AM7 SiC Whiskers
C	0.3	29.8
N	38.2	0.1
O	1.8	1.2

Theoretical levels of C in SiC and N in Si_3N_4 are 30.0 and 39.9 wt.%, respectively.

The surface chemistry of the Denka 9S Si_3N_4 powder was analyzed by X-ray photoelectron spectroscopy (XPS). The results, given in Table III, are not particularly surprising; the surface is primarily Si_3N_4 with some silicon oxynitride.

---

‡ Measurements performed by Multichem Laboratories, Inc., Lowell, MA.

* Neutron activation analysis performed at the Center for Trace Characterization, Texas A&M University, College Station, TX.

Table III

XPS Results for Denka 9S Si_3N_4 Powder

Species	Atomic Percent	Binding Energy (eV)	Comments
Si2p	27.9	101.3	Si_3N_4
Si2p	5.9	102.8	oxynitride
Si2p	1.5	104.0	
C 1s	4.5	284.6	
C 1s	1.1	288.6	
Ca2p3	0.6	347.3	
N 1s	29.8	396.9	Si_3N_4
N 1s	4.0	398.3	
O 1s	24.1	531.8	
F 1s	0.7	684.6	

The XPS data for AM7 SiC whiskers is given in Table IV. [Also presented is the data for three previously characterized American Matrix SiC whisker samples. AM5 is the designation for the as-received whiskers used in Task 1 of this program. These whiskers were etched and heat treated in argon at Allied-Signal for the second part of Task 1; they were then given the designation AM5E.]

Clearly, the HF etch has removed most of the surface SiO_2. The AM7 major-component-surface chemistry is fairly similar to that of the AM5E; it does not at all resemble that of the unetched AM5 whiskers which is dominated by SiO_2.

Considering the surface impurity levels, the Ca is the one major surprise. The high level, however, is not expected to cause problems. Fe appears to be low enough to avoid concern about it catalyzing degradation. The F level is much higher than on the AM5E whiskers. It is not clear why this is the case, although some of the fluorine may be tied-up with the Ca. We haven't been able to determine any positive or negative effects of fluorine in our composites so far.

Table IV

XPS Surface Chemistry Data for SiC Whiskers

Atomic % (Binding Energy in eV)

	AM7*	AM5E	AM5#
Si 2p	31.7(100.5)	29.4(100.4)	15.9(100.5)
Si 2p	2.7(102.2)	6.0(101.9)	17.3(103.2)
Si 2p		3.2(103.1)	
C 1s	29.2(282.4)	28.8(282.4)	13.6(282.4)
C 1s	4.6(284.4)	9.4(284.4)	2.8(283.9)
C 1s	1.1(290.2)		1.9(285.3)
O 1s	18.0(531.7)	16.3(531.9)	8.1(531.3)
O 1s			37.5(532.4)
N 1s	2.2(397.8)	3.7(397.5)	
Ca 2p3	5.5(347.5	0.9(348.3)	1.7(347.9)
Fe 2p3	0.3(711.9)		
F 1s	4.7(684.5)+	1.5(685.5)	
Al 2p		0.8(73.7)	

o Whisker Morphology

The AM7 were also examined by scanning transmission electron microscopy (STEM). The morphology was very similar to that of recent American Matrix SiC whiskers including the AM5 whiskers. One minor difference observed was an increase in the amount of Ca impurity present, which is consistent with the XPS surface chemistry.

---

* Received from American Matrix, Inc., Knoxville, TN in March 1989

\# Received from American Matrix, Inc., Knoxville, TN in March 1988

\+ Value taken from broad energy survey scan rather than high resolution scan; therefore, the accuracy will not be as high as for the other values shown.

o Whisker-Length Measurements

Whisker length distributions were measured for the AM7 whiskers and the green composite samples. Measuring the whisker length distribution in green composite samples was to assist process development to be described in the next subsection (Processing). Small amounts of whiskers or green samples were dispersed in NH_4OH solution. One or two drops of the suspension were deposited on a glass slide and allowed to dry. (The actual NH_4OH concentration was not determined. The dispersion was diluted until there was little overlap of whiskers on the slide. If the NH_4OH concentration became too low, the Si_3N_4 powder would tend to agglomerate onto the whiskers. When this became a problem, additional NH_4OH was added.) An Omnimet II™ image analysis system* was used to measure whisker length distributions. Particles or whiskers with aspect ratio less than 3 were ignored and assumed to be particulates.

As part of process optimization effort we experimented with mixing/milling procedures for the powder/whisker blends. These are summarized in Table V. We have performed whisker-length measurements to determine any deleterious effects of these procedures upon the whiskers.

Table V

Blending Procedures

Iteration	Deflocculant	Blending Method
1	A	standard ball mill
3	B	standard ball mill
4, 5	B	tumbled with 5 balls

(The only difference between iterations 4 and 5 is the amount of sintering aids added. In #4 the ratio of the amount of sintering aids to that of silicon nitride is constant. In # 5 the ratio of the amount of sintering aids to total weight is constant.)

The data for the as-received AM7 whiskers and for the whiskers in the green composites under iterations 1, 3, 4, and 5 are given in Table VI. The term "uncertainty" is an indication of statistical error related to sample size. The "standard deviation" is a measure of the width of the distribution. The third and subsequent iterations do appear to damage the whiskers less than

---

* Image analysis measurements were performed at Buehler Ltd., Lake Bluff, IL. Omnimet II is a registered trademark of Buehler Ltd.

iteration 1. Among the later iterations, there appears to be very little difference attributable to changes in the mixing/milling technique. The 30%-third-iteration data is much higher than that of the other samples. Since the number of whiskers measured in this case was low, it is probably a bad data point.

Table VI

Whisker Length Distribution Data

Whisker Content	Iteration #1	Iteration #3	Iteration #4	Iteration #5
10%	13	19+/-3 (13)	18+/-2 (15)	19+/-1 (15)
20%	14	20+/-2 (14)	17+/-2 (10)	
30%	15	26+/-4 (15)	19+/-2 (12)	
40%	18	17+/-1 (11)	19+/-2 (13)	
100%	19	(As Received AM7)		

Longest Dimension +/- Uncertainty (Standard Deviation of Distribution)

Uncertainty = (Longest Dimension) / (No. of Whiskers Measured)1/2

All dimensions in microns.

B) Processing

Due to the HF-etching and washing/infiltration procedures performed on the whiskers at American Matrix Inc. prior to shipping to Garrett Ceramic Components, it was found that the whiskers do no contain any detectable undesired foreign substance; therefore, not requiring any further washing/ cleaning. A series of sedimentation experiments were performed to determine the feasibility of reducing the whisker length distribution with a reasonable yield. The results indicated that the length distribution is already too narrow to be further reduced with a good yield. Thus, it was decided that the whiskers in the as-received state shall be used under this task.

The composite slips were prepared by blending the matrix GN-10 Si_3N_4 slip with the appropriate amounts of SiC_w, water and deflocculant. The GN-10 slip was prepared following the procedures established under the ATTAP subcontract at GCC (NASA/DOE DEN3-335 Subcontract 1774888). The composite slip was cast under pressure into a mold with four (4) cavities, each measured 2"x3". After casting, the composite plates were dried. After drying, plates were

inspected visually and by microfocus X-ray; and selected plates were sectioned for microstructural analysis. Figure 1 shows the generalized process flow chart.

An iterative experimental approach was used to establish an improved processing for green composites containing 10, 20, 30 and 40 wt.% SiC_w. In-process (monolithic and composite slips) as well as post-process (the dried green plates) characterizations were conducted. A total of five iterations had been conducted. The optimized green plates were used under Task 3A Parametric Densification Study, discussed later in this report.

o <u>First Iteration</u>

The baseline process (the process used under Task 1) was used to fabricate 10, 20, 30, and 40 wt.% SiC_w composites using the selected AM7 SiC whisker, and to identify areas of processing improvements. (Only 20 wt.% SiC_w loading composites were fabricated under Task 1) The slip properties are listed in Table VII.

Visual inspection of the plates did not find any external defects, however, internal cracks and voids were detected by a real time microfocus X-ray machine. It was found that the 10 and 20 wt.% SiC_w composites had cracks while the 30 and 40 wt.% SiC_w had voids. The cracks were attributed to the drying cycle used, while the voids were entrapped air because of the high viscosities of the 30 and 40 wt.% SiC_w composite slips. These internal defects probably existed in the green composites fabricated under Phase I and Task 1 of this Phase but were not known, because the higher resolution microfocus X-ray was not used.

One plate of each SiC whisker loading was sectioned along the vertical direction (casting direction) and the horizontal direction to evaluate whisker dispersion and orientation using an optical metallograph. It was found that the whiskers were uniformly dispersed in all four composites and there was no noticeable difference in whisker orientation between the vertical and horizontal sections of the composite plates. The lack of preferred orientation could be due to the thinner thickness of the plate (thus shorter casting time) as compared with the taller cylindrical billets fabricated under Task 1.

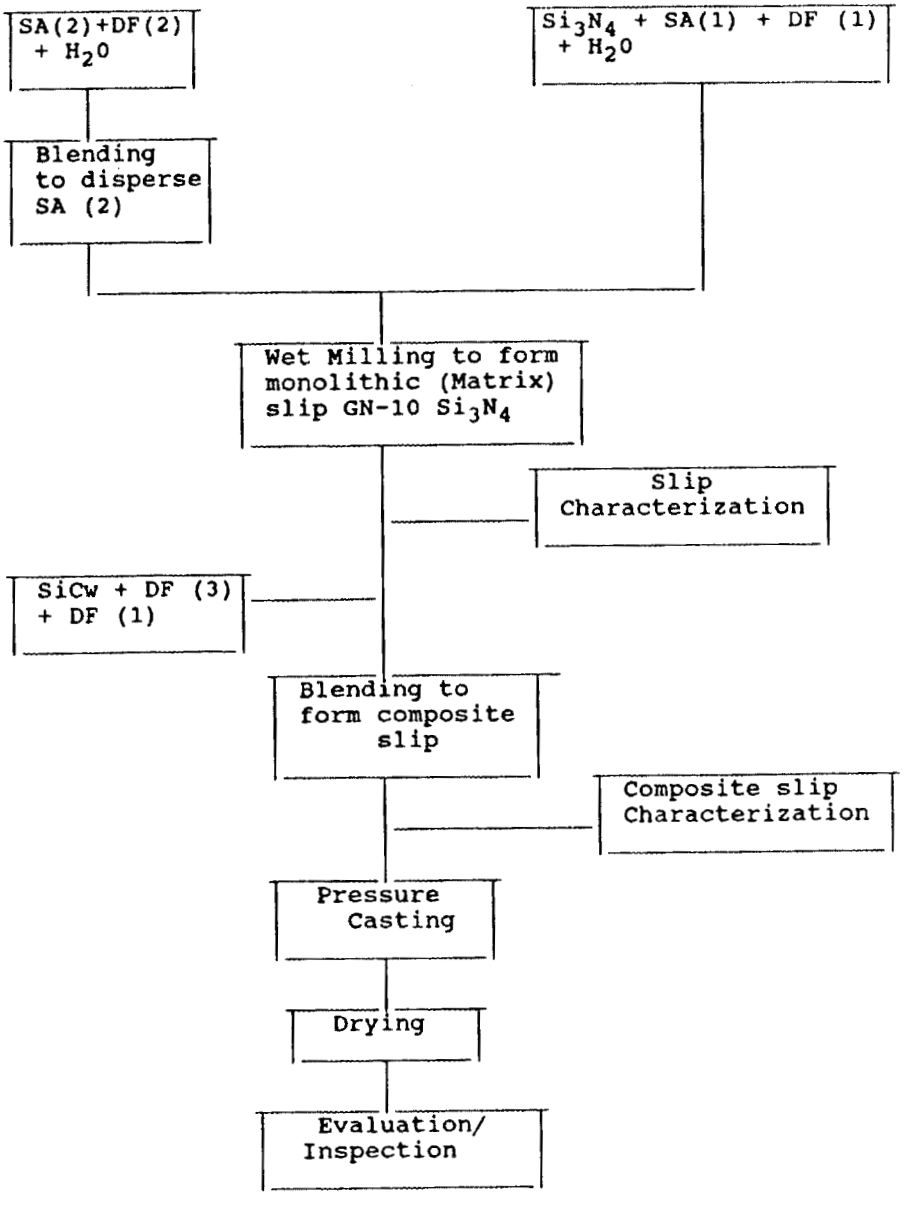

Note:
SA(n): Sinter Aid (n), where n= 1,2,3
DF(n): Deflocullant (n) where n= 1,2,3

Figure 1. Process Flow Chart

TABLE VII

FIRST ITERATION COMPOSITE SLIP PROPERTIES

Wt.% SiC_w	% Solids	Viscosity (cps)	pH	Sp. Gravity (g/cc)
10	74	363	10.38	2.01
20	70.1	691	10.25	1.90
30	64.6	1068	10.17	1.76
40	59.2	2684	10.28	1.66

o Second Iteration

In this iteration, the issues of internal cracks and voids were addressed. In addition experiments were conducted to estimate process boundaries in the slip properties and the green composite plates. Also, the effect of blending time was evaluated. A total of twelve batches of experimental composite castings were made.

To determine the effect of drying cycle on internal cracks, two plates of each batch (4 plates/batch) were dried using the baseline cycle (cycle #1) and the other two dried using an alternate drying cycle developed under the ATTAP program (cycle #2).

The approach to reducing the internal voids was to reduce the slip viscosity by modifying the slip preparation procedure, in particular the deflocculant chemistry. It was also found that the baseline deflocculant did not produce a consistent slip viscosity. A series of experiments was conducted to identify an alternate deflocculant system to be used when the whisker is blended with the monolithic GN-10 slip. The initial experiment showed that the alternate deflocculant produced a lower viscosity as well as more reproducible slip.

It is generally believed that a shorter blending time would minimize whisker damage. An experiment was conducted to evaluate whether the baseline 30 minute blending time was necessary to achieve a good quality slip. Ten and 20 minute blending time were tried and did not produce homogeneous slips. Thus, the baseline 30 minutes, which produced homogeneous slip, is the optimum blending time.

Green composite plates were inspected visually and then by real time microfocus X-ray. Again, no external defects were observed. The tendency to form internal cracks was reduced when drying cycle #2 was used. The amount of voids was reduced as the viscosity was reduced.

o Third Iteration

The alternate deflocculant developed under the second iteration was used to fabricate two complete sets of composite plates (10, 20, 30 and 40 wt.% SiC_w) to establish slip property boundaries. The viscosities of the slips ranged from 220-660 cps, compared with 363-2684 cps in the first iteration and 534-1200 cps in the second iteration, for all whisker loadings. The viscosity variation for a given whisker loading was much narrower than those observed in the second iteration. (The first iteration only had one batch per whisker loading.) The specific gravities and the pH values of the composite slips were all reproducible within experimental limits.

All composite plates were inspected by microfocus X-ray. Two drying cycles were used for each batch of composites to provide more data on drying cycle effect. Again, the amount of porosity decreased when the slip viscosity was reduced, and the internal cracks were only observed in one plate out of eight inspected. The cracked plate was dried using the baseline cycle (cycle 1).

o Fourth Iteration

Although significant improvements were made under iteration #3 in achieving higher reproducibility in composite slip properties and reduced internal defects in the green casting, it was felt that there is a potential for whisker damage during the standard 30 min. milling which was used to blend the whiskers with the matrix slip in the first three iterations. Under this iteration, a new blending technique was developed in which the composite slip was blended in a plastic bottle with five Si_3N_4 balls (5/8" dia.). A controlled amount of whiskers was added at a given time interval and the slip was rolled (tumbled) on a mill rack for a controlled length of time at a controlled RPM. To achieve good whisker dispersion, the solids contents of the composite slip were reduced by 5 wt.% from their counterparts in the third iteration. The slip properties and green casting densities were very reproducible as demonstrated in Table VIII. The viscosity range (100-270 cps) is much lower than that in the third iteration (220-660 cps). Lower viscosity is desired for further improving the quality of the castings. The achievement of good whisker dispersion was verified by SEM and optical metallography. The length distributions of whiskers in the composites were measured on samples taken from green castings using the technique described earlier. The results showed that the whiskers in the composites retained the starting length of whisker (average 19 μm). The data were shown in Table VI. In addition the quality of the castings were improved over those of the third iteration based on visual and X-ray inspections. The processing procedure established under this iteration was considered optimum and the composite castings will to be used under Task 3A.

TABLE VIII

FOURTH ITERATION

COMPOSITE SLIP PROPERTY AND GREEN CASTING DENSITY

WHISKER CONTENT (Wt %)	BATCH NO.	pH	VISCOSITY (CPS)	ZETA POTENTIAL	SPECIFIC GRAVITY (g/cc)	SOLIDS CONTENT (wt %)	GREEN DENSITY (g/cc)
10	1	10.04	120	8.7	1.93	69.0	1.89
	2	10.04	100	8.6	1.90	69.0	1.85
20	1	10.17	211	4.0	1.81	64.3	1.76
	2	10.22	220	8.9	1.80	64.3	1.69
30	1	10.47	242	10.4	1.68	58.7	1.51
	2	9.90	130	8.5	1.67	58.7	1.50
40	1	10.47	270	11.9	1.56	52.7	1.17
	2	10.20	130	9.9	1.57	52.2	1.24

o Fifth Iteration

The processing procedure established under the fourth iteration was used to fabricate a new series of composites in which the sintering aids level in the starting Si_3N_4 powder formulation, prior to blending with the whiskers, was increased proportionally to the whisker loading. The purpose of this sintering aids level adjustment was to maintain the concentration of sintering aids relative to the sum of Si_3N_4 and SiC whiskers in the composite the same as that in the monolithic GN-10. The composites made so far in this program were starting with standard GN-10 Si_3N_4 formulation. After SiC whiskers (without sintering aids) were blended into this standard GN-10 powder, the effective concentrations of sintering aids in the matrix were correspondingly diluted. This was the approach used in Phase I of this program as well as almost all of the literature work. With sintering aids level adjustment, the sintering aids concentration in the matrix should be closer to, if not identical to, that of the baseline monolithic GN-10 independent of whisker loading. This series of composites is required for Task 3A statistical matrix parametric densification study. Two batches of composites with each whisker loading (10, 20, 30, 40 wt.%) were fabricated for use under Task 3A. The slip behavior and casting properties were similar to those under the fourth iteration.

TASK 3 PARAMETRIC DENSIFICATION STUDY

Three subtasks (A, B, and C) shall be conducted to evaluate the effects of key densification parameters on microstructures/ properties of Si_3N_4/SiC(w) composites. An optimum process/whisker loading shall be selected for detailed property evaluation (subtask C) as well as specimen size and shape effect study (Task 4). Only Subtask A was conducted during this reporting period.

A) Statistical Matrix

A statistically designed HIP matrix experimental plan was submitted to ORNL and was subsequently approved for implementation. The plan consists of five HIP runs at 25 ksi, to be conducted at two stages. The first stage consists of four HIP runs. Based on the most pertinent results of these four runs (density, hardness, indentation toughness and optical microstructure), the HIP parameters for the fifth HIP run shall be selected. Each HIP run will contain eight different composite plates (approximately 2"x3" x1/2") plus one baseline GN-10 plate. The eight composite plates in each HIP run consist of 10, 20, 30, and 40 wt.% SiCw plates fabricated under 4th iteration (Task 2), and 10, 20, 30 and 40 wt.% SiCw plates fabricated under 5th iteration (Task 2). As already explained, the difference between 4th and 5th iteration samples was in sintering aids level. In the 4th iteration, the weight ratio of (sintering aids)/(Si_3N_4) was a constant regardless of the SiCw loading, while in the 5th iteration the weight ratio of (sintering aids)/(Si_3N_4 + SiCw) was a constant. After densification, in the 4th iteration samples, the effective concentration of sintering aids in the matrix phase will decrease with the increase in whisker loading. The approach used in 5th iteration was an attempt to maintain the sintering aids concentration in the matrix phase independent of the whisker loading.

A two level L-4 design was selected for the first stage four HIP experiments; the parameters were: T1^{o}C/t1 hr, T1^{o}C/t2 hr, T2^{o}C/t1 hr, and T2^{o}C/t2 hr. The high temperature (T2) and long hold time (t2) combination (T2^{o}C/t2 hr) has been the baseline HIP parameter at Allied-Signal for the monolithic matrix material (GN-10). A lower temperature, shorter hold time, and a combination of both (T1/t1) were selected for the other three HIP runs. These less severe HIP conditions were primarily chosen in an attempt to achieve weaker bonding between the whisker and the matrix, yet still achieve high density composites (>95% full density). A weaker interfacial bonding is believed to produce longer whisker pullouts which in turn would result in higher fracture toughness. It is anticipated that the microstructure of the matrix densified under these four HIP conditions will also be different. These microstructural variations would also have a significant impact on the fracture toughness and strength of the composites. Under this subtask, only small size specimens were fabricated. Therefore, only microhardness and

indentation toughness shall be used to obtain preliminary indication of the relationship between HIP parameters and the mechanical properties of the composites.

Densities of the as-HIP'ed plates are listed in Table IX and plotted in Figures 2 and 3. As a reference, percent of theoretical densities, based on rule-of-mixture, are also listed in Table IX. Because of the approximation used in the calculation, some of the composites exhibit densities greater than theoretical. It was encouraging to note that monolithic GN-10 achieved full density under all four HIP conditions, and also all the composite samples except four achieved densities greater than 3.2 g/cc. As expected, the 5th iteration samples achieved higher densities than the 4th iteration, especially those with 30 wt.% or greater SiC_w loading. Samples were cut from each plate and are in the process of detailed characterization which includes indentation toughness, hardness, Young's modulus, optical metallograph (whisker distribution and orientation), STEM (matrix microstructure, whisker and whisker/matrix interface).

TASK 4 SPECIMEN SIZE AND SHAPE EFFECT

Not initiated yet

TASK 5 ALTERNATE WHISKERS

The objective of this Task is to stay abreast of the whiskers with improved properties which may become available during the course of this program.

We have begun analysis of two sets of whiskers from Kobe Steel (Grades AT and A'T), two sets of whiskers from Tokai Carbon (TWS-100 Modified and TWS-400), and one set of whiskers from Keramont (Grade 9A).

Initial STEM examination was performed on two sets of whiskers. An improvement in the morphology was observed in (Grade AT, dated March 1989) whiskers supplied by Kobe Steel (compared with Kobe Steel whiskers analyzed earlier). Whisker diameters were more consistent and were on average a little less than 1 μm. The whisker lengths ranged from 5 to 50 μm. The amount of transition metal particles has been reduced. The Keramont (Grade 9A #49-51, received September 1989) whiskers had a greater range of diameters and lengths. Much debris was present.

TABLE IX

MEASURED HIP'ed DENSITIES (g/cc)

AND PERCENT OF THEORETICAL (%)‡

Wt% SiCw	T1 C/t1 h	T1 C/t2 h	T2 C/t1 h	T2 C/t2 h
0	3.31(100)	3.30(99.7)	3.30(99.7)	3.30(99.7)
		4th Iteration (SiCw/GN-10)		
10	3.29(99.7)	3.29(99.7)	3.30(100)	--
20	3.17(96.4)	3.27(99.4)	3.28 (99.7)	3.27(99.4
30	3.17(96.6)	3.21(97.9)	3.26 (99.4)	--
40	3.01(92.3)	3.05(93.6)	--	3.24(99.4)
		5th Iteration (SiCw/GN-10A)*		
10	3.30(100)	3.30(100)	3.30(100)	3.31(100.3)
20	3.30(100.3)	3.30(100.3)	3.29(100)	3.30(100.3)
30	3.21(97.9)	3.29(100.3)	3.30(100.6)	3.30(100.6)
40	3.26(100)	3.29(100.9)	--	3.29(100.9)

‡ BASED ON RULE-OF-MIXTURE

* PROCESSED USING THE SAME PROCEDURES AS IN 4TH ITERATION (OPTIMIZED GREEN PROCESS) EXCEPT THAT THE SINTERING AIDS LEVELS WERE ADJUSTED TO MAINTAIN A CONSTANT (SINTERING AIDS)(Si3N4 + SiCw) RATIO

TASK 6 NANOMETER DEPOSITION OF SINTERING AIDS

The objective of this Task is to develop nanometer deposition of the sintering aids through solution chemistry to promote grain boundary homogeneity resulting in improved high temperature properties and enhanced sinterability of GN-10, the matrix material of this program. The technology developed can be applied to a future GN-10 Si_3N_4 based composite effort.

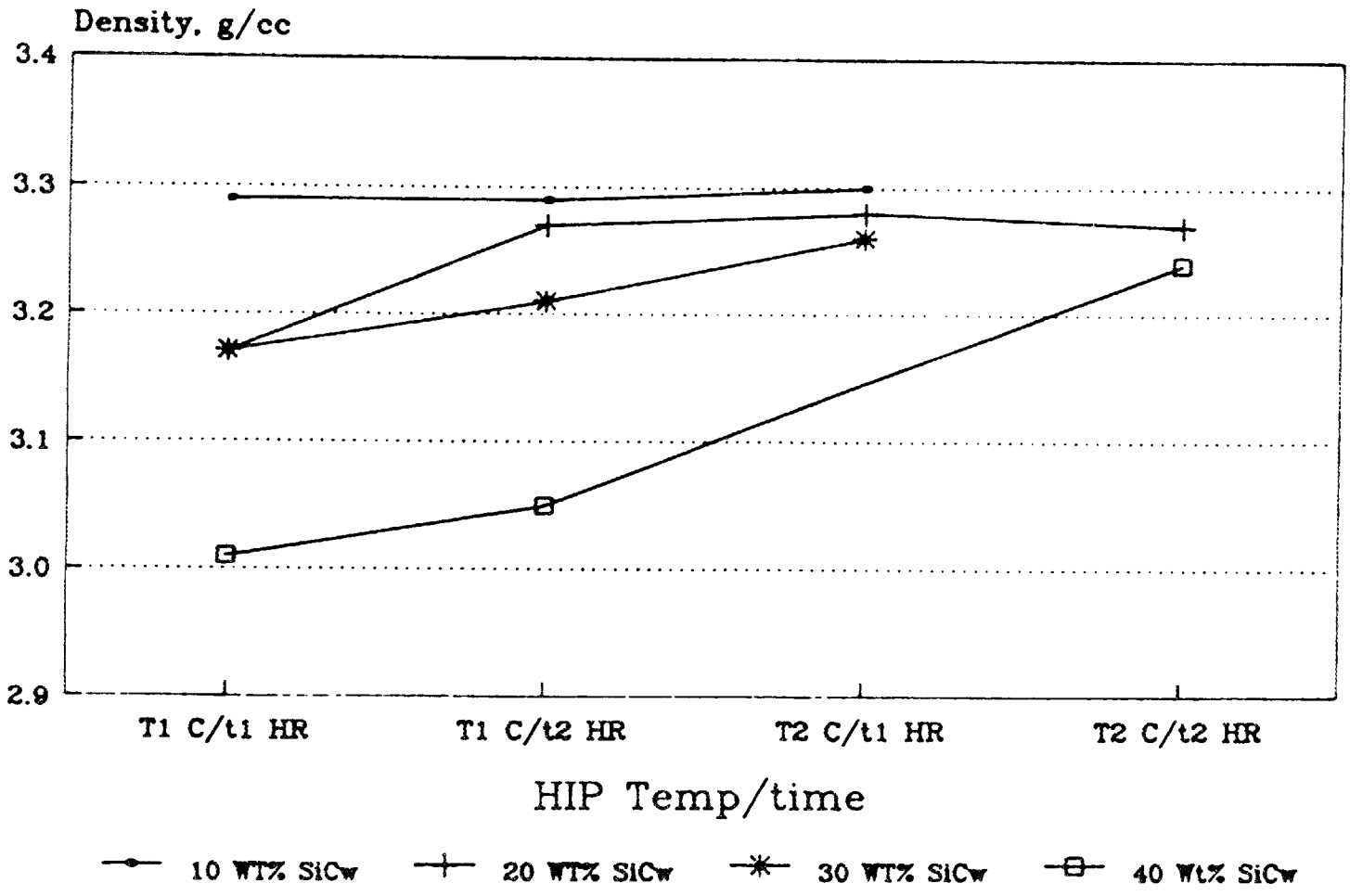

FIGURE 2
DENSITY VS. HIP PARAMETERS
(SiCw/GN-10, 4th Iteration)

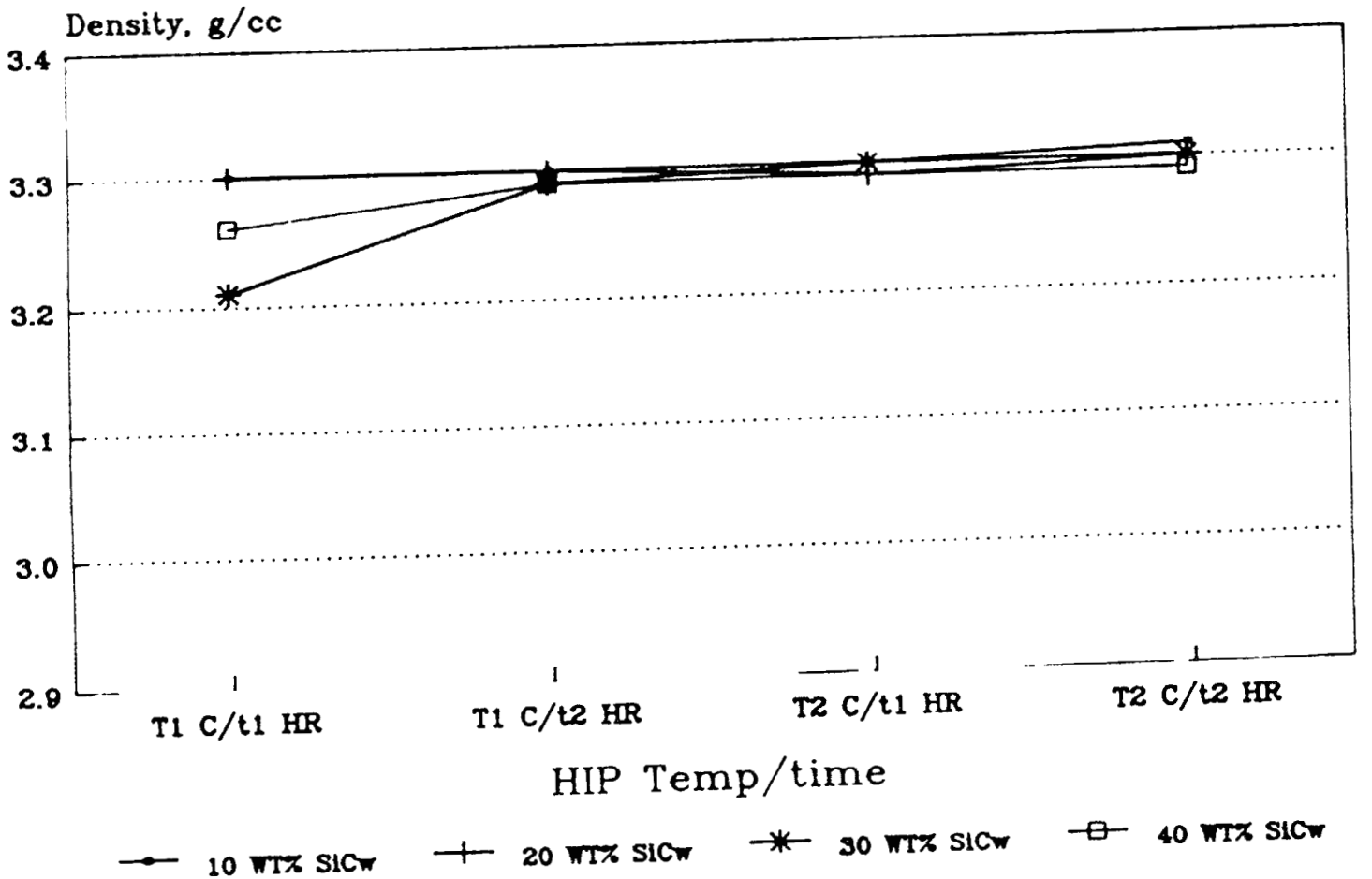

FIGURE 3
DENSITY VS. HIP PARAMETERS
(SiCw/GN-10A, 5th Iteration)

GN-10 sintering aids will be deposited on silicon nitride powders using precipitation, spray drying, or polymerization reactions. Initial work involved precipitation and characterization of compounds precipitated in the absence of silicon nitride. Mixed cation precipitates of the sintering aid composition were prepared. Differential thermal analysis shows that the decomposition of the co-precipitate was different than the individual components suggesting that an intimate mixture was achieved. In addition, precipitates have also been formed using an alternate anion. Thermal analysis will be used to investigate decomposition of the precipitates and homogeneity. We will use these methods to deposit sintering aids on silicon nitride powders and screen for uniformity and yield. Sufficient quantities will be prepared for slip casting studies.

TASK 7 IN-PROCESS CHARACTERIZATION AND PROCESS CONTROL DURING DRYING OF CAST CERAMIC PARTS

The objective of this Task is to determine the efficacy of ultrasonic methods for the real-time, on-line process control the drying of green ceramics fabricated by aqueous slip casting, the shape forming method used throughout this program. The technique developed can be applied to slip cast whisker reinforced Si_3N_4 composites in a future effort.

Experiments to monitor the baseline ultrasonic properties of aqueous slip cast plates are being designed. Four rectangular, green ceramic plates (2.X 3.X 0.5 inches) have been fabricated for preliminary experiments. Set-up of the humidity chambers, data acquisition protocol, and shrinkage measurement methods are in the planning stage.

STATUS OF MILESTONES

All milestones are on schedule.

PROBLEMS ENCOUNTERED

None

PUBLICATIONS/PRESENTATIONS

K. R. Karasek, S. A. Bradley, J. T. Donner, M. R. Martin, K. L. Haynes, and H. C. Yeh, "Composition and Microstructure of Silicon Carbide Whiskers," J. Materials Science, 24 1617-22 (1989).

S. A. Bradley, K. R. Karasek, M. R. Martin, H. C. Yeh, and J. L. Schienle, "Silicon Carbide Whisker Stability During Processing of Silicon Nitride Matrix Composites," J. Am. Ceram. Soc., 72 [4] 628-36 (1989).

Submitted to J. Materials Science: K. R. Karasek, S. A. Bradley, J. T. Donner, H. C. Yeh, and J. L. Schienle, "Characterization of Recent Silicon Carbide Whiskers."

Silicon Nitride-Metal Carbide Composites

S. T. Buljan, M. L. Huckabee, J. G. Baldoni, J. T. Neil
(GTE Laboratories, Inc.)

Objective/Scope

The objective of the proposed effort is to study the effect of sintering aids on microstructure and properties of Si_3N_4-SiC(w) composites and utilize the results obtained to design and synthesize an advanced composite of improved properties. It is also an objective of this effort to refine forming and consolidation processes and develop technology for prototype part fabrication.

Technical Highlights

High temperature creep studies have indicated different rates of devitrification of the intergranular glass phase of silicon nitride-based ceramics depending on the quantity and species of sintering aids employed. Based on these data, the controlled surface flaw technique (CSF) for measuring fracture toughness, which utilizes annealing to remove residual strain affected by the indentation, was deemed inappropriate and alternatives were explored.

Two (indented) bend bar techniques, the indentation strength (IS) [after G.R. Anstis, et al., J. Am. Ceram. Soc., 64 (9) p. 533 (1981)] and the modified indentation toughness (MI) [after R.R. Cook and B.R. Lawn, J. Am. Ceram. Soc., 66 (11) C-200 (1983)] techniques were evaluated. Preliminary testing showed that indenter geometry had no effect on the (IS) K_{IC} value obtained; therefore, 49N Knoop indentation was used, while a 49N Vicker indenter was employed for the (MI) test. Table 1 compares the results of these techniques to those obtained for the CSF test. The bend bars which were not post-indentation annealed, based on the assumption that the residual indentation stress in each was the same and that, while the absolute magnitudes of K_{IC} by CSF would be low, the relative differences would be representative. While the absolute magnitude of the K_{IC} values obtained was found to be technique-dependent, the relative differences between the monolithic and composite materials was not. Therefore, the (IS) method, based on its simplicity, was chosen.

Table 1: Comparison of Fracture Toughness Obtained by Various Bend Strength Techniques

Technique	AY6 (Code 051888A)	AY6+30 v/o SiCw (Code 040188P)	K_{IC} Difference
1) CSF (No Anneal)	4.9 ± 0.2	6.0 ± 0.2	22%
2) IS	6.3 ± 0.1	7.8 ± 0.4	24%
3) MI	7.2 ± 0.4	8.7 ± 0.6	21%

CSF: $K_{IC} = M\sigma(\pi a)^{1/2}/\phi$
IS: $K_C = 0.59\ (E/H)^{1/8}\ (\sigma P^{1/3})^{3/4}$
MI: $K_C = \sigma_m C_m^{1/2} + B$

Pursuing further exploration of the effects of intergranular phase on composite properties, silicon nitride-based ceramics containing either Y_2O_3 or MgO sintering aids, added on a volume equivalent basis, were densified by hot pressing or hot pressed and heat treated in a single cycle. Monolithic, SiC whisker-containing composite and composite matrix phase analog (AY6 or AM4 + 30 v/o Si_3N_4) materials were

evaluated. Each of these materials has an intergranular phase of different composition, i.e., adding SiCw or additional Si_3N_4 powder to preblended baseline powders decreases the amount of sintering aid admixture and increases the SiO_2 content (Table 2). In fact, these changes can effect a change in phase field by crossing a tie line in the X-Al_2O_3-SiO_2 (X≡MgO or Y_2O_3) phase diagrams. The amount of glass phase also varies. Given the fact that the intergranular phase controls to a large extent the fracture path, the data illustrate the importance of controlling this microstructural feature for mechanical property optimization.

All ceramic bodies were densified to greater than 98.5% of theoretical density. Phase analysis (XRD) showed no indication of devitrification, but the amount of the phases of interest is probably below the detection limit of this technique.

Table 2: Typical Sintering Aid Contents of Silicon Nitride-Based Ceramics

	Al_2O_3	MgO	Y_2O_3	SiO_2	SiO_2/Al_2O_3 + MgO or Y_2O_3
AY6	1.50	-	6.00	2.60	0.35
AY6 + 30 v/o SiCw	1.05	-	4.25	2.82	0.53
AY6 + 30 v/o Si_3N_4	1.05	-	4.25	2.66	0.50
AM4	1.53	4.36	-	2.60	0.44
AM4 + 30 v/o SiCw	1.14	3.07	-	2.85	0.68
AM4 + 30 v/o Si_3N_4	1.14	3.07	-	2.69	0.64

Room temperature mechanical property evaluation (Table 3) has indicated that the heat treatment cycle has an adverse effect on the room temperature properties of AY6. In this instance, the AY6-SiCw composite had a ~10% higher fracture toughness and equivalent strength compared to monolithic AY6, while it was appreciably (45%) tougher than the matrix phase analog. Considering the MgO-fluxed bodies, the monolithic AM4 exhibited low strength despite having a fracture toughness equivalent to AY6. In K_{IC} testing, a number of indented bend bars of the AM4 monolith failed to break at the Knoop indentation, indicating that the natural flaws are large (> ~100 μm) for this material, which accounts for its relatively low strength. Additions of SiCw or additional Si_3N_4 had little effect on fracture toughness, but these materials (E and F in Table 2) did have appreciably higher moduli of rupture than the baseline. Heat treating AM4 was observed to increase both fracture toughness (~15%) and strength (33%), while this procedure had little effect on the AM4-SiCw composite.

Table 3: Room Temperature Mechanical Properties of Silicon Nitride Ceramics (≥98.5% Theoretical Density)

Material	KIC(MPa.m1/2)[IS Method]MOR(MPa) [average of samples] HP	HP/HT
A) AY6	7.4 ± 0.1/981 ± 44	5.8 ± 0.1/847 ± 71
B) AY6 + 30 v/o SiCw	8.0 ± 0.1/994 ± 73	7.8 ±1.3/977 ± 68
C) AY6 + 30 v/o Si_3N_4	5.5 ± 0.2/845 ± 127	5.9 ± 0.8/755 ± 188
D) AM4	7.1 /590 ± 44	8.3 ± 0.3/789 ± 208
E) AM4 + 30 v/o SiCw	7.6 ± 0.3/882 ± 47	6.8 ± 1.0/803 ± 148
F) AM4 + 30 v/o Si3N4	7.3 ± 0.2/901 ± 102	5.1 ± 0.1/744 ± 86

AY6: 6.0 w/o Y_2O_3 + 1.5 w/o Al_2O_3 + Bal. Si_3N_4
AM4: 4.4 w/o MgO + 1.5 w/o Al_2O_3 + Bal. Si_3N_4
HP: Hot pressed at 1800°C/34.4 MPa/400 min. in N_2
HP/HT: HP + heat treated at 1200°C/240 min. in N_2

It was also determined that the heat treatment tended to reduce the Young's moduli (E) of these materials (Table 4). Surface energy, calculated from values of K_{IC} and E, was also observed to be affected by composition and/or densification route.

Table 4: Calculated Surface Energy (Fracture Energy) of Silicon Nitride-Based Ceramics Characterized in Tables 2 and 3

	HP			HP/HT		
Material	K_{IC} (MPa·m$^{1/2}$)	E+ (GPa)	γ* (10^3 erg/cm^2)	K_{IC} (MPa·m$^{1/2}$)	E+ (GPa)	γ* (10^3 erg/cm^2)
AY6	7.4	334.2	81.9	5.8	320.4	52.5
AY6+30 v/o SiCw	8.0	357.6	89.5	8.3	347.9	99.0
AY6+30 v/o Si_3N_4	5.5	321.1	47.1	5.9	309.2	56.3
AM4	7.1	330.0	76.4	8.3	327.3	105.2
AM4+30 v/o SiCw	7.6	356.9	80.9	6.8	345.2	67.0
AM4+30 v/o Si_3N_4	7.3	324.5	82.1	5.1	300.8	43.2

*$\gamma = K^2_{IC}/2E$ = surface energy
+E = Young's modulus (pulse-echo overlap technique)

Elevated temperature, 1400°C, modulus of rupture testing (four point loading) has shown that heat treating the yttria-containing Si_3N_4 ceramics can lead to increased strength and elastic limit (point of first deviation from linearity in the force-time MOR data). Table 5 compares the strength (ratio of 1400°C MOR to the room temperature value) and the elastic limit of the two series of Si_3N_4-based materials. The strength of the heat-treated AY6 monolith was 25% higher than that of hot-pressed AY6, while both the composite AY6 + SiCw and the composite matrix phase analog (AY6 + 30 v/o Si_3N_4) showed a 50% increase in strength compared to materials that were only hot pressed. In all cases, the cycle which included the heat treatment produced materials with increased elastic limits, by as much as 40% for the AY6 + SiCw composite. The heat treatment cycle had virtually no effect on the 1400° strength of the MgO-containing bodies. Since XRD could not verify that devitrification had indeed been affected via heat treatment, arrangements have been made for extensive TEM analysis of these ceramics at ORNL-HTML.

Table 5: Strength (MOR [1400°C]/MOR [25°C]) at 1400°C and Elastic Limit (E.L.) of Silicon Nitride Ceramics

	HP*		HP/HT**	
	MOR (1400°C)/MOR (25°C)	E.L. (MPa)	MOR (1400°C)/MOR (25°C)	E.L. (MPa)
A) AY6***	0.37	238 ± 9	0.46	282 ± 28
B) AY6 + 30 v/o SiCw	0.35	218 ± 18	0.52	305 ± 6
C) AY6 + 30 v/o Si_3N_4	0.40	342 ± 15	0.59	369 ± 17
D) AM4****	0.51	101 ± 6	0.38	100 ± 3
E) AM4 + 30 v/o SiCw	0.29	113 ± 3	0.32	106 ± 5
F) AM4 + 30 v/o Si_3N_4	0.39	111 ± 24	0.42	115 ± 10

*HP: Hot Pressed at 1800°C/34.4 MPa/400 min. in N_2
**HP/HT: HP + heat treated at 1200°C/240 min. in N_2
***AY6: 6.0 w/o Y_2O_3 + 1.5 w/o Al_2O_3 + Bal. Si_3N_4
****AM4: 4.4 w/o MgO + 1.5 w/o Al_2O_3 + Bal. Si_3N_4

Compressive creep testing has continued. Since one sample is normally used for as many as nine creep conditions (consecutively increasing stress or temperature), it was deemed important to establish the effect of the early creep conditions of stress and temperature on the creep dynamics observed under subsequent conditions. Four experiments were conducted to investigate this effect. In the first two experiments, two samples were annealed for four hours each at the temperature of creep prior to loading the sample. Following the anneal, one sample was loaded to 150 MPa, the other to 350 MPa. The steady-state creep rates of these experiments were then compared with the creep rates of a sample which had undergone a pre-creep anneal of 4 hours and a typical creep loading sequence (i.e., 50 to 350 MPa in 50 MPa increments). In the remaining two experiments, two more samples were annealed at the temperature of creep prior to loading. However, in these experiments, the anneal time was equivalent to the time the sample would be at temperature prior to that stress condition in a typical isothermal creep run involving only changes in stress. For the sample crept at 150 MPa, the anneal time was 34 hours and for the sample crept at 350 MPa, the anneal time was 56 hours. Table 6 shows a compilation of the steady-

state creep rates of these four experiments and a comparison to the steady-state creep rate of the sample in a normal stress exponent creep experiment.

Table 6: Steady-State Creep Rates for Various Anneal Times as Compared to Creep Rates with Prior Loading Histories

T (K)	Stress (MPa)	Anneal Time (hrs.)*	ε_{ss} (s-1)	ε_{ss} STD (s-1*)
1620	150	4	7.16E-8	6.17E-8
1620	350	4	2.19E-7	1.48E-7
1620	150	34	6.79E-8	6.17E-8
1620	350	56	1.40E-7	1.48E-7

*Standard steady-state creep rates represent creep rates with prior loading history (i.e., stress range of 50-350 MPa).

An analysis of the data shows that the values for strain rate at each of the four conditions of the samples strained under one condition and that of the single sample stressed under each of these individual conditions but also under several prior conditions are within the normal scatter of creep data for this multi-phase material. This is considering two samples of this same material subjected to the same pre-creep conditions of temperature, even if small amounts of strain (<1%) occur in one but not the other, the strain rates at the next higher level of stress will be virtually the same in both materials. However, as discussed in the next section, the temperature-time history of the silicon nitride base material has been determined to affect the time-dependent response to stress.

The creep kinetics of AY6-Si_3N_4 reinforced with 30 v/o SiC whiskers were evaluated with relation to annealing. In addition to experiments preceded by 4 and 50 hour anneals, studies have been conducted in which the samples were annealed for 75 and 100 hours prior to loading. Figure 1 shows the results of these four experiments. Since the curves for the samples annealed for 75 and 100 hours are approximately the same for most data points, the microstructure is believed to be set between 50 and 75 hours of annealing.

Analytical electron microscopy of an annealed (4 hours at 1620K) and a fully crept (50 to 350 MPa at 1620K) sample has revealed that a significant portion of the glass phase in the microstructure is continuous with one or more crystalline phases at triple junctions. Energy Dispersive Spectrometry of these pockets has shown the following average compositions:

Annealed Sample (At%)

N	~21.5%
O	~45.0%
Al	.8%
Si	15.4%
Y	17.3%

Crept Sample (At%)

N	~13.7%
O	~55.4%
Al	0.3%
Si	16.2%
Y	14.3%

These spectra were taken from pockets between Si_3N_4 grain pairs and between Si_3N_4 grains and whiskers.

In order to determine if microstructural evolution is the cause of the dramatic change in stress dependence initially observed at approximately 225 MPa (see Figure 1), one sample was crept (at 1620K) to the conditions before the break in the stress-dependence curve. This microstructure, as well as those from an as-received sample, and samples annealed and crept at 1620K, were closely examined to determine the evolution of the microstructure during creep. High resolution TEM has shown that an amorphous layer was present within the grain boundaries (Si_3N_4/Si_3N_4 and Si_3N_4/whisker) and on the outer edges of triple-point pockets in samples crept under conditions which correspond to those prior to the change in slope of the creep rate-stress curve. After the break, this film was not observed at either location!

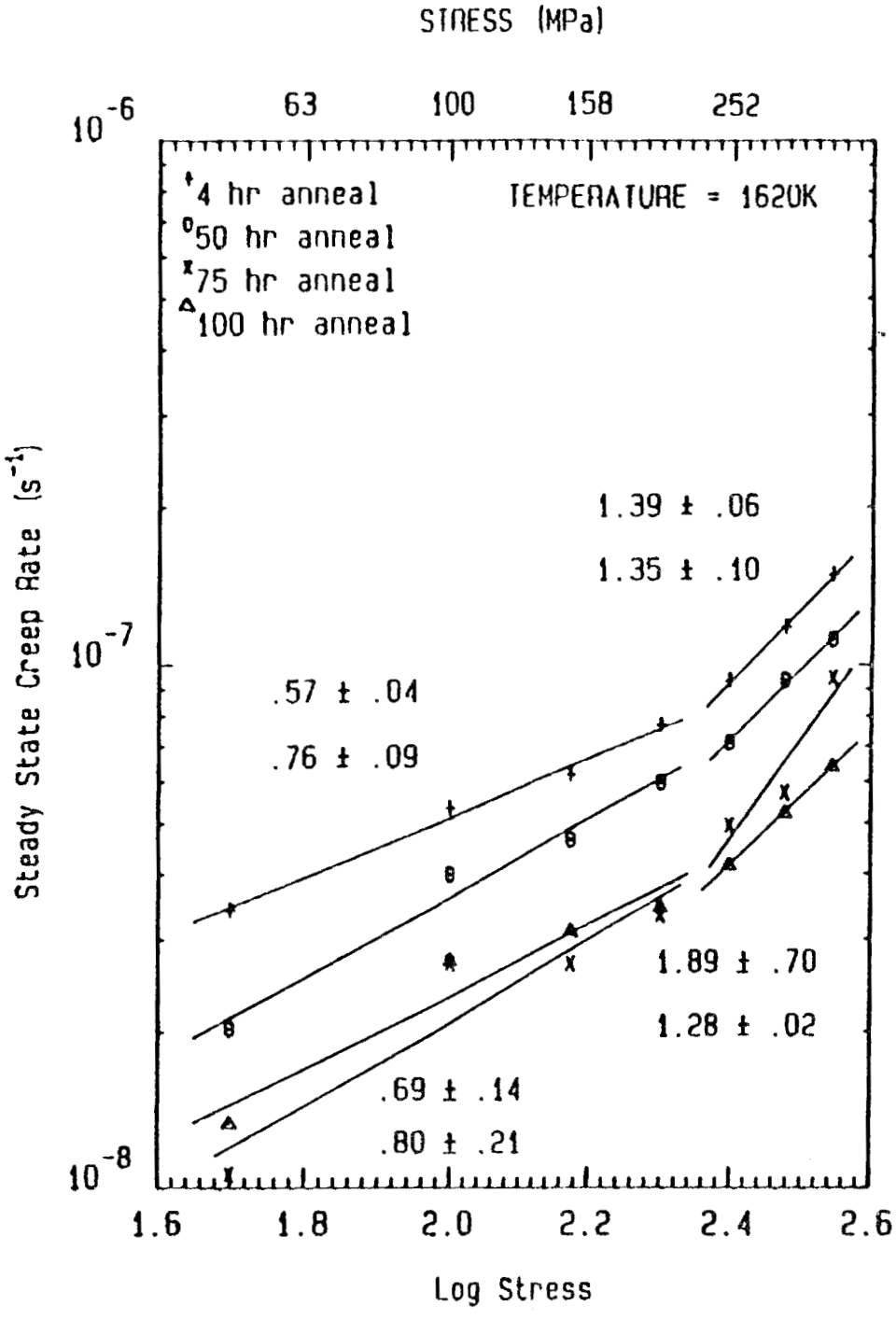

Figure 1: Effect of anneal time on steady-state creep rates and stress exponent of 30 vol % SiC whisker-reinforced Si_3N_4

Data has shown that the break in the stress dependence occurs almost exclusively at approximately 1% strain. An experiment was conducted in which 1% strain was induced in the material at low stress. The experiment did show the break to occur at a stress less than 225 MPa. This relationship between strain and the break may suggest that the film of amorphous phase is not crystallized but squeezed out of the microstructure to produce a stiffer microstructure through the formation of a β-Si_3N_4 grain skeleton as has been proposed for WC-Co cermets. This would result in and explain the observed increase in stress dependence.

The effect of anneal time on creep kinetics was further investigated. Anneals of 4, 50, 75 and 100 hours, at 1620°K were conducted preceding the loading sequence at the same temperature. The results of these four experiments are shown in Figure 2a. It can be seen that the location of the break does not change with anneal time, since annealing does not produce strain that would push out intergranular glass. However, steady-state creep rates decrease with increasing anneal time, suggesting that the microstructure is not in internal equilibrium after the four anneal times used.

Also during this reporting period the conversion of one creep system to operate in an air atmosphere was initiated and completed. One creep experiment has been completed. At 1620°K in the stress range of 50 - 350 MPa the material exhibited a bilinear behavior similar to that of the material crept in nitrogen. Figure 2b shows a comparison of steady-state creep rate versus log stress for this material crept in air and in nitrogen with all other parameters being the same. At all stress conditions, the sample crept in air exhibits higher creep rates. This phenomenon could be related to a loss of N_2 from the intergranular glass phase, present due to densification in a nitrogen-rich atmosphere, which would tend to lower the viscosity or effect a change in the kinetics of devitrification.

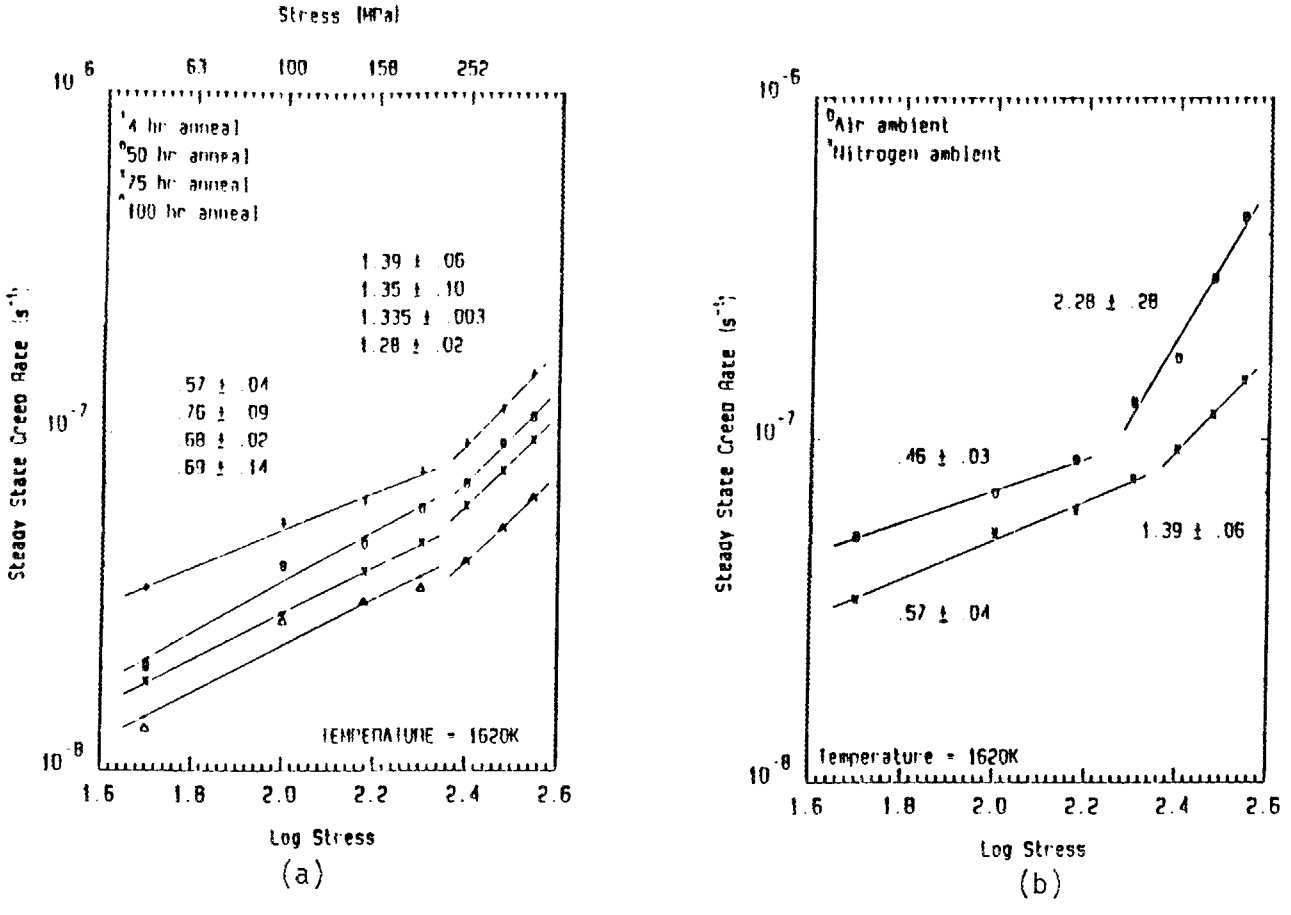

Figure 2 Compressive Creep Testing Results for AY6-Si_3N_4 + 30 v/o SiCw Composite: a) Effect of Annealing on the Steady State Creep Rate at 1620K; b) Effect of an Air Atmosphere on the Steady State Creep Rate at 1620K

Results of tensile (NIST) and compressive (NCSU) creep testing have indicated no reduction in creep rate due to whisker reinforcement. This is contrary to previously reported results for creep tests in bending where the composite exhibited considerably lower steady state creep rates. Preliminary four-point bending results (Table 7) of specimens cut from the same billets of material from which the tensile and compressive samples were machined are in agreement with the uniaxial testing results. The initial results showing enhanced creep resistance for the composite were obtained with materials prepared with GTE SN502 Si_3N_4 powder, while the ceramics used for the round robin testing were made with Ube E10 Si_3N_4 powder. The surface area of the Ube powder is appreciably larger than that of the SN502 powder in both the as-received and milled condition, 10.5 m^2/gm/14.0 m^2/gm and 4.0 m^2/gm/7.5 m^2/gm, respectively. In spite of the smaller particle size, monolithic AY6 prepared with the Ube powder has been observed to require a higher densification temperature to obtain complete α to β Si_3N_4 conversion (XRD) when hot pressed under the same pressure/time parameters which produce AY6 prepared with SN502 containing no detectable α-phase. The application of higher densification temperatures, possibly coupled with the different powder, results in monolithic Si_3N_4 microstructures which are appreciably different from those produced to date for Si_3N_4 hot-pressed bodies fabricated with SN502 powder. Fractography of bend bars broken at room temperature (Figure 3) indicates a microstructure for monolithic AY6 (Ube powder) which is very similar in appearance to that obtained for AY6 (SN502) + 30 v/o SiC whisker composites. A higher density of acicular β-Si3N4 grain pullout cavities and depressions by fracture around grains are observed for the Ube powder source monolith compared to the counterpart prepared with SN502 powder. This microstructural difference also resulted in increased room temperature mechanical properties with the fracture toughness and modulus of rupture of the Ube material being higher by 15% and 30%, respectively. The microstructures of these composites are being evaluated.

Table 7: Steady State Creep Rates (1200°C/206.7 MPa Imposed Stress) of Si_3N_4-Based Ceramics in Four-Point Bending

Material	Si_3N_4 Powder	Four Point Creep Steady State Strain Rate at 1200°C/206 MPa (10^{-9} sec^{-1})	
AY6 #1	SN502	16.8	→ 19.1 ± 6.1
AY6 #2	SN502	20.2 (ave. of 2)	
AY6 #3	Ube E10	3.3 (ave. of 2)	
AY6 + 30 v/o SiCw	SN502	2.2 ± 0.3	
AY6 + 30 v/o SiCw	Ube E10	4.7 ± 0.9	

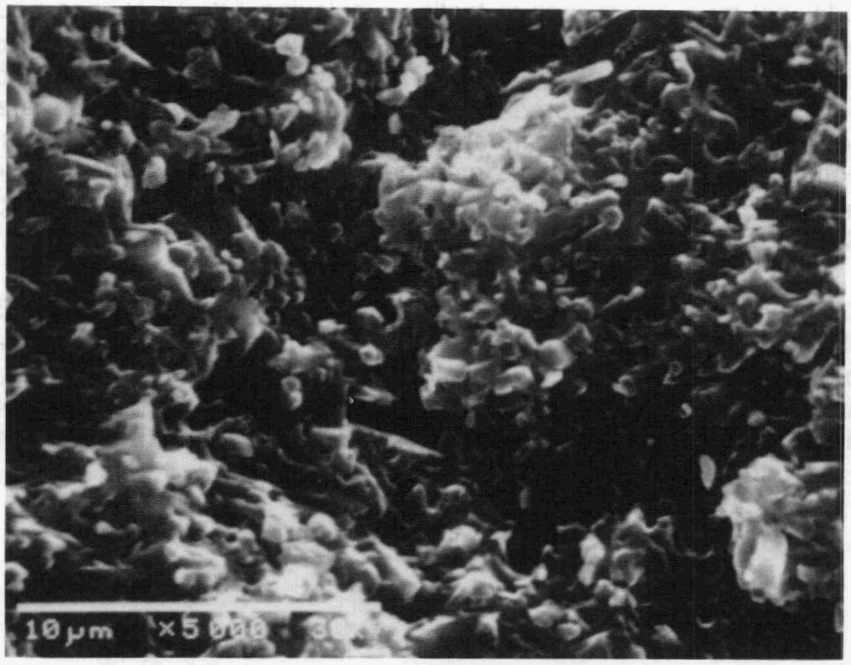

(a)

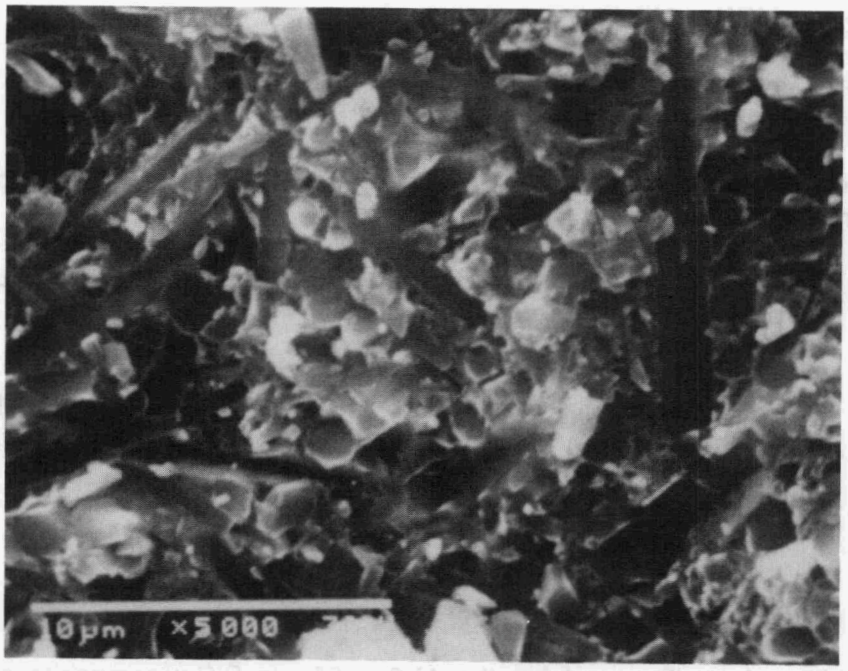

(b)

Figure 3: Fracture Surfaces of Monolithic AY6 Si3N4 Ceramics Broken at Room Temperature a) Prepared with SN502 Powder and b) Prepared with Ube E10 Powder

Additional modulus of rupture testing employing AY6-Si_3N_4 has been conducted with a fixture whose spans and load point size correspond to MIL-Std-1942 (MR) configuration B (quarter point loading with outer span = 40 mm and load point diameter = 4.5 mm) and compared to MOR values obtained using the standard GTEL fixture (outer span = 22.9 mm, inner span = 10.2 mm, load point diameter = 6.1 mm). Room temperature MOR was measured at a crosshead speed of 4.95 mm/min corresponding to calculated strain rates of 5.7×10^{-3} min^{-1} and 7.4×10^{-3} min-1 for the MIL-Std and GTEL fixtures, respectively.

The results (Table 8) indicate that the average strength is reduced by 13% when the larger MIL-Std-B size bend bar is tested. Although the calculated Weibull moduli appear to be significantly different, these values are statistically similar, since there is an estimated ±30% error for a 90% confidence level in this calculation with a 20-point data set. If an average Weibull modulus of 14 is assumed to be representative of both data sets, from the Weibull scaling law:

$$\frac{\sigma_1}{\sigma_2} = \left(\frac{v_2}{v_1}\right)^{1/m}$$

where

σ_1 = MOR of GTEL Std. = 1001 MPa
σ_2 = MOR of MIL Std. = expected value
v_1 = effective volume of GTEL Std.
v_2 = effective volume of MIL-Std.
m = Weibull modulus

Then the expected MOR of this AY6-Si_3N_4 is σ_2 = 853 MPa, which is in good agreement with the measured value.

Table 8: Comparison of MIL-Std-B and GTEL Four Point Modulus of Rupture

Fixture	Sample Size (mm)	MOR* (MPa)	2-Parameter Weibull Modulus	Effective Volume (mm^3)
MIL-Std-B	3.4x4.0x45.0	870±89	11.7	10.2
GTEL-Std.	1.3x2.5x25.0	1001±72	16.5	1.1

*Average of 20 samples

Additional studies involving the AY6 + 30 v/o SiCw composite material were directed at mechanical property evaluation of injection-molded material HIPed at different temperatures and times (constant pressure, 207 MPa). Variations of time and temperature for the cycles evaluated are illustrated in Figure 4 and are additive to the values used for cycle 1. For cycles 1 and 2, the measured densities for the bars

ranged between 98.2 and 98.5% of the calculated values, while the values for cycles 3 and 4 ranged between 97.6 and 99.0%.

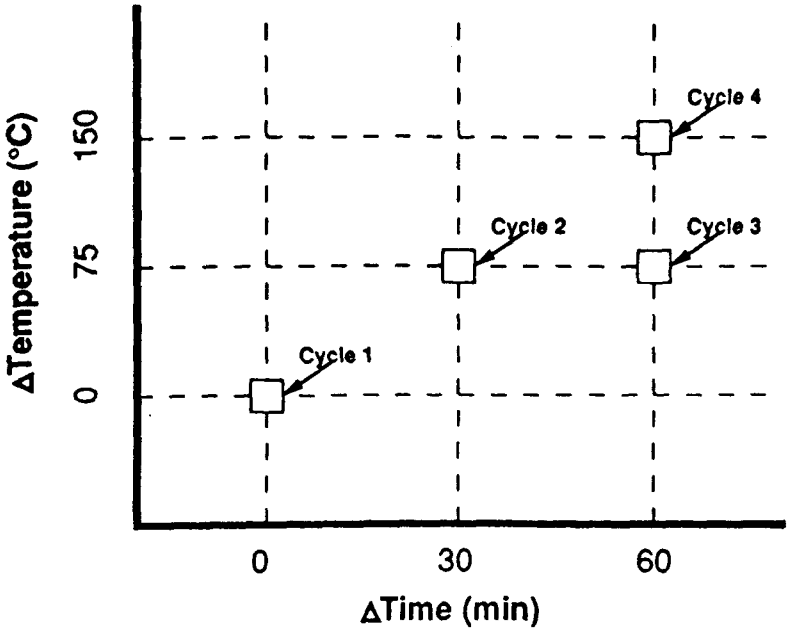

Figure 4: Variations of Temperature and Time for the HIP Cycles Investigated

Mechanical property values (Table 9) for the four cycles investigated show that cycle 1 (lowest temperature and shortest time) had a lower fracture toughness and MOR. Increasing the temperature and time over cycle 1 increased the fracture toughness and MOR. For cycles 2, 3 and 4, the data also suggest that increasing the temperature and time of the HIP cycle can increase the MOR. In particular, at 1400°C, cycle 4 samples show a four-fold increase of MOR.

Table 9: Room and Elevated Temperature Measurements for Injection-Molded AY6 + 30 v/o SiCw composite HIPed at Different Temperatures and Times (Constant Pressure = 207 MPa, Temperature and Time Variations for the Cycles Shown in Figure 4

HIP Cycle	Fracture Toughness* K_{IC} MPa·M$^{1/2}$)	Mechanical Properties Modulus of Rupture (MPa) 25°C	1200°C	1400°C
1	5.1±0.5(5)**	1053±87(7)	465±86(3)	110±2(3)
2	6.5±0.2(5)	1209±73(7)	616±105(3)	386±58(3)
3	64.±0.4(5)	1155±62(5)	670±75(3)	365±49(3)
4	62.±0.2(5)	1120±102(5)	638±51(3)	460±21(3)

*IS technique
**Number of parentheses represents number of samples tested.

The HIP cycle also effects the yield stress (elastic limit) observed during the 1400°C MOR test for the four cycles. No plastic deformation was observed up to 1200°C for any cycle investigated. For the test at 1400°C, examination of the data shows yield of the samples occurs when the average stress reaches 62 MPa for cycle 1, 230 MPa for cycle 2, 267 MPa for cycle 3, and 317 MPa for cycle 4. These differences are most likely due to the different character of the intergranular glass phase produced during the different HIP cycles. Differences in glass properties are also evident in the force time curves for high temperature (1400°C) four-point bend test as illustrated in figure 4 for cycle 1 and 5. The higher yield stress and MOR value at 1400°C observed for cycle 4 suggests that the higher temperature and longer time HIP cycle results in the formation of a more viscous, homogeneous glass phase which would lead to the improved mechanical properties observed.

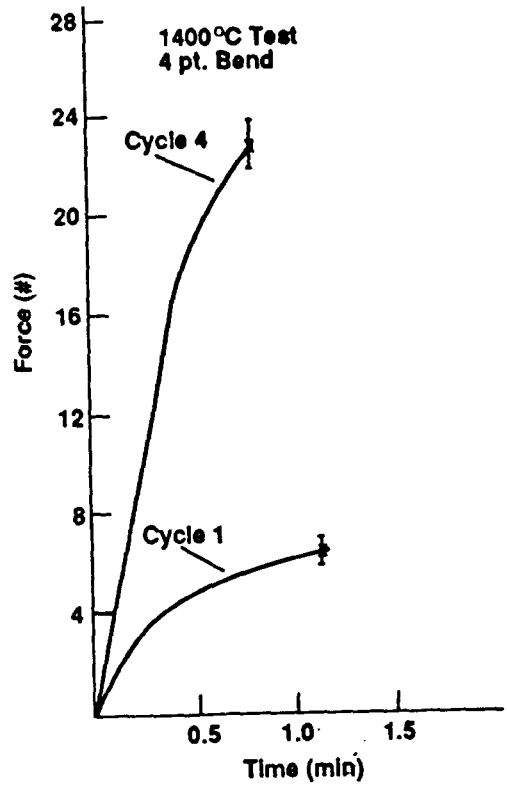

Figure 5: Force-Time Plots for 1400°C MOR Test in Four-Point Loading, Two different HIP Cycles

Further analysis of these specimens has also shown considerable differences in fracture mode between material prepared at the lower temperature, shorter time (cycle 1) and those fabricated at the higher temperature for longer times (cycle 4). Composites HIPed at low temperature fracture intergranularly and have several times greater pullout lengths of acicular grains indicating a relatively low strength of intergranular bond. Despite the shorter pullout lengths, the composites HIPed at higher temperature exhibit higher fracture toughness.

Testing of creep response at 1200°C and constant load 207 MPa shows (Figure 6) that composites densified at low temperature (cycle 1) exhibit poor resistance to creep and slow crack growth, leading to fracture in 1.5 to 3 hours, while improved creep/subcritical crack growth resistance is observed for the material HIPed at higher temperature for longer time.

These results again point to the importance of the intergranular phase (together with grain size/shape) in determining room and elevated temperature properties of silicon nitride ceramics.Limited observations to date suggest, for example, that the kinetics of glass phase homogenization is considerably more sluggish than what was generally assumed. It follows then that in order to be fully specified a composite has to be defined in terms of its major constituents (grain size/shape/distribution), composition, and processing history as well as quantity and species of minor components forming the intergranular phase.

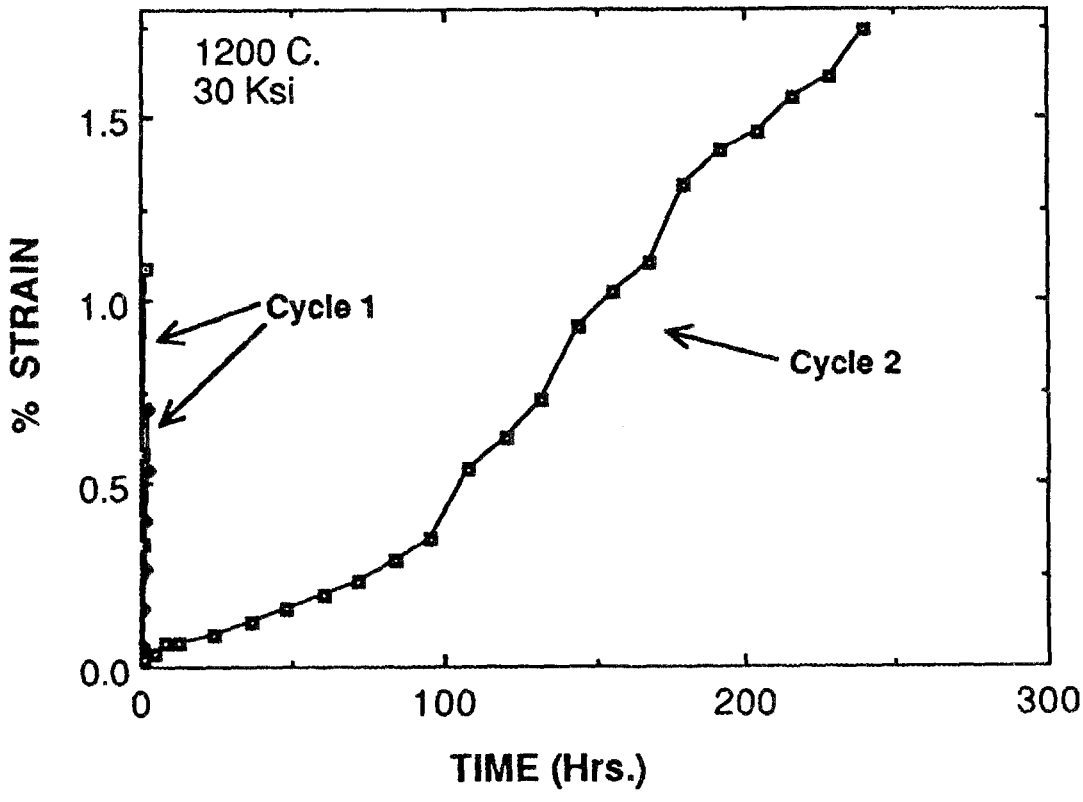

Figure 6: Comparison of Injection-Molded AY6 + 30 v/o SiC Whiskers HIPed at Low Temperature Short Time (Cycle 1) and High Temperature Longer Time (Cycle 4) Subjected to Creep at 1200°C

Another aspect of the current work includes optimization of forming by injection molding. Based on analyses of whisker orientation in injection-molded parts, a new gating configuration was developed for the fabrication of CATE axial turbine blades from whisker-containing composite material. The gate modification work concentrates on minimizing distortion in the airfoil section, which typically is not

machined after densification. Work on injection molding, which was delayed due to laboratory and equipment upgrade to more safely handle the compounding of the composite material containing SiC whiskers, has been resumed. Material has now been prepared and compounded and is being injection-molded in preparation for binder burnout and HIPing.

Status of Milestones

Overall execution of program is on schedule.

Communications/Visits/Travel

None.

Problems Encountered

None.

Publications

None.

Development of Toughened Si_3N_4 Composites by Glass Encapsulated Hot Isostatic Pressure

N. D. Corbin, G. J. Sundberg, K. N. Siebein, V. K. Pujari, G. A. Rossi and J. S. Hansen
(Norton Company)

OBJECTIVE/SCOPE

This two year program is to develop fully dense Si_3N_4 matrix SiC whisker composites which show enhanced properties over monolithic Si_3N_4 materials. Materials will be densified using high pressure glass encapsulation HIPing. The primary goal is to develop a composite with a fracture toughness > 10 MPa$\sqrt{m}$ and capable of operating up to 1400°C.

Studies will be conducted to tailor the whisker/matrix interface and determine the optimum whisker morphology for fracture toughness improvements. The effect of forming on whisker orientation, fracture toughness, and shape distortion will also be addressed.

TECHNICAL PROGRESS

1.0 EVALUATION PROCEDURES

Procedures for analytical evaluations and mechanical property determinations have previously been described in detail.(1) Flexural strength is determined using the U.S. Army recommended procedures for a cross-section of 3 mm x 4 mm.(2) Fracture toughness is determined by either an indentation method (3), a controlled flaw method (4), or by a chevron notch method (5) depending on material availability.

Fracture toughness testing of composites using the chevron notch method was performed using a two step technique. At first a slow cross head speed of .005 mm/min was used to precrack the specimen and a faster cross head speed, 0.5 mm/min, for fracture. This two step procedure was used to induce subcritical precracking followed by stable crack growth and fracture (6)(Figure 1). Figure 1 exhibits a truncated stable crack growth region characteristic of the precrack length. The results obtained using the previous single cross head speed

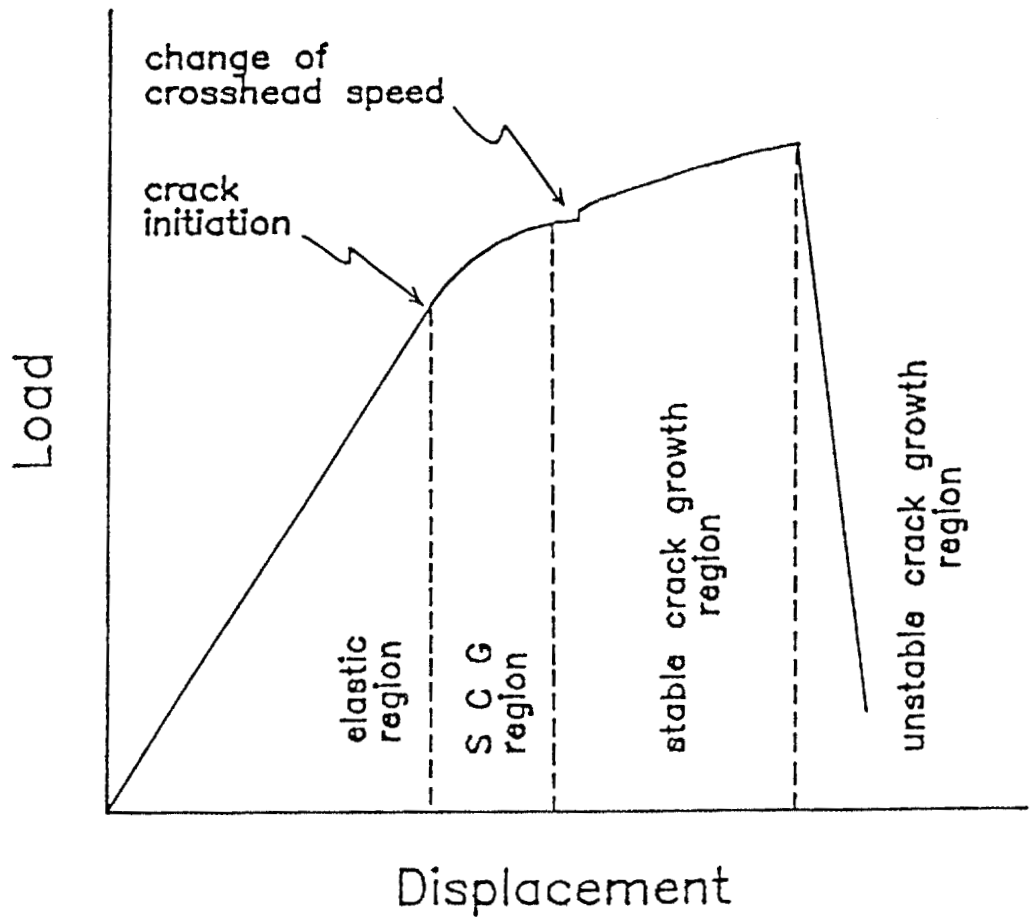

FIGURE 1 Load displacement curve for a two step chevron notch fracture toughness test. (6)

technique and the current two crosshead speed technique were similar for a Si_3N_4 monolith (NT154 (Si_3N_4 + 4 w/o Y_2O_3)). A greater number of valid toughness tests were performed with the two step technique than the single cross head speed technique.

Toughness may vary with the measurement technique used.(7) Consequently, the toughness data will be reported with the toughness of a readily available material, NC132, determined by the same measurement technique.

As previously detailed (8) a technique was developed for determining the surface composition of individual SiC whiskers by Scanning Auger Microanalysis (SAM). This method was used to evaluate additional whisker materials.

2.0 INTERFACES

BORON NITRIDE - A BN coating was applied to SiC whiskers by an outside vendor using a polymer pyrolysis process. Analysis by TEM showed the coating to be relatively uniform, continuous, and present on all the whiskers examined. In most areas the coating thickness ranged from approximately 30 - 35 nm. Figure 2 is a bright field micrograph of a typical BN coated whisker. There were some large areas of coating on the whiskers with thickness up to 350 nm. The BN coating was amorphous as determined by selected area diffraction. The average composition of the coating as determined by Auger analysis was: ~ 2 atomic percent (a/o) Si, 28 a/o C, 7 a/o O, 31 a/o B, and 33 a/o N. The ratio N:B = 1.06. The high carbon content is either residual from the polymer or due to absorption from exposure to the atmosphere.

A batch of BN coated SiC(w) applied by CVD at Norton Company with a thinner coating than earlier material was evaluated.(7) The coating was relatively uniform and continuous. All of the whiskers examined were coated. The coating morphology was platelike with the BN platelets oriented perpendicular to the SiC whiskers surface. The BN platelets were between 1.0-5.0 nm in diameter and ~50 nm long. The overall coating thickness ranged from 40 to 50 nm. Figure 3 is a brightfield micrograph of a whisker with the CVD BN coating. Selected area diffraction (SAD) was performed on an agglomerate of the coating, which was indexed as microcrystalline BN. The average composition of the coating as determined by Auger was: 29 a/o C, 6 a/o O, 34 a/o B, 32 a/o N. The N:B ratio is 0.94. The carbon content may be a result of the graphite heating element used in the CVD apparatus.

METAL/ALLOY - Metallic interfaces between SiC(w) and Si_3N_4 matrix are under evaluation to further define the interface properties necessary for improved fracture

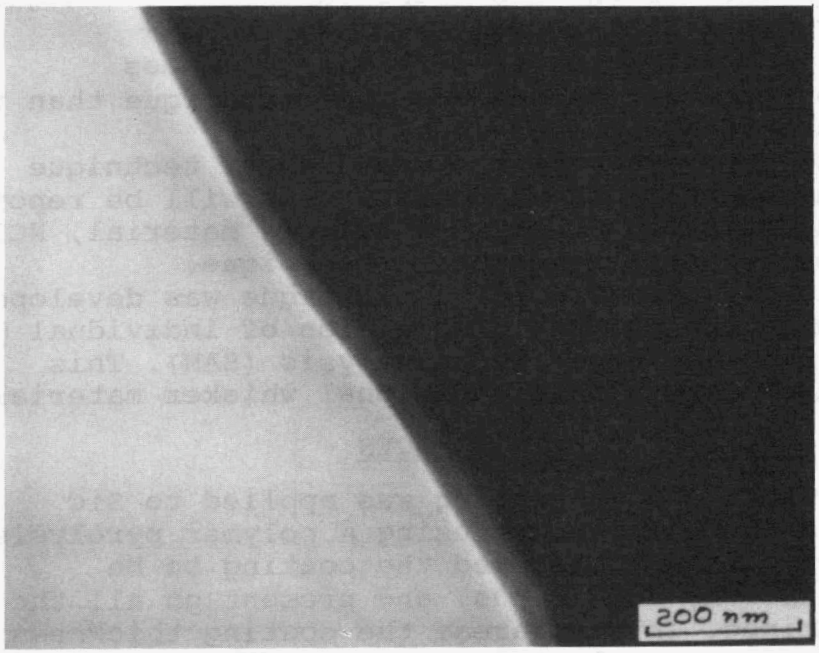

FIGURE 2 Bright field micrograph of a SiC whisker with a BN coating applied by a polymer pyrolysis method.

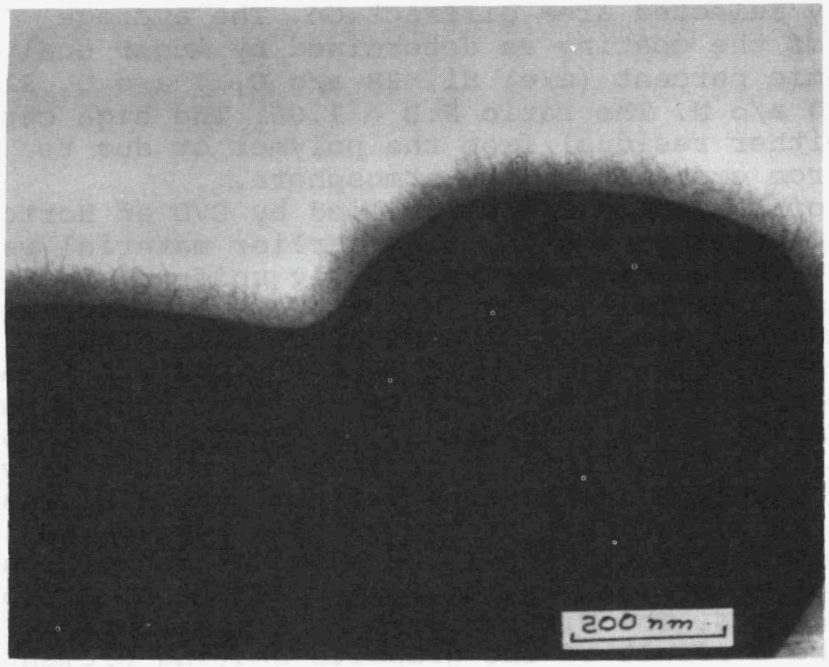

FIGURE 3 Bright field micrograph of a SiC whisker with a BN coating applied by a CVD method at Norton Company.

toughness. Although many of the selected metals or alloys may not be practical for high temperature application, insight can be provided into the effect of the interface on fracture toughness.

The use of metals and alloys as interface coatings may be divided into four categories.

1. layered structures (eg. GaS, Si_2Te_3, WSe_2)
2. ductile layers (eg. gold, silver)
3. brittle layers (eg. silicon, germanium, tungsten)
4. reactions to produce an in-situ carbon layer (eg. chromium, nickel)

Initial interest focussed upon finding materials other than BN and Carbon which had similar layered structures. These materials generally have weak interplanar forces which promote debonding and sliding when placed at an interface. There are some obvious silicates such as talc and mica which in principle fulfill this requirement but high temperature instability and anticipated reactivity with Si_3N_4 eliminate them from consideration. Many other layered structured materials exist that fall into the general classes listed in Table 1.(9) Unfortunately, many of these materials become unstable above ~500°C.

Those which show better high temperature stability contain tellurium and selenium which are toxic. Toxicity severely limits the practical use of such interfaces for improved materials. No practical materials with layered structures which would be appropriate for the interface between Si_3N_4 and SiC have been found.

The metallic coatings in Table 2, which fall into the categories 2, 3, and 4 above were applied to either SiC grain or whiskers by either PVD, CVD or electrolytic methods. After coating, the SiC was mixed with Si_3N_4 having 4 w/o Y_2O_3 sintering aid and HIPed. The effectiveness of the coating was determined by insertion of indentation cracks into polished sections and observing crack interactions with the microstructure. The results of the coatings to date are summarized in Table 2. Several coatings did show evidence of enhanced debonding and/or blunting at the interface.

3.0 MODELING OF RESIDUAL STRESSES

As previously noted (5), residual stresses in Si_3N_4/SiC(w) composites are sensitive to the coefficient of thermal expansion (CTE) of the intergranular phases. It has been observed in TEM that intergranular phases can form large single crystals which encompass

TABLE 1

LAYERED STRUCTURE MATERIALS

- Bivalent Metal Hydroxides
  $Mg(OH)_2$, $Mn(OH)_2$

- Transition Metal Dichalcogenides
  MCh_2 (M = Ti, Zr, Nb, Mo, W; Ch = Se, Te, S)

- III - VI Compounds
  GaS, GaSe, GaTe, InSe

- IV - VI Compounds
  PbO, Si_2Te_3, SnS_2, SnO

- Carbon, Boron Nitride

TABLE 2

Composites with Metal Interfaces

Metal Coating	SiC	Composite Code	Observations
Ni(B)	grain	(2256#58)	Coating diffused away from the interface during HIPing. Reaction with SiC produced Ni_5Si_2.
Cr	powder	(2229D#53)	Coating diffused away from the interface during HIPing. Cr reacted with SiC to produce CrSiC.
Si	whisker	(2231A#53)	Coating diffused away from the interface during HIPing.
W	grain	(2228#53)	Coating remained at interface, evidence of crack blunting.
Au	grain	(2258#58)	Coating remained at interface some evidence of enhanced debonding.
Silver	grain	(2262#64)	Coating present at interface, debonding evident.

multiple grain boundaries and surround Si_3N_4 grains in a monolith.(10) As a result it is necessary to know the CTE's of the intergranular phases as a function of crystallographic orientation. This is necessary because the Si_3N_4 grains or SiC whiskers may be in contact with each of the crystallographic orientations of the intergranular phase.

The expansion data for two phases which occur in Si_3N_4 when Y_2O_3 is used as the sintering aid, delta $Y_2Si_2O_7$ and yttrium apatite $Y_5(SiO_4)_3N$ were not available in the literature. The values were determined by a joint effort between Norton Company and the HTML facility at Oak Ridge National Laboratory (Table 3) (11-19). The specifics for this determination will be reported elsewhere. (13) In brief, the two phases were synthesized then evaluated for thermal expansion by determining lattice parameters from room temperature to 1200°C. The lattice expansions for delta $Y_2Si_2O_7$ were highly anisotropic. This anisotropy means the tensile stress at the interface where $Y_2Si_2O_7$ is sandwiched between SiC and Si_3N_4 can range from ~ 400 MPa to ~ 1500 MPa depending on crystal orientation. The expansion of the apatite phase is only slightly anisotropic as is typical for silicate apatites (20) and in very good agreement with the reported bulk data.(14)

Table 3 lists the thermal expansion coefficient of various Si_3N_4 intergranular phases. As can be seen there is a very large range of expansions available which greatly effect the residual stress in the composite system. The CTE of intergranular phases have been used to explain differences in the fracture toughness of Si_3N_4 monoliths.(16)

4.0 MATERIAL PROPERTY PROGRESS

TOUGHNESS - The toughness of a composite prepared with BN coated SiC(w) (2250C#68) is 4.8 MPa$\sqrt{m}$ by the control flaw method. This value does not show any improvement over monolithic material. The test bars were not fully dense. There is evidence of whisker pullout on the fracture surfaces but the effect of the coated whiskers may be masked by the porosity in the specimen. Additional BN coated SiC(w) are being prepared for further analysis in Si_3N_4.

Fracture toughness results from room temperature to 1370°C are presented in Table 4. The table incorporates the fracture toughness measurements made previously on Si_3N_4 monoliths NT154 (Si_3N_4 + 4 w/o Y_2O_3) and NC132 (Si_3N_4 + 1 w/o MgO) and various composites using the one cross head speed technique and new results using the

TABLE 3

Mean Expansion Coefficient for
Potential Phases in $Si_3N_4/SiC_{(w)}$ Composites

Expansion x 10^{-6}	Temperature Range	Direction	Phase	Reference
-17.5	0-1100°C	c	β-$LiAlSiO_4$	16
- 2.0	25-1100°C	a	β-$LiAlSi_2O_6$	16
0.6	RT-200°C	[100]	Y_2SiO_5	12
1.26	0-1000°C	a	Si_2ON_2	11
2.9	RT-1200°C	(010)	$\delta Y_2Si_2O_7$	13
3.23	0-1000°C	a	βSi_3N_4	11
>3.5	N/A	--	Y-Si-Al-O-N glass	17
3.61	0-1000°C	a	αSi_3N_4	11
3.70	0-1000°C	c	αSi_3N_4	11
3.72	0-1000°C	c	βSi_3N_4	11
3.89	0-1000°C	b	Si_2ON_2	11
3.99	0-1000°C	c	Si_2ON_2	11
4.06	20-1000°C	α_{33}	SiC (4H)	15
>4.1	N/A	--	Mg-Si-AL-O-N glass	17
4.4-4.5	N/A	--	SiC cubic (3C)	15
4.47	20-1000°C	α_{11}	SiC (4H)	15
4.55	0-1000°C	a	Silicon	1
5.8	20-1000°C	Bulk	$Y_2Si_3O_3N_4$	14
6.5	25-1100°C	c	β-$LiAlSi_2O_6$	16
6.6	20-1000°C	Bulk	$Y_8Si_4O_{14}N_4$	14
<7.0	N/A	--	Y-Si-Al-O-N glass	18
7.6	RT-600°C	c	$Y_5(SiO_4)_3N$	13
7.8	0-1100°C	a	β-$LiAlSiO_4$	16
8.2	20-1000°C	Bulk	$Y_5(SiO_4)_3N$	14
8.3	RT-600°C	a	$Y_5(SiO_4)_3N$	13
>8.5	N/A	--	Ca-Na-Si-O-N glass	17
8.6	RT-1000°C	Bulk	$Y_3Al_5O_{12}$	19
10.2	RT-1200°C	(100)	$\delta Y_2Si_2O_7$	13
10.7	RT-1200°C	(001)	$\delta Y_2Si_2O_7$	13
11.4	RT-200°C	[100]	Y_2SiO_5	12

TABLE 4

Toughness Results (MPa $(m)^{.5}$)

CODE	MATRIX (A)	SiC(w)	Controlled Flaw Room Temp.	CHEVRON NOTCH RT	1000 C	1200 C	1370 C	METHOD (B)
NC132	Si3N4	---	4.5	4.3(3)	---	3.9(3)	---	(1)
NT154	Si3N4	---	5.5	4.7(3)	4.1(3)	3.7(2)	4.1(3)	(1)
NT154	Si3N4	---	5.5	4.6(3)	---	---	---	(2)
7X014	SRBSN	30 v/o Tateho	5.2	4.6(3)	---	3.9(3)	4.1(3)	(1)
2154C#43	SRBSN	30 v/o Tateho	5.3	4.8(3)	---	3.5(2)	4.5(2)	(2)
2197#50*	Si3N4	30 v/o AMI	6.5	5.8(3)	5.2(2)	5.6(3)	4.7(3)	(1)
2247#57*	Si3N4	30 v/o ACMC	5.7	4.9(3)	---	6.0(2)	4.9(2)	(2)

- All samples except NC-132 have 4 w/o Y_2O_3 in matrix, NC-132 has 1 w/o MgO.
- Specimen cross section is 3 mm x 4 mm.
- Number of specimens tested in parentheses next to fracture toughness.

(A) SRBSN = composites prepared by blending SiC(w) with silicon, and sintering aid, nitriding, then HIPing to full density.
Si3N4 = blending Si3N4 powder with Sintering aid and whiskers prior to HIPing.

(B) 1 = one step method, 2 = two step method.

* Composites with carbon coated whiskers

two step technique. The specimen with treated American Matrix SiC whiskers (2197#50) had the highest room temperature fracture toughness. The two composite samples with Tateho whiskers in an SRBSN matrix had fracture toughnesses of, approximately 4.75, which was lower than the composite with the treated AMI whiskers. The fracture toughness of the composite with ACMC whiskers in a Si_3N_4 matrix was similar to the SRBSN matrix room temperature materials. The treated AMI whiskers seem to improve the room temperature toughness of the composites.

In general, the high temperature fracture toughness decreased with increasing temperature. One material, 2247#57, exhibited very high fracture toughness at 1200°C. The cause of the high 1200°C fracture toughness is under investigation. At 1200°C the fracture toughness of the C-coated AMI whisker composite and the ACMC whisker composites were 5.6 and 6.0 MPa, respectively, compared with 3.7 for the monolith.

OXIDATION - Oxidation screening tests of two composite samples were performed at 1400°C and 1000°C in air for 10 hours (Table 5). The influence of Carbon and BN at the fiber/matrix interface on the oxidation resistance was studied. One material contained carbon coated SiC whiskers (2261#61), and another sample contained BN coated SIC whiskers (2250#68). The weight change and surface appearance were monitored after heat treatment. The room temperature flexure strength of the composite with carbon coated SiC(w) was measured before and after oxidation. Phase analysis was performed using x-ray diffraction on the specimen oxidized at 1400°C.

In general, catastrophic oxidation did not occur as a result of the treatments. The composite with carbon coated SiC(w) appeared unaffected by the 1000°C treatment, the weight gains were very small averaging .002 grams with no significant change of flexure strength (Table 6). A few small white crystals were present on the surface of the test bars after oxidation. After the 1400°C treatment the surface had a discontinuous oxide layer that appeared predominantly amorphous upon which small crystals were present. The room temperature strength reduction from 92.1 ksi to 66.9 ksi after the oxidation treatment at 1400°C was accompanied by a small weight gain of 0.0006 grams. The 1400°C oxidized surface of the composite contained: beta silicon nitride (JCPDS 33-1160), alpha silicon nitride (JCPDS 9-250), SiC (JCPDS 29-1129), and alpha cristobalite (JCPDS 11-695).(21) The crystalline oxidation product was alpha cristobalite. The oxidation results were encouraging because the composite contained carbon coated whiskers and did not catastrophically oxidize at 1100°C

TABLE 5

Weight Changes and Surface Features of Oxidized Composites

Treatment	1000°C hrs		1400°C/10 hrs	
Sample	Weight Change	Surface Features	Weight Change	Surface Features
2261#61 (C-coated SiC)	+.00017g	a few white crystals	+.0006g	glassy surface crystal growth on surface
2250C#68 (BN-coated SiC)	-.00051g	partial coverage with oxide layer	-.0006g	glassy surface white & yellow crystals on surface

TABLE 6

Properties of Si_3N_4 Matrix Composite with Carbon Coated SiC(w)

Treatment	Weight Change (g)	Strength at Room Temperature MPa	(ksi)	Surface Appearance
unoxidized	--	635	(92.1)	--
oxidized 1000°C/10 hrs	+.0002	621	(90.1)	not affected by oxidation
oxidized 1400°C/10 hrs	+.0006	461	(66.9)	glassy phase at surface, some crystalline oxide growth

(Specimen Code 2261#61)

or 1400°C due to the presence of carbon. Catastrophic oxidation of Si_3N_4 with carbon has previously been reported.(22)

An oxide layer formed on the specimen with BN coated SiC(w) during both the 1000°C and the 1400°C treatment with an attendant loss of weight. The weight losses were low; .0005 grams after 1000°C treatment and .0006 grams after the 1400°C treatment. The light grey oxide layer that formed at 1000°C was not uniform and outlined dark grey macro grains. A discontinuous oxide layer with an amorphous appearance covered with yellow and white spots formed at 1400°C.

5.0 SUMMARY

Uniform, continuous BN coatings between 35 and 50 nm of thickness and B:N ratio ~1.0 have been applied to SiC whiskers by polymer pyrolysis and CVD methods. The BN coatings by polymer pyrolysis were amorphous and the CVD coatings were polycrystalline of platelike morphology. Appreciable carbon, 28 to 29 a/o, was present in the coating, the origin of which is under investigation.

The thermal expansion coefficient was determined for two phases which occur in Si_3N_4 with Y_2O_3 as a sintering aid, delta $Y_2Si_2O_7$ and yttrium apatite $Y_5(SiO_4)_3N$, that were not available in the literature. The maximum possible tensile stress from thermal expansion mismatch at the $SiC/Y_2Si_2O_7/Si_3N_4$ interface was calculated and found to be appreciable at 1500 MPa.

Carbon coated SiC whisker reinforced Si_3N_4 did not experience catastrophic oxidation during air heating at 1000°C and 1400°C for 10 hrs. Mean flexure strength reduced from 92.1 ksi to 66.9 ksi after the 1400°C - 10 hr oxidation treatment.

STATUS OF MILESTONES

All milestones are on schedule.

PUBLICATIONS/PRESENTATIONS

C. R. Hubbard and O. B. Cavin, Oak Ridge National Laboratory, and D. J. Devlin and N. D. Corbin, Norton Company, "Anisotropic Thermal Expansion of $Y_2Si_2O_7$ and $Y_5(SiO_4)_3N$ by High Temperature X-ray Diffraction, Presented at 38th Denver X-ray Conference, Denver, CO, August 4, 1989.

REFERENCES

1. N. D. Corbin and C. A. Willkens, "Development of Toughened Si_3N_4 Composites by Glass Encapsulated Hot Isostatic Pressure Final Report," ORNL/SUB/86-95906/1, Oak Ridge National Laboratory, Oak Ridge, Tenn., August 1988.

2. MIL-STD-1942 (MR), Flexural Strengths of High Performance Ceramics at Abient Temperature, Department of the Army, Washington, D.C., November 21, 1983.

3. G. Antis et al., "A Critical Evaluation of Indentation Techniques for Measuring Fracture Toughness: I, Direct Crack Measurements," *J. Am. Ceram. Soc.* **64**(9), 533-538, (1981).

4. Chantikul, et al., " A Critical Evaluation of Indentation Techniques for Measuring Fracture Toughness: II, Strength Method," *J. Am. Ceram. Soc.* **64**(9), 539-543, (1981).

5. N. D. Corbin et al., "Development of Toughened Si_3N_4 Composites by Glass Encapsulated Hot Isostatic Pressure," pp. 64-82 in *Ceramic Technology for Advanced Heat Engines Project Semiannual Progress Report for Period April 1988 to September 1988*, ORNL/TM-11116, Oak Ridge National Laboratory, Oak Ridge, Tenn., March 1989.

6. J. Sung and P. S. Nicholson, "Valid K_{Ic} Determination Via In-Test Subcritical Precracking of Chevron Notch Bend Bars," *J. Am. Ceram. Soc.* **72**(6), 1033-1036 (1989).

7. N. D. Corbin et al., "Material Development in the Si_3N_4/SiC(w) System Using Glass Encapsulated HIPing - Phase II," pp. 68-89 in the *Ceramic Technology for Advanced Heat Engines Project Semiannual Progress Report for Period October 1988-March 1989*, ORNL/TM-11239, Oak Ridge National Laboratory, Oak Ridge, Tenn., August 1989.

8. N. D. Corbin et al., "Development of Toughened Si_3N_4 Composites by Glass Encapsulated Hot Isostatic Pressure," pp. 39-50 in *Ceramic Technology for Advanced Heat Engines Project Semiannual Progress Report for Period October 1987-March 1988*, ORNL/TM-10838, Oak Ridge National Laboratory, Oak Ridge, Tenn., December 1988.

9. R. M. A. Lieth, Ed., *Preparation and Crystal Growth of Materials with Layered Structures*, D. Reidel Publishing Company, Dordrecht, Holland, 1977.

10. K. N. Siebein and R. L. Yeckley in "Proceedings of the Gas Turbine and Aeroengine Congress," Amsterdam, The Netherlands, June 6-9, 1988, ASME Paper #88-GT-184, Publisher ASME New York.

11. C. M. B. Henderson and D. Taylor, "Thermal Expansion of the Nitrides and Oxynitride of Silicon in Relation to Their Structures," Trans. *J. Brit. Cer. Soc.* **74**, 49-53 (1975).

12. H. M. O'Bryan, P. K. Gallagher, and G. W. Berkstresser, "Thermal Expansion of Y_2SiO_5 Single Crystals," *J. Am. Ceram. Soc.* 71(1), C42-C43 (1988).

13. C. R. Hubbard et al., "Anisotropic Thermal Expansion of $Y_2Si_2O_7$ and $Y_5(SiO_4)_3)N$ by High Temperature X-ray Diffraction," presented at the 38th Denver X-ray Conference, Denver, CO, August 4, 1989.

14. R. R. Wills, S. Holmquist, J. M. Wimmer and J. A. Cunningham, "Phase Relationships in the System Si_3N_4-Y_2O_3-SiO_2," *J. Mat. Sci.* 11, 1305-1309 (1976).

15. Z. Li, R. C. Bradt, "Thermal Expansion of the Hexagonal (4H) Polytype of SiC," to be published in the *Journal of Applied Physics*.

16. J. K. Kim, P. Greil and G. Petzow, "Formation and Characteristics of Silicon Nitride-Lithium Aluminum Silicate Ceramics: Part I, Sintering and Microstructure," *Adv. Ceram. Mat.* 2(4), 817-821 (1987).

17. D. R. Messier, "Review of Oxynitride Glasses," *Revue de Chimie Minerale* t.22, 518-533 (1985).

18. R. E. Loehman, "Prepartion and Properties of Yttrium-Silicon-Aluminum Oxynitride Glasses," *J. Amer. Ceram. Soc.* 62(9-10), 491-494 (1979).

19. D. Taylor, "Thermal Expansion Data-XI. Complex Oxides, A_2BO_5, and the Garnets," Trans. *J. Brit Ceram. Soc.* 86(1), 1-6 (1987).

20. D. Taylor, "Thermal Expansion Data XIII. Complex Oxides with Chain, Ring and Layer Structures and the Apatites," *Brit. Ceram. Trans. and Journal* 87(3), 81-110 (1987).

21. R. Jenkins et al. ed., *Powder Diffraction File*, Published by Joint Committee on Powder Diffraction Standards, International Centre for Diffraction Data, 1601 Park Lane, Swarthmore, PA, 1988.

22. H. Knoch and G. E. Gazza, "Carbon Impurity Effect on the Thermal Degradation of a Si_3N_4-Y_2O_3 Ceramic," AMMRC TR 79-27, Department of the Army, Washington, D.C., May 1979.

Fabrication of Si_3N_4/SiC Composites by Transient Liquid Phase Sintering

S. D. Nunn and T. Y. Tien (The University of Michigan)

Objective/Scope

The goal of this project is to obtain dense silicon nitride composites containing silicon carbide whiskers by transient liquid phase sintering. The systems SiAlON, SiAlON-Garnet ($Y_3Al_5O_{12}$) and SiAlON-Cordierite ($Mg_2Al_4Si_5O_{18}$) were selected for this study. Mixtures of the starting materials form a sufficient amount of liquid to aid densification at the sintering temperatures. After sintering, the liquid phase at the grain boundaries can be crystallized by heat treatment.

Technical Progress

1.0 CRYSTALLOGRAPHIC TEXTURE IN SINTERED COMPOSITES

Crystallographic orientation in hot pressed ceramics containing non-equiaxed particles has been reported for monolithic Si_3N_4,[1] SiC whisker reinforced Al_2O_3,[2] and SiC whisker reinforced Si_3N_4.[3] In all cases, it was reported that the strength and toughness values were higher when cracks in the test specimen were propagated perpendicular to the long axis of the oriented particles. In the present study, parallel orientation of both the whiskers and the matrix has been observed in pressureless sintered SiC whisker reinforced Si_3N_4 composites.

1.1 WHISKER ORIENTATION

The observation of whisker orientation in Si_3N_4/SiC_w composites when the green bodies were formed by pressure filtration of a slurry was described in an earlier report.[4] A schematic diagram of the pressure filtration apparatus is shown in Fig. 1. Because of their high aspect ratio, the SiC whiskers tend to be deposited with the long axis lying in the plane of the ceramic cake. The orientation was detected by analysis of x-ray diffraction patterns taken with different sample orientations. The whisker orientation was observed in both the green and in the sintered ceramics. It was found that the β-SiC <111> direction (length) was perpendicular to the pressure filtration direction, but that the whiskers were otherwise randomly oriented.

1.2 Matrix Orientation

More recent analysis of sintered composites has shown that the β-Si_3N_4 matrix which forms during sintering also exhibits crystallographic texture. Again, peak height variation in the x-ray diffraction patterns for different sample orientations was used to analyze the texture as shown in Fig. 2. The principal β-Si_3N_4 peaks (SN_{hkl}) and β-SiC peaks (β_{hkl}) are identified in the figure. The orientation of the Si_3N_4 grains and the SiC whiskers can be deduced by observing the shifts in the relative peak heights and comparing these to the known growth morphology of the two phases which is shown schematically in Fig. 3.

When the x-ray beam was incident on the face of the sample (top pattern in Fig. 2) the SN_{hk0} and the β_{220} peaks showed high relative intensities indicating that the corresponding planes were oriented favorably with respect to the x-ray beam, i.e., approximately parallel to the surface being analyzed. When the x-ray beam was incident on the edge of the sample the β_{111}, SN_{002}, and SN_{101} peaks showed enhanced intensity indicating that the corresponding planes were nearly parallel to the analyzed surface. The SN_{101} peak intensity is affected by the orientation because of the fractional c/a ratio (0.38) of the hexagonal β-Si_3N_4 crystal structure which results in a shallow interplanar angle (23.8°) between {101} and {002} planes.

Analysis of the peak height shifts indicates that the long axis of both the SiC whiskers and the Si_3N_4 grains lies in the plane of the sintered sample perpendicular to the original pressure filtration direction.

1.3 Effect on Fracture Toughness

The fracture toughness of a sintered composite showing crystallographic texture was measured using the indentation method.[5] The indents were made on the edge of the sample and aligned so that one axis of each indentation was parallel to the plane of crystallographic orientation and one axis was perpendicular to the orientation. Two sets of fracture toughness values were then calculated, one for the cracks parallel to the orientation and one for the cracks which were perpendicular to the orientation. The results are summarized in Table 1. The effect of the crystallographic texture in the sample is clearly evident in the measurements. The fracture toughness was from 37 to 70% higher when the cracks were perpendicular to the plane of orientation. This is in

agreement with properties reported for hot pressed ceramics which show crystallographic texture.[1-3]

2.0 Crystallization of Liquid Phase Sintering Aids

The models proposed for describing the mechanisms involved in the toughening of a ceramic matrix by whisker reinforcement all emphasize the importance of crack bridging and whisker pull-out in increasing the fracture energy.[6,7] The crack bridging phenomenon and pull-out are both dependent upon the properties of the whisker/matrix interface, particularly in terms of the bond strength and the stress state. The ability to predict and control the interfacial properties would enhance the ability to engineer the microstructure of these composites.

One possible method of varying the stress state at the whisker/matrix interface is by incorporating an interfacial phase with a thermal expansion coefficient which either matches (low stress) or is significantly different from (high stress) that of the matrix and reinforcing phases. A high tensile stress at the interface would reduce the bond strength between the whiskers and the matrix and should result in enhanced bridging and pull-out, thus increasing fracture toughness.

2.1 Effective Sintering Aids

The liquid phase sintering aid additions which are used to improve densification of the composites are believed to form a continuous intergranular phase. The sintering aids initially chosen for evaluation in this study, yttrium aluminum garnet and cordierite, were selected for a number of reasons:

1. The additives are effective sintering aids for monolithic Si_3N_4.
2. The additives are readily crystallized in monolithic Si_3N_4.
3. The additives have significantly different thermal expansion coefficients.

The thermal expansion coefficient of Si_3N_4 is $3.0 \times 10^{-6}/°C$, while that of SiC is $4.5 \times 10^{-6}/°C$. Cordierite has a thermal expansion coefficient of about $2.5 \times 10^{-6}/°C$, slightly less than that of Si_3N_4, while YAG has a much larger thermal expansion coefficient, $8.0 \times 10^{-6}/°C$. The difference in thermal expansion coefficient between the two sintering aids should allow evaluation of the possibility of microengineering the

matrix/whisker interface by modifying the stress state. Composites with a cordierite intergranular phase should have a low-stress or stress-free interface after cooling from the crystallization temperature, while the YAG-containing composites should develop significant tensile stresses at the interface upon cooling. This variation in stress state should result in differences in the measured fracture toughness, between composites made with the two different sintering aids and between the as-fired (glassy interface) and the annealed (crystalline interface) composites.

Both YAG and cordierite have been shown to be effective sintering aids in producing dense SiC whisker reinforced Si_3N_4 composites,[8] and crystallization of the YAG phase in the composites by annealing at 1400°C has been straight forward. However, attempts to crystallize the cordierite phase by annealing in the temperature range of 1200 to 1400°C have been unsuccessful. Instead, annealing the samples with the cordierite sintering aid produces a magnesium-aluminum-silicon oxynitride phase refered to as, N-phase, by Drew et al.[9] N-phase was described by them as a nitrogen petalite having an orthorhombic crystal structure and a proposed composition of Mg_2AlSiO_4N. This same phase (as determined by comparison of x-ray diffraction patterns) had also been reported by Nunn et al.[10] who described its compatibility with other phases in the Si, Al, Mg/O, N system. They were unable to determine the precise composition of the compound and refered to it as X*.

The x-ray diffraction patterns shown in Fig. 4 compare the phases which were detected in composites containing 20% SiC whiskers after they were sintered at 1850°C and annealed at 1350-1400°C. The sample containing YAG as the sintering aid (Fig. 4a) contains β-Si_3N_4, β-SiC, and garnet. However, the sample containing cordierite as the sintering aid (Fig. 4c) shows β-Si_3N_4, β-SiC, and N-phase; no cordierite was detected. Since the N-phase compound seemed to be readily crystallizable, an effort was undertaken to determine its composition and to measure its properties to assess whether the phase would be appropriate for use as a sintering aid in this study.

The N-phase composition was isolated and was found to lie on the join between silicon oxynitride, Si_2N_2O, and magnesium aluminum spinel, $MgAl_2O_4$. The compound has a 2:1 molar ratio of Si_2N_2O : $MgAl_2O_4$, and a composition of $MgAl_2Si_4O_6N_4$. The location of this compound in the Si, Al, Mg/O, N system is shown in the phase diagram in Fig. 5. The compound is located on the 50 eq.% oxygen/50 eq.% nitrogen

plane. It is interesting to note that the composition can also be expressed as $MgO \cdot Al_2O_3 \cdot SiO_2 \cdot Si_3N_4$.

The x-ray diffraction patterns in Fig. 6 show that compositions along the $Si_2N_2O/MgAl_2O_4$ join on either side of the N-phase composition form two phases when sintered. The 3:1 molar composition forms Si_2N_2O plus N-phase; the 3:2 compositon forms $MgAl_2O_4$ plus N-phase. The 2:1 composition is single-phase. The x-ray diffraction pattern of N-phase is shown in Fig. 7. The diffraction pattern was indexed based on an orthorhombic unit cell and the results are given in Table 2. The compound is believed to contain two formula units per unit cell and have a theorerical density of 2.93 g/cm^3. The measured density of a sintered sample having the N-phase composition was 2.85 g/cm^3.

2.2 Thermal Expansion Measurement

The thermal expansion coefficient of N-phase, $MgAl_2Si_4O_6N_4$, was measured over the temperature range of 25 to 1200°C by high temperature x-ray diffractometry and was found to be approximately 2.6 x 10^{-6}/°C. This is nearly the same as the thermal expansion of cordierite (2.5 x 10^{-6}/°C). Since both YAG and N-phase have been crystallized in the sintered composites by annealing at 1350-1400°C for 20 hours, they will be used to compare the effect of variations in thermal expansion coefficient on the strength and fracture toughness of the composite materials.

Status of Milestones

On schedule.

Communications/Visits/Travel

S. D. Nunn and T. Y. Tien, "Liquid Phase Sintering of SiC Whisker Reinforced Si_3N_4 Composites," Presented at the Annual Meeting of the American Ceramic Society, Indianapolis, IN, April, 1989.

S. D. Nunn and T. Y. Tien, "Development of Crystallographic Texture in SiC Whisker Reinforced Si_3N_4 Composites," Presented at the Annual Meeting of the American Ceramic Society, Indianapolis, IN, April, 1989.

S. D. Nunn attended the 1989 Gordon Conference on Novel Processing of Ceramic Materials in New London, NH from August 12-17, 1989 and presented a poster on "Liquid Phase Sintering of SiC Whisker Reinforced Si_3N_4 Composites."

Problems Encountered

None.

Publications

None.

References

[1] F. F. Lange, "Relationship Between Strength, Fracture Energy, and Microstructure of Hot Pressed Si_3N_4," *J. Am. Ceram. Soc.*, **56** [10] 518-22 (1973).

[2] P. F. Becher and G. C. Wei, "Toughening Behavior in SiC-Whisker-Reinforced Alumina," *J. Am. Ceram. Soc.*, **67** [12] C267-69 (1984).

[3] S. T. Bujlan et al., "Si_3N_4-SiC Composites," *Am. Ceram. Soc. Bull.*, **66** [2] 347-52 (1987).

[4] S. D. Nunn and T. Y. Tien, "Pressureless Sintering of Si_3N_4/SiC Whisker Composites," Semi-annual report submitted to ORNL under Contract No. SC-19X-SA125C, October, 1988.

[5] G. R. Anstis et al., "A Critical Evaluation of Indentation Techniques for Measuring Fracture Toughness: I, Direct Crack Measurements," *J. Am. Ceram. Soc.*, **64** [9] 533-538 (1981).

[6] A. G. Evans and D. B. Marshall, "The Mechanical Performance of Fiber Reinforced Ceramic Matrix Composites," *Mat. Res. Soc. Symp. Proc.*, Vol. 120 (1988) p. 213-246.

[7] G. C. Wei and P. F. Becher, "Development of SiC-Whisker-Reinforced Ceramics," *Am. Ceram. Soc Bull.*, **64** [2] 298-304 (1985).

[8] S. D. Nunn and T. Y. Tien, "Pressureless Sintering of Si_3N_4/SiC Whisker Composites," Semi-annual report submitted to ORNL under Contract No. SC-19X-SA125C, April, 1988.

[9] R. A. L. Drew, S. Hampshire and K. H. Jack, "Proceedings of the First International Symposium on Ceramic Compounds for Engine," Edited by S. Somiya, E. Kanai and K. Ando, KTK Scientific Publishers, Tokyo (1983) p. 394.

[10] S. D. Nunn, H. Honke, L. J. Gauckler and T. Y. Tien, "Subsolidus Phase Relations in Part of the System Si, Al, Mg/O, N," Presented at the Annual Meeting of the American Ceramic Society, Detroit, MI, 1978.

Table 1. Indentation fracture toughness of oriented samples.

Load (kg)	Number of Indents	Fracture Toughness (MPa√m)	
		Parallel	Perpendicular
15	5	5.72 +0.94	7.86 +0.31
25	4	4.65 +0.43	7.91 +0.42

Table 2. The indexed diffraction pattern of N-phase assuming an orthorhombic* unit cell.

h k l	d (calc)	d (obsv)	I/I1	h k l	d (calc)	d (obsv)	I/I1	h k l	d (calc)	d (obsv)	I/I1
0 0 2	7.0606	7.0548	3	1 2 4	2.0005	2.0005	4	2 0 8	1.4360	1.4361	4
0 1 1	5.1866	5.1820	5	0 1 7	1.8970	1.8975	18	1 2 8	1.4277	1.4282	9
0 1 3	3.5970	3.5973	85	2 2 0	1.8486	1.8480	7	3 2 0	1.4176	1.4172	23
1 1 1	3.5766	3.5739	80	1 1 7	1.7709	1.7711	18	0 0 10	1.4121	1.4117	10
0 0 4	3.5303	3.5298	100	2 1 5	1.7636	1.7629	2	0 4 0	1.3941	1.3948	7
1 1 3	2.9075	2.9068	40	0 3 3	1.7289	1.7285	22	3 2 2	1.3898	1.3897	3
0 2 0	2.7882	2.7867	9	2 2 3	1.7207	1.7218	2	0 3 7	1.3670	1.3666	14
0 2 1	2.7354	2.7395	3	2 0 6	1.7037	1.7045	2	2 2 7	1.3629	1.3623	2
0 2 2	2.5933	2.5916	4	1 3 3	1.6318	1.6317	3	1 0 10	1.3577	1.3579	6
0 1 5	2.5195	2.5189	4	2 1 6	1.6293	1.6294	2	1 4 0	1.3417	1.3413	3
2 0 0	2.4694	2.4695	39	0 1 9	1.5104	1.5101	2	1 4 2	1.3181	1.3185	4
1 2 0	2.4280	2.4275	41	2 1 7	1.5043	1.5046	9	3 2 4	1.3155	1.3151	9
0 2 3	2.3989	2.3995	4	3 1 3	1.4969	1.4973	14	0 4 4	1.2967	1.2969	4
1 2 1	2.3929	2.3928	6	0 2 8	1.4914	1.4913	3	3 1 7	1.2433	1.2434	9
2 0 2	2.3309	2.3321	8	2 3 0	1.4851	1.4857	2	1 2 10	1.2207	1.2211	5
1 2 2	2.2960	2.2957	10	1 3 5	1.4812	1.4810	3	2 4 0	1.2140	1.2137	3
1 1 5	2.2443	2.2441	4	2 3 1	1.4769	1.4768	6	4 1 1	1.2011	1.2011	1
2 1 3	2.0358	2.0363	20	1 1 9	1.4443	1.4440	4				

*The calculated unit cell dimensions were arbitrarily assigned as follows: a = 4.9387, b = 5.5764, and c = 14.1213.
The lattice parameters and d-spacings are given in Angstrom units.

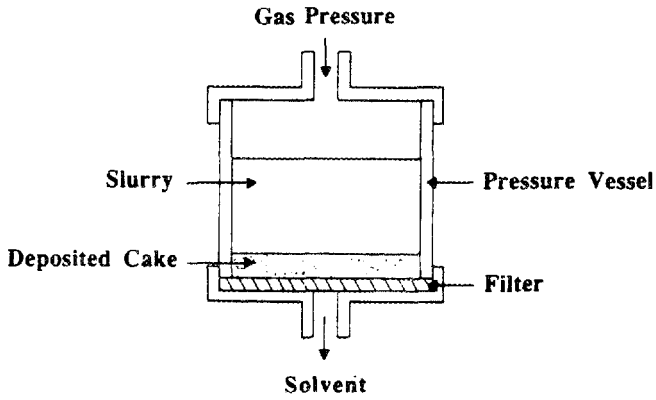

Figure 1. Schematic diagram of the apparatus used for forming the ceramic green body by pressure filtration.

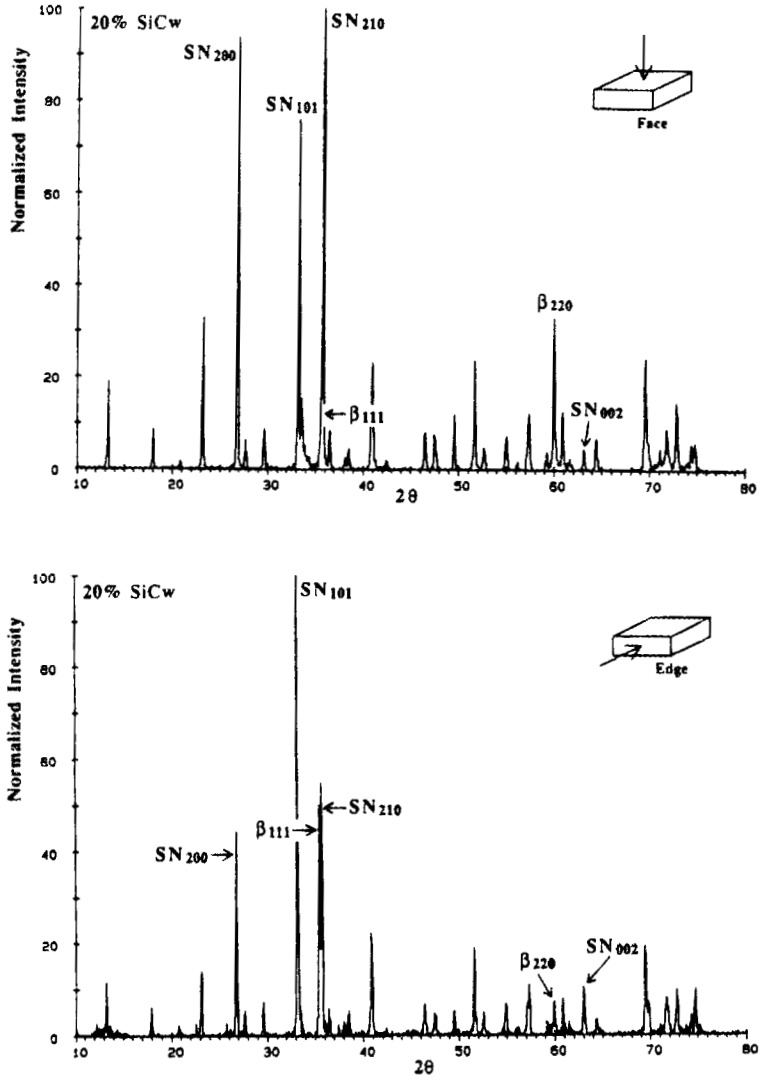

Figure 2. X-ray diffraction patterns of a Si_3N_4 matrix composite containing 20% SiC whiskers taken at two different sample orientations; one with the incident x-ray beam parallel to the pressure filtration direction (face) and one with the beam perpendicular to the pressure filtration direction (edge). The principal β-Si_3N_4 peaks are labeled SN_{hkl} and the principal β-SiC peaks are labeled β_{hkl}.

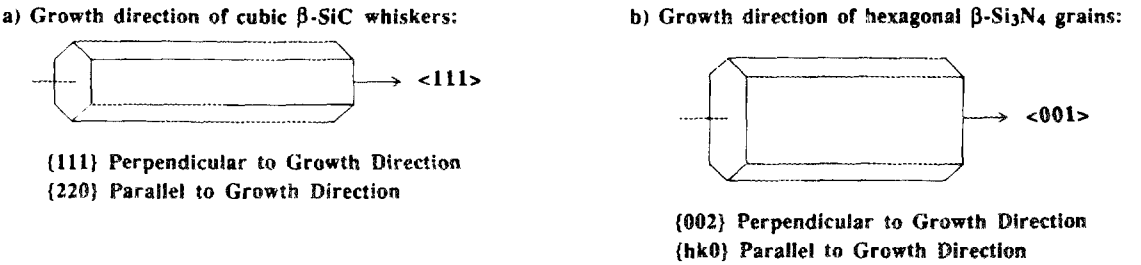

Figure 3. Anisotropic growth morphology of a) β-SiC and b) β-Si_3N_4 showing the growth direction and the families of planes which lie either perpendicular to or parallel to the growth direction.

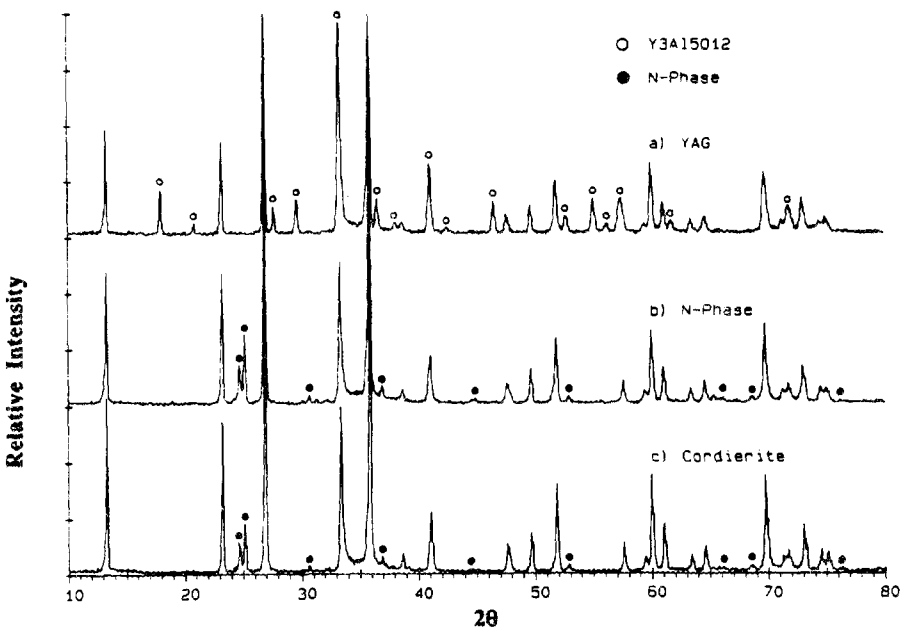

Figure 4. X-ray diffraction patterns of composites containing 20% SiC_w which were sintered at 1850°C for one hour and annealed at 1350-1400°C for 20 hours. Three sintering aids were used: a) YAG, b) N-phase, and c) cordierite. The principal phase is β-Si_3N_4. The peaks due to YAG (o) and N-phase (●) are indicated; cordierite was not detected. The β-SiC_{220} peak is seen at 60° 2θ.

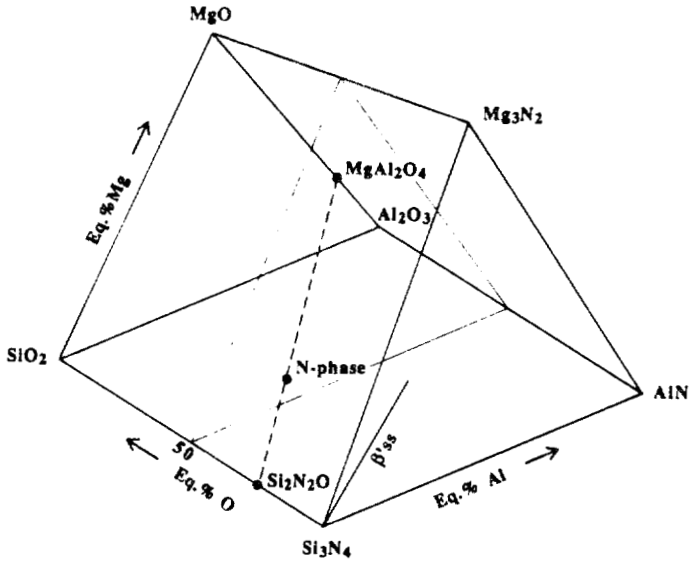

Figure 5. The quasiquaternary reciprocal salt representation of the Si, Al, Mg/O, N system showing the location of the N-phase compositon.

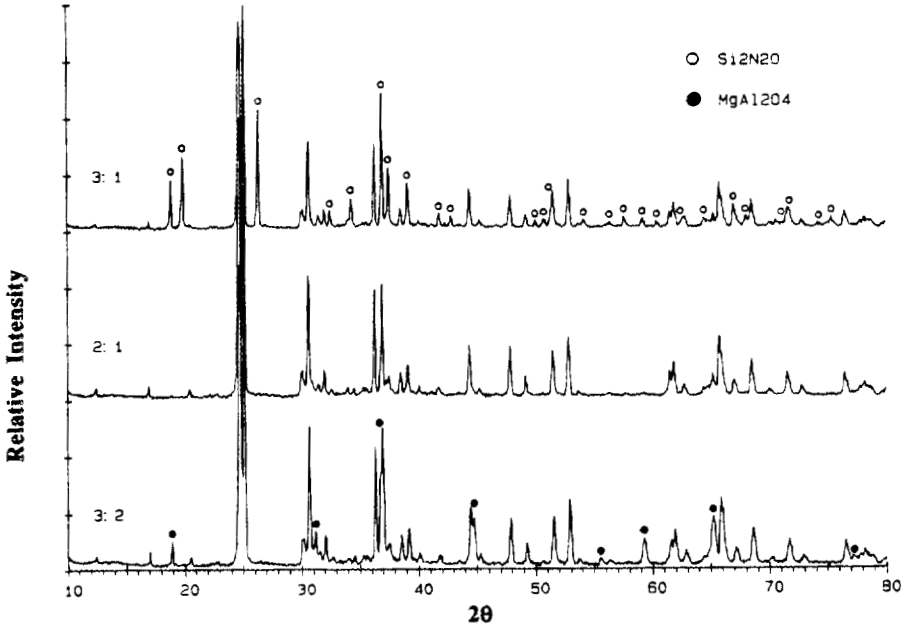

Figure 6. X-ray diffraction patterns of three compounds having Si_2N_2O:$MgAl_2O_4$ molar ratios of 3:1 (top pattern), 2:1 (middle pattern), and 3:2 (lower pattern). The principal phase in all of the patterns is N-phase. Peaks due to the secondary phases Si_2N_2O (o) and $MgAl_2O_4$ (●) are indicated.

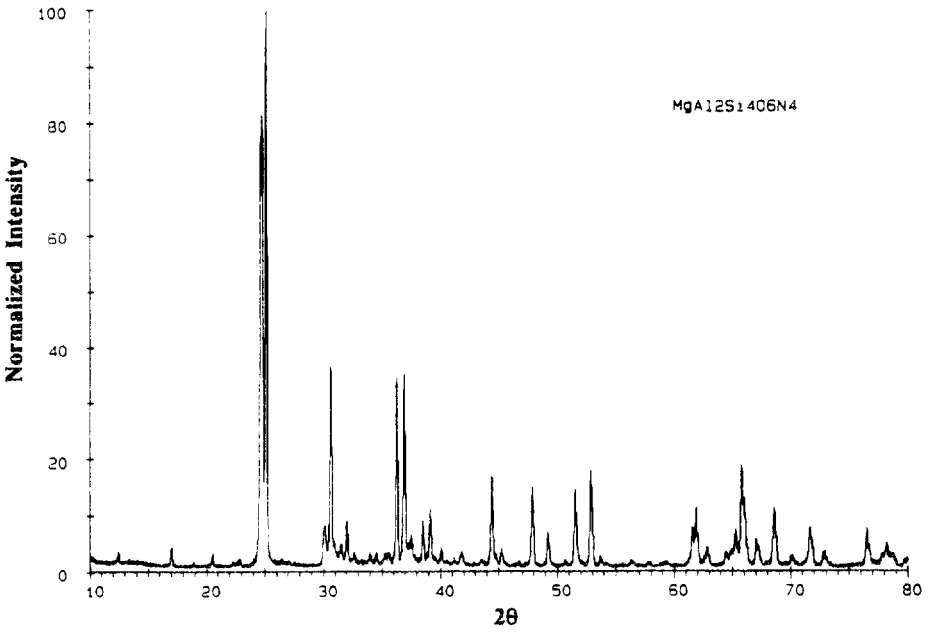

Figure 7. The single phase diffraction pattern of N-phase, $MgAl_2Si_4O_6N_4$.

1.2.3 Oxide Matrix

Dispersion-Toughened Ceramic Composite

T. N. Tiegs, W. H. Elliott, and P.A. Menchhofer (Oak Ridge National Laboratory)

Objective/scope

This work involves development and characterization of SiC whisker-reinforced ceramic composites for improved mechanical performance. To date, most of the work has dealt with alumina as the matrix because it was deemed a promising material for initial study. However, an effort in SiC whisker-reinforced silicon nitride and sialon is in progress. In addition, studies of whisker growth processes were initiated to improve the mechanical properties of SiC whiskers by reducing their flaw sizes.

Technical progress

Hot-pressed silicon nitride and sialon-SiC whisker composites. Specimens of silicon nitride and sialon, both with and without SiC whiskers, have been fabricated and tested at room and elevated temperatures for flexural strength. A summary of the flexural strength results on silicon nitride and sialon matrix composites is shown in Fig. 1. As shown, the flexural strengths are relatively stable up to approximately 1000°C. However, above 1000°C the strengths decrease for both the silicon nitride and the sialon materials. It is interesting to note that the flexural strengths for the monolithic materials (at 1200°C for the sialon and 1400°C for the silicon nitride) are greater than the composites. We believe this is due to the addition of SiO_2 that is associated with the SiC whiskers and the detrimental effect it has in changing the composition of the intergranular glass phase.

The effect of different whisker types from various manufacturers on the flexural strength is shown in Fig. 2. Again, the flexural strengths are relatively stable up to 1000°C, with slight decreases at higher temperatures, depending on the whisker type. The decrease is most dramatic for the American Matrix whisker composite and, like the composites shown in Fig. 1, it is related to the SiO_2 content of these whiskers. The other whisker types examined all have less associated SiO_2, and therefore the compositions of the intergranular glass phases are more refractory at elevated temperatures. Degradation of high-temperature creep and fatigue would also be affected in a similar manner due to SiO_2 additions from the whiskers. Consequently, removal of surface SiO_2 prior to composite fabrication is believed necessary to obtain optimum high-temperature properties in silicon nitride matrix composites.

The effect of SiC whisker content on high-temperature flexural strength of silicon nitride composites is shown in Fig. 3. The room-temperature strengths are comparable for the 10, 20, and 30 vol % composite materials. However, at 1000°C the 30 vol % composite shows a marked decrease in strength, while the 10 and 20 vol % materials are relatively stable. At 1200°C, the 10 vol % composite exhibits the highest strength, which is relatively unchanged from the room-temperature value. Silica additions to the intergranular glass phase are again thought to be responsible for the observed decrease in high-temperature flexural strength with increasing whisker content.

The effect of sialon matrix composition on the high-temperature strength was examined and is summarized in Fig. 4. As illustrated, the flexural strength of the Sialon A ($Si_{2.5}Al_{3.5}O_{3.5}N_{4.5}$) composite was drastically lower than the material containing less Al, Sialon AA ($Si_{4.5}Al_{1.5}O_{1.5}N_{6.5}$). However, Sialon A showed less of an effect of strength with temperature.

The quantity of the sintering aid also affects the high-temperature strength of the sialon matrix composites as shown in Fig. 5. At low levels of sintering aids (~0.5 % YAG), the composite densification is inhibited, and the result is a lower overall strength. However at 1200°C, the strength is nearly the same as the composites containing 2 % YAG sintering aid. The composite containing 8 % YAG had lower overall strength from room temperature up to 1200°C. The effect of changing the type of sintering aid on the high-temperature strength of sialon composites is shown in Fig. 6. While the sintering aid contents are not optimal, the results do illustrate the fact that the intergranular phase composition can be tailored to achieve improved high-temperature strength in sialon composites.

SiC Whiskers. As reported previously, flaws in SiC whiskers, such as internal inclusions and surface roughness, lead to strength degradation and, consequently, reduced effectiveness in increasing the fracture toughness in ceramic matrix composites. As part of the current work, SiC whisker growth studies have been started. The initial system consisted of colloidal SiO_2 and carbon black. Parameters to be investigated include catalyst type, atmosphere control, reactant geometry, and heating rates. Initial results show that SiC whisker growth is a two-stage process, where axial growth is very rapid followed by a slower lateral growth and an increase in diameter.

A series of whisker synthesis runs have been made using various catalysts. The catalysts include Fe, Fe_2O_3, Ni, Co, and CaO. Examination of the whisker growth by SEM revealed differences in morphology with catalyst type. These differences were most dramatic in the SiC whiskers catalyzed by Fe and CaO as shown in Fig. 7. TEM observations on these whiskers showed that only the CaO-catalyzed whiskers had any internal inclusions that are similar to those found in commercial materials.

Status of milestones

Milestone 123108 (complete study of mechanical properties of whisker sialon and silicon nitride composites) was completed on schedule.

Publications

T. N. Tiegs and D. M. Dillard, "Effect of Aspect Ratio and Liquid Phases on Sintering of Alumina-SiC Whisker Composites," submitted to *Journal of the American Ceramic Society.*

A draft report entitled, "Strength-Limiting Flaws in SiC Whiskers" by T. N. Tiegs, L. F. Allard, P. F. Becher, and M. K. Ferber is currently being reviewed.

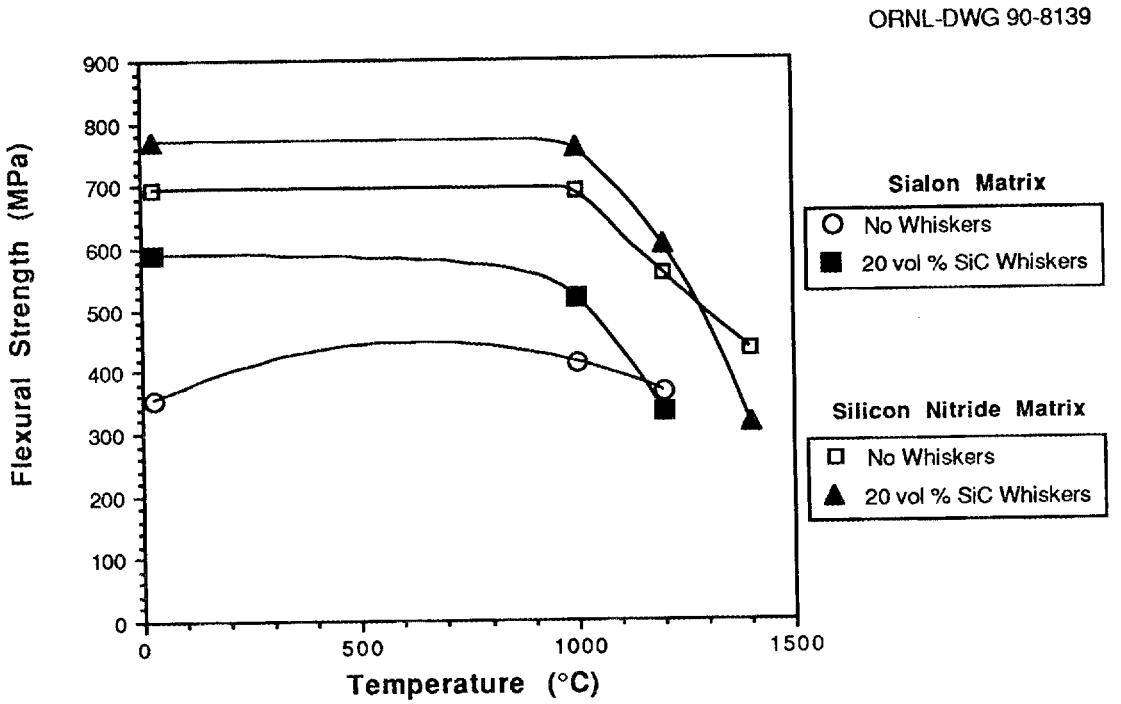

Fig. 1. High-temperature flexural strength of sialon ($Si_{4.5}Al_{1.5}O_{1.5}N_{6.5}$-2% $3Y_2O_3$-$5Al_2O_3$) and silicon nitride (Si_3N_4-6% Y_2O_3-2% Al_2O_3) materials with and without SiC whiskers. Whiskers are from American Matrix.

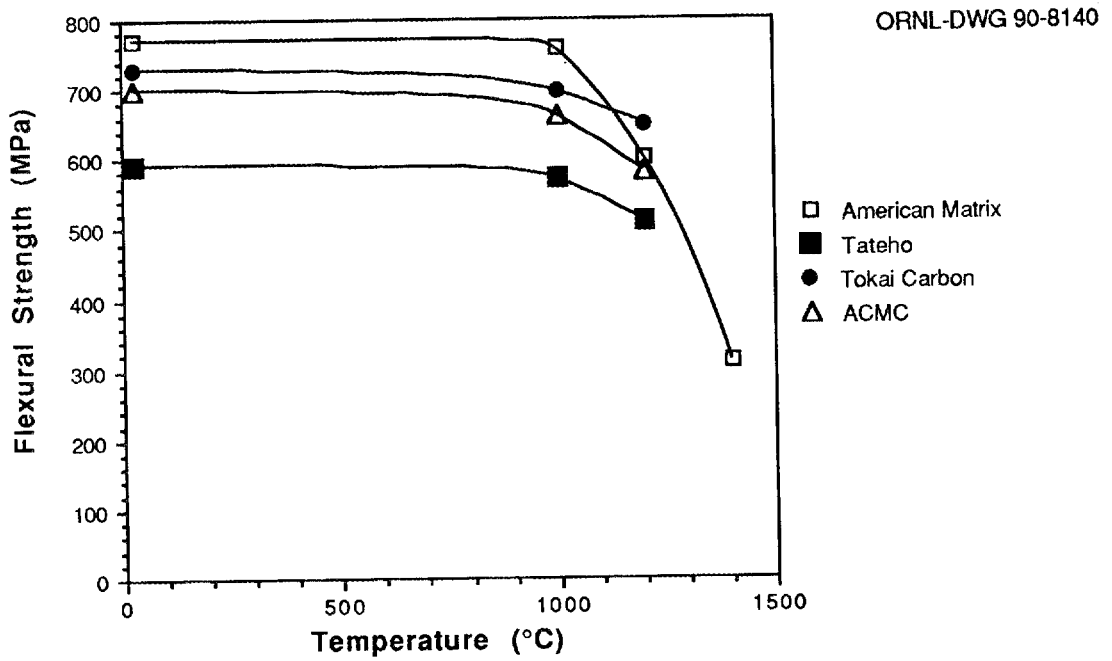

Fig. 2. High-temperature flexural strength of silicon nitride (Si_3N_4-6% Y_2O_3-2% Al_2O_3) materials with various types of SiC whiskers. Whisker content was 20 vol % for all composites. ACMC is Advanced Composites Materials Corporation.

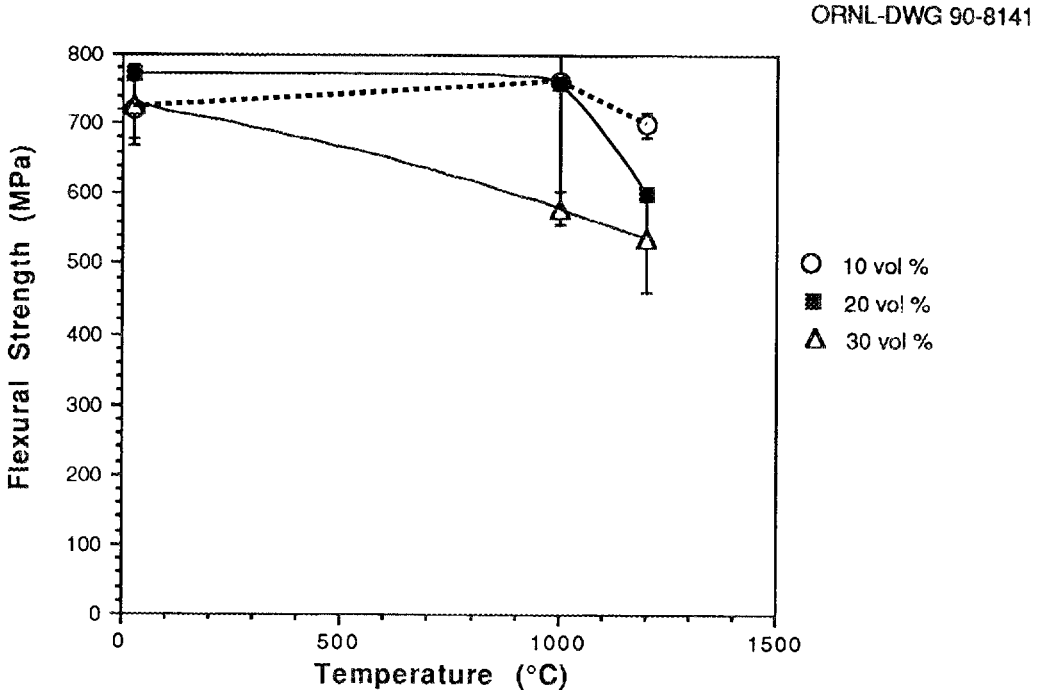

Fig. 3. Effect of SiC whisker content on high-temperature flexural strength of silicon nitride (Si_3N_4-6% Y_2O_3-2% Al_2O_3) composites. American Matrix SiC whiskers used in composites.

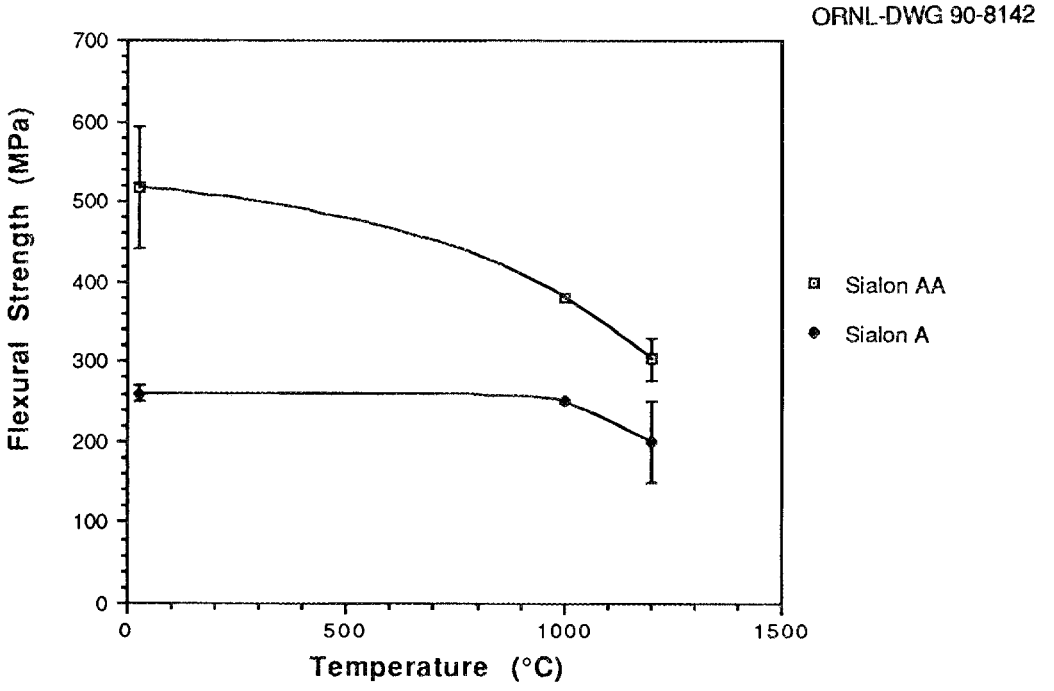

Fig. 4. High-temperature flexural strength of two sialon matrix composites. Sialon A–$Si_{2.5}Al_{3.5}O_{3.5}N_{4.5}$; Sialon AA–$Si_{4.5}Al_{1.5}O_{1.5}N_{6.5}$. Both compositions contain 20 vol % American Matrix SiC whiskers.

ORNL-DWG 90-8143

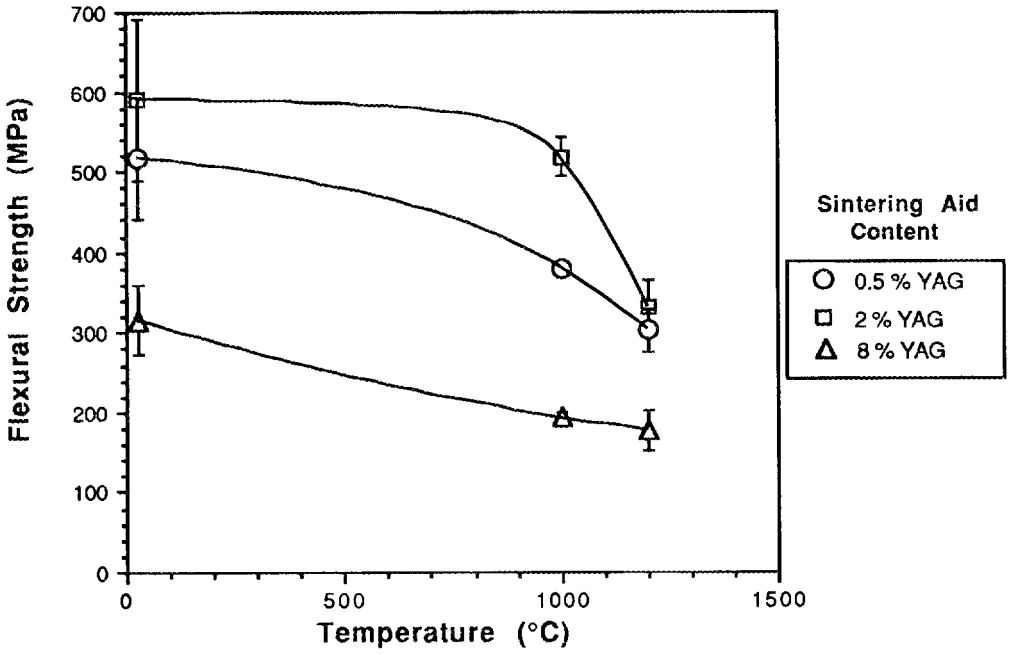

Fig. 5. Effect of sintering aid content on high-temperature flexural strength of sialon-20 vol % SiC composites. Sialon composition is $Si_{4.5}Al_{1.5}O_{1.5}N_{6.5}$, YAG is $3Y_2O_3$-$5Al_2O_3$, and whisker type is American Matrix.

ORNL-DWG 90-8144

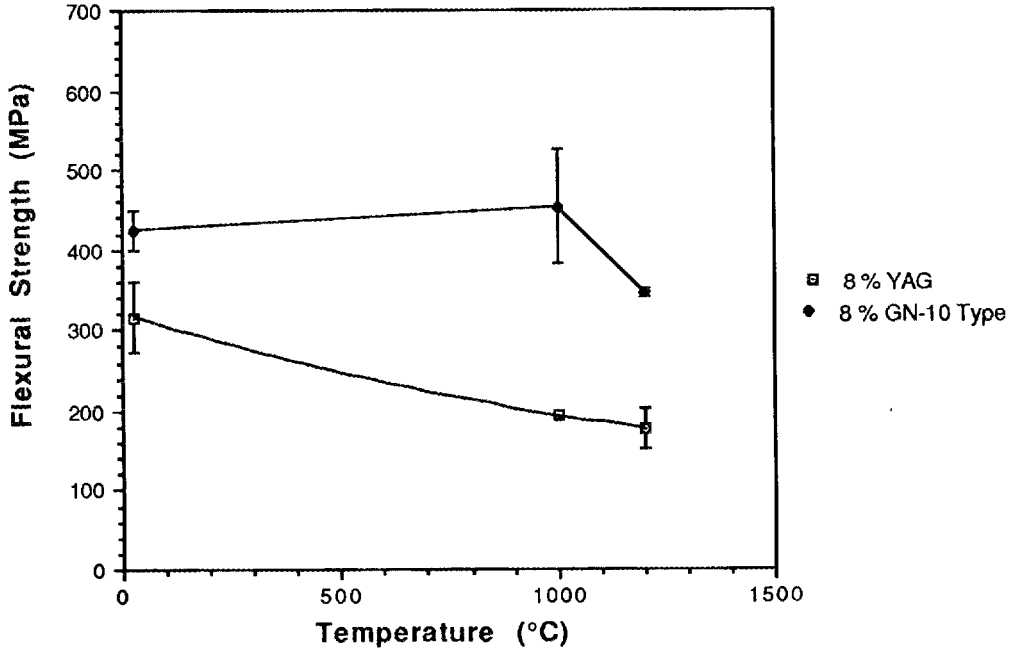

Fig. 6. Effect of sintering aid type on high-temperature flexural strength of sialon- 20 vol % SiC whisker composites. Sialon composition is $Si_{4.5}Al_{1.5}O_{1.5}N_{6.5}$, YAG is $3Y_2O_3$-$5Al_2O_3$, GN-10 is sintering aid designation given by Garrett Ceramic Components Division and whisker type is American Matrix.

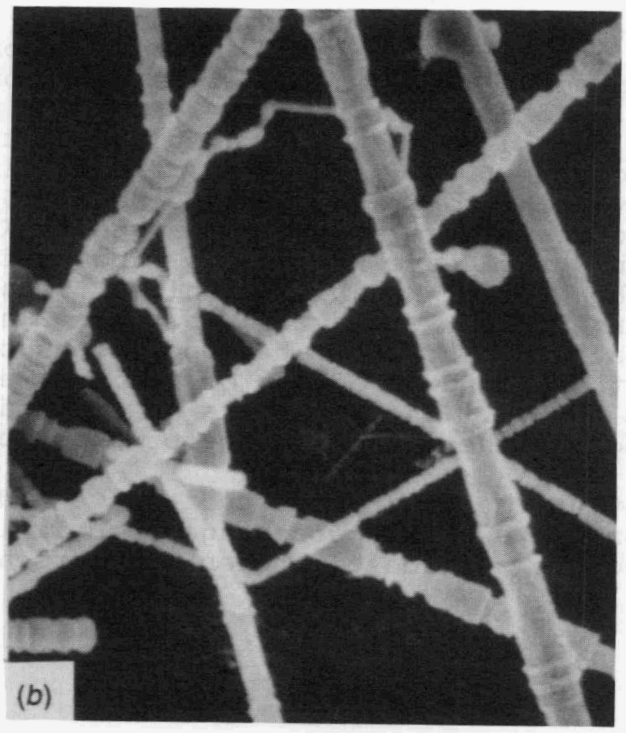

Fig. 7. Morphology of SiC whiskers grown using catalysts of (a) Fe and (b) CaO.

Processing of Improved Transformation-Toughened Ceramics

E. Lilley and G. A. Rossi (Norton Co., Advanced Ceramics)

OBJECTIVE/SCOPE

The objective of Phase IIA is to optimize the properties of two classes of transformation toughened ceramics, which were already studied in Phase I of this contract. These ceramics are Y-TZP (Y_2O_3 stabilized Tetragonal Zirconia Polycrystals) and Ce-ZTA (CeO_2-ZrO_2 toughened Al_2O_3).

For the Y-TZP materials, one of the main efforts will be to study the low temperature degradation and understand how it is affected by microstructure and composition. In the case of the Ce-ZTA ceramics, the main goal is to optimize the high temperature mechanical properties by minimizing the flaw size and controlling the microstructures.

TECHNICAL PROGRESS

1. Y-TZP

1.1 Mechanical Properties Development

Toughness measurements have been made on a variety of our Y-TZP materials of different composition and grain size. Two techniques have been used. First the double torsion technique which had been used previously to measure K_{IC} as a function of temperature up to 700°C. Secondly the micro indentation method with improvements by OKwon [1] of this laboratory. He has minimized the effect of slow crack growth and then used the Niihara et al equation for Palmquist cracks [2]. Variations of composition between 4.7 and 5.5w% yttria and grain sizes between 0.5 and 1.0 micron showed no observable systematic changes in K_{IC}. The micro indentation method gave K_{IC} values ranging from 7.4 to 8.8 MPa $m^{\frac{1}{2}}$. The work of Masaki and Shinjo [3] at Toray showed little change in K_{IC} with yttria between 3 and 5m% but there was a large increase at compositions below 3m%. Likewise, they found no effect of grain size between 0.2 and 0.7 micron on K_{IC}. Their results and ours are both contrary to the theories of transformation toughening.

In contrast to the toughness studies, we did find a strong correlation between the percentage monoclinic phase formed on the fracture surface of broken MOR bars and (i) yttria

concentration, and (ii) grain size. These results are shown in Figure 1 and 2. The data point at 4w% yttria is approximate since it was taken from a sample heated 5 hours at 1500°C which is expected to cause partitioning and so we have assumed that the resulting tetragonal phase has a composition of 4w%. In Figure 1 MG008, MG024 and MG026 each have a grain size of 1.0 micron whereas the overaged bar has about 2 microns grain size. It is interesting to see that at the higher yttria levels and smaller grain sizes there is a diminishing percentage of monoclinic formed on the fracture surface and yet the K_{IC} values are still 7-8 MPa $m^{\frac{1}{2}}$ as measured by micro indentation and double torsion.

We conclude that the measured toughness values are not simply a function of normal (irreversible) transformation toughening but that another mechanism must be operating too.

1.2 Low Temperature Degradation

Work has continued on measuring the low temperature degradation at 250°C in slightly humid nitrogen of various Y-TZP's made from arc melted, rapidly solidified crude. The depth of the monoclinic transformed surface layer was measured by optical microscopy on fracture surface of MOR bars after exposure for times up to 2500 hours. Recent results are included in Figure 3. The 5.5w% MG026 HIPped bars performed quite well but the best result is for the same powder classified to give a sintered grain size of ~0.5 micron (MG026/CLS/S). No transformation occurs in this material in 1000 hours. Exposures are being continued to 2000 hours.

In our current studies we have mainly relied upon fracturing bend bars to create a cross section which reveals the transformation zone in bars which have been exposed to moisture at different temperatures. Figure 4 is a low magnification SEM photograph of a bar of MG008/S previously held at 120°C/water for 1000 hours. The degraded zone (~80% monoclinic) is about 130 microns thick. The interface between the lighter transformed rim and the darker untransformed interior is shown in Figures 5 and 6 at different magnifications. The transformed region caused by the exposure to water has subsequently suffered in intercrystalline fracture whereas the untransformed interior has a predominantly transcrystalline fracture. It is evident that low temperature degradation has caused microcracking at the grain boundaries which leads to intergranular fracture when the MOR bar is broken.

A crack can be seen in Figure 6 running along the boundary between the transformed and untransformed regions. Compressive stresses build up within the transformed zone due to a volume expansion as the tetragonal phase transforms to monoclinic. However, it is likely that this crack occurred only after the breaking of the MOR bar since we do not see evidence of other extensive cracks which could have formed at this interface as it proceeded inwards.

Another way of examining the degraded surface layer is to probe it with a diamond indentor. This was done with different loads applied to a Vickers indentor. The calculated hardness and toughness (K_{IC}) values are shown in Table 1 for two different specimens. The first was our standard MG008/sintered exposed to slightly moist nitrogen at 250°C and the second was the same material immersed in water at 120°C for 500 hours.

Table 1

Test	Load Applied (kgm)	Hardness (GPa)	K_{IC} (MPa $m^{\frac{1}{2}}$)	Depth of Transformed Zone (Micron)
250°C/1000 hrs	5	13	14	100
	10	13	13	-
	20	13	10	-
	50	13	8	-
120°C/Water 500 hrs	5	8	7	120
	10	9	8	
	20	8	7	
Unexposed		13.5	8.5	0

The accuracy of the measurements of both the diamond impressions and of the crack lengths is not good because these are microcracked materials and suffer from irregularities. It was also necessary to use the modulus of dense zirconia of 220 GPa which is clearly too high. Consequently, the derived values of hardness and toughness are very approximate.

The two types of exposure, one in vapor the other immersed in water produce different types of degraded layers even when they are about the same thickness. The hardness results show that the immersed sample must have cracked much more than the 250°C vapor sample. In fact, with a load of 50 kg, the transformed layer of the immersion sample chipped off around the indent impression making it impossible to measure. The 250°C vapor sample also exhibits a reduction in hardness compared with the unexposed material, but this change is relatively small.

The vapor exposed material appears to have a high toughness when low loads are used when compared to the K_{IC} value of 8.5 MPa for the unexposed zirconia. Microcracking of the transformed layer, which is under residual compressive stress, inhibits the propagation of the indent crack.

These indentation results highlight the difference in degradation between the two types of exposure which leads to little change in modulus of rupture for the 250°C vapor exposure but to a marked decrease for the water immersion exposure.

2. Ce-ZTA Ceramics

2.1 Strength Enhancement by Improved Processing

It was previously shown (4) that the ceramics with the composition Z18.5CE62A (38 w/o ZrO_2 with 18.5 w/o CeO_2, and 62 w/o Al_2O_3) fabricated using a powder obtained by milling of a rapidly solidified (R/S) crude, exhibited a uniform microstructure and a higher strength compared to ceramics of a similar composition (Z16CE60A) made by dry pressing of a mechanically mixed powder (R/S 16 w/o CeO_2-ZrO_2 and AKP-30 Sumitomo Al_2O_3).

During this reporting period efforts were concentrated on further improvement of the wet powder processing, in order to maximize strength by reducing the number and size of the internal flaws and to meet the 1000°C strength goal of 500 MPa.

Particular care was exercised in trying to avoid foreign contamination during planetary milling with water of the crude previously calcined at 1050°C. The aqueous slurry was filtered through a 5 um filter and then used for pressure casting of billets, avoiding any exposure to the environment. Such precautions resulted in improved strength, a shown by Table 2 and both strength goals of 700 MPa at room temperature and 500 MPa at 1000°C were met. All billets were pressureless sintered at 1600°C/1 hr. Table 2 shows the progress made by switching from die pressing to pressure filtration and the improvement brought about by a clean processing procedure in the pressure casted materials.

Table 2

Influence of Processing on Flexural Strength of Ce-TZP/Al_2O_3 Composites Made With a Rapidly Solidified Powder

RT MOR	#	SD%	1000°C MOR	#	SD%	REMARKS
634	10	13	---	--	--	DP/CIP
482	9	24	---	--	--	UNF/PC
799	10	17	---	--	--	F/PC
903	7	14	402	10	20	F/PC
951	7	32	515	6	8	F/PC

Note: MOR values are in MPa; # = number of test bars; SD% = percent standard deviation; DP = die pressing; CIP = cold isostatic pressing; F = filtered suspension; UNF = unfiltered suspension; PC = pressure casted.

Fractographic analysis on the broken MOR bars has shown that in the ceramics made by filtering/pressure casting virtually all fracture origins are surface defects caused by machining. In most cases, such defects were localized in the bar chamfers, as shown by Figures 7 and 8. It appears therefore that careful wet processing has virtually eliminated the volume flaws (agglomerates, voids, inclusions, foreign particles) introduced in the dry pressing operations and shown in the previous semiannual report.

2.2 Transformability/Microstructure Relationship

The objective of this study was to understand the microstructure/property relationship in the Z18.5CE62A ceramics. Die pressed/ CIPed billets using the powder obtained by milling the crude calcined at 1050°C were sintered at 1600°C for 1, 3 and 6 hrs., in order to develop three different microstructures with progressively larger grain size. Samples from each material were analyzed by XRD for phase content and quantitative microstructural analysis (grain size distribution) was performed using SEM and an automatic image analyzer. Low temperature (Liquid N_2) dilatometry was also performed to study the transformability as a function of grain size and determine the M_s and M_f temperatures.

The results of this research, done at ORNL by G. A. Rossi in collaboration with Dr. P. F. Becher, have been analyzed and interpreted and the results are reported below.

Figures 9, 10 and 11 show the three microstructures and Figures 12, 13 and 14 the grain size distribution hystograms for ZrO_2 and Al_2O_3. Figures 15, 16 and 17 show the LN_2 dilatometry results.

Table 3 summarizes the results.

Table 3

Effect of Microstructure on t/m Transformation of CeO_2-ZrO_2 in Ce-ZTA Composites

MATERIAL	% m-ZrO_2 G	%m-ZrO_2 G+A	A.G.S. ZrO_2	A.G.S. Al_2O_3	C.G.S. G	C.G.S G+A	K_{IC}
1600/1	30	4	1.19	1.33	1.3	2.0	13.6* 6.7+ 8.6^
1600/3	47	17	1.55	1.56	1.3	2.0	10.7* 6.3+
1600/6	58	29	1.69	1.93	1.3	2.0	10.9* 6.4+

Note: G = ground surface; A = annealed at 1000°C; A.G.S = average grain size (um); C.G.S. = critical grain size for transformation (um); * = MCF (multiple control flaw) + = microindentation (Charles and Evans); ^ = microindentation (Palmqvist model).

The following conclusions can be drawn after this study:

1. The fraction of t-CeO_2-ZrO_2 grains transformed upon grinding increases with the grain size, as expected. Likewise, the fraction of m-ZrO_2 grains, spontaneously transformed on cooling after annealing the machined sample at 1000°C, increases with grain size.

2. The growth rates of the ZrO_2 and Al_2O_3 grains at 1600°C appear to be similar, as shown by the size ratio vs. soak time at 1600°C.

3. The ceramic fired at 1600°C/1 hr. shows a greater transformation toughening contribution, compared to those fired for 3 and 6 hrs., as shown by the larger expansion corresponding to the two temperatures M_b (burst) and M_s (start).

4. The critical grain size for spontaneous transformation in the three materials is about 2 um, whereas for transformations under grinding stress it is about 1.3 um. These values were obtained using the percent m-ZrO_2 from columns 2 and 3 of Table 3, calculated from XRD data, and the cumulative grain size distribution curves for the CeO_2-ZrO_2 grains. For example, for the 1600/1 material, which shows 30% m-ZrO_2 on the ground surface, assuming that 30% of the t-CeO_2-ZrO_2 grains have transformed, the cumulative curve indicates that 30% of the grains are larger than 1.3 um.

5. By comparing the low temperature dilatometry curves of these Ce-ZTA composites with those obtained by Becher et al. (5) on Ce-TZP ceramics with similar CeO_2 content, it appears that, for similar grain sizes, the t-CeO_2-ZrO_2 grains are more easily transformable in Ce-ZTA than the Ce-TZP. A possible explanation is the residual stress caused by the difference in elastic moduli and thermal expansion between ZrO_2 and Al_2O_3.

6. A clear relationship between transformability and fracture toughness was not found, except when K_{IC} was measured with the MCF method.

The study of grain size effect on transformation was also carried out for the Z16CE60A ceramic made with mechanically mixed powders (R/S 16 w/o CeO_2-ZrO_2 and AKP-30 Al_2O_3) sintered/HIPed at 1500°C. This material, whose microstructure is shown for the sake of comparison in Figure 18, had shown virtually no m-ZrO_2 on both ground and polished/annealed surfaces, as opposed to 30% and 4% m-ZrO_2, respectively, for ground and polished surfaces of the Z18.5CE62A ceramic fired at 1600°C/1 hr. This difference in transformability is likely due to the smaller grain size of the Z16CE60A sample, as shown by the two microstructures of Figures 9 and 18. In fact, annealing at 1550°C for different times samples of the Z16CE60A ceramic resulted in increased spontaneous transformation to m-ZrO_2, due to grain growth, as shown in the Table 4.

Table 4

Effect of Annealing Time at 1550°C on Transformability of the t-CeO_2-ZrO_2 Grains in the Z16CE60A Composite

Annealing time (hr.)	0	1	3	5
% m-ZrO_2	1.1	2.7	7.3	14.4

Note: Original sample (first column) was annealed at 1000°C. The samples annealed at 1550°C were about 1 cm^2 squares cut from a double torsion sample (50x25x1 mm) used for K_{IC} measurement.

2.3 Effect of Grain Size on Low Temperature Degradation (LTD) Resistance of Z18.5CE62A Composites

Since the study of the LTD resistance of Y-TZP ceramics is an important part of Phase IIA of this contract, some experiments were performed to evaluate the LTD resistance in autoclave of the Z18.5CE62A composites as a function of grain size. This was done for comparison purposes, even though it was not specifically requested by the Statement of Work.

Broken pieces of MOR bars of the Z18.5CE62A ceramics sintered at 1600°C for 1, 3 and 6 hrs. were subjected to two autoclave treatments as described in the following Table 5 and the percent m-ZrO_2 was measured by XRD before and after the autoclave test.

Table 5

Grain Size Effect on LTD Resistance in a Ce-TZP/Al_2O_3 Composite

SAMPLE	% m-ZrO_2 BEFORE	% m-ZrO_2 AFTER	REMARKS
Autoclave Test in Water at 150°C/.5 MPA/24 hrs.			
1600/1	30	36	Uncracked*
1600/3	47	54	"
1600/6	58	69	"
Autoclave Test in Water at 250°C/4 MPa/24 hrs.			
1600/1	30	--	Uncracked*
1600/3	47	74	"
1600/6	58	100	All cracked

Note: * = No cracks visible using optical microscopy

Considering the severity of these tests, which cause extensive degradation and destruction of Y-TZP's, it can be concluded that the LTD resistance of these Ce-ZTA composites is very good as long as the ceramics are not overaged.

STATUS OF MILESTONES

All milestones are on schedule. Billets of Z18.5CE62A sintered to theoretical density at 1500°C were mailed to Dr. P. F. Becher on 9/15/89 as final deliverables for Phase IIA of the contract. The last milestone is the delivery of the final report on 10/31/89 and is on schedule.

PUBLICATIONS

Two papers on the fabrication and properties of Ce-TZP/Al_2O_3 composites were presented at the Las Vegas Conference on Ceramics for Engines (authors G. A. Rossi and P. J. Pelletier) and at the 7th SIMCER in Bologna, Italy (author G. A. Rossi), at the end of 1988. Both papers have appeared in the Proceedings of the two conferences.

REFERENCES

[1] O. Kwon, M.V. Swain and J. Trogolo, American Ceramic Society Meeting, April, 1989, Indianapolis.

[2] K. Niihara, R. Morena and D. Hasselman, J. Mater, Sci Lett, 1; 13-16 (1982).

[3] T. Masaki and K. Shinjo, Advanced in Ceramics, 24B, 709-720, (1988).

[4] Semiannual Report, this contract, period Oct. 1988-Mar. 1989.

[5] P. F. Becher and G. M. Begun "Grain size Dependent Transformation Behavior in Polycrystalline Tetragonal Zirconia Ceramics", presented at the 91st Annual Meeting of the Am. Ceram. Soc., Indianapolis, IN.

Figure 1

EFFECT OF YTTRIA CONCENTRATION

ON THE MONOCLINIC % (XRD)

AT THE FRACTURE SURFACE

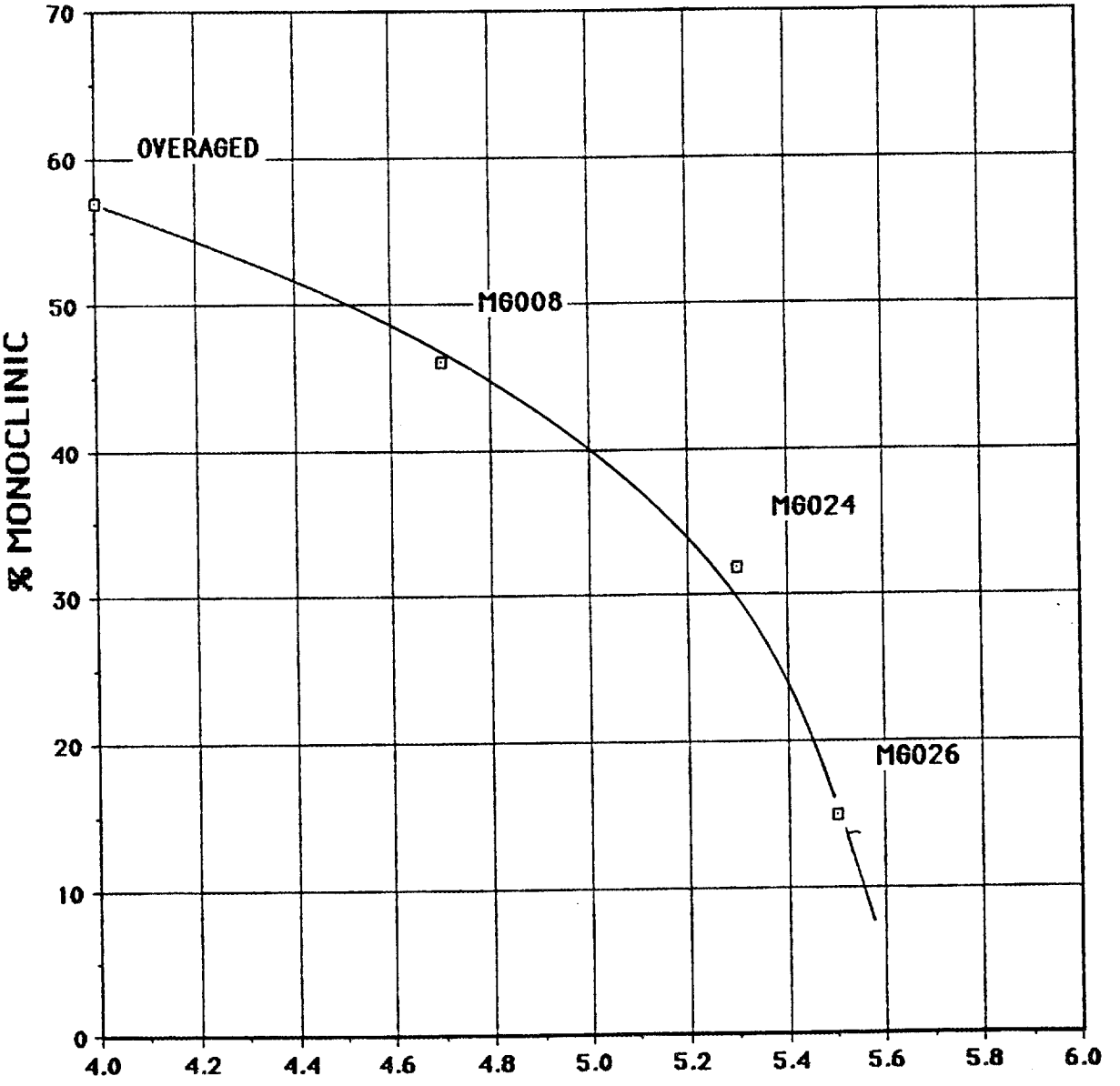

Figure 2

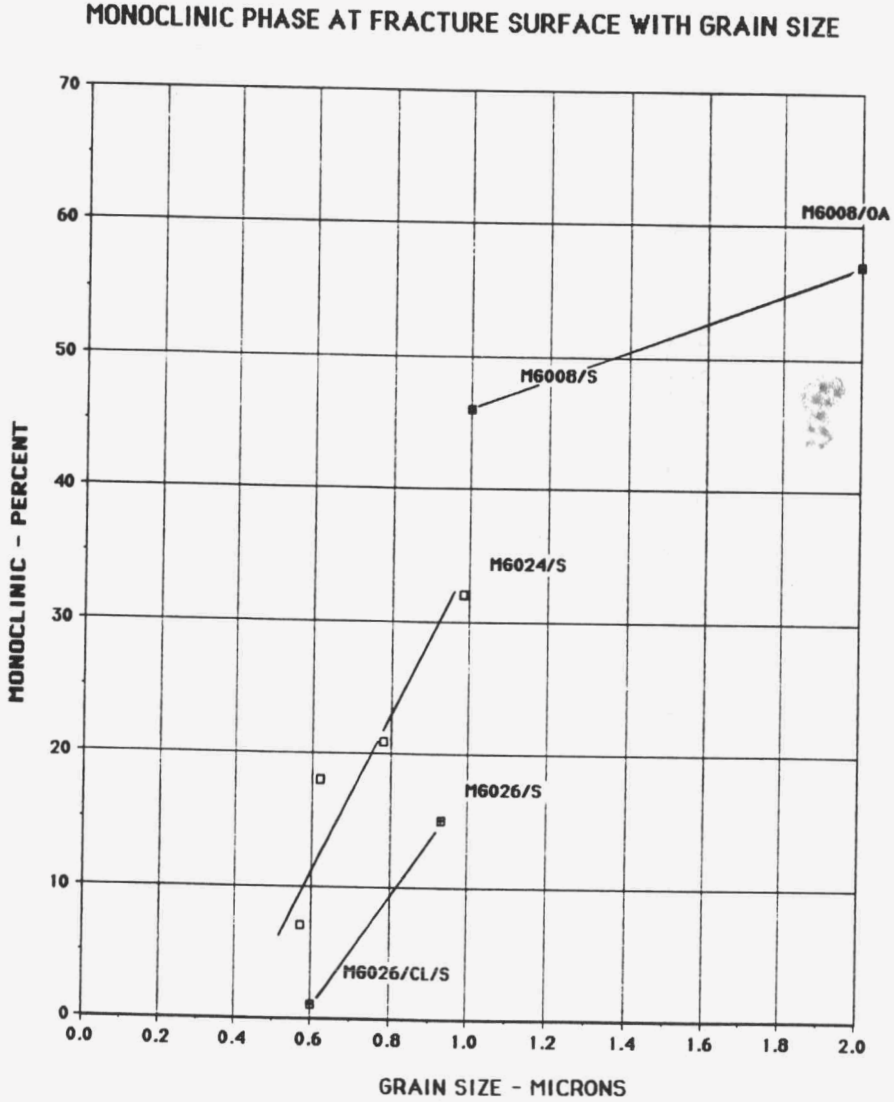

CODE VAR YZ %M/GS 421GR

EL/AB 4/21/89

Figure 3

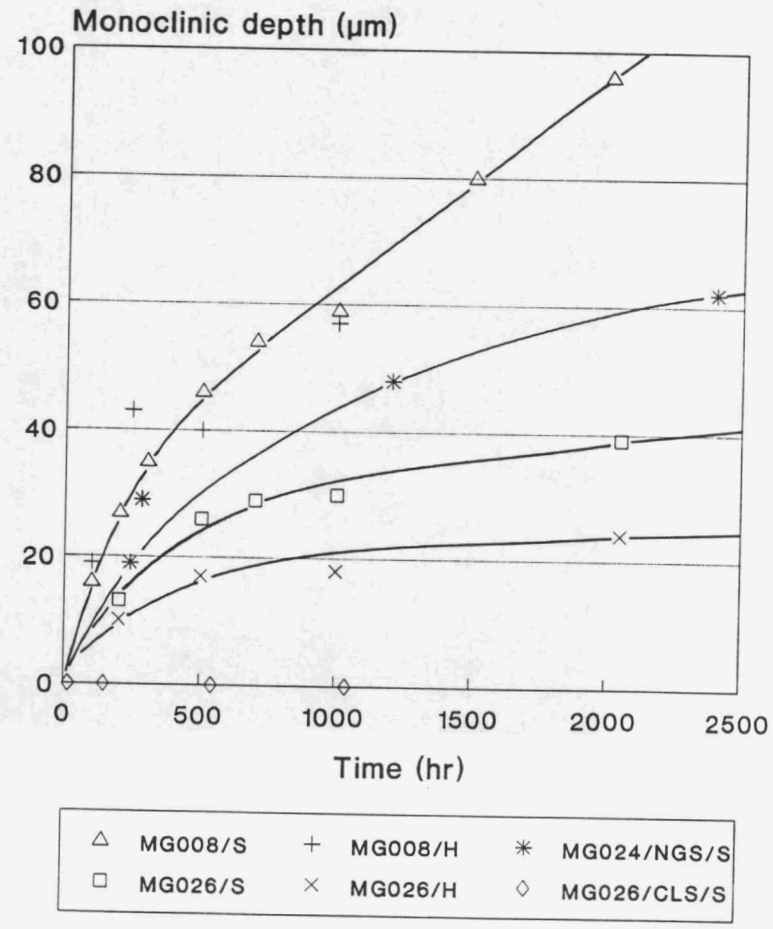

LTD Monoclinic Depth vs. Time
at 250 C/Oven

Figure 4: Fracture surface of MOR bar previously held for 1000 hrs. in water at 120°C. The rim of the bar has suffered low temperature degradation.

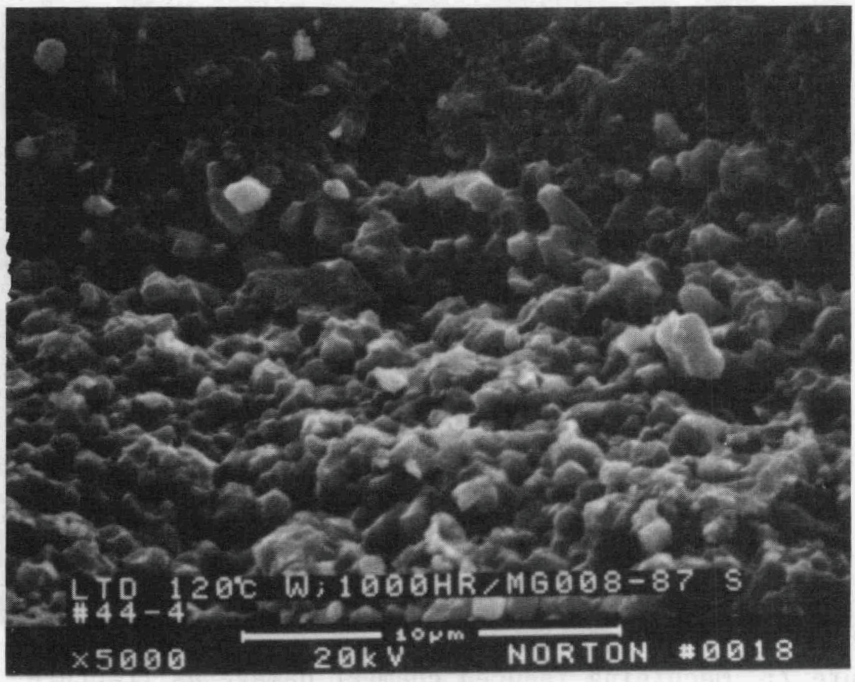

Figure 5: Same as Figure 4 but higher magnification showing the boundary between transformed (lower) and untransformed regions.

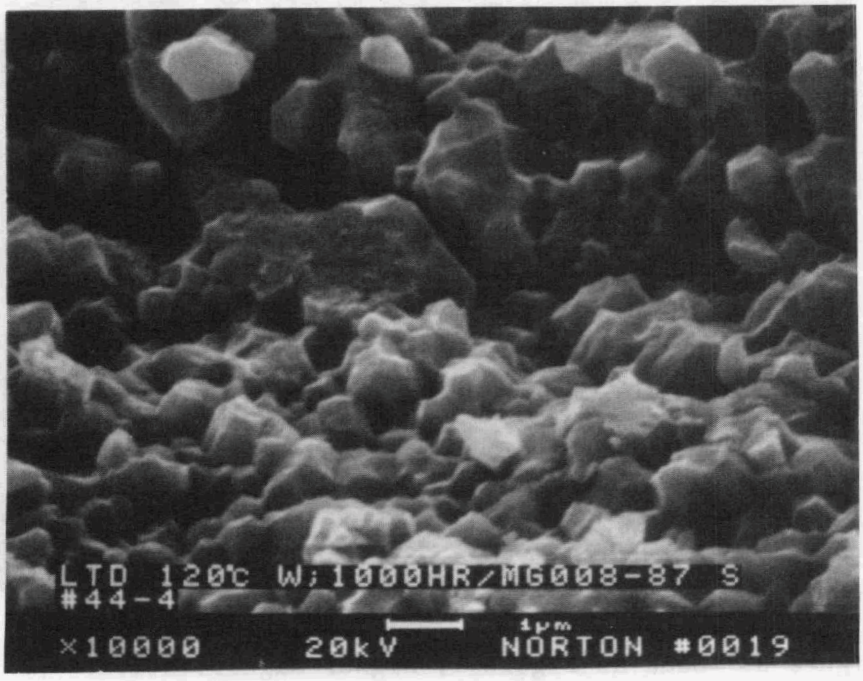

Figure 6: Same as Figure 4 but higher magnification. Notice the crack along the boundary between transformed and untransformed regions.

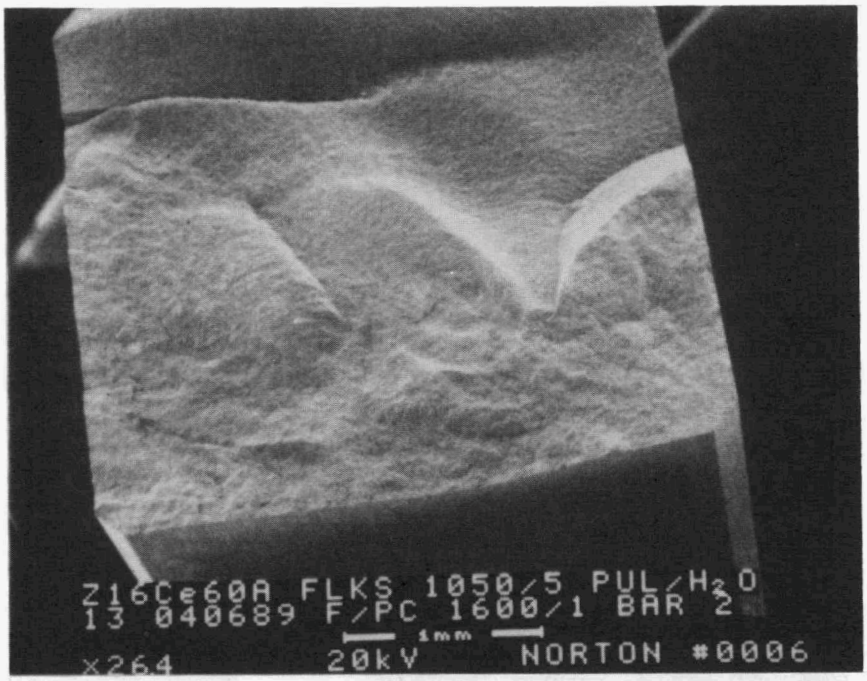

Figure 7: Machining induced chamfer damage as fracture origin.

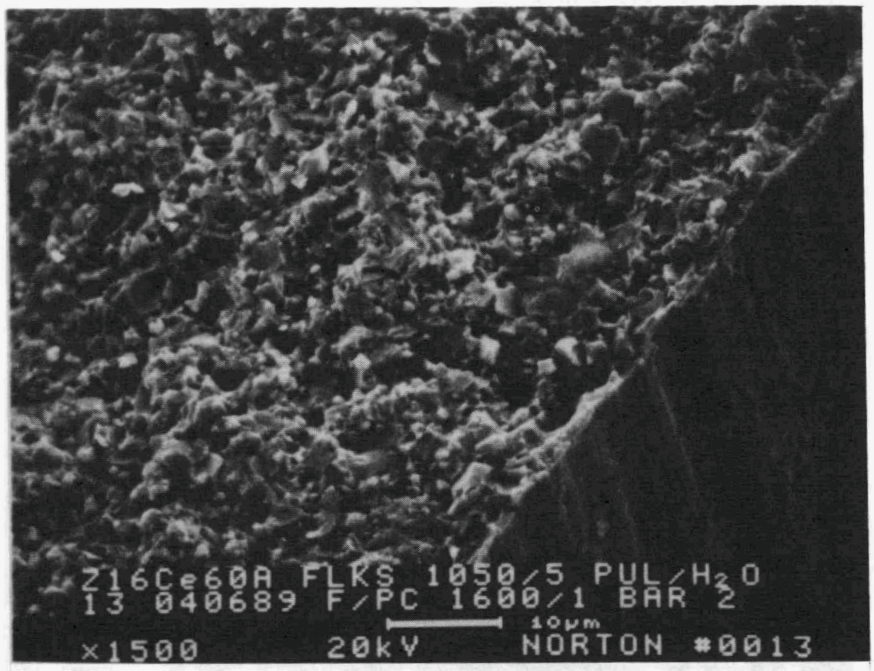

Figure 8: Same as Figure 1, higher magnification.

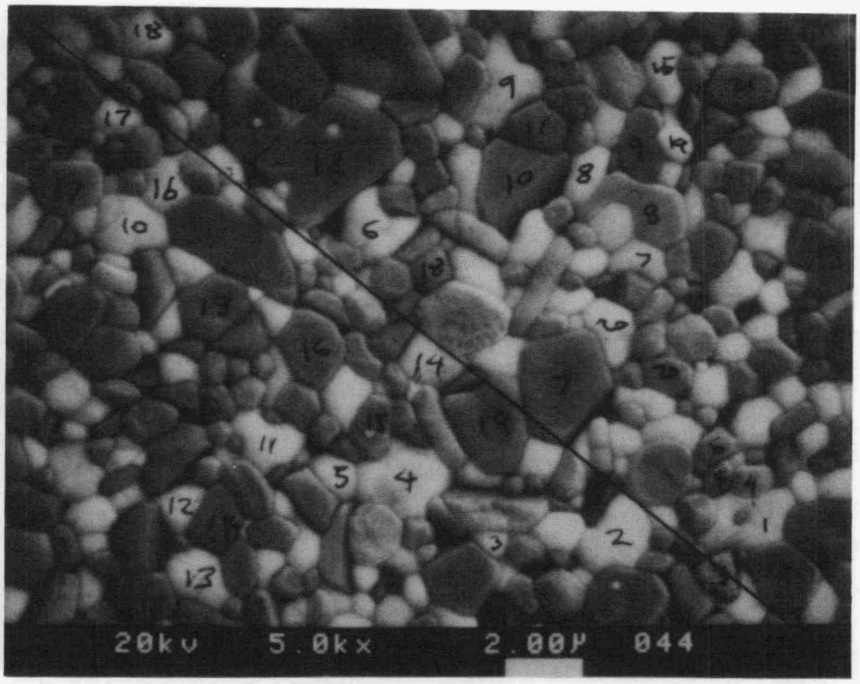

Figure 9: Microstructure (SEM) of Z18.5CE62A ceramic sintered at 1600°C/1 hr.

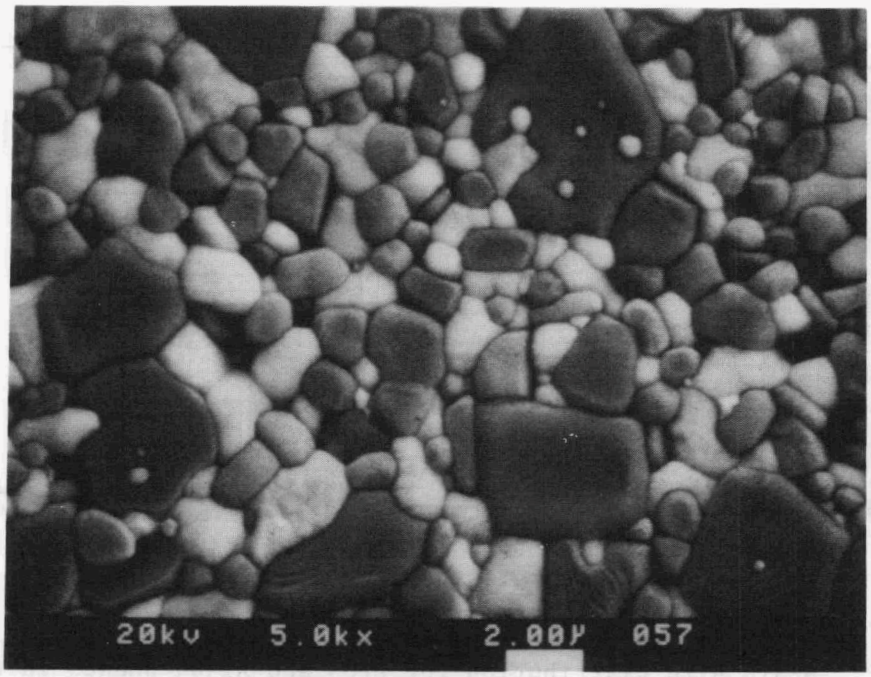

Figure 10: Microstructure (SEM) of Z18.5CE62A ceramic fired at 1600°C/3 hrs.

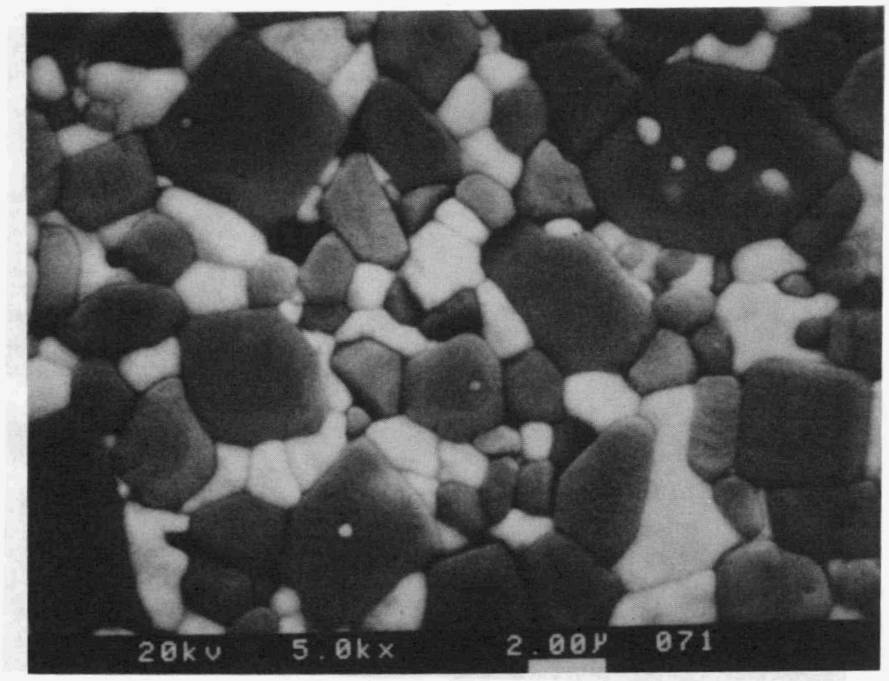

Figure 11: Microstructure (SEM) of Z18.5CE62A ceramic fired at 1600°C/6 hrs.

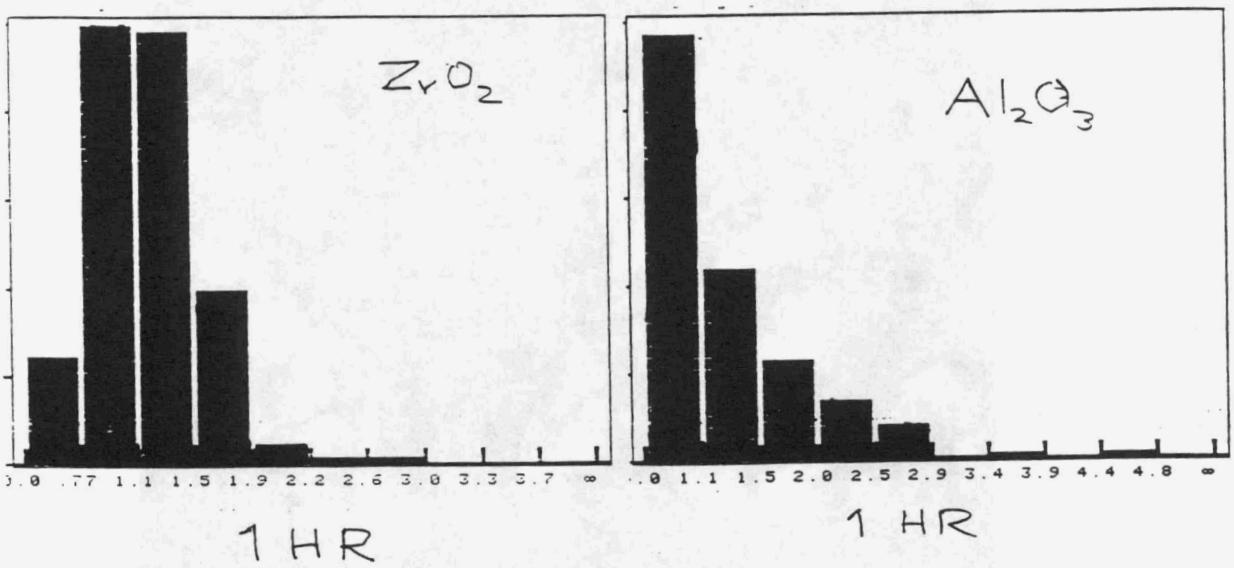

Figure 12: Grain size distribution for ZrO_2 and Al_2O_3 phases in the Z18.5CE62A ceramic fired at 1600°C/1 hr.

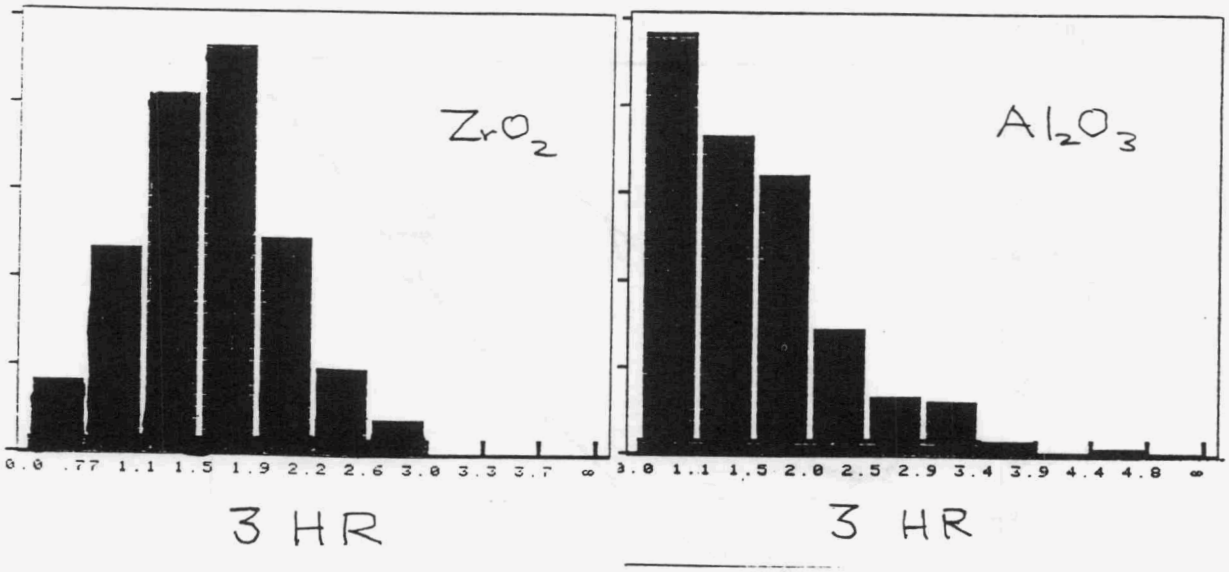

Figure 13: Grain size distribution for ZrO_2 and Al_2O_3 phases in the Z18.5CE62A ceramic fired at 1600°C/3 hrs.

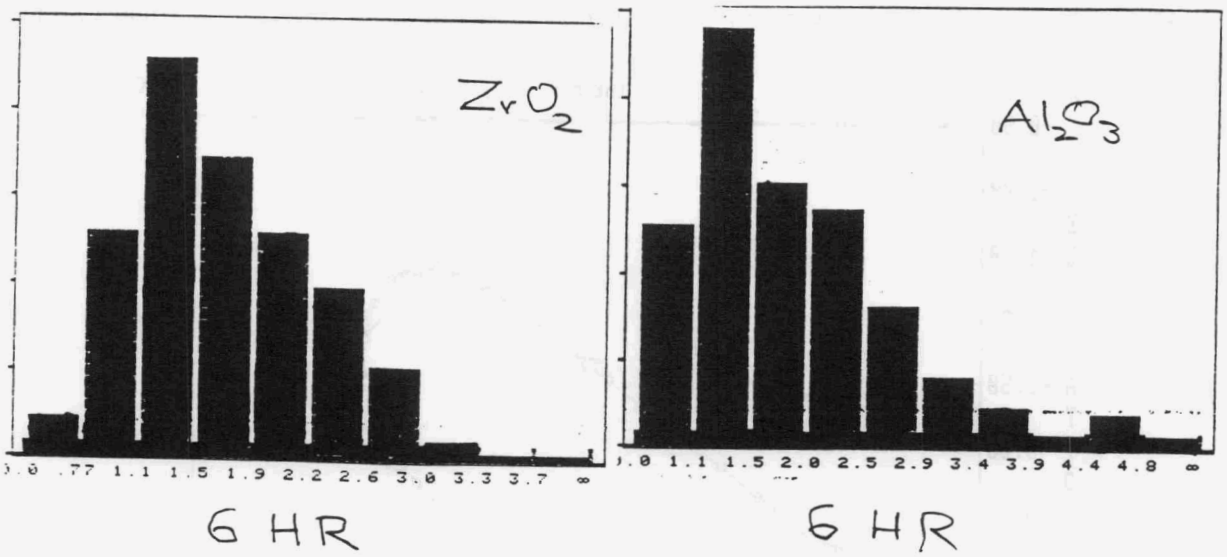

Figure 14: Grain size distribution for ZrO_2 and Al_2O_3 phases in the Z18.5CE62A ceramic fired at 1600°C/6 hrs.

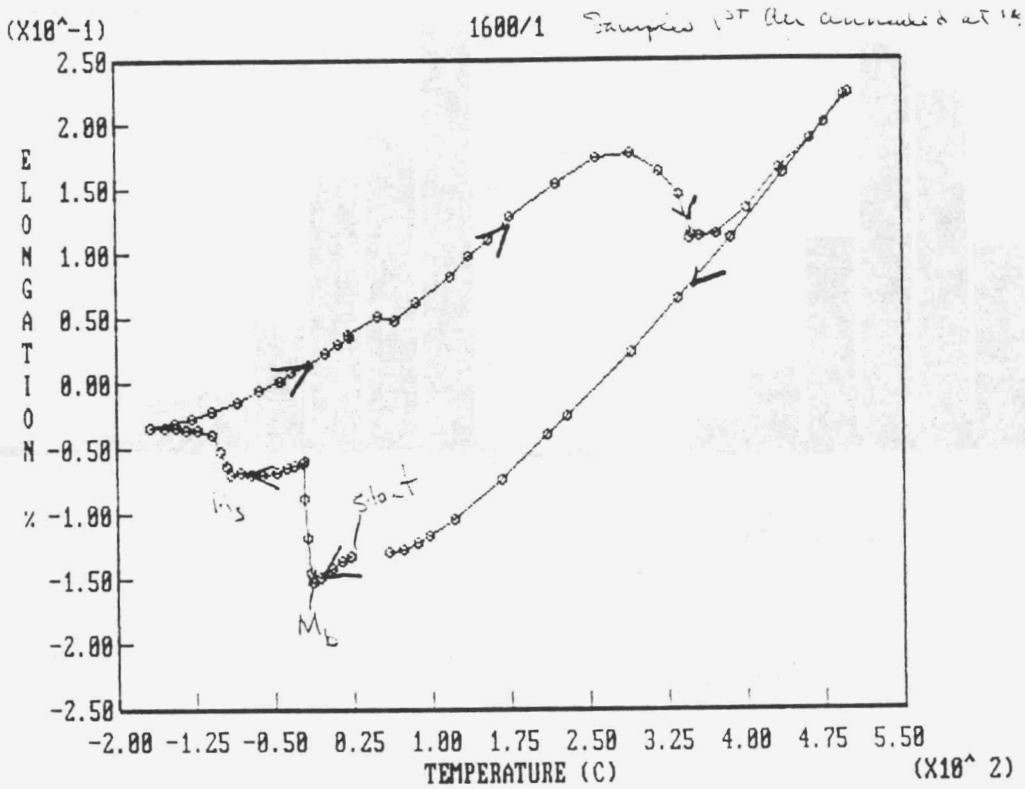

Figure 15: Liquid N_2 dilatometry curve for Z18.5CE62A ceramic fired at 1600°C/1 hr.

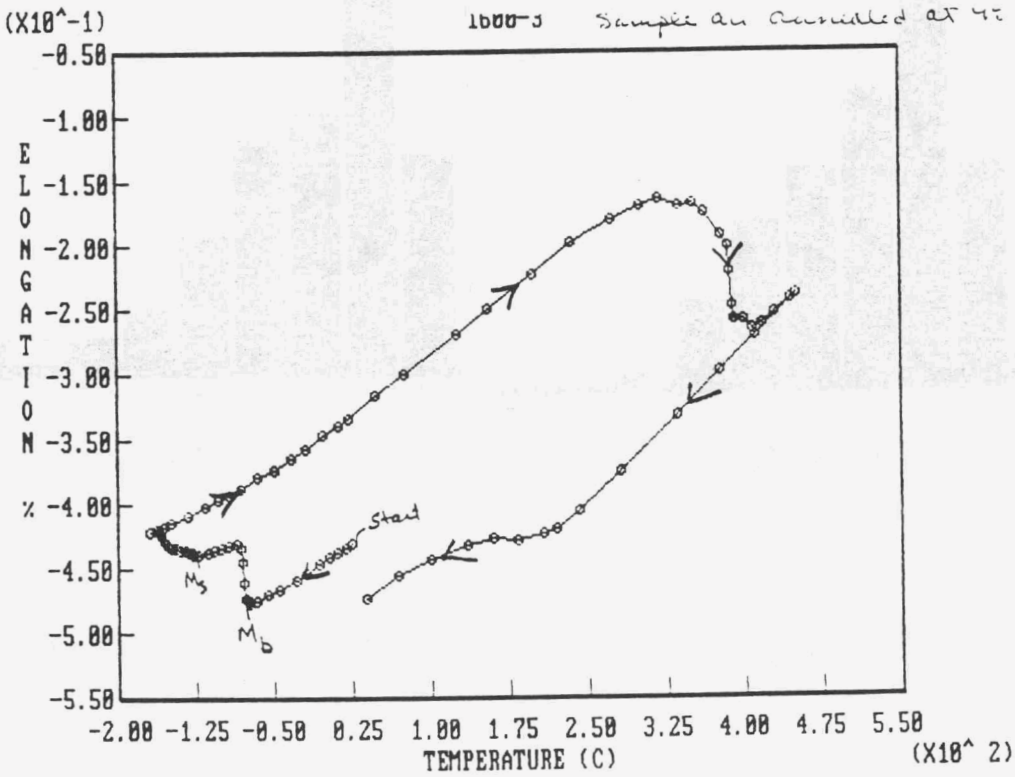

Figure 16: Liquid N_2 dilatometry curve for Z18.5CE62A ceramic fired at 1600°C/3 hrs.

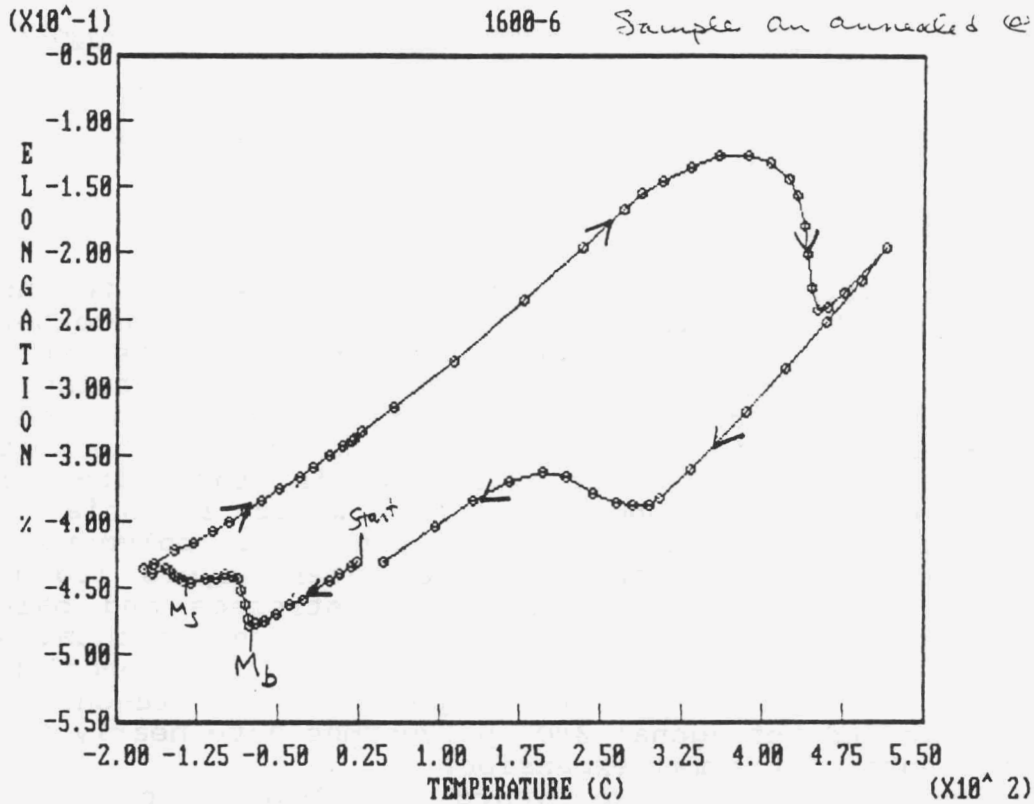

Figure 17: Liquid N_2 dilatometry curve for Z18.5CE62A ceramic fired at 1600°C/6 hrs.

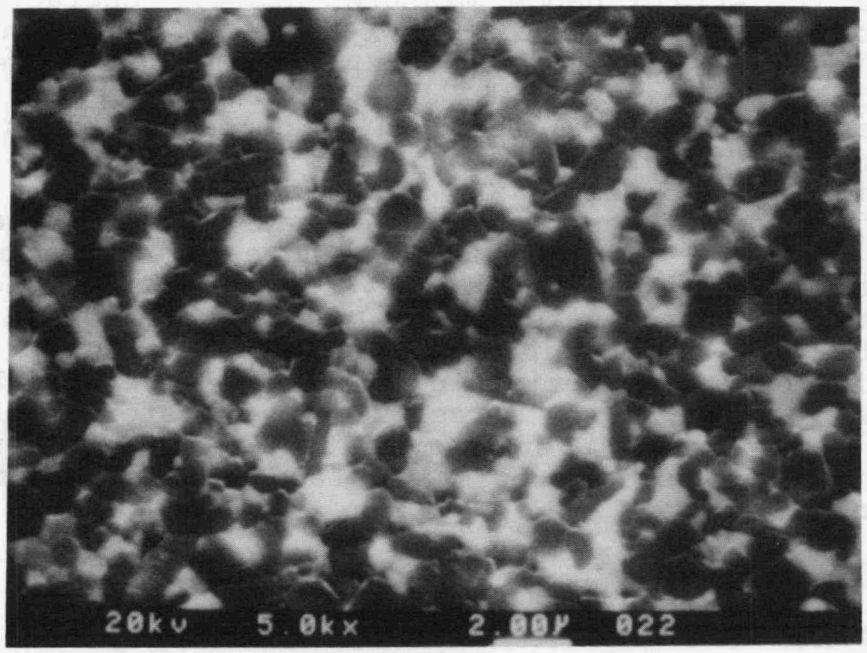

Figure 18: Microstructure (SEM) of Z16CE60A ceramic made with mechanically mixed CeO_2-ZrO_2 and Al_2O_3 powders, sintered/HIPed at 1500°C.

Processing and Characterization of Transformation Toughened Ceramics with Strength Retention to Elevated Temperatures

R. A. Cutler, C. B. Brinkpeter, S. L. Bruener and D. W. Prouse (Ceramatec, Inc.), A. V. Virkar and D. K. Shetty (Univ. of Utah)

Objective/Scope

Previous work[1] has shown that it is possible to increase the strength of Al_2O_3-ZrO_2 ceramics by incorporating transformation-induced residual stresses in sintered specimens consisting of three layers. The outer layers contained Al_2O_3 and unstabilized ZrO_2, while the central layer contained Al_2O_3 and partially stabilized ZrO_2. When cooled from the sintering temperature, some of the zirconia in the outer layers transformed to the monoclinic form while zirconia in the central layer was retained in the tetragonal polymorph. The transformation of zirconia in the outer layers led to the establishment of surface compressive stresses and balancing tensile stresses in the bulk. In theory, the residual stress will not decrease with temperature until the monoclinic to tetragonal transformation temperature is reached since monoclinic and tetragonal ZrO_2 polymorphs have nearly the same coefficients of thermal expansion.

During the first two years of ORNL funding it was demonstrated that 1) three layer composites could be made with retention of compressive surface stresses to temperatures of 750°C[2,3]; 2) residual stresses could be detected by strength testing[2,3], strain gauge measurements[4], characterization of monoclinic content by x-ray diffraction[2], or indentation/strength measurements[5]; 3) the three layer composites have excellent damage resistance[5]; and 4) significant (300-400 MPa) residual compressive stress which is not transformation-induced can be introduced by grinding monolithic Al_2O_3-15 vol. % ZrO_2(3.0 mol. % Y_2O_3).

The objectives of the present two year subcontract are 1) to increase the use temperature of three-layer composites by substituting HfO_2 for ZrO_2, 2) develop aqueous and nonaqueous slip casting techniques for three layer composites in order to obtain better layer uniformity and to maximize residual compressive stress by optimizing the outer layer thickness, 3) superimpose temperature stresses on transformation-induced stresses in three layer composites, and 4) demonstrate improved thermal shock resistance and damage resistance in optimized composites.

Technical Progress

Slip Casting

The difficulty in drying slip cast Al_2O_3-15 vol. % ZrO_2 three-layer plates without cracking was overcome by settering

the plates on ceramic (ZrO_2(3 mol. % Y_2O_3)) ball bearings. The ceramic ball bearings allowed the plates to move freely during binder burnout and sintering, thus reducing the friction between the plate and the setter. Monolithic plates of the outer (Al_2O_3-15 vol. % ZrO_2) or inner composition (Al_2O_3-15 vol. % ZrO_2(3 mol. % Y_2O_3)) could be sintered on setter plates without cracking, indicating that differential shrinkage between layers contributed to fracture initiation in the three-layer plates.

Three-layer bars with outer layer thicknesses of 300 μm and 125 μm, having room temperature strength as shown in Table 1, were tested at 1000°C. The three bars with an outer layer thickness of 300 μm had a mean strength of 561 MPa and a standard deviation of 92 MPa (the highest strength bar failed at 667 MPa and the lowest strength bar failed at 499 MPa). One of the three bars failed from the chamfer while the other two failed from the tensile surface. The three bars with an outer layer thickness of 125 μm had a mean strength of 584 MPa and a standard deviation of 10 MPa. The mean of all six bars was 577 MPa with a standard deviation of 48 MPa.

Testing of the outer layer monolithic specimens at 1000°C showed that the slip cast materials had a mean strength of 584 MPa with a standard deviation of 41 MPa (six bars). The strength retention for the monolithic outer material was much improved as compared to the three-layer bars and the monolithic inner layer bars (see Table 1). The strength differential between three-layer composites and monolithic outer layer bars at room temperature gives an indication of the residual stress achieved, since failure generally occurred from the tensile surface. The strength differential of 321 MPa at room temperature was non-existent at 1000°C, in accord with expectation, since the monoclinic ZrO_2 had transformed to tetragonal. High temperature x-ray diffraction has been used to monitor the m-->t transformation which occurs during heating, which is responsible for the decreasing residual stress[2]. The attainment of strength of approximately 575 MPa at 1000°C is significant since the best previous strength of three-layer composites at 1000°C was 320 MPa (see Figure 1). The improved uniformity of the outside layer, surface grinding, and improved dispersion of ZrO_2[6] are believed to be the principal reasons for the greatly improved high temperature strength.

Superposition of temperature stress (due to difference in thermal expansion mismatch) on transformation-induced stress (due to volume expansion differences between monoclinic and tetragonal ZrO_2) was demonstrated by using Al_2O_3-40 vol. % ZrO_2 as the inner layer material in three-layer composites where the outer layer was Al_2O_3-15 vol. % ZrO_2. Sintered bars made by powder pressing had densities of about 97% of theoretical (typical HIPed bars have densities greater than 99% of theoretical). The strength differential between three-layer bars with transformation-induced stress was 191 MPa and

Table 1
Strength Retention for Slip Cast Al_2O_3-15 $^v/o$ ZrO_2

Composition	Strength (MPa) 25°C	1000°C	% Room Temperature Strength at 1000°C
Outer[a]	733±78	584±41	79
Inner[b]	975±86	553±62	56.7
Three-layer[c]	1054±76	577±48	54.7

a. Al_2O_3-15 vol. % ZrO_2.
b. Al_2O_3-15 vol. % ZrO_2(3 mol. % Y_2O_3).
c. Three-layer composite with outer layers 125-300μm in thickness (total thickness of ≈5 mm).

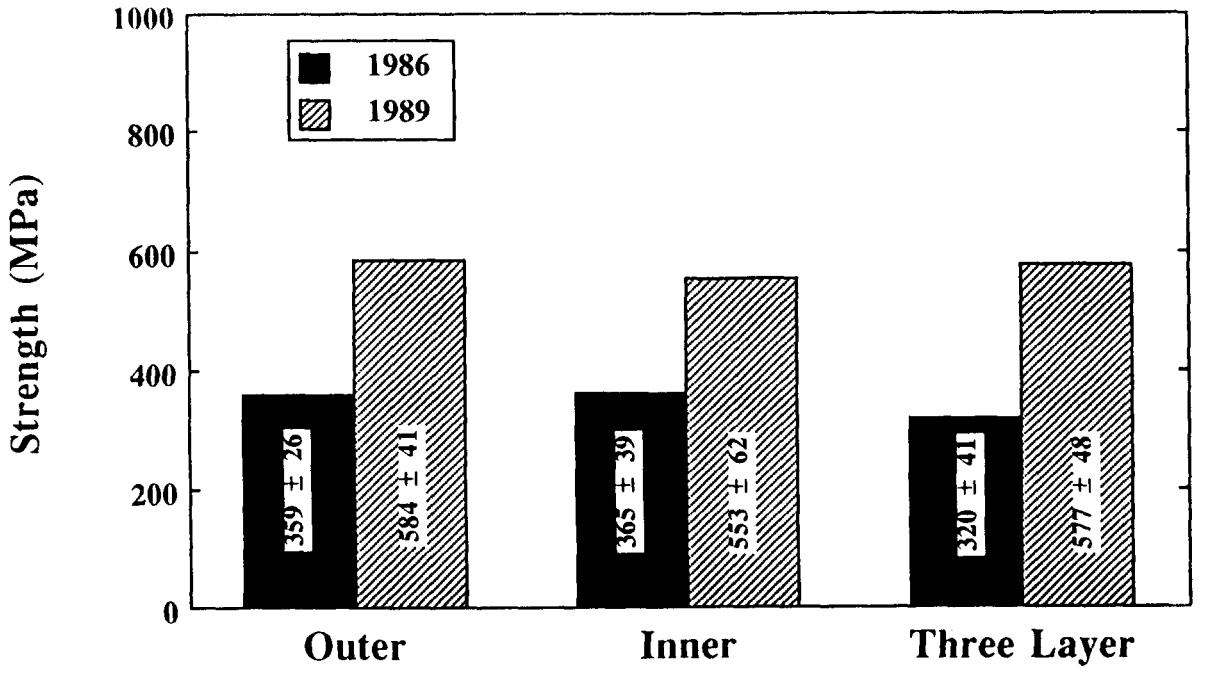

Figure 1. Strength improvement at 1000°C for monolithic and three-layer Al_2O_3-15 vol. % ZrO_2 composites. The outer monolithic bars were made with unstabilized ZrO_2 while the inner layer bars were made with ZrO_2(3 mol. % Y_2O_3). The outer layers of the three-layer composite are approximately 1/12 the total thickness. Strengths are similar at 1000°C for all three materials since this is above the m-> t ZrO_2 transformation temperature.

the differential with temperature-induced stress and transformation-induced stress was 444 MPa. As expected, it is therefore possible to superimpose temperature-induced stress on transformation-induced stress.

Superposition of temperature stress (due to difference in thermal expansion mismatch) on transformation-induced stress (due to volume expansion differences between monoclinic and tetragonal ZrO_2) was previously demonstrated using Al_2O_3-40 vol. % ZrO_2 as the inner layer material in three-layer composites where the outer layer was Al_2O_3-15 vol. % ZrO_2[6]. These bars were made by pressing powders uniaxially and isostatically prior to sintering. The temperature-induced stress enhance the strength of three-layer composites at low temperatures.

Slip cast three-layer composites were made with an inner material composed of ZrO_2(3 mol. % Y_2O_3)-40 vol. % Al_2O_3 and the outer material described above. The slip cast plates were sintered and cladless HIPed to greater than 99% of theoretical density.

The expected compressive residual stress in the outer layer of the bars is the combination of transformation-induced and temperature-induced stresses. The transformation-induced compressive stress, σ_t, in the outer layer, assuming a square wave stress distribution, is given[1] as

$$\sigma_t=-(E_1E_2d_2\Delta\epsilon_o)/[(1-v)(E_1d_1+E_2d_2)] \quad (1)$$

where E is Young's modulus, d is thickness, $\Delta\epsilon_o$ is the unconstrained strain in the outer layer from the transformation of ZrO_2, v is Poisson's ratio, and the subscripts 1 and 2 refer to the outer and inner layers, respectively. The temperature induced stress, σ_T, in the outer layer, also assuming a square wave distribution, is given as

$$\sigma_T=-[(E_1E_2d_2\Delta T)(\alpha_2-\alpha_1)]/[(1-v)(E_1d_1+E_2d_2)] \quad (2)$$

where ΔT is the temperature difference over which stress exist and α is the coefficient of linear thermal expansion. By superposition, the expected residual stress in the outer layer is

$$\sigma_1=-[(E_1E_2d_2)(\Delta\epsilon_o+\Delta T(\alpha_2-\alpha_1))]/[(1-v)(E_1d_1+E_2d_2)] \quad (3)$$

Taking E_1 as 340 GPa[4], E_2 as 275 GPa, ϵ_o as 1.5×10^{-3}[2], T as 1000°C, $\alpha_2-\alpha_1$ as 1×10^{-6}/°C, v as 0.25, d_1 as 500 μm and d_2 as 5 mm, the expected compressive residual stress in the outer layer is slightly over 1 GPa. The corresponding residual tensile stress in the inner layer is approximately 200 MPa.

Slip cast three-layer bars, with the predicted transformation-induced and temperature-induced stresses given above, were fractured in four-point bending at room temperature. Seven bars where failure initiated from the outer layer had a mean strength of 1,244 MPa with a standard

deviation of 103 MPa. The highest strength bar broke at 1,417 MPa and the lowest strength bar at 1,111 MPa. Two bars which failed just inside the interface had strengths of 1,118 and 1,053 MPa and one bar failed from within the inner layer at a stress of 858 MPa. Corresponding outer layer bars tested at the same time had a mean strength of 549 MPa and a standard deviation of 57 MPa (The lower strength of these outer layer bars compared to the same composition with data displayed in Table 1 is believed to be due to differences in degassing the slips leading to voids). The difference in strength between the three-layer bars which failed from the outer layer (1,244 MPa) and the outer layer bars (549 MPa) is an indication of the compressive residual stress in the outer layer of three-layer bars. This value of 695 MPa is 70% of the predicted value. More importantly, it shows that high strengths can be achieved in layered ceramic composites using a combination of transformation and temperature-induced stresses.

The dependence of strength on test temperature for these bars is shown in Figure 2 for three-layer and monolithic outer layer bars tested in four-point bending. As expected, the three-layer bars with temperature-induced stress superimposed

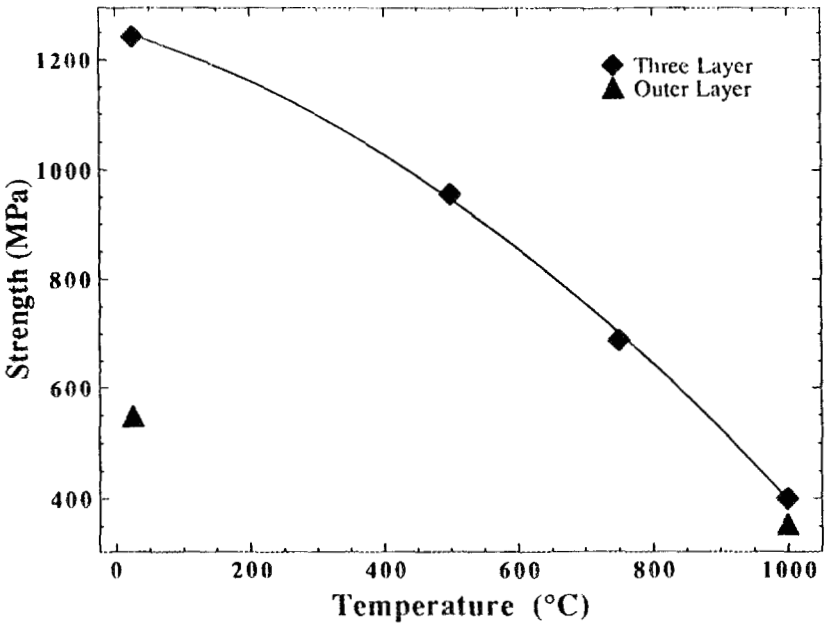

Figure 2. Strength as a function of temperature for monolithic and three-layer composite with temperature-induced stress superimposed on transformation-induced stress in outer layers. Monolithic and outer layers of three-layer bars are Al_2O_3-15 vol. % ZrO_2 while inner layer of is ZrO_2(3 mol. % Y_2O_3)-40 vol. % Al_2O_3.

on transformation-induced stress have a rapid degradation in strength with temperature. The low strength at 1000°C for the three-layer bars, relative to the values in Table 1, is due to the poor strength of the monolithic outer layer material.

Slip casting of three-layer plates and the resulting strength testing of bars cut from those plates has resulted in improved strength at room temperature (see Figure 3) and 1000°C (see Figure 1). Figure 4 shows a strength comparison between monolithic and three-layer Al_2O_3-15 vol. % ZrO_2 made by dry pressing and slip casting. The 10-20% strength improvement is due to improved uniformity in the thickness of the slip cast outer layers, as shown in Figure 5. The three-layer composite in Figure 5 has a higher volume fraction of ZrO_2 in the inner layer to outline the interface. The integrity of the smooth interface obtained by slip casting is seen by aligning indentation cracks with the interface. There is no tendency for the cracks to run along the interface.

The residual stresses present in the three-layer composite are clearly evident by indenting cross-sections. Assuming a simplistic analysis for indentation behavior, the indentation crack length, c_o, in the absence of residual stress is given by

$$c_o=[0.016(E/H)^{1/2}(P/K_{Ic})]^{2/3} \quad (4)$$

where E is Young's Modulus, H is hardness, P is the Vicker's indentation load, and K_{Ic} is the fracture toughness. In the presence of residual stress, σ_R, the half-penny crack after indentation is shorter in the outer layers which are under uniform compressive stress or longer in the inner layer which is under a lesser tensile stress. The crack length in the presence of residual stress, c, may be calculated by

$$(c_o/c)^2-(c_o/c)^{1/2}+\alpha=0 \quad (5)$$

where $\alpha=A\sigma_R[(P/K_{Ic}^4)(E/H)^{1/2}]^{1/3}$ and A is a nondimensional constant[5]. Previous work showed the shorter crack lengths which occur in the outer layers of three-layer composites by comparing indentation cracks on the outer surfaces of monolithic and three-layer Al_2O_3-15 vol. % ZrO_2 composites[5]. Indenting cross-sections shows the effect of strong residual stresses more dramatically (see Figure 6). Assuming typical values[5] of toughness (4.3 $MPa\cdot m^{1/2}$), Young's modulus (340 GPa), hardness (17 GPa), compressive stress (-500 MPa) in the outer layers and balancing tensile stress (100 MPa) in the inner layer (1/12-5/6-1/12 bars), c_o=115 μm, and c=73.7 μm in the outer layers and c=140.8 μm in the inner layer. By aligning cracks parallel and perpendicular to the surface (and interface), it is possible to see shorter cracks in the outer layers perpendicular to the interface/surface (i.e., in the direction where the residual compressive stress is closing the crack tip) and longer cracks in the inner layer perpendicular to the interface/surface (i.e., in the direction where the residual tensile stress is opening the crack tip). These

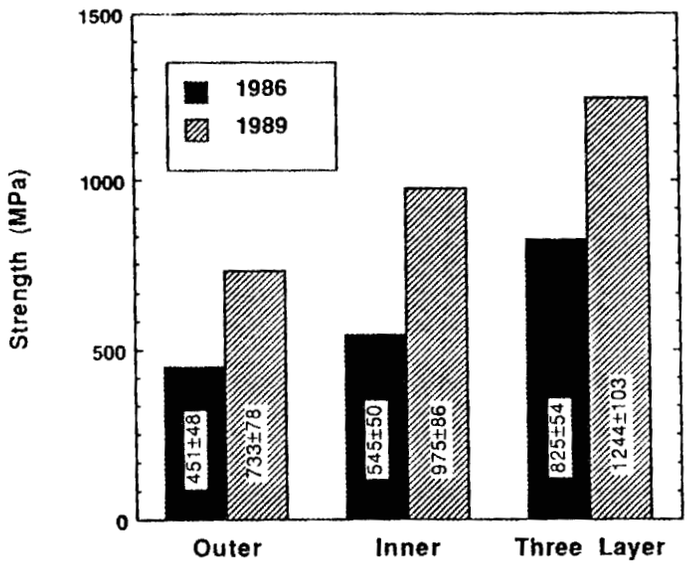

Figure 3. Strength improvements at room temperature obtained on monolithic and three-layer Al_2O_3-15 vol. % ZrO_2 composites made during ORNL funding.

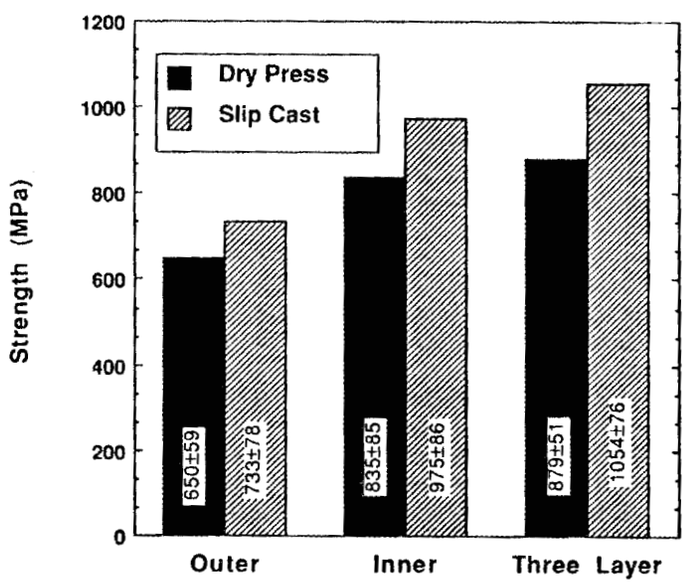

Figure 4. Room temperature flexural strength comparison of Al_2O_3-15 vol. % ZrO_2 fabricated by dry pressing and slip casting.

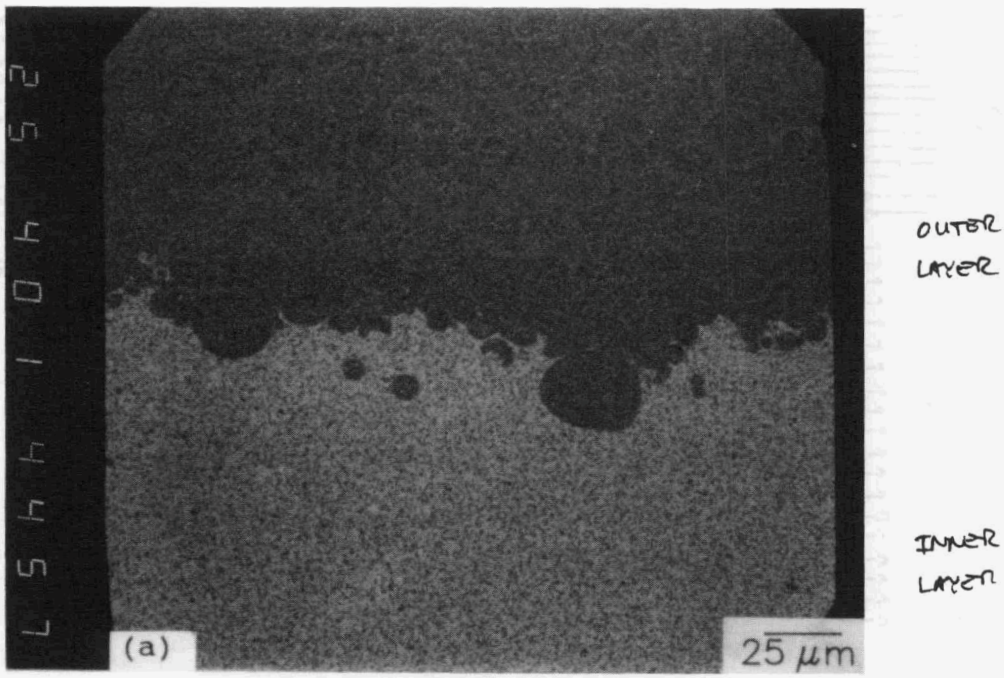

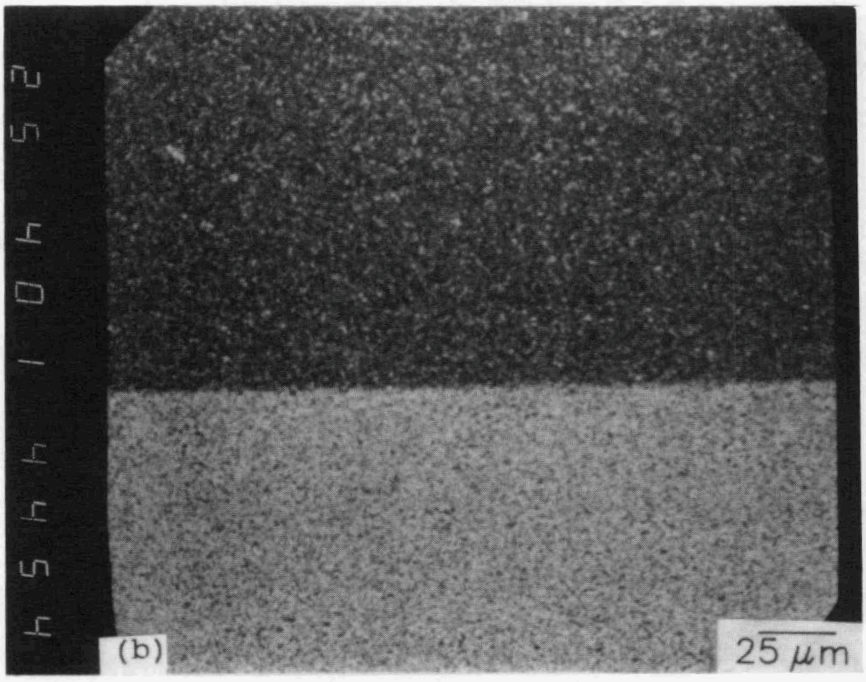

Figure 5. SEM micrographs of cross-sections of (a) dry pressed and (b) slip cast three-layer (outer layers of Al_2O_3-15 vol. % ZrO_2 and inner layer of ZrO_2(3 mol. % Y_2O_3)-40 vol. % Al_2O_3) composites (400X). Note smooth interface in slip cast composites and remnants of spray dried agglomerates in dry pressed outer layer.

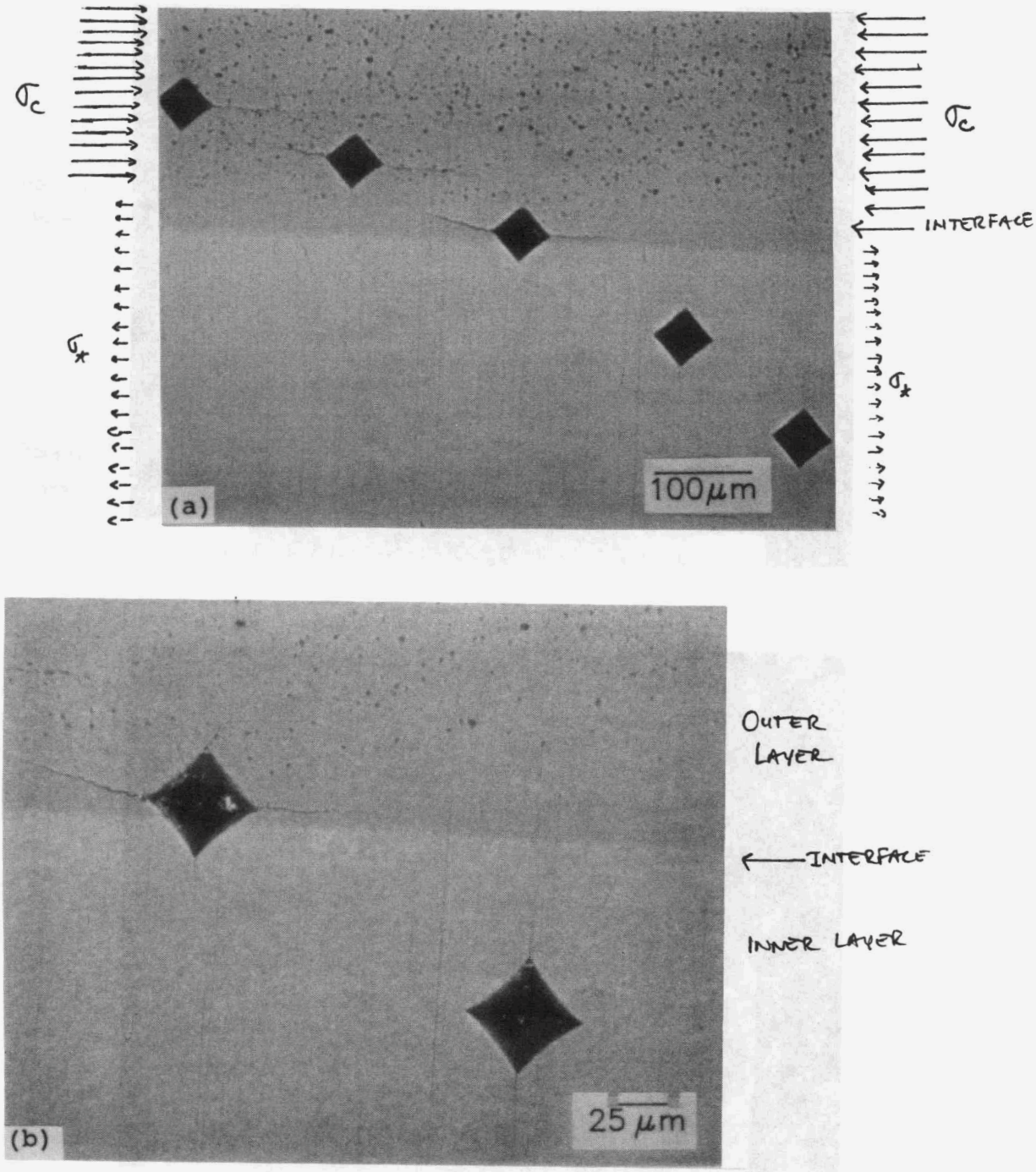

Figure 6. Optical micrographs of cross-sections of three-layer composites with indents oriented with cracks parallel and perpendicular to the interface/surface. (a,b) Same composition as three-layer composites shown in Fig. 5. (a) 150X, (b) 300X. Note change in crack lengths between inner and outer layers.

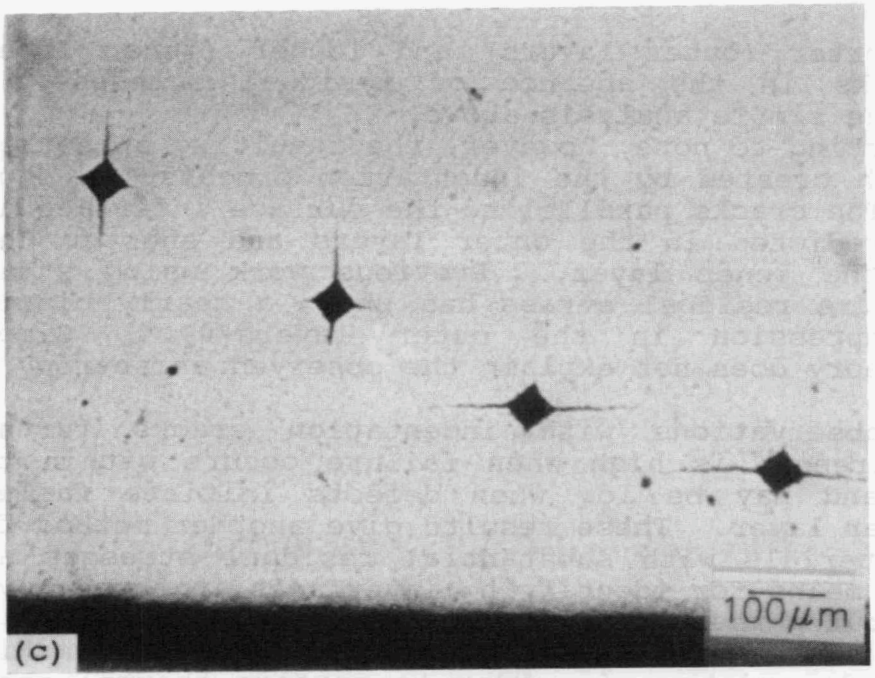

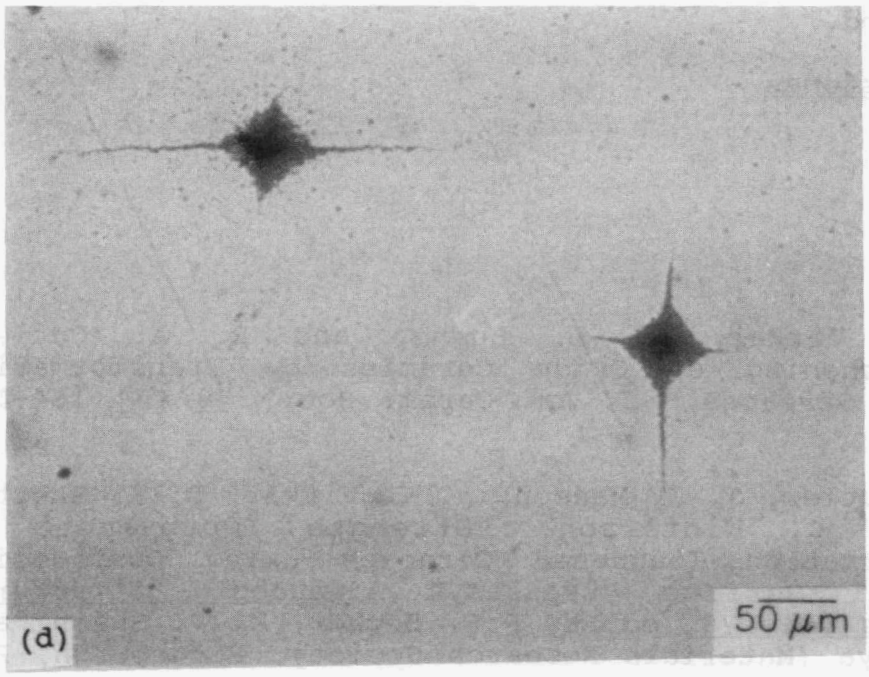

Figure 6 (cont). (c,d). Cracks in three-layer Al_2O_3-15 vol. % ZrO_2 after removing surface of indentation cracks to make cracks more visible. (c) 100X, (6) 200 X. Crack lengths are strongly influenced by residual compression (outer layers) and residual tension (inner layer).

cracks are shorter (outer layers) and longer (inner layer) than the cracks in the absence of residual stresses, as predicted by the simple analysis above.

It is interesting to note, however, the resulting anisotropy in crack length created by the indentation process, as shown in Figure 6. The cracks parallel to the surface/interface are longer than predicted in the outer layers and shorter than predicted in the inner layer. Previous work using strain gauges to measure residual stress has shown a nearly biaxial state of compression in the outer layers[4]. Simple indentation theory does not explain the observed anisotropy in crack lengths.

The above observations with indentation cracks further explain why strength is high when failure occurs within the outer region and may be low when defects initiate failure within the inner layer. These results give another method for identifying materials with substantial residual stresses and also provide a means for identifying interfaces in three-layer materials without phase contrasts (see Fig. 6(c,d)).

Slip casting molds were designed and fabricated for making encapsulated rods and bars in order to perform thermal shock testing which is scheduled for completion during the next reporting period.

Status of Milestones

On schedule

Publications

None

References

1. A. V. Virkar, J. L. Huang, and R. A. Cutler, "Strengthening of Oxide Ceramics by Transformation Induced Stresses," J. Am. Ceram. Soc., 70 [3] 164-170 (1987).

2. R. A. Cutler, J. J. Hansen, A. V. Virkar, D. K. Shetty, and R. C. Winterton, "Strength Improvement in Transformation Toughened Ceramics using Compressive Residual Surface Stresses," Advanced Structural Ceramics Vol. 78, ed. by P.F. Becher, M. V. Swain, and S. Somiya (Materials Research Society, Pittsburgh, PA, 155-163, 1987).

3. R. A. Cutler, J. D. Bright, A. V. Virkar, and D. K. Shetty, "Strength Improvement in Transformation-Toughened Alumina by Selective Phase Transformation," J. Am. Ceram. Soc., 70 [10] 714-18 (1987).

4. A. V. Virkar, J. F. Jue, J. J. Hansen and R. A. Cutler, "Measurement of Residual Stresses in Oxide-ZrO_2 Three-Layer Composites," J. Am. Ceram. Soc., 71[3] C-148-C-151 (1988).

5. J. J. Hansen, R. A. Cutler, D. K. Shetty and A. V. Virkar, "Indentation Fracture Response and Damage Resistance of Al_2O_3-ZrO_2 Composites Strengthened by Transformation-Induced Residual Stresses" J. Am. Ceram. Soc., 71[12] C-501-C-505 (1988).

6. R. A. Cutler, C. B. Brinkpeter, S. L. Bruner, D. W. Prouse, A. V. Virkar, and D. K. Shetty, "Processing and Characterization of Transformation Toughened Ceramics with Strength Retention to Elevated Temperatures," pp. 151-155 in Ceramic Technology for Advanced Heat Engines Project Bimonthly Technical Progress Report ORNL/CF-89/234 (Apr.-May 1989), Oak Ridge National Laboratory, Oak Ridge, TN.

1.2.4 Silicate Matrix

Low Expansion Ceramics for Diesel Engine Applications(VPI)
J.J. Brown (VPI and SU) and F.A. Hummel (Consultant)

Objective/scope

The major objective of this research is to investigate selected oxide systems for the development of a low expansion, high thermal shock resistant ceramic. Specifically, it is the goal of this study to develop an isotropic, ultralow expansion ceramic which can be used above 1200°C and which is relatively inexpensive.

Technical progress

This research program includes the synthesis, property characterization, and fabrication of candidate low thermal expansion ceramics from two systems based upon aluminum phosphate and zircon. In the aluminum phosphate system, the goal is to stabilize low thermal expansion, high temperature, high crystal symmetry phases via solid solution formation. In zircon, the crystal anisotropy and thermal expansion are reduced via solid solution formation. Based upon earlier data of the investigators, compositional ranges are evaluated by fabricating experimental specimens and determining phase content plus microstructure, thermal expansion, solidus temperature, and density. Those compositions which exhibit acceptable sintering, phase composition, and expansion characteristics are studied in more detail, including flexure strength, creep, thermal conductivity, and crystal structure. Finally, those ceramic compositions exhibiting the best combination of properties are evaluated as to their fabrication behavior in the form of specimens having masses up to about 0.5 kg.

Zircon (NZP) System

Two major systems of the NZP family, $RbZr_2(PO_4)_3$-$CsZr_2(PO_4)_3$ and $CaZr_4(PO_4)_6$-$MgZr_4(PO_4)_6$, had previously been identified to possess compositions with excellent thermal shock resistance and nearly zero thermal expansion up to 1200°C. During the reporting period, research was conducted to gain information on the phase equilibria relationships of the two systems, obtain single phase samples of desired solid solutions, and confirm the thermal expansion characteristics of stoichiometrically-varied NZP compositions.

Samples were synthesized by solid state reactions based on compositions $(Rb_{1-x},Cs_x)Zr_2(PO_4)_3$ and $(Ca_{1-x},Mg_x)\ Zr_4(PO_4)_6$. Reactant materials were

Rb_2CO_3, Cs_2CO_3, $CaCO_3$, $MgCO_3$, ZrO_2, and $NH_4H_2PO_4$. Previous starting materials were found to be highly hygroscopic and have been replaced by the more stable carbonates and phosphates. Samples were homogenized in acetone by mixing with a glass mortar and pestle. Final products were allowed to dry, then calcined in fused silica or platinum crucibles between 150°C and 550°C for 8 to 24 h. Samples were then reground and heat treated in alumina crucibles at temperatures and times shown in Tables 1 and 2 for $(Rb_{1-x},Cs_x)Zr_2(PO_4)_3$ and $(Ca_{1-x},Mg_x)Zr_4(PO_4)_6$, respectively. The resultant heat treated materials were ground into powders and characterized by standard x-ray diffraction (XRD) procedures. A Phillips x-ray diffractometer using CuK_α radiation was used to scan samples at a speed of 0.02° 2θ/s.

As shown in Tables 1 and 2, multiple phases occurred for some samples based on temperature and length of heat treatment. Secondary phases, which were common to both systems included ZrP_2O_7 and $Zr_2P_2O_9$. Generally, ZrP_2O_7 was found to occur at lower temperatures, often being replaced by $Zr_2P_2O_9$ at higher temperatures or for longer durations of heating. In most cases ZrP_2O_7 amounts were decreased or eliminated with longer heat treatments. $Zr_2P_2O_9$ was much more persistent and, in most cases, could not be eliminated with continued heat treatments. Relative amounts of $Zr_2P_2O_9$ based on x-ray intensity data appear to increase with further heating. The formation of this phase is possibly related to a loss of P_2O_5.

Heat treatments which yielded the best single phase or near single phase solid solution compositions were used to prepare samples for dilatometric analysis. After x-ray characterization, powders were mixed with an organic binder and several drops of distilled H_2O. Bars were formed with a die and pushrod compressed under 17 MPa (2500 psi) from a hydraulic press. The resulting bars were then calcined between 200°C to 550°C and sintered at a variety of temperatures for 12 h. Temperatures which yielded the best single phase bars were used to make samples for dilatometric analysis. Both systems required the addition of 1 wt% ZnO to obtain dense, well sintered bodies. Different sintering aids and heat treatments should be investigated to optimize density and minimize microcracking. ZnO is believed to aid densification by the formation of a liquid phase at high temperatures.

Sintered bars were cut to a standard size, and thermal expansion data were taken with a Netzsch dual pushrod differential dilatometer. A software package was used to correct the relative expansion and compute a coefficient of thermal expansion (CTE). The results of compositions based on the systems

$(Rb_{1-x},Cs_x)Zr_2(PO_4)_3$ and $(Ca_{1-x},Mg_x)Zr_4(PO_4)_6$ are shown in Tables 3 and 4, respectively. In both systems some compositions yielded nonlinear, slightly "U" shaped expansion curves. These curves exhibited both a negative and positive region of thermal expansion based on temperature. This phenomenon warrants further attention. Such anisotropic characteristics of NZP-type compounds are believed to be related to the rotation of ZrO_6 octohedra and PO_4 tetrahedra which occur in chains forming the material's structural framework.[1,2] Interstitial cations also affect thermal expansion due to their site selection and size. Cation selection for these materials was based on desired thermal expansion characteristics. Presently, more thermal expansion data are being collected to establish more accurate average thermal expansion values. Final results will be examined to determine the relationship between composition and thermal expansion.

In order to better understand the phase equilibria of the two systems, plots of lattice parameters vs composition were constructed. A compositional series from each system was prepared by a heat treatment which yielded the best single phase samples. These samples were then ground into a fine powder and mixed with a known internal standard (pure Al_2O_3 powder). With the use of XRD, precise 2θ values were recorded for each composition. Corrections for diffractometer error were made with the use of the internal standard. The **d** spacings were calculated from the 2θ values and CuK_α radiation. The corresponding Miller indices were obtained from the relative ASTM standard file cards. With the use of a computer program, a regression analysis was performed on the data to obtain the **a** and **c** parameters for each composition. These data are presented in Tables 5 and 6 and plotted vs composition in Figure 1 for $(Rb_{1-x},Cs_x)Zr_2(PO_4)_3$ and in Figure 2 for $(Ca_{1-x},Mg_x)Zr_4(PO_4)_6$. The plots in Figure 1 indicate complete solid solution between the Rb and Cs end members. With an increase in Rb concentration, the **a** parameter increases while the **c** parameter decreases. This information is consistent with Lenain's model for the NZP structure. As the size of the alkali ion decreases, the **c** parameter decreases and the **a** increases.[1,2]

A region of limited solid solution for the $(Ca_{1-x},Mg_x)Zr_4(PO_4)_6$ system is indicated by the plots in Figure 2. This region occurs with compositions high in Ca. Further investigation into the boundaries of this region are needed. The **a** and **c** parameters again agree with Lenain's model. For compositions containing more Mg, adjoining the solid solution region is an area where the slope of the curve is approximately zero suggesting a two-phase region. One phase is $CaZr_4(PO_4)_6$ solid solution (identified by XRD), while the other phase

is most likely $MgZr_4(PO_4)_6$. In low concentrations $MgZr_4(PO_4)_6$ is difficult to detect by x-ray techniques because it is masked by abundant, more intense $CaZr_4(PO_4)_6$ (solid solution) peaks. $MgZr_4(PO_4)_6$ may maintain a monoclinic structure, possibly similar to the $LiZr_4(PO_4)_6$ monoclinic phase. This is probably related to the small size of the Mg cation. It appears that the hexagonal lattice of $CaZr_4(PO_4)_6$ can receive only a limited amount of Mg cations. This matter deserves further investigation including an analysis to determine what sites are being occupied by Mg and Ca and how these positions affect the lattice framework.

High temperature phase stability of each system was determined by heating samples at elevated temperatures for several days. X-ray powder patterns of the resultant materials were then examined for signs of phase decomposition. For the $(Rb_{1-x},Cs_x)Zr_2(PO_4)_3$ system, a compositional series was heated at 1300°C for 114 h. All of the samples showed signs of decomposition with the formation of a new, unidentified phase. The $RbZr_2(PO_4)_3$ end of the series showed only slight signs of decomposition. As the amount of cesium in the sample was increased, decomposition of the original phase became greater. The $CsZr_2(PO_4)_3$ end of the series showed advanced signs of decomposition with a major reduction of the original single phase and the formation of an unknown secondary phase. Another compositional series was heat treated at 1200°C for 72 h, and then heated at 1250°C for 94 h. All but one of the samples remained a single phase, without significant signs of decomposition. These results suggest that the upper limit of stability for the Rb-Cs system lies at some temperature between 1250°C and 1300°C.

For the system $(Ca_{1-x},Mg_x)Zr_4(PO_4)_6$, samples were heat treated at temperatures and times shown in Table 2. At temperatures 1450°C, 1400°C, and 1350°C for 48 h, compositions high in Mg decomposed to $Zr_2P_2O_9$. Based on relative peak intensities from XRD data, more $Zr_2P_2O_9$ formed in samples heated at higher temperatures. Single phase $MgZr_4(PO_4)_6$ decomposed almost entirely into $Zr_2P_2O_9$ after 48 h at 1450°C. Further stability tests are being conducted along with weight loss analyses of compositions heated between 1300°C and 1450°C. Tentative data place the upper limit of stability for $MgZr_4(PO_4)_6$ at 1300°C to 1350°C. $CaZr_4(PO_4)_6$ and its solid solution with Mg showed no signs of decomposition after any of the heat treatments. Tentative data indicate that the upper temperature limit of stability for $CaZr_4(PO_4)_6$ and its solid solution with Mg is above 1450°C.

Table 1. Composition, heat treatment, and phase analysis of the $RbZr_2(PO_4)_3$-$CsZr_2(PO_4)_3$ system

Composition	Heat Treatment Temp.(°C)/Time(h)		Phases Present
$RbZr_2(PO_4)_3$		1100/24	RbZP*, ZrP_2O_7
		1100/48	RbZP, ZrP_2O_7
		1100/72	RbZP, ZrP_2O_7
	1100/3	1200/24	RbZP, ZrP_2O_7
	1000/3	1200/48	RbZP, ZrP_2O_7
	1000/3	1200/72	RbZP
	1000/2	1250/24	RbZP, ZrP_2O_7
	1000/2	1250/48	
	1000/2	1250/72	RbZP
	1000/3	1300/24	RbZP, ZrP_2O_7
	1000/3	1300/48	RbZP
	1000/3	1350/24	RbZP
	1000/3	1350/48	RbZP, $Zr_2P_2O_9$

(continued)

* (ZP = $Zr_2(PO_4)_3$)

$(Rb_{0.9},Cs_{0.1})Zr_2(PO_4)_3$		1100/24	RbZP(ss),ZrP_2O_7
		1100/48	RbZP(ss),ZrP_2O_7
		1100/72	RbZP(ss),ZrP_2O_7
	1000/3	1200/24	$(Rb_{0.9},Cs_{0.1})$ZP
	1000/3	1200/48	$(Rb_{0.9},Cs_{0.1})$ZP
	1000/3	1200/72	$(Rb_{0.9},Cs_{0.1})$ZP
	1000/2	1250/24	$(Rb_{0.9},Cs_{0.1})$ZP
	1000/2	1250/48	$(Rb_{0.9},Cs_{0.1})$ZP
	1000/2	1250/72	$(Rb_{0.9},Cs_{0.1})$ZP
	1000/3	1300/24	$(Rb_{0.9},Cs_{0.1})$ZP
	1000/3	1300/48	$(Rb_{0.9},Cs_{0.1})$ZP
	1000/3	1350/24	$(Rb_{0.9},Cs_{0.1})$ZP
	1000/3	1350/48	RbZP(ss),$Zr_2P_2O_9$
$(Rb_{0.8},Cs_{0.2})Zr_2(PO_4)_3$		1100/24	RbZP(ss),ZrP_2O_7
		1100/48	RbZP(ss),ZrP_2O_7
		1100/72	RbZP(ss),ZrP_2O_7
	1000/3	1200/24	RbZP(ss),ZrP_2O_7
	1000/3	1200/48	RbZP(ss),ZrP_2O_7
	1000/3	1200/72	RbZP(ss),ZrP_2O_7
	1000/2	1250/24	RbZP(ss),ZrP_2O_7
	1000/2	1250/48	RbZP(ss),ZrP_2O_7
	1000/2	1250/72	$(Rb_{0.8},Cs_{0.2})$ZP
	1000/3	1300/24	$(Rb_{0.8},Cs_{0.2})$ZP
	1000/3	1300/48	$(Rb_{0.8},Cs_{0.2})$ZP
	1000/3	1350/24	$(Rb_{0.8},Cs_{0.2})$ZP
	1000/3	1350/48	$(Rb_{0.8},Cs_{0.2})$ZP

$(Rb_{0.7},Cs_{0.3})Zr_2(PO_4)_3$		1100/24	$(Rb_{0.7},Cs_{0.3})ZP$
		1100/48	$(Rb_{0.7},Cs_{0.3})ZP$
		1100/72	$(Rb_{0.7},Cs_{0.3})ZP$
	1000/3	1200/24	RbZP(ss),ZrP_2O_7
	1000/3	1200/48	RbZP(ss),ZrP_2O_7
	1000/3	1200/72	RbZP(ss),ZrP_2O_7,$Zr_2P_2O_9$
	1000/2	1250/24	$(Rb_{0.7},Cs_{0.3})ZP$
	1000/3	1300/24	RbZP(ss),ZrP_2O_7,$Zr_2P_2O_9$
	1000/3	1300/48	$(Rb_{0.7},Cs_{0.3})ZP$
	1000/3	1350/24	RbZP(ss),ZrP_2O_7
	1000/3	1350/48	RbZP(ss),$Zr_2P_2O_9$
$(Rb_{0.6},Cs_{0.4})Zr_2(PO_4)_3$		1100/24	RbZP(ss),ZrP_2O_7
		1100/48	$(Rb_{0.6},Cs_{0.4})ZP$
		1100/72	$(Rb_{0.6},Cs_{0.4})ZP$
	1000/3	1200/24	RbZP(ss),ZrP_2O_7
	1000/3	1200/48	RbZP(ss),ZrP_2O_7
	1000/3	1200/72	$(Rb_{0.6},Cs_{0.4})ZP$
	1000/2	1250/24	RbZP(ss),ZrP_2O_7
	1000/2	1250/48	$(Rb_{0.6},Cs_{0.4})ZP$
	1000/2	1250/72	$(Rb_{0.6},Cs_{0.4})ZP$
	1000/3	1300/24	$(Rb_{0.6},Cs_{0.4})ZP$
	1000/3	1300/48	$(Rb_{0.6},Cs_{0.4})ZP$
	1000/3	1350/24	$(Rb_{0.6},Cs_{0.4})ZP$
	1000/3	1350/48	RbZP(ss),$Zr_2P_2O_9$

$(Rb_{0.5},Cs_{0.5})Zr_2(PO_4)_3$		1100/24	$RbZP(ss),ZrP_2O_7$
		1100/48	$RbZP(ss),ZrP_2O_7$
		1100/72	$RbZP(ss),ZrP_2O_7$
	1000/3	1200/24	$RbZP(ss),ZrP_2O_7$
	1000/3	1200/48	$RbZP(ss),ZrP_2O_7$
	1000/3	1200/72	$RbZP(ss),ZrP_2O_7$
	1000/2	1250/24	$RbZP(ss),ZrP_2O_7$
	1000/2	1250/48	$RbZP(ss),ZrP_2O_7$
	1000/2	1250/72	$RbZP(ss),ZrP_2O_7$
	1000/3	1300/24	$RbZP(ss),ZrP_2O_7$
	1000/3	1300/48	$RbZP(ss),Zr_2P_2O_9$
	1000/3	1350/24	$(Rb_{0.5},Cs_{0.5})ZP$
	1000/3	1350/48	$RbZP(ss),Zr_2P_2O_9$
$(Rb_{0.4},Cs_{0.6})Zr_2(PO_4)_3$		1100/24	$RbZP(ss),ZrP_2O_7$
		1100/72	$RbZP(ss),ZrP_2O_7$
	1000/3	1200/24	$RbZP(ss),ZrP_2O_7$
	1000/3	1200/48	$RbZP(ss),ZrP_2O_7$
	1000/3	1200/72	$(Rb_{0.4},Cs_{0.6})ZP$
	1000/2	1250/24	$RbZP(ss),ZrP_2O_7$
	1000/2	1250/48	$RbZP(ss),ZrP_2O_7$
	1000/2	1250/72	$(Rb_{0.4},Cs_{0.6})ZP$
	1000/3	1300/24	$(Rb_{0.4},Cs_{0.6})ZP$
	1000/3	1300/48	$(Rb_{0.4},Cs_{0.6})ZP$
	1000/3	1350/24	$(Rb_{0.4},Cs_{0.6})ZP$
	1000/3	1350/48	$RbZP(ss),Zr_2P_2O_9$

$(Rb_{0.3},Cs_{0.7})Zr_2(PO_4)_3$		1100/24	$RbZP(ss),ZrP_2O_7$
		1100/72	$RbZP(ss),ZrP_2O_7$,unknown
	1000/3	1200/24	$RbZP(ss),ZrP_2O_7$
	1000/3	1200/48	$(Rb_{0.3},Cs_{0.7})ZP$
	1000/3	1200/72	$RbZP(ss),ZrP_2O_7$
	1000/2	1250/24	$RbZP(ss),ZrP_2O_7$
	1000/2	1250/48	$RbZP(ss),ZrP_2O_7$
	1000/2	1250/72	$RbZP(ss),ZrP_2O_7$
	1000/3	1300/24	$RbZP(ss),ZrP_2O_7$
	1000/3	1300/48	$(Rb_{0.3},Cs_{0.7})ZP$
	1000/3	1350/24	$RbZP(ss),ZrP_2O_7,Zr_2P_2O_7$
	1000/3	1350/48	$RbZP(ss),Zr_2P_2O_9$
$(Rb_{0.2},Cs_{0.8})Zr_2(PO_4)_3$		1100/24	$RbZP(ss),ZrP_2O_7$
		1100/72	$RbZP(ss),ZrP_2O_7$,unknown
	1000/3	1200/24	$RbZP(ss),ZrP_2O_7$
	1000/3	1200/48	$RbZP(ss),ZrP_2O_7$
	1000/3	1200/72	$RbZP(ss),ZrP_2O_7$
	1000/2	1250/24	$RbZP(ss),ZrP_2O_7$
	1000/2	1250/48	$RbZP(ss),ZrP_2O_7$
	1000/2	1250/72	$RbZP(ss),ZrP_2O_7$
	1000/3	1300/24	$(Rb_{0.2},Cs_{0.8})ZP$
	1000/3	1300/48	$RbZP(ss),Zr_2P_2O_9$
	1000/3	1350/24	$RbZP(ss),ZrP_2O_7,Zr_2P_2O_9$
	1000/3	1350/48	$RbZP(ss),Zr_2P_2O_9$

$(Rb_{0.1},Cs_{0.9})Zr_2(PO_4)_3$		1100/24	RbZP(ss),ZrP_2O_7
		1100/72	RbZP(ss),ZrP_2O_7,unknown
	1000/3	1200/24	RbZP(ss),ZrP_2O_7
	1000/3	1200/48	RbZP(ss),ZrP_2O_7
	1000/3	1200/72	RbZP(ss),ZrP_2O_7
	1000/2	1250/24	$(Rb_{0.1},Cs_{0.8})$ZP
	1000/3	1300/24	$(Rb_{0.1},Cs_{0.8})$ZP
	1000/3	1300/48	RbZP(ss),$Zr_2P_2O_9$
	1000/3	1350/24	RbZP(ss),ZrP_2O_7,$Zr_2P_2O_9$
	1000/3	1350/48	RbZP(ss),$Zr_2P_2O_9$,unknown
$CsZr_2(PO_4)_3$		1100/24	CsZP,ZrP_2O_7
		1100/72	CsZP,ZrP_2O_7,unknown
	1000/3	1200/24	CsZP,ZrP_2O_7
	1000/3	1200/48	CsZP,unknown
	1000/3	1200/72	CsZP,unknown
	1000/2	1250/24	CsZP,ZrP_2O_7,unknown
	1000/3	1300/24	CsZP
	1000/3	1300/48	CsZP,$Zr_2P_2O_9$,unknown
	1000/3	1350/24	CsZP,ZrP_2O_7
	1000/3	1350/48	CsZP,$Zr_2P_2O_9$,unknown

Table 2. Composition, heat treatment, and phase analyses of the $CaZr_4(PO_4)_6$-$MgZr_4(PO_4)_6$ system

Composition	Temp (°C)/Time (h)	Phases Present
$CaZr_4(PO_4)_6$	1220/24	$CaZr_4(PO_4)_6$
	1220/48	$CaZr_4(PO_4)_6$
	1240/12	$CaZr_4(PO_4)_6$
	1240/24	$CaZr_4(PO_4)_6$
	1280/12	$CaZr_4(PO_4)_6$
	1280/24	$CaZr_4(PO_4)_6$
	1300/12	$CaZr_4(PO_4)_6$
	1300/24	$CaZr_4(PO_4)_6$
	1300/48	$CaZr_4(PO_4)_6$
	1350/12	$CaZr_4(PO_4)_6$
	1350/24	$CaZr_4(PO_4)_6$
	1350/48	$CaZr_4(PO_4)_6$
	1400/48	$CaZr_4(PO_4)_6$
	1450/48	$CaZr_4(PO_4)_6$
$(Ca_{0.9}, Mg_{0.1})Zr_4(PO_4)_6$	1220/24	$Ca_{0.9}Mg_{0.1}Zr_4(PO_4)_6$
	1220/48	$Ca_{0.9}Mg_{0.1}Zr_4(PO_4)_6$
	1240/12	$Ca_{0.9}Mg_{0.1}Zr_4(PO_4)_6$
	1240/24	$Ca_{0.9}Mg_{0.1}Zr_4(PO_4)_6$
	1280/12	$Ca_{0.9}Mg_{0.1}Zr_4(PO_4)_6$
	1280/24	$Ca_{0.9}Mg_{0.1}Zr_4(PO_4)_6$
	1300/12	$Ca_{0.9}Mg_{0.1}Zr_4(PO_4)_6$
	1300/24	$Ca_{0.9}Mg_{0.1}Zr_4(PO_4)_6$
	1300/48	$Ca_{0.9}Mg_{0.1}Zr_4(PO_4)_6$
	1350/24	$Ca_{0.9}Mg_{0.1}Zr_4(PO_4)_6$
	1350/48	$Ca_{0.9}Mg_{0.1}Zr_4(PO_4)_6$
	1400/48	$Ca_{0.9}Mg_{0.1}Zr_4(PO_4)_6$
	1450/48	$Ca_{0.9}Mg_{0.1}Zr_4(PO_4)_6$
$(Ca_{0.8}, Mg_{0.2})Zr_4(PO_4)_6$	1220/24	$Ca_{0.8}Mg_{0.2}Zr_4(PO_4)_6$, ZrP_2O_7
	1220/48	$Ca_{0.8}Mg_{0.2}Zr_4(PO_4)_6$, $Zr_2P_2O_9$
	1240/12	$Ca_{0.8}Mg_{0.2}Zr_4(PO_4)_6$, ZrP_2O_7
	1240/24	$Ca_{0.8}Mg_{0.2}Zr_4(PO_4)_6$, ZrP_2O_7
	1280/12	$Ca_{0.8}Mg_{0.2}Zr_4(PO_4)_6$
	1280/24	$Ca_{0.8}Mg_{0.2}Zr_4(PO_4)_6$
	1300/12	$Ca_{0.8}Mg_{0.2}Zr_4(PO_4)_6$
	1300/24	$Ca_{0.8}Mg_{0.2}Zr_4(PO_4)_6$
	1300/48	$Ca_{0.8}Mg_{0.2}Zr_4(PO_4)_6$
	1350/24	$Ca_{0.8}Mg_{0.2}Zr_4(PO_4)_6$
	1350/48	$Ca_{0.8}Mg_{0.2}Zr_4(PO_4)_6$
	1400/48	$Ca_{0.8}Mg_{0.2}Zr_4(PO_4)_6$, $Zr_2P_2O_9$
	1450/48	$Ca_{0.8}Mg_{0.2}Zr_4(PO_4)_6$, $Zr_2P_2O_9$

$(Co_{0.7}Mg_{0.3})Zr_4(PO_4)_6$	1220/24	$Ca_{0.7}Mg_{0.3}Zr_4(PO_4)_6$, $Zr_2P_2O_9$
	1220/48	$Ca_{0.7}Mg_{0.3}Zr_4(PO_4)_6$, $Zr_2P_2O_9$
	1240/12	$Ca_{0.7}Mg_{0.3}Zr_4(PO_4)_6$, ZrP_2O_7
	1240/24	$CaZr_4(PO_4)_6$(s.s.),$MgZr_4(PO_4)_6$(s.s.),ZrP_2O_7
	1280/12	$Ca_{0.7}Mg_{0.3}Zr_4(PO_4)_6$, $Zr_2P_2O_9$
	1280/24	$Ca_{0.7}Mg_{0.3}Zr_4(PO_4)_6$
	1300/12	$CaZr_4(PO_4)_6$(s.s.), $MgZr_4(PO_4)_6$(s.s.), ZrP_2O_7
	1300/24	$CaZr_4(PO_4)_6$(s.s.), $MgZr_4(PO_4)_6$(s.s.), ZrO_2
	1300/48	$Ca_{0.7}Mg_{0.3}Zr_4(PO_4)_6$, $Zr_2P_2O_9$
	1350/24	$Ca_{0.7}Mg_{0.3}Zr_4(PO_4)_6$, $Zr_2P_2O_9$
	1350/48	$Ca_{0.7}Mg_{0.3}Zr_4(PO_4)_6$, $Zr_2P_2O_9$
	1400/48	$Ca_{0.7}Mg_{0.3}Zr_4(PO_4)_6$, $Zr_2P_2O_9$
	1450/48	$Ca_{0.7}Mg_{0.3}Zr_4(PO_4)_6$, $Zr_2P_2O_9$
$(Ca_{0.6}, Mg_{0.4})Zr_4(PO_4)_6$	1220/24	$CaZr_4(PO_4)_6$(s.s.), $MgZr_4(PO_4)_6$(s.s.), ZrP_2O_7
	1220/48	$CaZr_4(PO_4)_6$(s.s.), $Zr_2P_2O_9$
	1240/12	$CaZr_4(PO_4)_6$(s.s.), ZrP_2O_7
	1240/24	$CaZr_4(PO_4)_6$(s.s.), $Zr_2O_2O_9$
	1280/12	$CaZr_4(PO_4)_6$(s.s.), $MgZr_4(PO_4)_6$(s.s.),$Zr_2P_2O_7$
	1280/24	$CaZr_4(PO_4)_6$(s.s.), $MgZr_4(PO_4)_6$(s.s.),
	1300/12	$CaZr_4(PO_4)_6$(s.s.), $MgZr_4(PO_4)_6$(s.s.), $Zr_2P_2O_9$
	1300/24	$CaZr_4(PO_4)_6$(s.s.), $MgZr_4(PO_4)_6$(s.s.), $Zr_2P_2O_9$
	1300/48	$CaZr_4(PO_4)_6$(s.s.), $Zr_2P_2O_9$
	1350/12	$CaZr_4(PO_4)_6$(s.s.), $MgZr_4(PO_4)_6$(s.s.), ZrP_2O_7
	1350/24	$CaZr_4(PO_4)_6$(s.s.), $Zr_2P_2O_9$
	1350/48	$CaZr_4(PO_4)_6$(s.s.), $Zr_2P_2O_9$
	1400/48	$CaZr_4(PO_4)_6$(s.s.), $Zr_2P_2O_9$
	1450/48	$CaZr_4(PO_4)_6$(s.s.), $Zr_2P_2O_9$
$(Ca_{0.5}, Mg_{0.5})Zr_4(PO_4)_6$	1220/24	$CaZr_4(PO_4)_6$(s.s.), $MgZr_4(PO_4)_6$(s.s.), ZrP_2O_7, $Zr_2P_2O_9$
	1220/48	$CaZr_4(PO_4)_6$(s.s.), $Zr_2P_2O_9$
	1240/12	$CaZr_4(PO_4)_6$(s.s.), $MgZr_4(PO_4)_6$(s.s.), ZrP_2O_7, $Zr_2P_2O_9$
	1240/24	$CaZr_4(PO_4)_6$(s.s.), $Zr_2P_2O_9$
	1280/12	$CaZr_4(PO_4)_6$(s.s.), $Zr_2P_2O_9$
	1280/24	$CaZr_4(PO_4)_6$(s.s.), $MgZr_4(PO_4)_6$(s.s.), ZrP_2O_7, $Zr_2P_2O_9$
	1300/12	$CaZr_4(PO_4)_6$(s.s.), $MgZr_4(PO_4)_6$(s.s.), ZrP_2O_7, $Zr_2P_2O_9$
	1300/24	$CaZr_4(PO_4)_6$(s.s.), $MgZr_4(PO_4)_6$(s.s.), $Zr_2P_2O_9$
	1300/48	$CaZr_4(PO_4)_6$(s.s.), $Zr_2P_2O_9$
	1350/12	$CaZr_4(PO_4)_6$(s.s.), $MgZr_4(PO_4)_6$(s.s.), $Zr_2P_2O_9$
	1350/24	$CaZr_4(PO_4)_6$(s.s.), $MgZr_4(PO_4)_6$(s.s.), $Zr_2P_2O_9$
	1350/48	$CaZr_4(PO_4)_6$(s.s.), $Zr_2P_2O_9$
	1400/48	$CaZr_4(PO_4)_6$(s.s.), $Zr_2P_2O_9$

$(Ca_{0.4}, Mg_{0.6})Zr_4(PO_4)_6$	1220/24	$CaZr_4(PO_4)_6$(s.s.), $MgZr_4(PO_4)_6$(s.s.), ZrP_2O_7, $Zr_2P_2O_9$
	1220/48	$CaZr_4(PO_4)_6$(s.s.), $MgZr_4(PO_4)_6$(s.s.), $Zr_2P_2O_9$
	1280/24	$CaZr_4(PO_4)_6$(s.s.), $MgZr_4(PO_4)_6$(s.s.), $Zr_2P_2O_9$
	1280/48	$CaZr_4(PO_4)_6$(s.s.), $MgZr_4(PO_4)_6$(s.s.), $Zr_2P_2O_9$
	1350/24	$CaZr_4(PO_4)_6$(s.s.), $MgZr_4(PO_4)_6$(s.s.), $Zr_2P_2O_9$
	1350/48	$CaZr_4(PO_4)_6$(s.s.), $Zr_2P_2O_9$
	1400/48	$CaZr_4(PO_4)_6$(s.s.), $Zr_2P_2O_9$
	1450/48	$CaZr_4(PO_4)_6$(s.s.), $Zr_2P_2O_9$
$(Ca_{0.3}), Mg_{0.7})Zr_4(PO_4)_6$	1220/24	$CaZr_4(Po_4)_6$(s.s.), $MgZr_4(PO_4)_6$(s.s.), $Zr_2P_2O_9$
	1220/48	$CaZr_4(PO_4)_6$(s.s.), $MgZr_4(PO_4)_6$(s.s.), $Zr_2P_2O_9$
	1280/24	$CaZr_4(PO_4)_6$(s.s.), $MgZr_4(PO_4)_6$(s.s.), $Zr_2P_2O_9$
	1280/48	$CaZr_4(PO_4)_6$(s.s.), $MgZr_4(PO_4)_6$(s.s.), $Zr_2P_2O_9$
	1350/24	$CaZr_4(PO_4)_6$(s.s.), $MgZr_4(PO_4)_6$(s.s.), $Zr_2P_2O_9$
	1350/48	$CaZr_4(PO_4)_6$(s.s.), $Zr_2P_2O_9$
	1400/48	$CaZr_4(PO_4)_6$(s.s.), $Zr_2P_2O_9$
	1450/48	$CaZr_4(Po_4)_6$(s.s.), $Zr_2P_2O_9$
$(Ca_{0.2}, Mg_{0.8})Zr_4(PO_4)_6$	1220/24	$CaZr_4(PO_4)_6$(s.s.), $MgZr_4(PO_4)_6$(s.s.), ZrP_2O_7, $Zr_2P_2O_9$
	1220/48	$CaZr_4(PO_4)_6$(s.s.), $MgZr_4(PO_4)_6$(s.s.), $Zr_2P_2O_9$
	1280/24	$CaZr_4(PO_4)_6$(s.s.), $MgZr_4(PO_4)_6$(s.s.), $Zr_2P_2O_9$, ZrP_2O_7
	1220/48	$CaZr_4(PO_4)_6$(s.s.), $MgZr_4(PO_4)_6$(s.s.), $Zr_2P_2O_9$
	1350/24	$CaZr_4(PO_4)_6$, $MgZr_4(PO_4)_6$(s.s.) $Zr_2P_2O_9$
	1350/48	$CaZr_4(PO_4)_6$(s.s.), $Zr_2P_2O_9$
	1400/48	$CaZr_4(PO_4)_6$(s.s.), $Zr_2P_2O_9$
	1450/48	$CaZr_4(PO_4)_6$(s.s.), $Zr_2P_2O_9$
$(Ca_{0.1}, Mg_{0.9})Zr_4(PO_4)_6$	1220/24	$CaZr_4(PO_4)_6$(s.s.), $MgZr_4(PO_4)_6$(s.s.), ZrP_2O_7, $Zr_2P_2O_9$
	1220/48	$CaZr_4(Po_4)_6$(s.s.), $MgZr_4(PO_4)_6$(s.s.), ZrP_2O_7, $Zr_2P_2O_9$
	1280/24	$CaZr_4(PO_4)_6$(s.s.), $MgZr_4(PO_4)_6$(s.s.), ZrP_2O_7
	1280/48	$CaZr_4(PO_4)_6$(S.S), $MgZr_4(PO_4)_6$(s.s.), $Zr_2P_2O_9$
	1350/24	$CaZr_4(PO_4)_6$(s.s.), $MgZr_4(PO_4)_6$(s.s.), $Zr_2P_2O_9$
	1350/48	$CaZr_4(PO_4)_6$(s.s.), $MgZr_4(PO_4)_6$(s.s.), $Zr_2P_2O_9$
	1400/48	$CaZr_4(PO_4)_6$(s.s.), $Zr_2P_2O_9$
	1450/48	$CaZr_4(PO_4)_6$(s.s.), $Zr_2P_2O_9$
$MgZr_4(PO_4)_6$	1220/24	$MgZr_4(PO_4)_6$(s.s.), $Zr_2P_2O_9$, ZrP_2O_7
	1220/48	$MgZr_4(PO_4)_6$(s.s.), $Zr_2P_2O_9$, ZrP_2O_7
	1280/24	$MgZr_4(PO_4)_6$(s.s.), $Zr_2P_2O_9$, ZrP_2O_7
	1280/48	$MgZr_4(PO_4)_6$(s.s.), $Zr_2P_2O_9$
	1350/24	$MgZr_4(PO_4)_6$(s.s.), $Zr_2P_2O_9$, ZrP_2O_7
	1350/48	$MgZr_4(PO_4)_6$(s.s.), $Zr_2P_2O_9$
	1400/48	$MgZr_4(PO_4)_6$(s.s.), $Zr_2P_2O_9$
	1450/48	$MgZr_4(PO_4)_6$(s.s.), $Zr_2P_2O_9$

Table 3. Computed thermal expansion data for compositions based on $(Rb_{1-x},Cs_2)Zr_2(PO_4)_3$

Composition	Average Bulk CTE (30-1000°C)	Avg CTE 30-500°C	Avg CTE 500-1000°C
	1250°C/24h heat treatment		
$(Rb_{0.8}, Cs_{0.2})Zr_2(PO_4)_3$	-1.3×10^{-7}	-1.1×10^{-6}	
$(Rb_{0.6}, Cs_{0.4})Zr_2(PO_4)_3$	$1.\times10^{-8}$	8.7×10^{-7}	
	1250°C/72h heat treatment		
$RbZr_2(PO_4)_3$	-5.5×10^{-7}	-1.2×10^{-6}	8.5×10^{-7}
$(Rb_{0.9}, Cs_{0.1})Zr_2(PO_4)_3$	-6.5×10^{-7}	-1.2×10^{-6}	
$(Rb_{0.8}, Cs_{0.2})Zr_2(PO_4)_3$	5.6×10^{-7}	$-1.\times10^{-6}$	$9.\times10^{-7}$
$(Rb_{0.6}, Cs_{0.4})Zr_2(PO_4)_3$	2.5×10^{-6}		
	1300°C/48h heat treatment		
$RbZr_2(PO_4)_3$	1.4×10^{-7}	-1.3×10^{-6}	7.1×10^{-7}
$(Rb_{0.7}, Cs_{0.3})Zr_2(PO_4)_3$	$-4.\times10^{-7}$	-1.1×10^{-6}	
$(Rb_{0.5}, Cs_{0.5})Zr_2(PO_4)_3$	$1.\times10^{-8}$	-1.5×10^{-6}	1.1×10^{-6}
$(Rb_{0.4}, Cs_{0.6})Zr_2(PO_4)_3$	4.6×10^{-7}	$-4.\times10^{-7}$	$1.\times10^{-6}$

Table 4. Computed thermal expanstion data for compositions based on $(Ca_{1-x},Mg_x)Zr_4(PO_4)_6$

Composition	Average Bulk CTE (30-1000°C)	Avg. CTE 30-700°C	Avg CTE 700-1000°C
	1280°C/24h heat treatment		
$CaZr_4(PO_4)_6$	-1.16×10^{-6}	-2.13×10^{-6}	1.06×10^{-6}
$Ca_{0.9}Mg_{0.1}Zr_4(PO_4)_6$	-7.9×10^{-7}	-8.3×10^{-7}	1.6×10^{-6}
$Ca_{0.8}Mg_{0.2}Zr_4(PO_4)_6$	-1.29×10^{-6}	-1.98×10^{-6}	1.09×10^{-6}
$Ca_{0.7}Mg_{0.3}Zr_4(PO_4)_6$	-9.6×10^{-7}	-7.2×10^{-7}	4.15×10^{-7}
$Ca_{0.6}Mg_{0.4}Zr_4(PO_4)_6$	1.0×10^{-7}	-5.0×10^{-7}	1.1×10^{-6}
$Ca_{0.5}Mg_{0.5}Zr_4(PO_4)_6$	2.6×10^{-7}	-7.7×10^{-7}	9.9×10^{-7}
$Ca_{0.4}Mg_{0.6}Zr_4(PO_4)_6$	1.36×10^{-6}		1.36×10^{-6}
$Ca_{0.3}Mg_{0.7}Zr_4(PO_4)_6$	1.69×10^{-6}		1.69×10^{-6}
$Ca_{0.2}Mg_{0.8}Zr_4(PO_4)_6$	2.06×10^{-6}		2.06×10^{-6}
$Ca_{0.1}Mg_{0.9}Zr_4(PO_4)_6$	2.3×10^{-6}		2.3×10^{-6}
$MgZr_4(PO_4)_6$	2.5×10^{-6}		2.5×10^{-6}

Table 5. Calculated lattice parameters for the $(Rb_{1-x},Cs_x)Zr_2(PO_4)_3$ compositions

Composition	a(Å)	c(Å)
$RbZr_2(PO_4)_3$	8.6466	24.477
$(Rb_{0.9}, Cs_{0.1})Zr_2(PO_4)_3$	8.648	24.46
$(Rb_{0.7}, Cs_{0.3})Zr_2(PO_4)_3$	8.641	24.47
$(Rb_{0.5}, Cs_{0.5})Zr_2(PO_4)_3$	8.626	24.63
$(Rb_{0.4}, Cs_{0.6})Zr_2(PO_4)_3$	8.613	24.70
$(Rb_{0.3}, Cs_{0.7})Zr_2(PO_4)_3$	8.606	24.79
$(Rb_{0.2}, Cs_{0.8})Zr_2(PO_4)_3$	8.599	24.84
$(Rb_{0.1}, Cs_{0.9})Zr_2(PO_4)_3$	8.5832	24.912

Table 6. Calculated lattice parameters for the $(Ca_{1-x},Mg_x)Zr_4(PO_4)_6$ compositions

Composition	a(Å)	c(Å)
$CaZr_4(PO_4)_6$	8.784	22.682
$(Ca_{0.8},Mg_{0.2})Zr_4(PO_4)_6$	8.789	22.618
$(Ca_{0.7},Mg_{0.3})Zr_4(PO_4)_6$	8.789	22.618
$(Ca_{0.6},Mg_{0.4})Zr_4(PO_4)_6$	8.789	22.618
$(Ca_{0.5},Mg_{0.5})Zr_4(PO_4)_6$	8.789	22.618

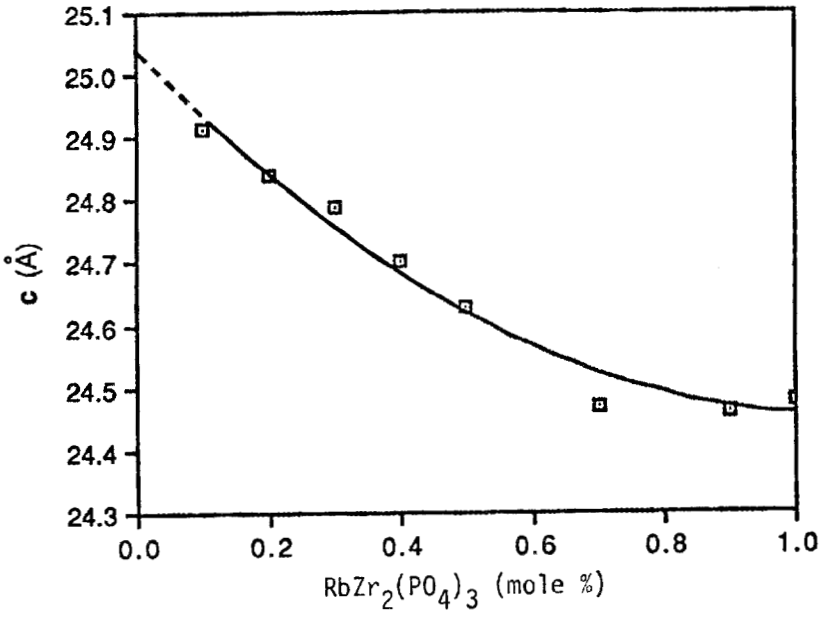

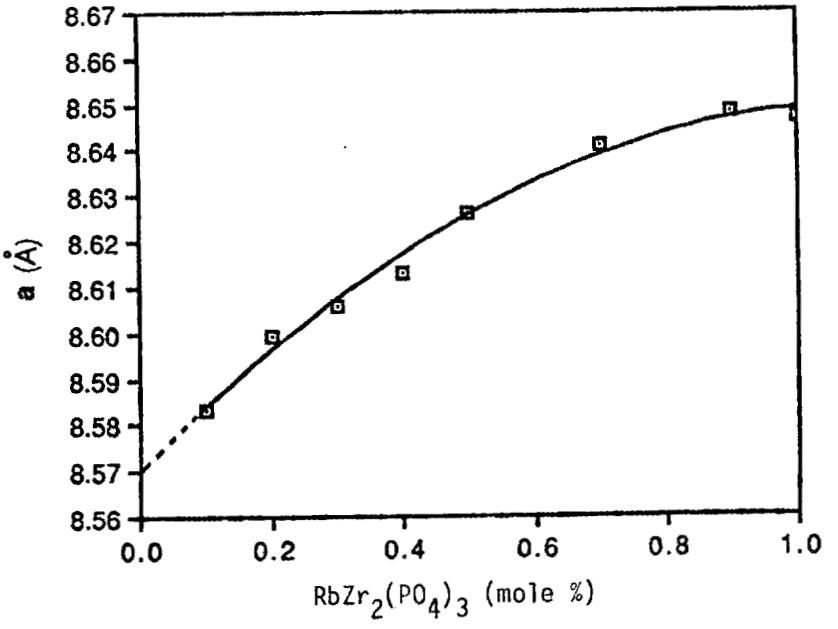

Figure 1. Lattice parameters for the $(Rb_x,Cs_{1-x})Zr_2(PO_4)_3$ compositions (tentative).

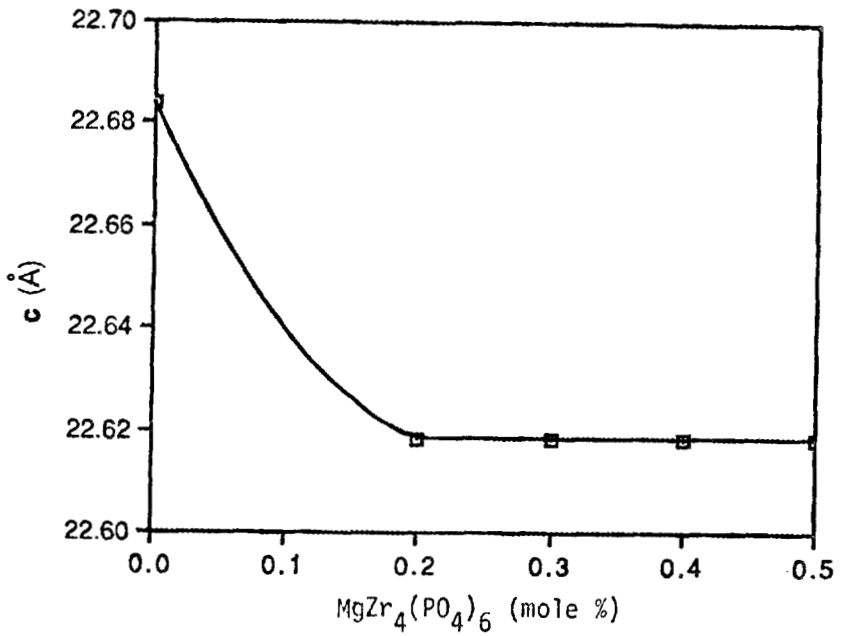

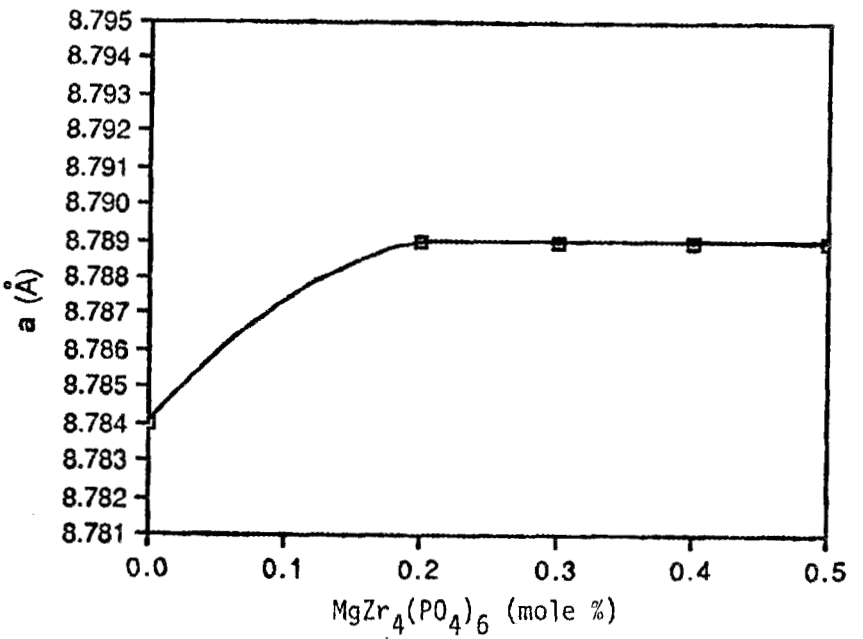

Figure 2. Lattice parameters for the $(Ca_x,Mg_{1-x})Zr_4(PO_4)_6$ compositions (tentative).

$AlPO_4$-β-$LiAlSiO_4$ System

Up to this time, research has concentrated on screening compositions in several crystal structure groups to identify high melting phases with low thermal expansion. Property characterization other than thermal expansion and phase identification has been on "as-prepared" samples. Various compositions of the chemically modified β-eucryptite ($AlPO_4$-β-$LiAlSiO_4$) were synthesized for the development of an isotropic, ultra-low expansion, and high thermal shock resistant ceramic. Sample composition, procesing, phase analysis, and thermal expansion details have been reported previously. From the results, the following conclusions were drawn:

1. The limit of solid solubility of $AlPO_4$ in β-$LiAlSiO_4$ is 54 mol%.

2. A decrease in SiO_2 content will reduce the negative thermal expansion.

3. Substitution of Mg^{++} for Li^+ lowers the negative thermal expansion; however, only 20 mol% of Li^+ can be replaced by Mg^{++}.

Thermal shock resistance and relative retained strength (normalized) were determined for the compositions $Li_{0.46}AlP_{0.54}Si_{0.46}O_4$, $Li_{0.5}AlP_{0.5}Si_{0.465}O_{0.393}$, and $Li_{0.41}Mg_{0.035}AlP_{0.52}Si_{0.48}O_4$. The composition selection was based on the following: (1) $Li_{0.46}AlP_{0.54}Si_{0.46}O_4$ contains the maximum $AlPO_4$ content, (2) sample $Li_{0.5}AlP_{0.5}Si_{0.465}O_{3.93}$ has the lowest negative thermal expansion thus far achieved, and (3) sample $Li_{0.41}Mg_{0.035}AlP_{0.52}Si_{0.48}O_4$ has partial substitution of Mg^{++} for Li^+, and very low thermal expansion. Results of thermal shock resistance and relative retained strength determinations are summarized in Table 7 and relative retained MOR values are shown in Figure 3, plotted as a function of the number of thermal shock cycles. Among the selected compositions, composition $Li_{0.41}Mg_{0.035}AlP_{0.52}Si_{0.48}O_4$ was found to have nearly zero thermal expansion and low anisotropy and to be stable to above 1200°C.

Generally, sample porosities in excess of 10% preclude the collection of any significant mechanical properties data. It is felt that the prime objective of the continuation of this research should be to develop the chemically-modified β-eucryptite-$AlPO_4$ compositions through processing, composition optimization, characterization, and parts fabrication to the point where they are attractive for testing in actual heat engines.

Because the β-eucryptite compositions are glass-forming and suitable for controlled recrystallization, this is likely to be the easiest and most economical process for densification. This task involves the addition of a suitable nucleation agent such as ZrO_2 or TiO_2, forming glass, and optimizing the recrystallization heat treatment to yield maximum strength and/or toughness. Therefore, glass-ceramic forming techniques have been initiated for the composition $Li_{0.41}Mg_{0.035}AlP_{0.52}Si_{0.48}O_4$.

Preliminary batch compositions included the addition of 4 wt% ZrO_2 as a nucleation agent. A glass resulted form heat treating the raw materials [$Al(OH)_3 \cdot nH_2O$, $NH_4H_2PO_4$, Li_3CO_3,$MgSO_4$, silicic acid, and ZrO_2] at 1625°C for 24 h (heating rate of 70°C/min). Glass fragments obtained from this procedure are crystaline following a single heat treatment of 850°C for 48 h. XRD analyses of the recrystallized glass-ceramics showed the crystalline phases to be β-eucryptite solid solution with a trace amount of $AlPO_4$.

It has recently been reported that all previous β-eucryptite compositions formed by solid state reaction contained about 10% Al_2O_3 as a second phase, along with trace amounts of $AlPO_4$. It is likely that the undesirable phases resulted from heat treating an incompletely reacted solid solution phase. During heat treatment, $AlPO_4$ decomposed into Al_2O_3 and P_2O_5. It, therefore, appears that to obtain the desired glass-ceramic phase composition, the raw materials must be fully reacted prior to glass-formation to form the $AlPO_4$-free β-eucryptite solid solution phase.

Since it is very important to maintain the desired composition until it reaches the glass-forming temperature in order to form the desired glass and glass-ceramics, the following tasks will be requried for further study:

1. Establish the heat treatment of the batch composition in order to get the desired β-eucryptite solid solution phase.

2. Establish the cooling rate of molten glass in order to get a satisfactory glass sample.

3. Establish the recrystallization temperature of the glass.

4. Prepare samples for thermal expansion, corrosion, and mechanical properties studies.

Table 7. Results of thermal shock experiments

Composition	Thermal Expansion (30-1000°C) $\alpha(\times 10^{-7}/°C)$	ΔT_{max}(°C)	Relative retained strength* (%)
$Li_{0.46}AlP_{0.54}Si_{0.46}O_4$	-5.8	1150	39.3
$Li_{0.41}Mg_{0.035}AlP_{0.52}Si_{0.48}O_4$	-2.3	1175	46
$Li_{0.5}AlP_{0.5}Si_{0.465}O_{3.93}$	-0.96	1175	63.4

*(MOR of specimen after 10 thermal shock cycle/MOR of specimen as originally formed) x 100%.

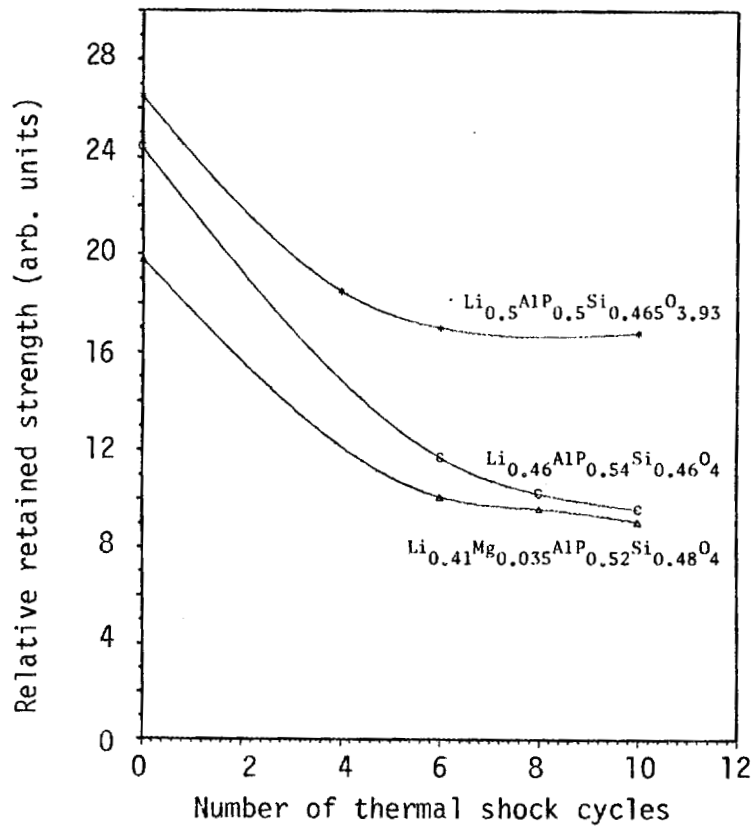

Figure 3. Relative retained strength of thermally shocked specimens.

Status of Milestones

Status of milestones is presented in Table 8 and Figure 4.

Publications

None this period.

References

1. J. Alamo and R. Roy, "Crystal Chemistry of the $NaZr_2(PO_4)_3$, NZP or CTP, Structure Family," *J. Mat. Sci.*, 21, 444-450 (1986).

2. T. Oota and I. Yamai, "Thermal Expansion Behavior of $NaZr_2(PO_4)_3$-Type Compounds," *J. Am. Ceram. Soc.*, 69[1], 1-6 (1986).

Table 8. Key to major milestones

VPI1.1	Process selection for phosphate- and silicate-based systems (Oct. 31, 1986)
VPI1.2	Process selection for mullite- and zircon-based systems (Oct. 31, 1986)
VPI2.1	Complete literature review (Oct. 31, 1986)
VPI3.1	Complete upgrade of characterization facility (Dec. 31, 1986)
VPI4.1	Complete initial screening of phosphate-based systems (Dec. 31, 1987)
VPI4.2	Complete initial screening of silicate-based systems (Dec. 31, 1987)
VPI4.3	Complete initial screening of zircon-based systems (Dec. 31, 1987)
VPI4.4	Complete initial screening of mullite-based systems (Dec. 31, 1987)
VPI5.1	Complete second-stage property and characterization evaluation of phosphate-based systems (Sept. 30, 1988)
VPI5.2	Complete second-stage property and characterization evaluation of silicate-based systems (Oct. 31, 1988)
VPI5.3	Complete second-stage property and characterization evaluation of mullite-based systems (Nov. 30, 1988)
VPI5.4	Complete second-stage property and characterization evaluation of zircon-based systems (Dec. 31, 1988)
VPI6.0	Complete scale-up specimen fabrication of most promising low-expansion ceramics (Feb. 28, 1989)

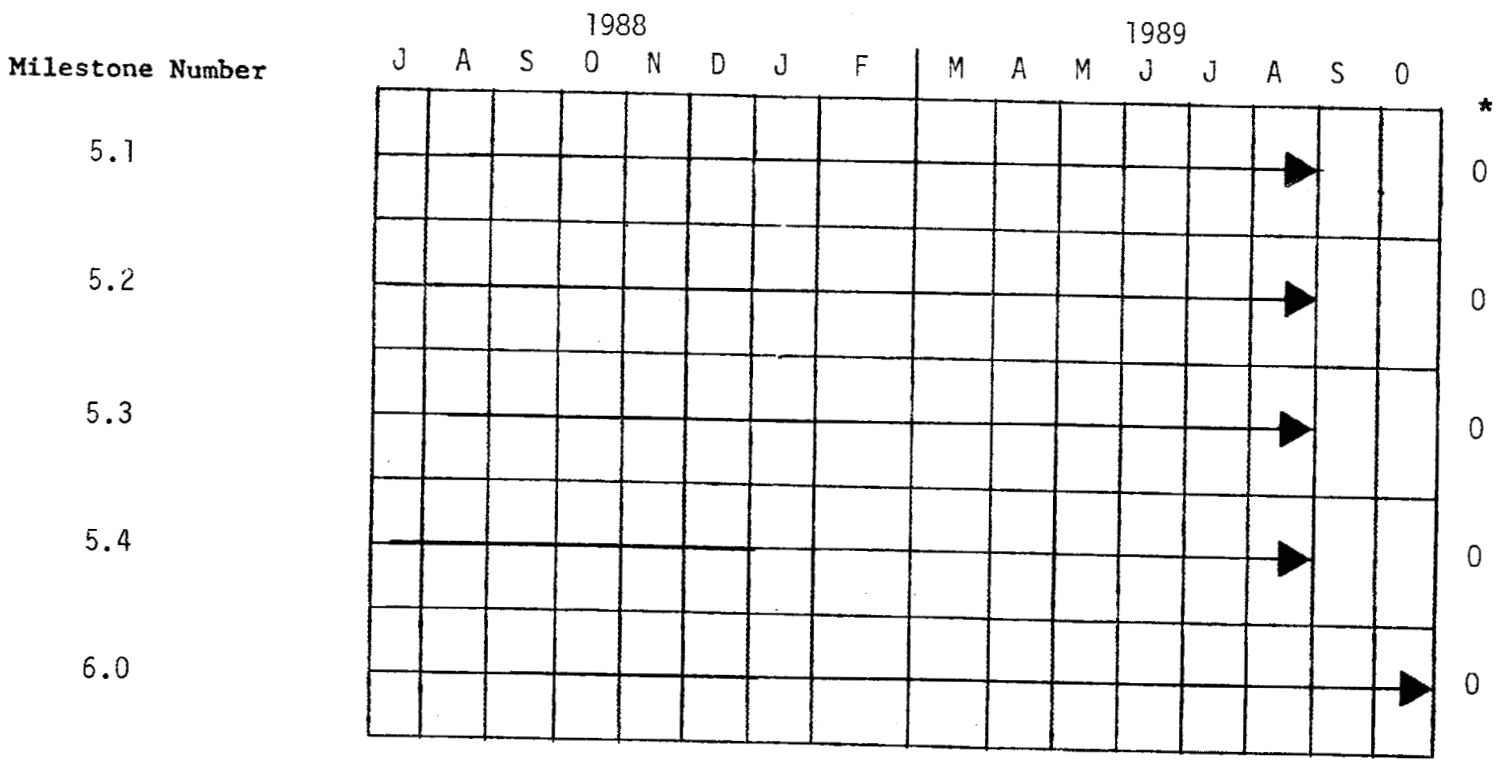

*On, Ahead of, or Behind Schedule.

Figure 4. Milestone status.

1.3 THERMAL AND WEAR COATINGS

1.3.1 ZrO_2 Base Coatings

Development of Adherent Ceramic Coatings to Reduce Contact Stress Damage of Ceramics
H. E. Rebenne, C. D'Angelo, J. H. Selverian (GTE Laboratories)

Objective/Scope

The objective of this program is to develop oxidation-resistant, high toughness, adherent coatings for silicon based ceramics. These coatings will be deposited on reaction bonded Si_3N_4 (RBSN), sintered SiC (SSC), and HIP'ed Si_3N_4 (HSN) and used in an advanced gas turbine engine. A chemical vapor deposition (CVD) process will be used to deposit the coatings. These coatings will be designed to provide the best mix of mechanical, thermal and chemical properties.

Technical Highlights

Contact stress tests of coated RBSN, SSC, and HSN at room temperature, 1000°C, and 1200°C were completed. These tests were performed by Garrett Turbine Engine Company using a modified Instron apparatus. The test included imparting a sliding point contact at the test temperature and measuring post-contact flexure strength at room temperature. The maximum sliding friction coefficient was also calculated. Results showed no improvement in the contact damage resistance of any of the substrates. However, the samples were oxidized at 1200°C for 100 hours in air prior to contact stress testing, and it is known that the coating cracks and spalls at these conditions. Hence, no firm conclusions will be drawn from these tests.

Contact Stress Testing

The contact stress testing from Phase I of the program was completed by Garrett Turbine Engine Company. Twenty coated bar and pin pairs of each substrate - RBSN, SSC, and HSN - were tested for contact stress using sliding point contact. The bar dimensions were 2" x 1/4" x 1/8". The test procedure was described elsewhere (1). Each sample had a ≈5 μm-thick AlN intermediate layer and a 1 μm-thick outer layer of Al_2O_3+ZrO_2 composite. The coated MOR bars were oxidized in static air at 1200°C for 100 hours before application of the stress. After oxidation, the coatings exhibited good adherence to the RBSN and SSC substrates and poor adherence to the HSN substrates. Room temperature flexure strength (using 4-point bending) was measured after application of the stress. The maximum sliding friction coefficient was also calculated.

Tables 1 - 3 show the strength loss and maximum friction coefficient measured for each set of conditions. The "As-coated strengths" were taken from samples that were oxidized at 1200°C for 500 hours and tested at 25°C and from unoxidized samples tested at 1000°C and 1200°C. These measurements were made at GTE Laboratories on a separate set of samples. All samples contact stress tested showed a strength loss of 30 - 50%. The increase in strength of the HSN samples tested at 1200°C (see Table 2) is not understood. The values of maximum friction coefficient reported are not necessarily the static "breakaway" friction coefficient measured during the test. In some cases, the apparent friction increased during the test, possibly due to embedment of the contact pin in the coating or to asperity effects resulting from coating damage. In some tests, the apparent friction coefficient rose to a value greater than the "breakaway" friction coefficient.

It was previously reported (2) that the Al_2O_3+ZrO_2 coatings flaked off the substrates and that the samples were fully oxidized after 100 hours of oxidation at 1200°C. Based on the previous oxidation data and the multiple factors involved in the contact stress testing (oxidation, contact stress, and variable friction), no firm conclusions will be drawn from this contact stress data.

We are currently evaluating the feasibility of measuring friction coefficients and resistance to contact damage using conventional ball-on-disk and pin-on-disk wear tests.

Table 1: Summary of contact testing and post-contact MOR strength testing for CVD coated RBSN.

Test Temp. (°C)	Applied Load (lbs)	Maximum Friction	As-coated Strength (MPa)	Retained Strength (MPa)	Contact Damage	Change in Strength (%)
25	25	0.44	197	154	yes	- 22
"	"	0.47	"	157	yes	- 20
"	"	0.54	"	137	yes	- 30
"	50	0.35	"	188	yes	- 5
"	"	0.43	"	130	yes	- 34
"	"	0.37	"	124	yes	- 37
"	60	0.50	"	116	yes	- 41
"	"	0.48	"	119	yes	- 40
"	"	0.45	"	131	yes	- 34
1000	25	1.36	245	150	yes	- 39
"	"	1.65	"	137	yes	- 44
"	50	0.82	"	164	yes	- 33
"	"	0.63	"	115	yes	- 53
1200	25	1.02	224	90	yes	- 60
"	"	1.03	"	105	yes	- 53
"	50	0.94	"	92	yes	- 59
"	"	0.81	"	95	yes	- 58

Microstructural Evaluation of Composite Layer

The microstructure of the Al_2O_3+ZrO_2 composite layer is being studied by TEM and analytical electron microscopy. During this reporting period, a sample of Al_2O_3+ZrO_2 coating on a TiC whisker-reinforced Al_2O_3 substrate was analyzed. This substrate was used because previous attempts at preparing a thin foil specimen of coated silicon

nitride-based materials were unsuccessful. The failure was attributed to uneven milling rates of the coating and substrate during ion beam milling.

Table 2: Summary of contact testing and post-contact MOR strength testing for CVD coated HSN.

Test Temp (°C)	Applied Load (lbs)	Maximum Friction	As-coated Strength (MPa)	Retained Strength (MPa)	Contact Damage	Change in Strength (%)
25	50	0.81	520	267	yes	- 49
"	"	0.43	"	564	no	+ 8
"	"	0.69	"	330	yes	- 37
"	60	0.71	"	318	yes	- 39
"	"	0.72	"	322	yes	- 38
"	"	0.65	"	368	yes	- 29
"	75	0.54	"	334	yes	- 36
"	"	0.71	"	310	yes	- 40
"	"	0.67	"	316	yes	- 39
1000	50	0.60	557	316	yes	- 43
"	"	0.68	"	----*	----	----
"	75	0.87	"	----*	----	----
"	"	0.85	"	109	yes	-80
1200	50	0.36	393	466	no	+19
"	"	0.48	"	453	no	+15
"	75	0.43	"	531	no	+35
"	"	0.42	"	545	no	+39

* Tested improperly

The coating was 3 μm thick and contained approximately 3 w/o Zr. It was found that the majority of the coating was essentially pure Al_2O_3 with the Zr concentrated at the interface between the coating and the substrate. The Zr was present as 30 nanometer particles containing impurities that were identified as silicon, tungsten, and probably oxygen. These impurities are probably introduced during deposition of the coating as a result of residue inside the CVD equipment from coating of other substrate materials. It has not yet been determined that the Zr is present as ZrO_2. An amorphous Si-rich phase was also present at the interface. This glass probably formed from the binder material

in the substrate. The grain size of the Al_2O_3 in the coating ranged from 40 to 200 nanometers with the majority being 50 nanometers. The phase of Al_2O_3 is still being determined.

These results are consistent with earlier studies done using electron microprobe. In particular, the ZrO_2 was found to be concentrated at the interface. This is due to the method of generating the Al- and Zr-containing source materials. A modification of the CVD process will therefore be necessary in order to obtain a homogeneous coating. The required modifications to the CVD reactor are currently being designed.

Table 3: Summary of contact testing and post-contact MOR strength testing for CVD coated SSC.

Test Temp (°C)	Applied Load (lbs)	Maximum Friction	As-coated Strength (MPa)	Retained Strength (MPa)	Contact Damage	Change in Strength (%)
25	40	0.23	328	248	yes	-24
"	"	0.48	"	180	yes	-45
"	"	0.50	"	209	yes	-36
"	50	0.35	"	195	yes	-41
"	"	0.49	"	178	yes	-46
"	"	0.30	"	192	yes	-41
"	60	0.55	"	202	yes	-38
"	"	0.76	"	183	yes	-44
"	"	0.51	"	162	yes	-51
1000	40	0.59	258	172	yes	-33
"	"	0.69	"	173	yes	-33
"	60	0.45	"	165	yes	-36
"	"	0.49	"	152	yes	-41
1200	40	0.85	320	141	yes	-56
"	"	0.89	"	115	yes	-64
"	60	0.64	"	169	yes	-47
"	"	0.91	"	155	yes	-52

Oxidation Resistance of the Coating

During Phase I, the oxidation resistance of the coating in static air was studied. The coating was found to be oxidation resistant for up to 500 hours at 1000°C, but not at 1200°C. The cause of failure is being studied in Phase II.
Thus far, tests indicate that the failure is due to oxygen penetration through the Al_2O_3+ZrO_2 composite layer to the AlN layer and oxidation of the AlN. Several pathways for oxygen penetration through the composite layer exist, including porosity, cracking, and diffusion. Some samples were examined for porosity in the composite layer using an electron microprobe analyzer, and no pores were detected. However, the detection limit was 1 μm diameter. Additional samples coated with the composite layer only on optically transparent substrates (single crystal sapphire) were examined in a light microscope, and no porosity was detected. Cracks were also searched for using scanning electron microscopy, but none were found. Additional samples are currently being examined for cracking. The possibility of oxygen diffusion, either grain boundary or lattice type, was theoretically evaluated. This was done by calculating the oxygen concentration in an Al_2O_3 coating as a function of temperature, time, and distance. The approach used was taken from Fisher (3). Three types of diffusion were included in the calculation: 1) diffusion from the surface down the grain boundary, 2) diffusion normal to the grain boundary into the grain, and 3) diffusion from the surface through the grain (bulk diffusion). Fisher's treatment was used for the first two types of diffusion, and the constant surface concentration solution to Fick's second law was used for the third type. For purposes of the calculation, the coating was treated as pure Al_2O_3. This is considered to be realistic for the coatings that were oxidation tested since the TEM analysis indicated that all of the ZrO_2 was concentrated at the interface (see above).

A computer program was written and oxygen concentration profiles calculated at temperatures of 1100°C, 1200°C, 1300°C, 1400°C, and 1500°C for times up to 2,048,000 hours and diffusion distances of 0.5 μm, 1.0 μm, and 1.5 μm. The following parameters were used: grain boundary width = 5×10^{-8} cm, bulk diffusivity for oxygen in Al_2O_3 at 1500°C = 3.5×10^{-16} cm^2/s, grain boundary diffusivity of oxygen in Al_2O_3 at 1500°C = 5.0×10^{-15} cm^2/s, activation energy for oxygen lattice diffusion in Al_2O_3 = 152,000 cal/mole K, preexponential factor for oxygen lattice diffusion in Al_2O_3 = 1.9×10^{3} cm^2/s, activation energy for oxygen grain boundary diffusion in Al_2O_3 = 57,600 cal/mole K, preexponential factor for oxygen lattice diffusion in Al_2O_3 = 6.3×10^{-8} cm^2/s. The activation energies and preexponential factors were taken from Oishi and Kingery (4). The calculations indicated that, at 1200°C, the oxygen concentration 0.5 μm below the surface of the coating is $<10^{-4}$ atomic per cent at 500 hours. At 1200°C and 1.0 μm below the surface, the oxygen concentration is zero after 500 hours and only 1×10^{-2} atomic per cent after 8000 hours. For a depth of 1.5 μm at 1200°C, the oxygen concentration is only 2×10^{-4} atomic per cent after 8000 hours. The oxygen concentration only becomes significant for a depth of 1.5 μm and a temperature of 1500°C after 8000 hours. This combination of time and temperature is well beyond the anticipated service range of these coatings. Hence, these results suggest that the coating should not fail due to oxygen diffusion through the composite layer.

Oxidation tests of the full coating configuration on all three substrates are currently underway to provide kinetic data for the oxidation behavior. In addition, a set of samples with a modified coating configuration is being coated in preparation for oxidation testing. This modification incorporates a pure Al_2O_3 layer between the composite and AlN to

provide an oxygen barrier. It is anticipated that this will improve the oxidation resistance of the coating.

Status of Milestones

First two milestones, due in December, 1989, are on schedule.

Communications/Visits/Travel

04/24-27/89 - H. E. Rebenne attended the annual meeting of the American Ceramic Society in Indianapolis and presented a talk entitled "High Temperature Oxidation of Ceramic Coatings on Si_3N_4- and SiC-Based Substrates." The coauthors were C. D'Angelo, H. J. Kim, and D. W. Oblas.

09/08/89 - H. J. Kim and H. E. Rebenne visited Oak Ridge National Laboratory to present a review of the program.

Problems Encountered

None.

Publications

None.

References

1. J. Schienle and J. Smyth, "High Temperature Coating Study to Reduce Contact Stress Damage of Ceramics," Final Report, DOE Contract DE-AC05-840R21400 (March, 1987).
2. C. D'Angelo, H. J. Kim, D. W. Oblas, H. E. Rebenne, and V. K. Sarin, "Development of Adherent Ceramic Coatings to Reduce Contact Stress Damage of Ceramics," Final Report, DOE Contract 86X95915C, submitted (March 1989).
3. J. C. Fisher, J. App. Phys., vol. 22(1), 74-7 (1951).
4. Y. Oishi and W. D. Kingery, J. Chem. Phys., vol. 33(3), 905-6 (1960).

Wear resistant Coatings

C. D. Weiss (Caterpillar, Inc.)

Objective/scope

The goal of this technical program is to develop wear-resistant coatings for piston ring and cylinder liner components for low heat-loss diesel engines.

Wear resistant coatings will be applied to metallic substrates utilizing plasma spraying, vapor deposition (CVD/PVD), and enameling processes. First, the adherence of each coating to the metallic substrate will be optimized. Methods which can be utilized for improving the adherence of these coatings include development of unique substrate preparation methods before application of the coating, grading coating compositions to match thermal expansion, compositional changes, laser or electron beam fusing and/or optimizing coating thickness. Once the adherence of each coating system is optimized, each coating will be screened for friction and wear at 350°C under lubricated conditions. Coatings which show promise after this initial screening will be further optimized to meet the friction and wear requirements. Then the optimized coating systems will be fully characterized for oxidation resistance, adherence, uniformity, and thermal shock resistance, as well as friction and wear.

Selection of the most promising coatings and coating processes will be made after the characterization task. Criteria for selection will include not only performance (i.e., wear adhesion, friction coefficient, thermal shock resistance and thermal stability) but manufacturability/ cost factors, as well. Utilizing both criteria a coating system having acceptable cost/benefit relationships will be selected.

Technical progress

Pin-on-disk friction and wear testing of the plasma sprayed and chemically vapor deposited coatings (Tables 1 and 2) has identified the following coatings as candidates for further friction and wear testing using the Hohman A-6 friction and wear machine:

Plasma sprayed high carbon iron-molybdenum,
Plasma sprayed Cr_2O_3-SiO_2,
Plasma sprayed PS212,
Chemical vapor deposited chrome nitride,
Mid-temperature chemical vapor deposited Ti(C,N).

Table 1. Friction and Wear Results - Plasma Sprayed Coatings 350°C/Lubricated

Coating Type	Pin	Friction Range	Disk Wear	Pin Wear
Cr_2O_3- SiO_2 Composite	ZrO_2	0.09 - 0.18	Low	Low
	440C	0.04 - 0.18	Med	Med
Ni - Cr Alloy	ZrO_2	0.09 - 0.15	Low	Low
	440C	0.11 - 0.15	Low	Med
High Carbon - Iron,Mo Composite	ZrO_2	0.04 - 0.13	Low	Low
	440C	0.04 - 0.18	Med	Med
High Mo Blend	ZrO_2	0.04 - 0.22	Low	Med
	440C	0.09 - 0.24	Low	Med
High Co , Mo, Cr, Alloy	ZrO_2	0.13 - 0.22	Med	Med
	440C	0.18 - 0.33	Med	Med
Hohman PS 212	ZrO_2	0.04 - 0.15	Med	Low
	440C	0.09 - 0.26	High	High
ZrO_2- TiO_2-Y_2O_3 Composite	ZrO_2	0.18 - 0.37	High	High
	440C			
Graded ZrO_2	ZrO_2	0.13 - 0.20	Med	Med
	440C	0.15 - 0.24	Med	High

Table 2. Friction and Wear Results - CVD Coatings 350°C/Lubricated

Coating Type	Pin	Friction Range	Disk Wear	Pin Wear
Mid Temperature Ti(C, N)	ZrO_2	0.07 - 0.1	Low	Low
	Al_2O_3	0.08 - 0.15	Low	Low
	440C	0.24 - 0.24	Med	High
Chrome carbide	ZrO_2	0.09 - 0.18	Med	Low
	Al_2O_3	0.11 - 0.22	Med	Low
	440C	0.24 - 0.31	Med	High
	Si_3N_4	0.13 - 0.59	Med	Med
Ti N / Ti C	ZrO_2	0.10 - 0.13	Low	Low
	Al_2O_3	0.08 - 0.11	Low	Low
	440C	0.18 - 0.22	Med	Med
Chrome nitride	ZrO_2	0.08 - 0.19	Low	Low
	440C	0.10 - 0.11	Med	Low

Additional pin-on-disk friction and wear testing of PVD zirconia coated mild steel and chemically vapor deposited W/WC H-13 tool steel specimens were completed with disappointing results.

The PVD zirconia on mild steel specimens were evaluated in a lubricated, pin-on-disk test, at 350°C, running against zirconia, alumina and 440C stainless steel counterfaces. The PVD zirconia coating recorded low friction and wear values running against the 440C counterface. Running against the alumina and zirconia counterfaces, the PVD zirconia coating also recorded low friction values. However, for both these counterfaces, the wear rate of the PVD zirconia coating initially was very low but increased rapidly as the test progressed. For this reason, both counterfaces wore through the PVD zirconia coating in a relatively short time.

The chemically vapor deposited W/WC coating exhibited a very rough surface finish (greater than 40 microinches) after the chemical vapor deposited coating was applied to the H-13 tool steel specimens. One possible reason for the rough surface finish was it was difficult to get a good bond between the H-13 tool steel and the W/WC coating and the specimens had to be recoated a number of times before acceptable coating adherence could be achieved. The rough surface finish caused the W/WC coating to record coefficient of friction values above 0.2 when run against either the zirconia or 440C stainless counterfaces. In addition, both counterfaces exhibited very high wear coefficients when run against the W/WC coating.

Both Solar Turbine's VPC coating and the University of Illinois' cobalt based enamel compositions recorded coefficient of friction values greater than 0.2 when evaluated against either a metallic or ceramic counterfaces during lubricated pin-on-disk testing, at 350°C. Addition of the hard, wear resistant particles (Table 3) to either composition did not reduce the coefficient of friction of the coating. As a result, all the VPC and/or enamel compositions, irrespective of the volume percent of hard-particle loading, exhibited unacceptable wear during pin-on-disk screening.

Table 3. Wear Resistant Enamel Compositions Evaluated

Base Enamel Compositions

Solar VPC
A.I. Andrew's Co Based Enamel

Hard Particle Additions

50 volume percent Si_3N_4
50 volume percent SiC
10, 20, 50, 70, and 80 volume percent Cr_2O_3
10, 20, 50, and 70 volume percent ZrO_2
50 and 70 volume percent Al_2O_3
20 volume percent Cr_2O_3 plus 20 volume percent BN

Four slurry sprayed enamels which had both wear resistant hard particles as well as solid lubricants added to the enamel composition were evaluated against both ceramic and metallic counterfaces in a lubricated pin-on-disk friction and wear test, at 350°C. This enamel composition recorded friction values below 0.1 and reasonably low enamel wear rates.

The Hohman A-6 testing was initiated with the development of a suitable procedure for operation at 350°C with a speed of 206 M/min and a load of 9.08 Kg. A room temperature calibration test was developed for the purpose of checking the machine operation. Baseline wear and friction data were obtained at 350°C using a plasma sprayed chrome carbide in a nickel-molybdenum matrix running against cast iron.

Hohman A-6 testing is continuing to evaluate the following material pairs:

High carbon iron-molybdenum plasma sprayed rub shoes against a chromia-silica plasma sprayed disk,

Chromia-silica plasma sprayed rub shoes against a chromia-silica plasma sprayed disk,

Chromia-silica plasma sprayed rub shoes against a chemically vapor deposited chrome nitride disk,

Chemically vapor deposited Ti(C,N) rub shoes against a chromia-silica plasma sprayed disk,

PS212 plasma sprayed rub shoes against a chromia-silica plasma sprayed disk.

All the plasma sprayed specimens which had been machined using a 200 grit wheel recorded high friction coefficients, which did not decrease with increasing test time. These high friction values caused the plasma sprayed specimens all to record unacceptable wear rates. Examination of the surfaces of the plasma sprayed specimens revealed that the high coefficient of friction values occurred because all the plasma sprayed specimens had an extremely rough surface finish. For this reason, the plasma sprayed specimens all were machined a second time to obtain the desired surface finish.

Status of milestones

MS1 Manufacture of 400 adherence test specimens- complete
MS2 Manufacture friction and wear test specimens- complete
MS3 Identify a minimum of 12 adherent coating systems-complete
MS4 Identify 12 coating systems for friction and wear optimization-complete
MS6 Manufacture simulated engine component specimens-complete

Publications

C.D. Weiss, "Wear Resistant Ceramic coatings for Diesel Engine Components", was presented at the International Conference on Metallurgical Coatings, 1989, April 19, 1989 in San Diego.

Development of Wear Resistant Ceramic Coatings for Diesel Engine Components

M.G.S. Naylor
Cummins Engine Company, Inc.

Objective/Scope

The objective of this program is to develop advanced wear resistant coatings for in-cylinder components for future, low heat rejection diesel engines. Coatings and substrates (for piston rings and cylinder liners) are to be developed to meet the following requirements:

1. low wear (as measured in laboratory rig tests at ambient temperature and 350°C). Wear coefficients in the range $5x10^{-12}$ to $5x10^{-11}$ $mm^3/mm/N$ are targeted (at 350°C).
2. low friction coefficients when tested under boundary lubricated conditions (target 0.1) and unlubricated conditions (target 0.2) at ambient temperature and 350°C.
3. good thermal shock resistance.
4. high adherence and compatibility with substrate materials up to 650°C
5. high uniformity and reproducibility

Technical Progress

Overview of Coating Development

Table 1 lists the wear coatings which have been under evaluation to this point in the program. Wear testing has been completed for the majority of the air plasma sprayed (APS) chromium oxides, some of the high velocity (HV) thermal sprayed cemented carbides and the slurry-sprayed silica-chromia-alumina (SCA) materials. Microstructural characterization has been completed for all the coatings which have been wear tested. Bond strengths have been measured for the APS chromium oxides, and a study of the effects of various spray parameters (powder composition, powder feed gas, powder feed rate, spray velocity and gun/nozzle selection) has been completed (see previous semiannual report). Property measurements (microhardness, tensile strength and elastic modulus at room temperature and 320°C, thermal expansion coefficient from 25 - 540°C, and thermal diffusivity) and microstructural characterization of the UTRC coatings (Table 1) are in progress.

Wear Testing

Wear tests have been performed on a wide variety of piston ring/cylinder liner coating combinations, using a Cameron Plint wear tester. The test conditions, which were chosen to represent the ring:liner engine environment close to the top ring reversal position, are detailed in Table 2. Wear tests were performed using a fresh commercial CE/SF quality 15W40 mineral oil based lubricant at two temperatures, and with the same oil taken from an engine test which produced severe oil degradation, to simulate the chemical environment of the engine more closely. In addition, tests were run with no lubrication, in order to rank the sliding wear properties of the different materials under "scuffing" conditions. A material with good scuff resistance is desirable in case of temporary loss of oil film in the engine (on start-up or under temporary conditions of extreme hot running, for example). Under the loading conditions at top ring reversal, it is extremely unlikely that sufficiently low wear rates can be obtained with any coating for extended engine operation without lubrication.

Coating	*Substrate*	*Supplier*
PLASMA SPRAYED		
APS UCAR Cr_2O_3	HK40 Stainless	APS Materials
APS Metco 106FP Cr_2O_3 - 2% SiO_2 - 2% other oxides	422 Stainless	UTRC
APS Metco 136 Cr_2O_3 - 5% SiO_2 - 3% TiO_2 (A)	HK40 Stainless	APS Materials
APS Metco 136 Cr_2O_3 - 5% SiO_2 - 3% TiO_2 (B)	HK40 Stainless	Boyd Machine
APS Cr_2O_3 - 15% Al_2O_3 - 4% SiO_2 - 3% TiO_2	HK40 Stainless	APS Materials
APS Cr_2O_3 - 33% Stellite 6 - 3% SiO_2 - 2% TiO_2	HK40 Stainless	APS Materials
APS Cr_2O_3 - 8% SiO_2 - 3% TiO_2	HK40 Stainless	APS Materials
APS Metco 143 ZrO_2 - 18% TiO_2 - 10% Y_2O_3	422 Stainless	UTRC
APS Armacor M	HK40 Stainless	APS Materials
APS Armacor T	HK40 Stainless	APS Materials
VPS Boron Carbide	HK40 Stainless	APS Materials
HIGH VELOCITY		
WC - 12% Co	HK40 Stainless	Boyd Machine
Cr_3C_2-WC-NiCrCo	HK40 Stainless	Boyd Machine
Diamalloy 3007 Cr_3C_2-NiCr	422 Stainless	UTRC
Diamalloy 2001 NiCrBSi	422 Stainless	UTRC
SLURRY-SPRAYED		
SiO_2 - Cr_2O_3 - Al_2O_3	Pearlitic Grey Cast Iron	Cummins
ION NITRIDED	Type 1 Niresist H13 Tool Steel	Cummins

Table 1. Ring and liner coating materials under evaluation.

Test Schedule for Each Coating:
Fresh CE/SF 15W40 mineral oil based lubricant at 200°C **Fresh** CE/SF 15W40 mineral oil based lubricant at 350°C **Engine-tested** CE/SF 15W40 mineral oil based lubricant at 200°C **Unlubricated**, 200°C
Test Conditions:
225 N on a 7.5 mm wide sample (30 N/mm) "Ring" sample has cylindrical radius of curvature of 50 mm "Liner" sample is flat 20 Hz frequency 5 mm stroke Lubricated tests: 6 hrs with 1 drop oil every 10 seconds Unlubricated tests: 10 - 30 minutes.

Table 2. Wear test conditions.

Before considering the wear results for advanced coating systems, it is worth reviewing the wear data already obtained for conventional diesel engine materials. Figure 1 shows the variation of wear coefficient with temperature for electroplated chromium piston rings sliding against pearlitic grey cast iron cylinder liners, with fresh CE/SF 15W40 oil (Cameron Plint data). Wear rates are very sensitive to temperature, varying over two orders of magnitude between room temperature and 360°C. Under the test conditions imposed, the system operated in the boundary lubrication regime over the whole temperature range, with friction coefficients in the range 0.1 to 0.3. For the lubricant and oil supply rate used in these tests, the "scuffing" temperature (the temperature above which an oil film could not be maintained and friction coefficients in excess of 0.5 were measured) was around 360°C.

This report compares the wear properties of various coatings under the above conditions. The effects of coating composition, microstructure and hardness on wear rates are discussed, and rankings of the materials tested are made under conditions of fresh oil lubrication, degraded oil lubrication and no lubrication. The final objective of the program is to develop a **wear system** (an optimized combination of ring material, liner material and lubricant) which is capable of meeting the above objectives.

APS Chromium Oxide Ring Coatings vs Pearlitic Grey Cast Iron Liners

A series of wear tests was performed at different temperatures, using a pure chromium oxide ring coating (UCAR powder) sliding against a conventional grey cast iron liner, with a fresh CE/SF 15W40 mineral oil based lubricant (Figure 2). By comparison with the baseline system (Figure 1), wear rates are generally lower for the ring material, but higher for the liner. The variation of liner wear with temperature is very small, which suggests that the liner wear mechanism does not involve thermal activation in this system. It is speculated that the predominant liner wear mechanism in this case is abrasion (see below).

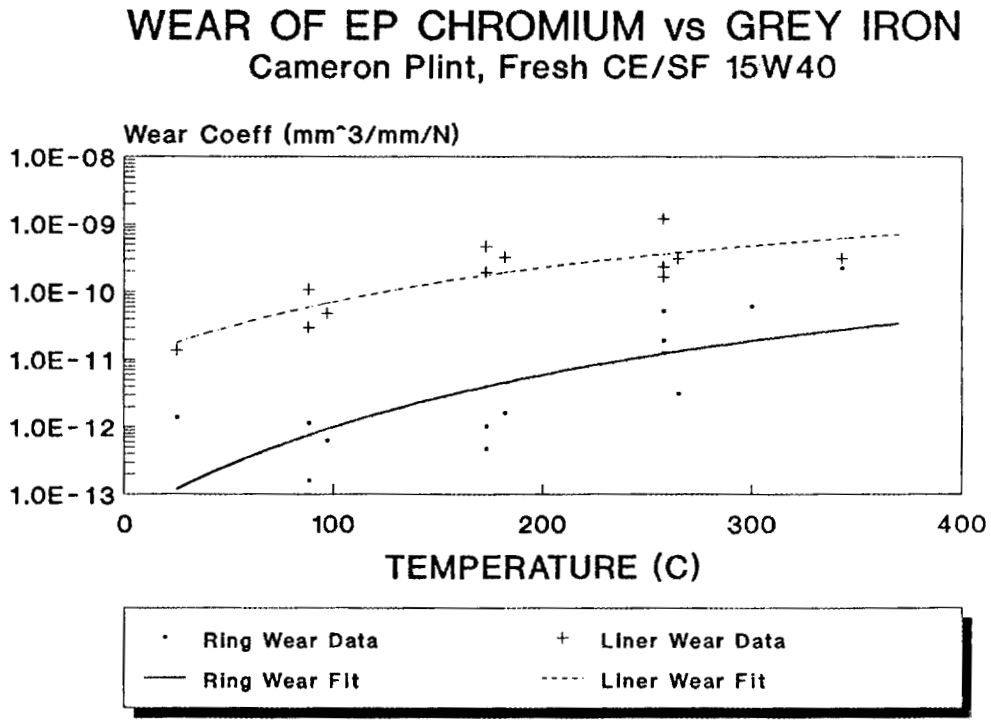

Figure 1. *Variation of wear coefficient with temperature for electroplated chromium rings vs grey cast iron liners, lubricated with fresh CE/SF 15W40 oil.*

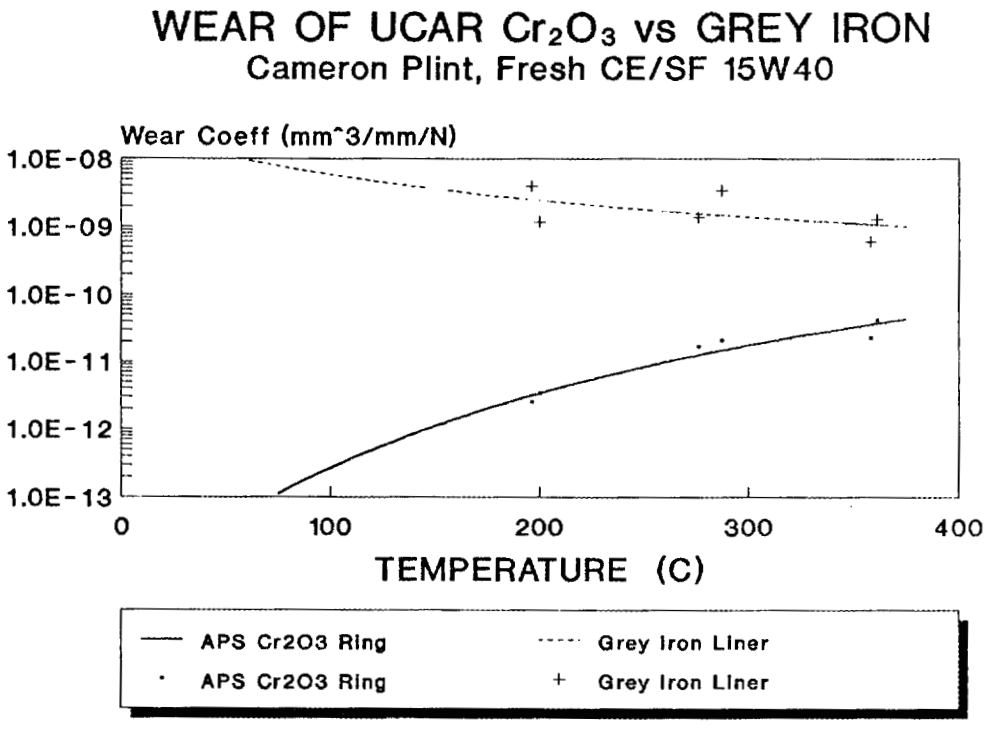

Figure 2. *Variation of wear coefficient with temperature for APS UCAR chromium oxide coated rings vs grey cast iron liners, lubricated with fresh CE/SF 15W40 oil.*

A variety of chromium oxide based materials was evaluated with the conventional grey iron liner counterface (Figure 3). In most cases, ring wear was lower than for electroplated chromium, but liner wear was higher. Surface roughness values for the coatings were in the range 0.25 - 0.5 μm (measured parallel to the sliding direction, i.e. parallel to the grinding marks on the machined surface). Experiments were performed with a hardened iron liner (42 HRC) in place of the pearlitic iron (approximately 10 HRC) for the UCAR coating. The hardness of the grey iron was not found to be a significant factor (Figure 3).

Two forms of Metco 136 coatings, from different suppliers using different spray systems, were evaluated (Figure 3). The material designated "A" was found to have lower wear rates than the other chromium oxides studied. Microstructural characterization of each coating is described below.

Wear rates for the Cr_2O_3 - 15% Al_2O_3 coating (formed by mixing 15 wt% Al_2O_3 with Metco 136 powder) were found to be similar to those for other Cr_2O_3 coatings, even though the hardness was increased from 960 $kgfmm^{-2}$ (Metco 136) to 1260 $kgfmm^{-2}$ (Metco 136 with 15% Al_2O_3) (Knoop, 100gf).

Wear tests using degraded, heavily soot-loaded oil from an engine test showed a considerable increase in ring and liner wear rates compared to tests in fresh oil for the conventional electroplated chromium/grey iron system (Figure 4). By comparison, the chromium oxide/cast iron tests generally showed little effect of oil degradation (Figure 4), which suggests that the advantages of using chromium oxide ring coatings over the conventional ring material would become more pronounced as the oil degrades in the engine.

Unlubricated tests with chromium oxide/grey iron combinations produced lower wear rates for coatings with additions of other oxides (Metco 136 and Cr_2O_3 - 15% Al_2O_3 - 4% SiO_2 - 3% TiO_2) than for pure Cr_2O_3 (Figure 5). However, even the best chromium oxide compositions gave the same wear coefficents as electroplated chromium.

Microstructural Evaluation of APS Chromium Oxide Coatings

SEM micrographs of each of the APS chromium oxide coatings are shown in Figures 6 - 9. The coatings generally contain pores and voids between the "splats" of solidified material. The Metco 136 materials showed variations in grey scales in backscattered electron SEM images, which were found to be caused primarily by variations in TiO_2 content. Comparing Figures 7 and 8, the two Metco 136 materials were found to be considerably different in microstructure. The "B" material contained large numbers of small, equiaxed particles, with a greater concentration of microcracks/voids, whereas the "A" material had a more lamellar microstructure. The "B" microstructure is thought to have been caused by unmelted particles being entrapped in the spray. The coating sprayed from a Metco 136 powder with 15 wt% Al_2O_3 is shown in Figure 9. The Al_2O_3 phase (darker) is clearly differentiated from the Cr_2O_3-rich material (lighter). Both phases have been melted in the plasma and have solidified without much mixing, and with no apparent cracking or debonding at the Cr_2O_3-Al_2O_3 interfaces.

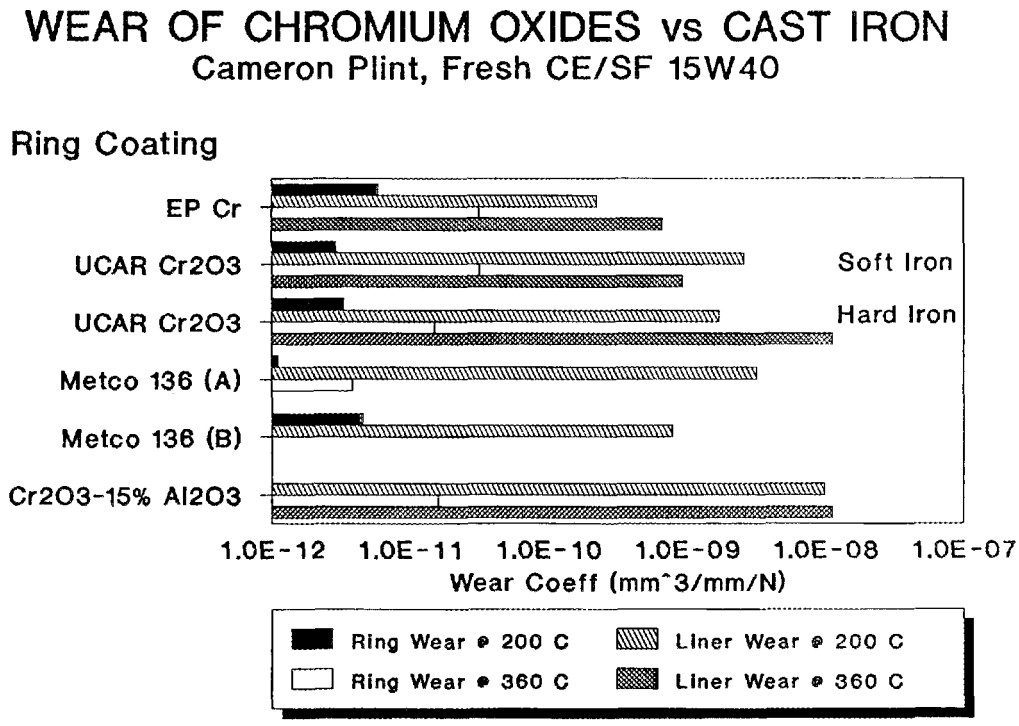

Figure 3. *Wear comparison of APS chromium oxide coatings and electroplated chromium sliding against grey iron liners at 200 and 360°C, lubricated with fresh CE/SF 15W40 oil.*

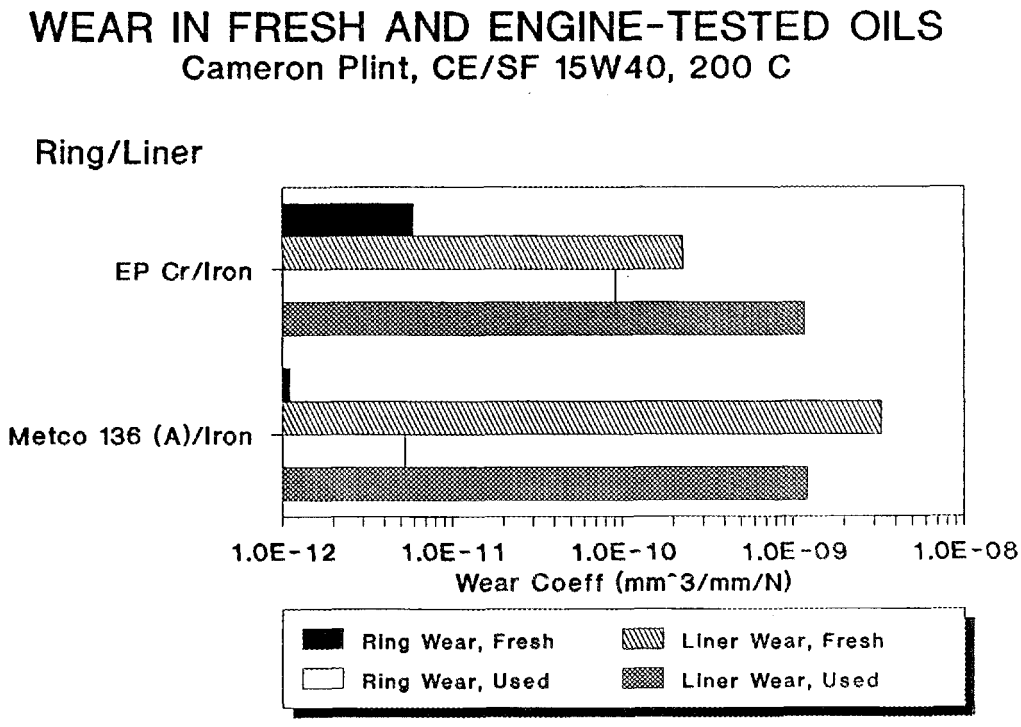

Figure 4. *Wear comparison of Metco 136 chromium oxide and electroplated chromium sliding against grey cast iron liners at 200°C in fresh and engine-tested oils.*

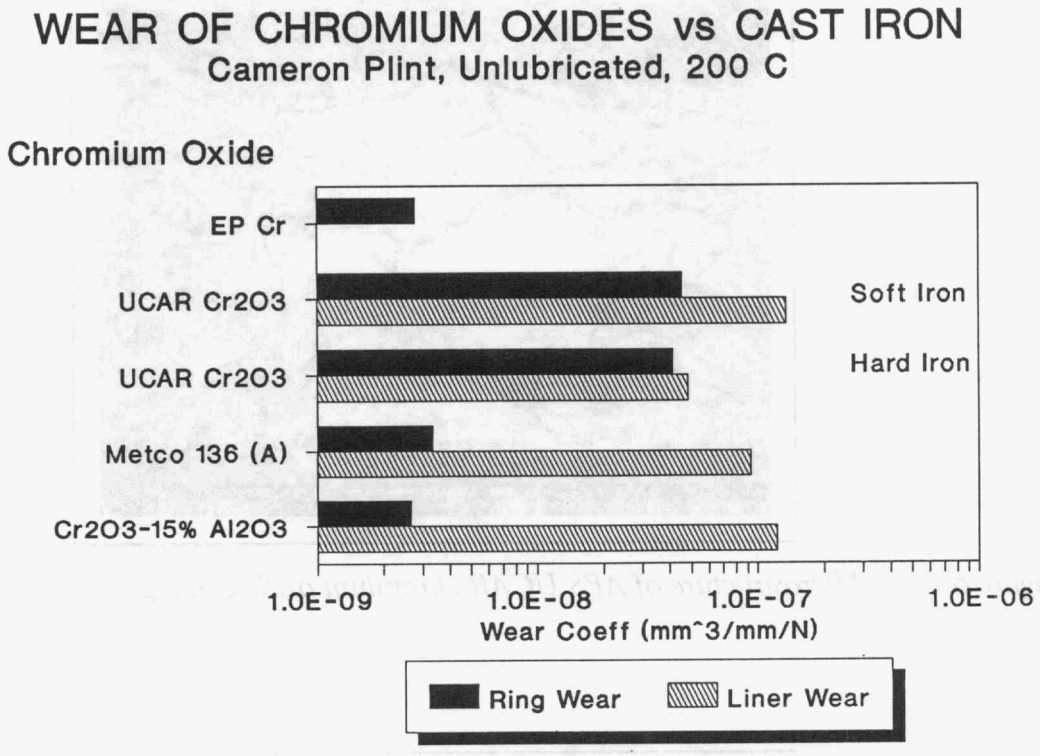

Figure 5. *Wear comparison of APS chromium oxide coatings and electroplated chromium sliding against grey iron liners at 200°C without lubrication.*

Examination of Chromium Oxide and Grey Iron Wear Surfaces

Figures 10 and 11 show SEM images of, respectively, Metco 136 (B) and pearlitic grey cast iron wear surfaces from a lubricated test at 260°C. The Cr_2O_3 surface shows a few large scratches with large areas of smooth, flat material (Figure 10). Within the flat areas, shallow flat pits suggest either a preferential polishing type of wear, or a delamination mechanism. The cast iron wear surface has been worn smooth, revealing the graphite flakes. Wear is thought to occur by a predominantly abrasive mechanism, although there is some evidence of a surface film (possibly oxide or transfer layer) on the wear scar.

Unlubricated tests resulted in a Cr_2O_3 wear surface typified by Figure 12. Large amounts of iron have transferred to the Cr_2O_3 surface to form thick, highly adherent transfer films which have clearly supported the wear contact for at least part of the time. Backscattered electron images (Figure 12) showed that the iron-containing films gave low atomic number contrast, and so were probably composed mainly of oxides. Elemental iron would have appeared much brighter than the Cr_2O_3 substrate. The Cr_2O_3 appeared macroscopically rough, but contained numerous areas with a "rounded" character, suggestive of debonding at the pre-existing "inter-splat" cracks/voids in the coating.

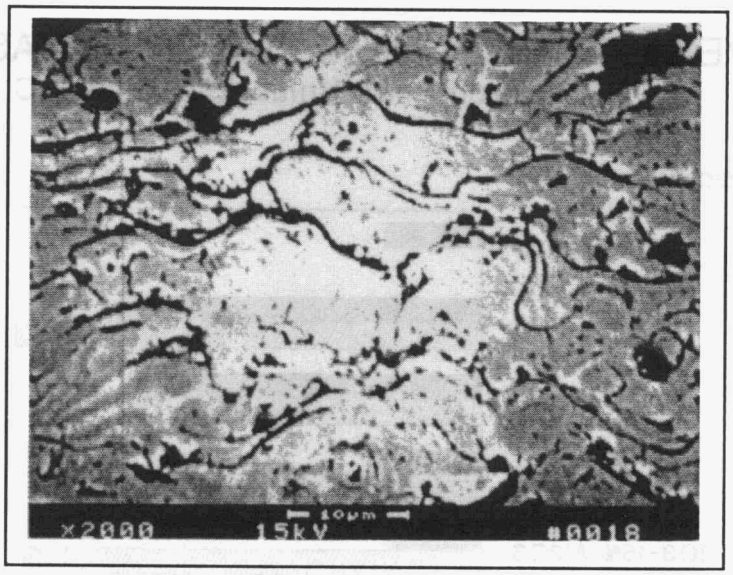

Figure 6. *Microstructure of APS UCAR chromium oxide coating.*

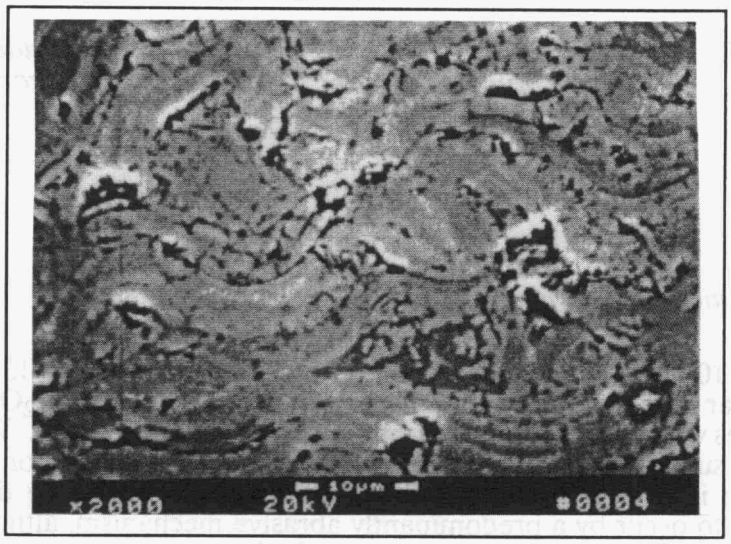

Figure 7. *Microstructure of APS Metco 136 chromium oxide coating (A).*

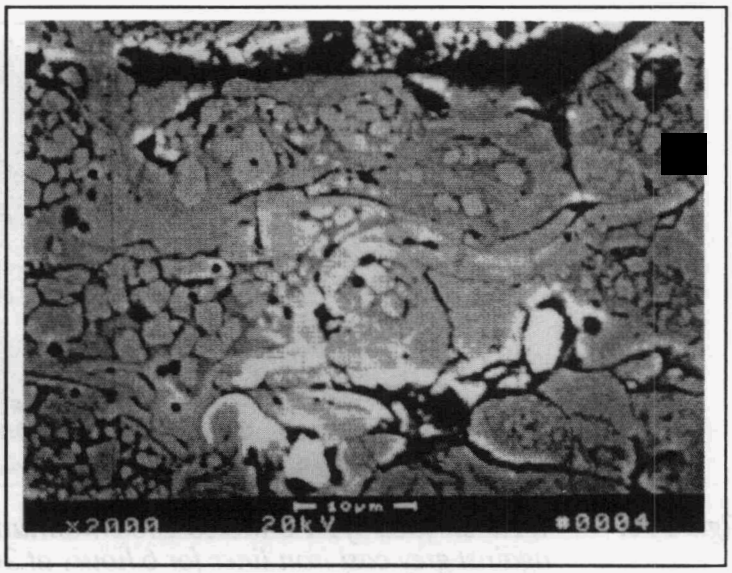

Figure 8. *Microstructure of APS Metco 136 chromium oxide coating (B).*

Figure 9. *Microstructure of APS Cr_2O_3 - 15% Al_2O_3 - 4% SiO_2 - 3% TiO_2 coating.*

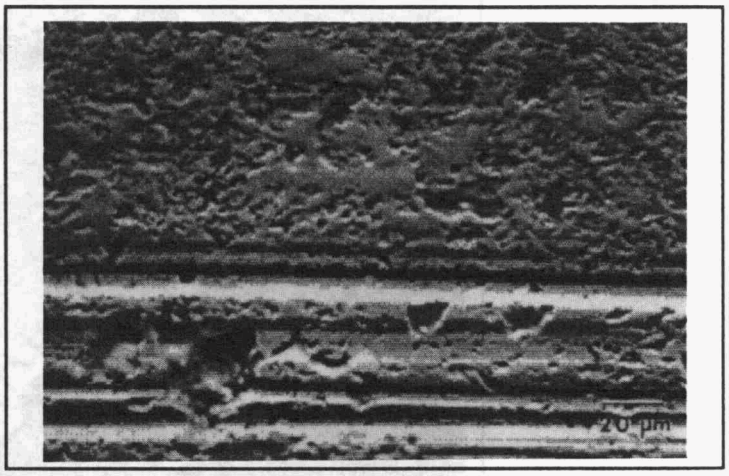

Figure 10. *Wear surface of APS Metco 136 chromium oxide (B) after sliding against grey cast iron liner for 6 hours at 260°C with fresh CE/SF 15W40 lubricant.*

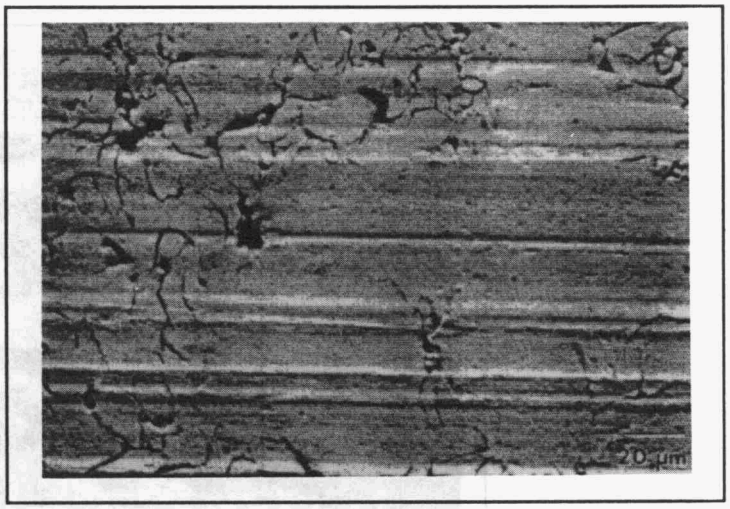

Figure 11. *Wear surface of grey cast iron liner after wear test against APS Metco 136 chromium oxide (B), 6 hrs, 260°C with fresh CE/SF 15W40 lubricant.*

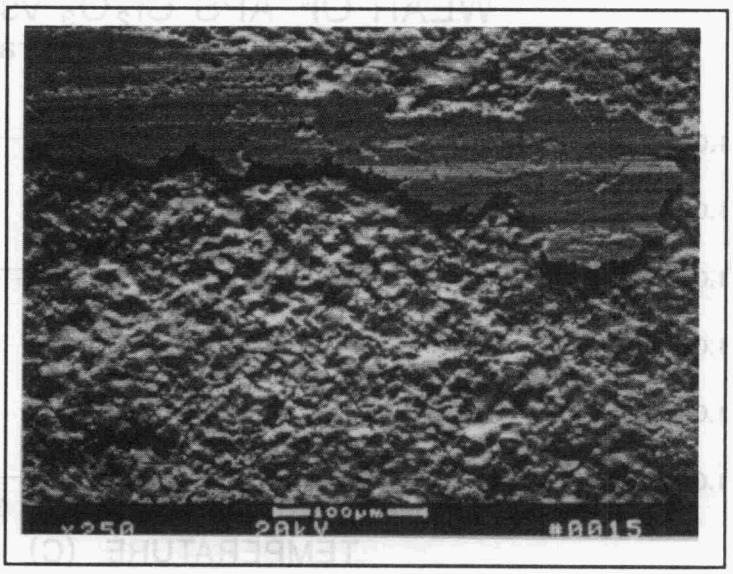

Figure 12. *Wear surface of APS Cr_2O_3 - 15% Al_2O_3 - 4% SiO_2 - 3% TiO_2 after sliding against grey cast iron liner for 20 minutes at 200°C with no lubricant.*

Wear of APS Chromium Oxide vs Slurry-Sprayed Silica-Chromia-Alumina

Lubricated wear tests were performed as a function of temperature for APS Cr_2O_3 ring coatings sliding against slurry-sprayed SiO_2 - Cr_2O_3 - Al_2O_3 (SCA) liner coatings. The results are shown in Figure 13, which is a compilation of data for the UCAR and Metco 136 (B) ring materials against the same 12 densification SCA coating. Both ring and liner coatings showed no sensitivity of wear coefficient to temperature over the range 30 - 350°C. Wear rates of the APS Cr_2O_3 and SCA coatings were identical (within experimental scatter).

Compared with the baseline EP chromium/grey iron and APS Cr_2O_3/grey iron systems with fresh oil lubrication, the Cr_2O_3/SCA system was found to give much lower liner wear, but much higher ring wear rates (Figure 14). Total wear coefficients (ring + liner) were approximately the same as for the baseline system.

Ring and liner wear rates were the same with engine-tested oil as with fresh oil for the Cr_2O_3/SCA system (Figure 15). With used oil, ring wear rates were approximately the same as for the baseline Cr/iron system, with much lower liner wear coefficients. Thus, the advantage of using a Cr_2O_3/SCA wear combination increases as the oil becomes degraded during engine operation.

Unlubricated tests with the APS Cr_2O_3/SCA combination resulted in Cr_2O_3 wear coefficients which were approximately the same as for the Cr_2O_3/grey iron system, but the SCA liner wear was much lower (Figure 16). Thus, total (ring + liner) wear for the Cr_2O_3/SCA system was much lower than for either the baseline Cr/iron or Cr_2O_3/iron wear couples. In these tests, the SCA material appeared to be more wear resistant than the Cr_2O_3 material.

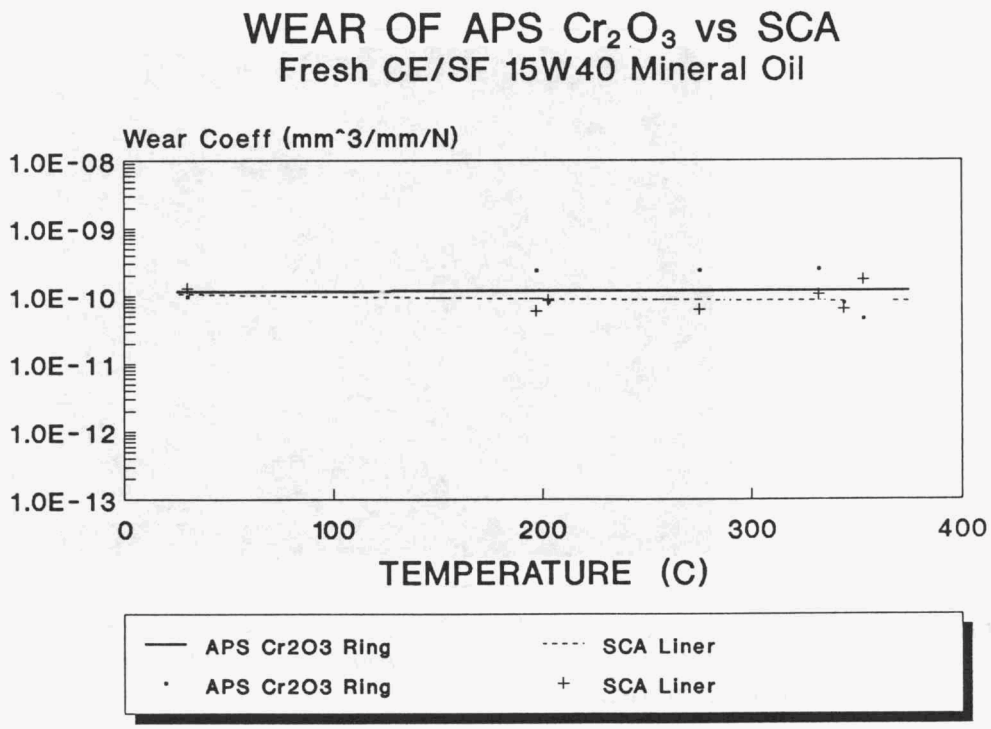

Figure 13. *Variation of wear coefficient with temperature for APS UCAR chromium oxide ring vs silica-chromia-alumina liner coatings, lubricated with fresh CE/SF 15W40 oil.*

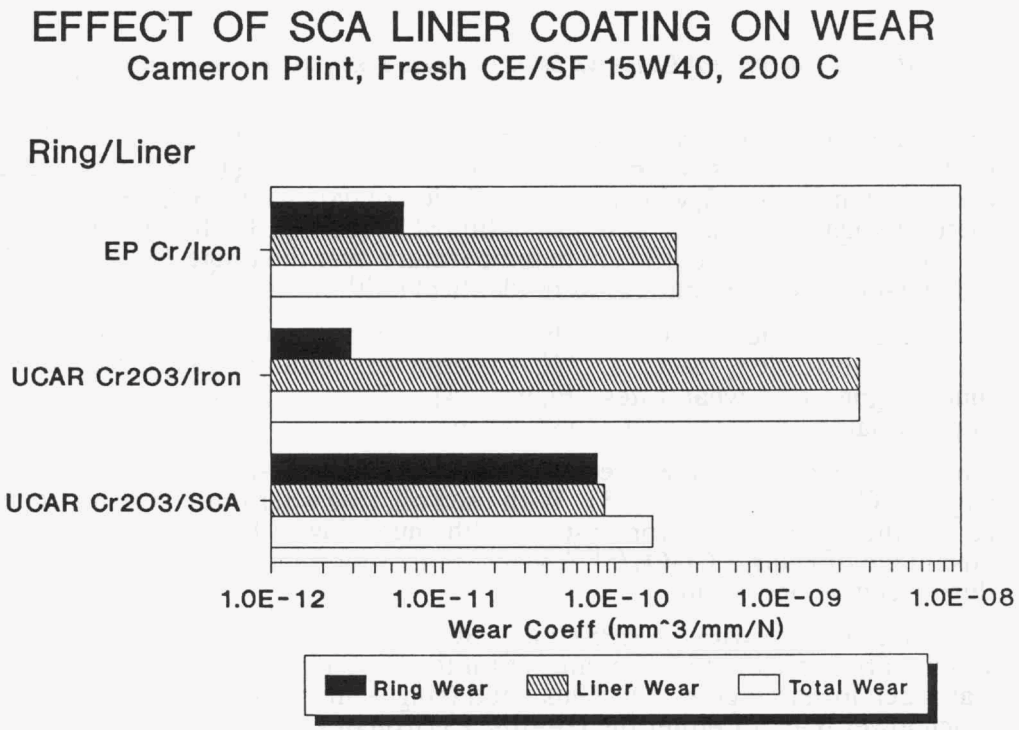

Figure 14. *Wear comparison of electroplated chromium vs grey cast iron, APS chromium oxide vs grey cast iron and APS chromium oxide vs silica-chromia-alumina ring/liner couples at 200°C in fresh CE/SF 15W40 oil.*

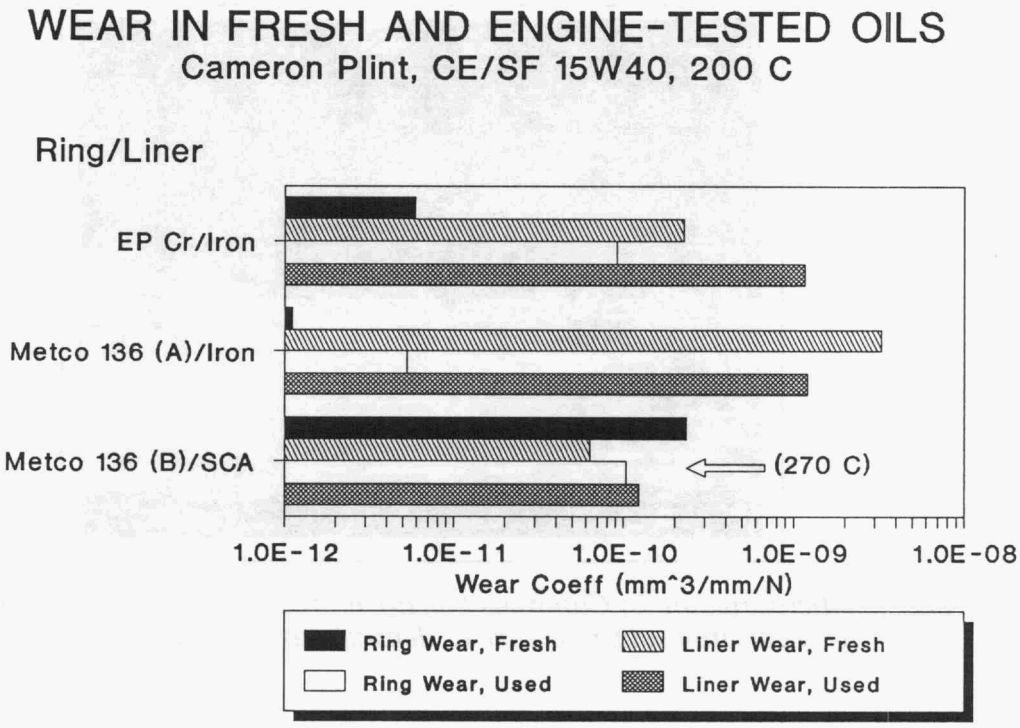

Figure 15. *Wear comparison of electroplated chromium vs grey cast iron, APS chromium oxide vs grey cast iron and APS chromium oxide vs silica-chromia-alumina ring/liner couples at 200°C in fresh and engine-tested oils.*

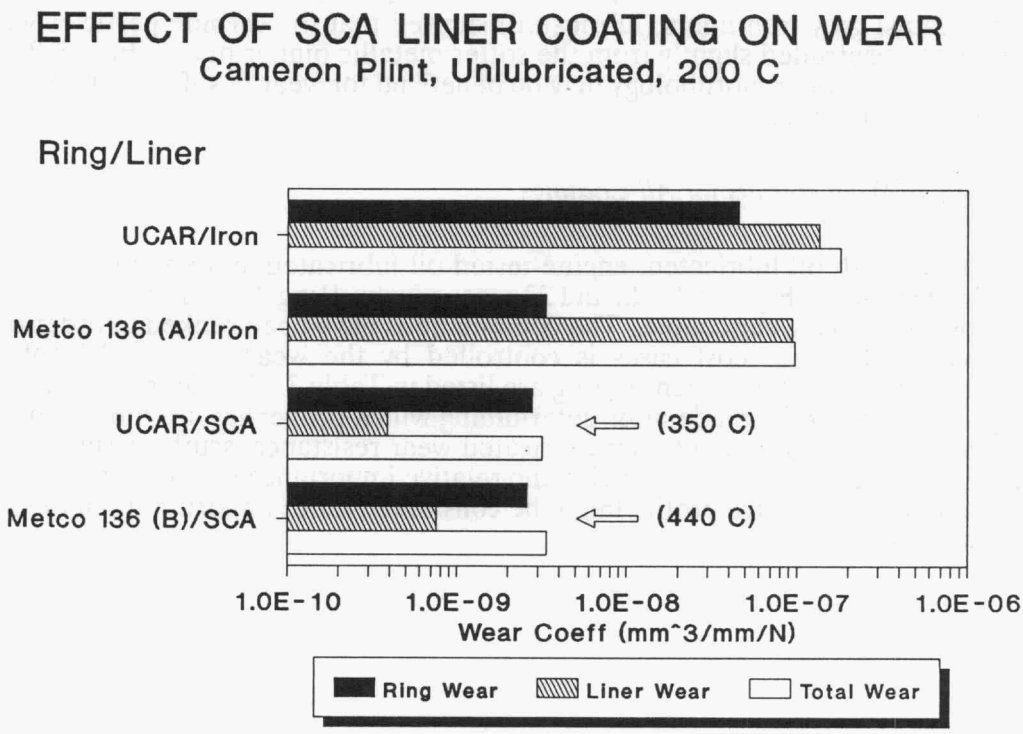

Figure 16. *Wear comparison of APS chromium oxide vs grey cast iron and APS chromium oxide vs silica-chromia-alumina ring/liner couples without lubrication.*

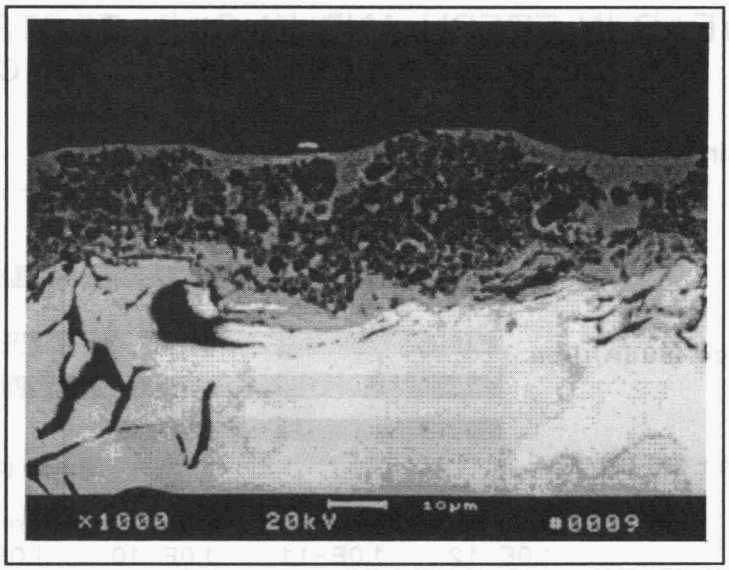

Figure 17. Microstructure of Cummins Silica-Chromia-Alumina coating on grey cast iron substrate after 12 densification cycles.

Microstructural characterization of the HV materials has been detailed in previous reports. For example, the WC-Co coating was comprised of 5 μm WC particles in a Co matrix with low levels of porosity (Figure 19). SEM micrographs of wear surfaces of the HV WC-Co tested against grey iron liners (lubricated) showed that the carbide particles were polished smooth and protruded slightly from the softer metallic binder phase (Figure 20). This type of "cobblestone" wear morphology may be beneficial for wear of softer counterface materials such as grey cast iron.

Summary of Wear Results for All Coatings

Results for fresh oil lubricated, engine-tested oil lubricated and unlubricated wear tests at 200°C are shown in Figures 21, 22 and 23 respectively. Ring, liner and total wear coefficients are shown for each wear couple. The combinations have been ranked in order of decreasing total wear, which in most cases is controlled by the wear rate of the softer material. Microhardness values for each coating are listed in Table 3. Selection of coatings for engine components should be made after determining which properties are most important for the application (e.g. high temperature lubricated wear resistance, scuff resistance, resistance to degraded oils, etc.) and after assessing the relative importance of each surface. For example, maintaining the ring face profile might be considered more important than low liner wear in some applications.

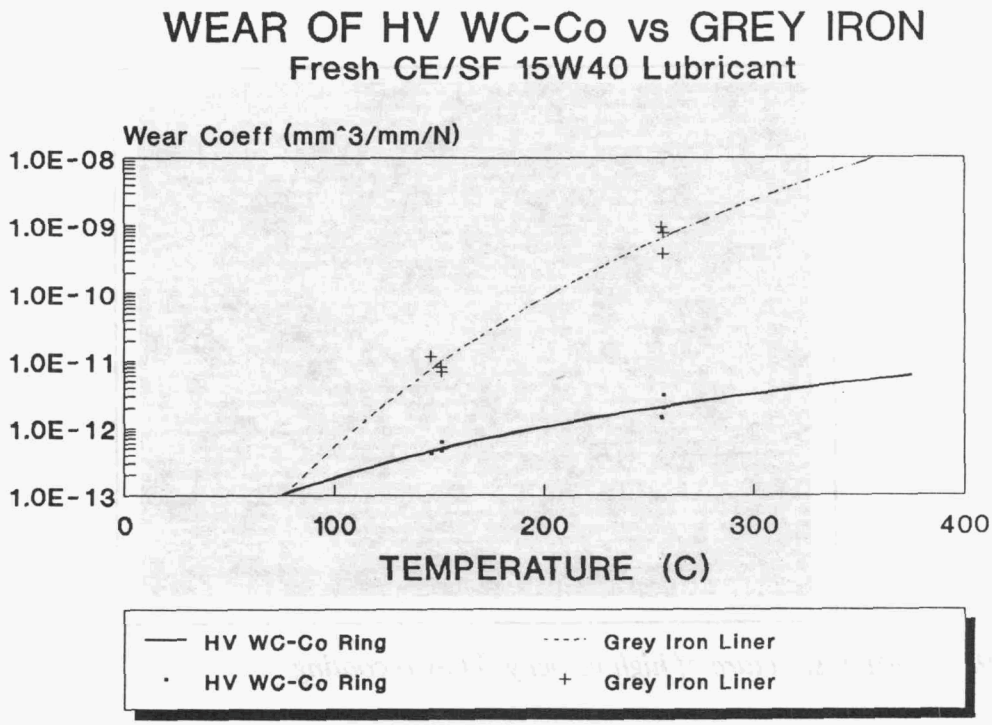

Figure 18. *Variation of wear coefficient with temperature for HV WC-Co rings vs grey cast iron liners, lubricated with fresh CE/SF 15W40 oil.*

Microstructural Evaluation of Slurry-Sprayed Silica-Chromia-Alumina Coating

Figure 17 shows an SEM micrograph of a polished section of an SCA coating densified 12 times. The phase distribution was estimated from EDS analysis to be 55 wt% Cr_2O_3, 41 wt% SiO_2 and 4 wt% Al_2O_3. The coating thickness was approximately 25 μm. The material is fine-grained (up to 5 μm grain size) and almost fully dense. A thin "skin" of pure Cr_2O_3 has formed at the surface of the coating.

High Velocity Thermal Spray Coatings

Two high velocity coatings have been evaluated to date: an 88% WC - 12% Co material and a WC-Cr_3C_2-NiCrCo material (both sprayed using a "Jetkote II" system). The variation of wear coefficient with temperature for the WC-Co material sliding against a pearlitic iron liner is shown in Figure 18. In contrast to the Cr_2O_3/iron and Cr_2O_3/SCA systems, ring and liner wear rates were a strong function of temperature. At 150°C, extremely low wear coefficients were obtained for both ring and liner materials, but at 250°C, liner wear rates were the same as for the baseline Cr/grey iron system. At the higher test temperature, the coating was found to have fractured during the test, and it is speculated that the sharp edges generated by this cracking caused the high liner wear rates observed. The variation of wear rate with temperature for the WC-Cr_3C_2-NiCrCo/grey iron combination was similar to the WC-Co/grey iron results, with somewhat higher coating wear. This coating was also found to crack at the higher test temperatures.

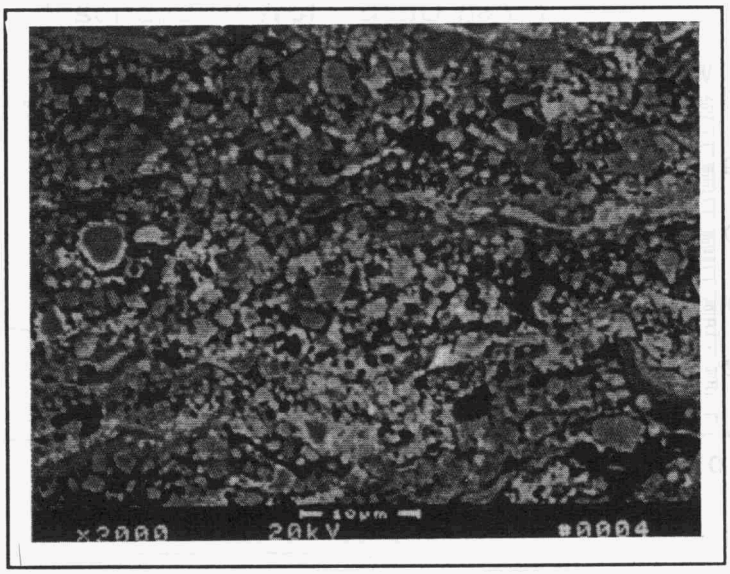

Figure 19. Microstructure of high velocity WC-Co coating.

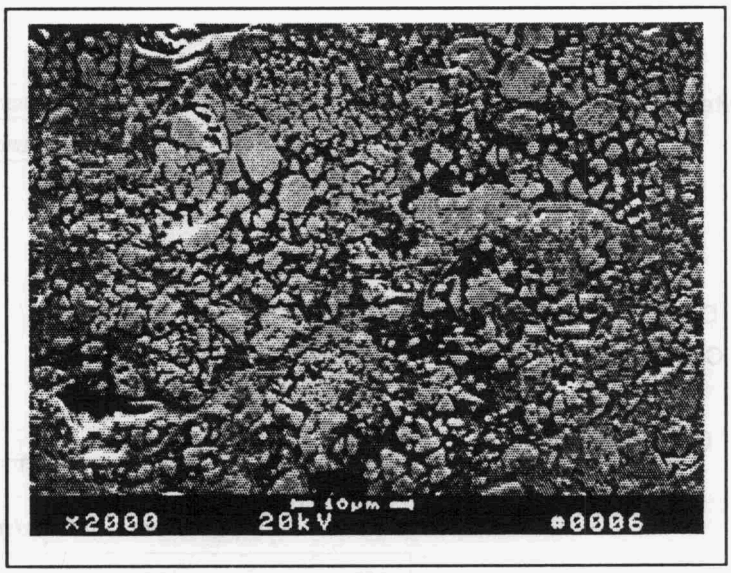

Figure 20. *Wear surface of HV WC-Co after sliding against grey cast iron liner for 6 hours at 150°C with fresh CE/SF 15W40 lubricant.*

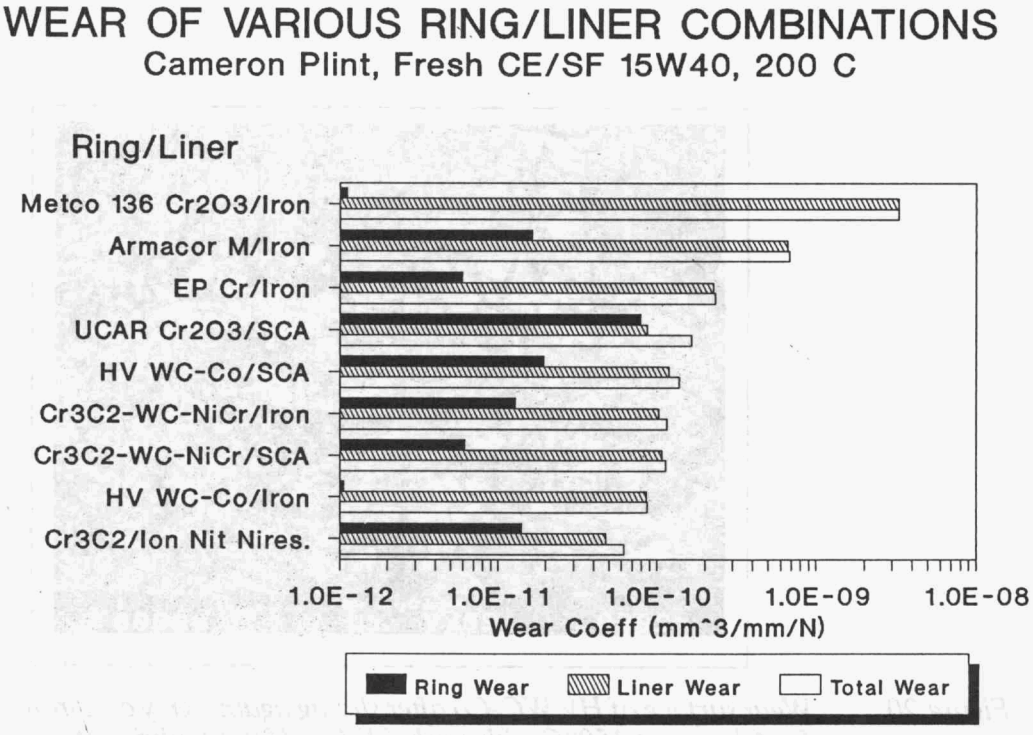

Figure 21. *Wear comparison of various ring/liner combinations at 200°C in fresh CE/SF 15W40 oil.*

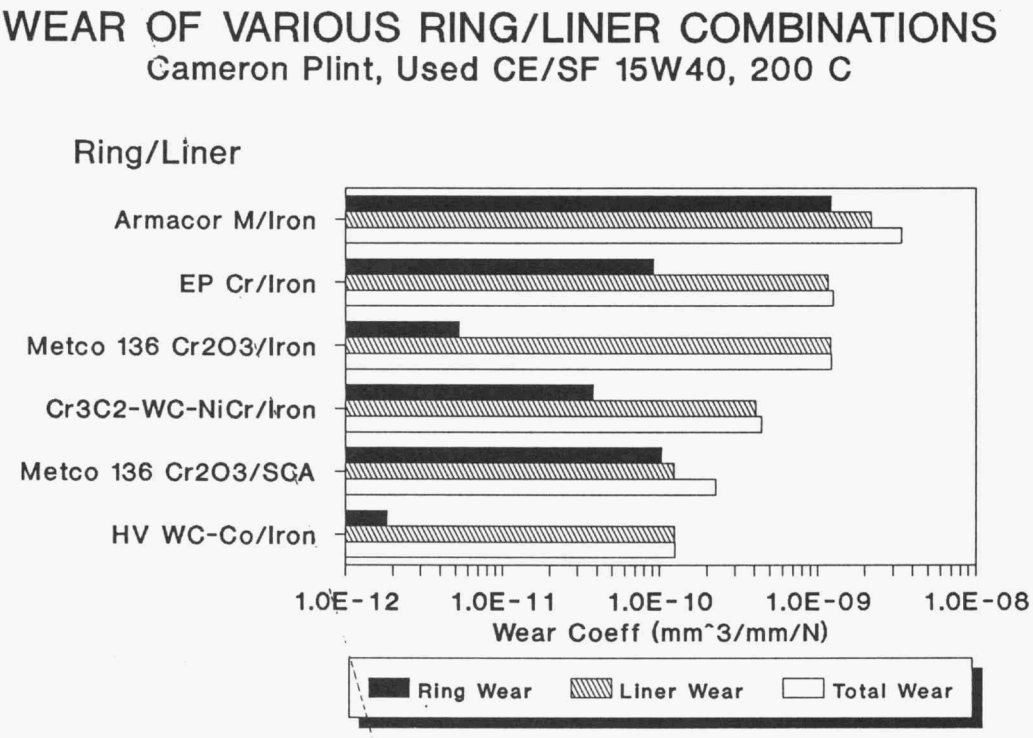

Figure 22. *Wear comparison of various ring/liner combinations at 200°C in fresh and engine-tested CE/SF 15W40 oils.*

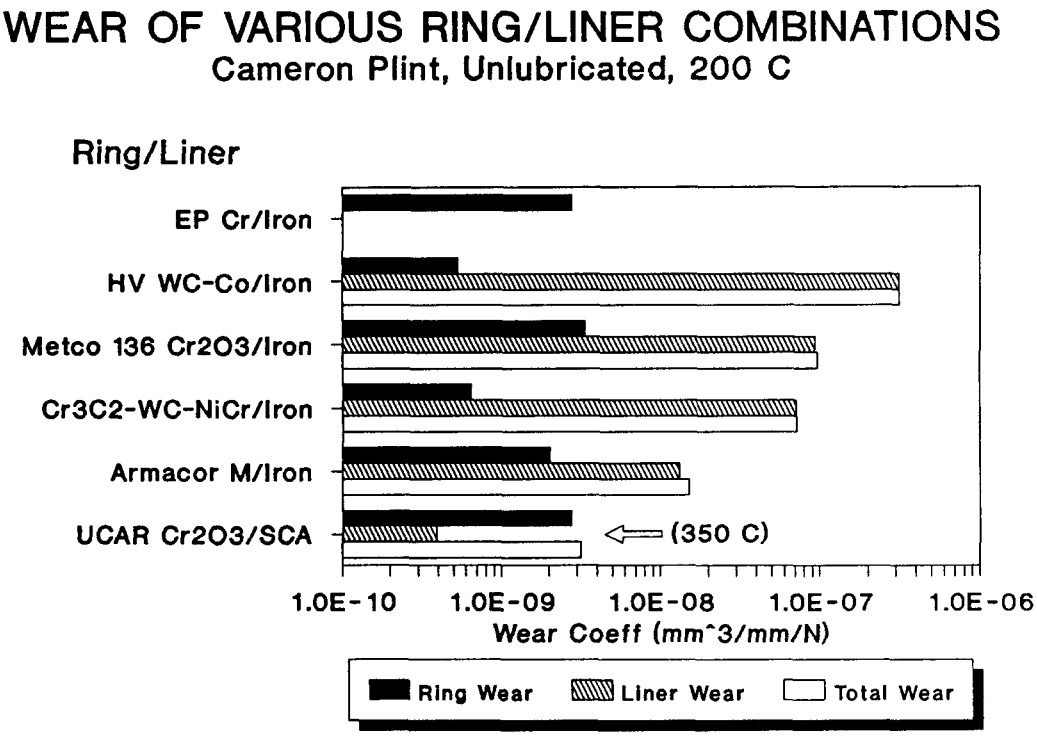

Figure 23. *Wear comparison of various ring/liner combinations at 200°C without lubrication.*

Coating	*Knoop Hardness at 100 gf load (kgfmm^{-2})*
APS UCAR Cr_2O_3	830
APS Metco 136 Cr_2O_3 (A)	960
APS Metco 136 Cr_2O_3 (B)	1010
APS Cr_2O_3 - 15% Al_2O_3	1260
Cummins SCA (8 densifications)	960
Cummins SCA (12 densifications)	960
Cummins SCA (16 densifications)	1030
HV WC - 12% Co	1120
HV Cr_3C_2 - WC - NiCrCo	1000
APS Armacor M	760

Table 3. *Microhardness of coatings.*

Status of Milestones

Task 1 Experimental Plan and Coating Deposition
Task 2 Characterization
Task 3 Selection of Coating
Task 4 Fabricate Components
Task 5 Reporting
Task 6 Quality Assurance

Tasks 1 (duration 18 months) and 2 (duration 16 months) are in progress. A no-cost extension of the contract has been requested to continue testing through August 30, 1990.

Publications

None

1.4 JOINING

1.4.1 Ceramic-Metal Joints

Joining of Ceramics for Heat Engine Applications
M. L. Santella (Oak Ridge National Laboratory)

Objective/scope

The objective of this task is to develop strong reliable joints containing ceramic components for applications in advanced heat engines. Presently, this work is focused on the joining of partially stabilized zirconia and silicon nitride by brazing. The technique of vapor coating ceramics to circumvent wetting problems that was developed for brazing zirconia at low temperatures will also be applied to brazing silicon nitride. The emphasis of this activity during FY 1989 will be on: (1) completing the initial assessment of zirconia joint strength, (2) high-temperature brazing of titanium-vapor-coated silicon nitride, (3) correlating braze joint microstructures with strength data to identify factors controlling joint strength, and (4) developing a method of calibrating the indentation fracture technique to determine the accuracy of residual stresses measurements in ceramic-to-metal joints.

Technical progress

ZrO_2 joints. Initial room-temperature flexure testing of ZrO_2-Fe braze joints suggested that there were two distributions for the joint strength data. This aspect of the joint strength data was studied more closely by additional testing. Ten ZrO_2-Fe joints were made and prepared into test bars for flexure testing. In three of these joints, the ZrO_2 joint surfaces were lapped to a 1-μm diamond finish. Lapping was done in an attempt to remove machining damage due to surface grinding that may have contributed to low joint strengths.

Initial and subsequent room-temperature flexure test data for ZrO_2-Fe braze joints were combined and plotted using the Weibull distribution function in Fig. 1. A linear regression was used to fit straight lines through the data. Additional testing confirmed that the joint strength data can be described by two statistical distributions. In the higher range, joint strength varied between 300 to 400 MPa with a Weibull modulus of 6.9, while in the lower range, joint strength varied from 25 to 300 MPa with a Weibull modulus of 1.0. The test results from twelve flexure bars taken from coupons in which the ZrO_2 joint surfaces were ground and lapped before being coated with titanium are shown as filled symbols in Fig. 1. Lapping the ZrO_2 joint surfaces had no apparent influence on joint strength compared with using as-ground joint surfaces. Metallographic examination of selected test bars and further analysis of the strength data is planned.

Si_3N_4 joints. The effects of joint surface finish is also being investigated for Ti-vapor-coated Si_3N_4 joints made with Au-25Ni-25Pd wt% braze filler metal. Nine joints were prepared for subsequent flexure testing. Joint surface finishes were as-ground, 30-μm diamond prepared by lapping, and 1-μm diamond polished. Initial testing will be done at room temperature.

Residual stress measurements. A portable hardness indenter was developed and integrated onto a tensile load frame. This arrangement permitted a tensile test specimen to be loaded axially and simultaneously probed with the hardness indenter. The size of the tensile test bars was nominally 6 × 6 × 150 mm. The material selected for the initial experiments was NC132, a silicon nitride from Norton Company. This material was selected because of its good availability and price and because it has been the subject of other studies of indentation fracture. The initial set of experiments involved making a series of Vickers indentations on the NC132 using a standard hardness testing machine and

comparing these results with indentations made at the same indenter loads on the tensile frame but without any axial loading. Generally, four or more indentations were made at each test condition. The indentation load was varied from 1 to 13 kg. The indentations and their associated cracks were measured on an optical microscope at 400× using a digital micrometer. These data were used to determine the hardness and to calculate an indentation fracture parameter $P/c^{1.5}$, where P is the indentation load and c is the indentation crack length. The variations of hardness and $P/c^{1.5}$ with indentation load are shown, respectively, in Figs. 2 and 3. Figure 2 shows that the hardness values generally decreased slightly with increasing indentation load and were about the same for testing done on the hardness machine and on the tensile frame. The average hardness values were in the range of 16 to 17 GPa, which agrees favorably with values reported elsewhere. Figure 3 shows that the indentation fracture parameter $P/c^{1.5}$ was basically invariant with indentation load and about the same for either testing configuration. Having $P/c^{1.5}$ be constant establishes that the toughness of this material can be described as $K_c = \chi P/c^{1.5}$ and implies that the data can be further analyzed as described in published literature on the indentation fracture of brittle materials. The actual $P/c^{1.5}$ values also compare favorably with published values for NC132. These experiments indicated that the tensile test frame/hardness testing facility can produce reliable data for unstressed material and that our techniques for analyzing such data are acceptable.

Tensile bars of NC132 silicon nitride were also loaded to stress levels up to 86.6 MPa and simultaneously subjected to Vickers hardness indentation at indentor loads up to 10 kg. At least four indentations were made at each combination of applied stress and indentor load. The indentor was oriented to produce cracks parallel and perpendicular to the axes of the tensile bars. According to indentation fracture mechanics, cracks perpendicular to the tensile axis of the bars should extend further from the Vickers indentation than cracks in unstressed material and the increased crack extension is related directly to the level of applied stress.

The results for residual stresses calculated from the indentation cracks at applied stresses of 49.4 MPa and 86.6 MPa are shown in Fig. 4. The dashed lines in these figures represent the applied stress level. Several important features of the data shown in Fig. 4 are apparent. There is a considerable amount of scatter in the data that was due to scatter in the indentation crack lengths. The calculated residual stress values appear to converge to a constant value at the higher indentor loads, but generally are an underestimate of the actual stress levels experienced by the specimens. The values of the calculated residual stresses depend directly on K_c, which was not determined experimentally and could be a source of some error. Further analysis of this data and refinements to the experimental technique are continuing. This work is being done in collaboration with K. C. Liu and K. Wu. Dr. Wu is an assistant professor of mechanical engineering at Florida International University in Miami and has been visiting ORNL this summer on the Oak Ridge Associated Universities Summer Faculty Research Program.

Status of milestones

On schedule.

Publications

The paper entitled, "Strength and Microstructure of Titanium-Vapor-Coated Silicon Nitride Braze Joints," was published in *Ceramic Materials and Components for Engines, Proceedings of the Third International Symposium.*

Unpublished work

The paper entitled, "Brazing of Titanium-Vapor-Coated Zirconia," was submitted for publication in the *Journal of the American Ceramic Society.*

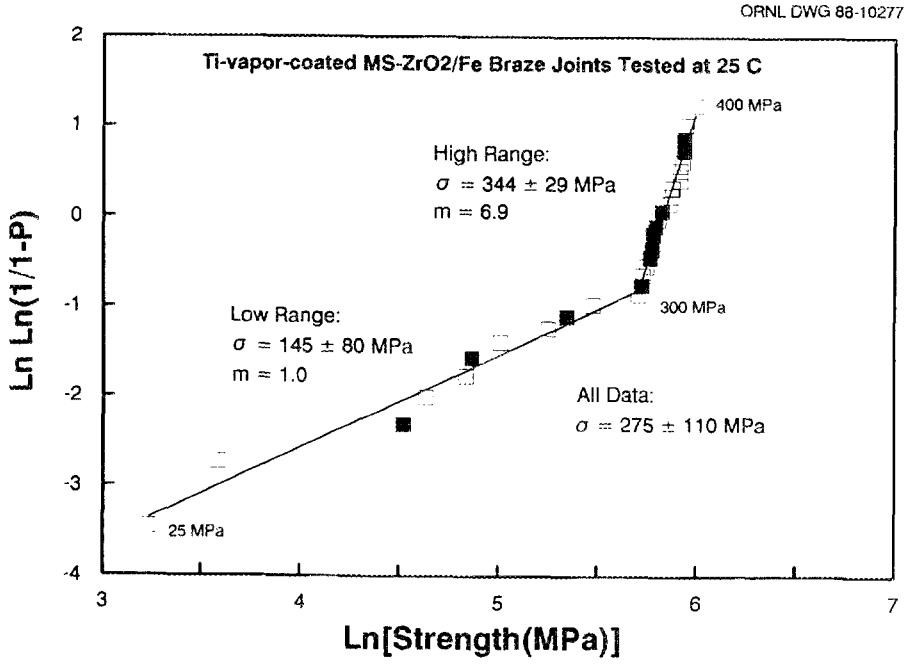

Fig. 1. Weibull distribution plot of strength data from ZrO_2-Fe braze joints tested at room temperature. Open symbols represent specimens with an as-ground finish on the joint surface. Filled symbols indicate a 1-μm finish on the joint surface.

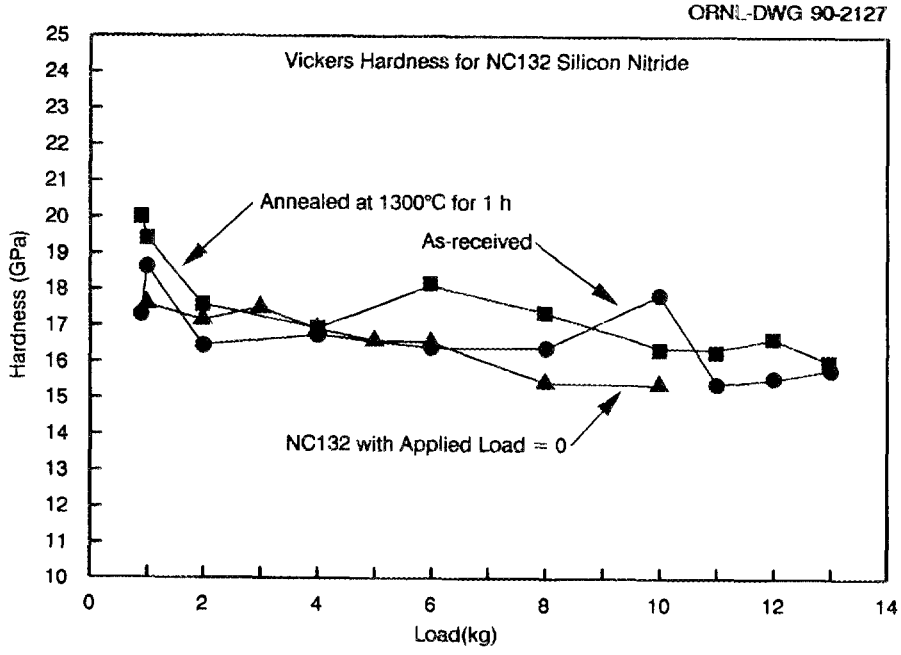

Fig. 2. Vickers hardness vs indentation load for NC132 Si_3N_4.

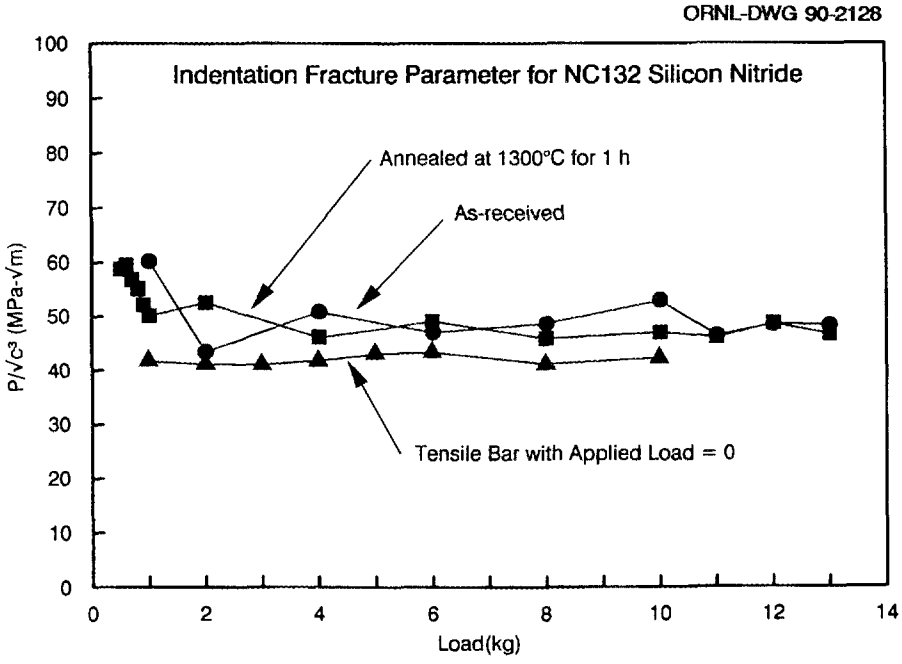

Fig. 3. Indentation fracture parameter $P/c^{1.5}$ vs load for NC132 Si_3N_4.

ORNL-DWG 90-2129

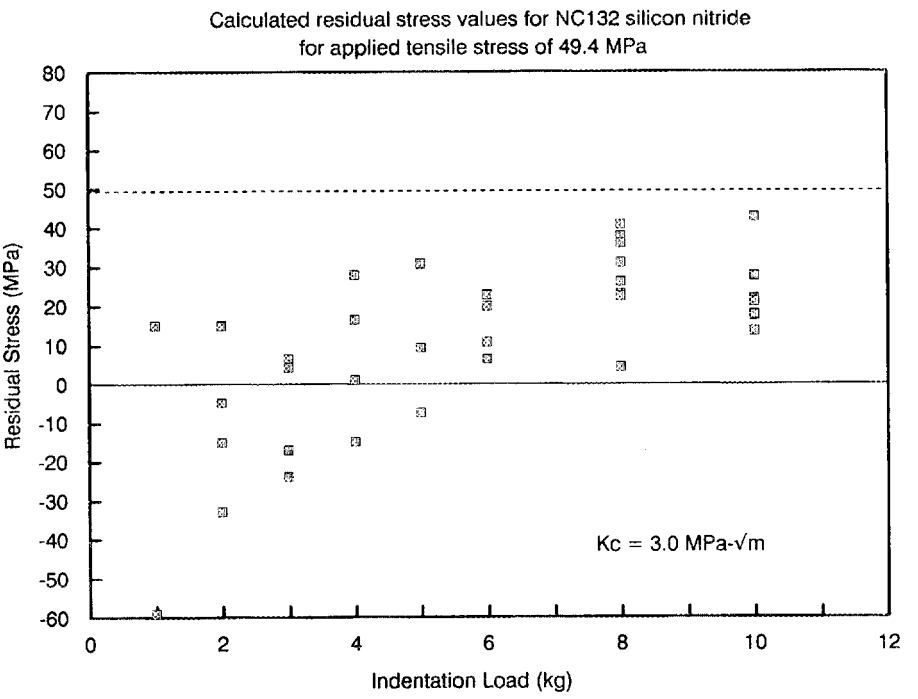

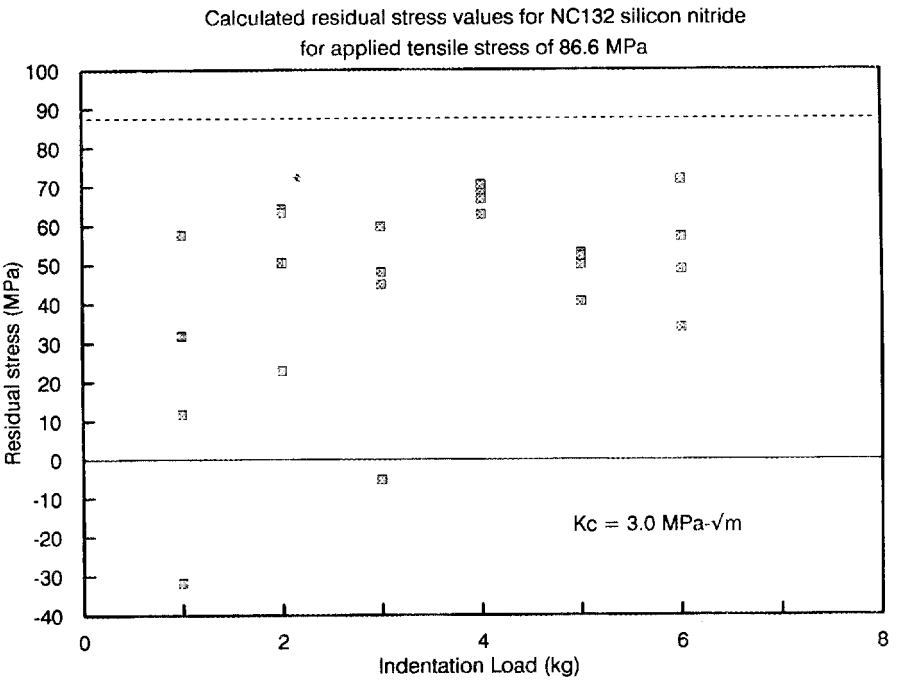

Fig. 4. Variation of calculated residual stresses with applied stress and indentation load for NC132 silicon nitride.

Analytical and Experimental Evaluation of Joining Silicon Nitride to Metal and Silicon Carbide to Metal for Advanced Heat Engines Application

S. Kang, H. Kim, J. H. Selverian (GTE Laboratories, Inc.)

Objective/Scope

The goal of this work is to demonstrate analytical tools for use in designing ceramic-to-metal joints, including the strain response of joints as a function of the mechanical and physical properties of the ceramic and metal, the materials used in producing the joint, the geometry of the joint, externally imposed stresses both of a mechanical and thermal nature, temperature, and the effects of joints exposed for long times at high temperatures in an oxidizing (heat engine) atmosphere. The maximum temperature of interest for application of silicon carbide to metal and silicon nitride to metal-containing joints is 950°C. The initial joint-fabrication work shall include "experimental" joints whose interfacial area is not less than two square centimeters. The work shall also include demonstration of the potential for scale-up of the joint size to interfacial areas of commercial significance, applicability of the analytical joint modeling tools, and the ability to use these tools to design and predict the mechanical and thermal behavior of larger joints. These joints, referred to as "scale-up" joints, shall have an interfacial area of at least twenty square centimeters.

Technical Highlights

The stress state of an interface void in a brazed joint has been evaluated. For an applied shear load, one crack tip experiences tensile loading and the other crack tip experiences compressive loading. The size of the shear yielded zone at each crack tip was calculated. The shear yield zone size increased dramatically as the applied shear stress approached approximately 75 % of the shear yield stress of the braze material.

The β and γ failure criteria were further refined based on a derivation using Dundur's parameter and J integrals.

Torsion tests were performed with Incoloy 909, Inconel 718, and PY6 at 650°C. PY6 is hot isostatic pressed and sintered Si_3N_4 with 6 Y_2O_3 and 2 Al_2O_3 added as sintering aids. PY6 was unaffected by the 650°C test temperature. Incoloy 909 and Inconel 718 both showed a 20 - 25 % drop in shear yield stress but no change in the rotational yield angle.

The thermal cycle tests of the 650 and 950°C Si_3N_4 systems are underway.

Brazed coupon samples were tested to increase the statistical base for the selection of the materials system. Task 2 samples were brazed. Cracks were found in the molybdenum interlayer ring and were evaluated metallographically.

A total of 53 cylindrical Task 2 specimens have been brazed. The information from this test series finalized the materials selection and provided an initial group of specimens needed for thermal fatigue tests.

Molybdenum will be used instead of nickel interlayers in joints with SiC and 30Au-34Pd-36Ni (Palniro 4), due to the severity of the reaction between nickel and SiC. Au-5Pd-2Ni braze with a Mo interlayer will be used with silicon nitride and Inconel 718 for the 950°C application. All compositions are in wt %.

The reaction at the braze-ceramic interface was determined by transmission electron microscopy (TEM) in Au-18Ni braze/Ti-coated SNW1000 and Au-18Ni braze/Ti-coated SiC brazed joints. SNW1000 is sintered Si_3N_4 with 4 wt % Y_2O_3 added as a sintering aid. TiN was formed at the interface in the Au-18Ni braze/Ti-coated SNW1000 joint and TiC was formed at the interface in the Au-18Ni braze/Ti-coated SiC brazed joint.

A study of the reactions between several braze alloys and the interlayer and structural alloy materials was initiated.

Design Criteria/Stress Analysis

Finite element analysis (FEA) of the braze joint assembly continues to be an integral part of our design effort. Figure 1a is a plot of the solid model and finite element mesh showing ceramic, metal, interlayer, and braze components. In each case, axisymmetric elements are used to model the process of cooling the brazed assemble to room temperature ($\Delta T \cong 1200°C$). Figure 1b shows the braze joint shape after cooling which has been superimposed on the finite element mesh of the original geometry. The metal component distorts a great deal to accommodate the stiffer ceramic component. We are utilizing FEM to asses alternate joint designs and materials.

Joint Defects

The effects of defects in the brazed joint was examined by a combination of analytical means and finite element analysis. The model for the defects was taken to be a region of unbonded area, a shrinkage crack or any other type of void present at the ceramic/metal interface. The braze was treated as an elastic perfect plastic material. The geometry of an interface void can be reduced to the analysis of simple shear, Figure 2. Analysis of the geometry in Figure 2 indicates that, at point A, the shear stress is bounded while the normal stress is unbounded.

To avoid the singularity at point A the geometry of an interface void was approximated by that shown in Figure 3. The normal stress is allowed to have a singularity at the crack tips (x = -a and b) and the shear stress is bounded at the interface. In the shear yield zones (-L,a) and (b,L) the shear stress is equal to the shear yield stress of the braze material. The boundary conditions describing this geometry are:

At the far field (x >> L):

$$\sigma_{xy} = \tau^{\infty}, \qquad \sigma_{xx} = \sigma_{yy} = 0$$

At the interface:

$$\begin{array}{lll} [\sigma \cdot n] = 0, & [u] = 0, & |x| > L \\ \sigma_{xy} = \tau_y, & [u_y]=0, & -L < x < -a \ \& \ b < x < L \\ \sigma \cdot n = 0, & [u_y] \geq 0, & -a < x < b \end{array}$$

In the shear yield zone:

$$\sigma_{xy} = \tau_y \qquad \text{for} \qquad u_x^+ - u_x^- > 0$$

$$\sigma_{xy} = -\tau_y \qquad \text{for} \qquad u_x^+ - u_x^- < 0$$

$$\sigma_{xy} < \tau_y, \ |x| > L$$

where τ_y is the shear yield stress of the interlayer material and u is the displacement. To satisfy the boundary conditions at the interface, Cauchy type singular integral equations were used. The material properties enter the analysis through the Cauchy equations through a set of two Dundur's parameters, α and β:

$$\alpha = \frac{G_1(1-\nu_2) - G_2(1-\nu_1)}{G_1(1-\nu_2) + G_2(1-\nu_1)}$$

$$\beta = \frac{1}{2}\frac{G_1(1-2\nu_2) - G_2(1-2\nu_1)}{G_1(1-\nu_2) + G_2(1-\nu_1)}$$

where G_1, G_2, ν_1, and ν_2 are materials parameters.

The size and nature of the shear yield zones was calculated for a joint between Incoloy 909 and PY6, $\alpha = 0.3007695$ and $\beta = 0.0999077$. The size of the shear yield zones are linear with applied shear stress until the applied shear stress approaches 90 % of the shear yield stress of the braze, Figure 4. At this point the size of the shear yield zone increases rapidly, reflecting the perfect

plastic behavior of the braze material and the onset of incipient failure. The mode I stress intensity factors at the crack tips, as a function of applied shear stress, are shown in Figure 5. A compressive state of stress exists at one of the crack tips while a tensile state of stress exists at the other crack tip. Note that that for $\beta = 0.0999077$ and $\tau^{\infty}/\tau_y > 0.45$ both stress intensity factors are positive.

Beta and Gamma Criteria

The β and γ analytical criteria were refined based on the derivation given below. Subscripts 1 and 2 refer to a metal and ceramic, respectively, brazed pair with an arbitrary shape or radius of curvature, r.

If the braze does not flow plastically, the stress concentration near the critical area is approximately represented by:

$$\tau = \frac{2\mu_1\mu_2}{(\mu_1+\mu_2)}(\alpha_1-\alpha_2)\,\Delta T\,\frac{L}{r}f(\beta^*)$$

where $f(\beta^*) = 1$; and so

$$\tau = \frac{2\mu_1\mu_2}{(\mu_1+\mu_2)}(\alpha_1-\alpha_2)\,\Delta T\,\frac{L}{r}$$

where τ is the principal shear stress, μ is the shear modulus, and β^* is a Dundur's parameter. Therefore, as $r \rightarrow o$, the stress concentration increases rapidly. This may cause the initiation of crack growth in the ceramic part.

If we introduce a braze layer that has a flow shear stress, τ_o, then the J-integral around the stress concentration area is expressed as

$$J = \tau_o\, L\, (\alpha_1-\alpha_2)\,\Delta T\, g(\alpha^*,\beta^*, \text{geometry}),$$

where α^*, β^* are dimensionless Dundur's parameters and g is a function bounded by unity.

As treated in nonlinear fracture mechanics, J can be regarded as a measure of the magnitude of the stress concentration. Therefore, the design strategy is to design a joint where J is as small as possible. This means τ_o, L, $(\alpha_1-\alpha_2)$, ΔT have to be small.

$$\frac{K_{IC}^2\,(1-\nu^2)}{EJ} > 1$$

where K_{IC} is the ceramic fracture toughness, ν is the ceramic Poisson's ratio and E is the ceramic Young's modulus.

$$\frac{K_{IC}^2\,(1-\nu^2)}{E\,\tau_o\,L\,(\alpha_1-\alpha_2)\,\Delta T\,g(\cdots)} > 1, \text{or}$$

$$\frac{K_{IC}^2\,(1-\nu^2)}{E\,\tau_o\,L\,(\alpha_1-\alpha_2)\,\Delta T} > g(\alpha^*, \beta^*, \text{geometry})$$

$$\text{for } L(\alpha_1-\alpha_2)\Delta T \le \gamma_f\, t$$

where t is the braze thickness and γ_f is the braze failure shear strain.

In general, we have to satisfy:

$$\frac{K_{IC}^2 (1-\nu^2)}{E\ \tau_o\ L\ (\alpha_1-\alpha_2)\ \Delta T} > \frac{K_{IC}^2 (1-\nu^2)}{E\ \tau_o\ \gamma_f\ t} > g(\alpha^*, \beta^*, \text{geometry})$$

where the first inequality is the modified β criterion and the second inequality is the modified γ criterion.

Based on the modified β criteria, in order to have a large effective torque transmitting area:

1) γ_f and t should be large.

2) E, τ_o should be small.

3) K_{IC} should be large.

4) $g(\alpha^*,\beta^*$, geometry) should be as small as possible.

Major geometry variables are t/L, curvature (r), and shape factors, g(···). We have designed the joint, using FEM, to minimize g(···).

Materials System Development

Task 2 : Sample Brazing

A total of 53 Task 2 cylindrical samples have been brazed to date. With these samples, it was possible to simultaneously observe the interactions between the braze, structural alloy, interlayer, and ceramic. This combination of materials, together with the vertical cylindrical geometry of the samples resulted in more extensive interactions between the braze, structural alloy, and interlayer materials than was seen with the horizontally oriented coupon samples.

A number of general conclusions can be made from an examination of the Task 2 brazed joints. The Mo interlayer was cracked in all of the brazed joints with a Mo interlayer. For example, the Mo interlayer in the Incoloy 909-(30Au-34Pd-36Ni)-Mo-PY6(Ti) brazed joint was cracked and porosity was evident in the braze, Figure 6. Cracks from the Mo interlayer had propagated into the ceramic member in the Inconel 718-(Au-5Pd-2Ni)-Mo-PY6(Ti) brazed joint.

The Ni interlayer was uncracked after the brazing cycle in all of the joints made to date, Figure 7. However, in Incoloy 909-(30Au-34Pd-36Ni)-Ni-SiC(Ti) joints, a very strong reaction was seen between the Ni and the SiC. A two phase mixture of nickel-silicide and graphite was formed. Based on the severity of this reaction, nickel interlayers should not be used with SiC when the braze alloy dissolves a large amount of nickel from the interlayer.

Palniro 4 (30Au-34Pd-36Ni) was unable to consistently bond to silicon nitride. Therefore, 30Au-34Pd-36Ni was replaced with Au-5Pd-2Ni for the 950°C silicon nitride application.

The Au-5Pd-2Ni braze alloy has been successfully used to join the Incoloy 909-Ni-PY6(Ti) system. However, a Mo interlayer was recommended to join PY6-Inconel 718 for the 950°C application. Mo was chosen over Ni for the interlayer material at 950°C, even though the Mo

interlayer exhibited radial cracks after brazing. A strong reaction between the Ni interlayer and the Au-5Pd-2Ni braze precluded using a Ni interlayer in the 950°C joint. This reaction is explained below.

In the brazing process, suppression of the braze melting point, due to alloying with elements of surrounding joint components, has a significant effect on overall brazing performance. Suppression of the melting point will prolong the solidification time of the braze, further accelerating alloying. This effect was demonstrated with the Inconel 718-Ni-PY6(Ti) system. Brazing was performed at 1180°C for 3-4 minutes in vacuum. This joint system resulted in excessive liquid phase formation, resulting in very poor bonding. Differential Thermal Analysis (DTA) of the braze alloyed with the Ni interlayer and with the Inconel 718 showed that the melting point had changed from 1140°C to 997°C (liquidus). X-ray fluorescence confirmed that the composition of the braze changed from 2% Ni to 26 % Ni.

The Incoloy 909-Ni-PY6(Ti) system gave reasonable joints with the Au-5Pd-2Ni braze, in contrast with the Inconel 718-Ni-PY6(Ti) system above. This is probably due to the difference in the Ni contents of Incoloy 909 (41%Fe-38% Ni-13% Co-4.7% Nb) and Inconel 718 (55% Ni-16% Fe-20 % Cr-5% Nb). Fe, Cr and Mo tend to increase the melting point of Au-based braze while Ni suppresses the melting point. Consequently, a Mo interlayer was chosen for the Inconel 718-(Au-5Pd-2Ni)-PY6(Ti) system at 950°C.

The final selections of the material systems based on the above, and on issues reported previously, are summarized in Table 2:

Table 2: Final material systems for brazed joints for use in testing program.

Ceramic	Structural Alloy	Interlayer	Braze
650°C Application			
PY6/Ti coating	Incoloy 909	Ni	Au-5Pd-2Ni
SiC/Ti coating	Incoloy 909	Mo	Au-5Pd-2Ni
950°C Application			
PY6/Ti coating	Inconel 718	Mo	Au-5Pd-2Ni
SiC/Ti coating	Inconel 718	Mo	30Au-34Pd-36Ni

Electron Microscopy of Brazed Joints

Cross-section samples were prepared for transmission electron microscopy from two different brazed joints. The interface between the braze and the ceramic is shown in Figure 8 for an Au-18Ni braze/SiC(Ti) joint. The reaction layer was identified by electron diffraction and electron energy loss spectroscopy as TiC. Figure 9 shows the cross-section of an Au-18Ni braze/SNW1000(Ti) joint. The reaction layer was identified as TiN.

A study of the interactions between the braze alloys and the structural and interlayer materials was initiated. To date, four different structural alloy-braze-interlayer combinations were investigated: (1) Incoloy 909-(Au-5Pd-2Ni)-Mo, (2) Incoloy 909-(Au-5Pd-2Ni)-Ni, (3) Inconel 718-(30Au-34Pd-36Ni)-Ni, and (4) Inconel 718-(60Pd-40Ni)-Ni.

A 0.004-inch thick piece of braze foil was sandwiched between a piece of the structural alloy and the interlayer material and vacuum brazed for 5 minutes at the appropriate temperature. The samples were sectioned, polished, and examined in a scanning electron microscope (SEM).

The Incoloy 909-(Au-5Pd-2Ni)-Ni system did not form intermetallic compounds. However, the braze dissolved both the Incoloy 909 and the Ni to an appreciable extent. The degree of dissolution was greater at the corner of the joint where there was excess braze.

The Incoloy 909-(Au-5Pd-2Ni)-Mo system formed Mo-Ni intermetallic compounds at the braze/Mo interface. The intermetallic compounds at the braze/Mo interface are cracked. These cracks probably formed during cutting and suggest the brittleness of this interface. The Au-5Pd-2Ni braze dissolved the Incoloy 909 and the Mo, as in the Incoloy 909-Ni system.

Both the Inconel 718-(30Au-34Pd-36Ni)-Mo and the Inconel 718-(60Pd-40Ni)-Ni systems did not appear to react to any significant extent. No reaction zone was seen between the braze alloys and the Inconel 718 or the Mo or Ni. In both systems, a limited amount of dissolution of the Inconel 718, Mo, and Ni was seen.

Performance Test

Torsion Testing of Base Materials

Torsion tests were performed at 650°C with Incoloy 909, Inconel 718, and PY6. These tests measured the base line properties of each material. The 650°C fracture strength of PY6 was the same as the room temperature fracture strength, the twisting moment at failure was 525 lb-in and 1.84 degrees of rotation. The torsional yield strength of Incoloy 909 and Inconel 718 were similar, 600 lb-in. At 650°C the torsional yield strength of Incoloy 909 and Inconel 718 were 20 - 25 % lower than at room temperature while the rotational yield angle was unchanged at 2-3 degrees. A 1" long by 0.25" diameter gauge section was used in these tests.

Shear Testing of Brazed Coupons

A group of coupon specimens were brazed and sheared to evaluate the remaining issues in materials systems development. These results are summarized in Table 1. The shear strengths of Ti-coated PY6 brazed to Mo with either Au-5Pd-2Ni or 30Au-34Pd-36Ni (Palniro 4) were excellent. Shear strengths at 500°C reached up to 24 ksi and 36 ksi, for Au-5Pd-2Ni and 30Au-34Pd-36Ni respectively. The PY6-(30Au-34Pd-36Ni)-Mo joint was strong enough to deform the Mo without breaking. Mechanical property results are reported for SiC-to-Mo joints. Comparable samples of SiC to nickel were not obtained because the large differential expansion between the SiC and Ni resulted in all of the coupon samples failing during cool down from the brazing temperature. It must be remembered that nickel and molybdenum are to be used as intermediate layers. Consequently, while these coupon samples provide a general indication of ability to bear load in the presence of residual stress, the stress conditions in these coupon joints are less severe than the actual Task 2 samples. Therefore Task 2 samples are required to finalize the system.

Thermal Fatigue of Braze Joint

Braze joints were made for thermal fatigue tests at 650°C and 950°C. The initial crack distribution was checked with micro-focus X-ray and an ultrasonic testing unit.

Ultrasonic testing was used to complement the results obtained from micro-focus X-ray. Ultrasonic testing is best-suited for the detection of cracks perpendicular to the pulse direction. It was found that acoustic pulses travel extremely fast in PY6 (Si_3N_4-6%Y_2O_3). The rapid propagation of the acoustic pulses resulted in a decreased time resolution of the reflected pulses and a

corresponding decrease in sensitivity. In addition, the effect of the interference from the metal braze made interpretation of the results more difficult.

Micro-focus X-ray detected cracks in the SiC systems, however, no cracks were detected in the Si_3N_4 systems. The lack of cracks in the Si_3N_4 systems could be due to either; no cracking in Si_3N_4, or to the cracks in the Si_3N_4 being smaller than the detection limit of the X-ray equipment, (40 μm).

Equipment for the thermal cycle tests has been set-up for tests between 335 and 650°C and between 545 and 950°C. The crack distribution will be checked after 10, 100, and 1000 thermal cycles by microfocus X-ray.

The thermal cycle tests of the 650 and 950°C Si_3N_4 systems are underway. Each set of samples has been cycled 10 times and no cracks were seen with microfocus x-ray. These same samples are currently being cycled 90 more times and will again be examined by microfocus x-ray.

Status of Milestones

Thermal Fatigue Tests:

All of the thermal fatigue samples have been brazed.
All of the Si_3N_4 samples have been examined by microfocus x-ray.
Testing of the 1st set of samples, 650 and 950°C Si_3N_4, is in progress.

Torsion Testing of Brazed Joints:

Initial set of samples has been brazed.
1st torsion tests will be run during the week of 10/16/89.

Mechanical Fatigue of Brazed Joints:

Fatigue waveform has been programed into the MTS machine.
1st fatigue tests will depend on outcome of torsion tests, will probably start week of 10/23/89.

Communications/Visits/Travel

S. Kang attended the American Ceramic Society Annual Meeting in Indianapolis. Two talks were presented, "Coating Development for SiC-Incoloy 909 system Braze Joints" and "Reactive Coatings for the Si_3N_4-Incoloy 909 System Braze Joints".

Professor. K.S. Kim from the University of Illinois visited on 5/26/89 and 8/31/89.

E. Dunn, S. Wayne and D. O'Neil visited Brown University on 9/25/89 to review the progress on the analytical mechanics and FEA task.

E. Dunn and H. Kim visited ORNL on 6/7/89 to present a progress report to D.R. Johnson and M. Santella.

Problems Encountered

None.

Publications

"Issues in Ceramic-to-Metal Jointing: An Investigation of Brazing a Silicon Nitride-Based Ceramic to a Low-Expansion Superalloy", S. Kang, E.M. Dunn, J.H. Selverian, and H.J. Kim, American Ceramic Society Bulletin, vol. 68(9), p. 1608-1617, 1989.

References

None.

Table 1: Shear tests with Au-34Pd-36Ni, Au-5Pd-2Ni, Pd-40Ni, and Au-18Ni brazes.

System	Load (lbs)	Area (in^2)	Shear Stress (ksi)	Comments
PY6(Ti)-(30Au-34Pd-36Ni)-Mo	4325	0.138	31.3	525°C
	2750	0.150	18.3	525°C
	4925	0.135	36.4	525°C
	>4800	0.132	>36	500°C, Mo substrate bent
	>4800	0.149	>30	500°C, Mo substrate bent
	650	0.145	4.4	room temperature
	1360	0.145	9.3	room temperature
PY6(Ti)-(30Au-34Pd-36Ni)-Ni	1825	0.157	11.6	525°C
	1225	0.157	7.8	525°C
PY6(Zr)-(30Au-34Pd-36Ni)-Mo	450	0.157	2.8	525°C
	2225	0.157	14.1	525°C
	2250	0.153	14.7	525°C
PY6(Ti)-(Au-5Pd-2Ni)-Mo	3000	0.153	19.6	525°C
	2925	0.153	19.1	525°C
	2900	0.139	20.8	525°C
	2710	0.132	20.5	500°C
	3055	0.123	24.8	500°C
	765	0.125	6.1	room temperature
	885	0.149	5.9	room temperature
	2350	0.149	15.7	room temperature
PY6(Zr)-(Au-5Pd-2Ni)-Mo	-------	--------	------	525°C, broke under preload during heat-up
	2560	0.128	20.0	525°C
	2800	0.131	21.3	525°C
PY6(Ti)-(Pd-40Ni)-Mo	2050	0.149	13.7	525°C
	4040	0.136	29.7	525°C
	2150	0.144	14.9	525°C

Table 1, continued: Shear tests with Au-34Pd-36Ni, Au-5Pd-2Ni, Pd-40Ni, and Au-18Ni brazes.

System	Load (lbs)	Area (in^2)	Shear Stress (ksi)	Comments
PY6(Ti)-(Pd-40Ni)-Ni	--------	--------	------	severe reaction between braze alloy and Ni, all samples broke with little force
SiC(Ti)-(30Au-34Pd-36Ni)-Mo	625	0.145	4.3	500°C, 3 other samples broke during preload
	700	0.149	4.7	room temperature
	117	0.149	0.8	room temperature
	500	0.145	3.4	room temperature
SiC(Ti)-(Au-5Pd-2Ni)-Mo	--------	--------	------	500°C, all 3 samples broke during preload
	845	0.132	6.4	room temperature
	320	0.149	2.1	room temperature
	745	0.138	5.4	room temperature
SiC(Ti)-(30Au-34Pd-36Ni)-Ni	--------	--------	------	thermal mismatch failure during cooling after brazing (all 3 samples)
SiC(Ti)-(Au-5Pd-2Ni)-Ni	--------	--------	------	thermal mismatch failure during cooling after brazing (all 3 samples)
SiC(Zr)-(Au-5Pd-2Ni)-Ni	--------	--------	------	thermal mismatch failure during cooling after brazing (all 3 samples)
SiC(Zr)-(Au-5Pd-2Ni)-Mo	--------	--------	------	500°C, all 3 samples broke under preload
SiC(Ti)-(Au-18Ni)-Mo	--------	--------	------	500°C, all 3 samples broke during preload
	110	0.143	0.8	room temperature
	490	0.149	3.2	room temperature

Note: the 500 and 525°C tests were conducted under an argon atmosphere.

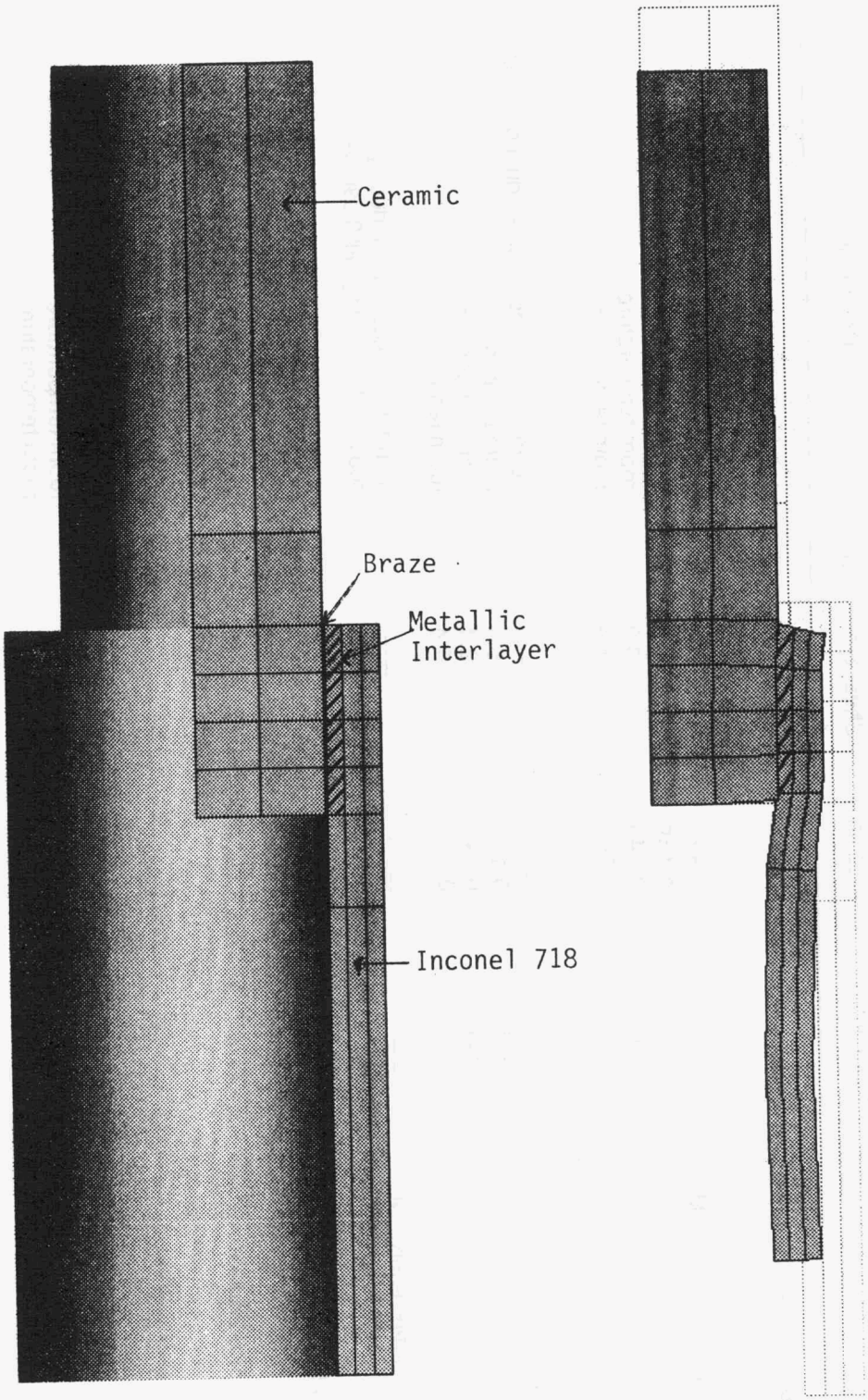

Figure 1. Fin ite element mesh of brazed joint.

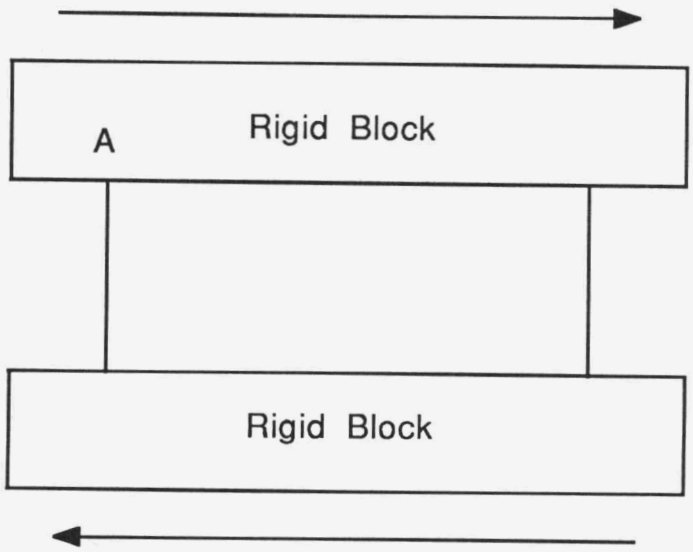

Figure 2. Direct shear problem.

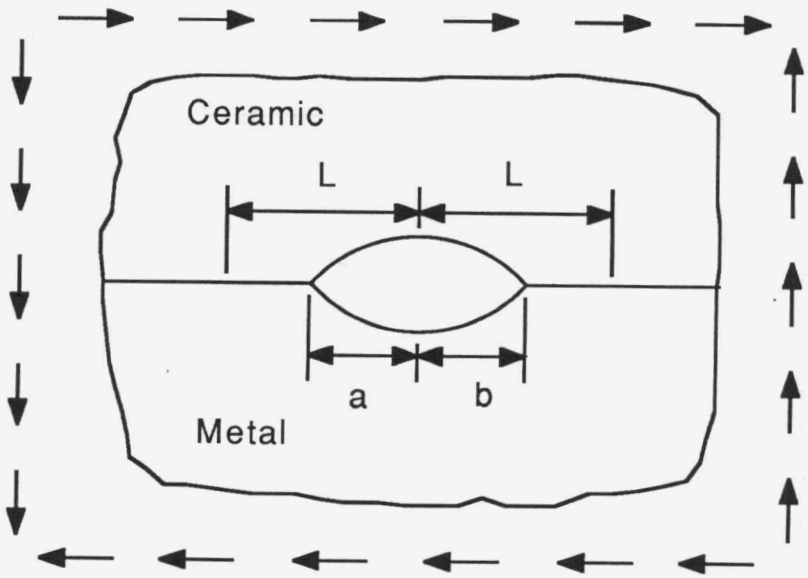

Figure 3. Mechanics model of interface crack of ceramic-metal joint.

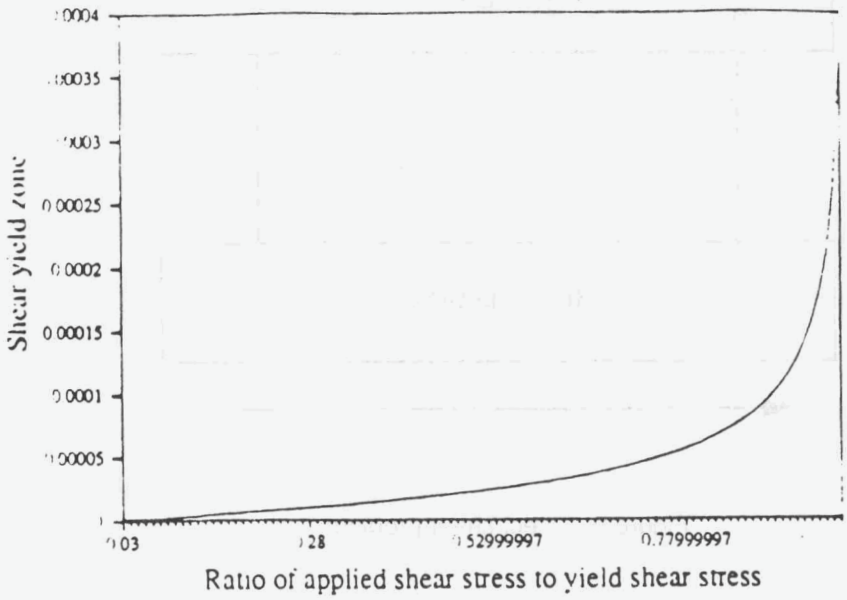

Figure 4. Shear yield zone size versus ratio of applied shear stress to shear yield stress for $\beta = 0.999077$.

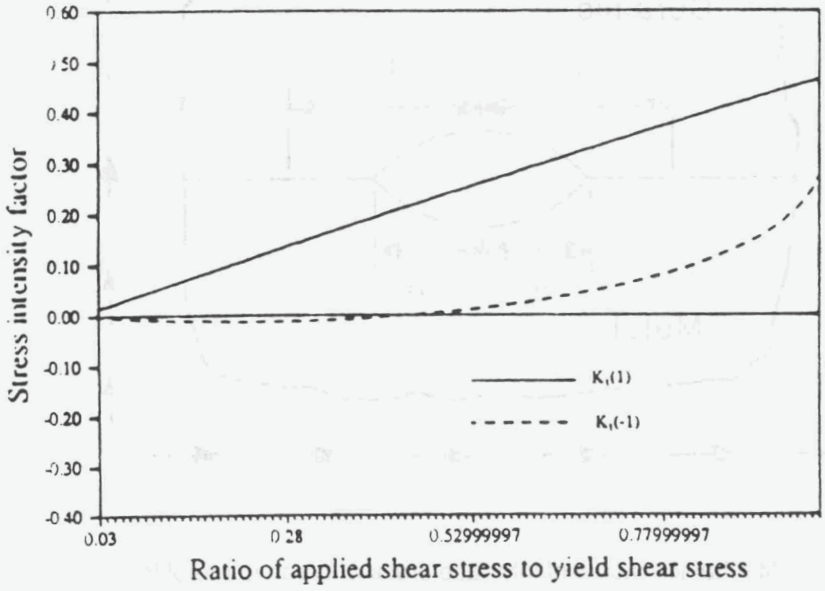

Figure 5. Normalized stress intensity factor versus ratio of applied stress to shear yield stress for $\beta = 0.999077$.

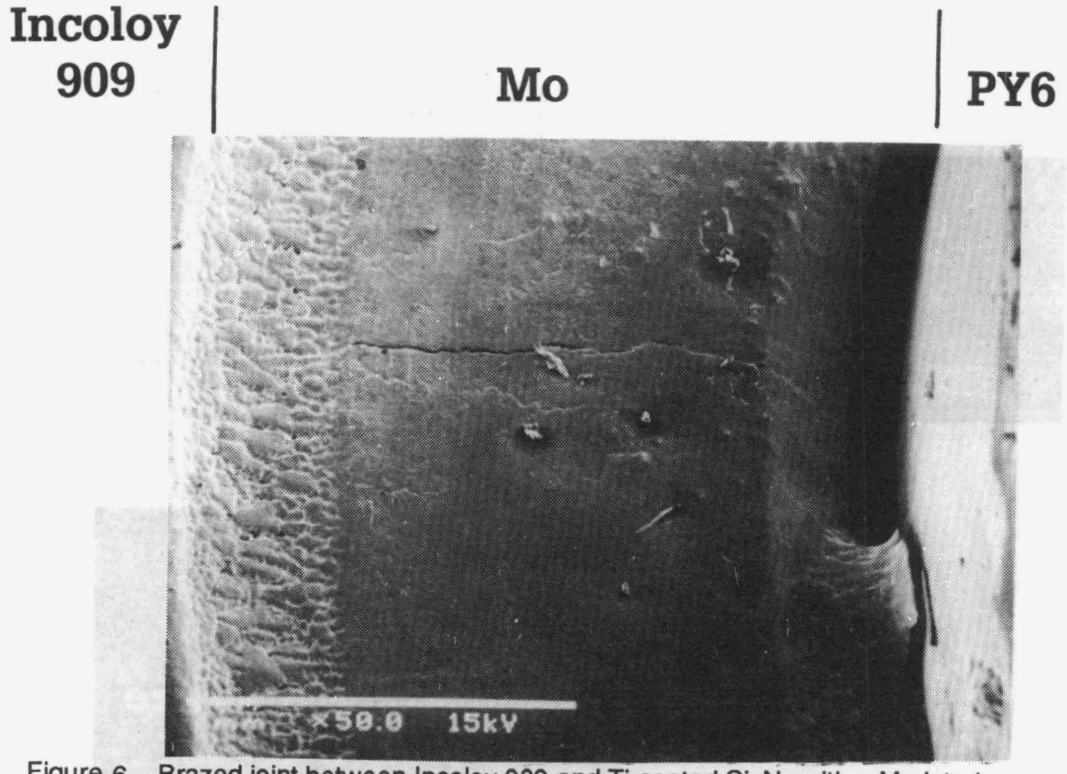

Figure 6. Brazed joint between Incoloy 909 and Ti-coated Si_3N_4 with a Mo interlayer and the 30Au-34Pd-36Ni braze.

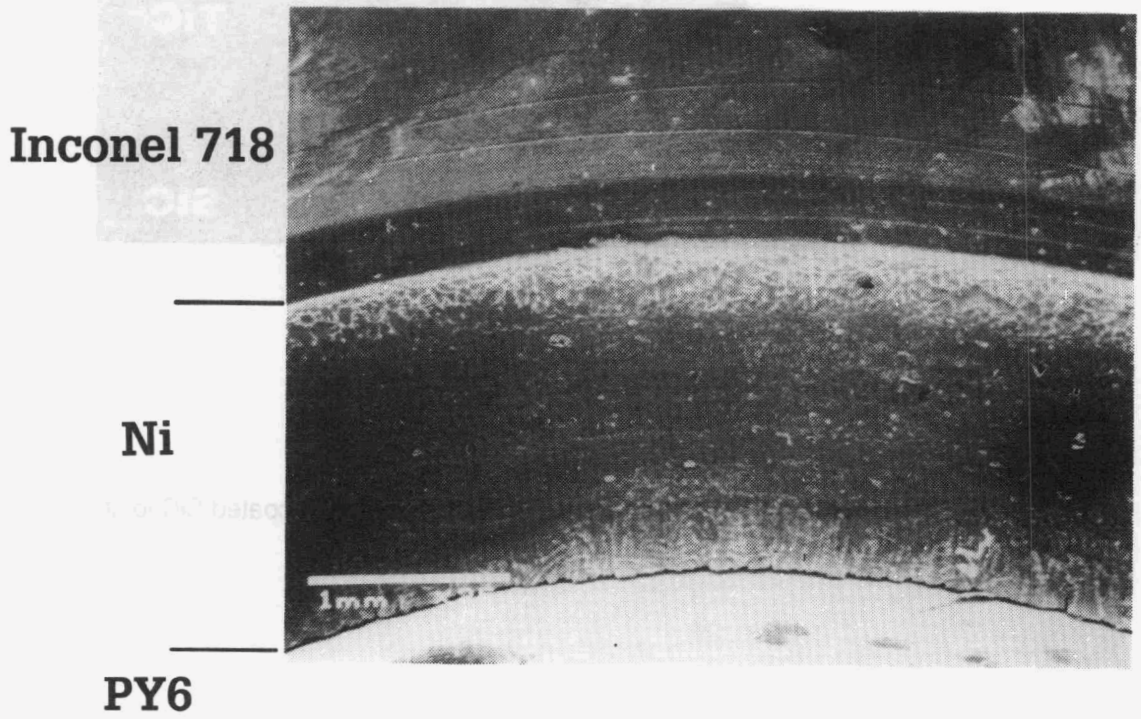

Figure 7. Brazed joint between Inconel 718 and Ti-coated Si_3N_4 with a Ni interlayer and the Au-5Pd-2Ni braze.

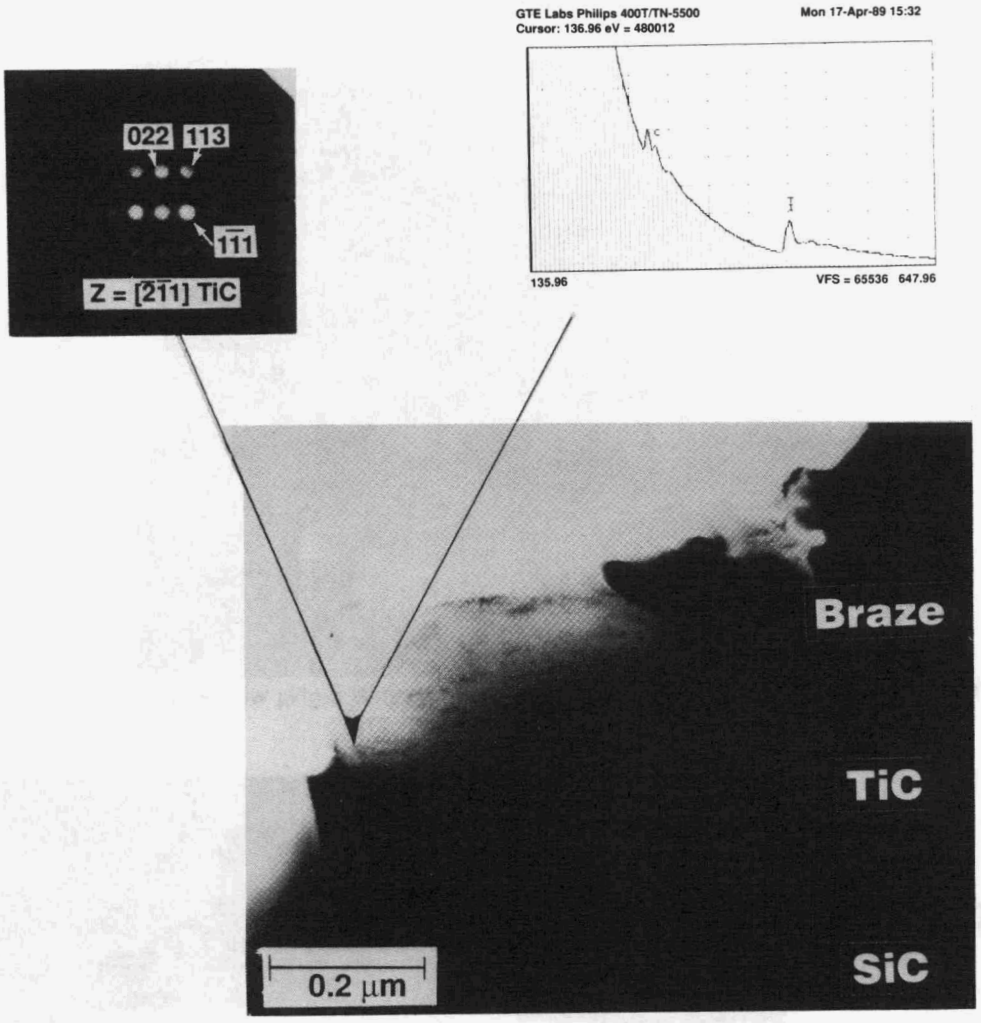

Figure 8. Cross-section TEM micrograph of Au-18Ni braze/Ti-coated SiC joint.

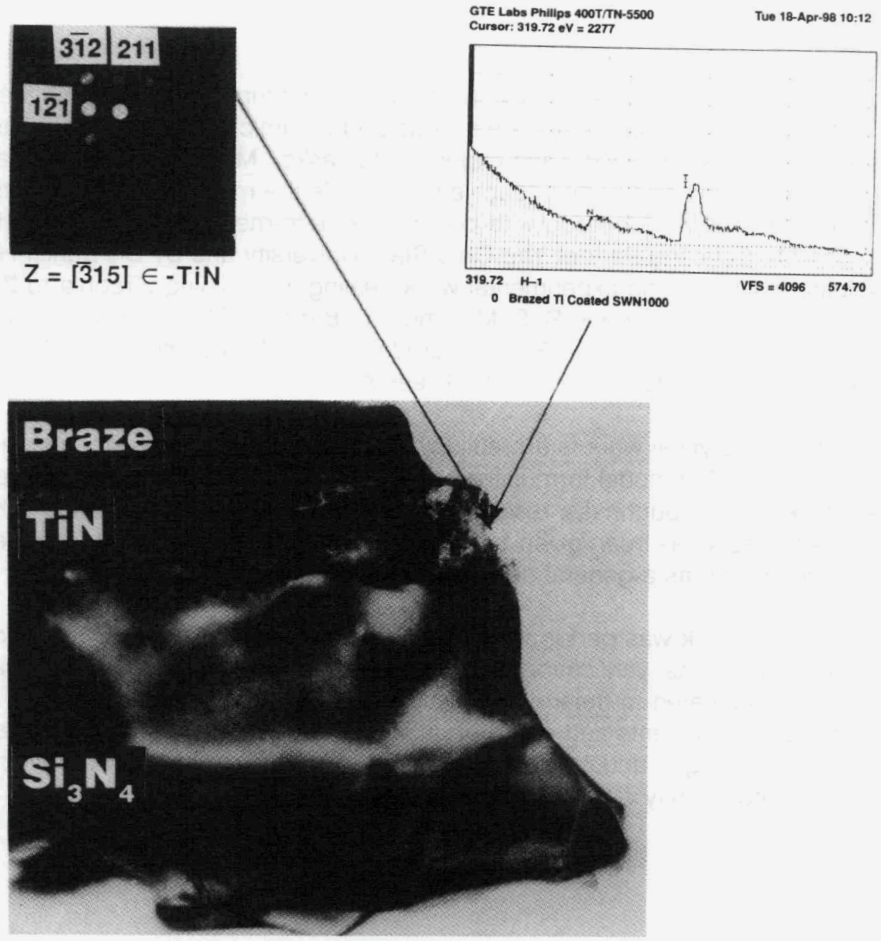

Figure 9. Cross-section TEM micrograph of Au-18Ni braze/Ti-coated Si_3N_4 joint.

Analytical and Experimental Evaluation of Joining Ceramic Oxides to Ceramic Oxides and Ceramic Oxides to Metal for Advanced Heat Engine Applications

A. T. Hopper, J.Ahmad, A. Rosenfield, and G. Majumdar (Battelle Columbus Division)

Objective/Scope

The objective of this project is the development of procedures necessary for the design of reliable, high strength ceramic oxide-to-ceramic oxide and ceramic oxide-to-metal joints. The research program consists of analytical and experimental tasks. Magnesia-Partially Stabilized Zirconia (PSZ) is the ceramic and nodular/ductile cast iron is the metal being used in this program. The experimental work dealing with ceramic oxide-to-metal joints was done by Dr. James Cawley and Mr. Eunsung Park of The Ohio State University and by Dr. Daniel Hauser of The Edison Welding Institute. The experimental work dealing with joining Zirconia to Zirconia was performed by Dr. S. L. Swartz and B. S. Majumdar of Battelle. Measurements of joint and constituent properties were done by Dr. B. S. Majumdar, Dr. A. R. Rosenfield, and Mr. Paul Held. Analytical modeling work was performed by Dr. Jalees Ahmad.

The goal of the analytical work is a predictive model that can be used in engineering design of ceramic joints. The model formulated represents a synergistic treatment involving applied stress, crack length, toughness, residual stress, and strength in a fundamentally sound manner. Special emphasis has been given to geometry and stress state independence, making the model widely applicable as a general design tool.

The experimental work was performed to provide both material property input to the design model and experimental verification of model predictions. To this end small scale and scaled up joints were fabricated to determine their mechanical behavior. Experiments included measurements of elastic constants and of stress-strain curves as a function of temperature, tensile strength, shear strength, and fracture toughness. Some experiments were also performed on specimens fabricated entirely of the interlayer materials.

Technical Progress

1.0 Analytical Efforts

A joint assessment and design model (JAD) has been developed and compared to verification experiments for ceramic-ceramic joints. In our development we have used the term joint failure to refer primarily to loss of load carrying capacity while strength will refer to a material or, in the present context, joint property. Joint failure will also refer to excessive dimensional change of the joint, especially in the metal-ceramic joints. While both failure types are addressed in the model, the emphasis in this discussion is primarily on loss of load carrying capacity.

Given a specimen geometry and the manner in which it is loaded, a joint's load carrying capacity is dictated by its strength (S_c) and toughness (G_c) properties. Which of the two properties dictates how and at what load failure occurs depends on their relative magnitude, flaw size (a) in the joint and residual stress (σ_R). Joint constituent (ceramic, metal, interlayer, reaction zones) properties and joining process variables (e.g., interlayer thickness and joining temperature) influence the load carrying capacity through their effect on toughness, strength, residual stress, inherent flaw size and stress at the failure location.

The literature suggests that in current model development efforts emphasis is on either the toughness or the strength aspect, or the two are treated independently. A key feature of the current approach has been to formulate a model which combines strength and toughness, and which represents a synergism of applied stress, crack length, toughness, residual stress, and strength in a self-consistent manner. Its validity is expected to be independent of specimen geometry and stress state. Special emphasis has been given to this independence in the development of the predictive model.

Formulation: As reviewed in reference [1], most of the early work on bimaterial interfaces relied on linear elasticity formulations and was predominantly analytical. Experimental work (e.g., see [2], [8], [9]) is relatively recent. Early analytical modeling efforts [3-5] were focused on explaining peculiar interface crack-tip stress field behavior predicted by the analyses. It is only within the last year or so (see [13] to [24]) that the subject has been treated with engineering rather than mathematical interest.

Recent literature on the subject of mixed mode fracture mechanics of bimaterial interfaces [1-24] suggests that the propensity for crack growth initiation (crack driving "force") can be expressed in terms of mixed-mode crack-tip energy release rate* (G) and a phase angle (Ψ) representing the "mixity", or ratio of shear and normal components of the crack driving force. While Ψ can have crucial effect on joint behavior and is part of our formulation, to simplify this presentation let us assume Ψ to be a constant.

Employing the above considerations as part of the basis, we invoke concepts in (engineering) nonlinear fracture mechanics [25, 26] to derive an expression for a joint assessment vector ($\bar{A}$) as follows:

$$\bar{A} = \left(\frac{G}{G_c}\right)^{1/2} i + \left(\frac{P}{P_c}\right) j \qquad (1)$$

in which P is a load parameter (related to joint stresses due to applied loads and residual stresses) and P_c is its critical value (related to joint strength). The assessment vector represents the propensity for joint failure. In a given direction, the smaller the magnitude of $\bar{A}$, the smaller is the propensity for joint failure.

For this report, let us set aside the directional considerations of the assessment vector, and focus on its magnitude. With sufficient generality one can express the magnitude (A) of the assessment vector as follows:

$$A^2 = \left(\frac{aF_M}{G_c} + \frac{1}{P^2_c}\right)P^2_M + \left(\frac{aF_R}{G_c} + \frac{1}{P^2_c}\right)P^2_R + \frac{2P_M P_R}{P^2_c} \qquad (2)$$

---

* Note that in the context of bimaterial interface cracks, the use of the classically defined Mode I and Mode II stress intensity factors (K_I, K_{II}) is (theoretically) inappropriate. This is due to the oscillatory nature of the elastic crack tip strain singularity and due to the inseparability of the normal and shear stress components near an interface crack tip.

in which the hitherto undefined quantities are as follows:

G_M = elastic energy release rate due to applied load

G_R = elastic energy release rate due to residual stress

P_R = loading parameter (P) corresponding to residual stress (σ_R)

P_M = Reference loading parameter (P) corresponding to a reference applied stress (σ)

$F_M = G_M/(aP_M^2)$

$F_R = G_R/(aP_R^2)$

The functions F_M and F_R express the geometry dependence of the energy release rate.

Assuming that $P_R << P_c$ (i.e., the joint doesn't fall apart due to residual stresses only!), equation (1) reduces to the following:

$$A^2 = \left(\frac{aF_M}{G_c} + \frac{1}{P_c^2}\right) P_M^2 + \left(\frac{aF_R}{G_c}\right) P_R^2 \qquad (3)$$

in which $P_c(\sigma_c)$ is now the critical value of P_m. In the absence of a flaw (i.e., a = 0), equations (2) and (3) say that failure is governed entirely by strength (σ_c). For a very strong joint (i.e., $P_c \rightarrow \infty$), the equations say that failure is governed only by toughness (G_c). For realistic situations between these two extremes, failure is governed by both σ_c and G_c.

To predict the failure load, P_m in equations (2) and (3) is replaced by P_f which is selected such that the vector $\bar{A}$ intersects the curve (in general, a surface) given by the following equation:

$$\frac{G}{G_c} = \frac{(P/P_c)^2}{\eta_E + \eta_N \left(\frac{P}{P_c}\right)^{N+1}} \qquad (4)$$

in which G and P are total values of energy release rate and the loading parameter and η_E and η_N are dimensionless parameters which have been derived based on small scale yielding and fully plastic fracture mechanics considerations, respectively. The parameter N represents the strain-hardening characteristic of the material.

A graphical representation of the model is shown in Figure 1. To predict failure conditions, one would find P (= P_f) such that the vector $\bar{A}$ intersects the curve, which is a plot of equation 4. To improve joint characteristics at a reference P (= P_m), one would try to minimize $\bar{A}$ with respect to constituent properties and joining process variables. Recall that the smaller the magnitude of A, the stronger the joint.

Application to Joint Design: Using the formulation just presented, knowing strength, toughness, and residual stress, failure prediction is relatively straightforward. What is more involved is minimization of $\bar{A}$, which is related to joint design. This complication is depicted in Figure 2, where it is indicated that joint constituent property variables, residual stress, geometric parameters and joining process variables influence the design parameters P_c, F_m, F_R, and P_R which appear in the expression for A. The relations of these variables with design parameters need to be established in order for the model to be useful in guiding joint design.

To illustrate the accuracy of the JAD Model prediction, consider the case of zirconia-zirconia joints. In these joints failure has been found to occur in the middle of the interlayer. Based on finite element analyses in this program, residual stress contributions to the driving force were found to be negligibly small and the stress state was found to be symmetric about the crack plane.

A series of finite element analyses was preformed to compute the energy release rate (G) for various combinations of specimen geometry variables (including interlayer thickness, t_i) and interlayer properties. The interlayer properties were, in turn, expressed as a function of the interlayer material's chemical composition. These analyses were performed after it was found that accurate representation of crack tip shielding is crucially important in accurately predicting the joint's load carrying capacity. If we represent the elastic energy release rate G in Equation 1 as follows:

$$G = f^2 P^2 (\pi a)(1-\upsilon_i)/2\mu_i \tag{5}$$

then for a ceramic-ceramic bend specimen, the finite element analysis results allow the dimensionless function f to be expressed as follows:

$$\frac{f}{f_H} = 1.0 + \left(0.376 + 2.340\,\frac{t_i}{2a}\right)\left(1 - \frac{\mu_i}{\mu_c}\right) - \left(2.504 + 3.870\,\frac{t_i}{2a}\right)\left(1 - \frac{\mu_i}{\mu_c}\right)^2 \tag{6}$$

in the range $0.016 \leq t_i/2a \leq 0.05$, where a represents the crack length. Note that f^2 is synonymous with F_M of Equations 2 and 3. In equations (1) and (2) P is applied load, μ is shear modulus, υ is Poissons Ratio and the subscripts i and c refer to the interlayer and ceramic (zirconia) materials, respectively. The dimensionless function f_H has the same meaning as f, but for a specimen without a joint. For the specimen design used in the experiments, the crack length to width (W) ratio was fixed at 0.3. For a/w = 0.3, f_H = 1.122. For the MASZ compounds used as interlayer materials, if V_z represents the volume fraction of zirconia, then

$$\frac{\mu_i}{\mu_c} \simeq 1 + \left(V_z^{-1}\right)\left(1.677 + 1.024\left(V_z^{-1}\right)\right) \tag{7}$$

in the range $0.67 \leq V_Z \leq 1.0$.

Together, equations (5), (6), and (7) provide the connection between interlayer material composition and interlayer thickness to the crack driving force (G). The crack driving force is then used in the JAD model described above.

As a first example, consider the case of a joint with $V_z = 0{\cdot}67$ and $a/2t_i$ of 0·024. Using (experimentally found) G_c for the interlayer material to be 42·6 J/M^2, use of the JAD model predicts the failure load for the specimen to be 130·33 N. The failure load measured in the joint experiment was 129 N. Note that this prediction required input data (G_c) not from an experiment on a joint, but from a test performed on a specimen made entirely of the MASZ interlayer material.

Using equations similar to (5) and (6) for the disk specimen (larger scale joint) but using the same G_c, the JAD model predicted the failure load of 1·58KN for a specimen with $t_i/2a$ of 0·011 and a/R of 0·5 with $V_z = 0{\cdot}67$. The measured failure load in this case was 1·44KN. It is currently being investigated whether this approximately 10 percent difference between JAD model prediction and the measured failure load is traceable to a specific (deterministic) variable, or if it should be accepted as a consequence of normal data scatter. Typical results of deterministic analyses being performed in this vein are shown in Figure 3. As shown in the figure, some of the data points correspond not to just one test, but to the average of many tests. Also, the plot contains data on three different types of specimens. Thus, correlation of measured and predicted failure loads appears to be quite good.

Results of Finite Element Analyses of Metal-Ceramic Disk Specimens: The metal-ceramic and ceramic-ceramic disk specimens (see Figure 4) are being used in support of the model validation activity for scaled up joints. For the metal-ceramic specimens, crack-tip stress intensity is expressible in terms of a vector Q (see reference 15) with components Q_1 and Q_2 defined as:

$$Q_1 = \frac{P}{\pi R} F_1 (a/R, \alpha, \beta) \sqrt{\pi a}$$

$$Q_2 = \frac{P}{\pi R} F_2 (a/R, \alpha, \beta) \sqrt{\pi a}$$

in which F_1 and F_2 are dimensionless functions of geometry and bimaterial constants α and β. For the specific α and β corresponding to cast-iron and zirconia elastic properties, the finite element results for two different a/R rations are shown in Figures 5 and 6. The double lines correspond to F_1 and F_2 at the two crack tips. These results were obtained using the finite element meshes shown in Figures 7 and 8 and a special interaction integral formulation developed by Prof. Shih at Brown University.

The results shown in Figures 5 and 6 are being used to define the dimensionless geometry factor F_M of the joint assessment and design model (see equations 2 and 3). F_1 and F_2 relate to F_m using the appropriate expression for energy release rate $G(Q_1, Q_2)$.

2.0 Experimental Effort

In support of the JAD model development and verification work, numerous tests and experiments have been performed on specimens manufactured by joining zirconia to zirconia and by joining zirconia to cast iron. In addition, some experiments have been performed on the joint constituents; zirconia, cast iron, braze metal, and ceramic interlayer material. Two kinds of specimens have been used in the experiments. Small bend bars having dimensions 2.5 x 5.1 x 38.1mm were used in four point bend tests for load-displacement and failure stress determinations, and fracture bars having dimensions 5.1x5.1x38.1mm with a notch of approximate depth 1.5mm at the joint were used for small scale fracture verification experiments. Scaled up joints

used for JAD model verification tests were in the form of disks (see Figure 4) having a diameter of 35.6mm and a thickness of 3.6mm. Disk specimens were either notched along the joint or were unnotched and they were tested in comparison with the joint either along the compression axis, or at an angle to the compression axis. Note that the bend bar cross sectional area is one tenth that of the disk specimen cross sectional area. As has been mentioned in previous reports on this program, the advantage of the disk specimen in joint characterization is that it allows easy changeover from normal to a mixed-mode type of loading, simply by rotating the joint plane with respect to the loading axis. Mixed mode loading is extremely important in joint characterization, particularly with different substrates, because even under nominally Mode I loading, the stress-singularity has a mixed mode character.

Table 1 lists the number of tests of different types that were performed at room temperature; load-displacement data were recorded for many of the tests listed. In addition to the approximately 160 tests that are listed in Table 1, approximately 60 tests were performed early on in this program; these earlier tests were conducted in the development stage of the joints, and the results were used to screen candidate joint material and joining technique. Besides the room temperature tests, approximately 30 tests were conducted at high temperature. For the zirconia-zirconia joints and their constituents, the high temperature tests were performed at 1000 C, while, for the zirconia-cast iron joints, the high temperature tests were conducted at 400 C.

2.1 Ceramic-Ceramic Joints

Ceramic-ceramic joints were fabricated using interlayers obtained by mixing a base magnesia-aluminia-silica (MAS) powder with various weight fractions of zirconia powder. The interlayers were designated MASZ-XX, where XX represents the weight fraction of zirconia in the MASZ mixture. The base MAS interlayer powder had the composition: 15 wt% MgO, 20% Al_2O_3, 56% SiO_2, and 9% TiO_2. It was fabricated by milling the respective oxides and calcination at 1100 C for four hours, followed by re-milling. Differential thermal analysis confirmed that the MAS melted at a temperature close to 1300 C; joining temperatures higher than this temperature were selected. Joining with the MASZ interlayers was accomplished by heating to temperatures between 1350 and 1400 C, with only minimal pressure (300 psi) applied, mainly to hold the parts together during joining. Good joint strength could not be achieved when a pure MAS interlayer was used, mainly because of the low viscosity of the MAS interlayer material at the joining temperature (and thus squeezing out of the interlayer material). The interlayer "squeeze-out" was minimized by the addition of ZrO_2 to the MAS interlayer powder. Addition of ZrO_2 also provided two other benefits. It reduced the thermal expansion mismatch and also provided greater elastic modulus compatibility between the interlayer and substrate. Three ZrO_2contents (50, 67, and 80 weight percent) designated MASZ-50, MASZ-67, and MASZ-80, and two joining temperatures (1350 and 1400 C) were investigated. The strength and modulus of interlayers and joints were found to increase with ZrO_2 contents. However, strength properties deteriorated with higher joining temperatures. These results will be used in the optimization scheme for designing joints. Microstructural analysis of the joints indicated significant interdiffusion of the interlayer constituents (especially silicon) into the Mg-PSZ, and also indicated the formation of zircon (i.e., $ZrSiO_4$) in the interlayer.

Bulk MASZ-50, MASZ-67, and MASZ-80 interlayers material were fabricated in the form of bars using standard ceramic processing methods. PVA binder was added to the MASZ powders and bars approximately 50.8x 10.2x10.2 mm were cold isostatically pressed. After binder burnout, the bars were sintered using the identical temperature cycles that were employed during joining. Although the theoretical density of the interlayer material is unknown (because of the complicated phase constitution), the shrinkage indicated that the interlayer bars were approximately 85-90 percent dense.

Mechanical characterization of the base materials included determination of σ-versus-ϵ curves for the base zirconia in the heat treated condition corresponding to the joining cycle, and determination of σ-versus-ϵ curves for the interlayers. Bend bars with strain gages were used to determine σ-versus-ϵ curves from the load-strain curves at room temperature. At 1000 C, σ-versus-ϵ curves were estimated from the load versus displacement curves. The σ-versus-ϵ curves were then approximated by the Ramberg-Osgood formula :

$$(\epsilon/\epsilon_o) = (\sigma/\sigma_o) + \alpha\,(\sigma/\sigma_o)^n \tag{8}$$

where σ_o and ϵ_o were determined from the proportional limit, and n and α were determined by a least-squares best-fit procedure. These parameters were subsequently used in the analytical computations.

Figures 9 and 10 illustrate the room-temperature stress-strain curves for the base heat-treated zirconia and MASZ-80 (fabricated with 80 weight percent zirconia) interlayer, respectively. The Ramberg-Osgood representation is shown in the figures. In particular, the parameters for the base heat-treated zirconia were : σ_o = 140.6 MPa, ϵ_o = 0.000698, α = 0.0832, and n = 1.62; E = 201.2 GPa. For the MASZ-80 interlayer, the parameters were : σ_o = 101.6 MPa, ϵ_o = 0.00072, α = 0.071, and n = 3.15; E = 141 GPa. Similar results were obtained for other interlayer materials; namely, interlayers with zirconia concentrations of 50 and 80 weight percent, and processed at 1350 C and 1400 C.

Load-displacement data were monitored during many of the bend tests and fracture toughness tests. A high accuracy LVDT-type gage, calibrated to a maximum displacement of 25 to 50-microns, was used to measure displacement of the center of the bend bar with respect to the upper loading pins. Non-linearities were observed in the load-displacement records, particularly for the notched bend bars used in the fracture toughness tests. Such non-linearities may have been the result of subcritical crack growth.

Load-versus-crack opening displacements also were monitored during the fracture toughness tests using the cracked disk specimen. This specimen geometry was used for the validation experiments. Also, it provided a means to evaluate whether the analytical model was able to predict load-displacement data under mixed-mode fracture conditions. It may be noted that in actual applications, loading is generally mixed mode in character.

Thermal expansion curves were obtained for the base zirconia, interlayers, and joints. These data were needed for the residual stress calculations. Peaks corresponding to zirconia phase transformations were observed for both the base zirconia and interlayer materials. Details will be available in the final report on this project.

From the bend strength data, Weibull plots of base materials and joints were obtained. Figure 11 summarizes some of the data. The average strength of the joint was always greater than that of the corresponding interlayer, although fractures propagated primarily through the 100-150 μm thick interlayer of the joint. We believe that this behavior is primarily a result of shielding of the interlayer, because of the lower modulus of the interlayer in comparison with the zirconia substrate. In fact, some of the analytical results obtained to date indicate extremely good correlation between measured joint strength and strength predicted based on shielding and bend strength of the interlayer material.

2.2 Ceramic-Metal Joints.

It had been reported earlier that erratic bonds were obtained when the zirconia was coated with a Ti-layer prior to brazing. An active filler metal approach was successful, using Incusil-ABA braze metal fabricated by GTE-Wesgo. This material has the nominal composition : 59.2 Ag, 27.5 Cu, 12.1 In, 1.2 Ti, all in weight percent. Neither the zirconia nor cast iron was coated prior to brazing in vacuum. All the large scale joints were successful (withstand the rigors of machining specimens) and a Weibull plot of bend strengths is shown in Figure 12.

Evaluation of the microstructure on the microprobe showed that most of the Ti in the braze metal segregated to the braze metal-zirconia interface during the brazing cycle. This most likely was responsible for providing good wettability between the braze metal and zirconia. It appears, in retrospect, that the active-filler metal approach is better than the indirect brazing approach using Ti-coated zirconia, because in the former approach the Ti is present in the braze metal, and is not oxidized by the environment; the Ti-layer is most likely oxidized prior to brazing in the indirect brazing approach. Careful examination of the fracture path indicated that room temperature failure occurred either in the zirconia next to the Ti-layer, or it occurred in the Ti-layer itself. Detailed micrographs will be provided in the final report.

Similar to the ceramic-ceramic joints, the constitutive response of the base zirconia, cast iron, and braze metal were determined in order to predict joint response based on stress-strain properties of the constituent materials. Tensile tests were performed on cast iron and Incusil-ABA, while bend tests were performed on the base zirconia. The temperature of testing ranged from room temperature to 400 C, the upper temperature limit for this type of joint. Figures 13, 14, and 15 illustrate the σ-vs-ϵ curves for the base zirconia, cast iron and braze metal at room temperature. Similar curves were obtained at other temperatures. The stress-strain data were fitted using the Ramberg-Osgood representation, and Figures 13 through 15 show that the curve-fitting is quite good. The parameters for zirconia were : σ_o = 301.8 MPa, ϵ_o = 0.00149, α = 0.0488, and n = 5.66; E = 201.9 GPa; for braze metal, they were : σ_o = 295.6 MPa, ϵ_o = 0.00374, α = 0.1546, and n = 19.58; E = 11.5 Msi; for cast iron, the parameters were : σ_o = 221.9 MPa, ϵ_o = 0.00136, α = 4.61, and n = 4.99; E = 163.3 GPa.

The load-displacement data were monitored during many of the bend tests and fracture toughness tests. Additionally, load versus crack opening displacement data were recorded for disk specimens, that were used for validation of the joint model. Figure 16 illustrates the result of a bend test, and it indicates that there was significant inelastic deformation. This inelasticity was expected based on calculation of residual stresses, and the magnitude of the applied load.

The thermal expansion curves for the base zirconia, braze metal, and cast iron were obtained over the temperature range room temperature to 730 C, the temperature of brazing. The thermal expansion was needed to predict the magnitude of residual stresses in the joints. In contrast to the heat-treated zirconia, no phase transformations occurred in the base zirconia in the temperature range 25 C to 730 C.

Status of Milestones

All joints, both small scale and scaled up, have been manufactured and tested. Tests have included determination of load-displacement response of joints and their constituents, bend strength, fracture toughness, and failure loads under mixed mode conditions. An engineering joint assessment and design has been formulated and verified on small-scale ceramic-ceramic joints. Current efforts are directed at verifying the model for ceramic-metal joints which involve nonlinear deformation. the final report will be written during November for submission at the beginning of December.

Publications

None.

References

1. Atkinson, C., 1989, "Cracks in Bimaterial Interface - An Overview," Advances in Fracture Research, Proceedings of ICF7, Vol. 4, pp. 3053-3061.

2. Cao, H. C. and Evans, A. G., 1989, "An Experimental Study of the Fracture Resistance of Bimaterial Interface," Mechanics of Materials, in press.

3. Comninou, M., 1977a, "The Interface Crack," Journal of Applied Mechanics, Vol. 44, pp. 631-636.

4. Comninou, M., 1977b, "Interface Crack with Friction in the Contact Zone," Journal of Applied Mechanics, Vol. 44, pp. 780-781.

5. Comninou, M. and Schmueser, D., 1979, "The Interface Crack in a Combined Tension-Compression and Shear Field," Journal of Applied Mechanics, Vol. 46, pp. 345-348.

6. He, M-Y,. and Hutchinson, J. W., 1989, "Kinking of a Crack out of an Interface," Journal of Applied Mechanics, to appear.

7. Hutchinson, J. W., 1989, "Mixed Mode Fracture Mechanics of Interfaces," to appear in Proceedings of the Acta/Scripta Metallurgical Conference on Bonding, Structure and Mechanical Properties of Metal/Ceramic Interfaces.

8. Liechti, K. M. and Hanson, E. C., 1988, "Nonlinear Effects in Mixed-Mode Interfacial Delaminations," International Journal of Fracture, Vol. 36, pp. 199-217.

9. Liechti, K. M. and Chai, Y. S., 1989, "Interfacial Crack Initiation under Biaxial Loading," manuscript in preparation.

10. Malyshev, B. M. and Salganik, R. L., 1965, "The Strength of Adhesive Joints using the Theory of Cracks," International Journal of Fracture Mechanics, Vol. 1, pp. 114-128.

11. Needleman, A., 1989, "An Analysis of Decohesion Along an Imperfect Interface," International Journal of Fracture, in press.

12. Parks, D. M. and Zywicz, E., 1989, "Elastic/Perfectly-Plastic Small Scale Yielding at Bi-Material Interfaces," Advances in Fracture Research, Proceedings of ICF7, Vol. 4, pp. 3081-3088.

13. Rice, J. R., 1968, "Elastic Fracture Mechanics Concepts for Interfacial Cracks," Journal of Applied Mechanics, Vol. 55, pp. 98-103.

14. Rice, J. R., Suo, Z. and Wang, J. S., 1989, "Mechanics and Thermodynamics of Brittle Interfacial Failure in Bimaterial Systems," to appear in Proceedings of the Acta/Scripta Metallurgical Conference on Bonding, Structure and Mechanical Properties of Metal/Ceramic Interfaces.

15. Shih, C. F. and Asaro, R. J., 1988, "Elastic-Plastic Analysis of Cracks on Bimaterial Interfaces: Part I -- Small Scale Yielding," Journal of Applied Mechanics, Vol. 55, pp. 299-316.

16. Shih, C. F. and Asaro, R. J., 1989a, "Elastic-Plastic Analysis of Cracks on Bimaterial Interfaces: Part II -- Structure of Small Scale Yielding Fields," Journal of Applied Mechanics, in press.

17. Shih, C. F. and Asaro, R. J., 1989b, "Elastic-Plastic Analysis of a Collinear Array of Cracks on a Bimaterial Interface," Materials Science and Engineering, Vol. A107, pp. 145-157.

18. Shih, C. F., Asaro, R. J. and O'Dowd, N. P., 1989, "Cracks on Bimaterial Interfaces: Plasticity Aspects," to appear in Proceedings of the Acta/Scripta Metallurgical Conference on Bonding, Structure and Mechanical Properties of Metal/Ceramic Interfaces.

19. Symington, M., Shih, C. F. and Ortiz, M., 1988, "Tables of Plane Strain Mixed-Mode Plastic Crack Tip Fields," Brown University Report, MRG/DMR-8714665/1.

20. Suo, Z. and Hutchinson, J. W., 1989, "Sandwich Test Specimen for Measuring Interface Crack Toughness," Materials Science and Engineering, Vol. A107, pp. 135-143.

21. Suo, Z., 1989, "Mechanics of Interface Fracture," Ph.D. Thesis, Harvard University, Cambridge, MA (Available through University Microfilms, Ann Arbor, MI).

22. Zywicz, E. and Parks, D. M., 1989a, "Elastic Yield Zone around an Interfacial Crack Tip," Journal of Applied Mechanics, in press.

23. Zywicz, E. and Parks, D. M., 1989b, "Elastic-Plastic Analysis of Frictionless Contact at Interfacial Crack Tips," International Journal of Fracture, in press.

24. Varias, A. G., O'Dowd, N. P., Asaro, R. J. and Shih, C. F., 1989, "Failure of Bimaterial Interfaces." Report to the U. S. Office of Naval Research (submitted for publication).

25. Dowling, A. R. and Townley, C. H. A., "The Effects of Defects on Structural Failures: A Two-Criteria Approach," International Journal of Pressure Vessel and Piping, Vol. 3, 1975, pp. 77-137.

26. Shih, C. F., Kumar, V., and German, M. D., "Studies on the Failure Assessment Diagram Using the Estimation Scheme and J-Controlled Crack Growth Approach," General Electric Company TIS Report, 1981.

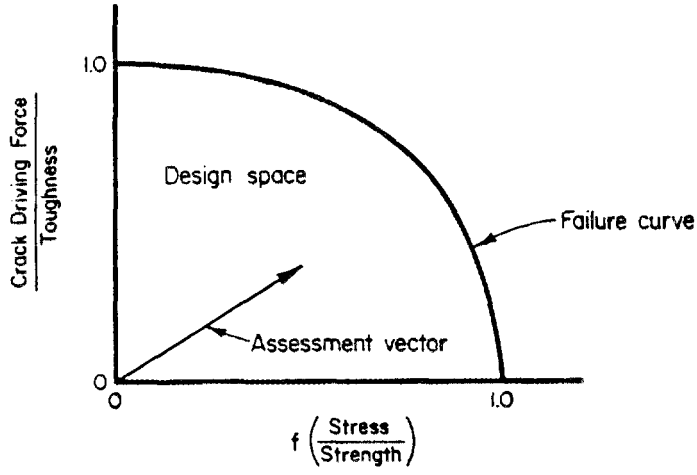

FIGURE 1. GRAPHICAL REPRESENTATION OF JOINT ASSESSMENT AND DESIGN MODEL.

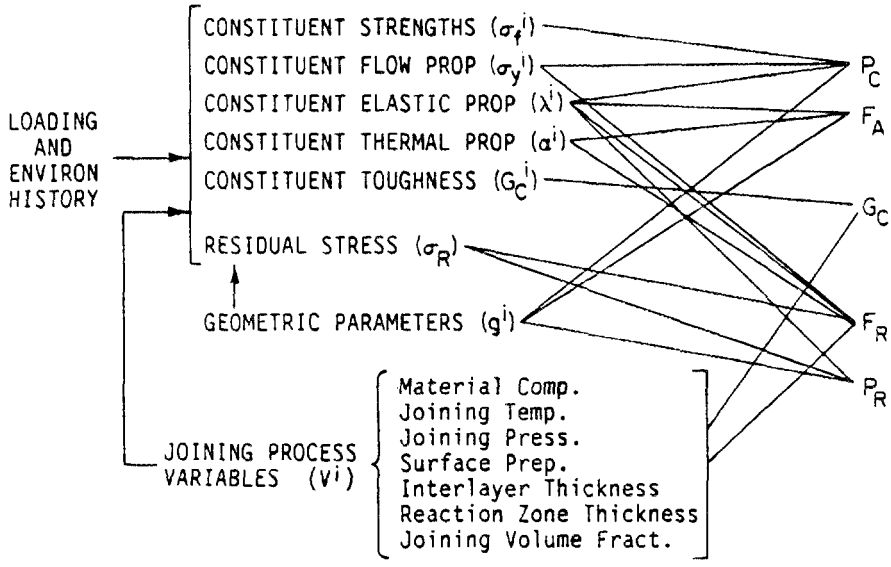

FIGURE 2. RELATION OF CONSTITUENT PROPERTIES, RESIDUAL STRESS, GEOMETRIC PARAMETERS AND JOINING PROCESS VARIABLES WITH DESIGN PARAMETERS.

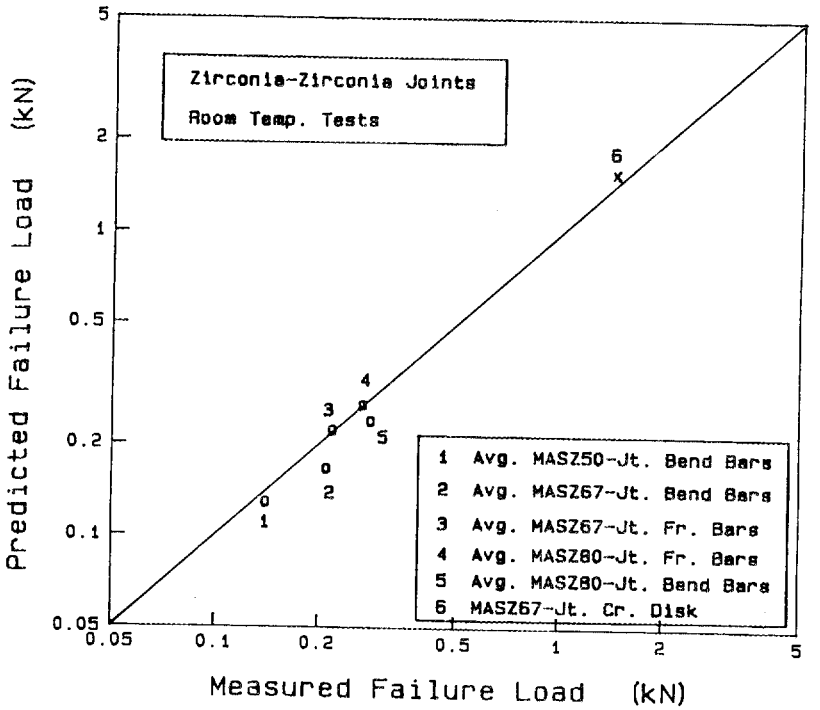

FIGURE 3. COMPARISON OF JAD MODEL PREDICTIONS AND EXPERIMENTAL DATA.

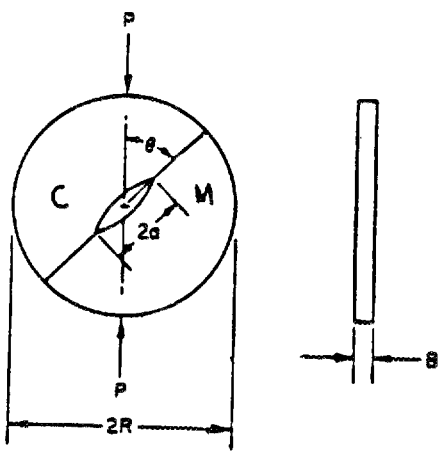

FIGURE 4. THE BIMATERIAL DISK SPECIMEN.

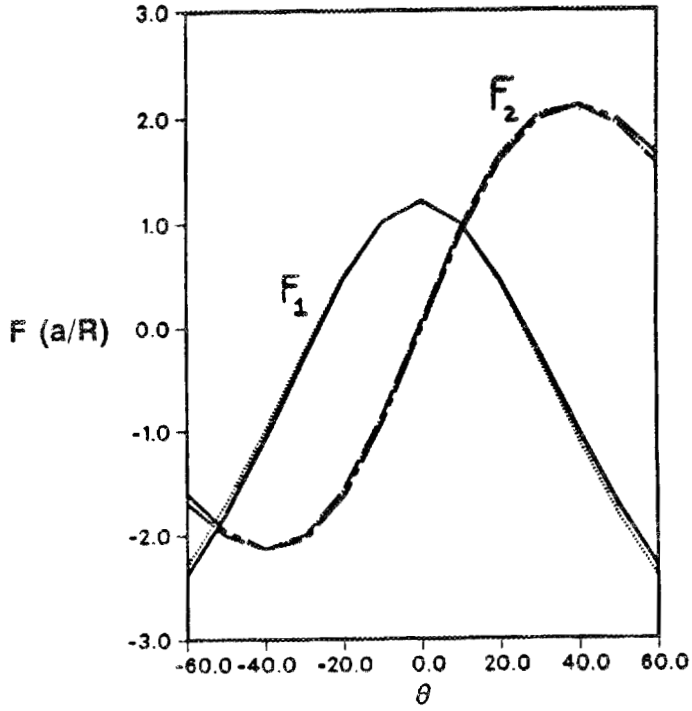

FIGURE 5. FINITE ELEMENT RESULTS OF GEOMETRY FACTORS F_1 AND F_2 AT THE TWO CRACK TIPS FOR BIMATERIAL DISK WITH a/R = 0.333.

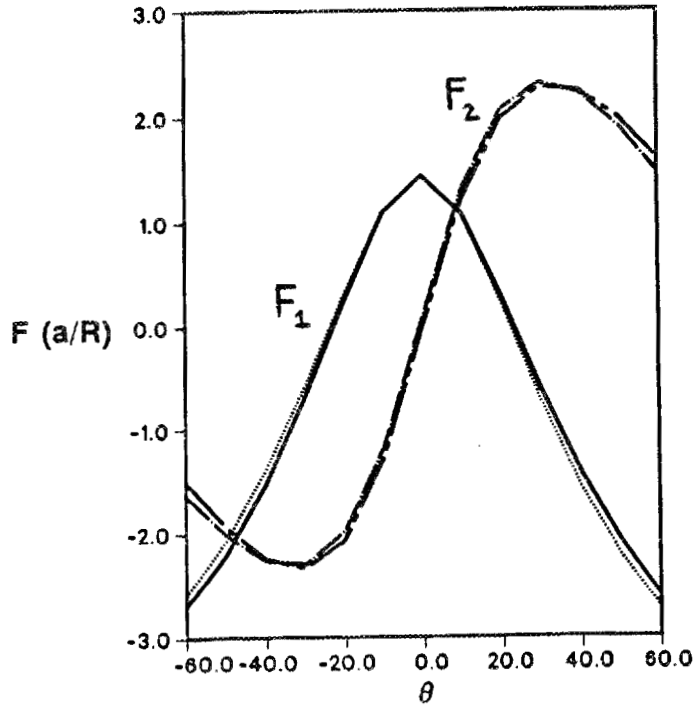

FIGURE 6. FINITE ELEMENT RESULTS FOR BIMATERIAL DISK WITH a/R = 0.5.

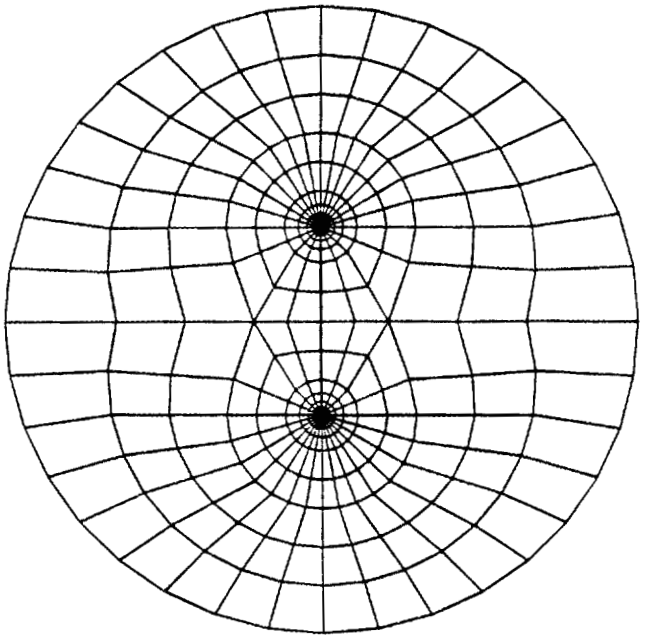

FIGURE 7. FE MESH FOR a/R = 0.333.

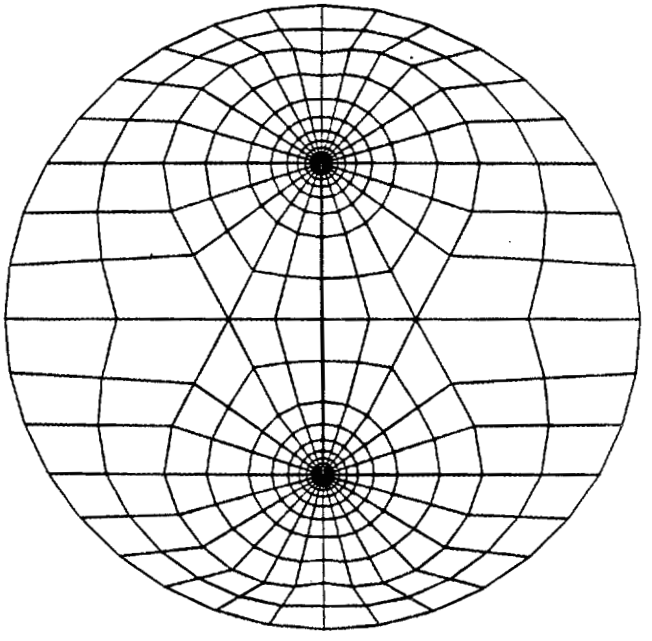

FIGURE 8. FE MODEL FOR a/R = 0.5.

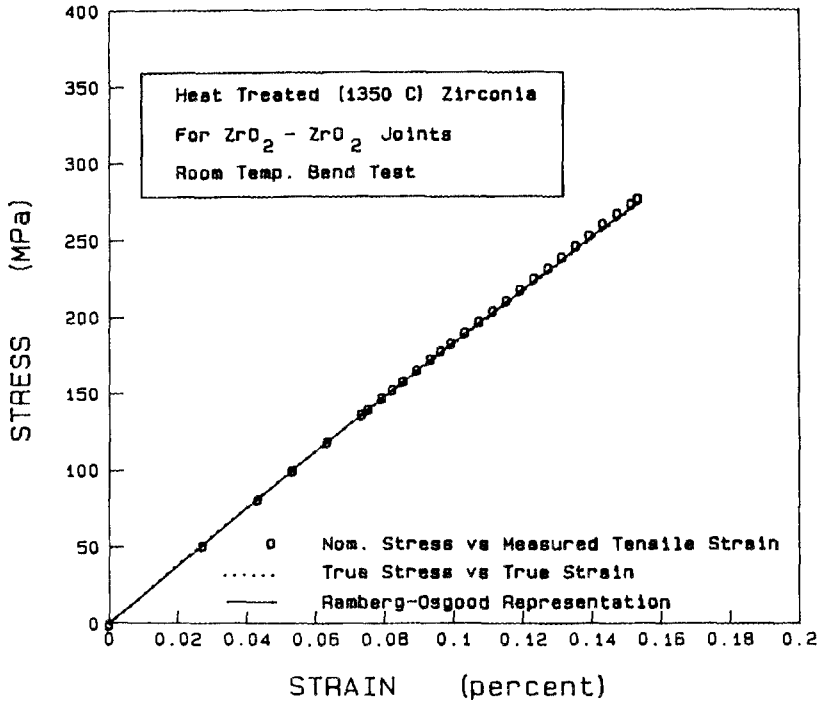

FIGURE 9. STRESS-STRAIN FOR PARTIALLY STABILIZED ZIRCONIA (PSZ), HEAT-TREATED AT 1350 c FOR 1-HOUR AND SLOWLY COOLED TO ROOM TEMPERATURE.

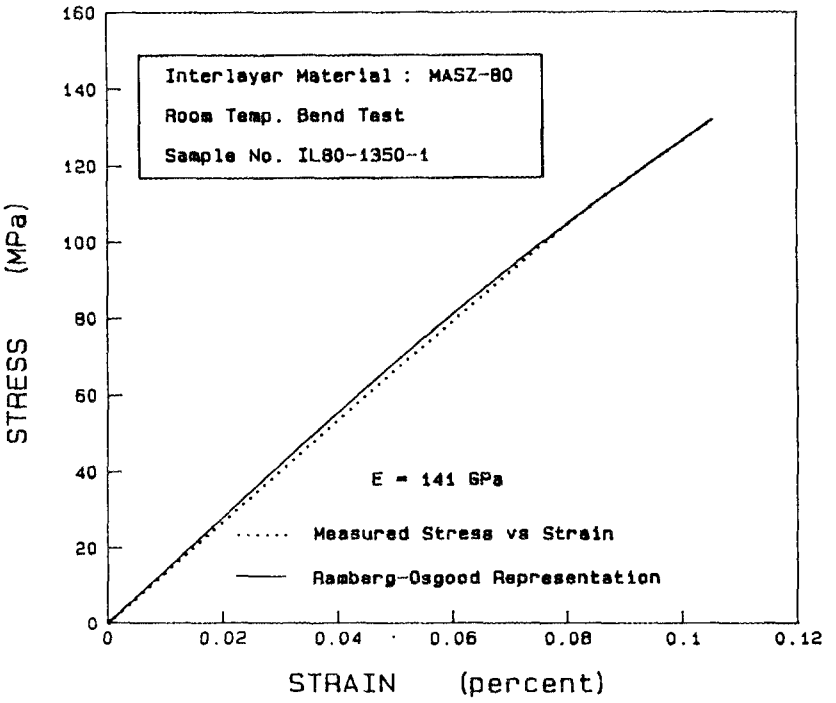

FIGURE 10. STRESS-STRAIN CURVE FOR MASZ-80 INTERLAYER MATERIAL THAT WAS USED FOR MAKING THE PSZ-PSZ JOINTS.

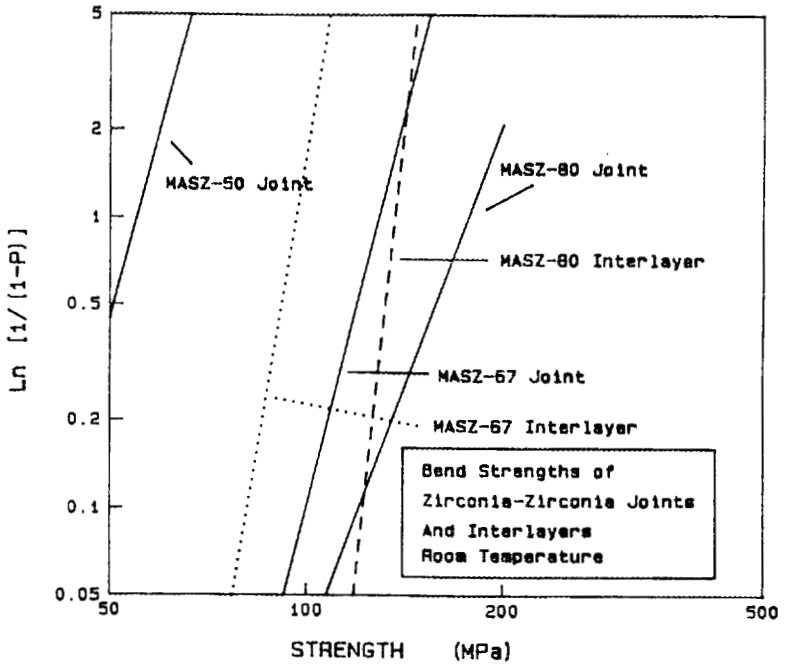

FIGURE 11. WEIBULL PLOT OF BEND STRENGTHS FOR PSZ-PSZ JOINTS AND INTERLAYER MATERIALS.

MASZ-67 joints refers to a PSZ-PSZ joint, fabricated using MASZ-67 interlayer. Similarly, MASZ-80 Joint refers to a PSZ-PSZ joint, fabricated using MASZ-80 interlayer. Note that the Weibull plot for a joint is shifted to the right of the corresponding interlayer.

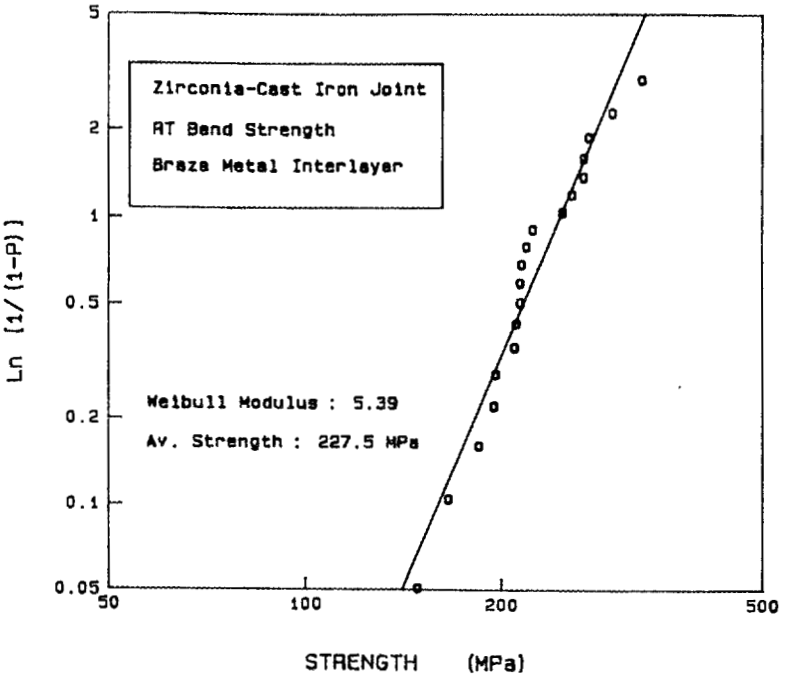

FIGURE 12. WEIBULL PLOT OF BEND STRENGTHS FOR PSZ-CAST IRON JOINTS

The plot includes data from three different joined billets.

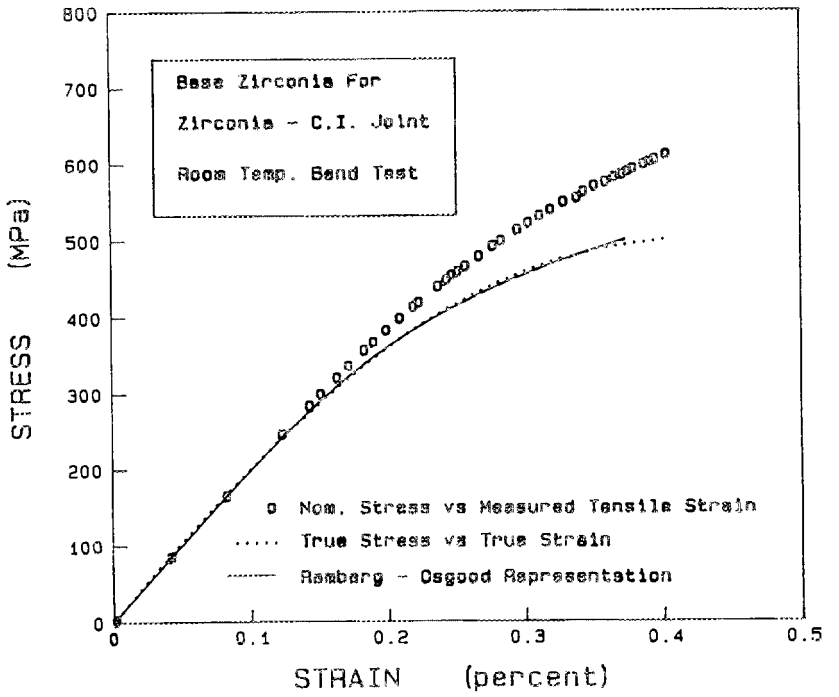

FIGURE 13. STRESS-STRAIN CURVE FOR BASE PSZ FOR THE PSZ-CAST IRON JOINT.

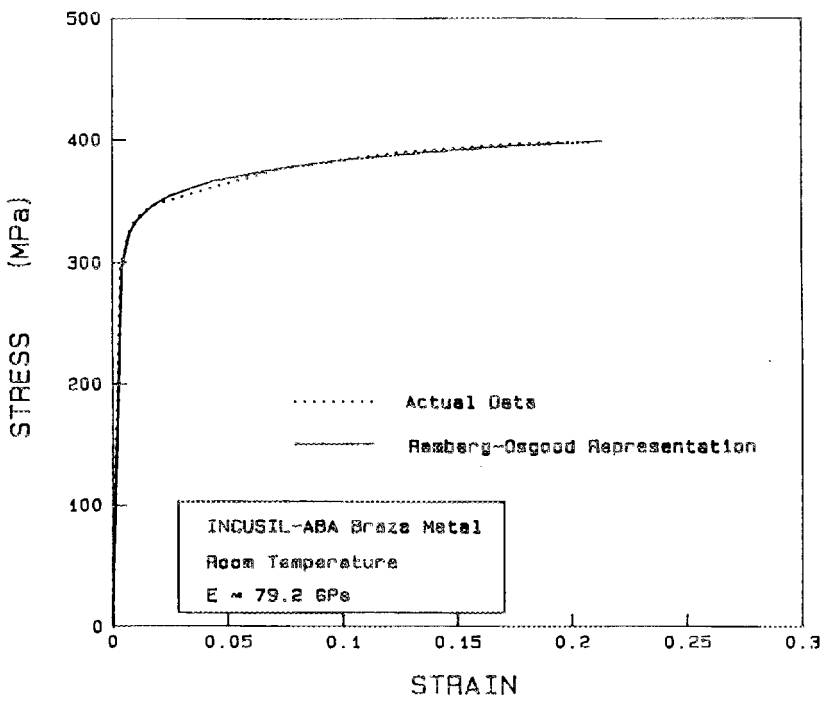

FIGURE 14. STRESS-STRAIN CURVE FOR THE INCUSIL-ABA BRAZE METAL, USED FOR FABRICATING PSZ-CAST IRON JOINTS.

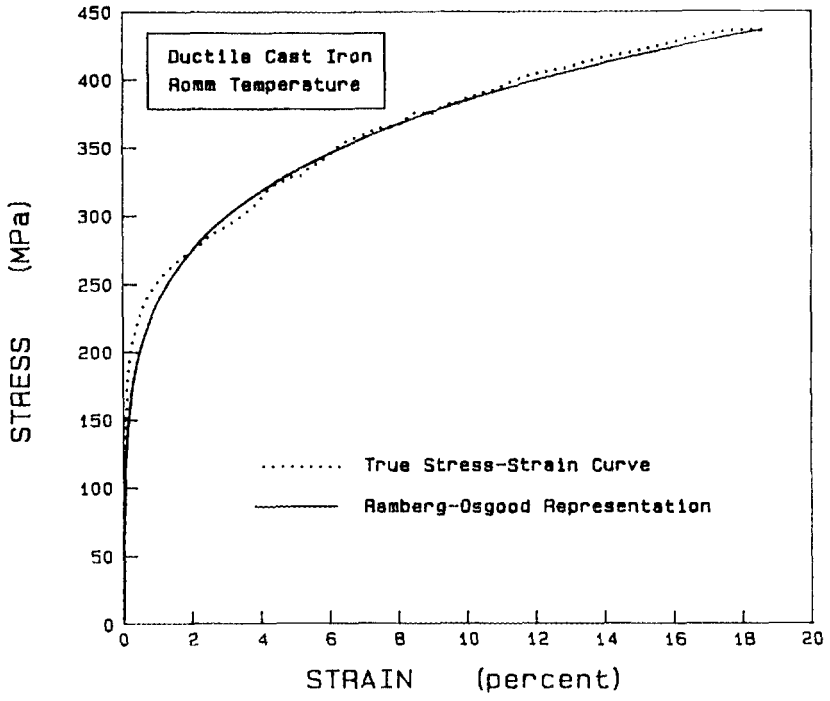

FIGURE 15. STRESS-STRAIN CURVE FOR CAST IRON, USED FOR THE PSZ-CAST IRON JOINTS.

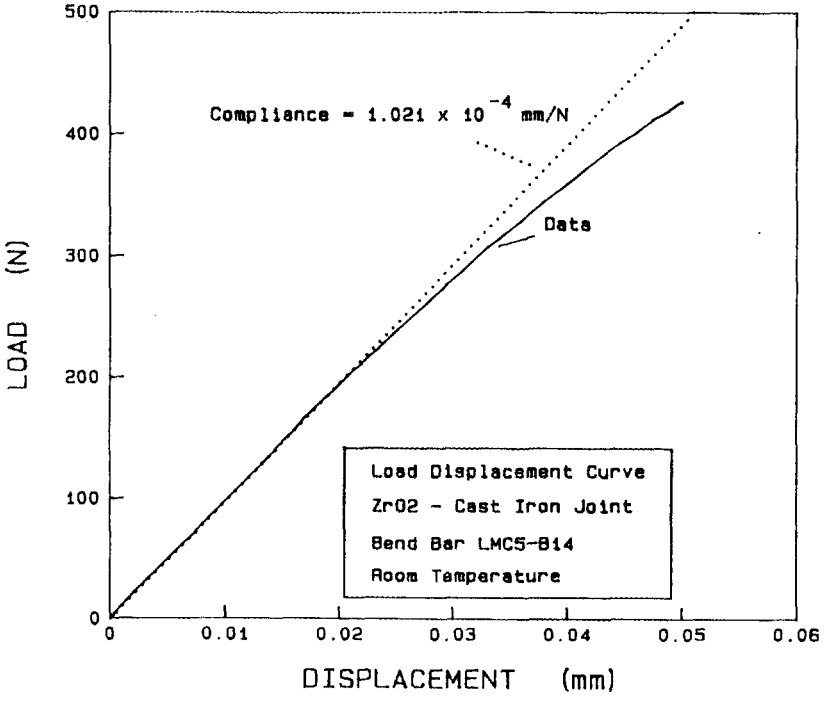

FIGURE 16. TYPICAL LOAD-DISPLACEMENT PLOT FOR A PSZ-CAST IRON JOINT.

The bend bar was size of 0.2001-in width, 0.0985-in thickness; 4-point bend test, with inner span of 0.75-inch and outer span of 1.25-inch. The joint was at the center of the 1.5-inch long bend bar.

TABLE 1. COMPLETED TEST MATRIX FOR MECHANICAL TESTS PERFORMED AT ROOM TEMPERATURE.

Geometry	Base ZrO2 For ZrO2/CI Joint	Cast Iron	Braze Metal	ZrO2/Cast Iron Joint	MASZ-67 Interlayer	MASZ-80 Interlayer	MASZ-50 Interlayer
Bend Bar	4	2	3	27	6	3	2
Fracture Bar	2	-	-	5	1	1	1
Uncracked Disk	-	-	-	3	-	-	-
Cracked Disk	1	-	-	6	-	-	-

Geometry	ZrO2-MASZ67-ZrO2 Joint	ZrO2-MASZ80-ZrO2 Joint	ZrO2-MASZ50-ZrO2 Joint	ZrO2-MASZ67(1400C) ZrO2 Joint	ZrO2-MASZ80(1400C) ZrO2 Joint	Heat Treated ZrO2 For ZrO2/ZrO2 Joints
Bend Bar	21	10	6	6	6	10
Fracture Bar	5	3	-	2	2	2
Uncracked Disk	2	1	-	-	-	-
Cracked Disk	8	2	-	-	-	-

ZrO2-MASZ67-ZrO2 Joint implies a zirconia-zirconia joint fabricated at 1350 C, using MASZ-67 Interlayer. Similar nomenclature is used for joints with MASZ-50 and MASZ-80 Interlayers. ZrO2-MASZ67(1400C)-ZrO2 Joint implies a zirconia-zirconia joint fabricated at 1400 C, using MASZ-67 Interlayer. Similar nomenclature is used for the joint with MASZ-80 Interlayer. Heat Treated Zirconia refers to the zirconia that received a 1350 C heat treatment, similar to the thermal cycle involved in the fabrication of zirconia-zirconia joints.

Analytical and Experimental Evaluation of Joining Silicon Carbide to Silicon Carbide and Silicon Nitride to Silicon Nitride for Advanced Heat Engine Applications

G. A. Rossi, C. H. Bates, M. R. Foley, G. J. Sundberg, and F. J. Wu (Norton Company)

OBJECTIVE/SCOPE

The purpose of this program is to develop techniques for producing reliable ceramic-ceramic joints and analytical modeling to predict the performance of the joints under a variety of environmental and mechanical leading conditions including high temperature, oxidizing atmospheres. The ceramic materials under consideration are silicon nitride and silicon carbide. The joining approach for silicon nitride is based on the ASEA hot isostatic pressing process while the plan for silicon carbide is to co-sinter green forms together. These joining methods were selected to produce joints which exhibit the minimum possible deviation in properties from those of the parent ceramic materials. Analytical models will be experimentally verified by measurements on experimental size and scale-up joints produced as part of this work.

Background

Because of their strength, oxidation resistance, and other desirable high temperature properties, silicon nitride and silicon carbide are under extensive study for use in advanced gas turbine and internal combustion engines. In both engine types there are requirements for joining the ceramics to themselves, other ceramics, and various engineering alloys. Existing bonding methods lack the high temperature capabilities required for use in advanced heat engines. Further, analytical modeling techniques to predict joint reliability and performance have not been developed. These technical needs have prevented consideration of economically fabricating large, complex ceramic engine components from smaller, less complicated segments. The current program will address these issues for silicon nitride to silicon nitride and silicon carbide to silicon carbide joints.

TECHNICAL PROGRESS

1. Sample preparation for mechanical testing

To satisfy the requirements of Task 1 (Characterization) three types of test samples are needed, MOR bars, "dog bone" creep specimens (NBS type), and cylindrical tensile specimens (ORNL/DOE type) for stress/strain measurement.

At the end of this reporting period all MOR bars had been machined, both joined and controls. Sufficient number of joined billets of Si_3N_4 and SiC, necessary for machining "dog bone" creep samples, were made and cut into slices of appropriate thickness. Each slice, containing the joint, will be machined into a creep specimen. As far as the cylindrical tensile specimens are concerned, about 70% of the joined SiC billets and 30% of the joined Si_3N_4 billets have been successfully fired and await machining. A last decision concerning the most appropriate machine shop, based on quality and cost considerations, will be made in October.

2. Mechanical Testing

By the end of September all fast fracture date for both Si_3N_4 and SiC had been obtained. For Si_3N_4, the joined MOR bars were tested at 25°C, 750°C and 1370°C. The control (no join) MOR bars were tested at 25°C and 1370°C. For SiC, the joined MOR bars were tested at 25°C, 750°C and 1530°C, whereas the controls were tested at 25°C and 1530°C. All bars were broken using 5 and 40 mm spans, with a cross-head speed of 0.5 mm/min. The 5 mm inner span was chosen, instead of the regular 20 mm for MIL 1942 B, in order to increase the probability of failure at the joint.

Table 1 reports the results obtained.

Thermal cycling of Si_3N_4 and SiC MOR bars is being done at AMTL in Watertown, MA and is not complete yet. The thermally cycled bars will be broken at room temperature.

Cyclic fatigue testing at room temperature on joined and control MOR bars of the two materials is expected to start in October. High temperature oxidation of joined and control MOR bars for both materials is also expected to start in October.

3. Analytical Modeling

3.1 Fast Fracture: Statistical analysis of fast fracture data has been completed for joined and control MOR. Results are presented in Table 1 and Weibull plots for the two materials in Figures 1 and 2. In general, joint failures are scarce but joined samples give lower MOR and average strengths than control samples for both materials. The statistical significance of the differences in their mean strength was calculated using the t-test distribution of means. Results are summarized in Table 2. At room temperature, the statistical analysis indicate that the joined samples have different flaw distribution properties from the control samples. Confidence percentages are

TABLE 1: FAST FRACTURE STATISTICAL DATA

MATERIAL	TEMP. °C	σ_{ave} Ksi (MPa)	STD. DEV. Ksi (MPa)	σ_{MOR} Ksi (MPa)	WEIBULL MODULUS m	NO. SAMPLES
NCX-5100 Joined	Room T.	136.4 (940.7)	9.0 (61.8)	140.5 (968.7)	17.0	45
	750	98.2 (676.8)	15.3 (105.4)	104.5 (720.8)	7.4	30
	1370	76.3 (526.3)	7.8 (54.1)	79.7 (549.8)	11.3	45
NCX-5100 Control	Room T.	140.2 (966.7)	9.1 (62.9)	144.5 (996.5)	15.8	30
	1370	82.6 (569.6)	7.4 (50.9)	85.7 (590.6)	16.2	30
NCX-4500 Joined	Room T.	50.9 (351.2)	8.3 (57.2)	54.4 (374.9)	6.8	45
	750	49.0 (338.1)	6.6 (45.3)	51.8 (356.9)	9.2	30
	1530	49.0 (337.6)	8.9 (61.2)	52.7 (363.4)	5.4	45
NCX-4500 Control	Room T.	57.6 (397.2)	9.3 (64.2)	61.4 (423.7)	7.2	30
	1530	50.3 (346.7)	8.8 (60.9)	54.0 (372.4)	6.2	30

TABLE 2: CONFIDENCE LEVEL OF DISIMILARITY BETWEEN JOINED AND CONTROL SAMPLES

NCX-5100	Room Temp.	91.93%
	1370°C	99.91%
NCX-4500	Room Temp.	99.82%
	1530°C	47.22%

99.93% and 99.82% for NCX-5100 and NCX-4500 respectively. At 1370°C NCX-5100 experiences a 40% degradation from room temperature in average strength on both joined and control samples. On the other hand, at 1530°C NCX-4500 control samples show a small variation (weakness) in strength from their room temperature strengths while joined samples appeared to remain unaffected.

Modeling of these materials will be performed by assuming that the joined and control samples have different fast fracture characteristics as inherent material properties differences until further microstructural characterization is done. Also, strength data will be used to model and understand the effect of different fracture criteria on the statistical predictions. This study is still underway. Additional fractographic analysis will be pursued to complete such study.

3.2 Creep Modeling: Check models, for which closed form solutions are known, are being developed to verify that the creep programs created predict simple creep strain behavior. Current available creep data is scarce and therefore additional verification runs will be done with the creep characterization data of our joints.

STATUS OF MILESTONES

A six month extension of this contract was granted by ORNL, due to the problems encountered in joining SiC to SiC and to the expected difficulties in fabricating and machining the cylindrical tensile specimens. In addition, some revisions of the original Statement of Work were proposed to, and accepted by, the ORNL manager. Consequently, the milestone dates have been shifted as shown below:

1.	Complete characterization testing	March	1990
2.	Complete testing, model validation 2 cm^2 joint	May	1990
3.	Complete 20 cm^2 joint experimental plan	June	1990
4.	Complete model development	June	1990
5.	Complete testing, model validation 20 cm^2 joint	Aug.	1990
6.	Delivery of final report	Oct.	1990

PUBLICATIONS

None

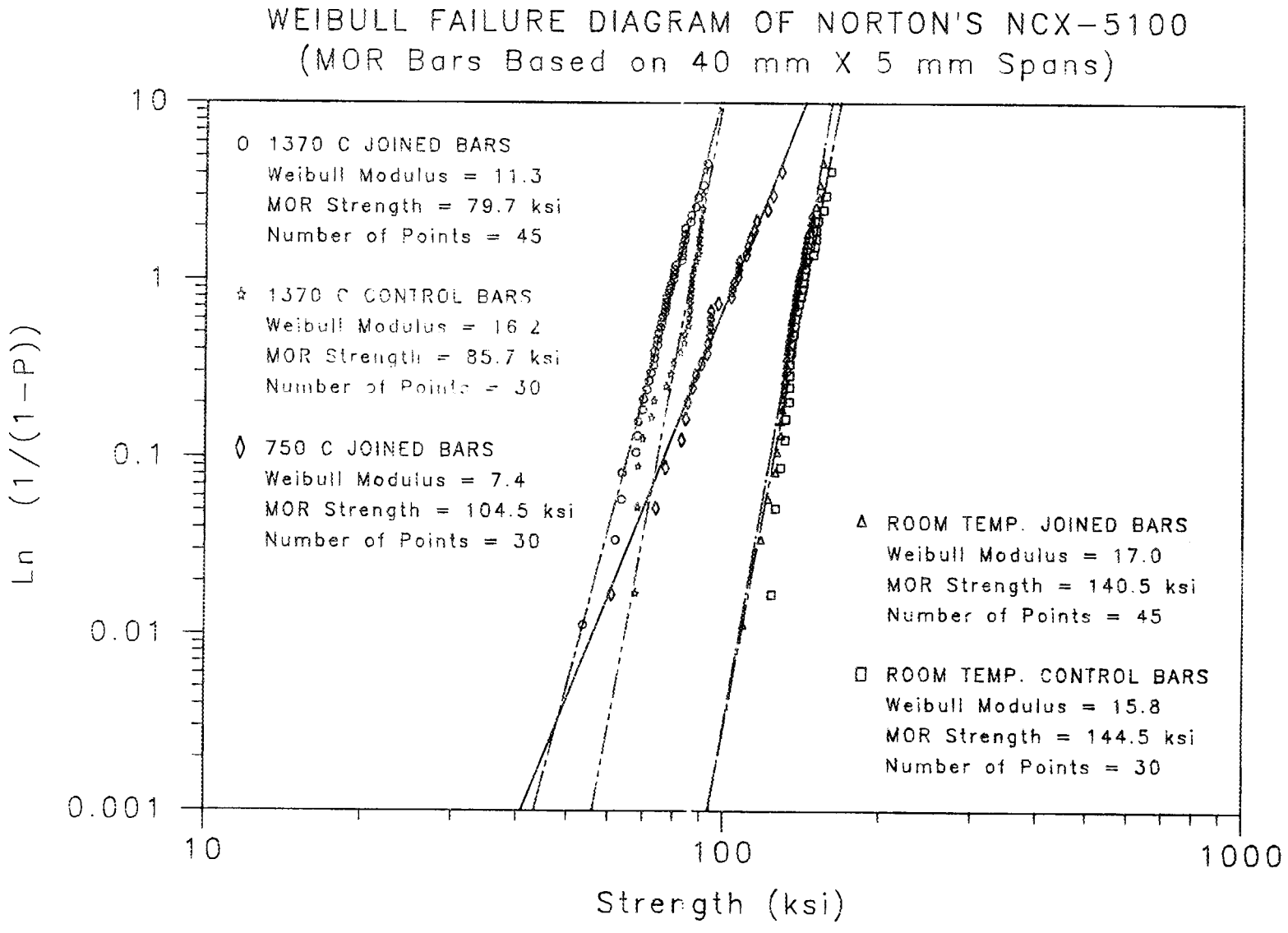
WEIBULL FAILURE DIAGRAM OF NORTON'S NCX-5100
(MOR Bars Based on 40 mm X 5 mm Spans)
O 1370 C JOINED BARS
Weibull Modulus = 11.3
MOR Strength = 79.7 ksi
Number of Points = 45
☆ 1370 C CONTROL BARS
Weibull Modulus = 16.2
MOR Strength = 85.7 ksi
Number of Points = 30
◊ 750 C JOINED BARS
Weibull Modulus = 7.4
MOR Strength = 104.5 ksi
Number of Points = 30
Δ ROOM TEMP. JOINED BARS
Weibull Modulus = 17.0
MOR Strength = 140.5 ksi
Number of Points = 45
□ ROOM TEMP. CONTROL BARS
Weibull Modulus = 15.8
MOR Strength = 144.5 ksi
Number of Points = 30
Ln (1/(1-P))
10
1
0.1
0.01
0.001
10
100
1000
Strength (ksi)

FIGURE 1

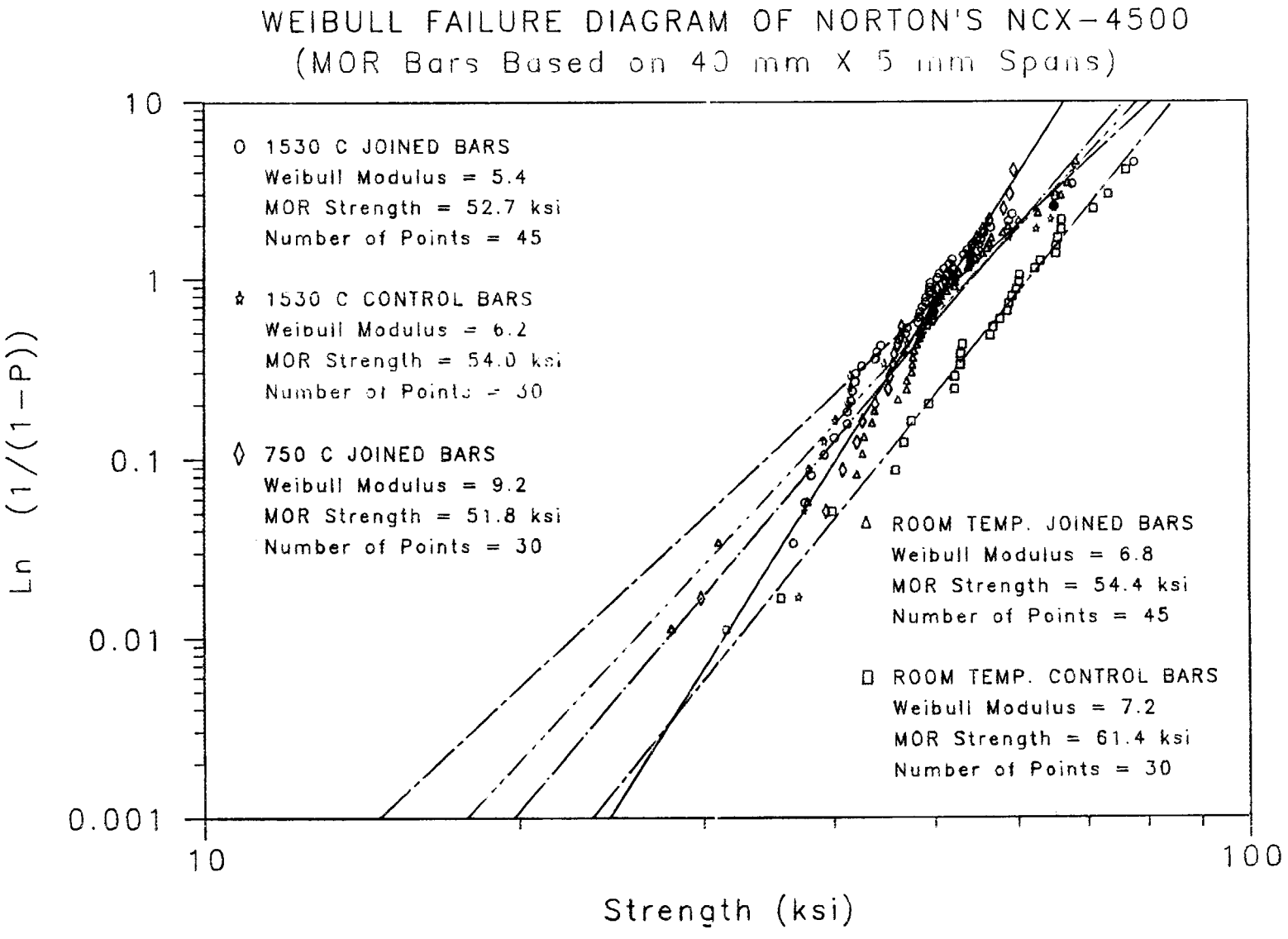
WEIBULL FAILURE DIAGRAM OF NORTON'S NCX-4500
(MOR Bars Based on 40 mm X 5 mm Spans)
O 1530 C JOINED BARS
Weibull Modulus = 5.4
MOR Strength = 52.7 ksi
Number of Points = 45
☆ 1530 C CONTROL BARS
Weibull Modulus = 6.2
MOR Strength = 54.0 ksi
Number of Points = 30
◊ 750 C JOINED BARS
Weibull Modulus = 9.2
MOR Strength = 51.8 ksi
Number of Points = 30
Δ ROOM TEMP. JOINED BARS
Weibull Modulus = 6.8
MOR Strength = 54.4 ksi
Number of Points = 45
□ ROOM TEMP. CONTROL BARS
Weibull Modulus = 7.2
MOR Strength = 61.4 ksi
Number of Points = 30
Ln (1/(1-P))
10
1
0.1
0.01
0.001
10
100
Strength (ksi)

FIGURE 2

2.0 MATERIALS DESIGN METHODOLOGY

INTRODUCTION

This portion of the project is identified as project element 2 within the work breakdown structure (WBS). It contains three subelements: (1) Three-Dimensional Modeling, (2) Contact Interfaces, and (3) New Concepts. The subelements include macromodeling and micromodeling of ceramic microstructures, properties of static and dynamic interfaces between ceramics and between ceramics and alloys, and advanced statistical and design approaches for describing mechanical behavior and for employing ceramics in structural design.

The major objectives of research in Materials Design Methodology elements include determining analytical techniques for predicting structural ceramic mechanical behavior from mechanical properties and microstructure, tribological behavior at high temperatures, and improved methods for describing the fracture statistics of structural ceramics. Success in meeting these objectives will provide U.S. companies with methods for optimizing mechanical properties through microstructural control, for predicting and controlling interfacial bonding and minimizing interfacial friction, and for developing a properly descriptive statistical data base for their structural ceramics.

2.1 MODELING

2.1.1 Modeling

Microstructural Modeling of Cracks

J.A.M. Boulet (University of Tennessee, Knoxville)

Objective/scope

The goal of the study is to develop mathematical procedures by which existing design methodology for brittle fracture could accurately account for the influence of protrusion interference on fracture of cracks with realistic geometry under arbitrary stress states. To predict likelihood of fracture in the presence of protrusion interference, a simulation will be developed. The simulation will be based on a three-dimensional model of cracks with realistic geometry under arbitrary stresses.

Technical progress

The system to be analyzed in the current phase of the project is a single, irregularly shaped, three-dimensional crack, initially closed, in an infinite medium subjected to remote, arbitrarily oriented, triaxial stress.

After reviewing various methods for solving three-dimensional elasticity problems, we concluded that only the finite element method (FEM) and the boundary element method (BEM) are sufficiently general for solving the problem at hand. Because it requires discretization of only the crack surface, the BEM should be more efficient than the FEM.

We have chosen a method for modeling the crack geometry. The crack surfaces will be represented as collections of triangular facets. Two methods of defining the facets will be employed. The first and simpler method will be used for development and evaluation of the numerical model. The second, more complicated method, will be used to represent realistic crack geometries in later stages of the project.

In the first method, the crack boundary will be represented as a many-sided regular polygon. The crack surfaces will then be constructed in four steps. First, a set of polygons geometrically similar to the crack boundary will be nested (uniformly spaced) inside the crack boundary. Second, the regions between neighboring polygons will be tessellated with identical isosceles triangles. Third, at selected positions on the crack, a tetrahedral protrusion will replace the triangle on one crack face while a congruent tetrahedral depression will replace the corresponding triangle on the other crack face. The variable parameters of this method are the number and positions of the protrusion/depression pairs, their heights, and their obliqueness.

The method described above is probably not adequate for representing highly irregular crack shapes. In the second method, we will allow the crack boundary and the polygons nested inside it to be irregular, and allow composite protrusion/depression to be built on multiple triangles. If necessary, we may allow the crack boundary to be nonplanar.

The kinematics of interference for two neighboring surfaces has been analyzed. When loads are applied and the regions bounded by the surfaces deform, two conditions must be met for the surfaces to interfere. One of these is that the surfaces must first come in contact with each other. The other condition is a constraint on the relative displacement vector for any two points (one on each surface) in contact. This constraint may be stated as follows. Let the contact point on one of the surfaces be designated by "A" and the contact point on the other surface by "B." Let the relative displacement vector be defined as the displacement of A minus the displacement of B. If the direction of the relative displacement vector is toward the interior of the region whose bounding surface contains B, then the two surfaces interfere. Mathematical representations of these two conditions have been derived and numerical algorithms for their implementation are being developed.

BEM computer programs that solve both two-dimensional and three-dimensional crack-face interference problems are under development.

Status of milestones

Work is on schedule.

2.2 CONTACT INTERFACES

2.2.1 Static Interfaces

Elastic Properties and Adherence of Thin Films and Coatings
D. L. Joslin (The University of Tennessee)

Objective/Scope

The objective of this research is the examination of the effects of ion bombardment on the structure of thin ceramic films on ceramic substrates. The material combinations will include oxide films that have (a) no solid solubility, (b) limited solid solubility, and (c) complete solid solubility with the substrate material (also an oxide). Techniques for determination of elastic and plastic properties of thin films or coatings on ceramic substrates and for the determination of the strength of the bond between the film and substrate, which are currently being developed, will be used to determine the hardness, elastic modulus, and adherence of each material combination. The main testing techniques will be the ultra-low load micro-indentation tester (Nanoindenter) and thermal cycling tests.

Technical Highlights

During this report period, several computer simulations of implantation processes were run to determine the implantation paramaters necessary for the mixing experiments planned for this research project. They include (1) oxygen into a chromium layer on sapphire, and (2) chromium into a Ti_xO_y/Al_2O_3 multilayered structure on silicon.

For (1), it is desired that the implanted oxygen come to rest at the Cr/Al_2O_3 interface. For a 100 nm-thick chromium film, the energy range for oxygen implantation at the interface is approximately 80 KeV (as calculated by TRIM[1]). The chromium layers deposited for system (1) were analyzed using Rutherford Backscattering Spectroscopy (RBS). From the analysis, it is known that the Cr layer already contains a small amount of oxide (approximately 15%) which may affect the implantation. These samples are now awaiting implantation. After the specimens are implanted, they will be examined using Rutherford Backscattering Spectroscopy (RBS) and Transmission Electron Microscopy (TEM) to determine whether mixing and/or compound formation has occurred.

For (2), it is desired that the implanted chromium come to rest at a position far beyond the first four layers of the specimen (distance greater than 100 nm). The energy required for this is approximately 350 KeV, as calculated by TRIM. A Ti_xO_y/Al_2O_3 multilayered structure on silicon was obtained from R. McKee for implantation and study. The sample was made up on 38 repetitions of alternating layers of crystalline Ti_xO_y and amorphous Al_2O_3. In the implanted area, the thickness of each layer was approximately 190 nm. The sample was implanted with 350 KeV Cr^{2+} at room temperature. Although TEM examination prior to implantation and after implantation showed the presence of the multilayered structure, RBS did not detect it either before or after implantation. From this sample, some evidence of mixing could be discerned. Analysis of a second sample, similar to this sample, is in progress.

Communications/Visits/Travel

None

Problems Encountered

None

Publications

None

2.2.2 Dynamic Interfaces

Studies of Dynamic Contact of Ceramics and Alloys for Advanced Heat Engines

K. F. Dufrane and P. A. Gaydos (Battelle)

Objective/Scope

The objective of the program is to develop an understanding of the friction and wear processes of ceramic interfaces based on experimental data. The supporting experiments are to be conducted at temperatures to 650°C under reciprocating sliding conditions reproducing the loads, speeds, and environment of the ring/cylinder interface of advanced engines. The test specimens are to be carefully characterized before and after testing to provide detailed input to the model. The results are intended to provide the basis for identifying solutions to the tribology problems limiting the development of these engines.

Technical progress

Apparatus

The apparatus developed for this program uses specimens of a simple flat-on-flat geometry, which facilitates specimen procurement, finishing, and testing. The apparatus reproduces the important operating conditions of the piston/ring interface of advanced engines. The specimen configuration and loading is shown in Figure 1. The contact surface of the ring specimen is 3.2 × 19 mm. A crown with a 32 mm radius is ground on the ring specimen to insure uniform contact. The ring specimen holders are pivoted at their centers to provide self-alignment. A chamber surrounding the specimens is used to control the atmosphere and contains heating elements to control the temperature. The exhaust from a 4500 watt diesel engine is heated to the specimen temperature and passed through the chamber to provide an atmosphere similar to that of actual diesel engine service. A summary of the testing conditions is presented in Table 1.

Materials

Rings and Cylinder Materials

The compositions of the various materials used in the study are presented in Table 2. A variety of monolithic and coating materials were selected to represent various chemical compositions and materials with previously demonstrated successful sliding performance.

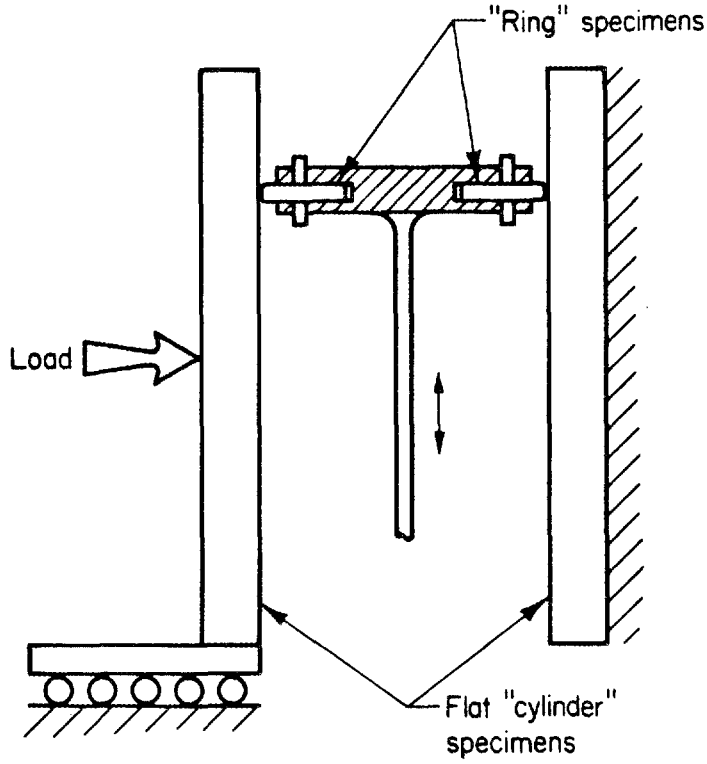

Figure 1. Test specimen configuration and loading

TABLE 1. SUMMARY OF TESTING CONDITIONS

Sliding Contact:	Dual flat-on-flat
"Cylinder" Specimens:	12.7 x 32 x 127 mm
"Ring" Specimens:	3.2 x 19 x 19 mm
"Ring" crown radius:	32 mm
Motion:	Reciprocating, 108 mm stroke
Reciprocating Speed:	500 to 1500 rpm
Average Specimen Speed:	1.8 to 5.4 m/s
Load:	to 950 N
Ring Loading:	to 50 N/mm
Atmosphere:	Diesel exhaust or other gases
Measurements:	Friction and wear (after test)

TABLE 2. MATERIALS FOR EVALUATION

Monolithic Ceramics	Coatings
YPSZ	Tribaloy 400
MPSZ	METCO 130 (13 TiO_2, 87 Al_2O_3)
ATTZ	METCO 501 (30 Mo, 12 Cr, bal Ni)
α SiC	Plasmalloy 312M ($MoSi_2$)
SiC/Al_2O_3	Cr_2O_3 (5 Cr, bal Cr_2O_3)
Sialon	Jet-Kote WC (12 Co, bal WC)
K162B (TiC - Ni/Mo)	Cr (Electroplated)
Si_3N_4	PS212 (Cr_3C_2 + BaF_2/CaF_2 + Ag)
	VR73 (WC/TaC/TiC/Co)
	VA 20 (WC/TaC/TiC/Ni)
	CA 815 (Cr_3C_2/Ni)
	Mo
	Duplex (WC and Mo)
	Ion Implanted (N in Cr_2O_3)

Wear Experiments

Previous Wear Results

In the first phase of the study the need for lubrication at the ring/cylinder interface was established by the high friction coefficients and wear rates measured during dry sliding of monolithic ceramics and ceramic coatings. With lubrication, the wear rates of ceramic coatings such as Cr_2O_3 and WC tested at 260°C were found to approach those measured in heavy duty truck engines with conventional ring/cylinder materials. With the need for lubrication, the maximum operating temperature with ceramics was found to be limited by the availability of suitable lubricants. A summary of the wear and friction data obtained under a variety of conditions is shown in Table 3.

Solid Lubricant Evaluation

Four different lubricants were obtained for evaluation. These solid lubricants were to be used as wipers to supply the stationary specimens with a film of dry lubricant. Solid lubricants of sufficient strength were also to be formed into actual ring specimens and run alone to obtain baseline wear rates. The experiments were expected to determine whether such films can control the wear on the ring specimens and whether the wipers would have a useful life at the needed transfer rates.

Efforts to modify Battelle's engine rig to accept spring loaded solid lubricants samples were unsuccessful. The geometry of the test ring constrains the total thickness of ring and lubricant wiper to 1/4 inch. The possible configurations of the ring/wiper combination were either a stacked pair of 1/8 inch specimens or an 1/8 inch wiper sandwiched between two 1/16 inch ring specimens. With the stacked configuration, the wiper was not supported sufficiently on one side and would break off due to bending moments. The sandwiched configuration supported the wiper sufficiently but left too little ring area available for a sound wear coating.

While no tests using a ceramic ring and lubricant wiper were run, evaluation of two self-lubricating materials was conducted during this reporting period. An MoS_2-metal (Molalloy from Pure Carbon) and a WeS_2/GaIn solid lubricant compact (D. J. Boes) were machined into ring specimens and run dry. All tests were run at room temperature to get a baseline comparison. The Molalloy used in this application did not appear to be providing enough lubricant to form a usable film for itself, much less an additional ring. Friction started high and increased throughout the one hour test, and loud "squealing" occurred. The Boes compact, on the other hand, ran as it was being lubricated with a liquid lubricant. The friction coefficient was actually better than many tests using liquid lubricant and become lower as the loading increased. The wear coefficient was also quite good for a self-lubricating material. Table 4 presents the results from the tests. Since the room temperature performance of the solid lubricant compact was encouraging, the evaluations were continued.

Tests were performed at higher temperatures to see if the compact's low friction and relatively low wear properties evident at room temperature remained as the temperature increased. Table 5 presents the high temperature data along with data from a typical room temperature test run under the similar load and speed conditions. A general reduction in the friction coefficient and increased wear rates are seen as the temperature increases. A softening of the material at higher temperatures or oxide

TABLE 3. COMPARISON OF APPROXIMATE RING WEAR COEFFICIENTS

Ring Material	Cylinder Material	Lubricant	Temperature, C	Ring Loading, N/mm	Friction Coefficient	Hardness Used in Calculation, kg/mm^2	Average Ring Wear Coefficient	
							Dimensionless	$mm^3/N\text{-}m$
Cr	Cast Iron	SAE 30	100	17.5	--	975	5×10^{-9} [a]	2×10^{-10}
Cr	Cast Iron	SDL-1	100	12.3	0.03 - 0.04	975	8×10^{-8}	3×10^{-9}
WC	SiC/Al_2O_3	SDL-1	260	14.5	0.04 - 0.09	2080	3×10^{-7}	5×10^{-9}
SiC/Al_2O_3 [b]	Cr_2O_3	SDL-1	260	12.3	0.03 - 0.08	2000	5×10^{-7}	8×10^{-9}
ESA	Cr_2O_3	SDL-1	260	12.3	0.03 - 0.06	2200	6×10^{-7}	9×10^{-9}
WC	Cr_2O_3	SDL-1	260	13.9	0.03 - 0.08	2080	6×10^{-7}	1×10^{-6}
Cr_2O_3 [c]	Cr_2O_3 [c]	SDL-1	260	12.3	0.04 - 0.08	2000	1×10^{-6}	2×10^{-8}
Cr_2O_3	Cr_2O_3	SDL-1	260	13.4	0.05 - 0.08	2000	1×10^{-6}	2×10^{-8}
VR73	Cr_2O_3	SDL-1	260	12.3	0.05 - 0.09	2200	1×10^{-6}	2×10^{-8}
Cr_2O_3	SiC/Al_2O_3	SDL-1	260	15.7	0.04 - 0.08	2000	1×10^{-6}	2×10^{-8}
Si_3N_4	Si_3N_4 [d]	SDL-1	260	15.7	0.04 - 0.08	2000	1×10^{-6}	2×10^{-8}
Si_3N_4	Si_3N_4	SDL-1	260	12.3	0.05 - 0.06	2000	3×10^{-6}	5×10^{-8}
αSiC	αSiC	SAE10	20	17.0	0.04 - 0.08	2700	3×10^{-6}	4×10^{-8}
Cr_2O_3	Cr_2O_3	LB625	260	12.3	0.02 - 0.16	2000	5×10^{-6}	9×10^{-8}
Duplex	Cr_2O_3	SDL-1	260	12.3	0.04	2000	1×10^{-4}	2×10^{-6}
Cr	Cast Iron	SDL-1	260	15.7	0.07 - 0.1	975	1×10^{-5}	4×10^{-7}
Cr_3C_2	Cr_2O_3	SDL-1	260	14.0	0.13	2650	2×10^{-5}	3×10^{-7}
Cr	Si_3N_4	SDL-1	260	12.3	0.14	975	1×10^{-4}	4×10^{-6}

(a) Typical actual diesel truck engine experience

(b) CC7000

(c) Nitrogen-ion implanted

(d) Surface modified by Ceraprep process

TABLE 4. ROOM TEMPERATURE SOLID LUBRICANT TESTS

MATERIAL	LOAD RANGE (N)	AVG. RPM	FRICTION COEFF.	WEAR COEFFICIENT $mm^3/N\text{-}m$	Dimensionless
Molalloy	92	300	0.24-0.60	1.9×10^{-5}	1.1×10^{-3}*
WSe_2/GaIn	150	289	0.07-0.15	2.8×10^{-6}	1.7×10^{-4}*
	196	492	0.05-0.10	8.1×10^{-7}	4.8×10^{-5}
	300	500	0.02-0.06	2.7×10^{-7}	1.6×10^{-5}
	300	500	0.02-0.07	4.2×10^{-7}	2.5×10^{-5}
	421	500	0.02-0.04	5.0×10^{-7}	2.9×10^{-5}
	196	500	0.03-0.06	2.6×10^{-7}	1.5×10^{-5}

* 1 hour break-in

TABLE 5. HIGH TEMPERATURE SOLID LUBRICANT TESTS
WSe_2/GaIn Compact

TEMP (C)	TEST LENGTH (MIN.)	FRICTION COEFF.	WEAR COEFFICIENT $mm^3/N\text{-}m$	Dimensionless
*25	240	0.05-0.10	8.1×10^{-7}	4.8×10^{-5}
260	240	0.05-0.13	1.5×10^{-6}	8.9×10^{-5}
260	240	0.06-0.09	1.8×10^{-7}	1.1×10^{-5}
315	240	0.03-0.07	1.1×10^{-6}	6.5×10^{-5}
360	240	0.03-0.10	3.2×10^{-6}	1.9×10^{-4}

* room temperature test for comparison

growth may explain the simultaneous reduction in friction coefficient and wear resistance. The compact showed relatively low wear for a solid lubricant, but it still wears too much to be a practical lubricant supply in long life over-the-road diesel trucks.

High Temperature Liquid Lubricant Evaluation

During this reporting period, the high temperature liquid lubricant evaluation was conducted. Plasma sprayed Cr_2O_3 coatings were used on both the ring and cylinder specimens, and five lubricants were evaluated. Only small research quantities of the special fluids were available so the number and duration of the tests were limited. The break-in period was also limited to 1 hour at room temperature to conserve lubricant. In some cases SDL-1 (polyolester) was used as the break-in lubricant, but the specimens were thoroughly cleaned before subsequent runs. Oil feed rate was adjusted according to need as determined from noise from the test chamber. The test temperature was limited by the coking temperature of the particular oil used or by the experimental rig's temperature capabilities. In addition to using Cr_2O_3 coatings for the wear specimens, ring load, engine motoring speed, and test environment were held constant for all of the tests. These parameters were 10.3 N/mm, 500 rpm, and diesel exhaust respectively.

Table 6 lists the lubricants that were evaluated, and Table 7 shows the friction and wear results from the tests. As seen in Table 7, one polyolester fluid (OS-75725L) performed better than all of the other lubricants tested at 260°C. Its performance was comparable with that of the SDL-1 in lubricating Cr_2O_3 specimens at the same temperature. The two polalkylene glycols allowed the ring specimens to wear at a rate about ten times faster than with the polyolester above. Another polyolester lubricant (OS-80001H) had the worst showing with specimen wear over 32 times greater than that with the OS-75725L. Unfortunately, the X-1P fluid was not tested at 260°C. The quantity received was only enough for one test, which was to be run at as high a temperature as possible.

TABLE 6. HIGH TEMPERATURE LUBRICANTS EVALUATED

BASE STOCK	SOURCE	MANUFACTURER DESIGNATION
Polyalkylene Glycol	Union Carbide	UCON LB-625
Polyalkylene Glycol	Union Carbide	UCON LB-650X
X-1P	Dow	X-1P Fluid
Polyolester	Lubrizol	OS-80001H
Polyolester	Lubrizol	OS-75725L

TABLE 7. WEAR RATES OF Cr_2O_3 RING SPECIMENS IN VARIOUS HIGH TEMPERATURE LUBRICANTS*

Lubricant	Temperature	Run Duration min.	Friction Coefficient	Average Ring Wear Coefficient Dimensionless	$mm^3/N\text{-}m$
OS-75725L	260	60	0.07 - 0.09	1.4×10^{-6}	2.4×10^{-8}
LB-625	100	480	0.06 - 0.08	2.9×10^{-6}	4.9×10^{-8}
X-1P	460	240	0.07 - 0.10	3.0×10^{-6}	5.1×10^{-8}
OS-75725L	370	240	0.13 - 0.25	1.2×10^{-5}	2.1×10^{-7}
LB-625	260	60	0.02 - 0.08	1.6×10^{-5}	2.7×10^{-7}
LB-650X	300	120	0.02 - 0.06	1.6×10^{-5}	2.7×10^{-7}
LB-650X	260	120	0.02 - 0.06	1.9×10^{-5}	3.3×10^{-7}
OS-80001H	370	120	0.07 - 0.10	2.1×10^{-5}	3.6×10^{-7}
LB-625	300	120	0.05 - 0.13	4.5×10^{-5}	7.6×10^{-7}
OS-80001H	260	120	0.07 - 0.09	4.5×10^{-5}	7.7×10^{-7}

*Diesel exhaust environment 10.3 N/mm ring loading 500 rpm motoring speed

The low specimen wear occurring during the low-temperature lubricated tests is the result of the ring specimens sliding hydrodynamically on a film of oil. As the temperature increases, the oil's viscosity decreases along with its ability to keep the wear surfaces separated. Faster evaporation at higher temperatures also reduces the amount of oil available in the wear interface and increases wear. On this basis, the lubricants generally became less effective in preventing wear of the ring specimens at high temperatures.

Two of the least effective lubricants at 260°C, the OS-80001H and the LB-650X, seemed to work better as the temperature increased, Table 2. As these oils typically left more deposits behind after a test run, it is conceivable that a protective layer of degraded oil was continually forming on the cylinder specimens during the testing. While this kind of deposit formation appeared to be beneficial in these wear tests, the cumulative buildup in actual engines could not be tolerated.

The X-1P fluid possessed good oxidative stability and good lubricating characteristics up to the highest testing temperature. The only test run with this fluid was at 460°C, and this temperature was limited by the experimental rig in the presence of a lubricant. The apparatus is capable of temperatures to 650°C but it would have necessitated heating the actual test chamber as opposed to simply preheating the incoming diesel exhaust. Oil vapors in direct contact with heating elements was considered a safety hazard. This was the hottest test ever run with liquid lubrication during this study, and the results were very encouraging.

Another small quantity of X-1P fluid has been obtained, and further characterization of its lubricating ability at high temperature will be conducted shortly. In addition, base stocks for the two formulated Lubrizol polyolesters have been obtained and will be evaluated in the future.

Status of Milestones

The study is progressing in accordance with the overall milestone schedule.

Communications/Visits/Travels

P. Gaydos attended a meeting at ORNL on May 2, 1989 to discuss the results of the Cummins Wear Coatings program. P. Gaydos and K. Dufrane attended a meeting at ORNL on June 4, 1989 to discuss the results of the Caterpillar Wear Coatings program.

Problems Encountered

None.

Publications

Submitted draft of paper entitled "High Temperature Lubrication of Cr_2O_3 in Advanced Heat Engine Applications" for the 1990 SAE conference.

2.3 NEW CONCEPTS

Advanced Statistical Concepts of Fracture in Brittle Materials
C. A. Johnson and W. T. Tucker (General Electric)

Objective/Scope

The design and application of reliable load-bearing structural components from ceramic materials requires a detailed understanding of the statistical nature of fracture in brittle materials. The overall objective of this program is to advance the current understanding of fracture statistics, especially in the following four areas:

- Optimum testing plans and data analysis techniques.
- Consequences of time-dependent crack growth on the evolution of initial flaw distributions.
- Confidence and tolerance bounds on predictions that use the Weibull distribution function.
- Strength distributions in multiaxial stress fields.

The studies are being carried out largely by analytical and computer simulation techniques. Actual fracture data are then used as appropriate to confirm and demonstrate the resulting data analysis techniques.

Technical Highlights

Work during this reporting period concentrated on finalizing the use of likelihood methods in obtaining confidence and tolerance limits for "Class IV" problems and in completion and delivery to ORNL of computer code to obtain Weibull point estimates for Class IV problems. An initial report on the use of likelihood methods to obtain confidence limits was given in a recent bimonthly report. The estimation methods employed in the (ORNL) computer code were developed under this program and details on the algorithms can be found in various Semiannual reports of the ceramic Technology for Advanced Heat Engine Contract such as Reference 1. The likelihood methods will be discussed first and then information on the (ORNL) computer program will be covered.

Recall that Class IV problems are those where the fracture data include specimens from multiple sizes and loading geometries, where the component of interest may be of yet a different size and loading configuration. As indicated in earlier bimonthly reports the conditional integration method is generally approximate for the Class IV situation as is the likelihood ratio method. Also, as indicated in an earlier bimonthly report, the likelihood ratio method has been programmed and shown to be in good agreement with the parametric bootstrap method described in Reference 2. To date one procedure appears to be viable for the integration method. In this approach, based on the location-scale model, the unknown argument of terms involving the "k-factor" or structure factor of a particular specimen is replaced

with a suitable approximation involving the maximum likelihood estimate of the Weibull modulus. An implementation of this form of the integration method has now been programmed.

Integration methods are established by conditioning on ancillary or approximate ancillary statistics. The present approximate integration method is based on the fact that the distributions of $\hat{m}/m$ and $\hat{m}\ln(\hat{\sigma}_p/\sigma_p)$ are approximately (asymptotically) independent of m and σ_0. In this setup $\sigma_p = \sigma_0\ [(1/kV)\ln(1/(1-p))]^{1/m}$ and gives the quantile at proportion p. (A confidence interval on σ_p is then a type of tolerance interval, and these confidence intervals are the subject of the study.) Then these results can be employed to show that the $a_i = (x_i/\hat{\sigma}_p)^{\hat{m}}$ are approximate (asymptotic) ancillary statistics. This leads one to consider the distribution of $s_1 = \hat{m}\ln(\hat{\sigma}_p/\sigma_p)$ and $s_2 = -\ln\hat{m}/m$ conditional on any n-2 of the a_i. Since the form of the resulting distribution is exactly that of the Class III solution (reported in References 3 and 4) with the addition of terms that involve the k-factor, the joint distribution of (s_1,s_2) is exact for Class IV problems. This is an important and, somewhat, unexpected result. However, as it stands it cannot be used to obtain exact confidence and tolerance bounds for Class IV problems--the k-factor is a function of the unknown m. As previously indicated one approximate method employing the maximum likelihood estimator, $\hat{m}$, appears to be viable in obtaining approximate asymptotic bounds. This method is under further theoretical and simulation study.

Both the likelihood ratio and integration methods of obtaining confidence/tolerance limits are programmed in the same computer code. This code was used to analyze several subgroups as well as the entire data set of 137 specimens of sintered SiC described in earlier bimonthly and semiannual reports (and employed in Ref. 2 in the study of the bootstrap methods). The data set consisted of three different specimen sizes (Mil Std 1942 MR specimens A, B, and C) tested in two different geometries (three and four-point bending) for a total of six different combinations of specimen size and testing configuration. Each group contained approximately 18 specimens with the exception of the four-point B group which comprised 48 specimens.

A graphical comparison of the parametric bootstrap to the likelihood ratio and integration methods of analysis of the entire SiC data set is shown in the accompanying two figures. As reported in Reference 1, fractography indicated that the strength controlling flaws were predominately located on specimen surfaces. Therefore, the specimen "size" axis is stressed area. The fracture strengths are drawn as open data points, different symbols identifying the six different sizes and configurations. The Weibull modulus and σ_0 were estimated using the maximum likelihood method for combined data as described in Reference 1. The upper line is the predicted position of the median (0.5 quantile) as a function of stressed area, while the lower line is the predicted position of the 0.05 quantile behavior. The 95 percent confidence bounds on the 0.05 quantile are included on each figure as solid triangles for the likelihood methods and as overlain smooth curves for the bootstrap method. The bounds can be used to state the uncertainty in the 0.05 quantile strength for any stressed area of interest. These Class IV approaches of analysis combine data from both SiC specimen geometries and make strength predictions with confidence bounds on components with arbitrary sizes and geometries. For this study the "component" loading is that of uniform tension, since no allowance was made for the loading geometry in the calculation of the confidence bounds.

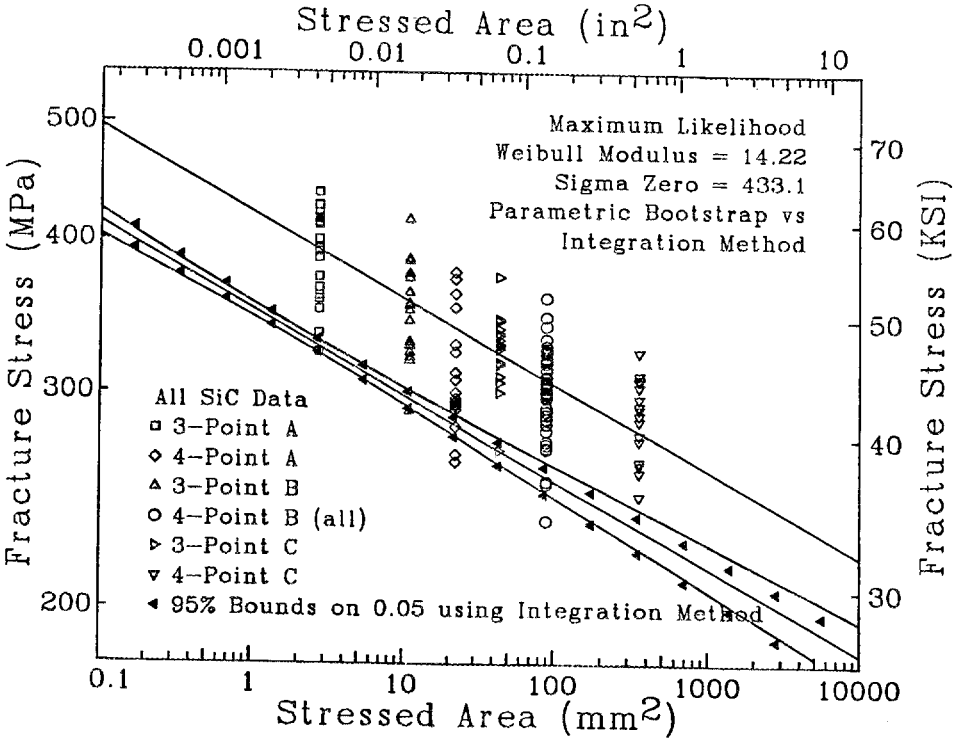
Stressed Area (in2)
0.001
0.01
0.1
1
10
Maximum Likelihood
Weibull Modulus = 14.22
Sigma Zero = 433.1
Parametric Bootstrap vs
Integration Method
All SiC Data
3-Point A
4-Point A
3-Point B
4-Point B (all)
3-Point C
4-Point C
95% Bounds on 0.05 using Integration Method
Fracture Stress (MPa)
500
400
300
200
Fracture Stress (KSI)
70
60
50
40
30
0.1
1
10
100
1000
10000
Stressed Area (mm2)

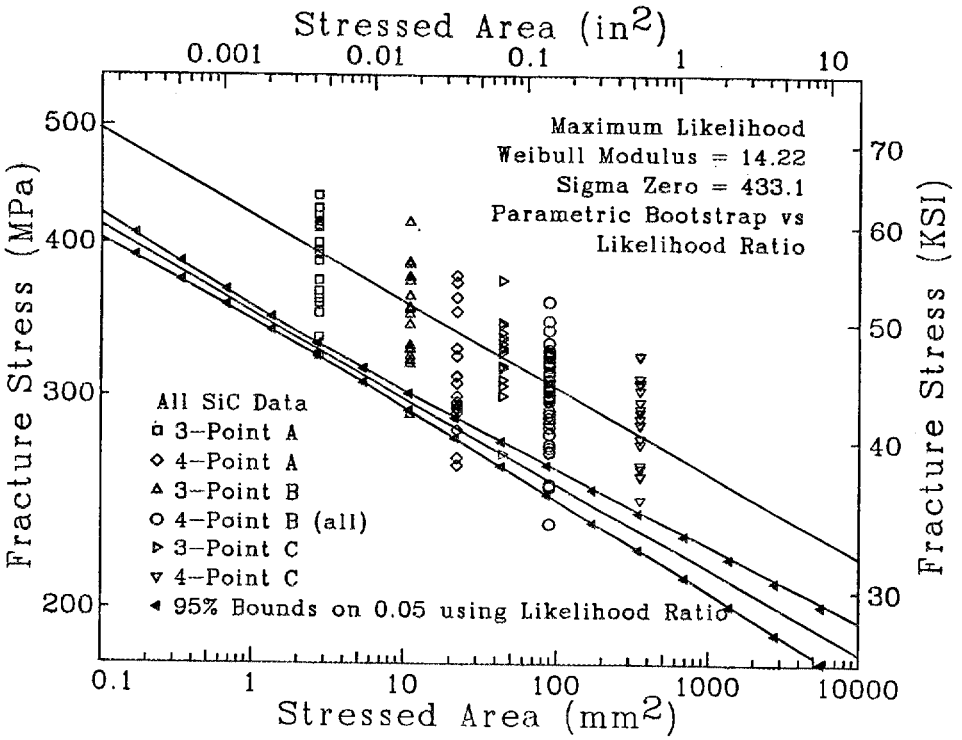
Stressed Area (in2)
0.001
0.01
0.1
1
10
Maximum Likelihood
Weibull Modulus = 14.22
Sigma Zero = 433.1
Parametric Bootstrap vs
Likelihood Ratio
All SiC Data
3-Point A
4-Point A
3-Point B
4-Point B (all)
3-Point C
4-Point C
95% Bounds on 0.05 using Likelihood Ratio
Fracture Stress (MPa)
500
400
300
200
Fracture Stress (KSI)
70
60
50
40
30
0.1
1
10
100
1000
10000
Stressed Area (mm2)

Perusal of the figures indicates that the limits obtained by the parametric bootstrap and likelihood ratio methods generally agree and both of these sets of limits are skewed relative to those of the conditional integration method. This skewness is due primarily to bias in the bootstrap and likelihood ratio approaches. It is well known that the likelihood ratio method produces biased limits and much theoretical work has gone into determining corrections for bias (the so called Bartlett correction, e.g., Reference 5). Also it is possible to correct the bootstrap limits for bias and initial results concerning this are reported in a recent bimonthly. Finally, when the conditional integration method is exact there is no bias in the limits. The method discussed herein is, however, an approximate one. Thus there may be some bias in the conditional integration limits.

To study the bias and overall performance of the likelihood methods a simulation study was carried out. The study was performed by considering only the 3-point bending portion of the data reported in the figures. This was done so that comparisons to previous Class III results can also be made and the effects of bias more clearly studied. However, not all Class IV formulae reduce to those of the Class III situation when there is only one loading geometry for the testing conditions. This comes about from the fact that in Class IV problems the k-factor is directly employed and in Class III problems the k-factor is set to one (and effectively ignored). This is clearly seen in the estimate of σ_p from the Class IV situation in the Class III context given by $\hat{\sigma}_p = [r(\hat{m})\ln(1/(1-p))\sum R_i x_i^{\hat{m}}/n]^{1/\hat{m}}$ where $r(m) = k_s(m)/k(m)$ and $R_i = V_i/V$. Here s denotes the common geometry of the sample specimens and $k(m)$ is associated with the loading geometry of the component, and V denotes the respective sizes of specimens and component. This formula comes directly from application of the definition of σ_p (given previously). Now $r(m)$ is not one since the loading geometry of the component is that of uniform tension and the loading geometry of the specimens is that of 3-point bending. But in the Class III situation there is no term involving $r(m)$. Thus, there is a fundamental difference between the Class III and Class IV situations. However, it should be pointed out that the "correct" estimate of m is obtained, since the terms involving the k-factor algebraically cancel out in the likelihood equation. It is only strength estimates that are affected and they are such that a true σ_0 is estimated in the Class IV case. The σ_0 estimated in the Class III situation applies to only the Class III case. Moreover, differences also occur in the computation of confidence and tolerance limits on strengths in the two situations, even in the case where both the component and specimens have the same loading geometry.

The primary results of the simulation study are reported in Tables 1 and 3. Tables 2 and 4 give a compression of the results shown in Tables 1 and 3. Since in Class IV problems the loading geometry is an important consideration, the initial simulation study was set up to be analogous to the testing situation of the 137 specimens reported in the figures. The specimen sizes are those of the 3-point bending areas and are shown in the heading of the tables. One study was done with a total sample size of five and the other was done with the same number of specimens as observed for the three 3-point sizes. It was the intent of the former case to study the "small" sample size properties of the methods. For both methods two independent runs were made at the seven component sizes shown in the tables. This was done so as to get an indication of simulation trial to simulation trial variability. Each simulation run consists of 500 individual trials and in all cases the confidence coefficient was 0.95. For this setup the standard error for an estimated coverage probability is 0.0069821 for an individual limit and

0.0097467 for an interval. These values can be used as guides in checking the veracity of the procedures investigated in the simulation studies. Also for all trials only a single quantile, 0.05, was studied. Each run was begun with a different random number seed, generally, the ending seed of the previous run.

Inspection of Table 1 indicates that the performance of the integration method is possibly satisfactory with the total sample size of five. For the 28 individual cases of lower and upper bounds only three were statistically significant at an 0.05 significance level. The expected number of misses is 1.4. Also there appears to be no significant trend indicating a bias in the limits. However, the same is not true for the likelihood ratio (lr) method. The lr method experienced some 18 significant results. Also the range of the simulated coverage probabilities was far greater than that of the integration method. Finally, there is a definite skewness in the lr coverages as a function of size. This indicates that these limits have a bias that changes as size changes. There could also be a constant bias, i.e., an offset that is independent of size; this is also true for the integration limits. Simulation results for the Class III situation indicate that the lr method is essentially exact for total sample sizes of the order reported in Table 3. Inspection of Table 3 indicates in the Class IV situation studied in this table that the lr method has not quite converged. There are still some five significant results and possibly some signs of bias. Moreover, the results for the integration method indicate that asymptotic convergence has, for practical purposes, been met. There were only 2 cases of significant results and no signs of trends in the coverages. All in all the results were very encouraging concerning the integration method.

The coverage results of the two individual runs shown in Tables 1 and 3 were compressed to those of Tables 2 and 4 in order to more thoroughly study the possible bias. (This is proper since all individual simulation runs were statistically independent. However, it is clear that the results reported in Tables 2 and 4 are not independent of those reported in Tables 1 and 3.) Shown in Tables 2 and 4 are only the respective coverages. Now the simulation trial size is 1000 so that the standard error for an estimated coverage probability is 0.0049371 for an individual limit and 0.0068920 for an interval. With regard to the integration method there are five significant results (combining the runs pushed some cases right at the boundary over) in Table 2 and two in Table 4 respectively for the 14 cases of individual lower and upper bounds. The expected number of misses is now 0.7 so that zero or one, or possibly two significant results is permissible. However, five are just too many. This points out that the conditional integration method is approximate in the Class IV situation. Again there are no real signs of trends in the coverages for the the integration limits in either table. Since this was the case an average of the lower and upper coverages was obtained. For Table 2 the average of the lower bounds is 0.969 and the average of the upper bounds is 0.981. This indicated why in Table 2 there were a total of five significant results: on average the lower limits were biased low and on average the upper limits were biased high. The respective averages from Table 4 are 0.973 and 0.978. These are clearly very close to the true value of 0.975.

The results for the lr method indicate its much more approximate nature. There are 11 significant results in Table 2 and six in Table 4. Further, there are definite trends in the coverages as a function of size and as a result no average coverages were obtained. Again the conclusion is that, practically, the integration method has converged for the sample size configuration of 18, 18, 18 specimens. And the lr method has not at this same sample size

setup. Moreover, the lr method has a definite bias over the component sizes studied. These results are consistent with and corroborate the findings shown in the figures concerning the full data set.

In order to more definitively characterize the approximate nature of both approaches a larger simulation study will be carried out. In this larger study a fuller range of total sample sizes and component-specimen loadings will be investigated. Also a study to compare more directly with the Class III results (Ref. 3) will be made. Preliminary results along this line indicate that the Class IV likelihood ratio limits are somewhat more accurate than the Class III likelihood ratio limits. But even without these more encompassing studies, it is concluded that the integration and likelihood ratio methods offer valid and useful ways for estimating confidence and tolerance limits for Class IV problems of strength analysis.

As previously indicated, a computer program for analyzing Class IV fracture strength data and estimating Weibull parameters and component strengths was completed during this reporting period and delivered to ORNL for distribution. The program name is "WeibEst" which is an abbreviation of Weibull Estimator. The Weibull two-parameter distribution function was assumed throughout the analysis. WeibEst accepts fracture data from many different specimen geometries and combines the three types of inherent information present in the forms of scatter within groups, specimen size dependence of average strength, and loading geometry dependence of average strength in order to estimate Weibull parameters. Maximum likelihood and two linear regression estimators are included. Where appropriate, the analysis is carried out three times for each estimator, corresponding to the three most common size-scaling assumptions: volume, surface area and edge length distributions of strength limiting defects. Details on the algorithms used in this program can be found in prior semiannual reports such as Reference 1.

WeibEst is written in Fortran 77 and has been successfully compiled on several different machines and compilers. The executable form of the program that is available for distribution is for execution on IBM-PC's and compatibles. It was compiled using Microsoft Fortran Version 4.01 and will run on any PC or compatible using 8088 through 80486 processors running PC-DOS or MS-DOS and containing at least 256K of RAM. Math coprocessors (80x87) are supported but are not necessary for execution. The output is purely character oriented, so no graphics support is necessary in this version.

The input strength data plus specimen size and geometry data must be available as an input data file. Input data files can be "built" during execution of WeibEst or they can be built or edited prior to execution using a text editor of the user's choice.

All Class IV estimators need values of the structure factor, k, as a function of the Weibull modulus, m. (In addition, the maximum likelihood estimator needs the quantity dk/dm as a function of m.) k is a dimensionless quantity in the two-parameter Weibull distribution function describing the fraction of the specimen volume, area or edge length that is effectively at the maximum stress in the structure. Unfortunately, very few k values can be evaluated analytically in closed form. Uniform tension and bending of rectangular and circular cross-section beams are some of the exceptions where k and dk/dm can be evaluated in closed form. WeibEst has built-in functions to evaluate k and dk/dm as a function of m for these special-case geometries where closed-form solutions exist.

In order for WeibEst to handle the infinite variety of other geometries that exist, the capability of "specials" was added. WeibEst still requires a means of calculating a k and a dk/dm as a function of m. In specials, these k-m relationships are transmitted to WeibEst in the form of a table. Finite element methods or numeric methods are used to calculate volume, area, and edge length k values for several different m values that safely bound the expected m value. This information is transmitted to WeibEst in table form in the input data file. WeibEst then uses cubic spline smoothing and interpolation methods to determine k and dk/dm for any value of m within the range of table inputs. In fact, the spline methods work remarkably well in estimating k and dk/dm even beyond the table values, but the worst possible errors are difficult to predict. Therefore, WeibEst generates a warning message if the final m value is outside the tabled values.

Important outputs of the program execution can be stored in an output data file for later printing, editing, etc. Program execution includes four sections: reading the input data file; analyzing and displaying results of individual sub-groups of data (groups that have the same size and loading geometry); analyzing and displaying results of the combined data using each of the different estimators; and estimation of component (or specimen) strengths at various probabilities of failure that may be of interest.

Status of Milestones

The milestone on delivery of software and documentation for Class IV estimators has been completed and the software and documentation have been delivered to M.K. Ferber. Also the milestone on determining confidence bounds on strengths for Class IV problems employing likelihood methods has been completed.

Publications

None.

References

1. C.A. Johnson and W.T. Tucker, "Advanced Statistical Concepts of Fracture in Brittle Materials", in Ceramic Technology for Advanced Heat Engines Project, Semiannual Progress Report for April 1987 through September 1987, pp 200-208.

2. C.A. Johnson and W.T. Tucker, "Advanced Statistical Concepts of Fracture in Brittle Materials", in Ceramic Technology for Advanced Heat Engines Project, Semiannual Progress Report for October 1988 through March 1989.

3. C.A. Johnson and W.T. Tucker, "Advanced Statistical Concepts of Fracture in Brittle Materials", in Ceramic Technology for Advanced Heat Engines Project, Semiannual Progress Report for October 1987 through March 1988, pp 253-259.

4. Tucker, W. T. and C. A. Johnson (1988), "Confidence Bounds on Strength Estimates," *S.A.E. Proceedings 26th Automative Technology Development Contractors' Meeting,* **P-**

219, 205-210.

5. Barndorff-Nielson, O. E. and D. R. Cox (1984), "Bartlett Adjustments to the Likelihood Ratio Statistic and the Distribution of the Maximum Likelihood Estimator," *J. R. Statist. Soc.,* **46,** 483-495.

Table 1

DIFFERING SPECIMEN AND COMPONENT SIZES
n=2 at 2.7242, n=1 at 10.9359, n=2 at 43.5809
Total n=5

Component Size	Method											
	Integration						Likelihood Ratio					
	Run 1			Run 2			Run 1			Run 2		
	I	L	U	I	L	U	I	L	U	I	L	U
0.01	472	483	489	477	489	488	463	495	468	443	497	446
	.944	.966	.978	.954	.978	.976	.926	.990	.936	.886	.994	.892
0.10	473	481	492	472	483	489	453	490	463	452	493	459
	.946	.962	.984	.944	.966	.978	.906	.980	.926	.904	.986	.918
1.00	479	488	491	477	486	491	456	489	467	455	487	468
	.958	.976	.982	.954	.972	.982	.912	.978	.934	.910	.974	.936
10.0	474	478	496	479	486	493	457	465	492	465	474	491
	.948	.956	.992	.958	.972	.986	.914	.930	.984	.930	.948	.982
100.0	472	482	490	472	482	490	446	452	494	460	466	494
	.944	.964	.980	.944	.964	.980	.892	.904	.988	.920	.932	.988
1000.0	484	492	492	480	491	489	465	468	497	465	467	498
	.968	.984	.984	.960	.982	.978	.930	.936	.994	.930	.934	.996
10000.0	465	476	489	473	488	485	448	452	496	452	460	492
	.930	.952	.978	.946	.976	.970	.896	.904	.992	.904	.920	.984

Table 2

DIFFERING SPECIMEN AND COMPONENT SIZES
n=2 at 2.7242, n=1 at 10.9359, n=2 at 43.5809
Total n=5

Component Size	Method					
	Integration			Likelihood Ratio		
	I	L	U	I	L	U
0.01	.949	.972	.977	.906	.992	.914
0.10	.945	.964	.981	.905	.983	.922
1.00	.956	.974	.982	.911	.976	.935
10.0	.953	.964	.989	.922	.939	.983
100.0	.944	.964	.980	.906	.918	.988
1000.0	.964	.983	.981	.930	.935	.995
10000.0	.938	.964	.974	.900	.912	.988

Table 3

DIFFERING SPECIMEN AND COMPONENT SIZES
n = 18 at 2.7242, n = 18 at 10.9359, n = 18 at 43.5809
Total n = 54

Component Size	Method											
	Integration						Likelihood Ratio					
	Run 1			Run 2			Run 1			Run 2		
	I	L	U	I	L	U	I	L	U	I	L	U
0.01	468	482	486	482	489	493	467	487	480	482	492	490
	.936	.964	.972	.964	.978	.986	.934	.974	.960	.964	.984	.980
0.10	473	486	487	473	487	486	470	487	483	468	487	481
	.946	.972	.974	.948	.974	.972	.940	.974	.966	.936	.974	.962
1.00	475	483	492	472	480	492	465	483	482	458	477	481
	.950	.966	.984	.944	.960	.984	.930	.966	.964	.916	.954	.962
10.0	470	485	485	476	485	491	468	482	486	473	482	491
	.940	.970	.970	.952	.970	.982	.936	.964	.972	.946	.964	.982
100.0	476	487	489	484	492	492	473	483	490	483	490	493
	.952	.974	.978	.968	.984	.984	.946	.966	.980	.966	.980	.986
1000.0	477	487	490	472	481	491	479	483	496	472	479	493
	.954	.974	.980	.944	.962	.982	.958	.966	.992	.944	.958	.986
10000.0	485	498	487	476	488	488	487	496	491	472	480	492
	.970	.996	.974	.952	.976	.976	.974	.992	.982	.944	.960	.984

Table 4

DIFFERING SPECIMEN AND COMPONENT SIZES
n = 18 at 2.7242, n = 18 at 10.9359, n = 18 at 43.5809
Total n = 54

Component Size	Method					
	Integration			Likelihood Ratio		
	I	L	U	I	L	U
0.01	.950	.971	.979	.949	.979	.970
0.10	.946	.973	.973	.938	.974	.964
1.00	.947	.963	.984	.923	.960	.963
10.0	.946	.970	.976	.941	.964	.977
100.0	.960	.979	.981	.956	.973	.983
1000.0	.949	.968	.981	.951	.962	.989
10000.0	.961	.986	.975	.959	.976	.983

3.0 DATA BASE AND LIFE PREDICTION

INTRODUCTION

This portion of the project is identified as project element 3 within the work breakdown structure (WBS). It contains five subelements, including (1) Structural Qualification, (2) Time-Dependent Behavior, (3) Environmental Effects, (4) Fracture Mechanics, and (5) Nondestructive Evaluation (NDE) Development. Research conducted during this period includes activities in subelements (1), (2), and (3). Work in the Structural Qualification subelement includes proof testing, correlations with NDE results and microstructure, and application to components. Work in the Time-Dependent Behavior subelement includes studies of fatigue and creep in structural ceramics at high temperatures. Research in the Environmental Effects subelement includes study of the long-term effects of oxidation, corrosion, and erosion on the mechanical properties and microstructures of structural ceramics.

The research content of the Data Base and Life Prediction project element includes (1) experimental life testing and microstructural analysis of Si_3N_4 and SiC ceramics, (2) time-temperature strength dependence of Si_3N_4 ceramics, and (3) static fatigue behavior of PSZ ceramics.

Major objectives of research in the Data Base and Life Prediction project element are understanding and application of predictive models for structural ceramic mechanical reliability, measurement techniques for long-term mechanical property behavior in structural ceramics, and physical understanding of time-dependent mechanical failure. Success in meeting these objectives will provide U.S. companies with the tools needed for accurately predicting the mechanical reliability of ceramic heat engine components, including the effects of applied stress, time, temperature, and atmosphere on the critical ceramic properties.

3.1 STRUCTURAL QUALIFICATION

Microstructural Analysis of Structural Ceramics

B.J. Hockey, Jr. and S.M. Wiederhorn
(The National Institute of Standards and Technology)

Objective/Scope:

The objective of this part of the program is to identify mechanisms of failure in structural ceramics subjected to mechanical loads at elevated test temperatures. Of particular interest is the damage that accumulates in structural ceramics as a consequence of high temperature exposure to stresses normally present in heat engines.

Design criteria for the use of ceramics at low temperature differ from those at high temperature. At low temperature ceramics are elastic and brittle; failure is controlled by a distribution of flaws arising from processing or machining operations, and the largest flaw determines the strength or lifetime of a component. By contrast, at high temperature where ceramics are viscoelastic, failure occurs as a consequence of accumulated, or distributed damage in the form of small cavities or cracks that are generated by the creep process. This damage effectively reduces the cross-section of the component and increases the stress that must be supported. Such increases in stress are autocatalytic, since they increase the rate of damage and eventually lead to failure as a consequence of loss in cross section. When this happens, the individual flaw loses its importance as a determinant of component lifetime. Lifetime now depends on the total amount of damage that has occurred as a consequence of the creep process. The total damage is now the important factor controlling lifetime.

Recent studies of high temperature failure of the non-oxide ceramics intended for use for heat engines indicates that for long term usage, damage accumulation will be the primary cause of specimen failure. Mechanical defects, if present in these materials, are healed or removed by high temperature exposure so that they have little influence on long term lifetime at elevated temperature. In this situation, lifetime can be determined by characterizing the damage and the rate of damage accumulation in the material at elevated temperatures. In ceramic materials such as silicon nitride and SiAlON, such characterization requires high resolution analyses because of the fine grain size of these materials: hence the need for transmission electron microscopy as an adjunct to the mechanical testing of ceramics for high temperature applications is apparent.

In this project, the creep and creep-rupture behavior of several ceramic materials will be correlated with microstructural damage that occurs as a function of creep

strain and rupture time. Materials to be studied include: SiAlON; hot-pressed silicon nitride; sintered silicon carbide. This project will be coordinated with WBS 3.4.1.3, Tensile Creep Testing, with the ultimate goal of developing a test methodology for assuring the reliability of structural ceramics for high temperature applications.

Technical Progress

Over the past six months, analytical transmission electron microscopy was used to characterize a SiC whisker reinforced silicon nitride that had been subjected to tensile creep at 1200°C and 1250°C. A similar study was conducted on hot-pressed, reaction bonded silicon nitride. The latter material was supposed to be the monolithic counterpart of the whisker reinforced material, however, a microstructural examination of the monolith indicated that the microstructure differed significantly from the matrix of the whisker reinforced material. Both materials studied in this project were supplied by J.G. Baldoni of the GTE Laboratories.

Preliminary studies on both the as-received and the crept samples of monolithic silicon nitride, revealed a bimodal grain structure, composed of a matrix of equi-axed, submicron Si_3N_4 grains and much larger, 1 to 10 µm tabular Si_3N_4 grains. The submicron matrix in the monolithic material is similar to the matrix found in the whisker reinforced material. The presence of Si_3N_4 grains that correspond to randomly oriented, basal platelets suggests abnormal grain growth during the processing of the monolithic Si_3N_4 material. The question of whether abnormal grain growth occurs as a result of differences in hot-processing conditions, or as a consequence of subtle changes in sintering aid composition are currently being pursued. In this regard, the residual glass composition (primarily a yttria-silicate glass) in the "as-received" monolithic material is devoid of CaO, which is present in minor concentrations in the whisker reinforced material as a contaminant associated with the SiC whiskers. Differences may also exist in minor concentrations of Al_2O_3 in the binder glass. Comparisons of the monolithic and whisker reinforced materials also revealed a considerable difference in porosity. Whereas little inherent porosity was found in the SiC whisker reinforced material, clusters of intergranular voids were found distributed within the matrix of the monolithic material.

Despite these differences, it is nevertheless interesting to note that both materials exhibit a "composite type" structure: one containing a distribution of 1 to 25 µm long SiC whiskers; the other containing a distribution of 1 to 10 µm Si_3N_4 platelet shaped grains. Examination of both materials indicated that creep cracks proceed from full

facet cavities, either along favorably oriented SiC whisker interfaces in the whisker reinforced material, or along favorably oriented grain boundaries separating abnormally large Si_3N_4 grains in the monolithic material. The increased lifetime of the monolithic material appears to be related to both the smaller dimensions of the crack like interfacial cavities and to their apparent arrest within the finer-grained structure of this material.

The nature, extent, and effect of crystallization of the intergranular binder phase was also investigated during the past six months. Crystallization that occurs during high temperature creep has a pronounced effect on the creep rate, increasing resistance to creep deformation. To date, examination of crept samples of both materials has shown that devitrification to an apparently "pure" yttria silicate crystal occurs rapidly within the larger interstices of both materials, effectively transforming the interstices into a multi-phase crystalline grain structure. High resolution observations indicate the persistence of a thin, amorphous interfacial layer between all crystalline phases, including narrow (≤ 1 nm) interfaces between adjacent Si_3N_4 grains. Thus, while devitrification greatly reduces the volume of glass present in these materials, the process of grain boundary sliding by which deformation and cavitation occur is still controlled by an amorphous interfacial phase.

Future efforts in this project will concentrate on characterizing differences between the two materials, focussing on compositional and microstructural changes that occur during high temperature creep. It is anticipated that this comparative study will be completed by the next Semi-Annual report.

Status of Milestones

All milestones are currently on schedule. Microstructural analyses by analytical transmission electron microscopy have been applied to SiC whisker reinforced Si_3N_4 after tensile creep. Similar analyses are being applied to a monolithic counterpart (milestone 311101) of the whisker reinforced Si_3N_4. The results of this study will be described in a talk at the Ceramic Science and Technology Congress, Anaheim, CA, November 1989. A paper on this work will be published in the Proceedings of the 14th Annual Conference on Composites and Advanced Ceramics, January 1990 (Milestone 311102).

Publications

A paper entitled "Effect of Microstructure on the Creep of Siliconized Silicon Carbide" has been submitted to the Journal of the American Ceramic Society.

Physical Properties of Structural Ceramics

R. K. Williams and R. S. Graves (Oak Ridge National Laboratory)

Objective/scope

The structural ceramics which will be used in the combustion chambers of advanced heat engines must also thermally isolate the metallic parts of the engine from the high temperature combustion gases. The ceramics being considered for this application are complex materials which are toughened by the presence of a second phase. The purpose of this task is to develop an improved understanding of the factors which determine the thermal conductivities of these structural materials at high temperatures. This study is required because the thermal conductivities of the ceramics of interest are generally not known at high temperatures, and the theory has not yet been sufficiently developed to yield reliable predictions. The influences of second phase type, content, and shape, and of parallel energy transport by photons are of particular importance. At present our understanding of these variables is at best only qualitative. The two areas which will be investigated are the role of photon transport at high temperatures and the influence of second phase additions.

Technical progress

A study of the thermal conductivity of transformation toughened Al_2O_3-Cr_2O_3 solutions has been concluded. This material was of some interest for insulated diesel applications, and previous work[1] showed that the thermal conductivity was lower than expected from a theoretical calculation. This calculation involved assuming that the ZrO_2 toughening phase was insoluble in the Al_2O_3-Cr_2O_3 matrix, and the validity of this assumption has been investigated experimentally.

It was necessary to prepare a sample especially for this study because the thermal conductivity samples were not suitable for microprobe analysis. Baikowski CR-10 Al_2O_3, Zircar ZYP unstabilized ZrO_2, and $Cr(NO_3)_3 \cdot 9H_2O$ were mixed by adding the nitrate in a methanol solution. The product was dried and fired in air at 1150°C for 2 hours to decompose the nitrate and dissolve the Cr_2O_3 in the Al_2O_3. The product was then broken up and hot pressed at 1600°C for 10 minutes. The nominal composition was Al_2O_3-30 mol % Cr_2O_3 + 10 vol % ZrO_2, and the relatively low concentration and relatively large particle size of the ZrO_2 made it possible to obtain reliable microprobe data.

The ternary system and the Cr_2O_3-ZrO_2 binary have not been studied. There is no mutual solubility in the Al_2O_3-ZrO_2 system. The microprobe data indicate that there is a small amount of miscibility in the ternary system at 1600°C. The ZrO_2 particles had an average cation analysis of 3.3 at. % Cr and 1.8 at. % Al. The properties of the Al_2O_3-Cr_2O_3 matrix phase largely determine the thermal conductivity, and the microprobe analysis showed 0.6 at. % Zr, 27.7 at. % Cr, and 71.7 at. % Al. The presence of Zr in this phase probably accounts for the observed thermal conductivity reduction. Phonon-point defect scattering depends on the difference between the mass of individual defects and the average mass of the lattice. In the Al_2O_3-Cr_2O_3 system this scattering is mostly due to the Cr^{+3} ions, and Zr^{+4} should scatter much more strongly because the mass difference is larger. Also, accommodating Zr^{+4} in the lattice requires the creation of cation vacancies, and these defects also scatter strongly.

A study of the low expansion ceramics developed at VPI[2] has also been concluded. The original sample of $(Rb_{0.5}Cs_{0.5})\ Zr_2\ (PO_4)$ supplied by VPI was not suitable. A second sample of this compound was 43% denser and had a crushing strength of 30 ksi. Thermal conductivity, λ, data were obtained over the temperature range 304-363 K and fitted to the equation:

$$\lambda^{-1} = 0.3706 + 5.57 \times 10^{-4} T .$$

In this equation λ is in $Wm^{-1}K^{-1}$ and the temperature, T, is in Kelvins. The thermal conductivity of this material is comparable to that of cubic zirconia.

References

1. D. R. Johnson, *Ceramic Technology for Advanced Heat Engines Project Semiannual Progress Report for October 1988 Through March 1989*, ORNL/TM-11239 (August 1989).

2. J. J. Brown, R. E. Swanson, and F. A. Hummel, *Ceramic Technology for Advanced Heat Engines Project Semiannual Progress Report for April through September 1988*, ORNL/TM-11116 (March 1989), p. 125.

Project Data Base

B. L. Keyes (Oak Ridge National Laboratory)

Objective/scope

The objective of this task is to develop a comprehensive computer data base containing the experimental data on properties of ceramic materials generated in the overall effort. This computer system is intended to provide a convenient and efficient mechanism for the compilation and dissemination of the large amounts of data involved. The data base will be made available in electronic form to all project participants. In addition, periodic hard copy summaries of the data, including graphical representation and tabulation of raw data, will be issued to provide convenient information sources for project participants.

Technical progress

The first draft of the fourth data base semiannual summary report was written, compiled, and completed during this semiannual period. This report contains experimental test data and background information from the data base on alumina-based alloys, including whisker-reinforced aluminas and mullites.

The data base now contains about 3925 test results on 282 different batches of ceramic materials. Approximately 52% of these are on zirconia-based ceramics, 3% are on silicon carbides, 12% are on silicon nitrides, 7% are on whisker-reinforced silicon nitrides, 25% are on alumina-based ceramics (including whisker-reinforced materials and mullites), and 1% are on other ceramics. Table 1 gives a detailed breakdown, by material class, of the data presently stored in the system. A list of materials within a material class will be made available to users upon request.

Completion of the proposed computer-based user interface, originally planned for December 1989, has been delayed due to time contraints. Until the interface is completed, a hardcopy users guide, in progress now, will be available for those who need to use the data base. This guide will contain the various file structures, definitions and standard units for all the fields, a map of the data base, and tips on how to use various features of the system. Since the data base operates within the dBASE IV™ structure, the user's guide will be slanted toward the dBASE format. Users of other data handling programs such as Lotus 1-2-3™ or EXCEL™ will find the guide useful in linking fields in different files together. (The data base is relational, composed of many different files, each with its own specific purpose.) Work on the field information section is presently nearing completion. We are trying to have the guide available by mid-to-late November.

While compiling the field information for the user's guide, we found several inconsistencies in the files, all very minor, but annoying. One of our main goals during the next bimonthly period, is to clean up all those inconsistencies and optimize the files. During this period, we also plan to make a detailed survey of the existing information in the data base to determine what information is still needed to produce complete material/test profiles.

Another project planned for the future is to create a better link between the IBM/PC-type computers and the Apple Macintosh computers. The data base resides on an IBM PC/AT with a dual 20-Mb Bernoulli disk drive to allow more space for larger data bases. To be useful to the engineering/designer community, the data base must be importable and exportable in most major IBM and Apple formats because both are heavily used in research and industry. This IBM-to-MAC link has recently become more important since more microcomputer users are now using Macintoshes.

Data collection and input for the next semiannual data base summary report will begin soon and will feature an update on zirconia-based ceramics. We welcome data from all participants in the CTAHE program, and will gladly work with anyone willing to contribute to the data base.

Status of milestones

The fourth semiannual data base summary was completed through the first draft and was submitted on time. The next semiannual report, due in April1990, will feature an update on zirconia-based ceramics.

Publications

B. L. P. Keyes, "Ceramics Technology for Advanced Heat Engines Project Data Base: September 1989 Summary Report." Oak Ridge National Laboratory, Oak Ridge, Tennessee, to be published.

TABLE 1. CTAHE DATA BASE SUMMARY AS OF SEPT. 30, 1989

Material Class	Creep	Cyclic Fatigue	Density	Dynamic Fatigue	Elasticity	Fracture Toughness	Interrupted Fatigue	Material Characteristics	MOR 3 Pt Bend	MOR 4 Pt Bend	Tensile
Alumina	1	15		9	24	20		19		371	28
Alumina + reinforcing fibers			7			39		91		144	11
Alumina + Zirconia										7	
Mullite					2	1		2	1	4	
Mullite + reinforcing fibers					11	16		48	9	22	
Silicon Carbide			5	13		5		7		65	
Silicon Nitride	27	19	15	16	2	45		29	10	174	16
Silicon Nitride + reinforcing fibers		15	2		16	31		44		34	50
Zirconia		43	158		92	54	215	37		1276	28
Zirconia + reinforcing fibers						5		5		2	
Other										5	
Totals	28	92	187	38	147	216	215	282	20	2104	133

Material Class	Oxidation Rate	Poisson's Ratio	Shear Modulus	Thermal Conductivity	Thermal Contraction	Thermal Diffusivity	Thermal Expansion	Thermal Shock	Wear Resist.	Weld Shear	X-Ray Diffraction
Alumina				3			1	2			
Alumina + reinforcing fibers				34		18	4	6			
Alumina + Zirconia					23		21				
Mullite											
Mullite + reinforcing fibers											
Silicon Carbide							18				17
Silicon Nitride	1	2	1	9		10	34		2		49
Silicon Nitride + reinforcing fibers	3	17	16	9		17	14				
Zirconia										57	72
Zirconia + reinforcing fibers											
Other									2		
Totals	4	19	17	55	23	45	92	8	4	57	138

Total number of records on file: 3924

3.2 TIME-DEPENDENT BEHAVIOR

Characterization of Transformation-Toughened Ceramics
Jeffrey J. Swab (U.S. Army Materials Technology Laboratory)

Objective/Scope:

Because of their unusual combination of properties, transformation toughened zirconia, specifically yttria tetragonal zirconia polycrystal materials (Y-TZP), are considered candidate materials for components of advanced diesel engines. However, Y-TZPs are susceptible to a loss of strength and toughness after long times at elevated temperatures. Accordingly, tasks were initiated to define the extent and magnitude of these potential losses.

The first task exposed a variety of Y-TZPs to 1000°C for 100 and 500 hours to determine if room temperature strength and toughness changed after exposure. The second task was to determine the performance of these Y-TZPs under a combination of elevated temperature and stress. This was to be completed using Stepped-Temperature Stress-Rupture and Stress-Rupture tests. The third task is to examine ZTA materials using the same test matrix.

Technical Highlights:

1) Two Y-TZP materials, the sintered/hip'ed YZ110 from Norton Co. and the hot pressed material from Hitachi, were examined to determine the time dependent behavior at 600° and 700°C. Both have quite similar time-dependent behavior between 800° and 1200°C as indicated by the stepped-temperature stress rupture results (Figure 1). However, the stress rupture behavior of the Norton material is significantly better at 700° than that of the Hitachi (Figure 2 & 3). The Norton material was able to support a stress of 600 MPa for 1,000 hours without failure, but, the Hitachi could only support 400 MPa for 1,000 hours without failure. A difference in grain size may account for this difference in behavior. The Norton material has an average grain size of ~ 1.0 μm while the Hitachi is much finer at ~ 0.3 μm. It has been shown that there is a critical grain size (D_c) necessary for the retention of the tetragonal phase. Above D_c it is increasingly difficult to retain the tetragonal phase. Therefore, it may be easier for the tetragonal grains in the Norton material to transform, resulting in higher time-dependent strength because there is a larger contribution from the transformation toughening phenomenon. Further work is needed to determine if other factors such as processing, yttria content, impurity content and grain boundary chemistry play a role in this improved behavior.

Stress rupture tests on the Norton material at 600°C show further a improvement in the time-dependent behavior (Figure 4). At this temperature one specimen showed it could support 700 MPa for 1,000 hours without failure. Tests at this temperature are currently underway on the Hitachi material.

2) Two ZTA materials manufactured by Kyocera-Feldmuehle, (KF), code: BN70 and Ceramatec, (CZA), code: CZA-600, were obtained from characterization. The density, MOE and room temperature strength has been determined for the as received state (AR) and after 500 hours of exposure at 1000°C (500/1000). The results are listed in Table 1, also included is data on a high purity, fully dense alumina produced by Coors for comparison.

Table 1.

Material	Density (g/cc) AR	Density (g/cc) 500/1000	MOE (GPa) AR	MOE (GPa) 500/1000	Strength AR	Strength 500/100
KF	3.94	3.94	353	355	512	461
CZA	4.17	4.17	339	343	441	433
ALUMINA	3.93	3.93	---	---	332	339

As expected both ZTAs had a higher average room temperature strength than the pure alumina, but after exposure the KF showed a strength loss while the CZA did not. Further analysis is needed to explain this difference.

Stepped-temperature stress-rupture testing of these ZTAs between 600° and 1200°C has been completed and is plotted in Figures 5 & 6. The KF material had typical time-dependent failures while the CZA had an anomalous behavior. Also creep was evident as a result of the STSR tests for the CZA but not the KF. These differences are probably due to microstructural variations. However, microstructural analysis has been delayed due to limited availability of the in-house SEM.

Comparison of the STSR results for these ZTAs with that of the Y-TZPs from the June-July 1988 Bimonthly report shhows that both ZTAs have slightly better stress carrying capabilities at 1100° and 1200°C than all but the Hitachi Y-TZP.

Due to a lack of interest in oxide based materials by the heat engine community, work on these materials will be considered complete once fracture toughness has been determined for both ZTAs. Primary emphasis will then shift to silicon nitride and silicon carbide based materials with any work on oxide materials being secondary.

References:

1. Lange, F.F., "Transformation Toughening - Size Effects Associated with the Thermodynamics of Constrained Transformations," J. Mat. Sci., 17, 225-234 (1982)

Status of Milestones:

Room temperature strength before and after treatment and STSR tests have been completed on the ZTAs but fracture toughness determinations were delayed due to problems encountered in specimen preparation. This has been rectified and toughness evaluations are proceeding.

Communications/Visitors/Travel:

Visited with Ted Lilley, Ken Manwiller and Oh-Hun Kwon at Norton, Co. to discuss the previously mentioned stress rupture results on the YZ-llO material.

A phone conversation with Jerry Brockmeyer of the Rocketdyne division of Rockwell International shows that they are interested in having some of the transformation-toughened silicon nitrides that were developed under subcontract 86X-22009C tested at elevated temperatures using stress rupture type testing. The material of interest is a composite of

Si_3N_4 with 45 w/o ZrO_2 stabilized with Y_2O3. This material has room temperature strengths as high as 1000 MPa, fracture toughness to 6 MPa*m 1/2, and high strength up to 1400°C with various sintering aids.

Problems Encountered:

I am unable to obtain enough time on the SEM for appropriate fractographic and microstructural analysis since the technician which ran the unit is no longer employed at MTL and no one has bee hired to fill the position.

Publications:

Swab, J.J., "Properties of Yttria-Tetragonal Zirconia Polycrystal (Y-TZP) Materials After Long-Term Exposure to Elevated Temperatures," MTL TR89-21, March 1989.

STEPPED-TEMPERATURE STRESS-RUPTURE

YZ110-H AS RECEIVED

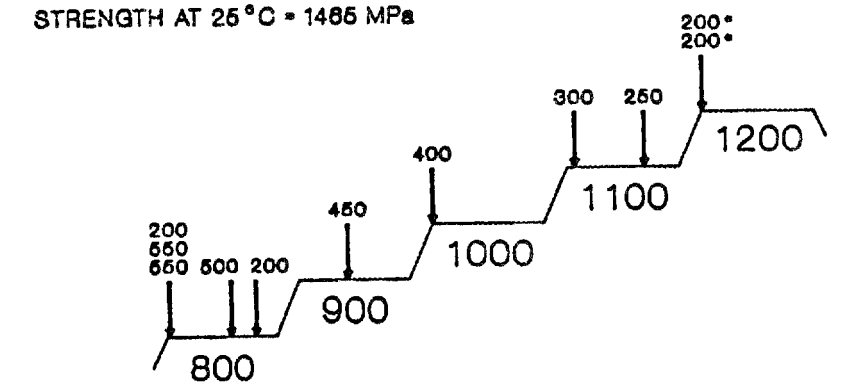

HITACHI 1985

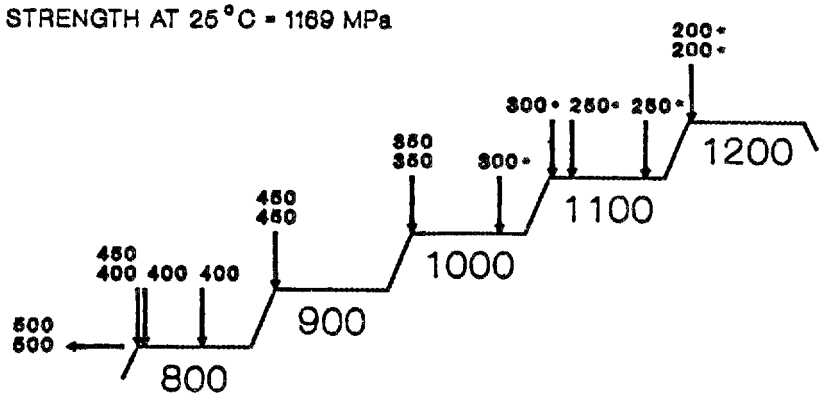

• CREEP FRACTURE
• TEST TERMINATED DUE TO CREEP
+ CREEP PRESENT
STRESS IN MPa
TEMPERATURE IN °C

Figure 1.

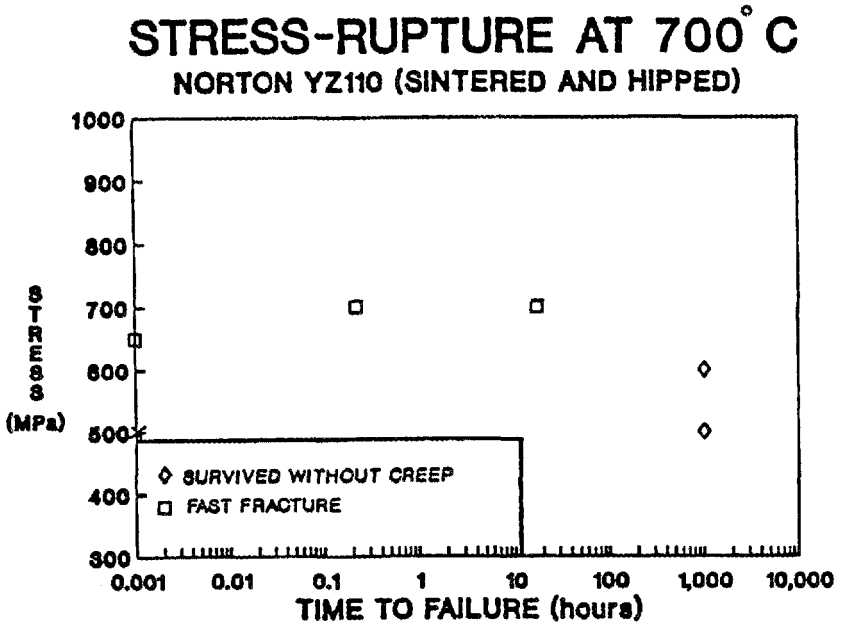

X- Fast Fracture Strength at 700°C as reported by Norton in the Feb-March 1989 Bimonthly. (Corrected for MIL STD 1942 Type B Flexure Bar)

Figure 2.

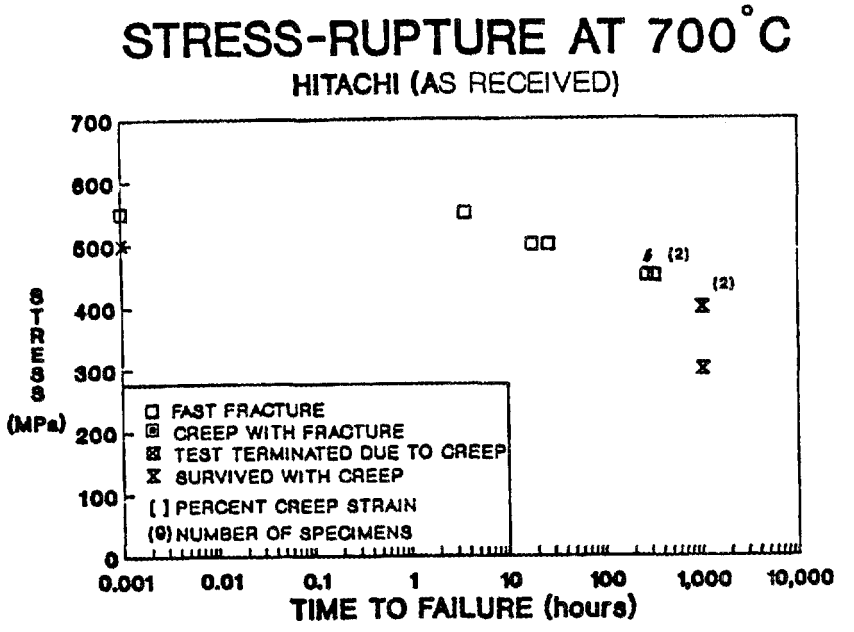

X- Fast Fracture Strength at 700°C.

Figure 3.

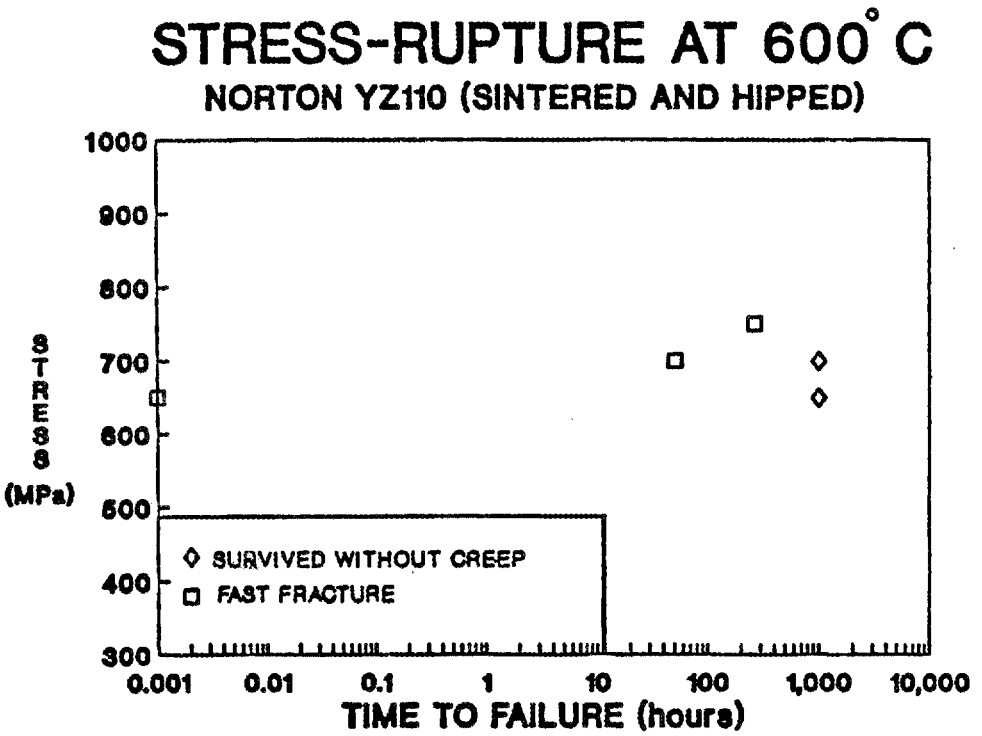
STRESS-RUPTURE AT 600° C
NORTON YZ110 (SINTERED AND HIPPED)
STRESS (MPa)
1000
900
800
700
600
500
400
300
0.001
0.01
0.1
1
10
100
1,000
10,000
TIME TO FAILURE (hours)
SURVIVED WITHOUT CREEP
FAST FRACTURE

Figure 4.

STEPPED-TEMPERATURE STRESS-RUPTURE

KYOCERA-FELDMUEHLE

STRENGTH AT 25 °C = 512 MPa

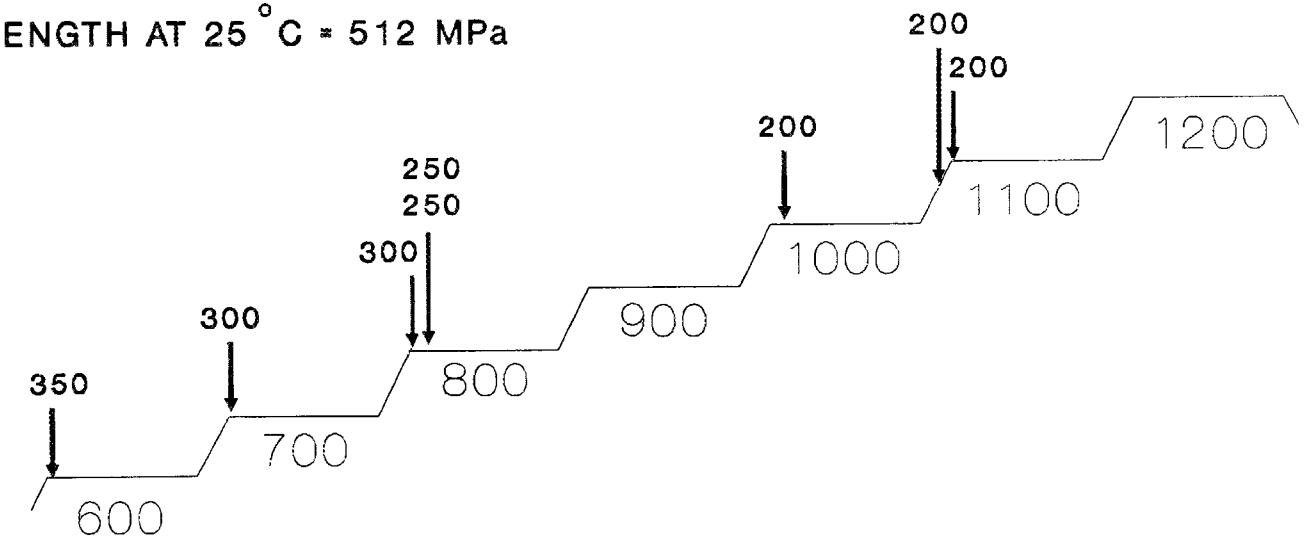

- • CREEP FRACTURE
- * TEST TERMINATED DUE TO CREEP
- + CREEP PRESENT

STRESS IN MPa

TEMPERATURE IN °C

FIGURE 5

STEPPED-TEMPERATURE STRESS-RUPTURE

CERAMATEC (CZA)

STRENGTH AT 25 °C = 441 MPa

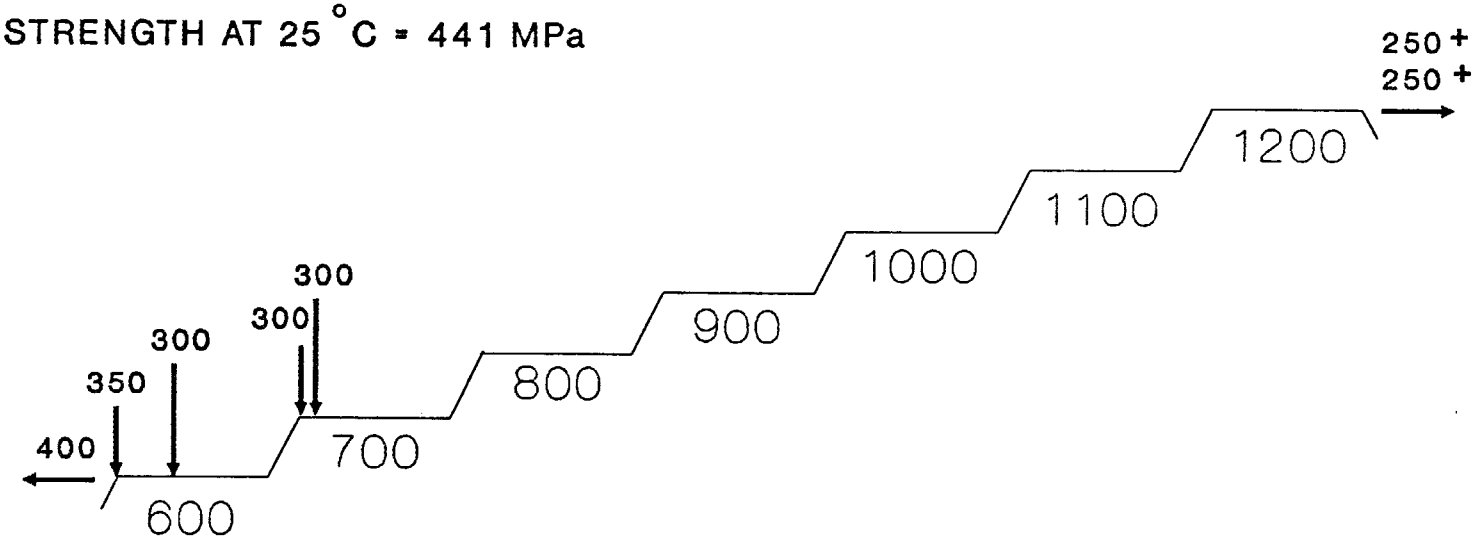

- • CREEP FRACTURE
- * TEST TERMINATED DUE TO CREEP
- + CREEP PRESENT

STRESS IN MPa

TEMPERATURE IN °C

FIGURE 6

Fracture Behavior of Toughened Ceramics

H. T. Lin, P. F. Becher, and W. H. Warwick (Oak Ridge National Laboratory)

Objective/scope

Ceramic composites, such as fiber and whisker-reinforced ceramics, particulate phase composites, and ceramics with similar grain structures, offer important advantages for heat engine applications. Chief among these is the improved fracture toughness that can be achieved by appropriate design of microstructural and material parameters. Previous studies show that these materials often exhibit substantial improvements in damage, thermal shock, and slow crack growth resistances. However, design of such systems must also consider the factors that influence performance at elevated temperatures.

In response to these needs, studies are conducted to determine the mechanical properties, for example, creep, delayed failure, strength, and toughness, at elevated temperatures for these toughened ceramics. Particular emphasis is placed on understanding how microstructure and composition influence the mechanical performance at elevated temperatures and the stability of these properties for extended periods at these temperatures. The knowledge gained from these studies provides input on how to modify materials to optimize their mechanical properties for the temperature ranges of interest.

Technical progress

Previous studies of alumina composites reinforced with 20 vol % SiC whiskers indicated that long-term exposures to flexure stresses at 1200°C resulted not only in permanent deformation but also in a significant degradation in mechanical properties.[1,2] The observed permanent deformation resulted from creep cavitation and microcracking at grain boundaries which led to failure. In order to ensure and improve long-term reliability at temperatures above 1100°C in air, the creep behavior of SiC whisker-reinforced alumina must be understood and controlled. Creep tests in four-point loading configuration at selected stress levels and at temperatures of 1200, 1300, and 1400°C in air of 20 vol % SiC whisker-reinforced alumina vs unreinforced, single-phase alumina have been conducted. The purpose of the polycrystalline fine-grained alumina study was to elucidate the deformation mechanism of alumina matrix and, furthermore, to provide a baseline for understanding the effect of SiC whiskers on the creep behavior of composites.

Figure 1 shows the variation in strain rate vs time for both SiC-reinforced alumina composite (2 μm) and fine-grained alumina (1.5 μm) at temperatures of 1200 and 1300°C and at a stress level of 100 MPa. Strain rate vs time curves of both materials indicate a primary creep stage which transitions to secondary creep stage (steady state creep) with increasing time of test for both materials. The results also show a well-developed, secondary creep stage is achieved. The secondary creep rates of the alumina composites are two orders of magnitude lower than that of the alumina shown in Fig. 1. Thus, the creep resistance of polycrystalline alumina can be significantly improved through the addition of SiC whiskers. On the other hand, the fine-grained alumina always exhibits substantial permanent deformation strain (>3%, limited only by test fixture, not by sample failure) while strain of $\leq$0.5% results in failure in reinforced alumina.

Figure 2 shows the tensile surface features of the polycrystalline alumina that has been polished and then deformed at 1300°C to 3.1% strain. Such observations clearly show intergranular cavitation, which is generally restricted to the neighborhood of well-developed cracks. In all instances, the cavity distributions are inhomogeneous. Grains are observed to slide out of the surface as a result of grain-boundary sliding (GBS). Surface features also reveal grain rotation. Such grain offsets and rotation confirm that GBS makes an important contribution to the creep and deformation of the polycrystalline alumina. TEM studies on similar tensile surface sections of the alumina also reveal intergranular cavities, triangular

voids at triple points, and voids associated with precipitates, as shown in Fig. 3. Triple-point cavities present further evidence of GBS which is not fully accommodated by other diffusion processes. Note that dislocations are rarely observed in the alumina grains. This indicates that GBS, rather than dislocation slip and/or climb, is the dominant process when such materials are subjected to flexure/tensile stress.

The reduction in the ability of grain-boundary sliding, and hence, creep rate in the composites, can be attributed to them acting as hard-pinning particles on the grain boundary surfaces and as rigid rods which penetrate across the boundary planes. Both types of whisker-grain boundary orientations are observed in the composites. The propensity for crack generation in the composites also has its roots in the reinforcing effects that limit GBS and decrease the creep rates. Figure 4 shows a TEM micrograph of tensile surface regions of whisker-reinforced alumina tested at 1300°C. Cavitations at matrix-whisker interfaces, triple-grain junctions, and grain interfaces are noted. In general, the alumina composites exhibit a higher number density of cavities and well-developed microcracks and macrocracks as compared to the alumina. This may be due to the fact that the addition of SiC whiskers into fine-grained alumina acts to introduce more stress concentration sites; consequently, this leads to a higher number density of cavitation and microcracking. It is also apparent that alumina composites exhibit smaller cavity size than those of single-phase alumina. In addition to the greater number of potential cavitation sites, the reduction in cavity size may be influenced by a decrease in plastic deformation of the composites ($\leq$0.5%) vs that of the alumina (>3%). The microcracks join together to generate numerous large-scale cracks, with the most critical crack resulting in failure. This process is likely enhanced for surface flaws by the oxidation of SiC whiskers and the formation of amorphous phases on the surface of the flexure bars. Such amorphous phases would locally accelerate creep damage.

It is seen that creep deformation in flexure in both the alumina and the composite occurs through GBS and by nucleation, growth, and coalescence of grain-boundary cavities. Such processes eventually lead to crack formation and growth and, finally, to failure. The lifetime of these materials at elevated temperatures is dictated first by minimizing creep and eventually by creep damage accumulation. The presence of grain-boundary SiC whiskers significantly retards the grain-boundary sliding, leading to a substantial decrease in steady creep rates. This feature allows the composite to be utilized at higher temperatures than the monolithic alumina while avoiding excessive deformation. The whiskers also promote cavitation and decrease the strain to failure. However, the use of such materials demands that permanent deformation first be excluded at the elevated temperatures over the desired stress range.

Sintering aids, that is, Y_2O_3 and MgO, are sometimes used to enhance the densification rate and limit grain growth of the matrix of the alumina-based composites. This is partly accomplished by the formation of grain-boundary glassy phases containing Y, Al, and Si. Creep tests in four-point flexure in air at 1300°C were also conducted on alumina composites (20 vol % SiC whiskers) containing sintering aids (i.e., 0.4 wt % MgO and 0.4 wt % Y_2O_3) to understand how the sintering aids influence the creep resistance of alumina composites under the testing conditions employed in this study.

The creep data for alumina composites with and without sintering aids at 1300°C is shown in Fig. 5 as a log-log plot of steady creep rate vs applied stress. Results indicate that the creep rate of alumina composites is increased by approximately two to three orders of magnitude with the addition of sintering aids as compared to the composite without additives. In addition, the composite containing sintering aids exhibits a higher stress exponent ($n \approx 4.3$) than that of composite without sintering aids ($n \approx 2$). This suggests that the contribution of the various creep processes in these two materials is quite different. The higher creep rate and stress exponent found in the composite containing sintering aids are attributed to the observed substantial content of amorphous phases at grain boundaries as compared to composites made without sintering aids. The presence of intergranular glassy

phase is known to enhance the creep processes of ceramics at elevated temperatures. For example, similar high stress exponent, $n \approx 4.8$, was also observed in a glass-bonded, 96% aluminum oxide.[3] A creep is enhanced by the presence of intergranular amorphous phases in Si_3N_4 ceramics and Si_3N_4-SiC whisker composites with the Y_2O_3 plus Al_2O_3 sintering aids.[4-6] Results of the sintering aids study suggest either that the sintering aids need to be modified or that a subsequent heat treatment needs to be devised to crystallize the amorphous phases to achieve the optimal properties for high temperature applications.

Status of milestones

A shift in Milestone No. 321308 was requested in September with a new target date of June 1990. This request was due to a delay in the receipt of high temperature dilatometers.

Publications

Paper entitled, "Creep Behavior of a SiC Whisker Reinforced Alumina," submitted to *J. Am. Ceram. Soc.*

References

1. P. F. Becher and T. N. Tiegs, "Temperature Dependence of Strengthening by Whisker Reinforcement: SiC Whisker Reinforced Alumina in Air," *Adv. Ceram. Mater.* 3(2), 148-54 (1988).

2. P. F. Becher, P. Angelini, W. H. Warwick, and T. N. Tiegs, "Elevated Temperature Delayed Failure of Alumina Reinforced with 20 vol % SiC Whiskers," *J. Am. Ceram. Soc.*, in press.

3. S. M. Wiederhorn, B. J. Hockey, R. F. Krause, Jr., and K. Jakus, "Creep and Fracture of a Vitreous-Bonded Alumina Oxide," *J. Mater. Sci.* 21, 810-24 (1986).

4. N. J. Tighe, S. M. Wiederhorn, T. J. Chuang, and C. L. McDaniel, "Creep Cavitation and Crack Growth in Silicon Nitride," pp. 587-604, in *Mat. Sci. Res. Vol. 18: Deformation of Ceramic Materials II*, eds. R. E. Tressler and R. C. Bradt, Plenum Press, New York, 1984.

5. M. H. Lewis, G. R. Heath, S. M. Winder, and R. J. Lumby, "High-Temperature Creep and Fracture of $\beta'Si_3N_4$ Ceramic Alloys," pp. 605-16 in *Mat. Sci. Res. Vol. 18: Deformation of Ceramic Materials II*, eds. R. E. Tressler and R. C. Bradt, Plenum Press, New York, 1984.

6. R. D. Nixon, S. Chevacharoenkul, M. L. Huckabee, S. T. Buljan, and R. F. Davis, "Deformation Behavior of SiC Whisker Reinforced Si_3N_4," pp. 295-302 in *MRS Proceedings: Advanced Structural Ceramics, Vol. 78*, eds. P. F. Becher, M. V. Swain, and S. Somiya, Materials Research Society, Pittsburgh, 1987.

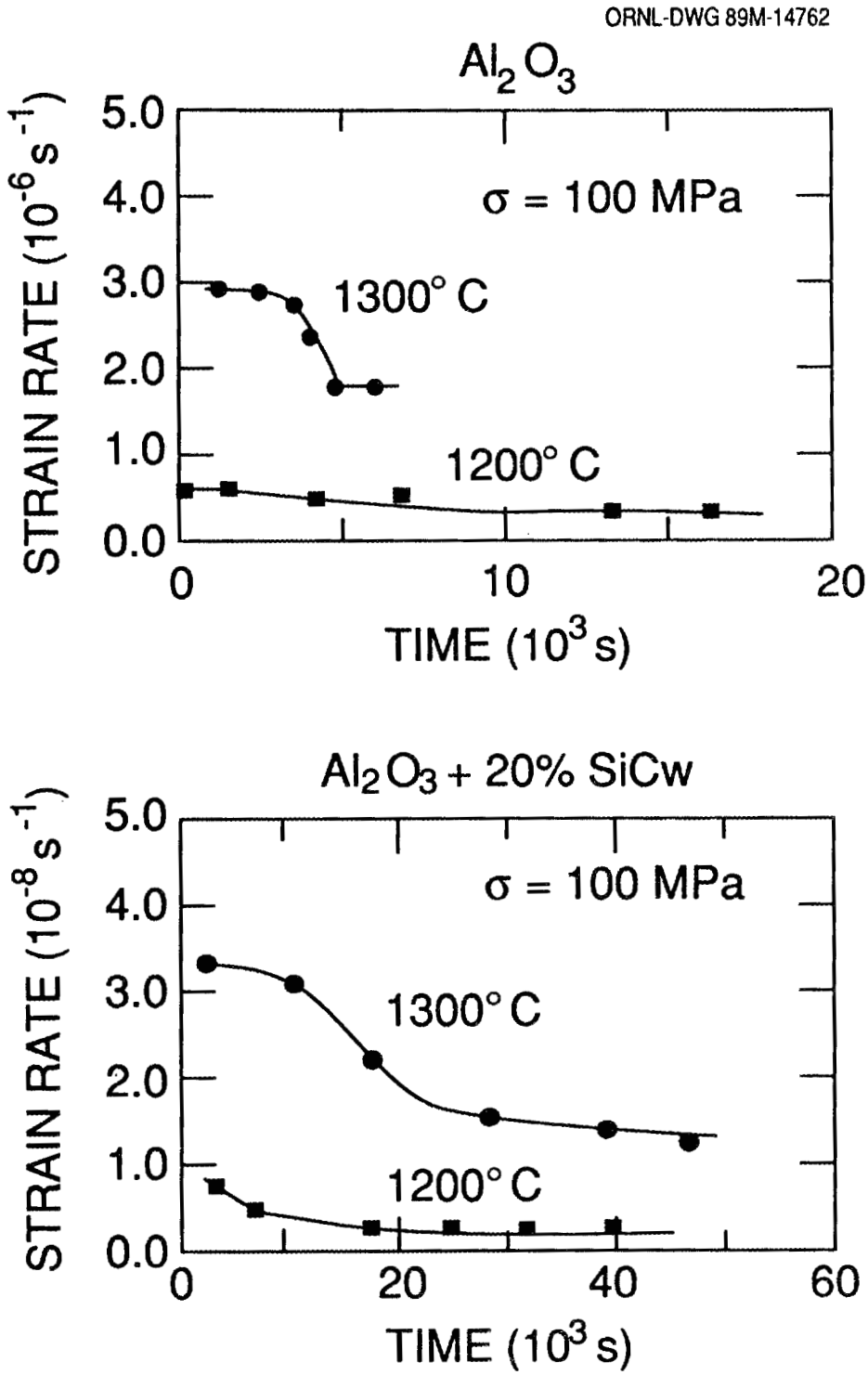

Fig. 1. Strain rate vs time creep curves for polycrystalline fine-grain alumina and SiC whisker-reinforced alumina. Note creep rate of alumina is significantly reduced through the addition of SiC whiskers.

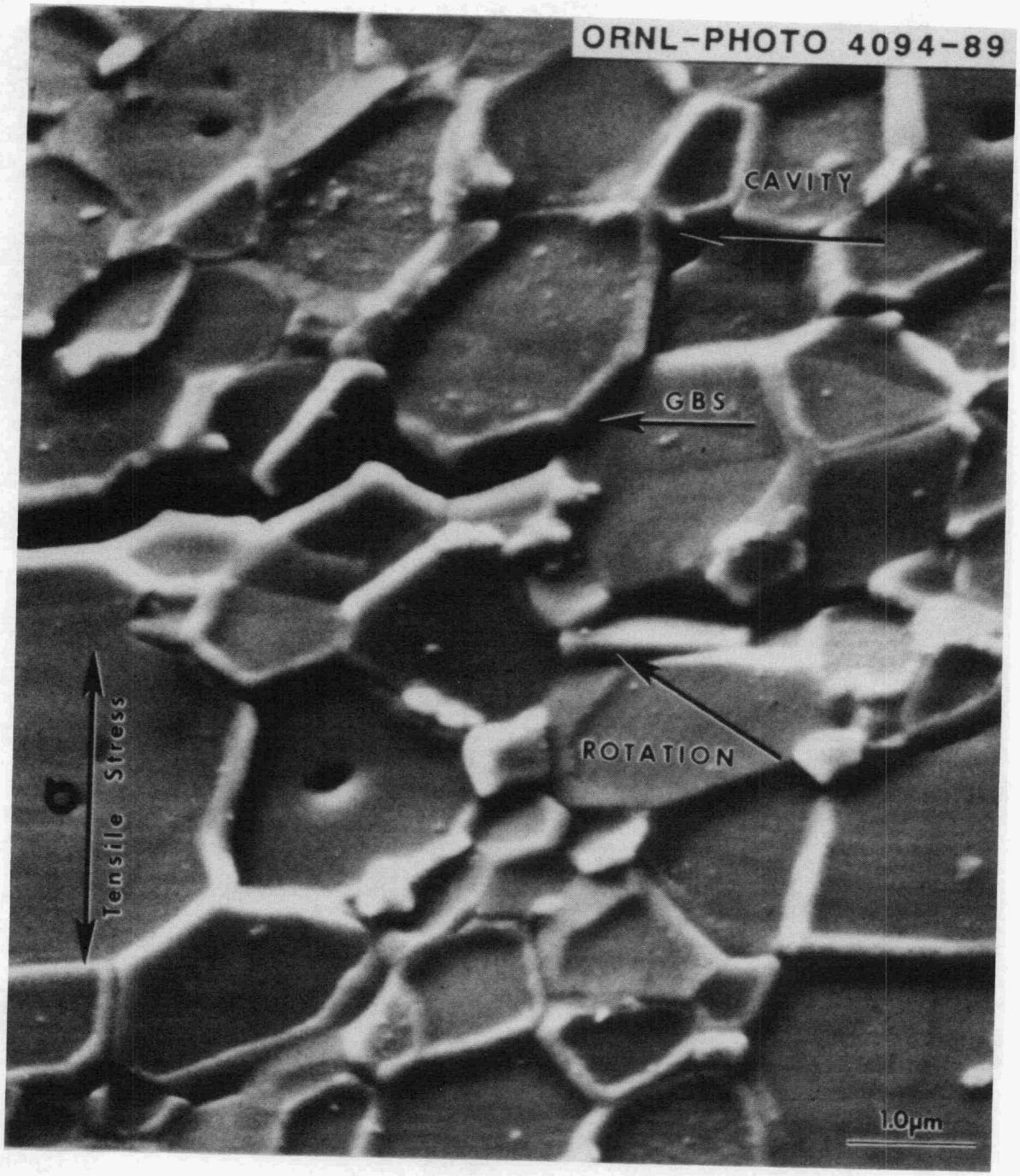

Fig. 2. SEM micrograph of tensile surface regions of polycrystalline alumina tested at 1300°C to strain of 3.1%. Grain-boundary sliding is evidenced by sliding of grains out of the surface.

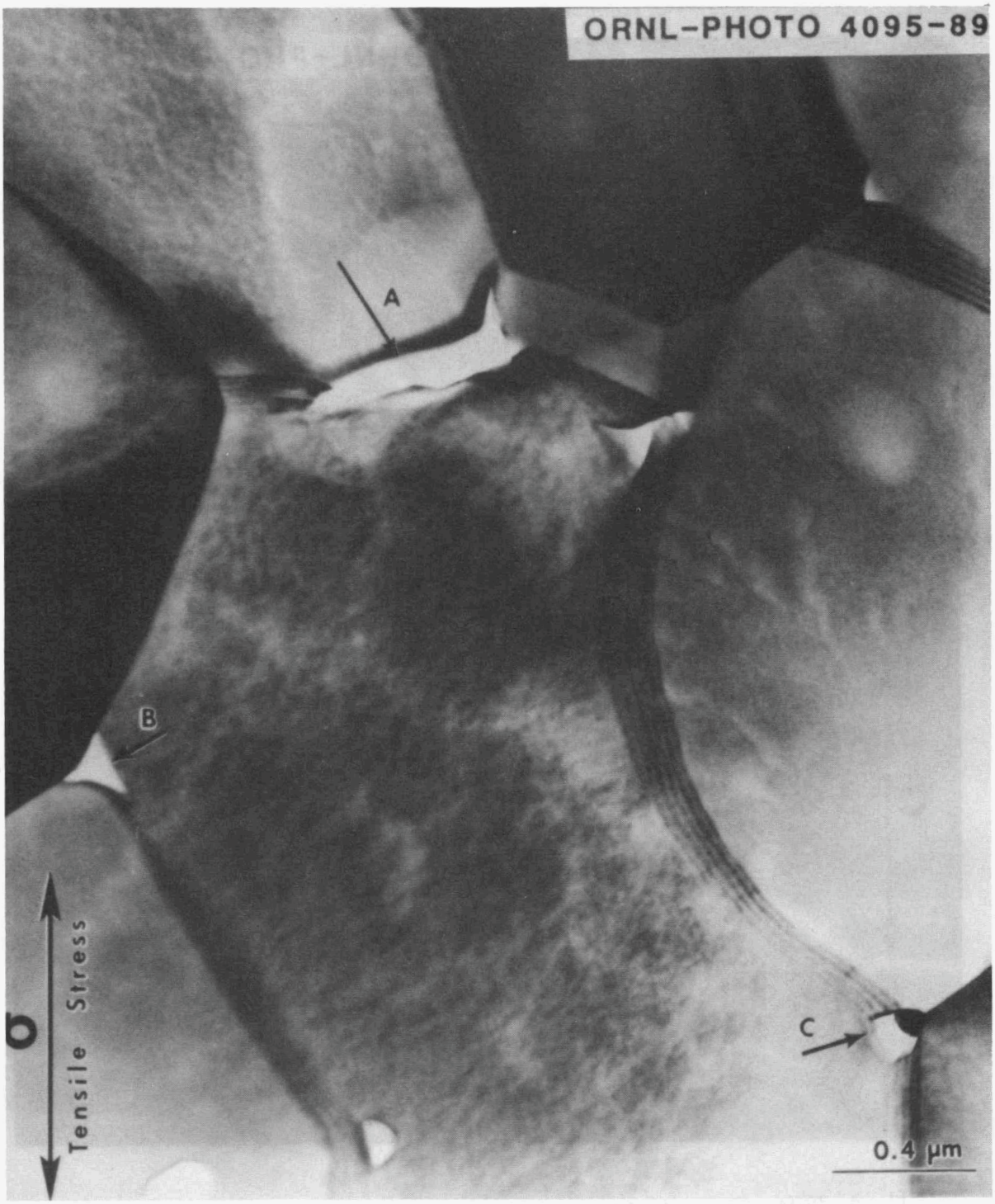

Fig. 3. TEM micrograph of tensile surface regions of polycrystalline alumina tested at 1300°C. Note cavitation occurs at grain boundaries, triple grain junctions, and precipitates.

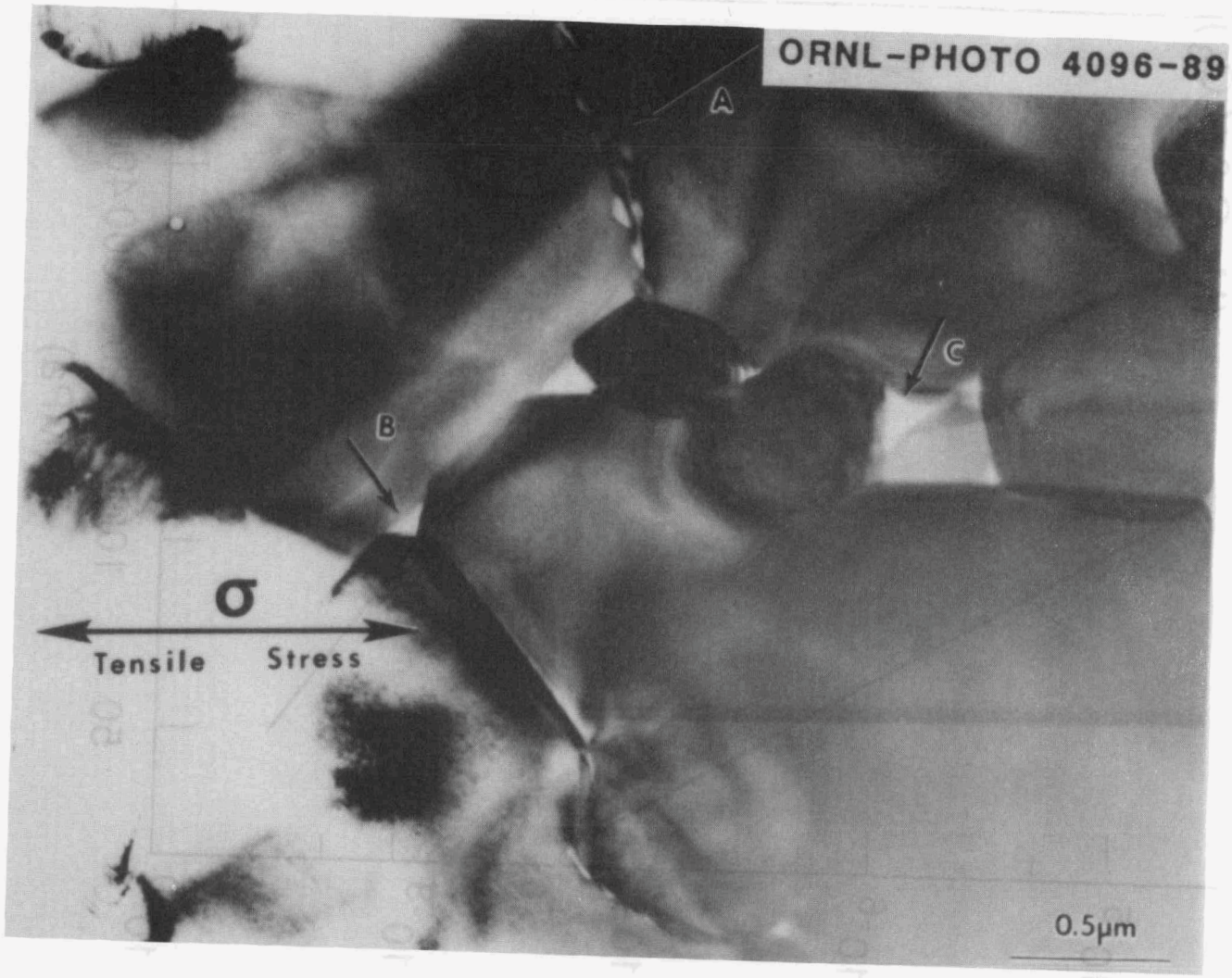

Fig. 4. TEM micrograph of tensile surface regions of SiC whisker-reinforced alumina tested at 1300°C. Note cavitation occurs at matrix-whisker interfaces, triple grain junctions, and grain interfaces. Grain boundaries are decorated with small polyhedral cavities.

ORNL-DWG 89M-16917

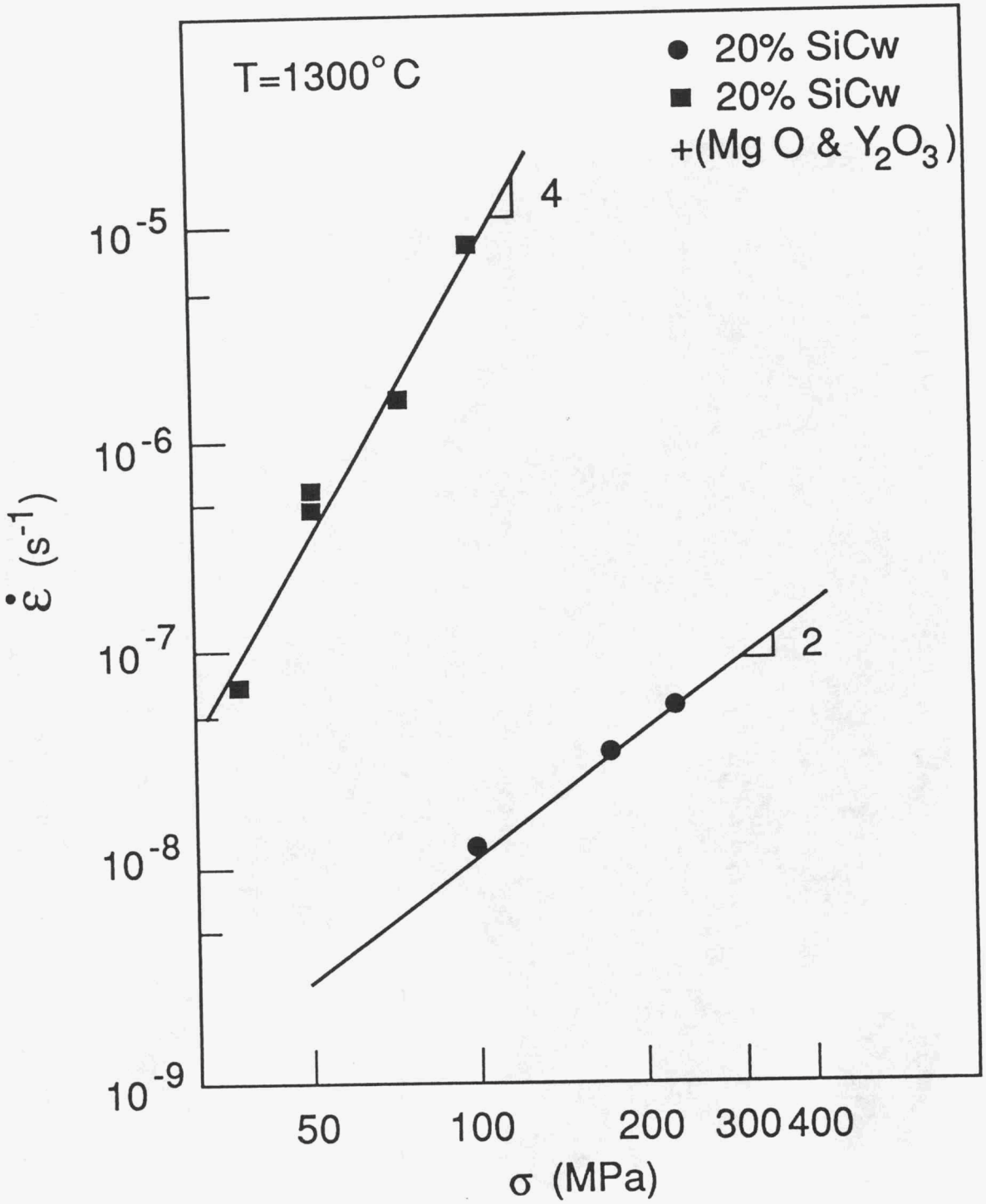

Fig. 5. Stress rate vs stress relation for creep deformation of SiC whisker-reinforced alumina with and without sintering aids at 1300°C.

Cyclic Fatigue of Toughened Ceramics

K. C. Liu and C. R. Brinkman (Oak Ridge National Laboratory)

Objective/scope

The objective of this task activity is to develop, design, fabricate, and demonstrate the capability to perform tension-tension dynamic fatigue testing on a uniaxially loaded ceramic specimen at elevated temperatures.

Three areas of research have been identified as the main thrust of this task: (1) design, fabrication, and demonstration of a load train column which truly aligns with the line of specimen loading; (2) development of a simple specimen grip that can effectively link the load train and test specimen without complicating the specimen geometry and hence, minimize the cost of the test specimen; and (3) design and analysis of a specimen for tensile cyclic fatigue testing.

Technical progress

An exploratory test matrix designed to generate tensile and cyclic fatigue data has been completed on Norton/TRW NT-154 Si_3N_4. Specimens designated as CP-series were fabricated by a cold isostatic pressing process prior to HIPing and those fabricated by slip casting as the PC-series. Because the total number of PC specimens was limited, only tensile tests were performed for this series. Test parameters and test results were summarized in Tables 1 and 2 for uniaxial monotonic tensile tests and in Table 3 for cyclic fatigue tests. Two different stressing rates of 7.5 and 2100 MPa/min were used in tensile tests to investigate the effects of stressing rate on the tensile strength of this material. A much higher stressing rate of 21,000 MPa/min was used in cyclic fatigue tests.

Results of uniaxial tensile testing. All tensile data obtained to date were plotted in Fig. 1. Discussions were given previously concerning the tensile strength of CP-specimens related to MOR strength obtained by various laboratories. Comparisons of data given in Fig. 1 show that slip cast specimens (PC-series) yielded tensile strengths marginally higher than that of CIPed specimens (PC-series) at temperatures below 1300°C. The situation was inconclusive at 1300°C due to the lower fracture strength obtained for specimen PC-2. A cursory examination of optical fractographs of specimen PC-2 indicated that the low fracture strength was attributed to a large fracture initiating a defect located near the center of the fractured cross-section.

Uniaxial stress-strain behavior of the material at elevated temperatures is shown in Fig. 2. Testing under the high stressing rate at 2100 MPa/min showed the material behaved like an elastic solid. As the stressing rate was decreased to 7.5 MPa/min, plastic deformation became barely perceptible in the high stress range for CIPed specimens tested at 1200 and 1300°C (curves B and D). In contrast, slip cast specimens appeared to be more viscoplastic in the high temperature range as shown in curves E and H for specimens PC-3 and PC-7, respectively. This might be the reason that the tensile strength of PC specimens was generally higher compared to that of CP specimens. The values of elastic modules tabulated in Tables 1 and 2 were determined from the stress-strain curves whenever they were available.

Cyclic fatigue testing. Cyclic fatigue tests were continued. As in the previous tests, two modes of cyclic loading conditions were used: (a) a constant amplitude cyclic loading in tension-tension with an R-ratio of about 0.1 at a stressing rate of 21,000 MPa/min, and (b) cyclic loading from low to high stress levels in multiple steps generally known as "coaxing." Test parameters and results were tabulated in Table 3, and the test data were

plotted in Fig. 3. The closed symbols indicate that failure occurred at the test condition indicated; whereas, the open symbols attached with an arrowhead indicate the end point of each intermediate cyclic loading, and that specimen failure did not occur at the indicated test condition. Intermediate loading steps were interconnected by short broken lines, which in all cases ended at the closed symbols, indicating specimen failure. Partially-filled symbols indicate the tensile fracture strength of specimens tested at the slow stressing rate.

The fatigue curves depicted in Fig. 3 were determined visually based on the trend portrayed by the data points in the same temperature group. Therefore, they must be regarded only as approximations at this time and will be subject to revisions as more data are generated. Specimen CP-15 was not included in the approximate curve fitting for the 1300°C data because it failed prematurely due to surface damage as pits resulting from the interaction between the specimen and the alumina probing rods used in the mechanical strain extensometer. The alumina rods will be replaced with SiC rods in future testing. In the meantime, the mechanical strain extensometer was used in subsequent tests only for a short period of time to record the initial cyclic stress-strain curves. The strain extensometer was then disengaged from the test specimen. To best describe the fatigue behavior at 1370°C, data were bracketed by a scatter band.

Electron microscopy. Optical (OM) and scanning electron microscopy (SEM) were performed on specimens CP-10 and CP-14 tested at 1200°C in tension at a fast (2100 MPa/min) and a slow (7.5 MPa/min) testing rate, respectively, and are illustrated in Figs. 4 and 5. Those of specimens CP-8 and CP-12 tested at 1370°C are given in Figs. 6 and 7, respectively. Fracture surfaces of all specimens tested in tension show that internal and subsurface defects were the origins of fracture initiation sites, as shown in Figs. 4–7. Flat mirror regions at fracture initiation sites are smaller for specimens tested at 1200°C compared with those for specimens tested at 1370°C. Similarly, they are smaller for specimens tested at the fast stressing rate compared with those for specimens tested at the slow stressing rate. Slow crack growth was apparently a dominant mechanism of fracture at 1370°C under the slow stressing rate. General observations show that the porosity is small, a couple of microns or less in diameter, and uniform throughout the bulk, resulting in high tensile strength. Therefore, a cluster of relatively large defects, ranging from 10 to 30 microns, was usually a potential fracture initiation site. Transgranular fracture was a prevailing mode of fracture for specimens tested at 1200°C. However, as temperature increased to 1370°C, a mixed mode of transgranular and intergranular fractures became more evident in the crack mirror region.

To investigate the effect of coaxing on the fatigue behavior of this material, each coaxing test was paired with a control test using the same stress level: CP-16 (coaxed) vs CP-20 (uncoaxed), CP-21 vs CP-22, and CP-24 vs CP-26, respectively. Observation clearly indicates that coaxing enhanced the cyclic fatigue lifetime by nearly one to two orders of magnitude. Testing of specimens CP-27 and CP-29 was intended to determine the high-cycle fatigue lifetime of the material at 1370°C. However, in both cases, the specimens underperformed far below our expectations.

Tensile testing of SiC whisker-reinforced alumina. A hot-pressed plate (150 mm^2 by 16 mm) of silicon carbide whisker-reinforced alumina, designated as PAD-AS30W, was received from CERCOM of Vista, California. A batch of seven specimens was made from the plate, following detailed NDE inspection by ultrasonics. Figure 8 shows an ultrasonic scan on a focal plane at a depth of about 2.5 mm from the plate surface. Large dark spots indicate defects which may be poorly dispersed SiC whisker clumps or inclusions. Noted that the images of the defects as seen in Fig. 8 were exaggerated by the technique with the actual sizes being much smaller. Examinations under a light microscope showed that all specimens had small, shallow, surface defects. Nevertheless, the specimens were tested in

the as-machined condition without surface polishing. It was intended to see if the tensile strength would be influenced by such surface flaws.

A total of six specimens was tested in pure tension. Three specimens were instrumented with strain gages to plot the stress-strain relationship and to determine the modulus of elasticity of the material. The remaining three specimens were tested with a mechanical strain extensometer for the purpose of comparing measurements with strain gage data. The test results are summarized in Table 4. The average tensile strength was 431 MPa (62.5 ksi), which was about 40% higher than that of monolithic alumina. Values of the tensile strength show a high degree of reproducibility in comparison to previous values obtained from monolithic materials. This implied that the Weibull modulus would be high for this material. The values of elastic modulus given in Table 4 were determined from measured stress-strain curves.

Examination of the fractographs shown in Figs. 9 and 10 indicated that all tensile fractures were initiated from large internal flaws, as shown by open arrowheads. Random locations of the fracture origins, with respect to a fixed reference testing position, indicated the fractures were not biased by test equipment and fixtures. Further detailed studies indicated that the tensile strength was inversely proportional to the size of the fracture initiating flaw. The small defect that is barely visible in Fig. 9 (1) was apparently responsible for the high tensile strength in specimen 1 and vise versa in the other cases. Probably by coincidence, the fracture initiating defects in specimens 2 through 6 show about the same shape and size, resulting in remarkable reproducibility of the tensile strength data.

A remaining tensile specimen was subjected to cyclic fatigue loading in tension to a peak stress of 330 MPa (48 ksi) at a stressing rate of 21,000 MPa/min. The peak stress is equivalent to about 77% of the average tensile fracture strength calculated from the test data given in Table 4. A total of 115,000 cycles has accumulated to date, and the test is continuing.

Status of milestone

321408 - Elevated-temperature fatigue and tensile tests on an advanced toughened ceramic material were completed as scheduled.

321409 - A draft report covering results of elevated-temperature tests on toughened ceramic material has been completed and will be reviewed for publication.

Publications

H. Pih and K. C. Liu, "Laser Diffraction Methods for High Temperatures Strain Measurement," in *Proceedings of 1989 Spring Conference on Experimental Mechanics*, Society of Experimental Mechanics, Cambridge, Mass., May 30-June 1, 1989, ISBN 0-912053-24-0, pp. 87-93.

Submitted the abstract entitled, "High Temperature Tensile Strength and Fatigue of Silicon Nitride," for preprints of the 1989 ATD-CC meeting, Dearborn, Mich., October 23-26, 1989.

References

1. K. C. Liu and C. R. Brinkman, "Cyclic Fatigue of Toughened Ceramics," Ceramic Technology for Advanced Heat Engines Project," *Semiannual Progress Report for October 1988 through March 1989*, ORNL/TM-11239, Oak Ridge National Laboratory, pp. 351-360, August 1989.

Table 1. Tensile tests of Norton/TRW NT-154 CIPed silicon nitride at room and elevated temperatures

Specimen	Temperature (°C)	Modulus of elasticity GPa (10^6 psi)	Stress rate MPa/min	Tensile strength MPa (ksi)	Total strain at failure (%)	Plastic strain (%)
CP-18	RT	-	2100	933 (135.3)	-	0
CP-5	1100	298.3 (43.3)	2100	642 (93.1)	0.214	0
CP-10	1200	292.9 (42.5)	2100	623 (90.4)	0.212	0
CP-14	1200	274.6 (39.8)	7.5	503 (72.9)	0.199	0.016
CP-6	1300	281.2 (40.8)	2100	529 (76.7)	0.186	0
CP-13	1300	234.4 (34.0)	7.5	288 (41.8)	0.152	0.029
CP-8	1370	261.6 (37.9)	2100	320 (46.5)	0.13	0.007
CP-12	1370	209.4 (30.4)	7.5	203 (29.4)	0.252	0.155

Table 2. Results of tensile tests on NT-154 slip cast silicon nitride at elevated temperatures

Specimen	Temperature (°C)	Modules of elasticity GPa (10^6 psi)	Stress rate MPa/min	Tensile strength MPa (ksi)	Total strain at failure (%)	Plastic strain (%)
PC-5	1100	290.4 (42.1)	2100	721 (104.6)	0.247	0
PC-6	1100	247.4 (35.9)	7.5	560 (81.3)	0.226	0
PC-1	1200	---	2100	419 (60.7)*	---	---
PC-4	1200	254.9 (36.9)	2100	525 (76.1)*	---	---
PC-10	1200	---	2100	638 (92.5)	---	---
PC-9	1200	224.5 (32.6)	7.5	524 (76.1)	0.231	0
PC-2	1300	---	2100	382 (55.4)	---	---
PC-3	1300	211.9 (30.7)	7.5	295 (42.8)	0.242	0.102

*The maximum stress attained at the moment of buttonhead failure.

Table 3. Summary of cyclic fatigue tests of Norton/TRW NT-154 silicon nitride tested at elevated temperatures

Specimen	Temperature (°C)	Cyclic stress to failure MPa (ksi)	Intermediate cyclic stress MPa (ksi)	Number of cycles at intermediate cyclic loading	Number of cycles to failure
CP-16	1200		414.3 (60.1)	80,000	(80,000)a
		452.3 (65.6)		28,691	108,691
CP-19	1200	474.64 (68.9)			270
CP-20	1200	448.7 (65.1)			8,605
CP-15	1300		277.0 (40.2)	346,000	(346,000)
			292.2 (42.4)	119,300	(465,300)
		307.3 (44.6)		1,467	466,767
CP-21	1300		338.1 (49.0)	1,024,490	(1,024,490)
			357.5 (51.8)	233,240	(1,257,730)
			372.4 (54.0)	191,000	(1,448,730)
		387.5 (56.2)		44,383	(1,493,113)
CP-22	1300	387.5 (56.2)			278
CP-23	1300	361.2 (52.4)			762
CP-24	1370		207.0 (30.0)	467,600	(467,600)
			219.9 (31.9)	216,200	(683,800)
		243.3 (34.0)		131,766	815,566
CP-26	1370	234.0 (34.1)			2,349
CP-27	1370	211.5 (30.7)			51
CP-29	1370	211.8 (30.7)			238

[a]Number of cycles accumulated at the end of intermediate loading.

Table 4. Uniaxial tensile strength of SiC whisker-reinforced alumina (CERCOM, PAD-AS530W) tested at room temperature.

Specimen	Modulus of elasticity GPa (10^6 psi)	Tensile strength MPa (ksi)	Total strain at failure (%)
CC-1	397 (57.5)	453 (65.7)	0.114[a]
CC-2	396 (57.5)	433 (62.8)	0.109[a]
CC-3	403 (58.4)	426 (61.8)	0.106[a]
CC-4	381 (55.3)	423 (61.4)	0.111[b]
CC-5	427 (61.9)	421 (61.0)	0.099[b]
CC-6	431 (62.5)	431 (62.5)	0.1[b]

[a]Indicates strain measured by strain gages.

[b]By a mechanical strain extensometer.

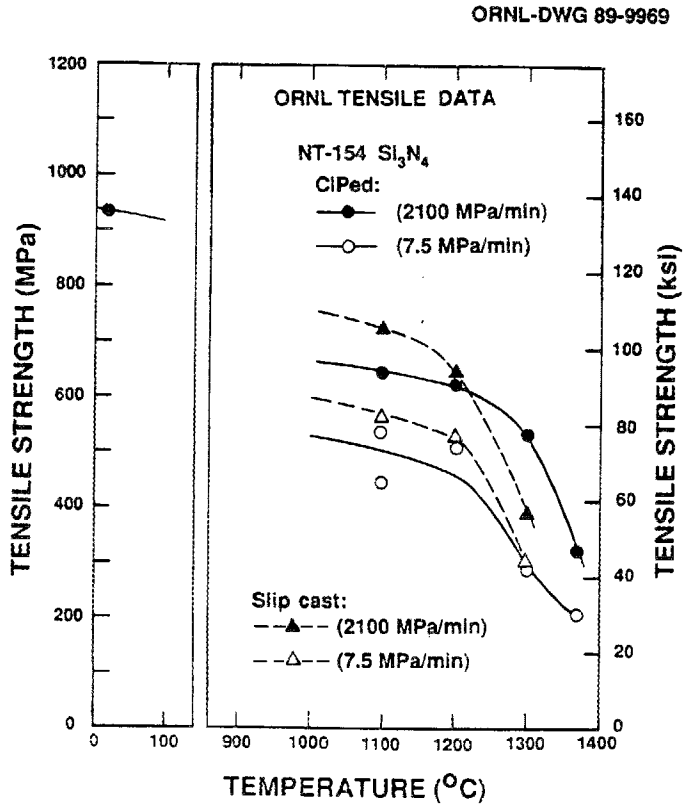

Fig. 1. Comparison of tensile data for CIPed and slip cast NT-154 silicon nitride tested at elevated temperatures.

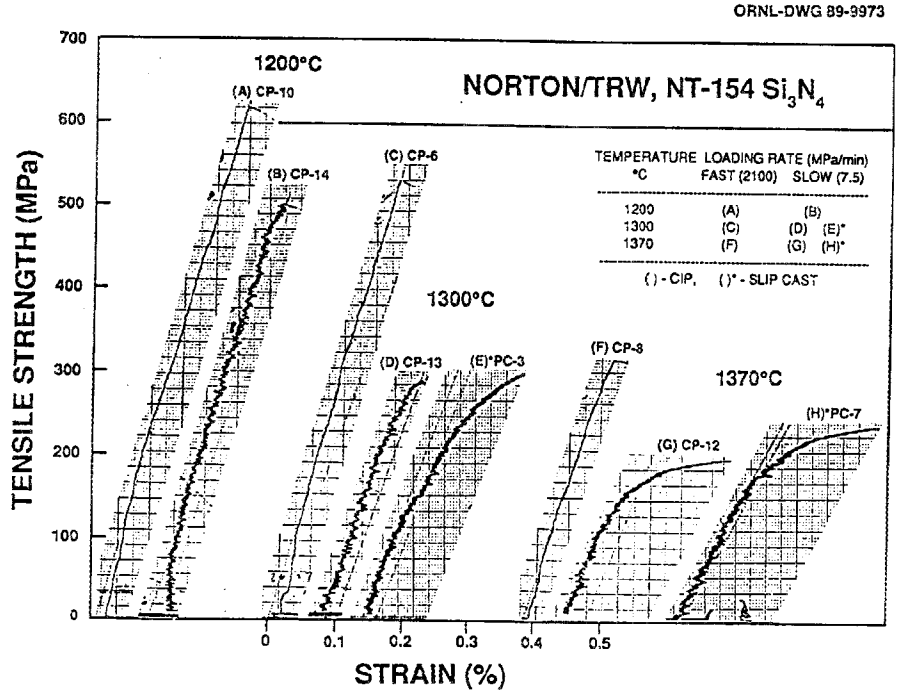

Fig. 2. Uniaxial tensile stress-strain curves of NT-154 silicon nitride tested at elevated temperatures.

ORNL-DWG 89-9969

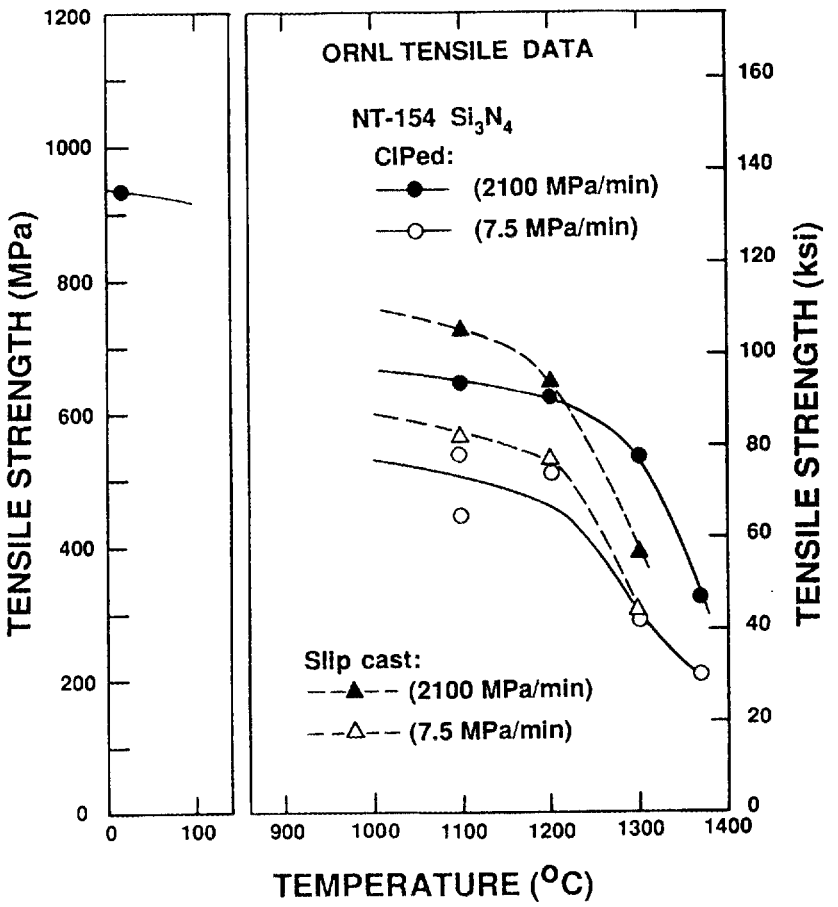

Fig. 3. Tensile strength and fatigue behavior of NT-164 CIPed silicon nitride tested at elevated temperatures. Partially filled symbols indicate slow tensile tests at 7.5 MPa/min.

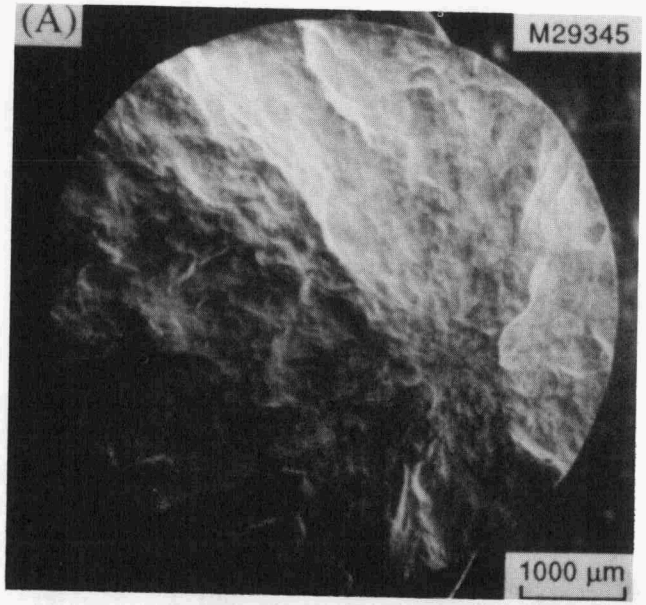

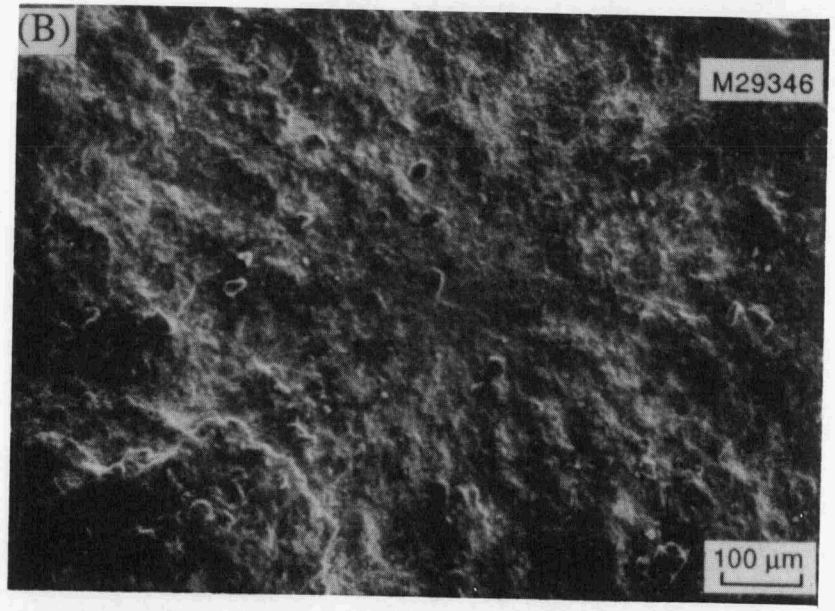

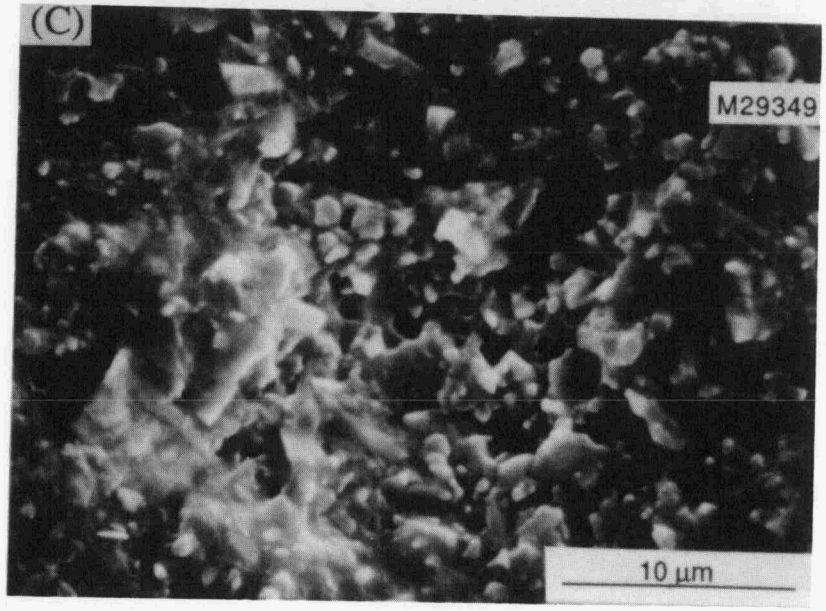

Fig. 4. (a) Fracture surface of specimen CP-10 tested at 1200°C in uniaxial tension at a fast stressing rate (2100 MPa/min), (b) fracture initiation site in a small crack mirror region of about 400 µm in diameter, (c) fracture origin.

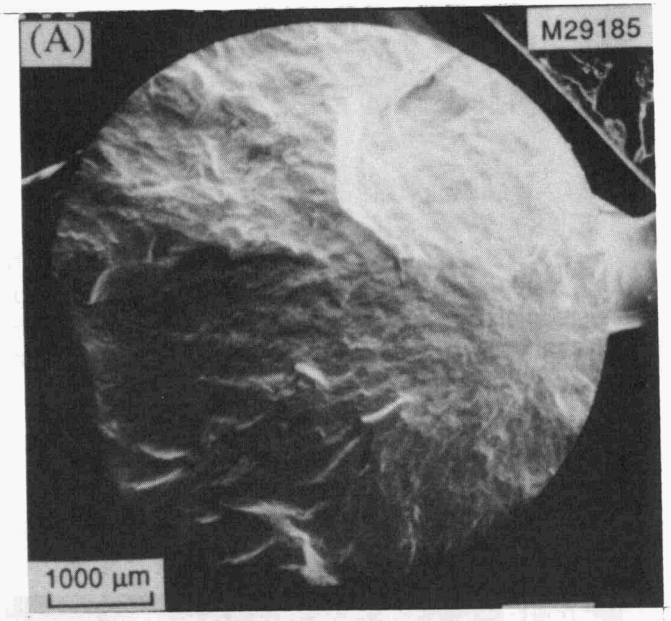

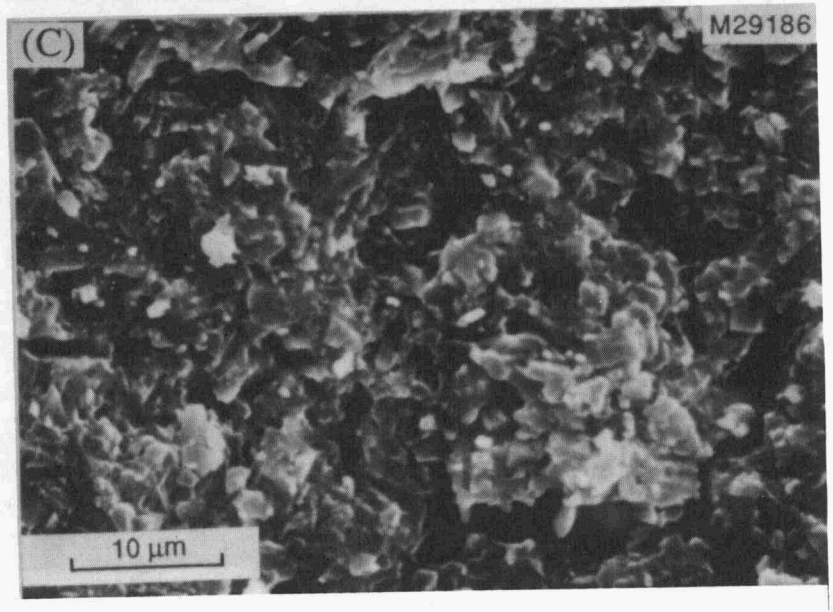

Fig. 5. (a) Fracture surface of specimen CP-14 tested at 1200°C in uniaxial tension at a slow stressing rate (7.5 MPa/min), (b) crack mirror region, (c) internal defects at the center of fracture origin.

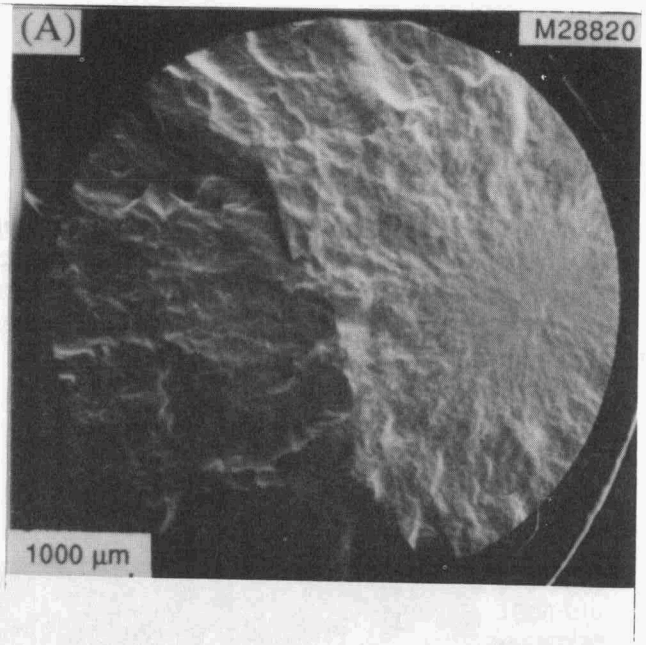

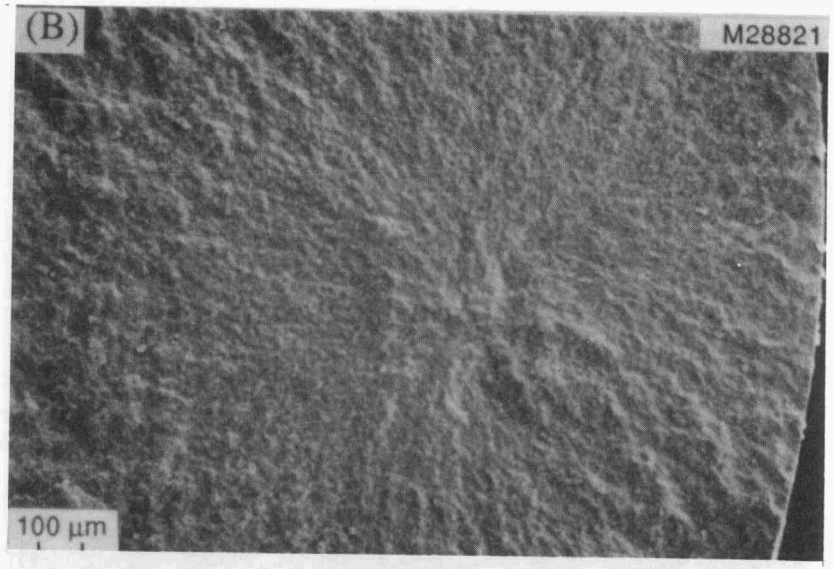

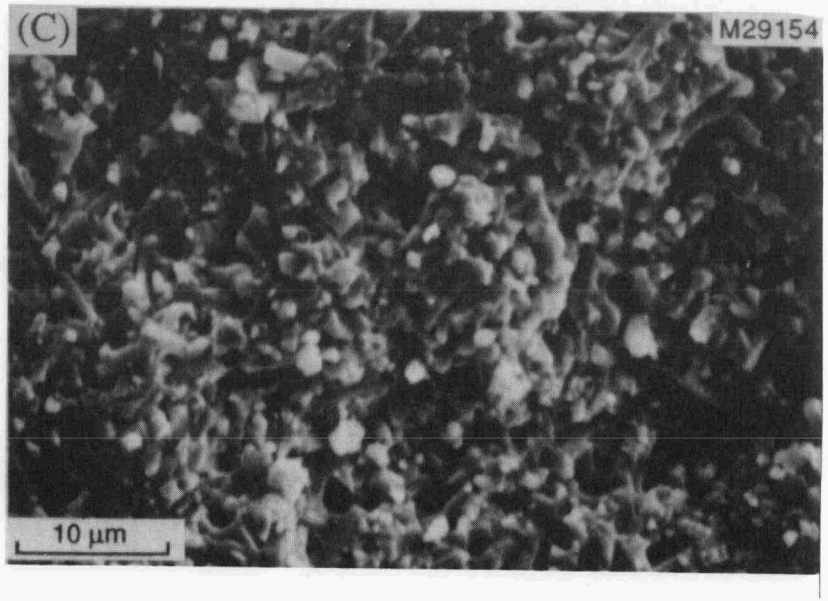

Fig. 6. (a) Fracture surface of specimen CP-8 tested at 1370°C in uniaxial tension at a fast stressing rate (2100 MPa/min) (b) fracture initiation site showing a large crack mirror region of about 1300 µm in diameter, (c) area near the center of fracture origin.

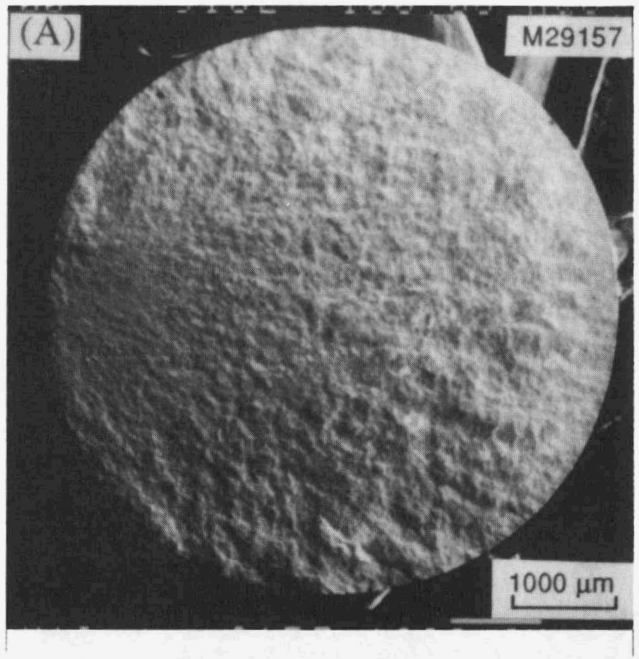

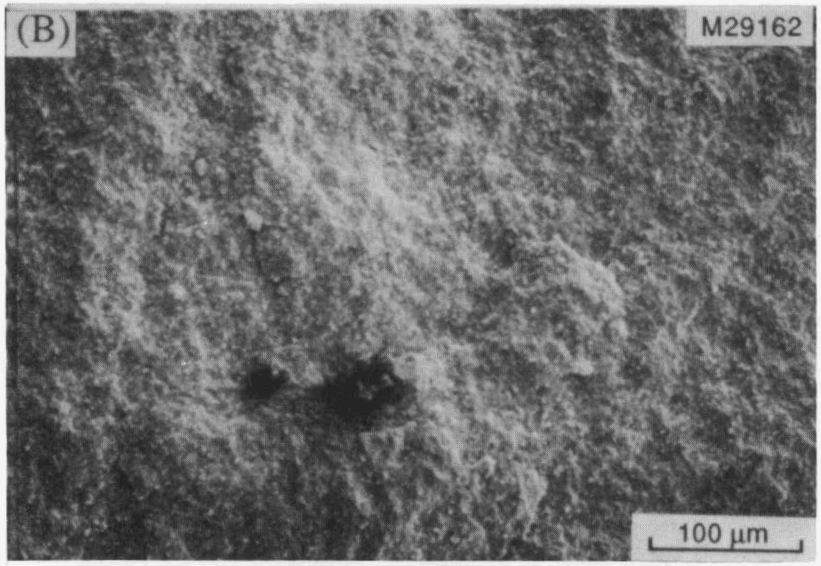

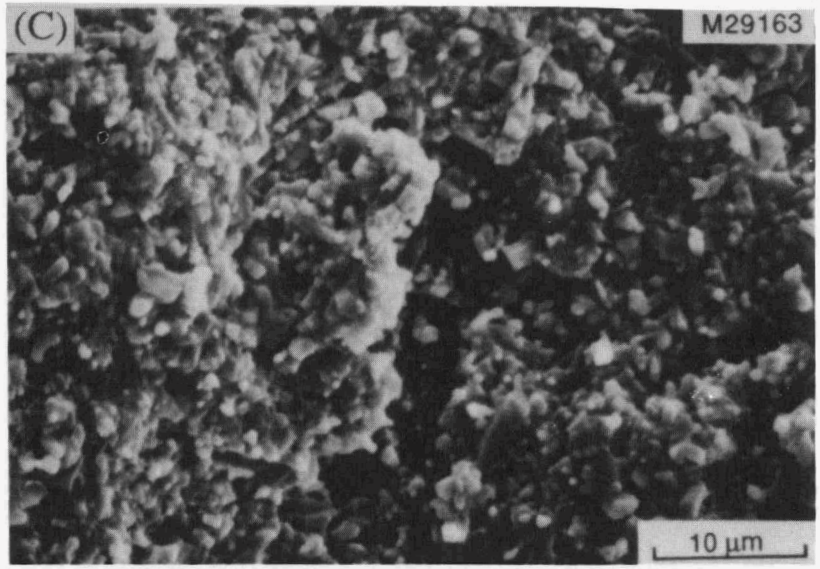

Fig. 7. (a) Fracture surface of specimen CP-12 tested at 1370°C in uniaxial tension at a slow stressing rate (7.5 MPa/min), (b) fracture initiation site showing a cluster of large defects, (c) typical defects in the region of fracture origin.

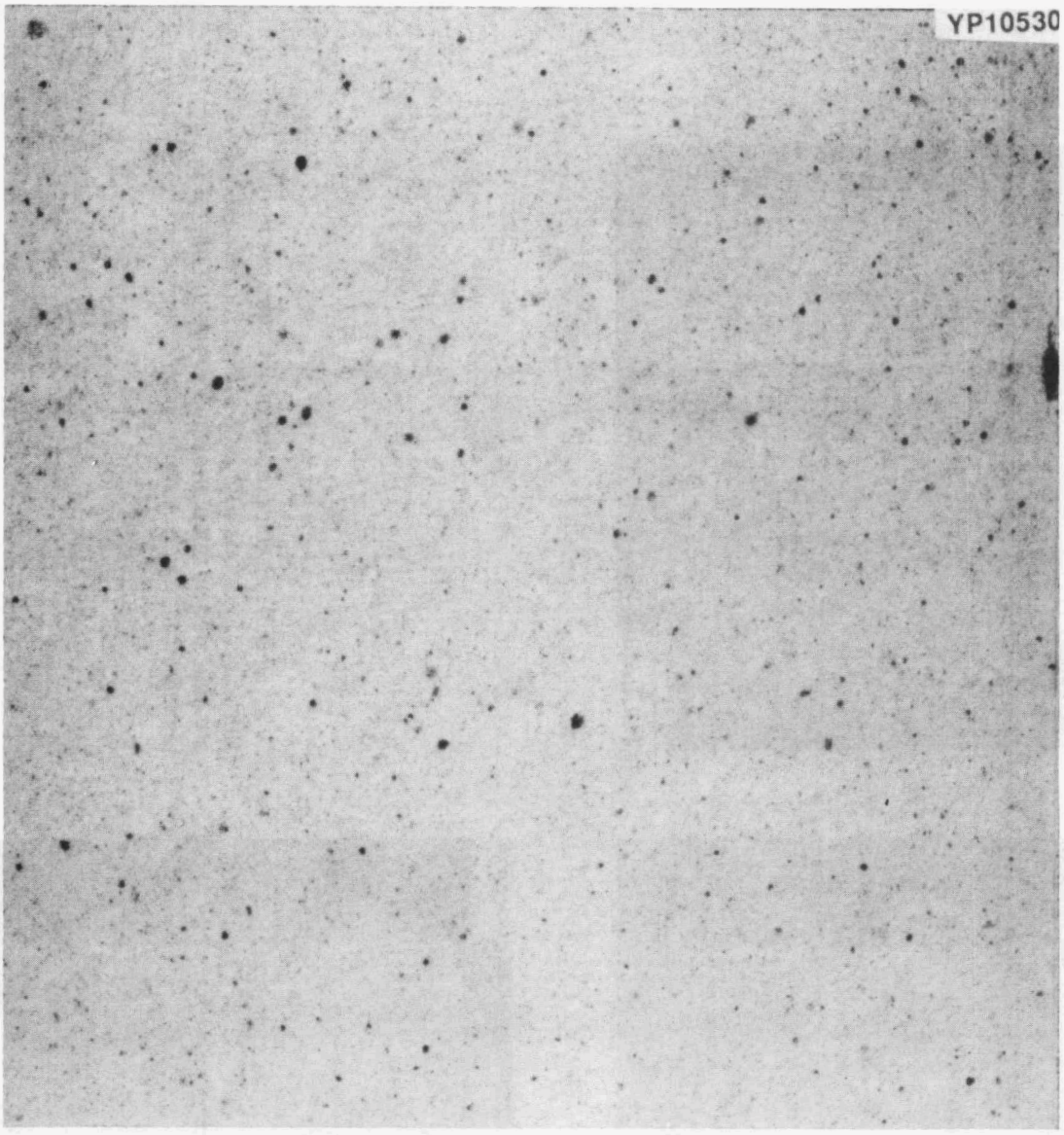

Fig. 8. Results of an NDE inspection by ultrasonic scanning showing large spot images of whisker clumps.

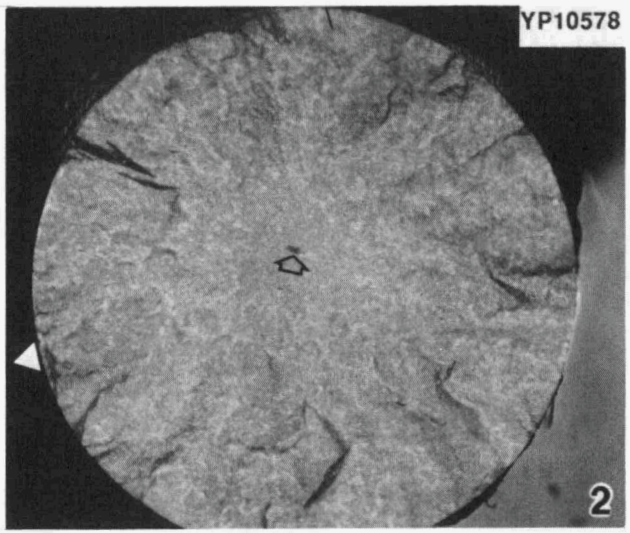

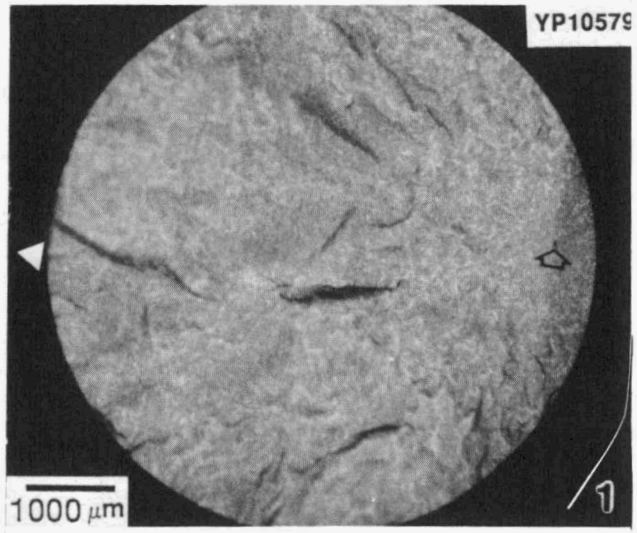

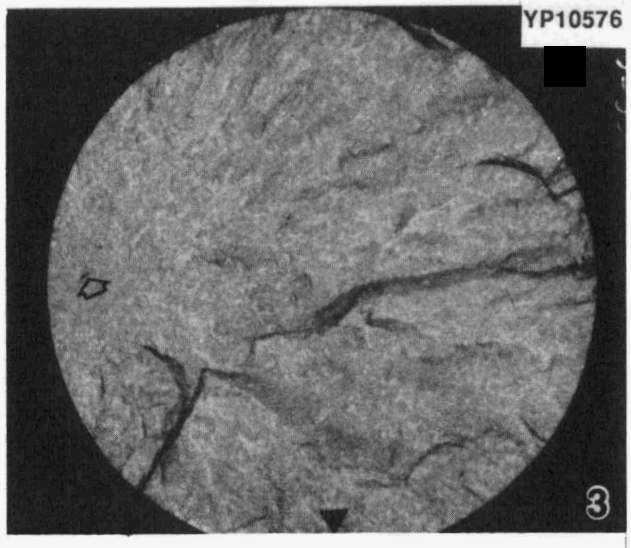

Fig. 9. Fractographs of whisker-reinforced aluminia specimens 1 through 3. Fracture initiating flaws are indicated by open arrowheads and the reference testing position by solid triangles.

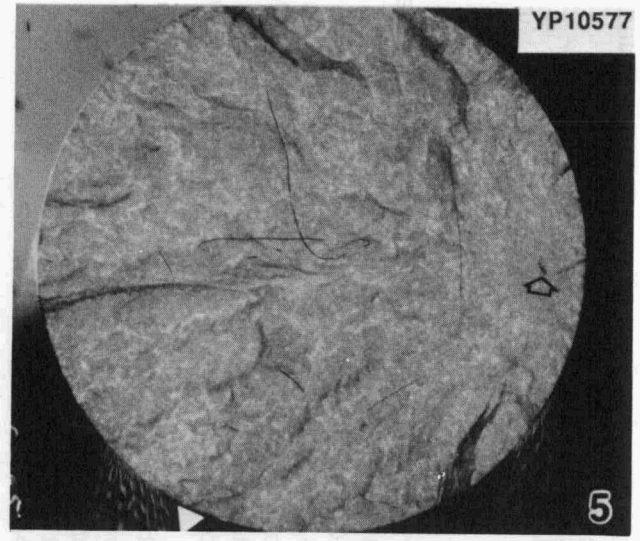

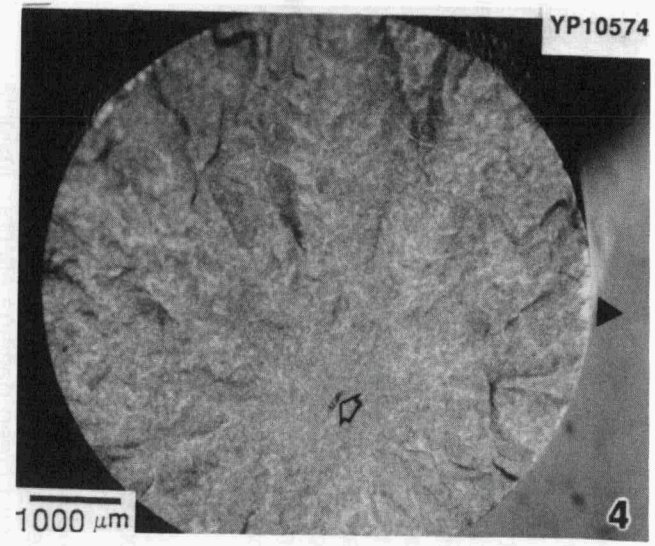

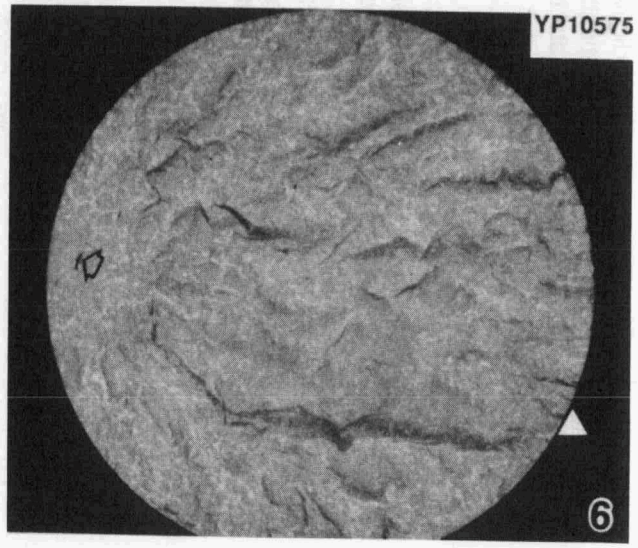

Fig. 10. Fractographs of specimens 4 through 6. All the fracture origins are seen at the center of a flat mirror region surrounded by a rugged terrain.

Rotor Data Base Generation

M. K. Ferber, M. G. Jenkins, and R. L. Martin (Oak Ridge National Laboratory)

Objective/scope

The goal of the proposed research program is to systematically study the tensile strength of a silicon nitride ceramic as a function of temperature and time in an air environment. Initial tests will be aimed at measuring the statistical parameters characterizing the strength distribution of three sample types (two tensile specimens and one flexure specimen). The resulting data will be used to examine the applicability of current statistical models, as well as sample geometries for determining the strength distribution.

In the second phase of testing, stress rupture data will be generated by measuring fatigue life at a constant stress. The time-dependent deformation will also be monitored during testing so that the extent of high-temperature creep may be ascertained. Tested samples will be thoroughly characterized using established ceramographic, scanning electron microscopy, and transmission electron microscopy techniques. A major goal of this effort will be to better understand the microstructural aspects of high-temperature failure including:

(1) extent of slow crack growth;
(2) evolution of cavitation-induced damage and fracture;
(3) transition between brittle crack extension and cavitation-induced growth; and
(4) crack blunting.

The resulting stress rupture data will be used to examine the applicability of a generalized fatigue-life (slow crack growth) model. If necessary, model refinements will be implemented to account for both crack blunting and creep damage effects. Insights obtained from the characterization studies will be crucial for this modification process. Once a satisfactory model is developed, separate stress-rupture (confirmatory) experiments will be performed to examine the model's predictive capability. Consequently, the data generated in this program will not only provide a critically needed base for component utilization in automotive gas turbines but also facilitate the development of a design methodology for high-temperature structural ceramics.

Technical progress

Due to problems with delivery of the silicon nitride tension and flexure specimens, initial tests involved the measurement of the creep behavior of a 94% aluminum oxide. Specifically, the steady-state creep rate at 1000°C was measured as a function of applied stress utilizing tension, compression, and flexure samples. One objective of this study was to evaluate the long-term stability of the capacitance extensometers used to measure tensile specimen deflection. In addition, the resulting data were used to examine the applicability of mathematical expressions relating the stress dependence of creep rate measured in tension and compression to that measured in flexure.

Plots of strain versus time associated with the tension, compression, and flexure samples are shown in Figs. 1(a), (b), and (c), respectively. These tensile data not only indicate the ability of the capacitance extensometer to resolve changes in the material deformation but also verify the elimination of the difficulties associated with ambient temperature changes noted in preliminary studies.[1] At the lowest stress level, the steady-state strain rate is about 8×10^{-10}/s, which is an excellent demonstration of the capability of the system to measure very low strain rates.

The data in Fig. 1 were used to determine the stress sensitivity of the steady-state creep rate. As shown in Fig. 2, the stress exponent associated with the tensile creep was 5.5, which is indicative of cavitation processes related to the presence of the glassy second phase.[2] Although the flexural creep exponent was similar to that for tension, the steady-

state tensile strain rates measured at a given stress were larger than those measured in flexure. This difference apparently reflects the influence of the compressive stresses present in the flexure sample. Finally, the creep exponent for the compression specimens was approximately 1, which indicates a diffusional process. Therefore, the major effect of the tensile stresses was to induce cavitation, thus accelerating the creep rate in the tension and flexure samples. By utilizing the equations given in Ref. 3, it was possible to predict the stress dependency of the flexural creep rate from the tension and compression data. The results (dashed line in Fig. 2) were in excellent agreement with the experimental data.

A series of room-temperature, tensile strength tests of a high purity aluminum oxide were also initiated this reporting period. The primary objective of these tests is to gain a better understanding of the factors responsible for recent buttonhead failures. Particular emphasis is being placed upon evaluating the buttonhead strength of gageless samples fractured using both straight and tapered collets (Fig. 3). The latter design has a distinct advantage in that the compressive stresses, which are generated in the shank region, assist in gripping the sample. In the straight collet design, the sample is supported entirely in the buttonhead radius. The match between specimen and collet radius is thus critical to achieving uniform loading. A key concern with this design is the effect of contact stresses upon the overall load carrying capability of the buttonhead.

Three variations in the straight collet testing arrangement were evaluated. The standard arrangement consisted of stainless steel collets and a single piece cover plate (see Fig. 3). In the second arrangement, "soft" copper collets (with single piece cover plate) were used to minimize line and point loading due to dimensional mismatches. A potential problem with this configuration involves the large gap between the cover plate and specimen shank (Fig. 3) which is required to accommodate the buttonhead when loading the specimen into the grip. As a result, the copper collet is only partially supported during testing. To eliminate this problem, a third grip arrangement using a split cover plate with the copper collets was evaluated. The cover plate/shank gap was reduced from approximately 2 mm (single plate) to <0.5 mm, thus providing more uniform loading into the collet.

All test samples required for this study were machined from straight rods using a numerically-controlled four-axis grinder. The gage section was eliminated from these samples to increase the probability that fracture initiated in the buttonhead region. Results of recent finite element modeling have shown that the nominal tensile stress is concentrated in this region due to contact mismatch between the collets and the specimen. Consequently, by comparing the fracture strengths obtained using each grip design, the relative magnitude of the associated stress concentration could be determined.

Prior to testing, each sample was checked for dimensional consistency using a high resolution optical comparator with an associated numerical processor. This optical comparator system uses either projection or surface illumination at magnifications of X5 to X50 to accurately determine dimensions with a resolution of +/-0.001 mm, which is less than the tolerance range called for on the specimen drawings. Two important features of this system are the data processor and the optical screen sensor. The data processor automatically calculates such critical dimensions as radii and angles between intersecting surfaces with minimal operator interaction. The optical screen sensor eliminates operator guesswork by consistently determining specimen edges through the detection of the change in light intensity with a resolution of 0.001 mm. The dimensional data are automatically recorded on a personal computer in a spreadsheet format for subsequent statistical evaluation.

As shown in Fig. 4, the following dimensions were measured for each alumina tensile sample:

(1) the radius associated with buttonhead/shank transition (r_{bt});
(2) the angle between the shank centerline and buttonhead (0_{bh}); and
(3) the shank diameter (d_s).

The parameters r_{bt} and 0_{bh} were measured at 90° intervals at each end of the specimen while d_s was measured at 180° intervals. Figure 5 illustrates the excellent match between the required and machined dimensions associated with the buttonhead radius.

The final step prior to testing involved the mounting of four strain gages spaced 90° apart on the central region of the tensile sample. These gages provided for the measurement of bending strain while the sample was loaded to failure. A sophisticated strain gage conditioning system with a programmable "front-end processor" was used to simultaneously condition the strain gage signals; calculate the percent bending strain; and record the strain, percent bending error, and the applied load.

Figure 6(a) shows the fracture loads obtained for each grip design. It is clear that the use of the tapered collets significantly reduced the level of stress concentration in the buttonhead region. As a result, the fracture loads were substantially higher than those associated with the straight collet grips utilizing either copper or stainless steel collets. These results are now being compared to predictions based upon the finite element modeling (see discussion below). In the case of the straight collet design, the substitution of copper collets for the stainless steel resulted in a slightly improved strength performance. A further improvement was observed when the single cover plate was replaced by the split cover plate. However, as shown in Fig. 6(b), slightly different trends were observed when the average percent bending at fracture was considered. For example, the lowest average bending was observed for the tapered collet and straight Cu collet (single piece cover plate) grip designs. The use of the split cover plate led to increased bending. This arrangement may have allowed the collets to move relative to one another, thereby reducing alignment of the sample in the grips. Therefore, in the case of the straight collet grips, there appears to be a trade-off between maintaining low specimen bending and achieving a high-loading capability in the grip.

Finite element analysis (FEA) techniques were applied to ascertain the stress states in the straight and tapered collet gripping systems. A PC-based finite element code[4] running in the protected mode of the Intel 80386 processor was used in conjunction with a sophisticated preprocessor to perform the geometric modeling of the specimen and the gripping systems.

The axisymmetric (y axis along the longitudinal axis of the specimen), quarter-symmetry models composed of approximately 7500-9500 degrees-of-freedom, and two-dimensional, four-noded plane elements were used to model the structure of the specimen and collets. Nonlinear, frictional, gap elements were used to model the interface between the specimen and collet. Ultralow stiffness two-dimensional truss elements were used to mathematically constrain the otherwise physically unconstrained parts of the collet.

The linear-elastic material properties of the specimen were those of an isotropic silicon nitride at room temperature with an elastic modulus, E, of 310 GPa and a Poisson ratio, v, of 0.27, while the properties of the collets were those of steel in which E = 200 GPa and v = 0.3. As noted, the truss elements were used only for mathematical constraint, thus $E = 1 \times 10^{-6}$ and v = 0.3.

Due to the nonlinear behavior of the gap elements, the pressure loads on the collets were applied as incremental steps, with the structural equilibrium state reached at each step through an iterative process. The size and number of time steps, as well as the refinement of the element mesh, were determined through a manual, trial and error method of examining the convergence of the displacement outputs.

The two models, which include the specimen and gripping systems, are shown in Figs. 7 and 8. Figures 9 and 10 illustrate the variation of the normalized maximum principal stress at the surface of the specimen as a function of normalized, longitudinal distance from the center of the specimen [x(l/2)].

Two anomalies in the stress state should be noted in Figs. 9 and 10. The first is that for both gripping systems the uniform, uniaxial stress state in the gage section ($0<x/(l/2)<0..212$) is perturbed as the gage section begins the transition into the large

radius leading to the shank. This perturbation results in a surface stress, which is approximately 5% greater than the uniaxial gage section stress. This indicates that the distribution of the locations of gage-section failures will tend to skew towards the surface of this transition for a defect-free material and a perfectly, uniaxially-aligned testing system.

The second stress anomaly is in the area of the buttonhead radius. As shown in Fig. 9 for the straight collet system, the stress concentration, kt (i.e., the ratio of the maximum principal stresses), between the buttonhead and the gage section, is about 0.72 when a coefficient of friction, m, equal to 0.5, is used for the collet/specimen interface. For the case of m = 0.0 (frictionless), kt = 0.69, thus showing that friction may not be as critical a contribution to the stress state as the inherent stress concentration of the geometry and the loading condition of the straight collet system. For the tapered collet system, kt = 0.75 when the collet is allowed to contact one point at the outer edge of buttonhead from the beginning of the loading sequence, thus simulating the installation of the collets with no regard to preloading of the collet against the specimen. However, if a slight preload of 100 N is simulated at the collet/specimen interface, kt = 0.35, since a greater portion of the load is transferred directly into the shank of the specimen.

Concurrent FEA modeling at the University Dayton Research Institute (UDRI)[5] has shown that kt = 0.53 for a hydrostatic pressure loading in the buttonhead radius. Hydrostatic loading is nearly analogous to that of the BN powder gripping system reported by Lange et al.[6] and later successfully used by Japanese researchers in a round-robin series investigation of tensile testing facilities.[7] The advantage of the powder-grip system is that the criticality of the dimensional match between the collet and the shank and/or buttonhead radius is substantially reduced. It is believed that the BN powder can successfully distribute a uniform load into the buttonhead region while maintaining the proper uniaxial alignment of the load without introducing eccentricity in the specimen alignment.

Future work includes FEA modeling so as to verify the stress state in the buttonhead region for the powder grip arrangement. In addition, existing FEA models will be used to ascertain the effect of the bending error on the magnification of the stress perturbation at the gage section transition area. The existing models for the straight and tapered collet systems will also be used in conjunction with various material properties (including plastic deformation) in order to verify the success of UDRI in reducing buttonhead failures by using deformable, straight copper collets.

Status of milestones

None.

Publications

1. M. G. Jenkins, M. K. Ferber, R. L. Martin, R. M. Poteat, and V. J. Tennery, "Numerical and Empirical Verification of the Stress State in a Ceramic, Button-head, Tensile Specimen," to be published in the *Proceedings of the Twenty-Seventh Automotive Technology Development Contractors' Coordination Meeting* to be held in Dearborn, Mich., October 1989.

2. M. G. Jenkins, M. K. Ferber, R. L. Martin, R. M. Poteat, and V. J. Tennery, "Evaluation of the Stress State in a Button-head, Tensile Specimen for Monolithic and Composite Ceramics," to be published in the *Proceedings of the 14th Annual Conference on Composites and Advanced Ceramic Materials*, Cocoa Beach, Fla.

3. M. K. Ferber, M. G. Jenkins, and V. J. Tennery, "Comparison of Tension, Compression, and Flexure Creep for Alumina and Silicon Nitride Ceramics," to be published in the *Proceedings of the 14th Annual Conference on Composites and Advanced Ceramic Materials*, Cocoa Beach, Fla.

References

1. M. K. Ferber, "Rotor Data Base Generation," pp. 302–6 in *Ceramic Technology for Advanced Heat Engines Project Semiannual Progress Report for Period October 1987–March 1988*, ORNL/TM-10838, Oak Ridge National Laboratory, Oak Ridge, Tenn., December 1988.

2. F. F. Lange, D. R. Clark, and B. I. Davis, "Compressive Creep of Si_3N_4/MgO Alloys," *J. Mater. Sci.* **15**, 611–5 (1980).

3. T. Chuang, "Estimation of Power-Law Creep Parameters from Bend Test Data," *J. Mater. Sci.* **21**, 165–75 (1986).

4. Cosmos/M 1.52A, Structural Research & Analysis Corp., Santa Monica, Calif. (1989).

5. Unpublished results, N. L. Hecht, University of Dayton Research Institute, "Environmental Effects in Toughened Ceramics," W.B.S. Element 3.3.1.4, Ceramic Technology for Advanced Heat Engines Project, October 1989.

6. F. F. Lange and E. S. Diaz, "Powder-Cushion Gripping to Promote Good Alignment in Tensile Testing," *J. of Test. Eval.* **6**(5), 320–3 (1978).

7. "Investigation of High Temperature Tensile Testing Procedures," in *The Report of Research and Investigation on Standardization of High Performance Ceramics*, Asahi Glass Company, Ltd., IHI Company, Ltd., and NGK Insulator Company, Ltd., Japan (1986).

ORNL-DWG 90-8128

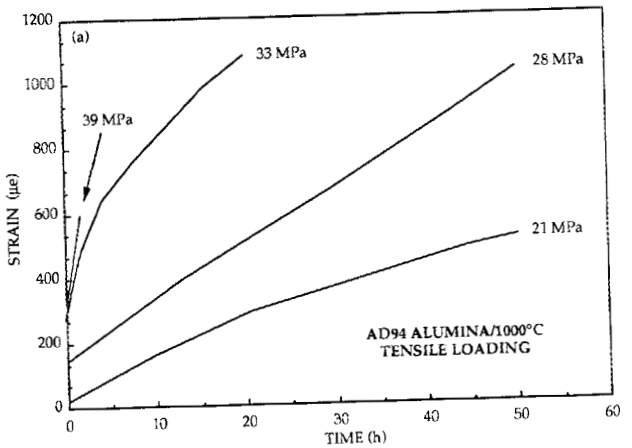

ORNL-DWG 90-8129

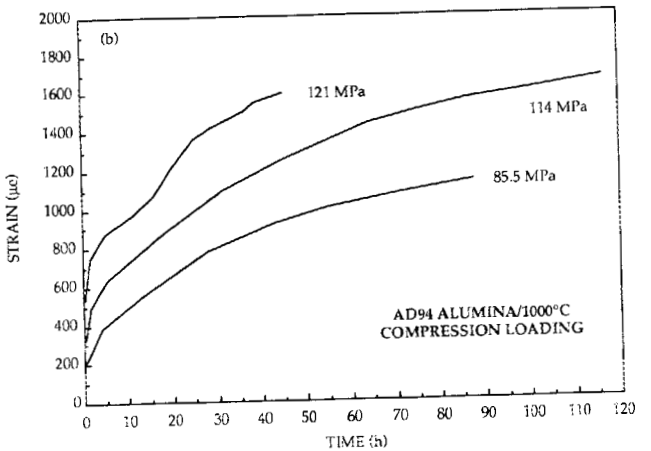

ORNL-DWG 90-8130

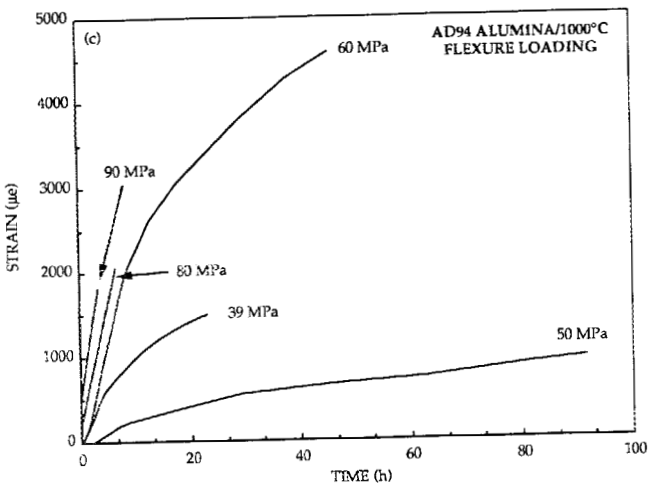

Fig. 1. Creep deformation as a function of applied stress at 1370°C for (a) tension, (b) compression, and (c) flexure loading.

ORNL-DWG 90-8131

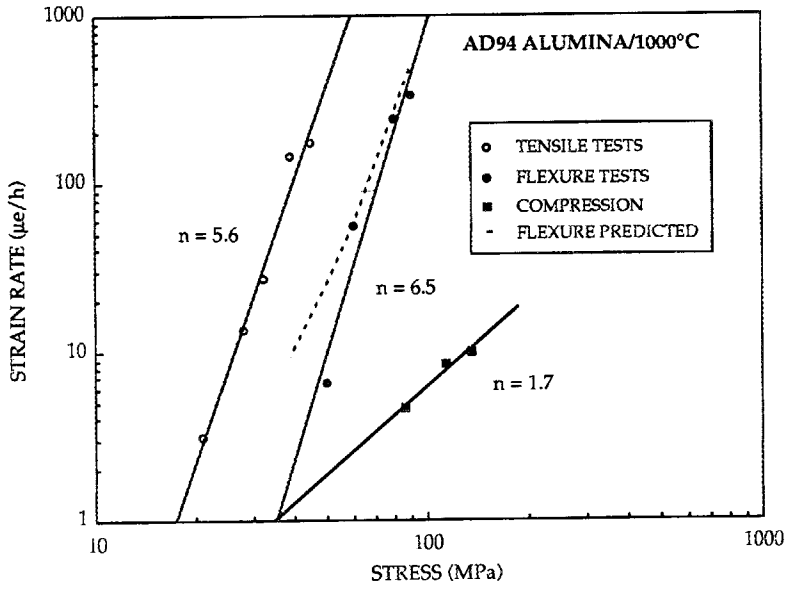

Fig. 2. Predicted creep behavior for flexure loading was in good agreement with experimental data.

ORNL-DWG 90-8132

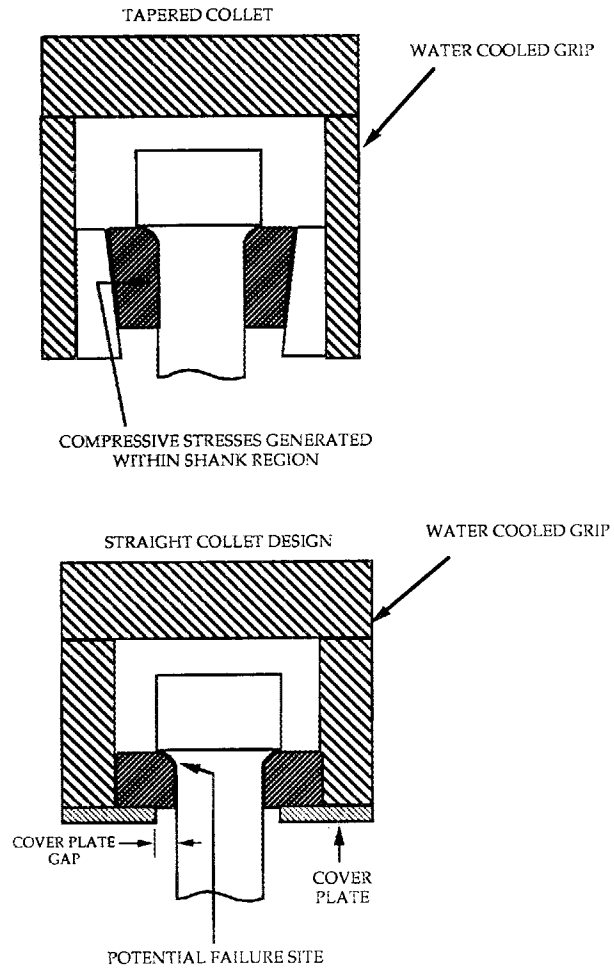

Fig. 3. Schematic illustration of two grip designs used in current tensile test equipment.

ORNL-DWG 90-8133

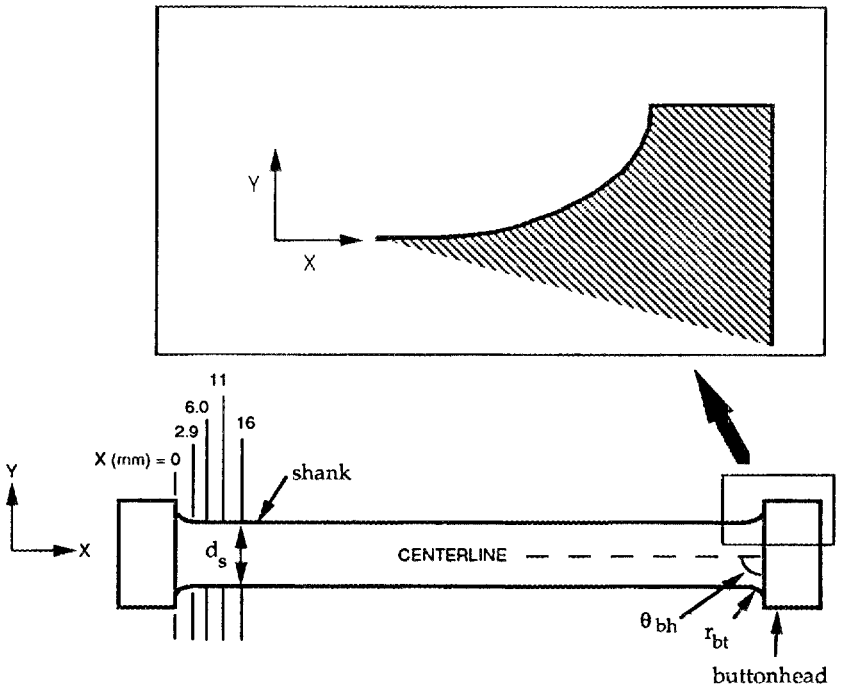

Fig. 4. Several critical dimensions associated with the buttonhead tensile samples were measured prior to testing.

ORNL-DWG 90-8134

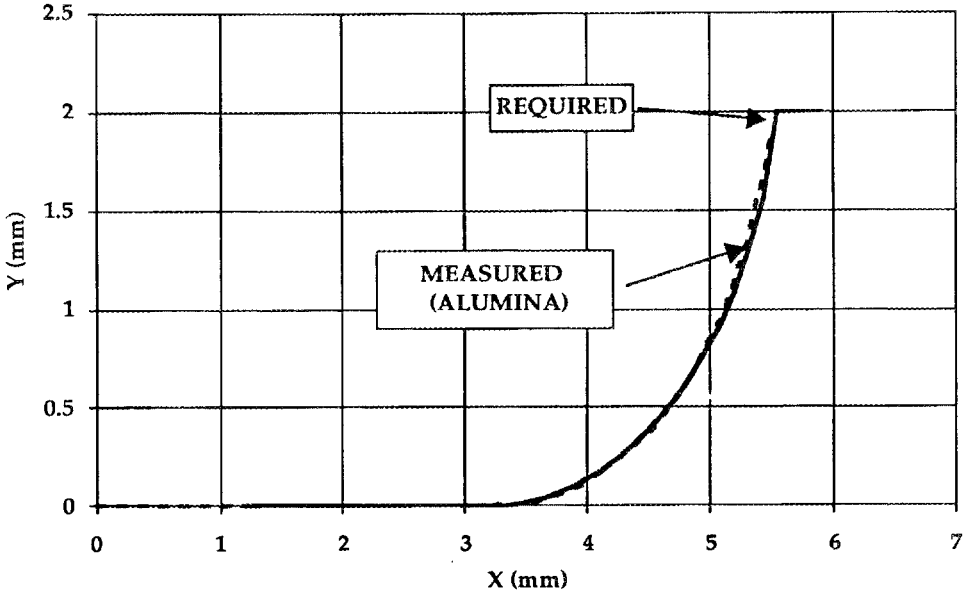

Fig. 5. Machined radius of alumina buttonhead specimen was very closely matched to required dimension.

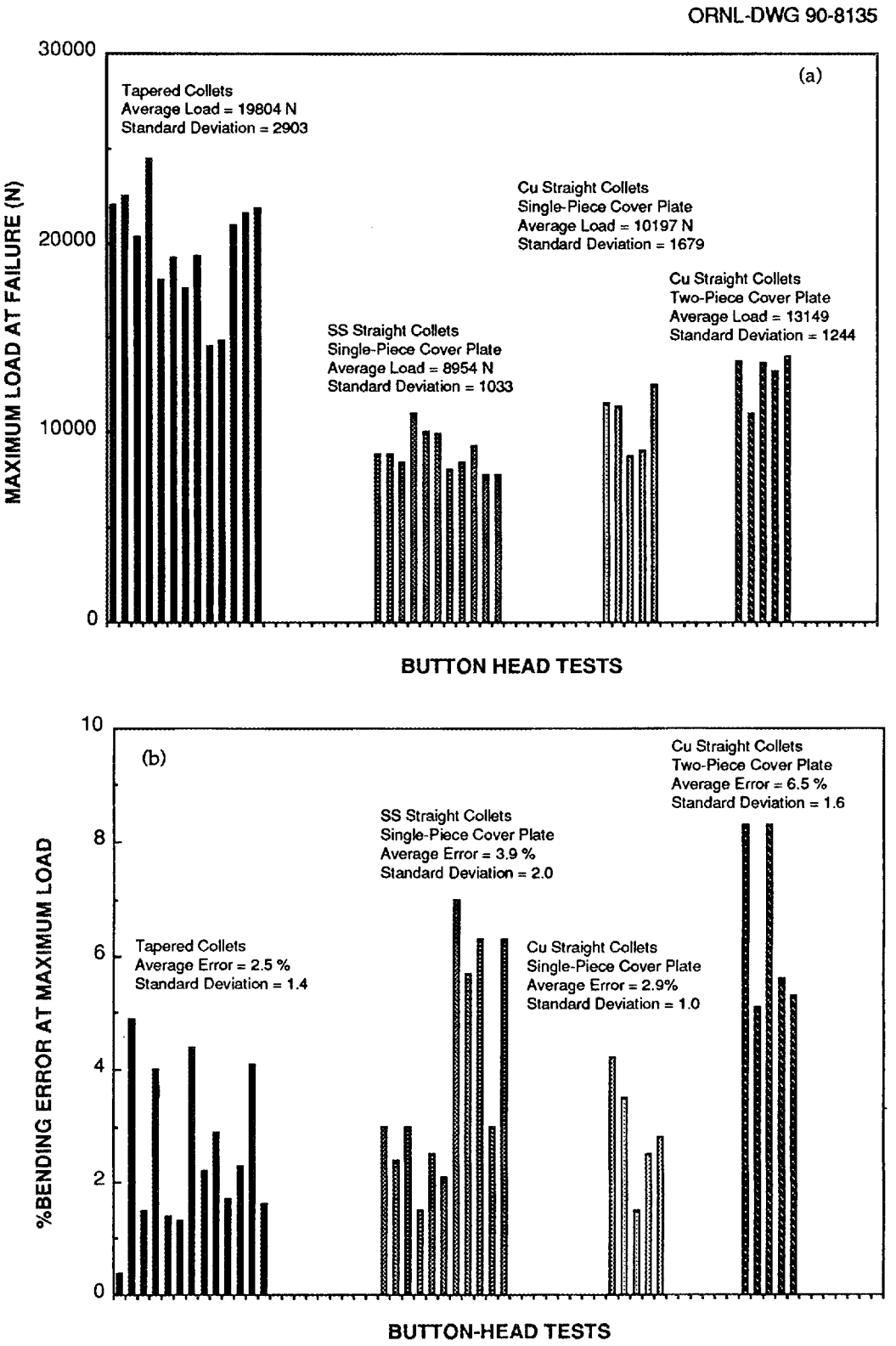

Fig. 6(a). Fracture loads associated with the tapered collet system were consistently higher than those for the straight collet grips. (b) The % bending at fracture was lower for the tapered collet and straight collet (with single cover plate) grip configurations.

ORNL-DWG 90-8136

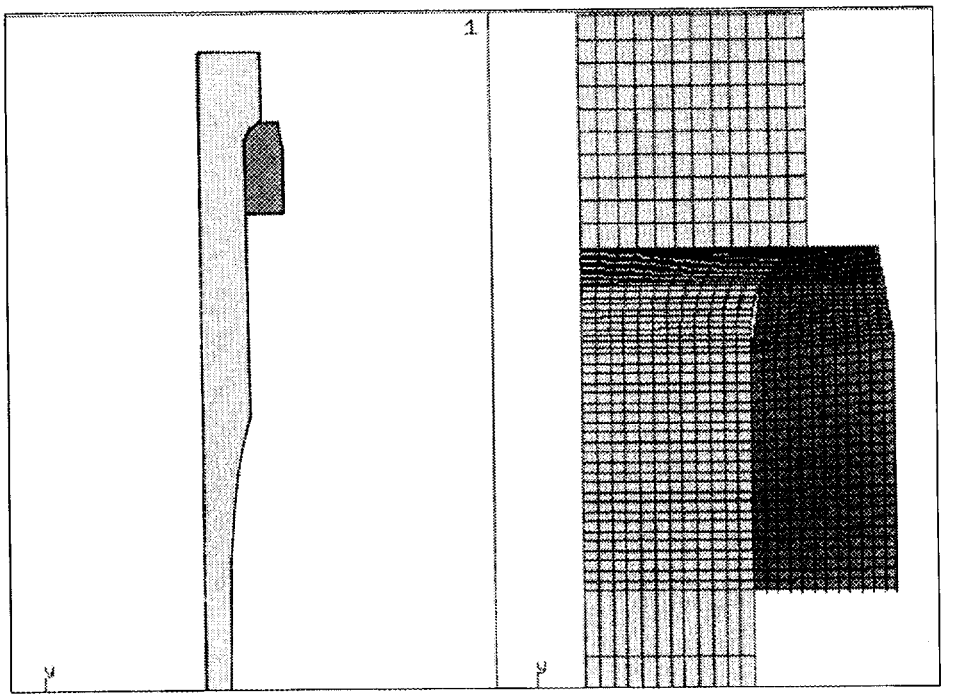

Fig. 7. Numerical model used for straight collet design.

ORNL-DWG 90-8137

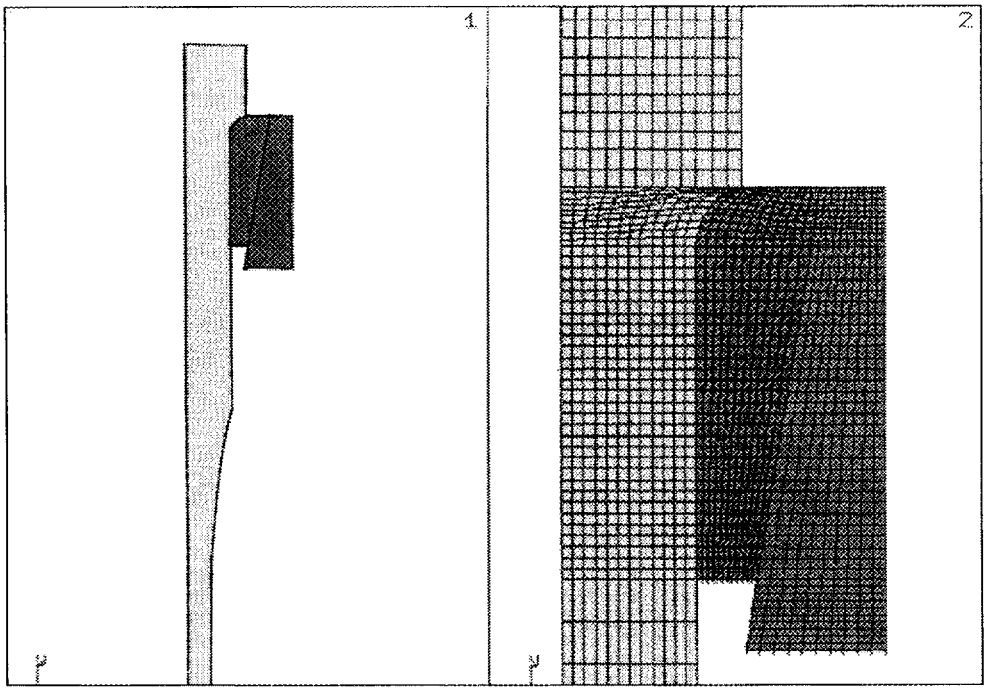

Fig. 8. Numerical model used for tapered collet design.

ORNL-DWG 90-8138

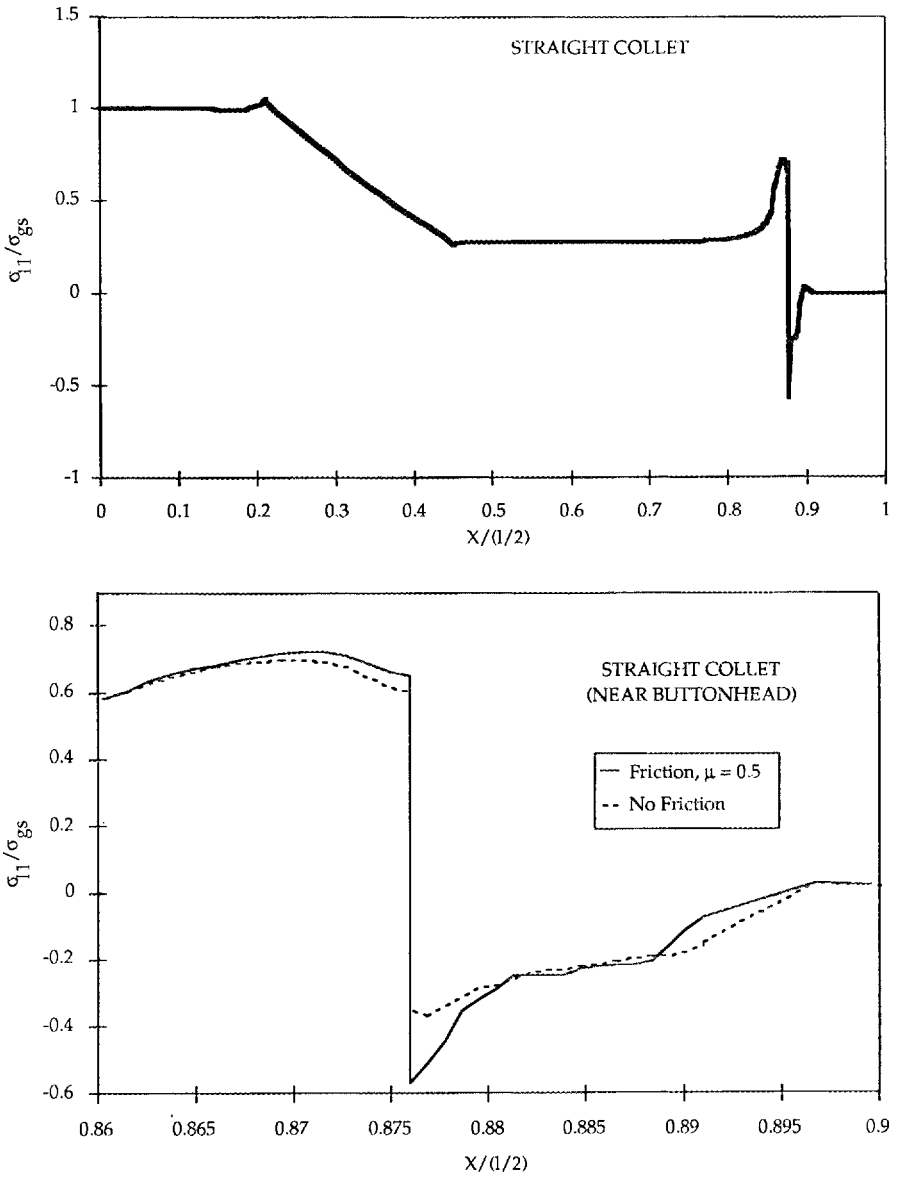

Fig. 9. Variation of the normalized maximum principal stress at the surface of the specimen in straight collet grip as a function of normalized, longitudinal distance from the center of the specimen.

ORNL-DWG 90-8139

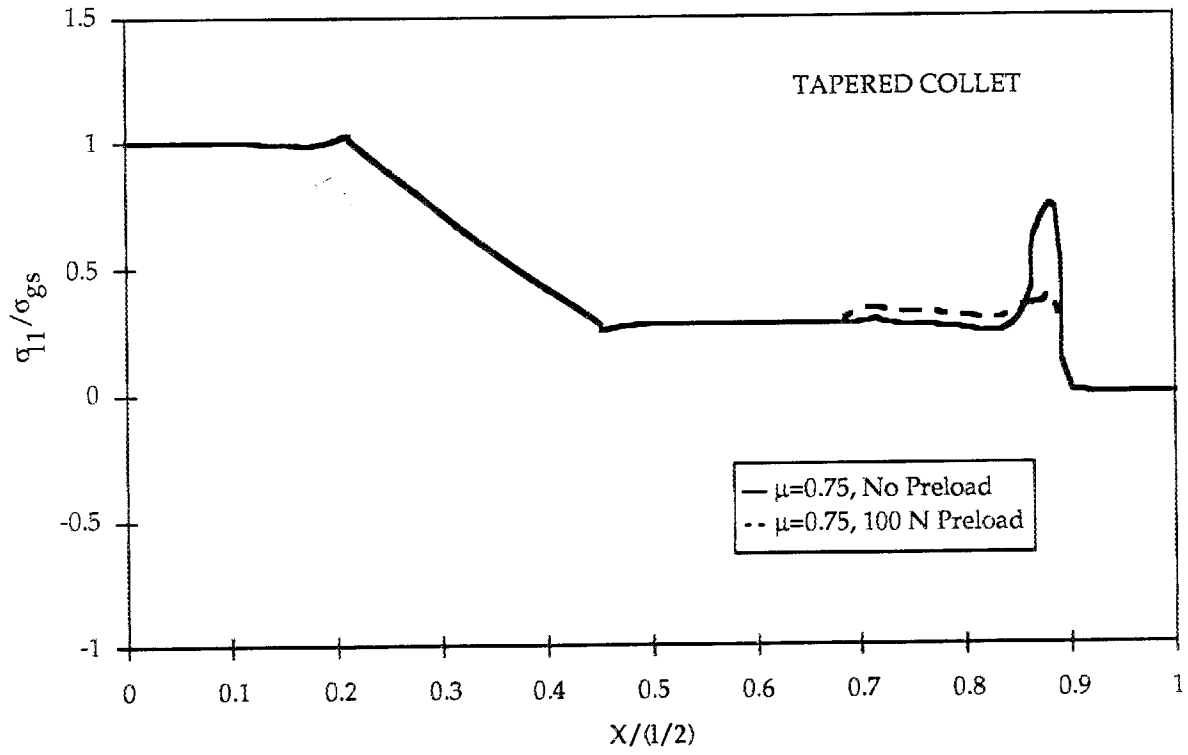

Fig. 10. Variation of the normalized maximum principal stress at the surface of the specimen in tapered collet grip as a function of normalized, longitudinal distance from the center of the specimen.

Toughened Ceramics Life Prediction

J. A. Salem (NASA Lewis Research Center)

Objective/Scope

The purpose of this research is to understand the room temperature and high temperature [≧1370°C (2500°F)] behavior of toughened ceramics, in particular SiC-whisker toughened Si_3N_4, as the basis for developing a life prediction methodology. A major objective is to understand the relationship between microstructure and the mechanical behavior within the bounds of a limited number of materials. A second major objective is to determine the behavior as a function of time and temperature. Specifically, the room temperature and elevated temperature strength and reliability, the fracture toughness, slow crack growth and the creep behavior will be determined for the as-manufactured material. The same properties will also be evaluated after long-time exposure to various high temperature isothermal and cyclic environments. These results will provide input for parallel materials development and design methodology programs. Resultant design codes will be verified.

Technical Highlights

The strength and toughness of Garrett Si_3N_4 and 30% SiC_w/Si_3N_4 were measured from 25 to 1400 °C. Whisker additions did not improve room or elevated temperature, fast fracture properties.

Material and NDE

GN-10 silicon nitride (Si_3N_4) powder was blended with 30 vol. % SiC whiskers by ACMC*. The resulting powder was slip cast into 50 mm diameter, 75 mm height billets, glass encapsulated by the ASEA method and HIPed. Densities of the monolithic and composite materials were 3.31 and 3.27 g/cm^3, respectively. Typical microstructures are illustrated in Figure 1. The microstructure was revealed with a modified plasma etching technique [1]. The whisker distribution in the composite was somewhat heterogeneous, with whiskers distributed randomly in some regions and oriented in others, Figure 2.

Strength and fracture toughness specimens were machined so that the longitudinal axes were perpendicular to the billet diameter. Test specimens were inspected with radiography, optical and acoustic microscopy. Velocity measurements did not detect anisotropy or heterogeneity of the materials, however, radiography revealed some variations. NDE results were reported in the October 1988 to March 1989 Semiannual Report.

Strength and Toughness

Four-point bend strength was determined in accordance with mil standard 1942 at temperatures from 25 to 1400°C. Between three and

ten specimens were tested per temperature. The specimens measured 3x4mm in height by width and were tested over spans of 20 and 40mm (size B). Flaw type (surface or volume) was determined with optical microscopy or scanning electron microscopy when necessary.

Fracture toughness was determined by the chevron-notch method [1]. Because of slight variations in chevron-notch geometry, the stress intensity factor coefficients were determined with the straight-through crack assumption [2]. Specimens measured 3x6x20x40mm in thickness, width, and spans. Three to six specimens were tested per temperature. The specimens were tested at a stroke rate of 0.05 mm/min. The low stroke rate used for chevron-notch testing was required to insure stable crack extension.

A summary of bend strength and fracture toughness test results are given in Table I and Figure 3. Strength of the monolithic and composite materials were similar at all test temperatures. The failure initiation sites were porous regions, coarse grained regions, and agglomerates, Figure 4.

Fracture Toughness of the materials were comparable as a function of temperature, Figure 3. Fracture toughness, calculated from maximum load and minimum stress intensity coefficient, decreased with temperature to 1200°C. However, at 1400°C the toughness appeared to increase substantially. Evidently the combination of slow stroke rate and high temperature resulted in creep deformation during crack extension. Significant amounts of whisker pullout were not apparent on the 25°C or 1200°C fracture surfaces, Figure 5. Oxidation of the fracture surface made interpretation of the 1400°C fracture surface difficult. Attempts to etch the oxide layer are being made. Interestingly, one strength test specimen exhibited whisker pullout around the failure origin, Figure 5B.

Conclusion

The addition of 30 vol. % SiC whiskers to this silicon nitride did not substantially improve room or elevated temperature strength or toughness. Whisker agglomerates occasionally acted as failure origins. Whisker pullout was not consistently observed on fracture surfaces. Either longer whiskers, different bonding, or improved microstructures may be required to improve the fracture properties via whisker additions.

Status of Milestones

Milestones are behind schedule.

Communications/Visits/Travel

Visited NIST to discuss strength and creep testing and observe mechanical testing facilities.

Problems Encountered

One of the PI's has transferred to another position, leaving this project temporarily under-staffed. A search for a replacement is underway. Machining damage to specimens of Garrett material was encountered.

References

1. K. N. Siebein and W.M. Lovington, "Plasma Etching of Si_3N_4," In Microstructural Science, Vol. 16: Metallography of Advance Materials, ed. by H.J. Cialone, pp. 319-329, 1988.

2. D. Munz, R.T. Bubsey and J.L. Shannon, Jr., "Fracture Toughness Determination of Al_2O_3 Using Four-Point-Bend Specimens with Straight Through and Chevron-Notches," J. Am. Ceram. Soc., Vol.63, No. 5-6, pp.300-305, 1980.

Publications

None

Table I. Strength and Toughness with standard deviation.

Property/ Material	Temperature, °C 25	800	1000	1200	1400
Strength MPa					
Si_3N_4	732±61	715±52	679±15	617±35	405±68
SiC/Si_3N_4	698±85	671±45	702±14	628±44	344±27
Toughness $MPa \cdot m^{.5}$					
Si_3N_4	6.5±.3	6.5±.4	5.7±.5	5.8±.1	10.1±1.3
SiC/Si_3N_4	7.1±.5	5.6±.2	6.2±	5.7±.4	10.7±.4

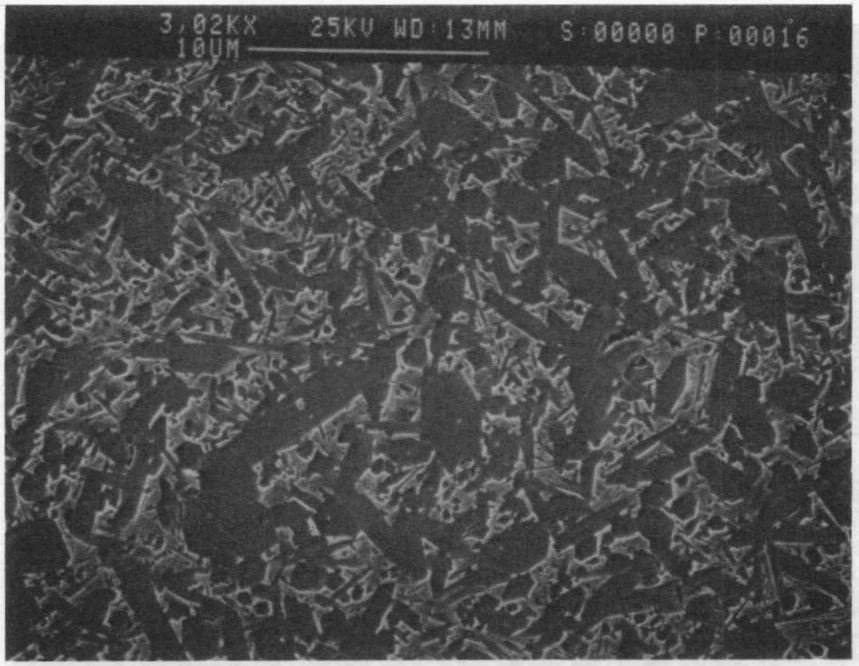

A.

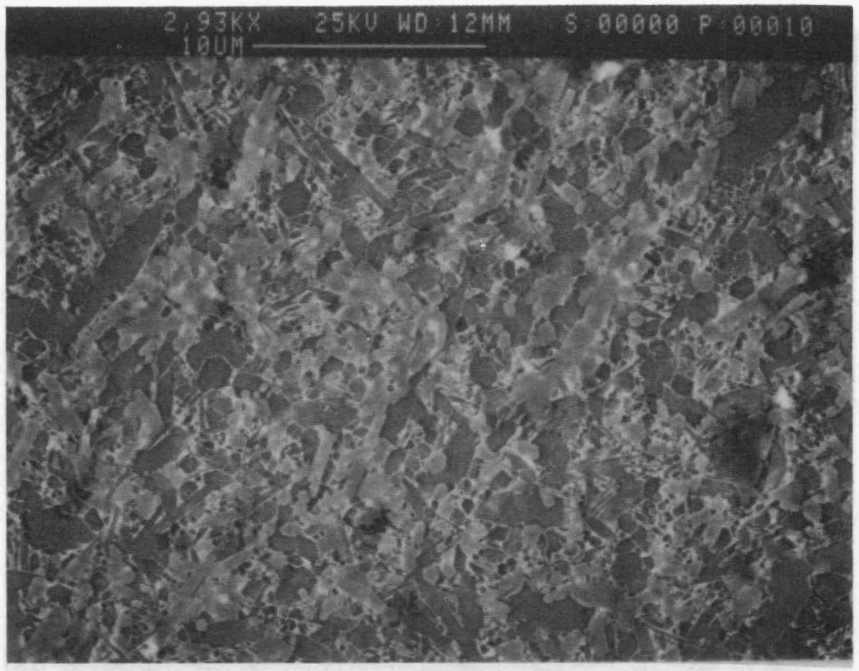

B.

Figure 1. Microstructure of Garrett materials:A) Si_3N_4 and B) SiC_W/Si_3N_4, where darkest regions are Si_3N_4, grey regions are SiC whiskers, and light regions are intergranular phase.

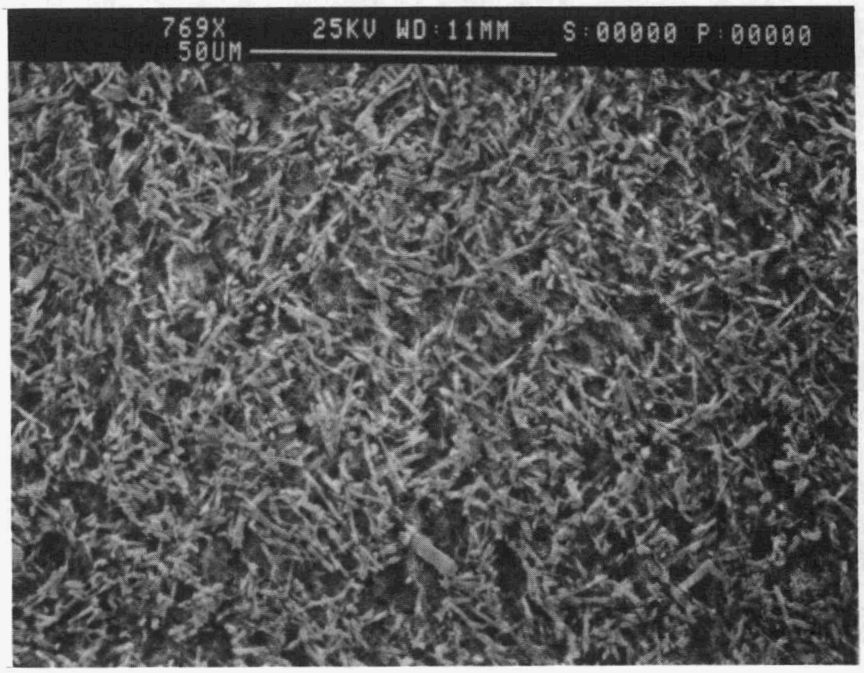

A.

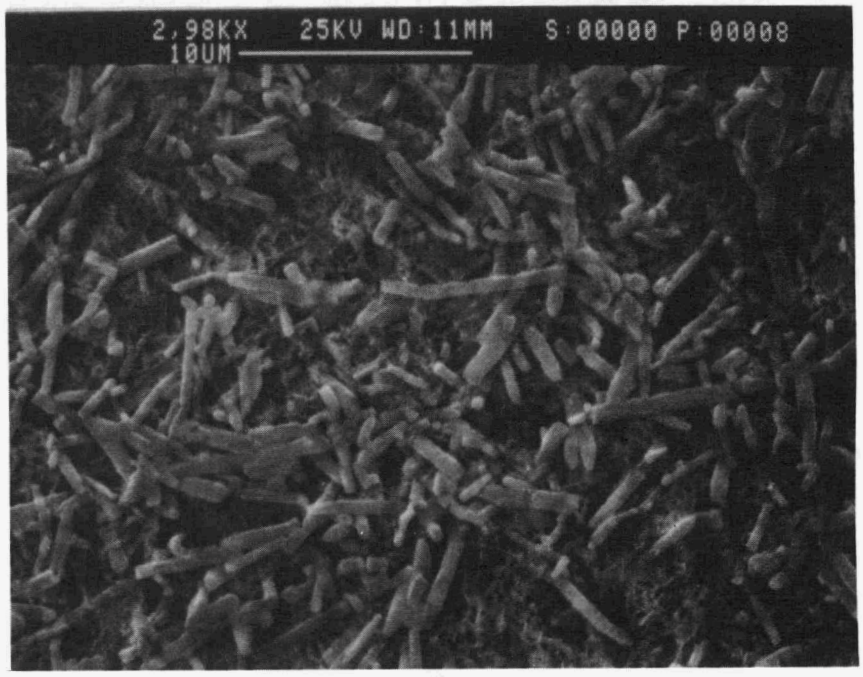

B.

Figure 2. Whiskers in SiC_w/Si_3N_4 exposed via plasma etching.

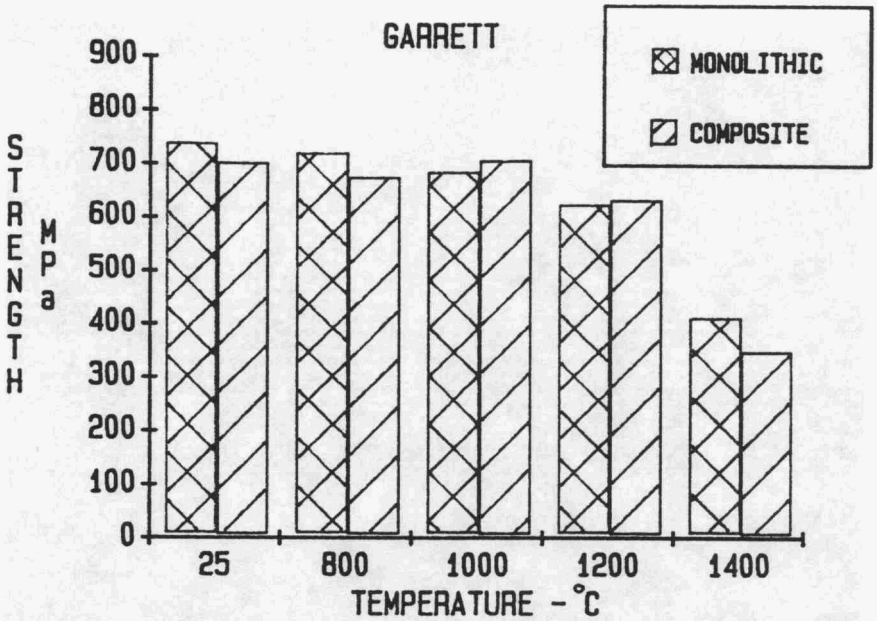

A.

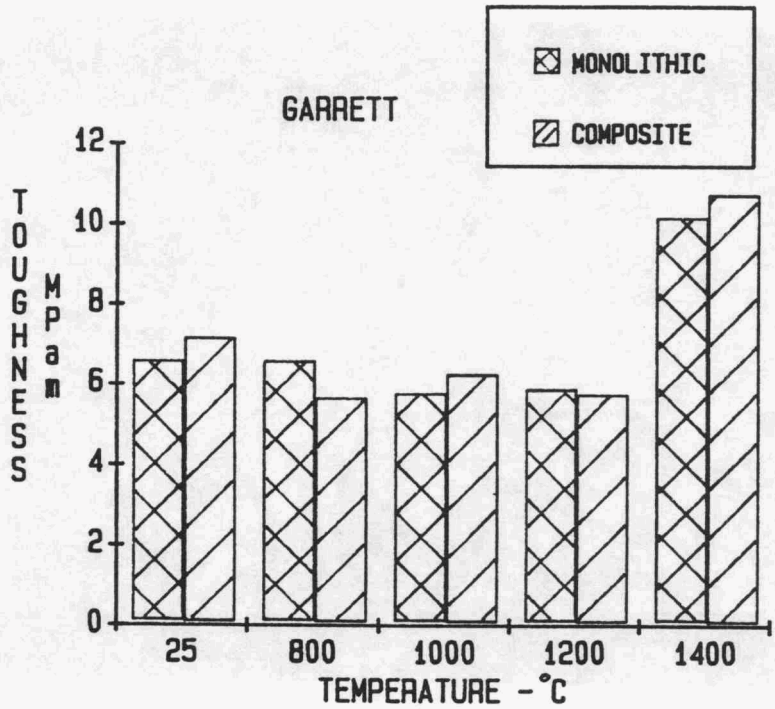

B.

Figure 3. Strength and fracture toughness of Si_3N_4 and SiC_W/Si_3N_4.

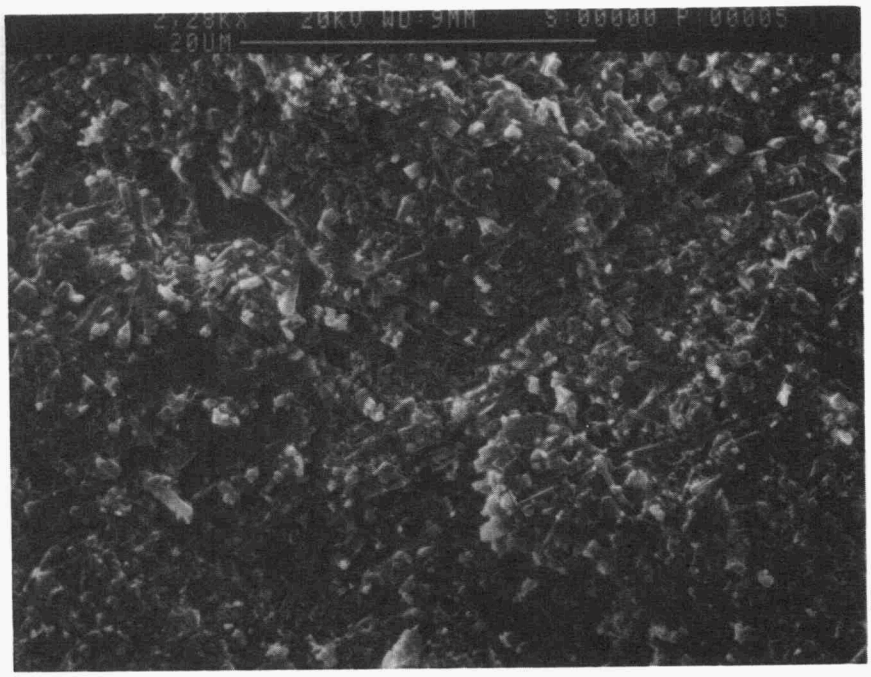

A.

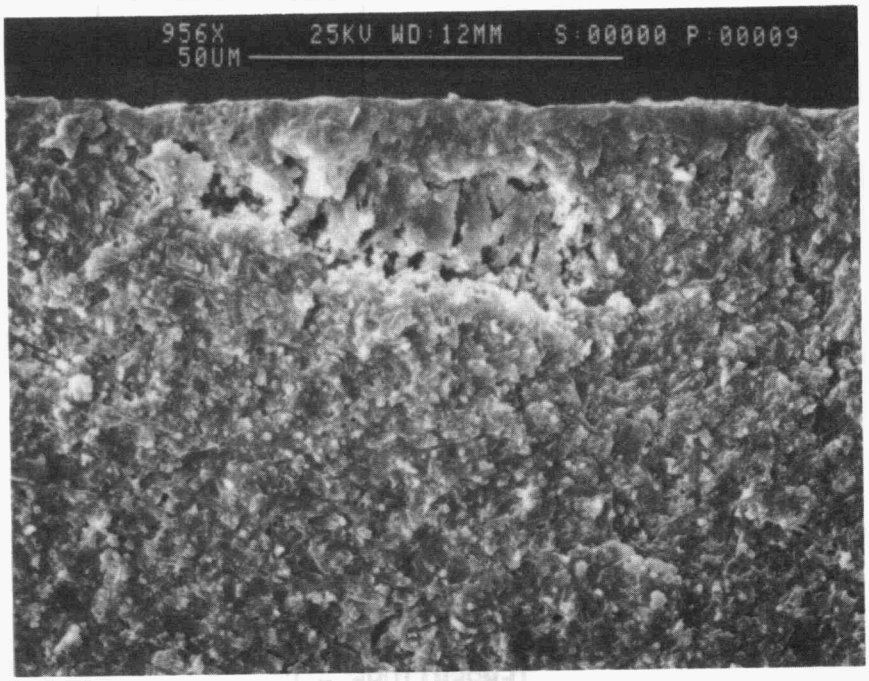

B.

Figure 4. Failure origins in SiC_w/Si_3N_4: A) coarse grain region, and B) porous region.

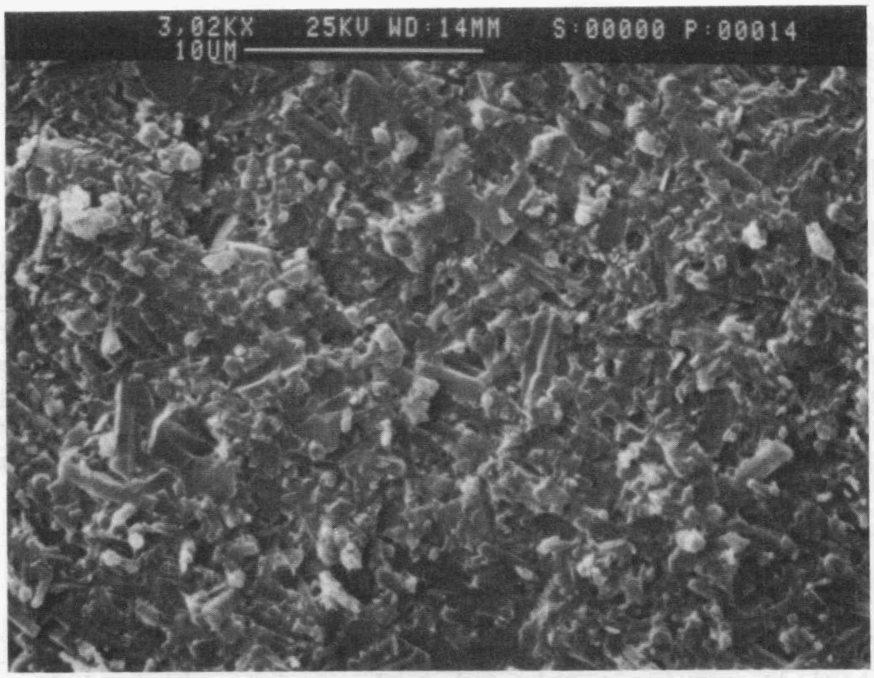

A.

B.

Figure 5. Fracture topography of SiC_W/Si_3N_4: A) fracture toughness test (25°C), and B) Strength test. Note whisker exposed near failure origin.

Life Prediction Methodology

D. L. Vaccari and P. K. Khandelwal (Allison Gas Turbine Division of General Motors Corporation)

Objective/scope

The objective of this project is to develop and demonstrate the necessary nondestructive examination (NDE) technology, materials data base, and design methodology for predicting useful life of structural ceramic components of advanced heat engines. The analytical methodology will be demonstrated through confirmatory testing of ceramic components subject to thermal-mechanical loading conditions similar to those expected to occur in actual vehicular service. The project addresses fast fracture, slow crack growth, creep, and oxidation failure modes.

Technical progress

Design methodology and data base development

To acquire valid design-quality tensile data, high strength silicon nitride materials require a uniaxial test specimen which will reliably and repeatedly fail in the gage section for temperatures from 20 to 1400°C.

A feasibility study was conducted at Southern Research Institute (SoRI) to develop a tensile specimen for effective testing of the GTE PY6 silicon nitride hot isostatically pressed (HIP) processed material which has been selected to develop the life prediction methodology under this program. GTE supplied three circular blanks from their inventory that were fabricated using the Oak Ridge specimen tool. The PY6 material was HIP processed and used SN502 powder. These blanks did not reflect the significantly improved current manufacturing process of PY6 material using UBE powder, which will be the standard bill of material for this program. The blank was approximately 7.2 in. in length with a head diameter of 0.68 in. and a gage diameter of 0.363 in. A specimen was designed around the blank and machined as shown in Figure 1. The average measured density of the material was 3.128 g/cc. The average modulus calculated from the ultrasonic time-of-flight measurement through the length of the specimen was 44 msi.

The tensile evaluations were performed in a gas-bearing tensile facility. Special loading components, including the collets, were designed and machined to test these specimens. The machining was done within 0.0005 in. The loading train was checked for its concentricity and alignment after each test. Strain was measured using a pair of clip-on extensometers mounted on special flags. The specimens were tested at a stress rate of 30,000 psi/min. The tensile results are summarized in Table 1. One specimen failed in the gage and the other two in the head. The first specimen, TN-AX-3, failed in the gage section at 36.92 ksi from a semicircular flaw located at the edge of the specimen.

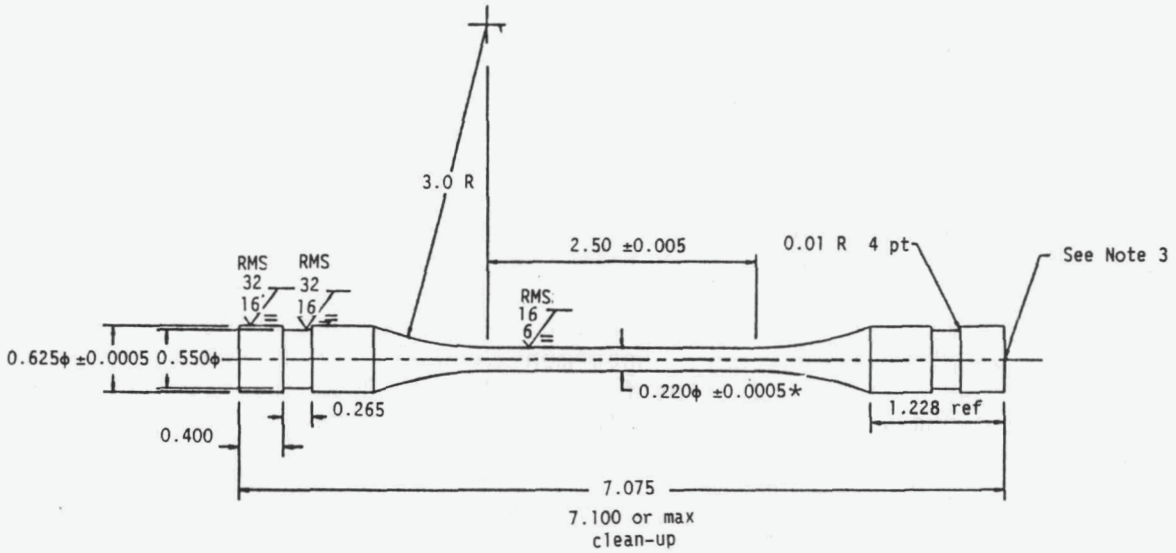

Notes:

*1. Diameters true and concentric to ±0.0005 in.
2. Do not undercut radius at tangent points
3. Both ends to be flat and perpendicular to ±0.0005 in.
4. Axial grind gage and radius together with 6.0ϕ wheel
5. All dimensions are in inches
6. Tolerances unless otherwise noted:
   Decimals ±0.001 in.
   Diameters ϕ0.001 in.
   Lengths ±0.002
7. 6 to 9 rms surface roughness parallel to centerline in gage

Figure 1. Tensile specimen configuration.

Table 1.
Tensile results for GTE PY6 silicon nitride.

Spec No.	Gage diameter (in.)	Ultimate tensile strength (psi)	Initial elastic modulus (msi)	Strain-to-failure (in./in.)	Failure location and dist to edge in inches	Remarks
TN-AX-1	0.2200	>53,980	43.94	>0.00123	Head failure	S.G. E-47,47 and 43 msi
TN-AX-2	0.2200	>38,690	43.80	>0.00089	Head failure	
TN-AX-3	0.2190	>36,920	43.73	>0.00085	EDGE, 0.0005	Fracture surface flaw

Notes: 1. TN-AX-1 had three strain gages for use in bending check during tensile testing.

A close examination of the collets revealed that they were a little big for the existing compression nuts. The collets were redesigned and fabricated before the other specimens were tested. The second specimen tested, TN-AX-1, was strain gaged 120-deg apart to obtain the percent bending in the specimen. The specimen failed in the head at 53.98 ksi with a maximum bending strain of 3.9% at maximum stress. The third specimen, TN-AX-2, failed in the head at 38.69 ksi. The tensile modulus of the specimens was very consistent with an average value of 43.8 msi, which is in good agreement with both the ultrasonic and strain gage measurements.

Fractography of the three specimens was conducted using optical and scanning electron microscopy. Specimen TN-AX-3 failed from a near edge flaw as shown in Figure 2. The flaw is about 0.0005 in. from the edge and about 0.004 x 0.0025 in. in dimension. The other two specimens, TN-AX-1 and TN-AX-2, failed in the head from natural flaws, poor machining, or improper loading. Microscopic examination of these specimens up to 1000X has shown that flaws were present in the head that contributed to the failure of the specimen in the undesired area.

Based on the limited testing conducted, the following three factors (listed in order of importance) most likely contributed to the failure of the specimens:

- o material anomalies in machined head surfaces
- o improperly fitting collets
- o machining tolerances in the head region in all the specimens

The recommendations from these observations are as follows. The specimen design for the rough tensile blank configuration should avoid more of the outer edge material. The machining marks in the 0.010 in.

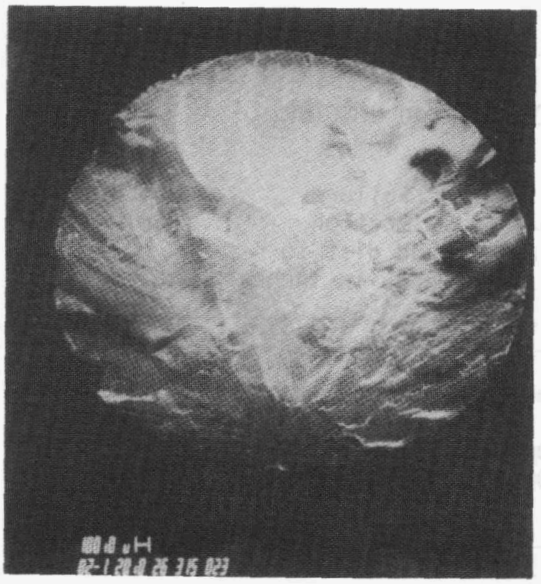

TN-AX-3 AT 20X

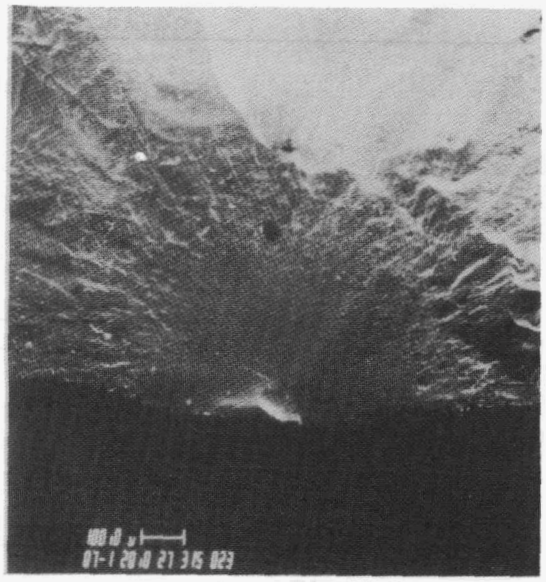

TN-AX-3 AT 70X

Figure 2. Tensile gage section fracture surface of GTE PY6 TN-AX-3 at 20X and 70X.

radius should be minimized. A light buffing of the radius while the specimen is centered in the lathe would ensure a more uniform polish to the radius. The radius in the grip section should have tolerances that the machine shop can machine with accuracy. The collet lip contact should allow for the maximum radius in the grip section plus 0.005 in. of additional clearance.

A recommended specimen design is given in Figure 3. The specimen used in this study was given in Figure 1. Notice that the specimen length on this recommended specimen has been reduced to 5.4 in. from the 7.2 in. blank length. The shorter length specimen is easier to machine by producing less wheel chatter and less bow due to the grinding wheel pressure. The shorter length also requires less material removal and avoids the possible poorer quality end material. The specimen head diameter was reduced to 0.600 in. from the 0.625 in. diameter to allow for possible bowing in the specimen blank, which was noticed in the previous blanks, and also to avoid additional outer skin blank material. Reducing the gage section diameter from 0.220 in. to 0.1875 in. causes an increase in the grip area to gage area ratio from 6.25 to 7.69. The gage length is 2.20 in. so that the strain signal can still be measured over a 2.00 in. gage length. This gage length is very important for long term creep tests where the signal-to-noise ratios are very low for long periods of time.

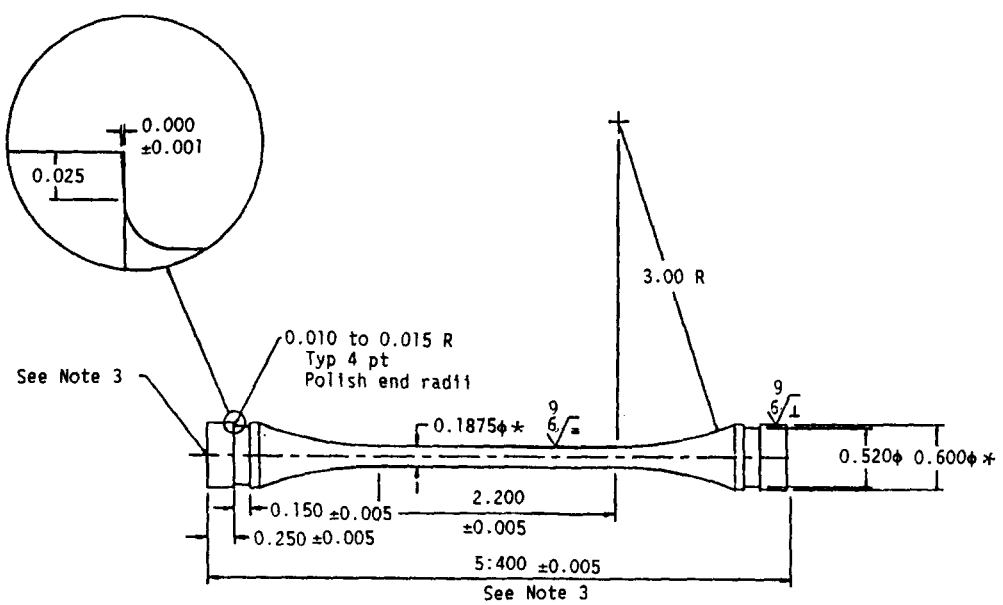

Notes:

*1. Diameters true and concentric to ±0.0005 in.
2. Do not undercut radius at tangent points
3. Both ends to be flat and perpendicular to ±0.0005 in.
4. Axial grind gage and radius together with 6.0ϕ wheel
5. All dimensions are in inches
6. Tolerances unless otherwise noted: decimals ±0.001 in., on diameters ±0.002 in., on lengths ±0.002

Figure 3. Recommended silicon nitride specimen configuration for GTE PY6 rough blank material.

Analytical tools

NASA released a new version of CARES this past reporting period. The FORTRAN source code was loaded onto the Allison computer system. The exec received from NASA has been modified to run under our CMS system. At present CARES will only run on CMS but can be made to run in the batch mode with some changes to the driver's JCL. Several problems have been encountered in getting CARES to run on our system using data generated by NASTRAN, also run on our system. These problems are discussed in the following paragraphs along with the action taken to overcome them.

The module generated by CARES required 12M of computer core and would not run under CMS. All dimensions in CARES are fixed and were set for a maximum of 2000 elements. By changing this maximum to 500, we were able to get the core required down to 4M, which would allow running under CMS. Running under CMS allows quicker turnaround on analyses. For very large analyses, however, CARES can be run in the batch environment where the dimensions are set back to 2000.

One of the subroutines in CARES was generating divide-by-zero error messages. These messages were a point of concern even though they did not seem to affect the answers--the example problems still checked with the manual. After a great deal of effort the compiler (VS FORTRAN OPT(3)) was found to be moving a divide outside a loop. This meant that the divide was being performed every time the routine was entered, even when the statement it was being used in was bypassed by an IF test. There were a couple of possible solutions to this problem. One was to change the compiler so that the divide was not moved. Another choice was to initialize the variable to something other than 0.0. We chose the second option as the best fix for our case so that the choice of compilers would not matter. This information was passed on to Noel Nemeth at NASA. He was not aware the compiler could do this, because he was not having the problem (i.e., he was using a different compiler). He did have another CARES user reporting divide checks and was going to provide that person with the possible fixes we provided.

We also discovered that the print file generated by NASTRAN could not be read by CARES. We examined the format statements used by CARES and found that they were one column off. By adding a blank column to the entire file, we were able to get CARES to read the file and run correctly. After talking to NASA again, we decided that the program was expecting to have a carriage control character in the first column, which we did not have. We found that this carriage control character could be gotten in the first column if a READPRT command was used instead of a READ command to get the file from the reader where NASTRAN put it. This works only if you change the RECFM to fixed (F) instead of variable (V) format. In all cases you must modify the NASTRAN-generated print file for CARES to read it. NASA is aware of the problem and we have discussed changing the input formats to account for this column difference.

After these problems were overcome, the example problems sent with the source code and manual were run and checked against the results in the manual. All of them agreed with the manual. The next step was to run one of the same problems using Allison's in-house proprietary code STRATA. Since the CARES program is public domain software, it will be the analytical tool used for this project. All of Allison's past experience is based on STRATA, and, therefore, we first wanted to get a correlation between the two programs. The example chosen for this comparison used the Principle of Independent Action as this is the only method available in STRATA. The problem involved a simple rotating disk of constant thickness. The NASTRAN/CARES solution used 8 hex and 18 shell elements to model a 15-deg sector of the disk. The shell elements are placed on the surface of the model with no stiffness to obtain the surface stresses used to calculate surface probability of survival. Two different models were generated for STRATA, one using axisymmetric elements and one using solid hex elements. The results from these analyses for NC-132 silicon nitride material properties are shown in Table 2.

Table 2.
Comparison of CARES and STRATA probability of survival calculation.

	Probability of survival		
Type of analysis	Volume	Surface	Total
NASTRAN/CARES	84.68	96.96	82.10
STRATA solids	86.52	97.17	84.08
STRATA axisymmetric	86.52	97.20	84.10

As shown in Table 2, the two types of elements from STRATA get the same results but these do not agree exactly with CARES. Exploring the reason for the difference, we found that the volumes of the structures were not the same and the number of subvolumes used in the analyses were different. STRATA uses nine subvolumes, one for each integration point. CARES uses 27 equal subvolumes for the solid elements. To determine what effects these two things had on the probability calculations, we made a number of different analyses using both STRATA and NASTRAN/CARES. In NASTRAN/CARES we varied the sector size as well as the number of elements in the sector. In STRATA we ran a number of different element types, changed the sector size, and also changed the number of elements in the model. The results from these runs are presented in Table 3.

Table 3.
Additional comparison of CARES and STRATA.

Program	Type of prob	No. of elem	Volume-- (in.^{3})	Max hoop stress	Probability of survival--% Vol	Surf	Total
NASTRAN/ CARES	15 deg sector	8	0.05004	61667	84.68	96.96	82.10
	5 deg sector	8	0.05055	61173	85.79	97.29	83.47
	1 deg sector	8	0.05061	61094	85.95	97.33	83.66
	20 deg sector	8	0.04960	61969	83.91	96.65	81.00
	15 deg sector	12	0.05005	61132	85.87	97.05	83.33
	1 deg sector	12	0.05062	60839	86.81	97.39	84.54
STRATA	Cubes 15 deg	8	0.05062	61589	86.52	97.17	84.08
	Cubes 5 deg	8	0.05062	61599	86.52	97.17	84.08
	Tri 10 nodes	16	0.05062	61441	86.53	97.18	84.09
	Tri 6 nodes	16	0.05062	61608	86.56	97.17	84.12
	Tri 6 nodes	66	0.05062	61739	86.54	97.17	84.09
	Quad 12	8	0.05062	61447	86.52	97.20	84.10
	Quad 8	8	0.05062	61599	86.57	97.18	84.12

As shown in Table 3, the STRATA results for all runs are nearly the same. It does not matter if it is a sector or axisymmetric model, or how big the sector is, or the number of elements in the model. The answers are always essentially identical. The same cannot be said for the NASTRAN/CARES analyses. The volume of the model changes with sector size. This volume approaches the correct number (0.05062) as the size of the sector gets smaller. This seems to indicate that NASTRAN calculates the volume using the chord length of the sector instead of the arc length. These same incorrect volumes are then used in CARES. The sector size also has some effect on the stress values, which, when combined with the volumes, causes some of the difference in the probability of survival calculation. Running NASTRAN with 12 elements in the sector instead of 8 does not change the volume but does cause a small change in stress, making the probability of survival different. Using the 12 elements in one degree sector, the probability of survival calculation

agrees very well with STRATA. Except for the way NASTRAN calculates volumes, we feel both CARES and STRATA are working correctly with the difference being in the way the subvolumes are determined and the stress assigned to each subvolume. This difference could cause the two programs to give slightly different answers with the same model, as shown in Table 3. However, with a fine enough finite element mesh, the two programs will give essentially the same probability of survival results. We have talked with Noel Nemeth of NASA about this problem with the volume calculation. He was unaware of it, and is not sure what he can do about it since the problem is in MSC/NASTRAN, and not CARES.

CARES also has the capability of calculating the Weibull material constants from modulus of rupture (MOR) test results. A set of raw material data (not the material to be used in this project) was regressed with STRATA and with two different methods in CARES. The results are presented in Table 4. Effort continues to understand the differences.

Table 4.
Calculation of Weibull material constants.

Material constant	Allison		CARES			
			Least squares		Max likelihood	
	Volume	Surface	Volume	Surface	Volume	Surface
Weibull slope	15.72	8.39	13.24	7.51	12.79	7.95
Charact strength	111.0	115.3	112.2	117.2	112.3	116.9
Unit charact strength	70.19	96.21	65.98	95.87	64.93	96.64

Status of milestones

The program is currently on schedule.

Publications

None

Life Prediction Methodology

D. Carruthers, A. Comfort, J. Cuccio, and H. Fang (Garrett Auxillary Power Divisions, Allied-Signal Aerospace Company

Objective/Scope

The feasibility of using ceramic components and the application of probabilistic design methods were first demonstrated by Garrett in the DARPA/Navy Ceramic Engine and DOE/NASA AGT101 programs. These programs highlighted the need for improved material properties and advanced design methods to assure adequate ceramic component life in engine use. Ceramic manufacturers are improving material properties through their own R&D efforts as well as government-funded programs in processing ceramics (e.g., DOE/ORNL Ceramic NDE/Processing program). Garrett Auxiliary Power Division (GAPD) has defined a program to develop the methodology required to adequately predict the useful life of ceramic components used in advanced heat engines.

GAPD's approach consists of materials characterization and behavior modeling, combined with component analysis and risk integration tools. Uniaxial and biaxial stress states will be evaluated to develop models for fast fracture, slow crack growth, creep deformation, and oxidation. The accuracy of the methodology will be verified by testing simulated components under stress and temperature conditions representative of gas turbine engine operation.

Technical Highlights

Material Testing and Analysis:
H. Fang and D. Carruthers

Material Selection

NT154 sintered silicon nitride from Norton/TRW Ceramics is the material selected for this program. NT154 fulfills the requirements of being produced by a domestic ceramic supplier and of being a material suitable for an Advanced Turbine Technology Application Project (ATTAP) component.

Test Matrix

Milestone 2, Finalize Specimen Test Plan was completed and a purchase order has been sent to Norton/TRW Ceramics. To aid in finalizing the test matrix, GAPD consulted a number of experts in ceramic behavior modeling and testing. The General Electric Corporate Research and Technology Center (GE-CRD) and Dr. D. Shetty (University of Utah) aided in determining the quantities and geometries required to accurately model material behavior and predict component lives. The Oak Ridge National Laboratory High Temperature Materials Laboratory (ORNL-HTML), Dr. S. Wiederhorn (National Institute of Standards and Technology), Norm

Hecht (University of Dayton Research Institute), Dr. S. Suresh (Brown University), and Dr. D. Shetty (University of Utah) were consulted regarding test methods to ensure accurate test results are obtained. In addition, reviews of material processing and machining plans to provide uniform material properties throughout the test matrix were held with Norton/TRW Ceramics. The finalized test matrix is shown in Tables 1 and 2.

Material Testing

All test procedures are being reviewed to ensure the procedures are complete and will generate accurate data. Current efforts are being focused on the flexure testing procedure. Lessons learned from the IEA Annex-II round-robin flexure testing have been incorporated into the flexure test procedure.

Data Analysis and Methodology Developement:
J. Cuccio, N. Menon, A. Obabueki, and D. Wu

Analyses were performed to support final definition of the test matrix. Specimen quantities and geometries have been finalized based on these analyses, as discussed in the following paragraphs.

A study was conducted to determine the number of flexure and tensile specimens required to generate volume flaw strength data for NT154. A target of 20 percent internal failure for censored data analysis was selected from numerical simulations of bimodal data sets. These simulations indicated that censoring techniques cannot accurately be used if the material exhibits less than 10 percent internal failures. The analyses also showed that greater than 30 percent internal failures provides little advantage over 20 percent internal failures.

The study also showed that the number of specimens tested influences the probability of observing 20 percent or more internal failures. While an entire population of specimens may have more than the needed 20 percent internal failures, a sampling of n specimens from this population may exhibit less than 20 percent internal failures. The probability P(x) of observing x fraction of internal failures is:

$$P(x) = C_n^r \cdot (P_{int})^r \cdot (P_{surf})^{n-r}$$

$$C_n^r = n! \cdot (r! \cdot (n-r)!)$$

n = sample size
r = number of samples from n that will fail from internal flaws
P_{int} = fraction of the population that will fail from internal flaws
P_{surf} = fraction of the population that will fail from surface flaws

This equation was used to generate the frequency versus percent internal failures plot shown in Figure 1. These analyses indicate that a sampling of 50 or more specimens is needed to be reasonably confident that 20 percent or more internal failures will occur from a sampling taken from a population with 25 percent internal failures.

TABLE 1. FINALIZED SPECIMEN TEST MATRIX

Type of Test			Temperature, C					
			Room	1093	1205	1260	1315	1370
			No. of Specimens					
FAST FRACTURE								
4-pt Bend	Size A	(Longitudinal)	60					
4-pt Bend	Size B	(Longitudinal)	60	30	60	30	30	30
4-pt Bend	Size B	(Transverse)	40					
4-pt Bend	Size B	(45 Degree)	40					
4-pt Bend	Size E	(Longitudinal)	100					
Tensile				100		40		
TOUGHNESS								
Chevron Notch			10	10	10	10	10	10
Diametral Compression			30		28	14		
Precracked Tension/Torsion			20					
STRESS RUPTURE	Time, hr	Stress, σ						
Tensile	1	σ1			10	10	10*	10*
	10	σ2			10	10	10*	10*
	100	σ3			5	5	5*	5*
	500	σ4			5	5	5*	5*
FLAW GROWTH		Stress, σ						
Tensile, Rectangular Gage	In Air	σ2			3	3	3	
		σ3			3	3	3	
	Inert Gas	σ2			3	3	3	
		σ3			3	3	3	
Tensile, Square Gage	In Air	σ2			3	3	3	
		σ3			3	3	3	
OXIDATION		Time						
		t_1		10	10	10	10	10
		t_2		10	10	10	10	10
		t_3		10	10	10	10	10

*Strain will be measured on 2 specimens from each set.

TABLE 2. CONFIRMATORY SPECIMEN TEST MATRIX

Type of Test	Temperature, C					
	Room	1093	1205	1260	1315	1370
	No. of Specimens					
PLATE BENDING	40					
UNNOTCHED TENSION/TORSION	30					
NOTCHED TENSILE						
$K_T = 2$	20		10			
$K_T = 3$	20		10			
SPIN DISK						
Fast Fracture	15		10		10	
Stress Rupture ω_1			4		4	
Stress Rupture ω_2			4		4	

The effect of specimen size on percent internal failures was also calculated. The percent internal failures for NT154 tensile and flexure specimens is plotted in Figure 2. The Weibull parameters used to generate these curves were calculated from tensile data provided by Norm Hecht at the University of Dayton Research Institute. The flexure data points included on the plot were obtained from NT154 data at GAPD.

From these analyses, flexure and tensile specimen quantities and sizes were defined, as reported in Table 1.

In support of test procedure development for fast-fracture testing, analyses were performed to determine the percentage of chamfer failures that is acceptable in flexure specimens. Excessive chamfer failures could mask the surface failures of interest, and severely hinder the verification of size scaling methods. An excessive amount of chamfer failures could result from incomplete testing procedures, debris in the test fixture, fixture wear, or poor chamfer machining. Analyses have been performed to determine the percentage of chamfer failures that should occur if the chamfer has the same flaw distribution as the tensile surface of a flexure specimen.

Analysis indicates that the geometry of the chamfer does not produce a significant stress concentration. The stress distribution in the chamfer was determined in order to calculate chamfer failure probabilities. A 3-dimensional finite element stress analysis was performed for three flexure specimen sizes with a 0.005 inch chamfer. The results verified that the stress gradient varies linearly from the tensile surface to the center of the specimen, without any influence from the chamfer.

After verifying the stress field in the chamfer, the percentage of surface failures that should initiate in the chamfer was calculated using Weibull theory. The percentage of chamfer failures for a range of Weibull surface moduli are plotted in Figure 3. The chamfer was assumed to have the same strength distribution as the rest of the specimen surface, and the effect of internal flaws was assumed to be negligible. These plots can be used to determine if a data set is contaminated by non-representative chamfer failures.

Non-representative chamfer failures can be caused by either improper testing or machining damage. The flexure test procedure is being reviewed and refined as needed to ensure accurate test results are obtained. The chamfer machining procedure has been reviewed and modified, using a slower downfeed rate to machine the chamfer. Thirty NT154 bars were machined using this modified procedure, and testing is in progress.

NDE Methods Development and Application:
J. Minter

Nondestructive evaluation (NDE) is an integral step in applying life prediction methodologies because it can be used to characterize the material and to assess the initial flaw distribution of the material. Selected NDE techniques will be quantified such that the minimum detectable flaw size and probability of detection are known. These techniques can then be used to reduce the component failure

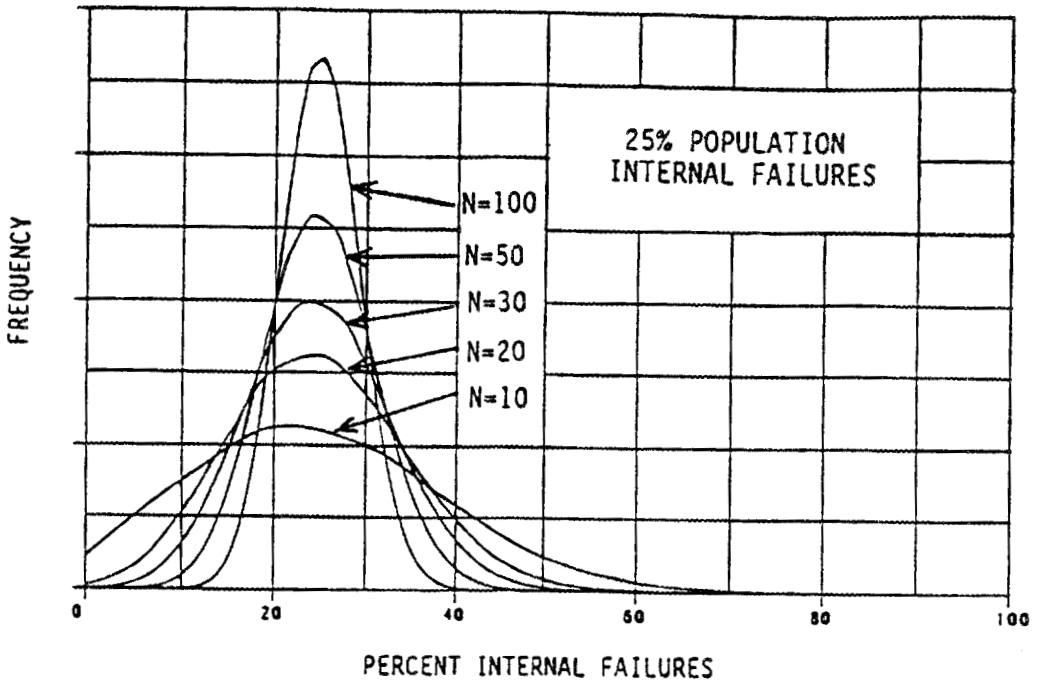

Figure 1. These frequency functions for various sample sizes N taken from a population with 25 percent internal failures demonstrate the need for testing a sufficient number of samples to ensure that 20 percent or greater internal failures occur.

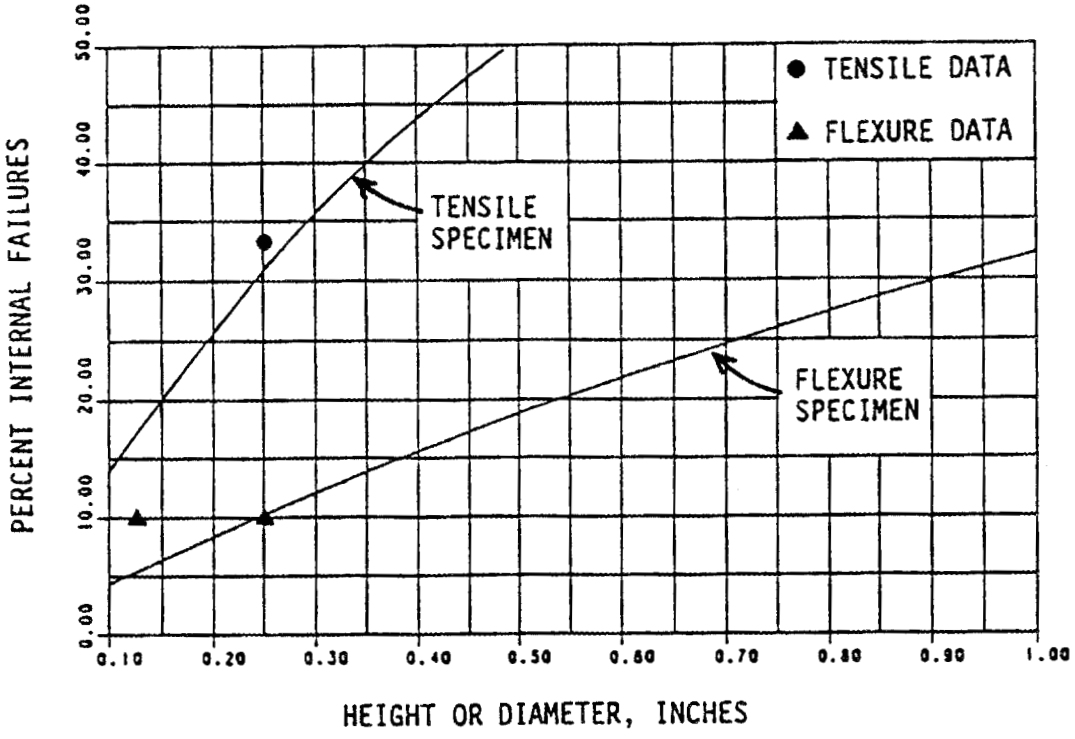

Figure 2. The effect of specimen size on percent internal failures was calculated for NT154.

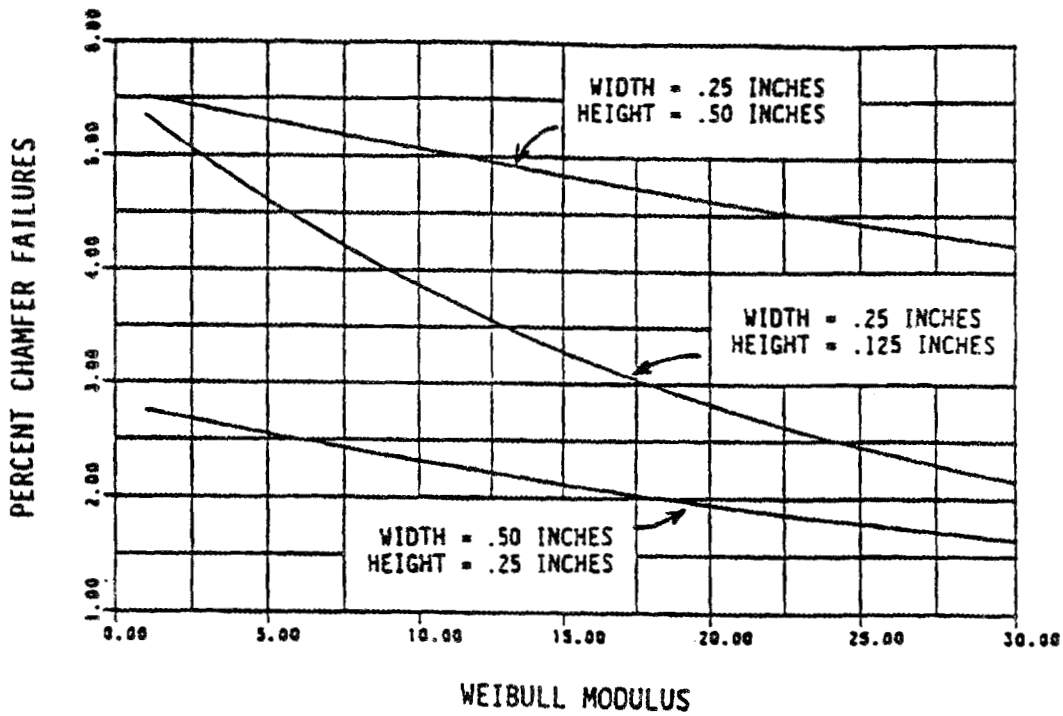

Figure 3. Less than 5 percent of all surface failures should initiate from the chamfer of a flexure specimen with a 0.50 x 0.25 inch cross section.

probability, by eliminating components with defects larger than a critical size. In addition, NDE techniques will be used to characterize material conditions that cause a reduction in material properties but may not be discrete flaws.

NDE techniques that will be studied include: ultrasonic, radiographic, flourescent penetrant inspection (FPI), computed tomography, surface acoustic waves (acoustic microscopy), and acoustic emission techniques. Our initial efforts are focused on acoustic emission and acoustic microscopy.

Acoustic emission experiments were initiated on 1/4 x 1/4 x 2 inch chevron notch specimens to determine whether acoustic emission can be correlated with crack size during growth. The experimental procedure used controlled load flexure testing to break the bars. Acoustic emission events were monitored directly on the test bar and through the fixture to assess the attenuation effects of the fixture interface. The results indicated that further evaluation of transducer coupling to the specimen and improved data filtering techniques are required. Efforts are continuing in this area.

An acoustic microscopy study has been designed to evaluate the effect of different surface finish conditions on the ability of the acoustic microscope to detect surface and near surface defects. The data from the experiment will be used to correlate acoustic microscopy data to surface condition, defects, and material strength. The study has been divided into two tasks; the first will identify the effect of surface conditions on defect detectability, and the second will correlate

defect size and material strength with acoustic microscopy data. The study will use NT154 with Vickers indentations as shown in Figure 4. The matrix for the first task is defined in Table 3. The study will be reviewed with General Electric (GE) NDE Systems and Services once they are under subcontract, prior to conducting the study.

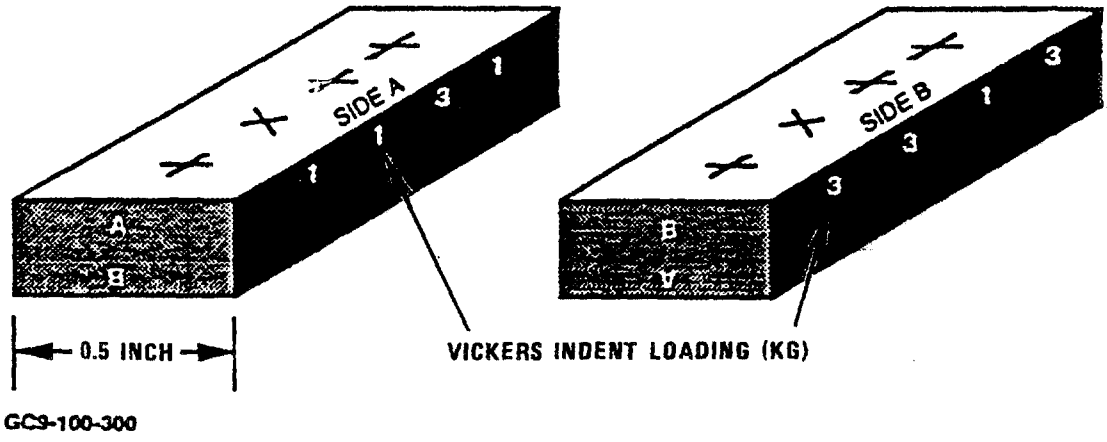

Figure 4. Vickers indent positioning for acoustic microscopy study.

TABLE 3: SPECIMEN MATRIX FOR ACOUSTIC MICROSCOPY SURFACE FINISH STUDY.

		Normal Machining	Aggressive Machining	Polished
No Heat Treatment	As Indented	X	X	X
	Indent Removed	X		X
Heat Treated	After Indent	X	X	X

Status of Milestones

Milestones 1 and 2 have been met. All other milestones are on schedule.

Publications

None.

3.3 ENVIRONMENTAL EFFECTS

Environmental Effects in Toughened Ceramics

N. L. Hecht (University of Dayton)

Objective/scope

Since 1985, the University of Dayton has been involved in a three-phase project to investigate the effects of environment on the mechanical behavior of commercially available ceramics being considered for heat engine applications. In the first phase of this project, the effects of environment on the mechanical behavior of transformation-toughened ZrO_2 ceramics were investigated. In the second phase, two Si_3N_4 ceramics (GTE-PY6 and Norton/TRW-XL144) and one SiC ceramic (Hexoloy-α-SiC) were evaluated. In the third phase the tensile, flexural, and fatigue strength of nine SiC and Si_3N_4 ceramics (see Table 1) were evaluated at temperatures ranging from 20°C to 1400°C. Microstructure, chemistry, and physical properties were also investigated.

During the past six months (April 1989 through September 1989) evaluations of three SiC and six Si_3N_4 ceramics were completed. In addition, the development of optical interferometry techniques to monitor strain was completed.

Experimental procedures

Flexural strength measurements are made using two Instron Universal Testing Machines (Model 1123) following MIL-STD-1942(MR). Elevated temperature measurements (1000°C to 1400°C) are conducted in two ATS #3320 high-temperature furnaces. Flexural strengths are measured on test specimens 3 x 4 x 50 mm with the tensile surface

---

"Research sponsored by the U.S. Department of Energy, Assistant Secretary for Conservation and Renewable Energy, Office of Transportation Systems, as part of the Ceramic Technology for Advanced Heat Engines Project of the Advanced Materials Development Program under contract DE-AC05-84OR21400 with Martin Marietta Energy Systems, Inc., Work Breakdown Structure Subelement 3.3.1.4"

Table 1. Candidate SiC and Si_3N_4 Ceramics Selected for Evaluation

Carborundum Hexoloy α-SiC	Cold formed (injection molded or isostatic pressing) and pressureless sintered α-SiC with additions of B and Al (200 tensile and 200 flexure specimens)
Carborundum Hexoloy ST	Cold formed and pressureless sintered α-SiC and TiB_2 (60 flexure specimens)
GTE PY6	Injection molded and hipped β Si_3N_4 with additions of Y_2O_3 (200 tensile and 200 flexure specimens)
Norton/TRW NT154	Sintered and HIP'ed Si_3N_4 (100 flexure and 100 tensile specimens)
CVD SiC	SiC prepared by chemical vapor deposition techniques (60 flexure specimens)
Howmet SN-4	Cold formed (die pressing/isostatic pressing) sintered and HIP'ed Si_3N_4 with 10% oxide sintering aids (Al_2O_3 and Y_2O_3) (60 flexure specimens)
Ceradyne Ceralloy 147-3	Cold formed (isopressing/slip casting/injection molding) sintered Si_3N_4 with additions of Y_2O_3 and Al_2O_3 (60 flexure specimens)
Kyocera SN252	Cold formed (isopressed/slip cast/ etc.) and sintered Si_3N_4 with additions of Yb_2O_3, Y_2O_3, and Al_2O_3 (Note: the sintering process is controlled to promote the growth of a β Si_3N_4 whisker phase in the Si_3N_4 matrix) (60 flexure specimens)
NGK Spark Plug EC-152	Gas pressure sintered Si_3N_4 with additions of Al_2O_3 and Y_2O_3 (60 flexure specimens)

ground and polished to a 16-microinch finish [MIL-STD-1942(MR) specimen size B]. The long edges of the tensile surface are rounded and polished to minimize edge failures. Flexural strength is measured using four-point bend test fixtures, and the test specimens are loaded at machine crosshead speeds of 0.004, 0.0004, and 0.00004 cm/sec. For room temperature measurements, the bend fixtures are made of steel. For measurements at 1000°C, 1200°C, and 1400°C, the bend fixtures are made of SiC. The four-point bend fixtures have an outer span of 4 cm and an inner span of 2 cm.

The dynamic fatigue analysis of each material is determined from the fast, medium, and slow loading rate strength data. The dynamic fatigue can be characterized by a ln-ln plot of fracture strength (σ_f) versus loading rate ($\dot{\sigma}$) which is expressed by the relationship:

$$\sigma_f = A'\dot{\sigma}^{\left(\frac{1}{n+1}\right)} \tag{1}$$

where A′ is a constant. The constant, n, is a measure of the stress corrosion susceptibility of the material. Large values of n are synonymous with lower stress corrosion or fatigue.

The tensile strength measurements are made using an Instron Electro-Mechanical Test System (Model 1361) equipped with Instron "Super-Grip" universal coupling and water-cooled holders for high-temperature tensile testing. For high-temperature measurements an Instron high-temperature short furnace is used.

Tensile stress rupture has been initiated to evaluate the fatigue behavior of the NT-154 and Hexoloy SA materials. These measurements are made using the Instron Electro Mechanical Test System at temperatures from 1200°C to 1400°C. For the NT-154 Si_3N_4 tensile stress rupture is being measured at 1200°C, 1250°C, and 1300°C at applied stress levels of 300 MPa. At 1400°C applied stress levels of 200 MPa were used because of premature failure by the NT-154 material.

Fracture origins are determined by optical microscopy and SEM (JEOL/SM-80 with EG&G Ortec System 5000 Microanalysis System). The strength values are evaluated to determine Weibull parameters. Maximum likelihood estimates of the shape parameter, m (modulus), and the scale parameter, β_0 (the 63rd percentile for the distribution of breaking strength), are determined in this analysis.

The elastic modulus of the candidate materials is measured by a Grindo-Sonic (Model MR35T) Transient Impulse/Elastic Modulus Apparatus. The hardness of the candidate materials is measured by a Vicker's microindent hardness tester.

The microstructure and chemistry of the candidate materials are also studied. Polished sections from representative specimens are viewed by optical microscope (Nikon Epiphot), and freshly fractured sections are viewed by scanning electron microscope (JEOL JSM-840). X-ray fluorescence (EDXA) spectra are obtained using an EG&G Ortec System 5000 attachment to the JSM-840. Test specimens are examined by x-ray diffraction with a Norelco/Philips Electronic Instruments XRD System using CuKα radiation (40 KV, 25 μA) for analysis from 20° 2θ to 58° 2θ. In addition, further chemical analysis of selected specimens is obtained using high-resolution scanning Auger spectroscopy (JEOL JAMP-30).

Thermal expansion is measured from 25°-1400°C using a Theta Industries Dilatronic II (Model 6024). Fracture toughness is measured by both the controlled flaw method and the microindent method. An indent load of 2000 grams is used in both methods.

Technical progress

In the past six months, the flexural strength and dynamic fatigue measurements for all nine candidate materials and the tensile strength measurements for Hexoloy SA and NT-154 have been completed. Computer-generated graphs summarizing the flexural strength results have been compiled and are presented in Figures 1 through 9. The results of the

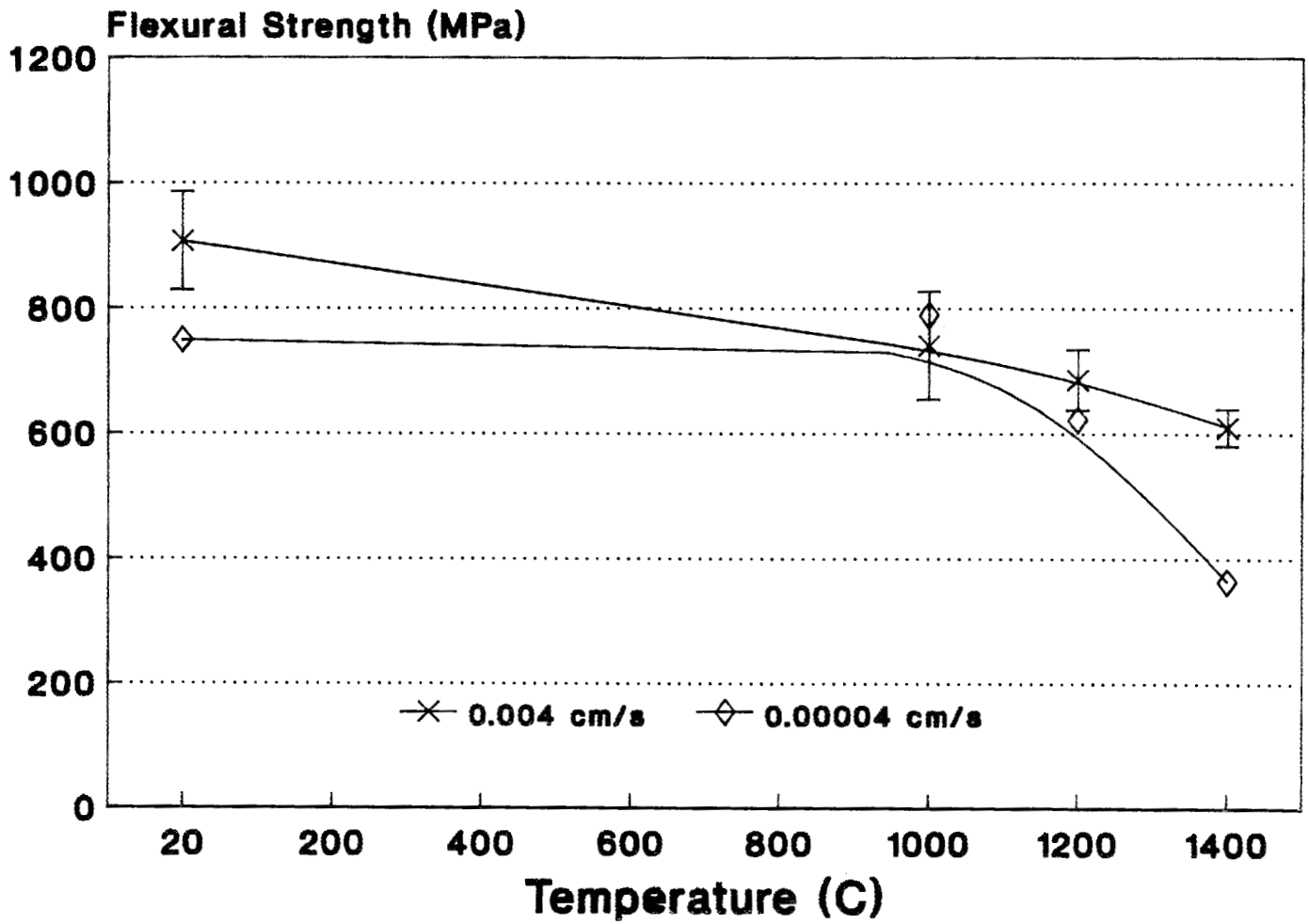

Figure 1. Flexural strength of Norton/TRW NT-154.

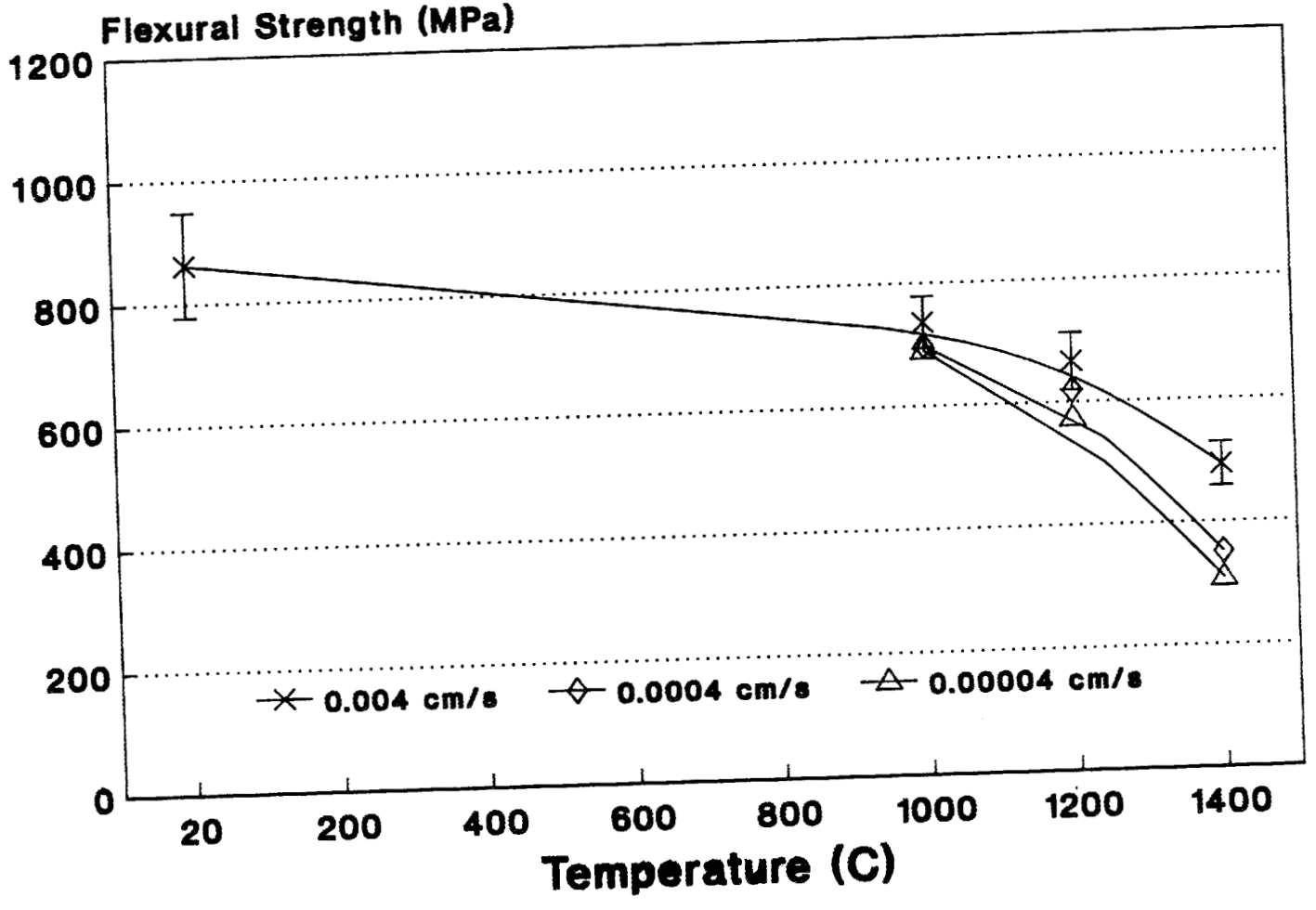

Figure 2. Flexural strength of GTE PY6.

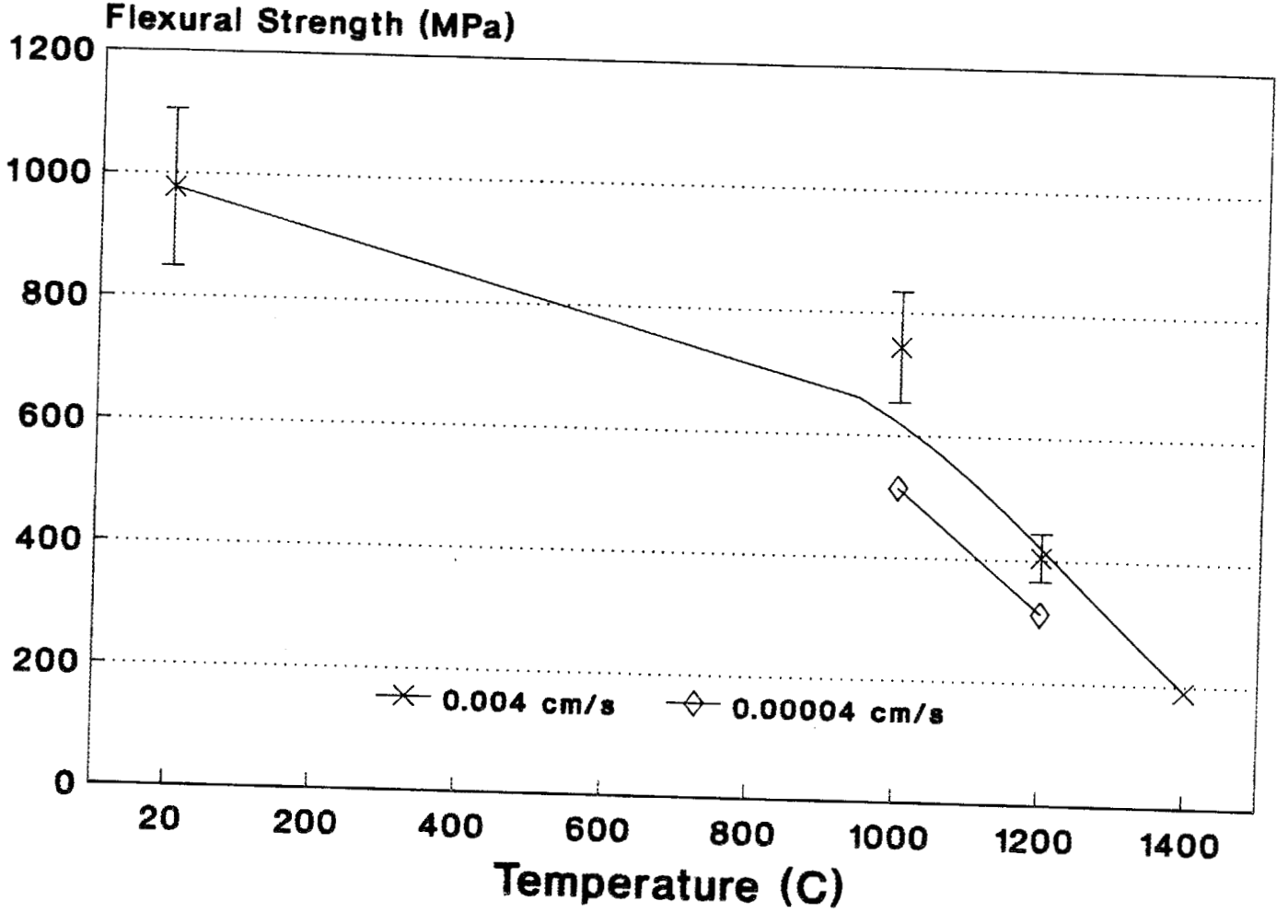

Figure 3. Flexural Strength of Howmet SN-4.

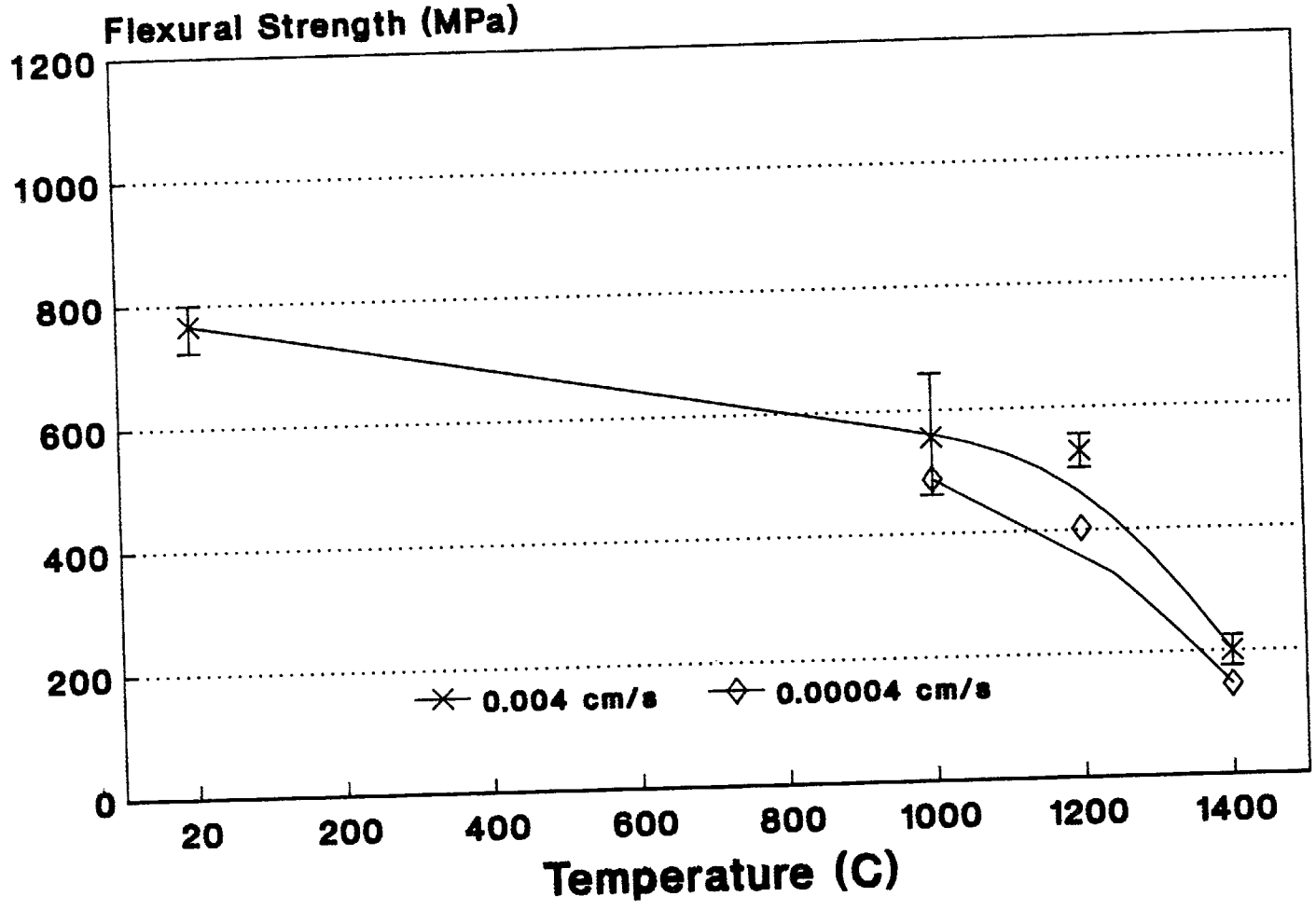

Figure 4. Flexural strength of Ceradyne 147-3.

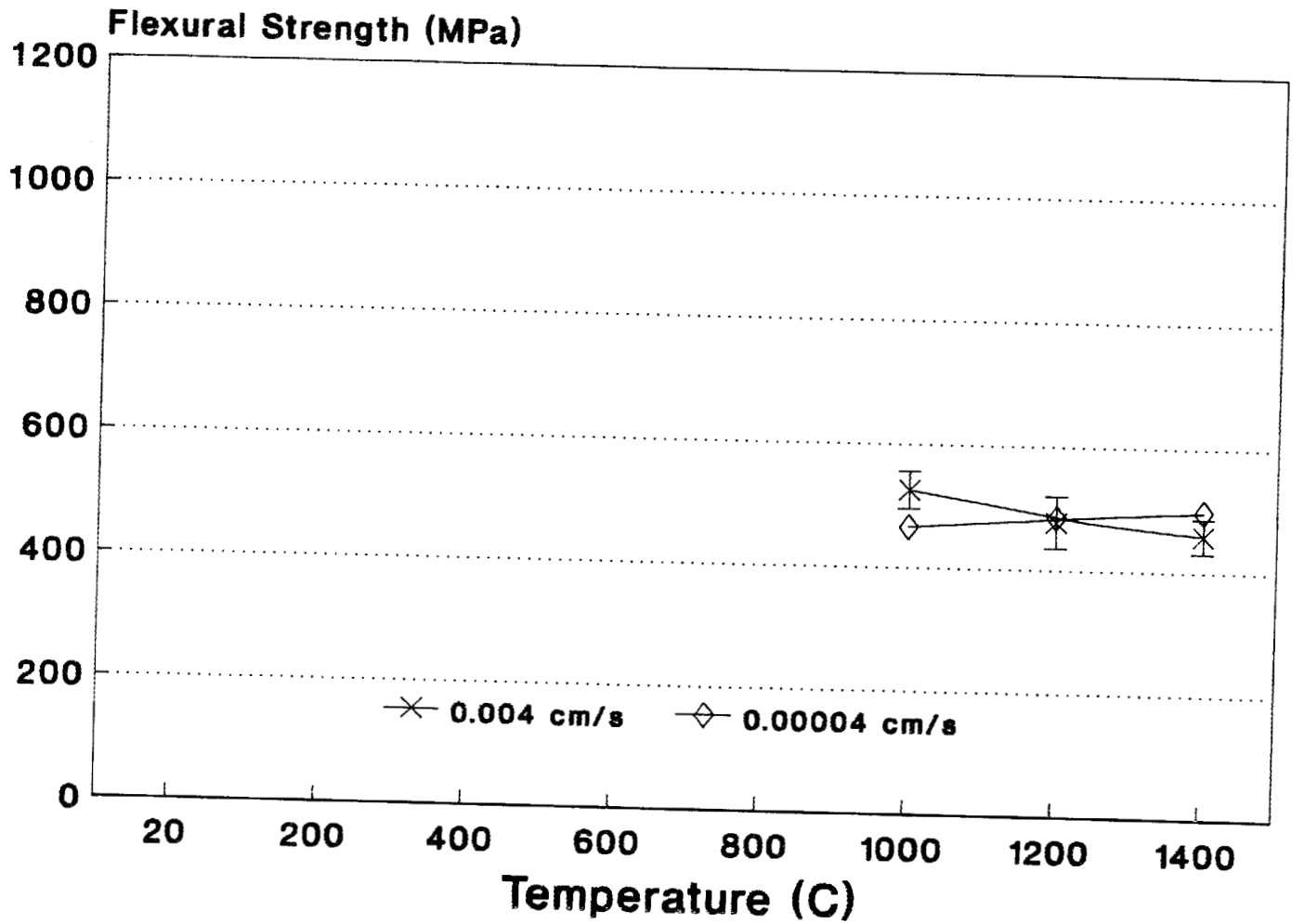

Figure 5. Flexural strength of Kyocera SN-252.

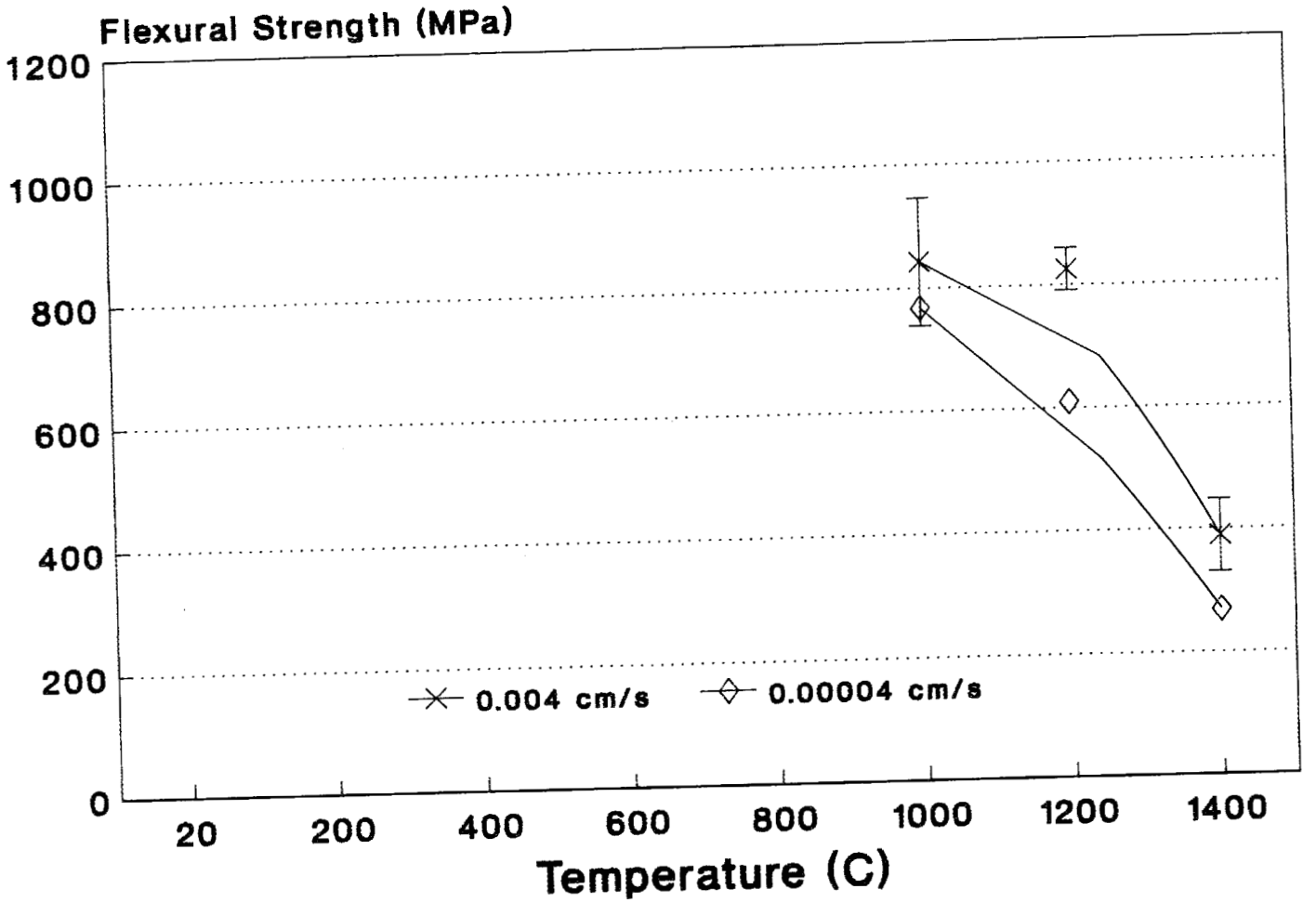

Figure 6. Flexural strength of NTK EC-152.

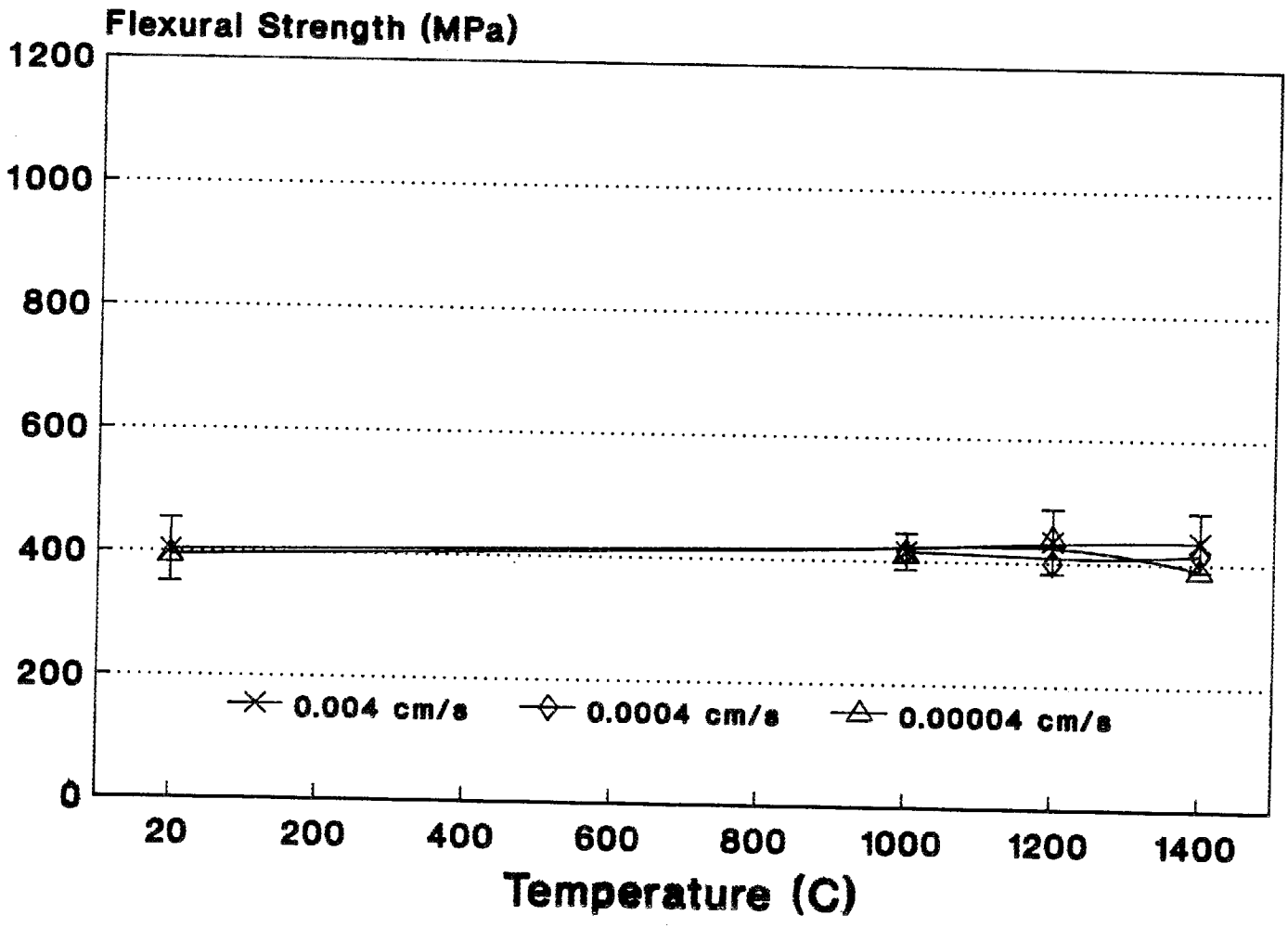

Figure 7. Flexural strength of Hexoloy SA.

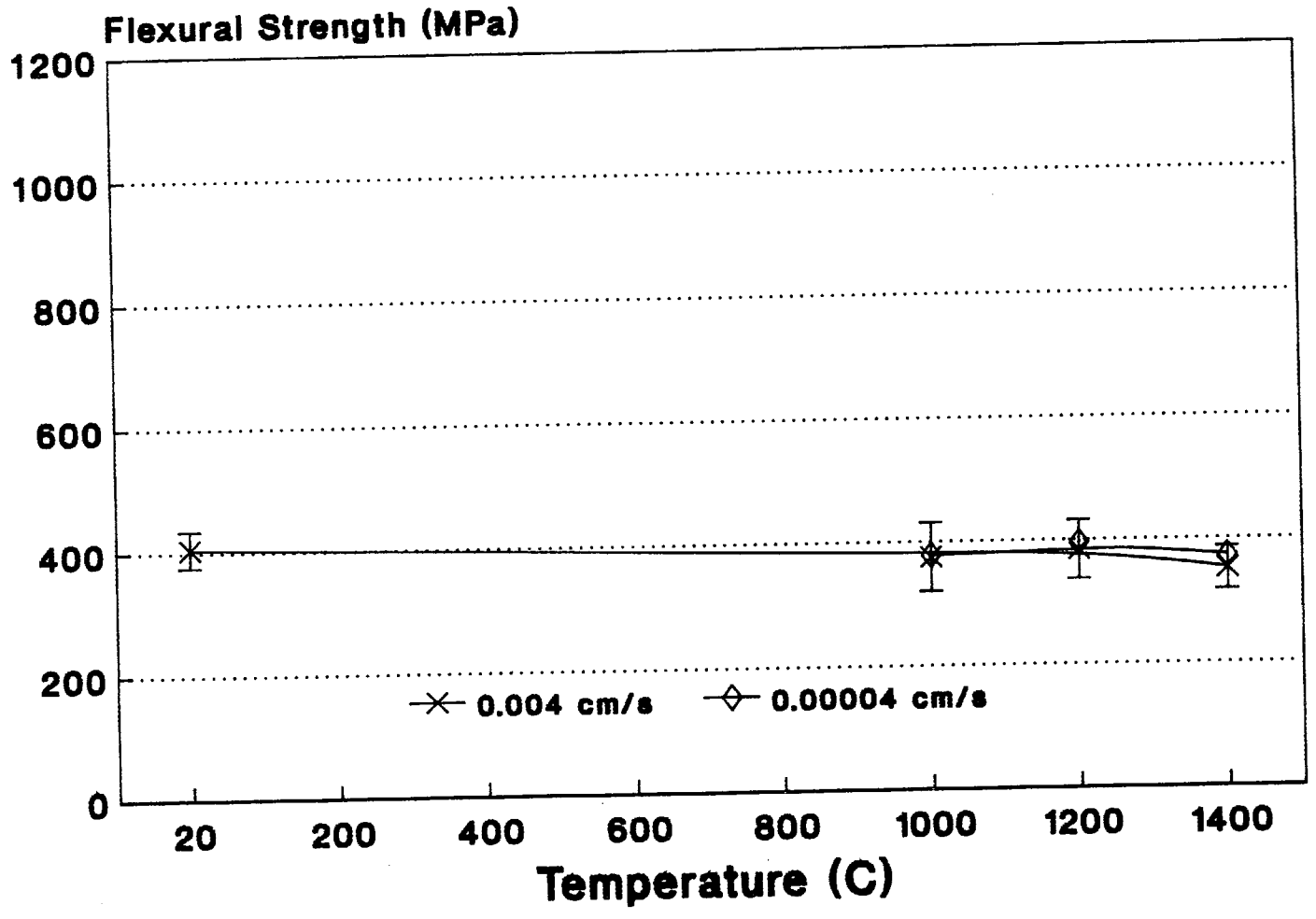

Figure 8. Flexural strength of Hexoloy ST.

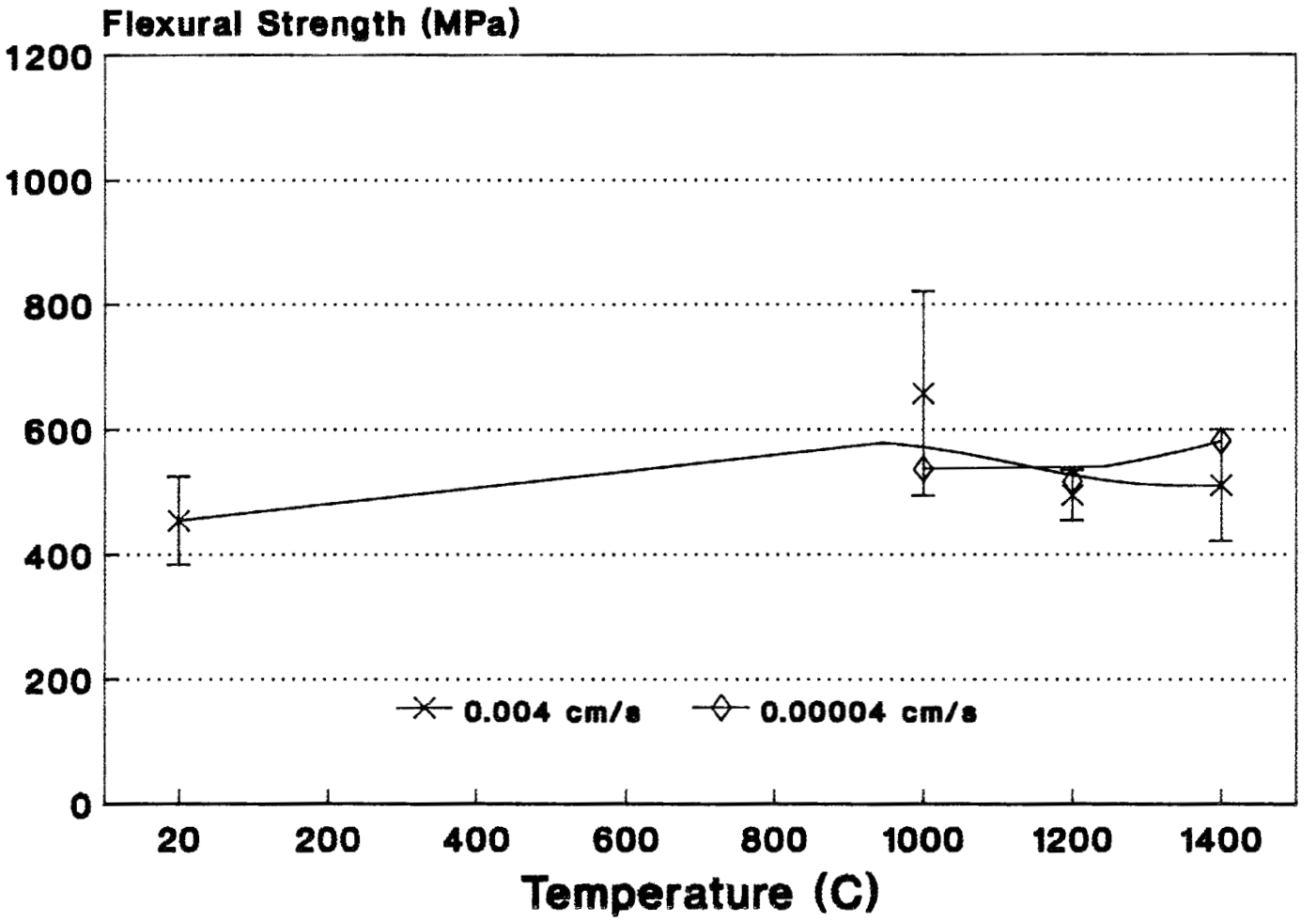

Figure 9. Flexural strength of CVD Inc. SiC.

tensile strength measurements for the Hexoloy SA and NT-154 are presented in Figures 10 and 12. Weibull plots for the tensile strength measurements obtained for Hexoloy SA and NT-154 are presented in Figures 11 and 13. The darkened symbols shown in Figures 11 and 13 denote the specimens which failed from volume-initiated flaws. The results of the Weibull analysis obtained from the flexural strength measurements are presented in Table 2. The results of the dynamic fatigue analysis obtained from the flexural strength measurements are presented in Table 3. Table 4 is a summary of the physical property measurements made, and Table 5 is a summary of the semiquantitative chemical analysis obtained for the candidate materials.

During this reporting period tensile stress rupture measurements of NT-154 specimens were initiated. Eighteen tensile specimens have been evaluated. Six specimens (#1 through #6) have been evaluated at 1400°C. The first three specimens were to be loaded at 300 MPa for an exposure time of 100 hours. However, all three specimens failed during loading before reaching 300 MPa. As a result, three additional tensile specimens were loaded to only 200 MPa for planned exposures up to 100 hours. Four specimens (#7 through #10) were loaded to 300 MPa for tensile stress rupture testing at 1200°C for 100 hours. Three of the specimens (#7, #8, #10) endured the 100-hour exposure and were subsequently loaded to failure. In addition, three specimens (#11, #12, #13) were tested at 1250°C and five specimens (#14 through #18) were tested at 1300°C. None of these tensile specimens survived the 100 hours. The results of these tensile stress rupture tests are compiled in Table 6 and displayed graphically in Figure 14. All of the fractured specimens are being examined optically. Typical fractographs obtained at the different test temperatures are shown in Figures 15 through 18.

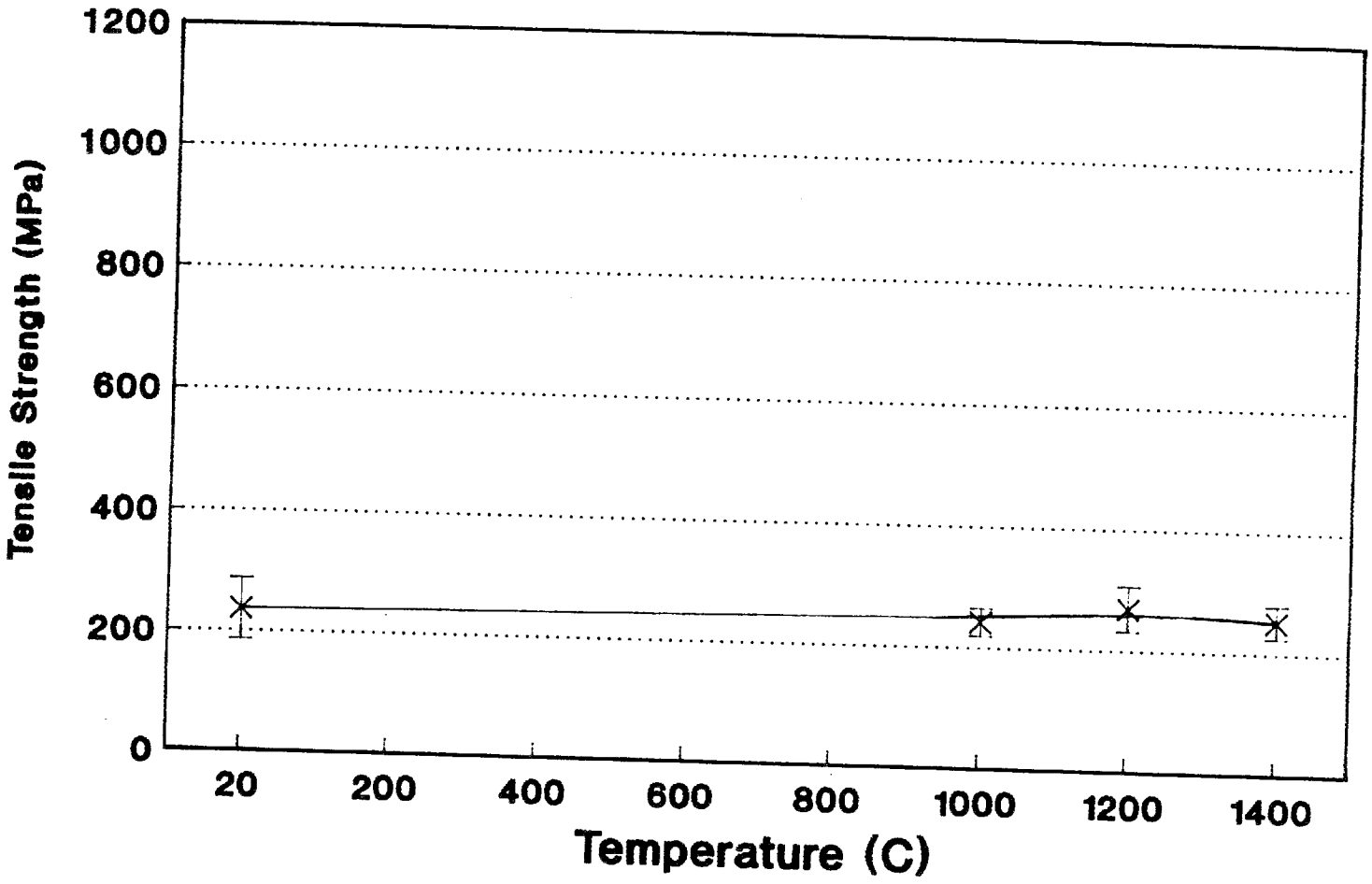

Figure 10. Tensile strength of Hexoloy SA, actuater speed 0.00004 cm/s.

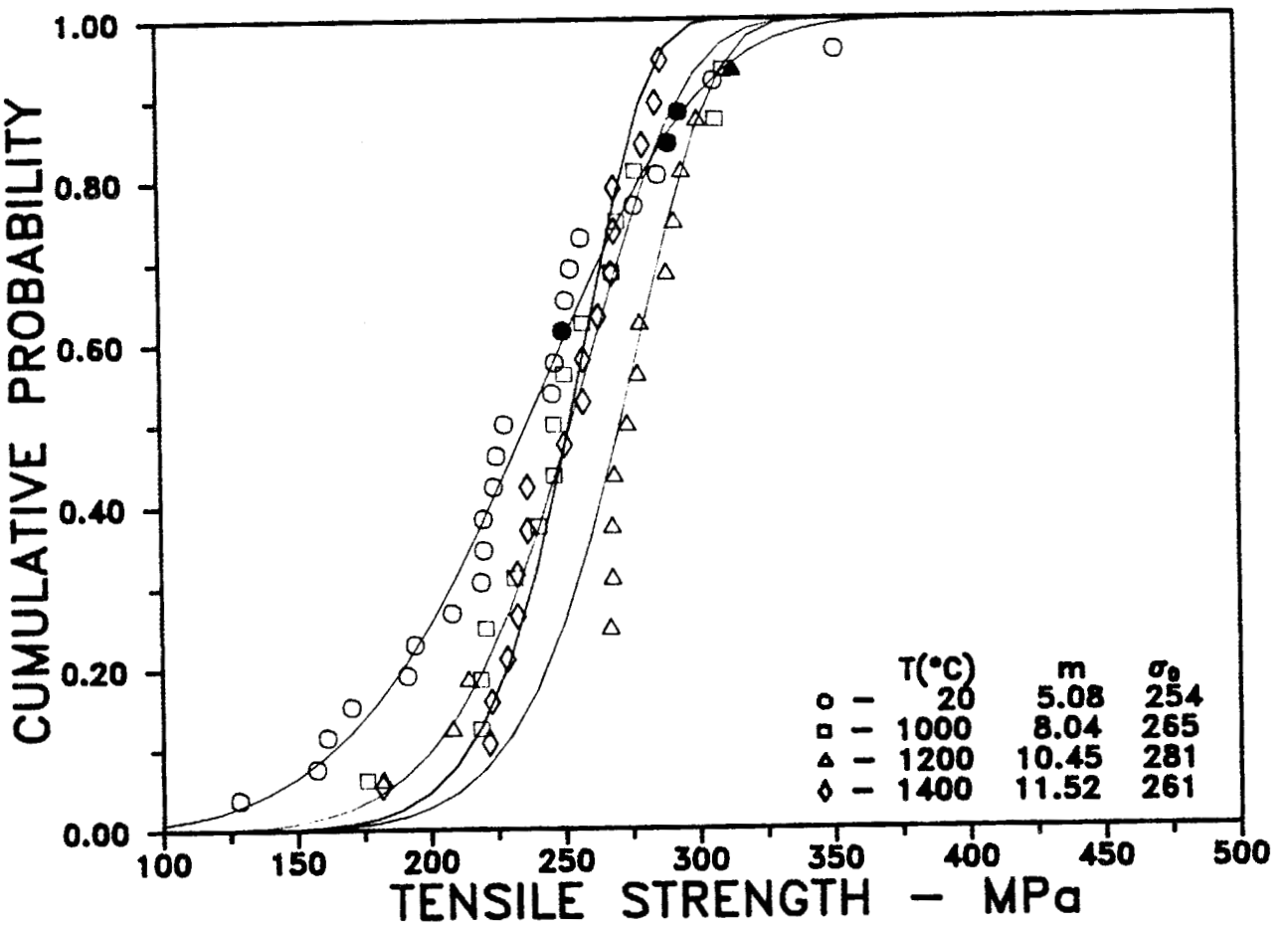

Darkened symbols - volume failures

Figure 11. Weibull plots of Carborundum Hexoloy SA - tensile strength in air.

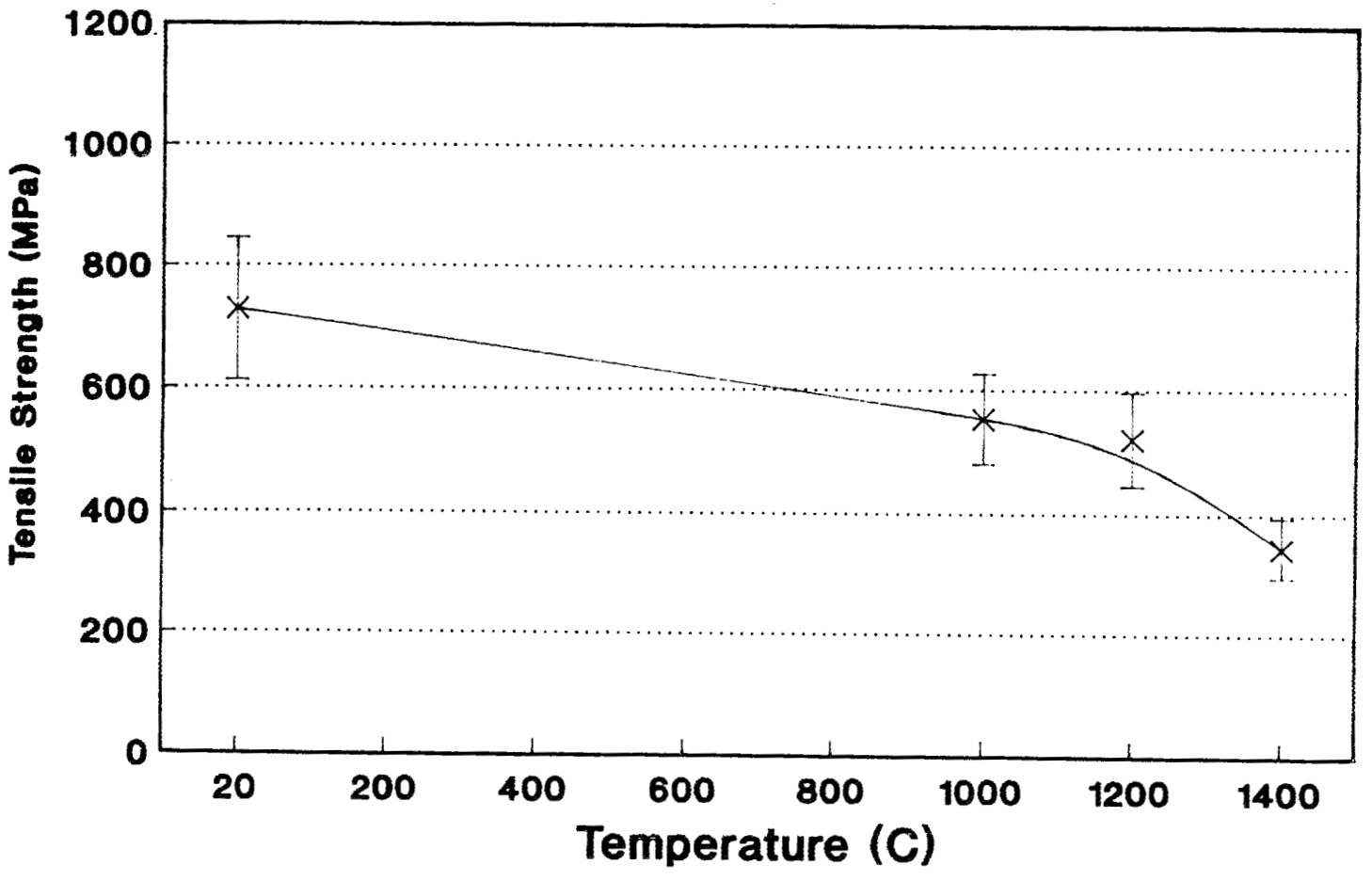

Figure 12. Tensile strength of Norton/TRW NT-154, actuater speed - 0.004 cm/s.

Table 2. Weibull Statistics for SiC and Si_3N_4 Flexural Test Specimens

Material Designation	Temperature C	Loading Rate Mpa/sec	Weibull Modulus m	Weibull Scale-data S_0 - MPa	Weibull Scale-area δ_0 - MPa
Hexoloy SA	21	190	8.83	424	147
	1000	1.71	12.50	428	202
		17.1	11.03	436	186
		171	18.13	429	255
	1200	1.43	9.80	465	179
		14.3	8.67	424	144
		143	8.79	457	158
	1400	1.33	15.23	405	218
		13.3	12.18	432	200
		133	10.87	457	193
SN-252	1000	1.33	20.53	478	303
		133	19.19	540	331
	1200	1.19	19.94	499	311
		119	12.56	497	236
	1400	1.14	20.78	511	325
		114	18.68	472	285
NT-154	21	143	15.27	940	508
	1000	1.33	34.68	804	613
		133	13.13	773	378
	1200	1.19	17.14	640	370
		119	18.69	707	428
	1400	1.14	6.87	391	100
		114	23.11	624	415
SN-4	20	143	11.30	976	426
EC-152	1000	1.33	15.20	795	429
		133	9.86	887	343
	1200	1.19	17.35	627	365
		119	24.74	842	576

Note: Weibull statistics were not calculated for test conditions with six or fewer test results.

Table 2. Weibull Statistics for SiC and Si_3N_4 Flexural Test Specimens (Concluded)

Material Designation	Temperature C	Loading Rate Mpa/sec	Weibull Modulus m	Weibull Scale-data S_0 - MPa	Weibull Scale-area δ_0 - MPa
GTE PY6	21	143	12.25	900	418
	1000	1.33	47.11	699	572
		13.3	10.16	732	291
		133	18.72	756	457
	1200	1.19	17.83	591	349
		11.9	22.15	634	414
		119	22.47	684	450
	1400	1.14	15.71	320	176
		11.4	12.14	367	169
		114	15.61	509	279
HEXOLOY ST	1000	1.71	8.31	401	130
		171	7.68	399	118
	1200	1.43	9.47	416	155
		143	10.83	403	170
CVD Inc. Si	21	190	8.13	482	153
	1000	1.71	4.04	593	59
		171	4.84	719	105
	1200	1.43	4.50	568	72
		143	14.59	513	269
	1400	1.33	12.54	611	289
		133	6.97	547	143
Ceradyne 147-3	1000	1.3	8.82	514	178
		133	6.75	595	149
	1200	1.2	10.53	423	174
		119	23.49	541	363
	1400	114	9.01	211	75

Note: Weibull statistics were not calculated for test conditions with six or fewer test results.

Table 3. Slow Crack Growth Parameter (n) Values

Material	Temperature	n Values
Sohio Hexoloy SA	21	Slope not significantly greater than zero
	1000	Slope not significantly greater than zero
	1200	Slope not significantly greater than zero
	1400	41
Kyocera SN-252	1000	37
	1200	Slope not significantly greater than zero
	1400	Slope significantly less than zero (n = -58)
Howmet SN-4	1000	12
	1200	17
Norton NT-154	21	25
	1000	Slope not significantly greater than zero
	1200	46
	1400	7.6
NGK-SP EC-152	1000	50
	1200	14
GTE PY6	1000	73
	1200	30
	1400	8.8

Table 3. Slow Crack Growth Parameter (n) Values (Concluded)

Material	Temperature	n Values
Sohio Hexoloy ST	1000	Slope not significantly greater than zero
	1200	Slope not significantly greater than zero
	1400	Slope not significantly greater than zero
CVD Inc. SiC	1000	Slope not significantly greater than zero
	1200	Slope not significantly greater than zero
	1400	Slope not significantly greater than zero
Ceradyne/147-3	1000	36
	1200	15

Table 4. Property Data Obtained for Candidate SiC and Si_3N_4 Ceramics

Property Measurement	Materials					
	Hexoloy SA	Hexoloy ST	GTE PY6	Norton/TRW XL-154	Howmet SN-4	Kyocera SN-252
Density g/cc	3.17	-	3.27	3.23	3.23	-
Young's Modulus (GPa)	427	-	301	310	294	-
Hardness (kg/mm^2)	2727	2619	1513	1620	1605	1537
Coefficient of Thermal Expansion (10^{-6}/°C from 20°-1400°C)	5	-	3.3	-	-	-
Fracture Toughness CF/MI* (MPa $\cdot\sqrt{m}$)						
20°C	2.6/3.4	-/4.4	3.2/5	3.2/4.3	3.7/6.8	-/5
1400°C	3.1/3.0	-	-	3.6/5.6	-	-

*CF - Controlled Flaw Method
MI - Microindent Method

Table 5. Semiquantitative Chemical Analysis of the As-Received Candidate Materials

Material	Si_3N_4	Al_2O_3	Y_2O_3	Yb_2O_3	SiC	TiB_2
Kyocera SN-252	93.06	0.40	0.30	6.24	--	--
Howmet SN-4	90.65	5.26	4.10	--	--	--
NTK-EC-152	90.65	4.40	4.94	--	--	--
GTE PY6	76.23	--	23.77	--	--	--
Norton/TRW NT-154	84.34	--	15.66	--	--	--
Hexoloy SA	--	--	--	--	100	--
Hexoloy ST	--	--	--	--	79.3	20.7
Ceradyne 147-3	84.48	1.77	13.75	--	--	--
CVD SiC	--	--	--	--	100	--

Table 6. Interim Results of Tensile Stress Rupture Testing for NT-154

Test Sequence Number	Temperature (°C)	Stress Level (MPa)	Time (min)	Stress @ Failure (MPa)	Failure Mode
1	1400	-	0*	290	Volume
2	1400	-	0*	279	Volume
3	1400	-	0*	216	Volume
4	1400	200	4.3	200	Surface
5	1400	200	0.6	200	Surface
6	1400	200	0.2	200	Surface
7	1200	300	6000	388	Vol. @ Inclusion
8	1200	300	6000	485	Vol. @ Inclusion
9	1200	300	3379	300	Surface
10	1200	300	6000	572	Vol. @ Inclusion
11	1250	300	5040	300	Surface
12	1250	300	3372	300	Volume
13	1250	300	702	300	Volume
14	1300	300	184	300	Surface
15	1300	300	226	300	Volume
16	1300	300	31	300	Volume
17	1300	300	48	300	Volume
18	1300	300	72	300	Volume

*Failed during loading.

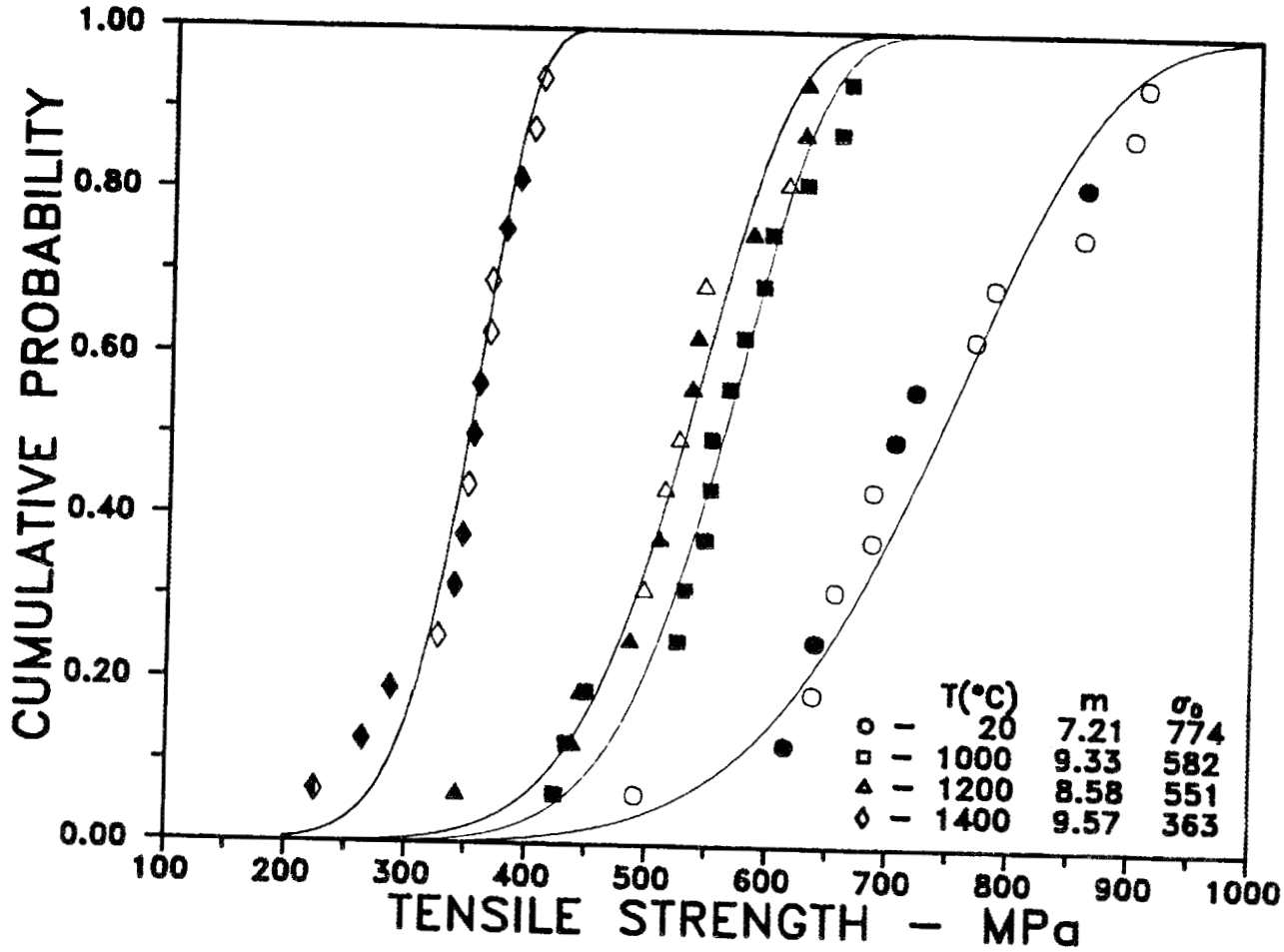

Darkened symbols - volume failures

Figure 13. Weibull plots of Norton/TRW NT-154 - tensile strength in air.

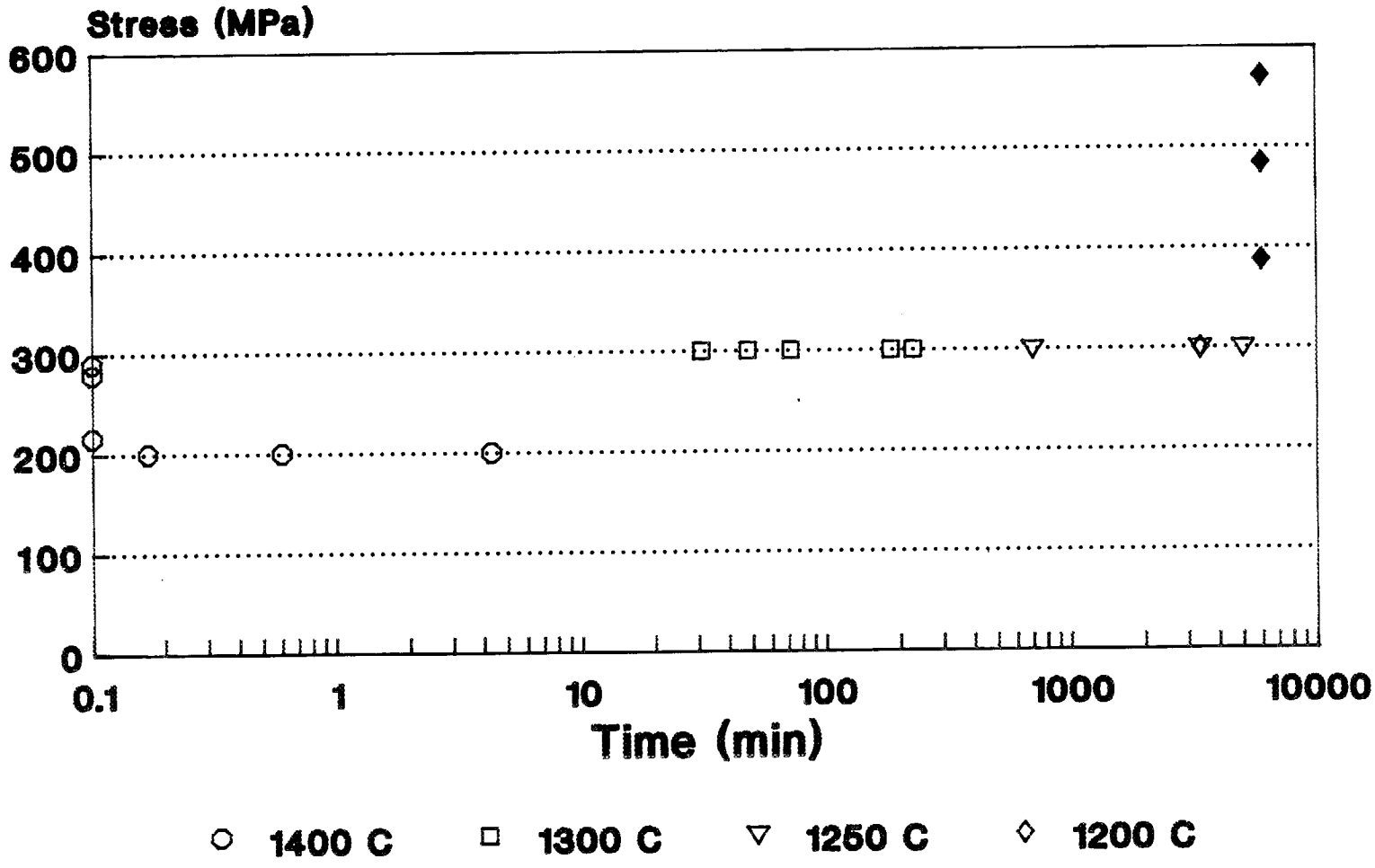

Figure 14. Tensile stress rupture behavior of NT-154.

Figure 15. NT-154 @ 1200°C, tensile stress rupture @ 300 MPa.

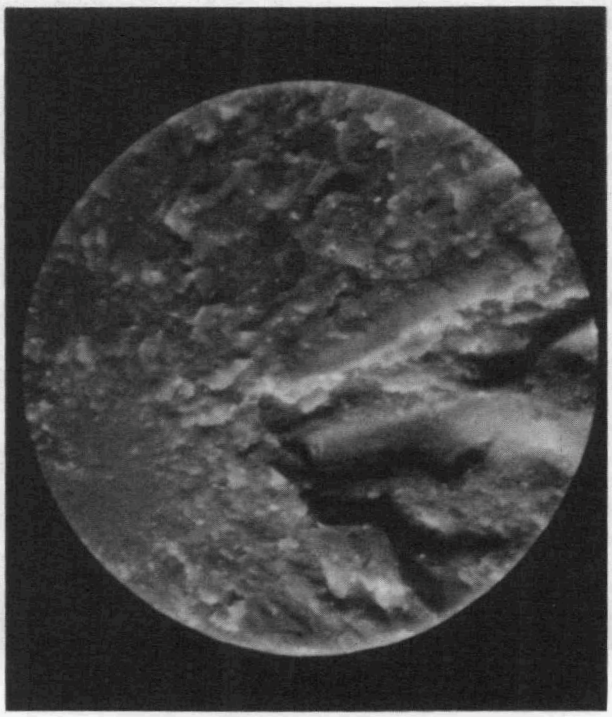

Figure 16. NT-154 @ 1250°C, tensile stress rupture @ 300 MPa.

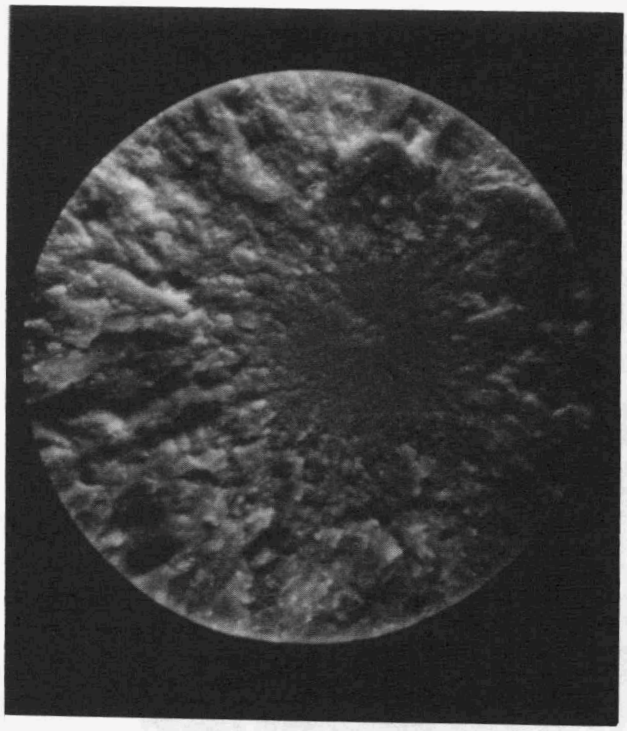

Figure 17. NT-154 @ 1300°C, tensile stress rupture @ 300 MPa.

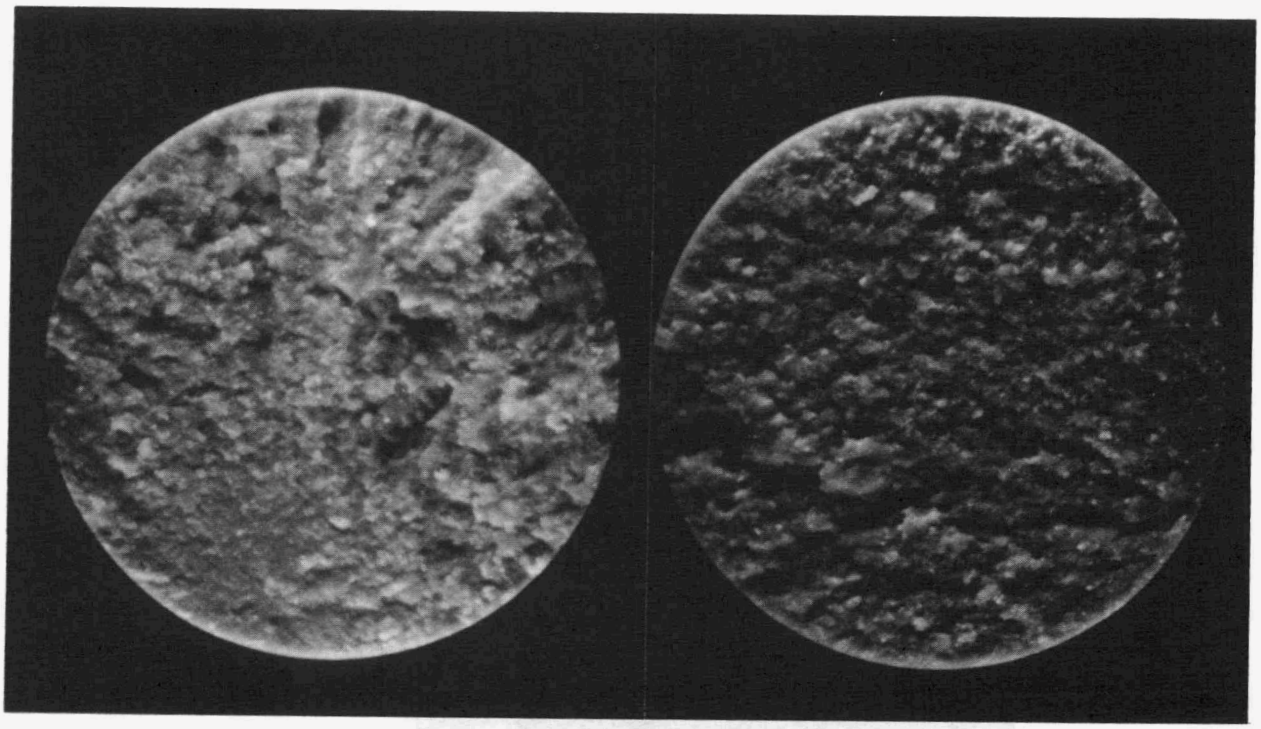

(a) (b)

Figure 18. NT-154 @ 1400°C, (a) tensile stress rupture @ ~300 MPa, (b) tensile stress rupture @ ~200 MPa.

Discussion of results

Strength:

The measured flexural strength values (Figures 1 and 7) were compared with the tensile strength values for NT-154 and Hexoloy SA (Figures 10 and 12). The results of these measurements are presented in Table 7.

Table 7. Comparison of Tensile and Flexural Strength Values Measured for NT-154 and Hexoloy SA

Temperature (°C)	NT-154 Tensile (MPa)	NT-154 Flexural (MPa)	NT-154 Ratio (%)	Hexoloy SA Tensile (MPa)	Hexoloy SA Flexural (MPa)	Hexoloy SA Ratio (%)
20	726	907	(83)	234	400	(59)
1000	552	741	(74)	250	412	(61)
1200	520	686	(76)	275	441	(62)
1400	343	610	(56)	250	390	(64)

As seen in Table 7, for the NT-154 material tensile-to-flexural-strength ratio decreases with increasing temperature (83%-56%); however, for the Hexoloy SA material there is a small increase in tensile-to-flexural-strength ratio with increasing temperature (59%-64%). From a review of the literature it was observed that tensile strength will vary from 50 to 90% of the measured flexural strength for a wide range of tensile gage volumes. As shown in Table 7, the Hexoloy SA had an average tensile-to-flexural-strength ratio of 61.5% for the temperatures studied. This value is somewhat lower than average and is probably due to the poor machining that was observed for the Hexoloy SA tensile specimens. The NT-154 material had a room temperature tensile-to-flexural-strength ratio of 83%, a 1000°C and 1200°C ratio of 75%, and a 1400°C ratio of 56%. It is believed that the high room temperature strength and high tensile-to-flexural-strength ratio are due to the heat treatment (50 hours @ 1000°C) given

to the NT-154 specimens after surface machining. The heat treatment blunts the surface flaws and enhances the low-temperature tensile strength. As the test temperature is increased, the effect of the heat treatment becomes less significant. At 1000°C and 1200°C the strength ratio is more typical of the average values reported. At 1400°C the tensile strength drops significantly and the strength ratio also drops dramatically. These results would suggest a change in tensile failure mechanism versus flexural failure.

As shown in Table 7, both the tensile and flexural strength of NT-154 decreased with increasing temperatures above 1000°C. However, the strength of Hexoloy SA does not vary greatly with temperature. The high-temperature behavior observed for NT-154 can be attributed to the viscosity of a glassy phase in the Si_3N_4 grain boundaries. The strength retention observed in the Hexoloy SA test specimens at elevated temperatures can probably be attributed to the reported flaw-healing characteristics of this material at elevated temperatures.

The fracture toughness values obtained (Table 4) by microindent tended to be higher than the values obtained by the controlled flaw method. It is believed that the lower values obtained by the controlled flaw method are due to residual stresses introduced into the surface of the controlled flaw specimens [1]. A limited review of the literature indicates that fracture toughness values for Si_3N_4 range from 3-6 MPa $\sqrt{m}$. Fracture toughness values for SiC range from 2-4 MPa $\sqrt{m}$. Norton/TRW reported a value of 5.2 MPa $\sqrt{m}$ for NT-154 by the controlled flaw method. Norton/TRW uses a load of 10 kg for indentation. It is suggested that the value (3.2 MPa $\sqrt{m}$) obtained for NT-154 by controlled flaw is due to the generation of smaller crack size in our test procedure. Evans has suggested that the different values reported for fracture toughness of the same material may be due to R-curve behavior. Similar results have also been reported by Cook, et al. [2] showing the variation of K_{Ic} with indent load. It is apparent that K_{Ic} can vary significantly depending on test method.

The tensile stress rupture results (Table 6) obtained for the NT-154 was troubling. At 300 MPa load, severe strength degradation was observed at temperatures above 1200°C. As shown in Figures 15 through 18, failure at 1200°C was by brittle fracture, while at and above 1250°C failure appears to be due to void formation. These results are consistent with the results reported in the literature [3,4] for Y_2O_3-doped Si_3N_4. As concluded by Wiederhorn et al., [3] in 1983, 1200°C appears to be the safe upper limit for using these Y_2O_3 doped Si_3N_4 for structural applications.

Weibull Analysis:

A theoretical analysis to evaluate the probability of volume-flaw initiated failures in SiC and Si_3N_4 tensile and flexural test specimens was conducted. The effort employed a two-parameter Weibull statistical strength model and assumed that test specimens were subject to bimodal failure, originating either at surface flaws or at volume flaws. The analysis compared the volume-mode failure probability for tensile specimens and 3 mm x 4 mm cross-section flexural specimens in two orientations. The analysis employed statistical strength characteristics of nominal low-, mid-, and high-strength candidate materials at 1200°C. Special attention was focused on the effect of testing four-point bend flexural specimens with the 3-mm specimen dimension as the tensile surface to increase the fraction of volume-mode failures. It was assumed that test specimens had surface-mode statistical strength characteristics equal to those determined from flexural test results with the 4-mm dimension as the tensile surface. This analysis, completed before tensile test results for NT-154 were obtained, employed a systematic variation of assumed volume-mode statistical strength Weibull parameters that covered a wide range of likely values.

The results of tensile tests on NT-154 specimens provided the first useful indication of the surface-mode and volume-mode statistical strength characteristics of test program materials. Tensile test results at 20°C, 1200°C, and 1400°C indicated bimodal

strength characteristics. All tensile specimens failures at 1000°C were initiated in the tensile gage volume. Although the number of specimens (15 tested for a given temperature, and loading condition) is not large enough to support a good statistical analysis, the results provide the basis for preliminary evaluations of volume-mode Weibull statistical strength characteristics.

The results appear to indicate that the volume-mode Weibull parameters, m (modulus), and $\beta_0 V$ [test statistics scale parameter, the stress at which the probability of specimen failure is (1 - 1/e)] are similar to the values for the combined set of samples and for surface-mode strength. The results indicate that the Weibull modulus values are lower than those measured for flexural specimens at the same temperatures.

The preliminary Weibull parameters determined from the test results were used as input values for the bimodal-Weibull model mentioned above. Results obtained compared reasonably well with actual tensile test results, considering the large uncertainties due to the relatively small sample size. The results of the analysis indicate that the probability of volume-mode failures in standard flexural specimens [MIL-STD 1942(MR), specimen size B] is very small. This is consistent with the flexural test results which appear to indicate 100% surface-mode failures. Volume-mode failures that occur in four-point bend specimens are likely to be initiated very close to the tensile surface and may be difficult to differentiate from surface-mode failures. The theoretical model also indicates that the use of the non-standard 3-mm tensile surface orientation is not likely to increase the volume-mode failure fraction to a significant level for the materials being evaluated.

Finite Element Analysis:

As a result of excessive buttonhead failures during the initial phase of our tensile testing project, re-evaluation of our tensile

testing methodology was initiated. A photoelastic analysis of buttonhead specimens and the gripping collets is in progress and a finite element structural analysis was completed.

Buttonhead failures which occurred in the early part of the tensile testing appeared to be the result of high surface stresses acting on surface imperfections caused by machining in the buttonhead fillet. A finite element structural analysis [5] was conducted to determine the state of stress in the button fillet, particularly the location and magnitude of the principal stresses, for a variety of potential loading conditions which the collet could impose on the specimen.

Four loading cases were considered and the applied load for each case results in a uniform axial gage section stress of 1000 psi (see Figure 19): (1) uniform axial tension, in which 159 psi pulls at the ends of the specimen (to serve as an ideal baseline case); (2) hydrostatic pressure, in which 364 psi is applied to fillet and shank over the region bounded by the collet/shank interface; (3) ring contact pressure, in which 6740 psi is applied uniformly over a 0.0055-in-wide ring representing the initial contact region between the collet and specimen fillet, are due to a slight (1.67%) mismatch and a large (10%) mismatch in collet and fillet radii; and (4) ideal Instron collet pressure in which 524 psi is applied uniformly over those interface regions which should ideally contact the collet radius and specimen fillet and the collet and specimen shanks, but not the region bounded by the collet flat.

Several assumptions are made in performing these analyses: (1) the problem is axisymmetric; (2) the material behavior is linear elastic; (3) friction forces may be ignored, providing conservative results; and (4) the failure mode is that of surface tensile stresses

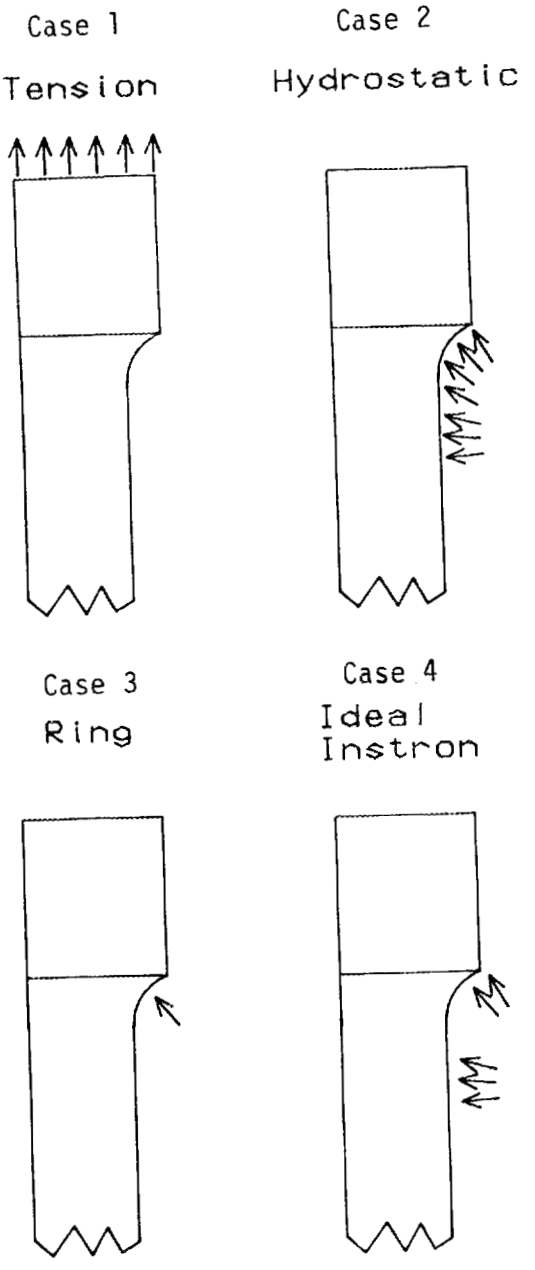

Figure 19. Buttonhead load distributions.

pulling open a surface flaw, thereby initiating and propagating a crack which leads to failure in the button head fillet.

The finite element models consist of a large number (6000-6500) of 4-node axisymmetric elements to ensure good resolution of stresses. Material properties for SiC (E = 62 Msi, ν = 0.14) were used for this model. Because of symmetry conditions, only half of the specimen cross section is explicitly modeled (see Figure 20).

The modeling and analyses were performed using the Algor SuperSAP finite element analysis system running on an Everex 386 personal computer. Hardcopy output is obtained on an HP LaserJet Series II printer and HP 7550A plotter.

From the maximum principal stress contour plots (Figures 21 through 25), it was found that for all four loading cases, the highest surface tensile stresses occur at the base of the button head fillet adjacent to the specimen shank, which coincides with the region of stress concentration predicted by elasticity theory. Stress concentration factors for each load case are presented in Table 8. The factors are the ratio of the maximum surface tensile stress in the fillet (σ_{cr}) to either the gage section axial stress or the shank axial stress.

Table 8. Stress Concentration Factors Obtained for the Buttonhead Tensile Specimens

Case	σ_{cr} (psi)	K_{gage}	K_{shank}
1	440	0.44	1.57
2	530	0.53	1.89
3	740	0.74	2.64
3b	760	0.76	2.71
4	850	0.85	3.03

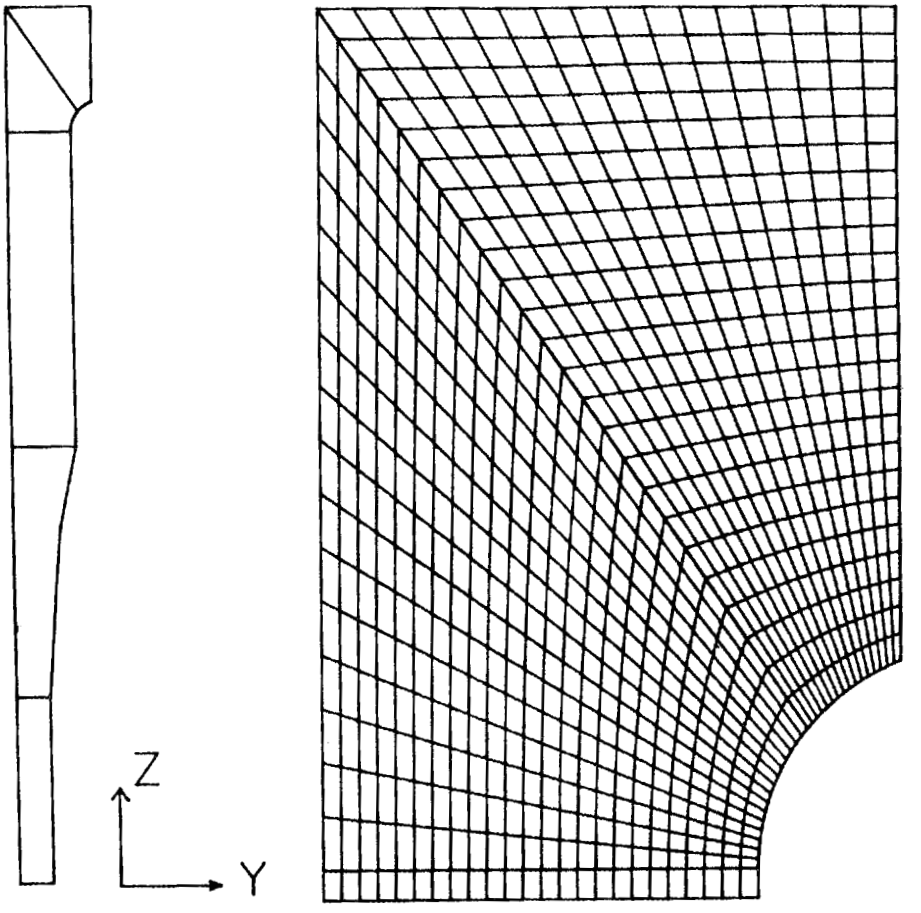

Figure 20. Buttonhead axisymmetric mesh.

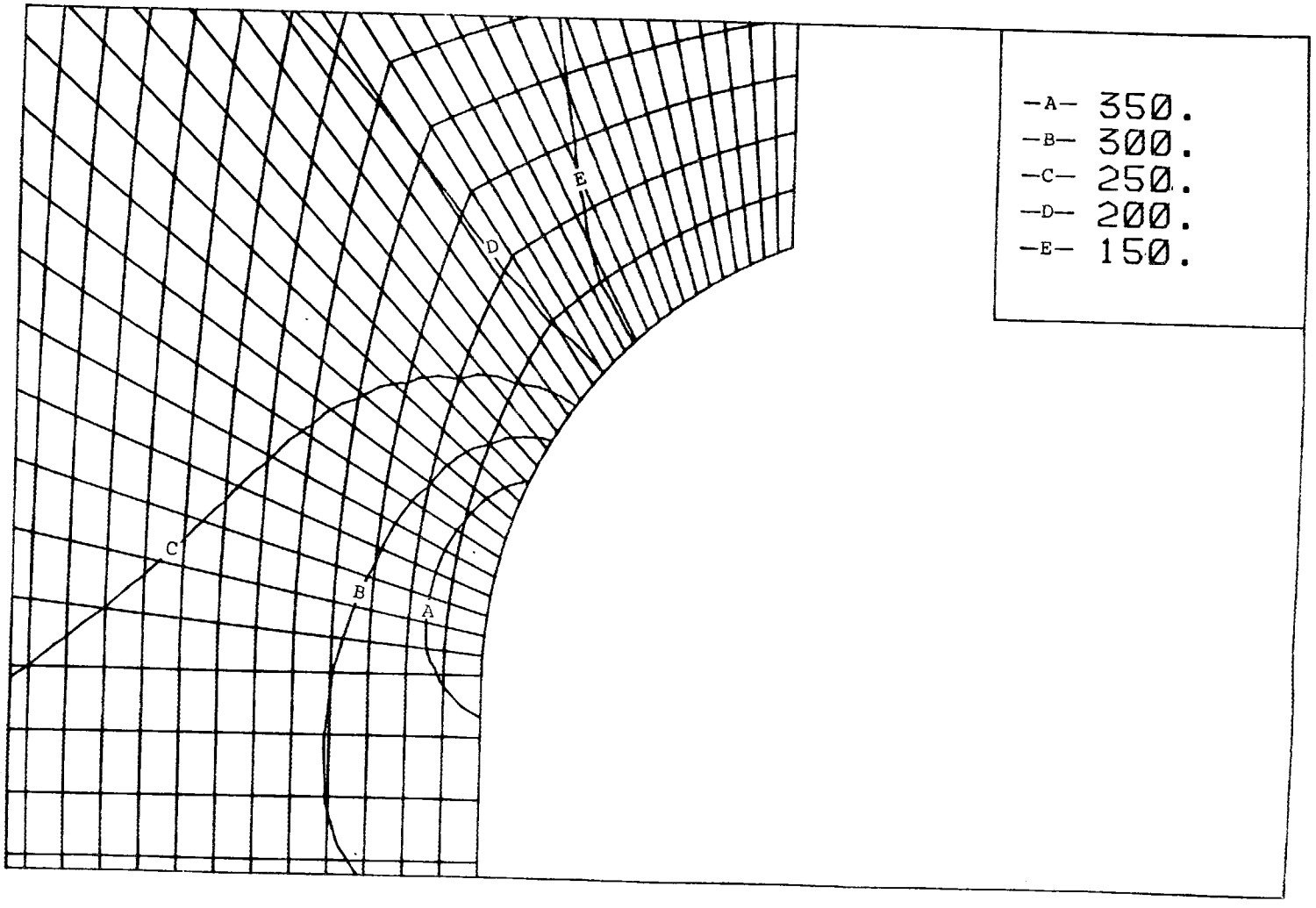

Figure 21. Maximum principal stress contours for the tension load case.

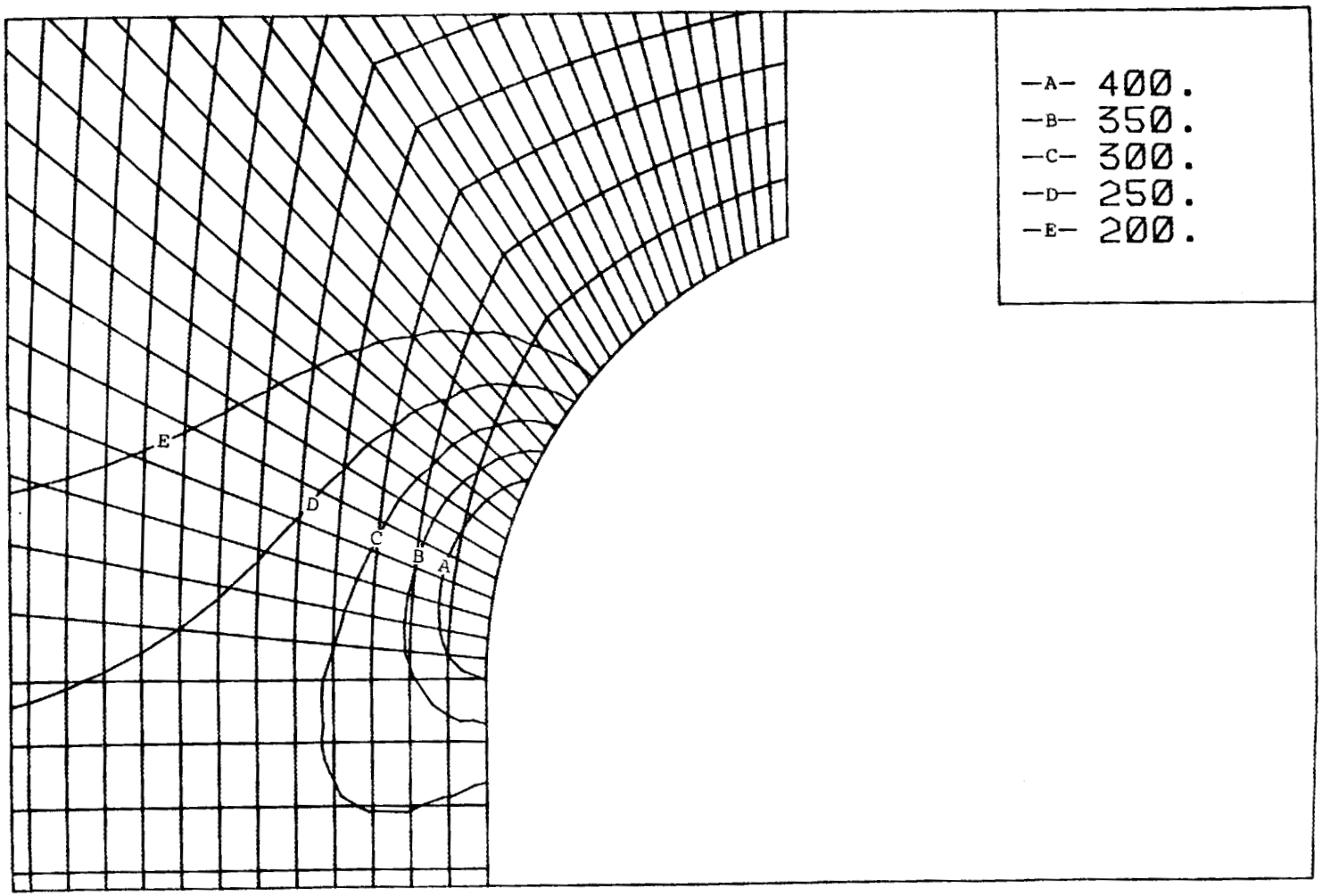

Figure 22. Maximum principal stress contours for the hydrostatic load case.

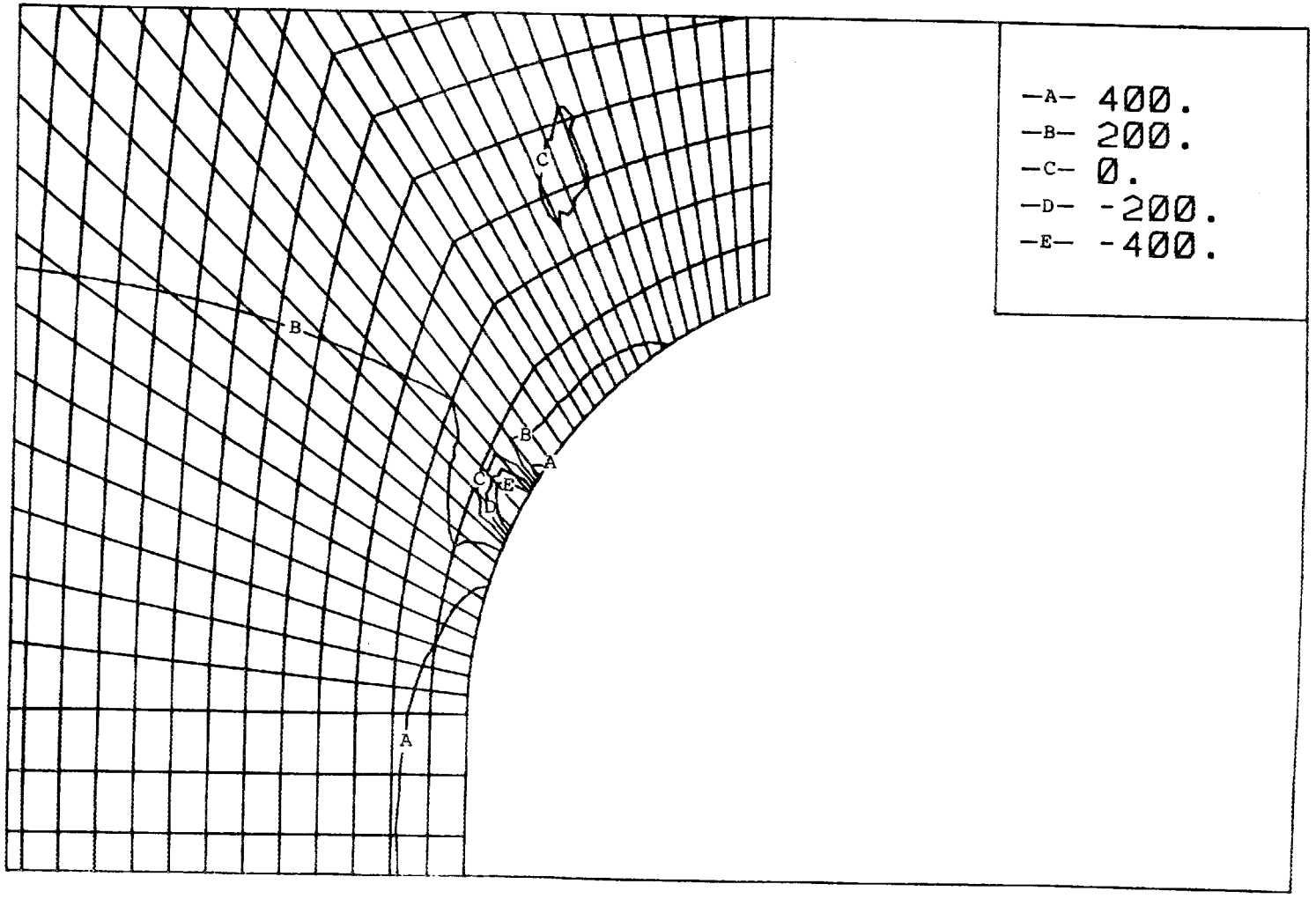

Figure 23. Maximum principal stress contours for the ring load case, 1.67% radius mismatch.

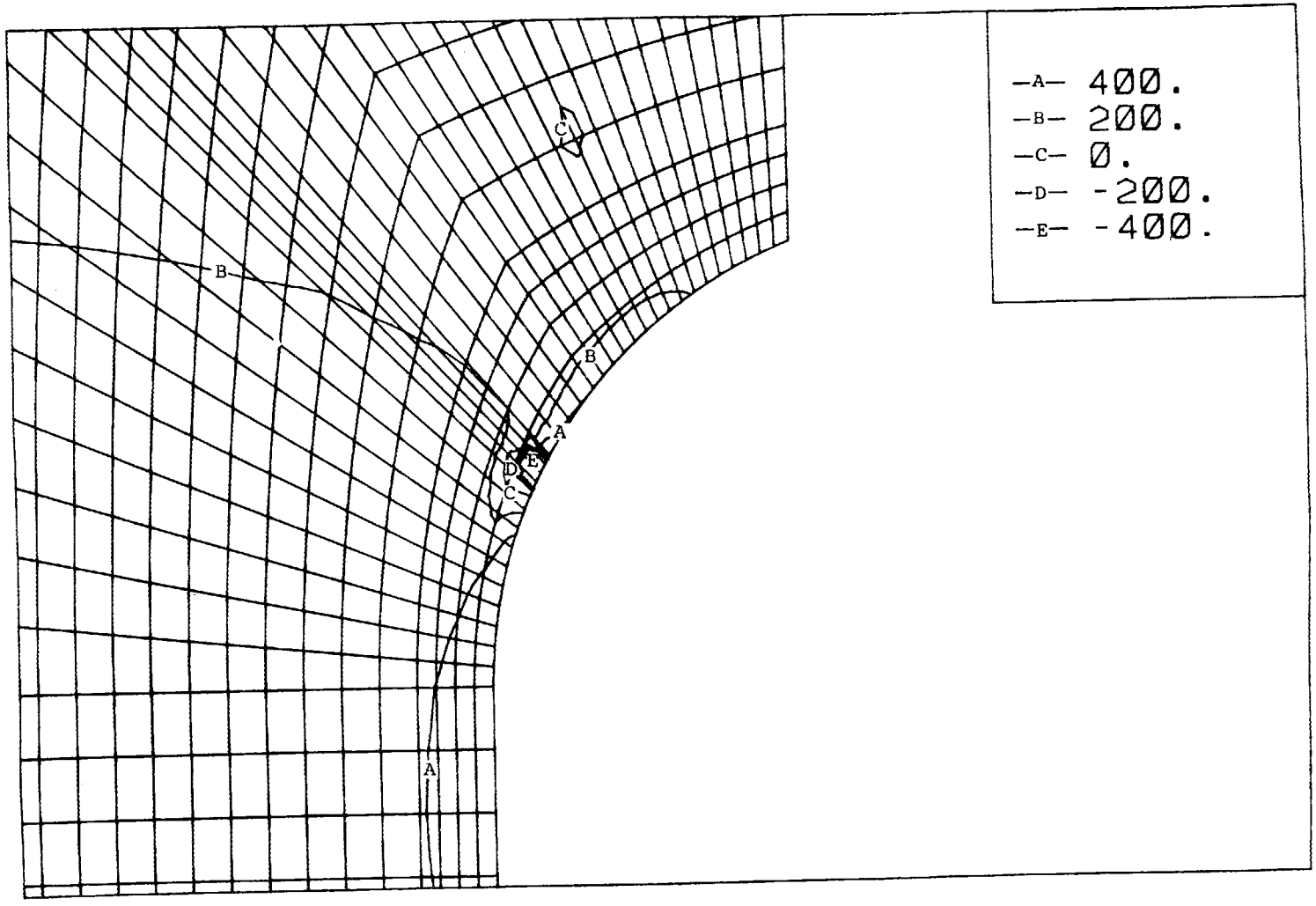

Figure 24. Maximum principal stress contours for the ring load case, 10% radius mismatch.

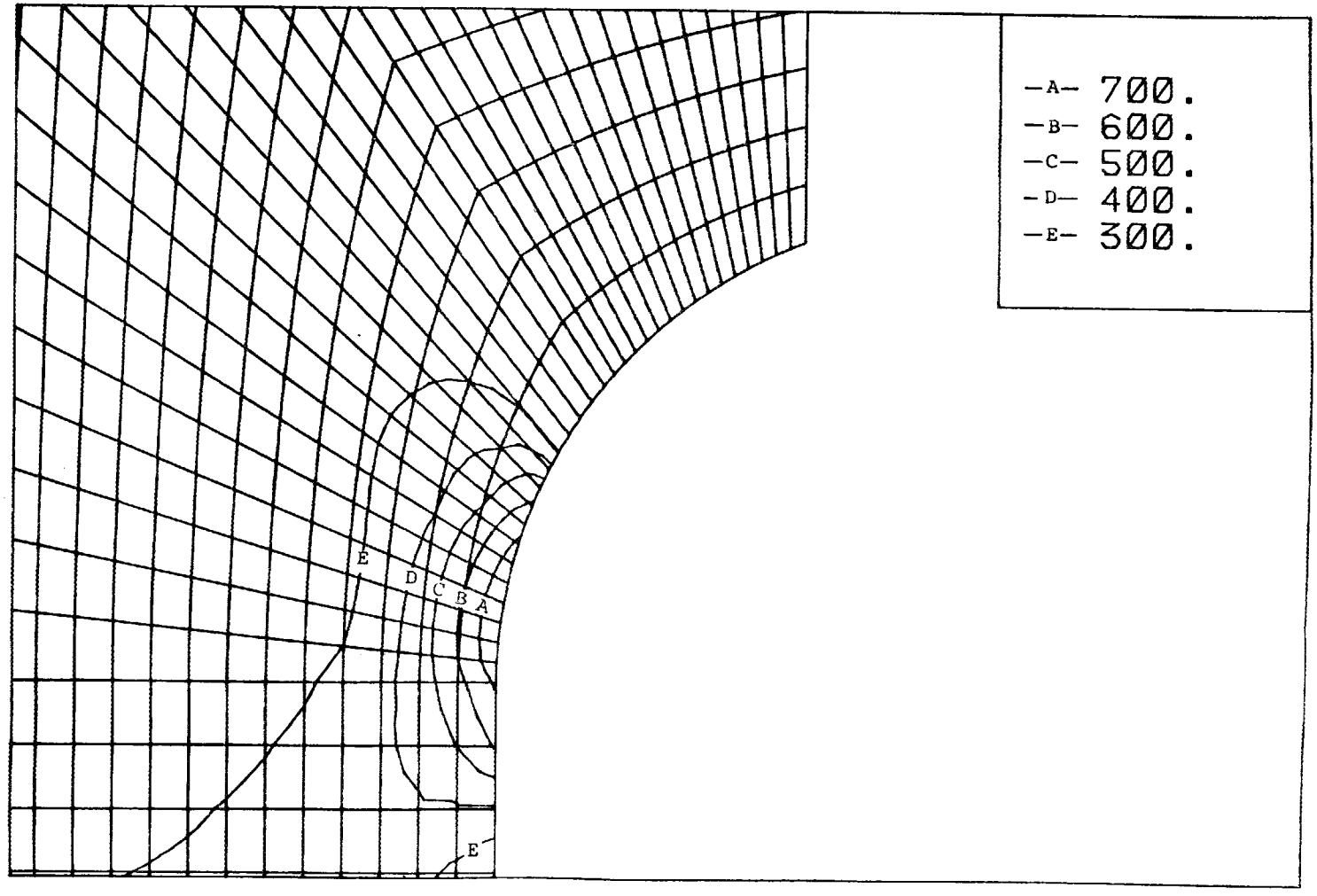

Figure 25. Maximum principal stress contours for the ideal Instron load case.

All K_{gage} values are less than 1.0, indicating that the gage section axial stress is higher than the fillet surface tensile stress, so that failure should occur in the gage section. Failures in the button fillet indicate that factors other than the state of stress, such as machining marks, are contributing to such undesirable failures.

As expected, the uniaxial tension case (Case 1) results in the least surface tensile stress on the fillet. The highest surface tensile stresses on the fillet occur for the ideal Instron collet loading (Case 4). Loading through the collet radius and shank (but not through the flat) results in an additional tensile stress (a bending or membrane stress) at the base of the fillet opposite the collet flat. This additional stress adds to the surface tensile stress due to the axial loading and the stress concentration, producing the highest surface tensile stresses of any of the four load cases. In addition to the above results, an unforeseen result was found during the course of this analysis. The centers of the radius of curvature for the collet and the fillet of the buttonhead specimen do not match. Due to the mismatch, an initial point contact is generated, as shown two-dimensionally in Figure 26.

In comparison to the ideal Instron collet loading, the hydrostatic pressure loading (Case 2) uniformly applied a smaller pressure over a broader area (including the region opposite the Instron collet flat). As a result, the tensile surface stress at the base of the fillet is less than that for the Instron collet case, even though loads are being applied directly to the fillet base.

Although the most likely tensile failure location for the ring loading case is at the base of the fillet, a different failure mode could be induced by the ring load. The highly localized compressive loads induce large compressive stresses in the specimen, which may lead to local bearing failure of the specimen. In addition, the ring loads induce a high shear stress in the specimen, which could result in a cleavage failure. Classical contact stress analysis

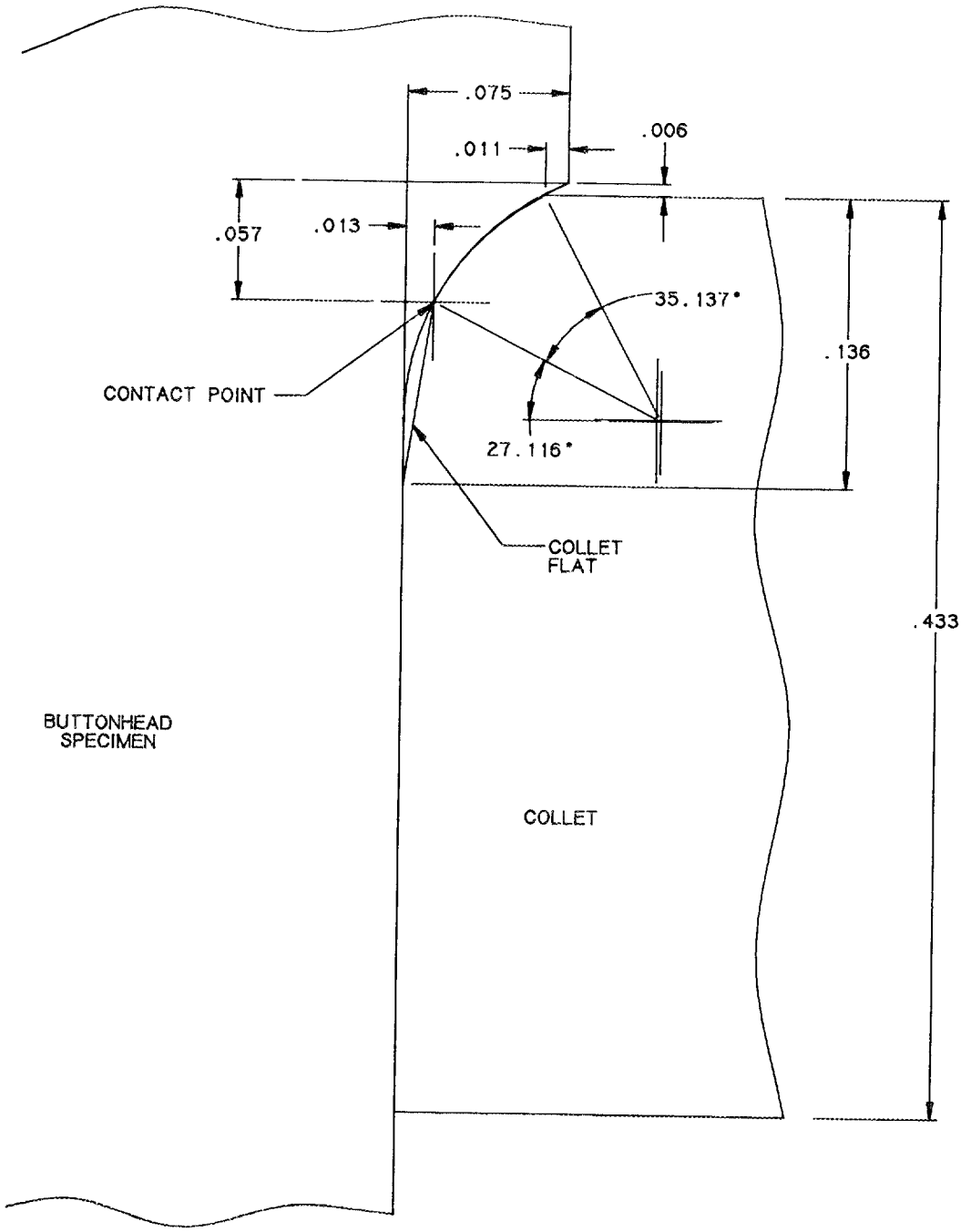

Figure 26. Buttonhead/collet interface.

also indicates that the maximum shear stress occurs below the surface, so that it is possible for failure to initiate internally (if the shear stress exceeds the material's shear strength).

Based on the results to date, it is recommended that the load applied to the buttonhead specimen fillet by the collet be as uniformly distributed as possible. Means of accomplishing this are (a) use ductile collet materials (such as the malleable copper collets now used for all tensile testing); (b) eliminate the Instron collet flat (i.e., continue the radius around tangent to the collet shank); and (c) match the collet and specimen radii as closely as possible (especially for hard, high-modulus collet materials, like steel). Further, it is recommended that a failure analysis of the failed buttonhead specimens be conducted to determine the location and mode of failure. Correlating these results with the finite element analysis results could ascertain the cause of the undesirable buttonhead failures and provide guidance in choosing potential solutions to the problem.

The modification of our tensile test methodology to using properly annealed copper collets has eliminated all buttonhead failures for the NT-154 material. In addition, approximately 80% of buttonhead failures for the Hexoloy SA have also been eliminated. The 20% failure rate for the Hexoloy SA was attributed to the poor machining at the root radius of the buttonhead.

References

1. Petrovic, J. J., et al., "Effects of Residual Stresses on Fracture from Controlled Surface Flaws," J. Am. Ceram. Soc. 59 (3-4), pp. 177-179, 1976.

2. Cook, R. F., et al., J. Mater. Res., 2(3), May/June 1987.

3. Widerhorn, S. M., Tighe, N. J., J. Am. Ceram. Soc., (66)12, pp. 884-889, December 1983.

4. Quinn, G., AMMRC TR 80-15, Army Materials and Mechanics Res. Ctr., (NTIS ADA-117463) April 1980.

5. Braisted, W. and Bouchard, M., Memorandum: Current Progress on Buttonhead Finite Element Analysis, UDRI, 14 July 89.

Low Heat Rejection Diesel Coupon Test

C. R. Brinkman, G. M. Begun, R. L. Graves, B. H. West, and K. C. Liu (Oak Ridge National Laboratory)

Objective/scope

The objective of this task is to expose various structural ceramics to conditions found in small diesel engines. Commercially available ceramics, as well as new candidate monolithic and whisker-toughened ceramics, will be fabricated into small MOR bars, nondestructively examined, and exposed to a variety of operating conditions within small diesel engines. Subsequent to exposure, the bars will be nondestructively and destructively examined and the results compared to an unexposed data base.

Technical progress

PSZ-TS (Lot 1). Work was concluded covering the exposure of this material to the combustion conditions of diesel engine No. 2 (i.e., a two-cylinder indirect-injection and air cooled unit) for 100 h. The engine burned a synfuel 50/50% blend of Philip's D-2 diesel fuel (reference) and an aromatic. The aromatic blend was a 53.5% (wt) Philip's Light Cycle Oil (LCO), and 46.5% (wt) Exxon Heavy Aromatic Naptha (HAN). Subsequent to exposure, the bars were subjected to Raman spectroscopy scans to determine any localized increases in apparent monoclinic content as was previously reported[1] for an engine which burned reference D-2 diesel fuel. A localized increase was found in monoclinic content some 12 to 15 mm from the clamped end of the bar as previously shown.[2]

Results from four MOR tests are compared in Table 1 with the MOR control specimens (as fabricated) and 14 MOR results from bars exposed to the control diesel fuel environment. The results are limited, but they show that the synfuel environment was somewhat less deleterious to the strength (i.e., specimens exposed to a synfuel combustion environment showed a 15% decrease while specimens exposed to the control or reference combustion environment showed a 32% decrease in strength) in comparison to the as-fabricated material.

PSZ-TS (Lot 2). Exposure of a total of eighteen bars of this material was completed in either engine No. 1 (single cylinder) or engine No. 2 (two cylinder). The objective of this effort was to determine if specific engine conditions (i.e., single versus two cylinder) made any significant difference in the post exposure strength of a material known to be sensitive to the environment.[1] The exposure time was again 100 h. Results of subsequent room temperature four-point bend tests are compared with control specimens in Table 1 and plotted as Weibull curves in Fig. 1. Results given in Table 1 indicate a 34 and 29 percent reduction in strength after exposure in engines No. 1 and 2, respectively, in comparison to as-fabricated or control specimens.

Figures 2 and 3 show Raman spectroscopy profiles of apparent monoclinic content as a function of distance from the fixed end of bars both before and after exposure for 100 h in engine No. 2. Note the increased monoclinic content some 10 to 18 mm from the fixed end of the bar subsequent to exposure.

Figure 4 shows similar Raman spectroscopy scans prior to engine exposure for bars No. 218 and 219. These bars were scheduled for insertion in engine No. 1. Exposure of specimens 218 and 219 was begun but halted after 62 h of exposure due to catastrophic failure of the specimens in the engine. This was most unfortunate as results from these tests were expected to give definitive evidence of any engine-to-engine variations in the post exposure behavior of this material. It was not clear what caused premature failure of these specimens. All installation procedures were identical to previous procedures, with no noted anomalies. Engine repairs are underway and expected completion is mid-October.

Figure 5 compares the fracture locations of bars exposed in engines No. 1 and 2. Note that fracture locations of bars inserted in engine No. 1 tend to be random, but in contrast, nine out of twelve (75%) of the bars exposed in engine No. 2 failed approximately 15 to 20 mm from the fixed end of the bar (i.e., near attachment locations within the engine). These differences suggest that somewhat different environments existed in the two engines. Additional temperature measurements are planned to help define these differences. Figure 6 shows locations of failure of specimens 218 and 219 that failed during exposure in engine No. 1.

Silicon Nitride (WESGO SNW-100). A total of 32 bars have now been exposed for 100 h in the reference diesel fuel combustion environment. These bars have all been subject to four-point bend rupture at room temperature, and results are compared in Table 1 with unexposed or control fracture data. The comparison given in Table 1 shows only a slight (1%) increase in mean fracture strength in comparison to the unexposed material, which is not significant and probably within scatter of the data. Figure 7 is a Weibull plot comparison of the exposed and unexposed rupture strengths. While Figure 8 is a photograph of the post exposed specimens, note the lack in any preferential failure location.

References

1. C. R. Brinkman et al., "Influence of Diesel Engine Combustion on the Rupture Strength of Partially Stabilized Zirconia," *Amer. Ceram. Soc. Bull.*, 68(8) 1440-1445, (1989).

2. C. R. Brinkman et al., Low Heat Rejection Diesel Coupon Test, *Ceramic Technology for Advanced Heat Engines Project Semiannual Progress Report for October 1988 through March 1989*, ORNL/TM-11239, August 1989, pp. 469-478.

Table 1. Results of four-point bend tests[a] conducted on MOR bars of several different materials

Number of observations	Material condition	Weibull modulus		y-intercept		Average strength (MPa)	Standard deviation (MPa)	Reduction in average[b] strength (%)
		Linear regression	Maximum likelihood	Linear regression	Maximum likelihood			
				PSZ-TS (Lot 1)				
53	As-fabricated	31.7	48.6	-202.7	-310.2	587.3	20.3	0
4	Engine-exposed for 100 h[c]	10.4	15.3	-65.3	-95.5	501.0	52.6	15
14	Engine-exposed for 100 h[d]	3.5	4.2	-21.6	-25.4	401.8	120.5	32
				PSZ-MS				
40	As-fabricated	29.2	29.7	-191.1	-194.5	682.9	28.6	0
4	Engine-exposed for 100 h[c]	85.4	100.0	-550.8	-644.4	626.7	8.2	8
20	Engine-exposed for 100 h[d]	19.8	22.0	-124.7	-141.9	625.0	38.7	9
				PSZ-TS (Lot 2)				
20	As-fabricated	24.7	25.6	-159.8	-165.6	629.6	30.9	0
6	Engine #1 exposed for 100 h[d]	4.9	5.2	-30.0	-31.8	413.9	91.4	34
12	Engine #2 exposed for 100 h[d]	5.5	6.7	-34.0	-41.0	444.3	88.3	29
18	Engine #1 and #2 combined exposed for 100 h[d]	5.6	6.0	-34.7	-36.8	434.2	87.9	31

Table 1. (continued)

Number of observations	Material condition	Weibull modulus		y-intercept		Average strength (MPa)	Standard deviation (MPa)	Reduction in average[b] strength (%)
		Linear regression	Maximum likelihood	Linear regression	Maximum likelihood			
				GTE WESGO SNW-1000[e]				
40	As-fabricated	10.8	11.2	-67.8	-70.5	506.5	56.3	0
32	Engine-exposed for 100 h[d]	9.9	14.2	-62.3	-89.3	512.7	54.6	1[f]

[a]Tests were conducted with a crosshead speed of 8.47×10^{-3} mm/s or a strain rate of 1.1×10^{-4} s^{-1}.

[b]Reduction in strength in comparison to as-fabricated material.

[c]Fuel was a 50/50 percent blend of Phillip's D-2 Diesel Fuel (reference fuel) and an aromatic blend.

[d]Fuel was control diesel (reference fuel).

[e]Material from Lot Number 174-MA-1607 and re-heat-treated to sintering temperature.

[f]Increase

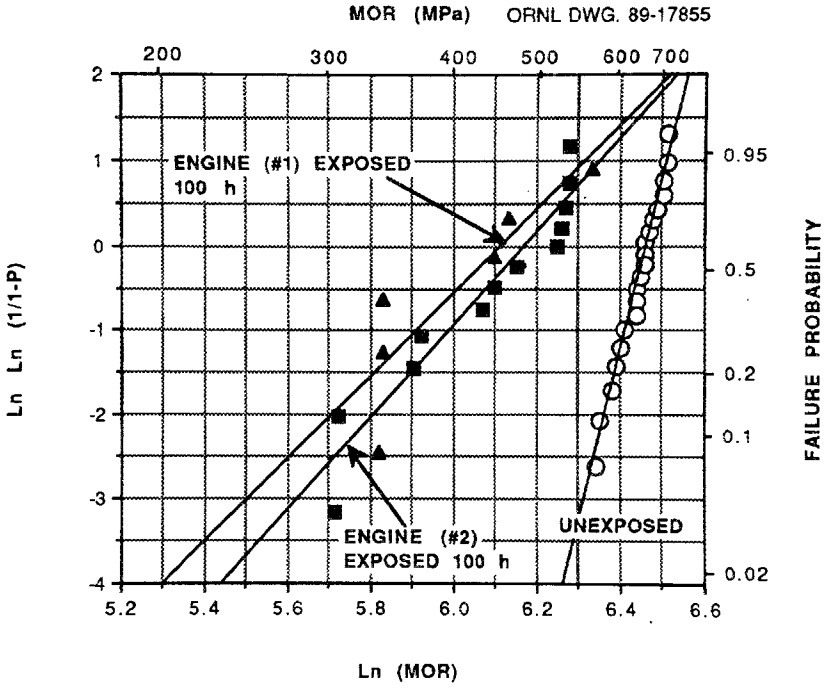

Fig. 1. Weibull plot comparing fracture strength of Nilcra, PSZ-TS grade (Lot 2), previously exposed for 100 h in a single cylinder (#1 and two cylinder (#2) diesel engine in a reference diesel fuel combustion environment with similar results from unexposed material.

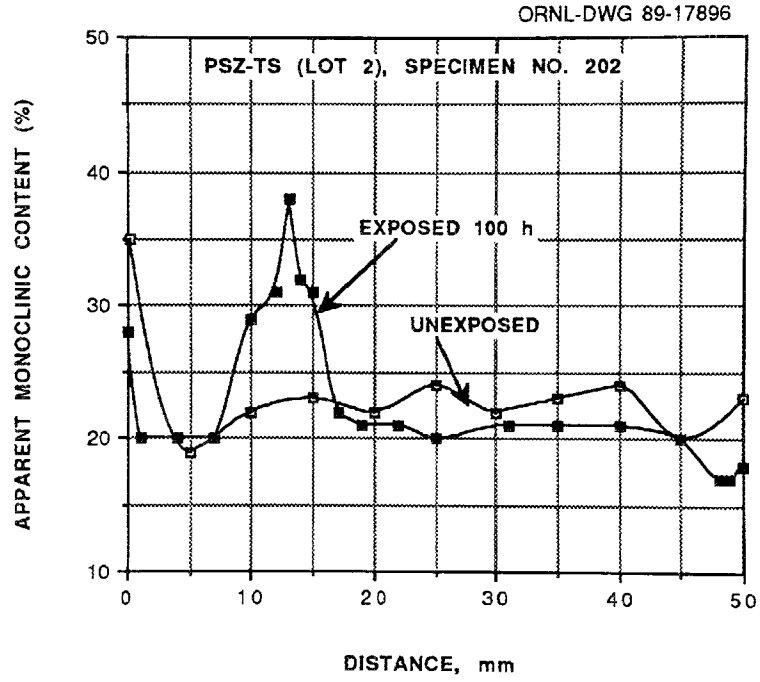

Fig. 2. Raman spectroscopy profiles before and after exposure showing apparent monoclinic content as a function of distance from the fixed end of a bar inserted in engine No. 2 for the time indicated.

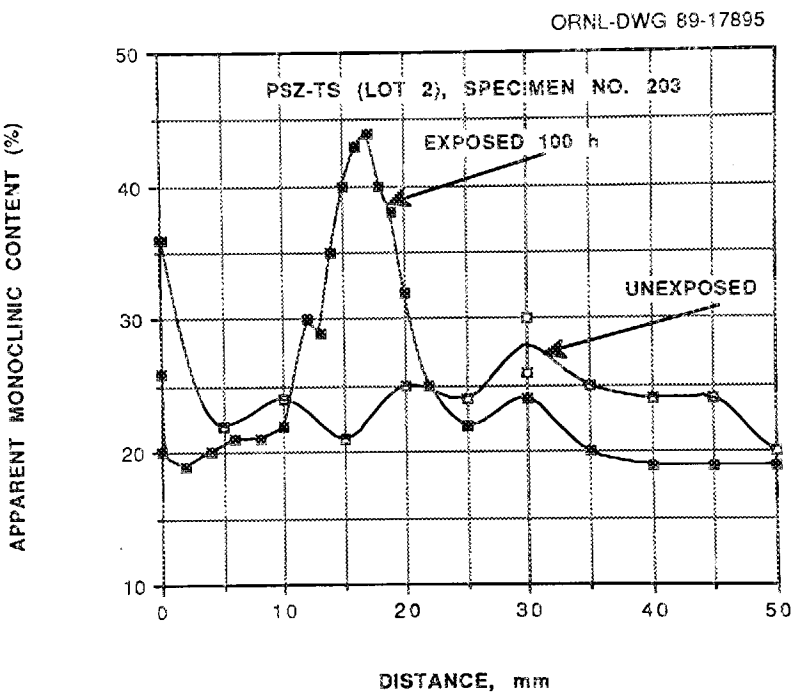

Fig. 3. Raman spectroscopy profiles before and after exposure showing apparent monoclinic content as a function of distance from the fixed end of a bar inserted in engine No. 2 for the time indicated.

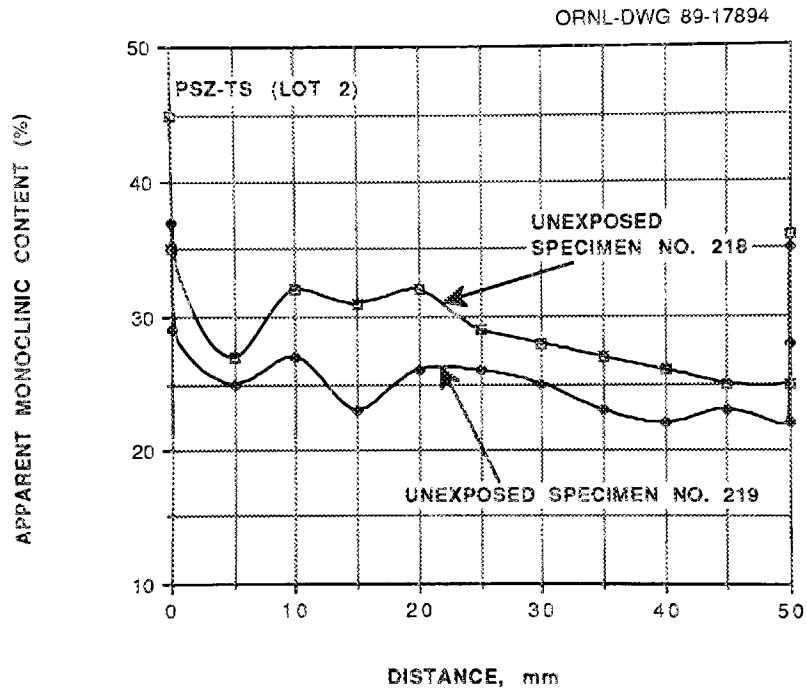

Fig. 4. Raman spectroscopy profiles before engine exposure showing apparent monoclinic content as a function of distance along bar. Bars were subsequently inserted in engine No. 1, but failed during engine exposure.

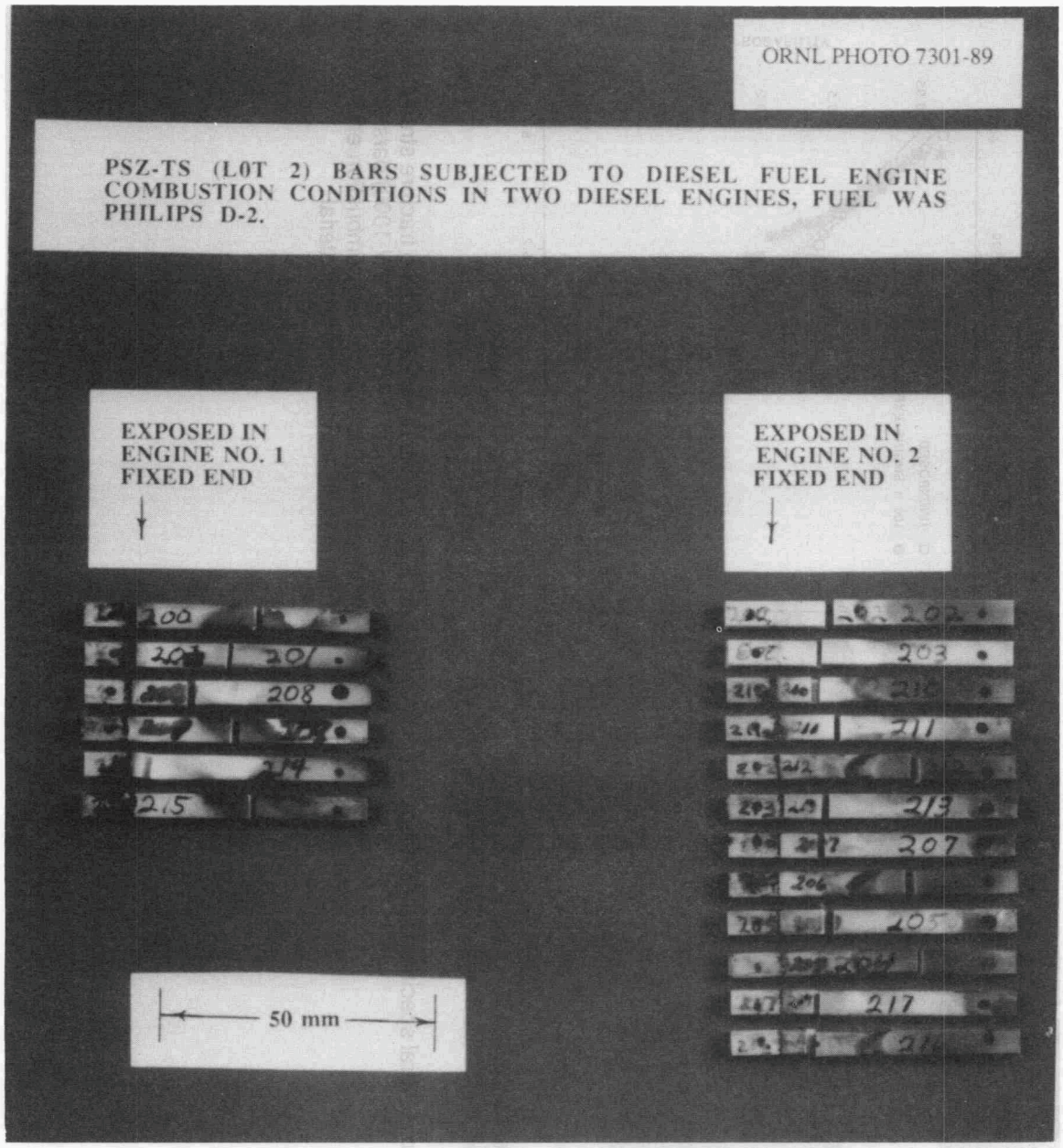

Fig. 5. Comparison of the fracture locations of PSZ-TS bars exposed in two engines. Note preferential four-point bend fracture locations of specimens exposed in enging No. 2.

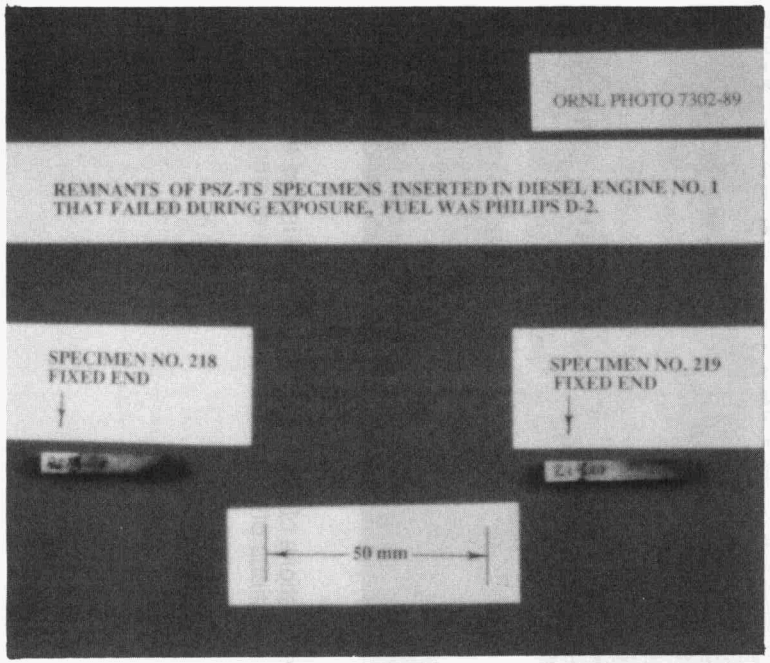

Fig. 6. Photographs of several specimens that failed during exposure.

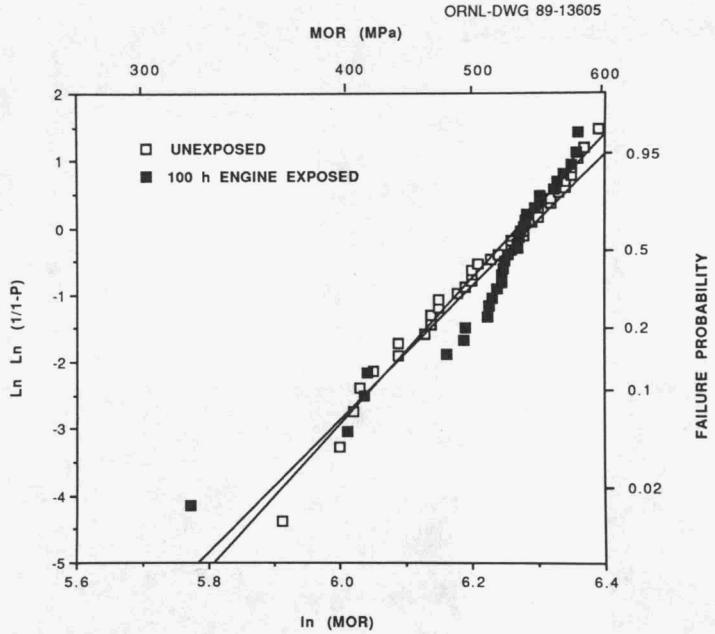

Fig. 7. Weibull plot comparing fracture strengths of thirty-two silicon nitride (WESGO SNW-1000) bars exposed for 100 h in a reference diesel fuel combustion environment with similar results from unexposed material.

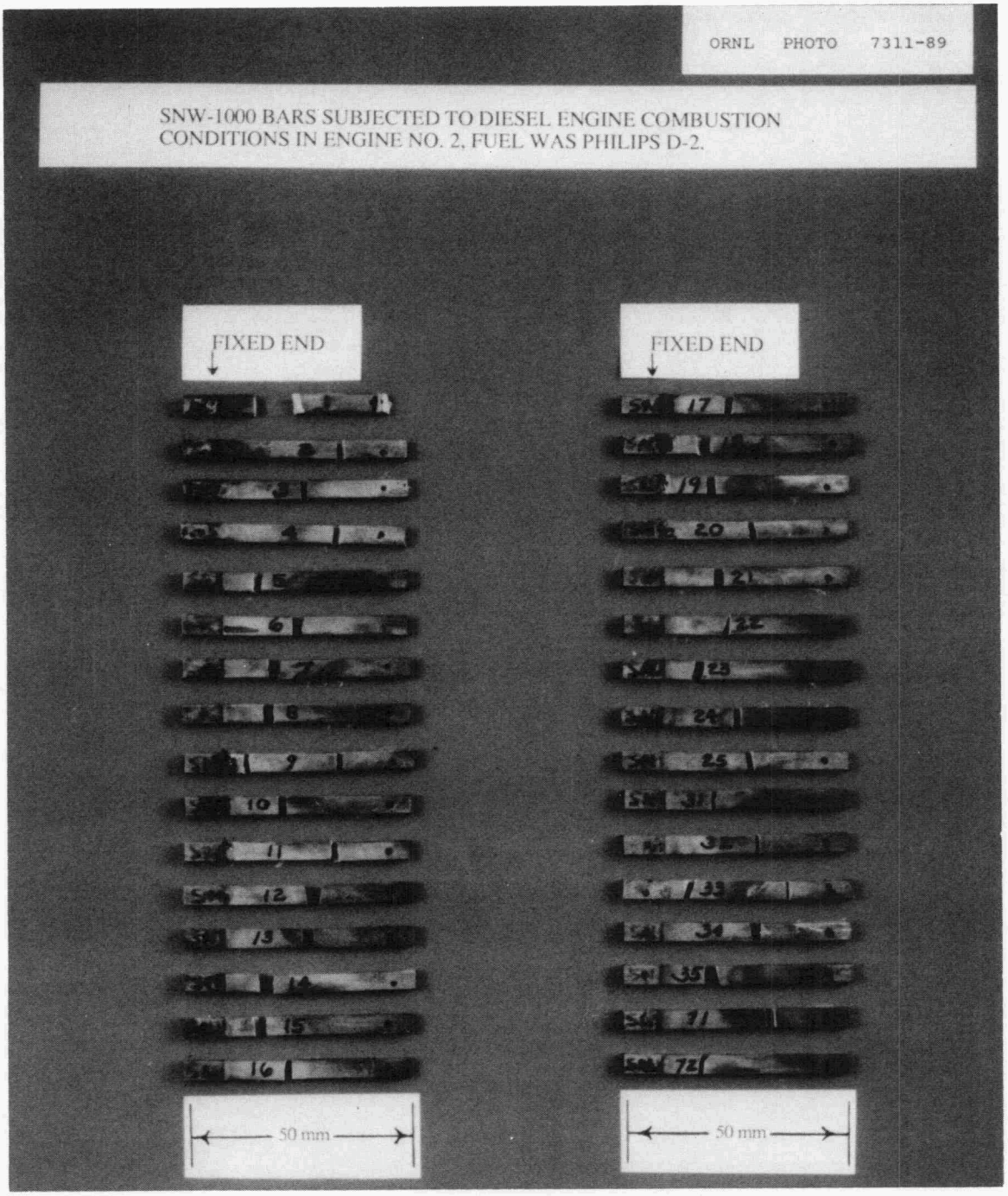

Fig. 8. Showing failure locations of post-exposed specimens of SNW-1000.

3.4 FRACTURE MECHANICS

Testing and Evaluation of Advanced Ceramics at High Temperature in Uniaxial Tension

J. Sankar, A. D. Kelkar, V. S. Avva, and Jun Gao (Department of Mechanical Engineering, North Carolina A & T State University, Greensboro, North Carolina 27411)

Objective/Scope

The purpose of this effort will be to test and evaluate advanced ceramic materials at temperatures up to 1500 ^{o}C in uniaxial tension. Testing may include fast fracture strengths, stepped static fatigue strength along with analysis of fracture surfaces by scanning electron microscope. This effort will comprise of the following tasks:

Task 1. Specifications for Testing Machine and controls + (procurement)
Task 2. Identification of Test Material (s) + (procurement of specimens)
Task 3. Identification of Test specimen configuration
Task 4. Specifications for Testing grips and Extensometer + (Procurement)
Task 5. Specifications for Testing Furnace (Procurement) and controls
Task 6. Development of Test Plan
Task 7. High Temperature Tensile Testing
Task 8. Reporting (Periodic)
Task 9. Final Report

It is anticipated that this program will help in understanding the behavior of Ceramic materials at very high temperatures in uniaxial tension.

Technical Progress

During the reporting period, efforts were undertaken to study the accuracy of the laser extensometer measurements from room temperature to very high temperatures. This was done by comparing the gap measured by the laser extensometer against the same gap as measured by a standard micrometer which was located outside the furnace. A pair of alumina rods were used, one of which was held in a standard micrometer. The gap between the tips of the two rods could be increased or decreased by turning the micrometer wheel. Calibration of the laser system was done at room temperature, 500, 800, 1000,1100,1200,1300, and 1400 deg.C.

Figure 1 shows the set up used to verify the accuracy of the laser extensometer. Figure 2 shows the close up view of the set up. Figures 3 through 7 show the micrometer and zygo readings taken simultaneously at the temperatures of 25, 1100, 1200, 1300 and 1400 deg.C. The time between each reading was approximately 2 to 3 minutes. The readings were taken after about 45 minutes of stabilization time at the test temperature. This helped to accommodate the thermal expansion of the

alumina rods, if any, at these temperatures. It was observed that the gaps measured simultaneously by the laser system and the standard micrometer matched up to temperature of 1100°C (Figure 4). Tests carried out at 1200°and above indicate (Figures 5-7) that there is a slight variation between the Zygo and micrometer readings. It is thought that above 1200°C, the air density fluctuations that develop in the path of the laser beam during the tests probably attributed to this variation in Zygo readings.

During this reporting period, tests were also carried out to evaluate the stability of laser system over a long period of time at high temperatures since our task this year is to conduct high temperature creep tests on Si_3N_4. It is thought that this kind of evaluation is essential to see the effectiveness of laser system at very high temperature over a long period of time. The results obtained for 1200°C and 1300°C are given in Figure 8. It can be observed that gap measured by the laser extensometer increased with time. After a period of 3-4 hours, the variation becomes more stable. Tests were also carried out to evaluate the effect of having a steady flow of air near the testing furnace on the Zygo laser extensometer readings at elevated temperature (1200°C and 1300°C). A fan was placed near the furnace to create the steady flow of air. The results are given in Figure 9. It can be observed that in case of the air flow, the stabilization time is shorter and the deviation of the readings are much less.

An inhouse testing program for the creep test was also developed. The verification of the program, which can be run on the Micro-PDP/11 computer attached to the MTS 880 testing machine has been completed.

Status of Milestones

Tasks 1-7 are complete.

Communications/Visitors/Travel

Dr. Ken Liu of ORNL visited A&T to help set up the laser extensometry calibration. Progress of the present research were also discussed during this time.

Problems Encountered

None

Publications & Presentations

None

Research sponsored by the U. S. Department of Energy under prime contract DE-AC05-84OR21400 with the Martin Marietta Energy Systems, Inc., subcontract 19X-89867C.

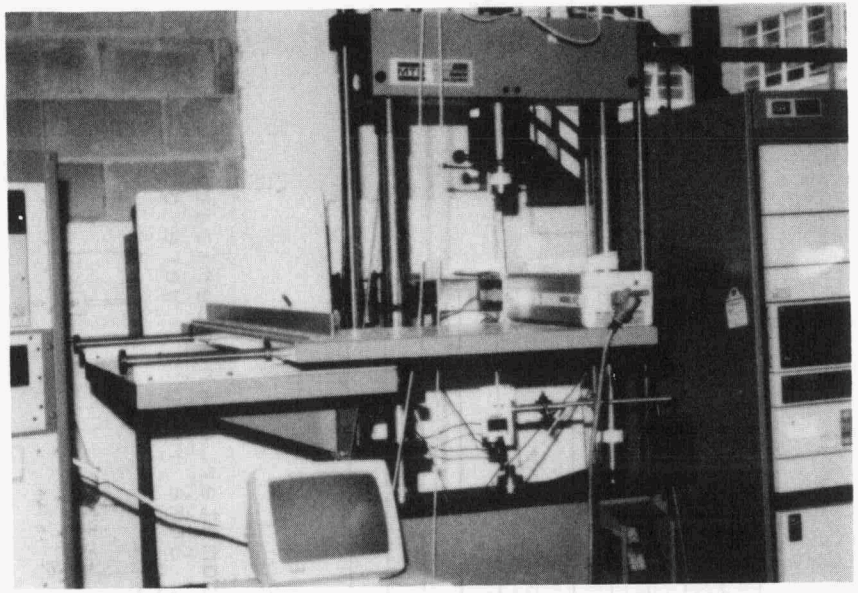

Figure 1. Set up for verifying the accuracy of the laser Ectensometer

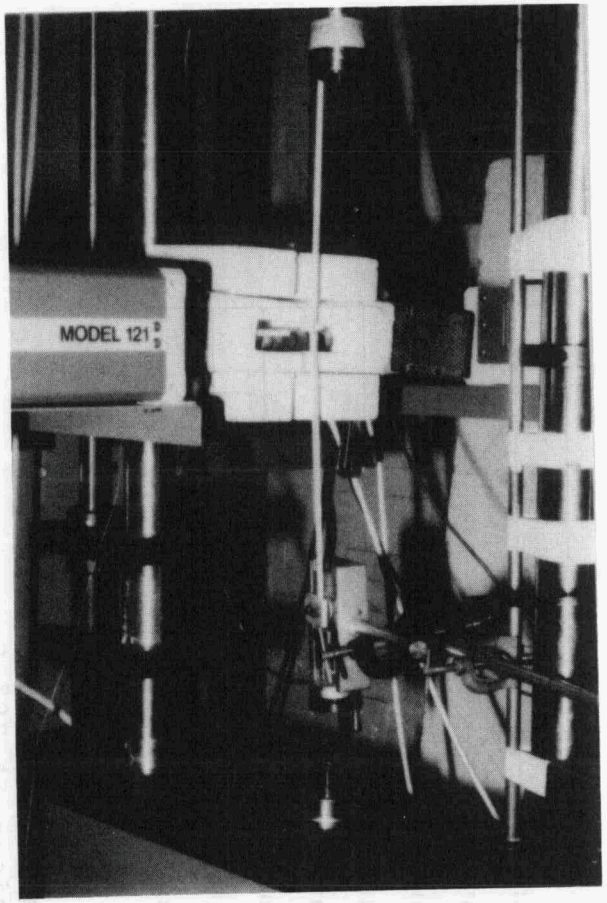

Figure 2. Close up view of the set up

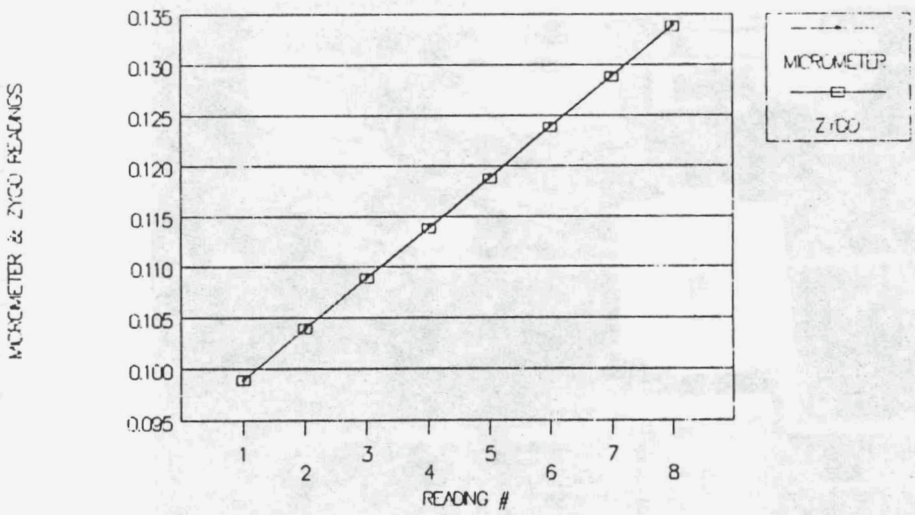

Figure 3. Laser Extensometer characterization comparison at 25° C

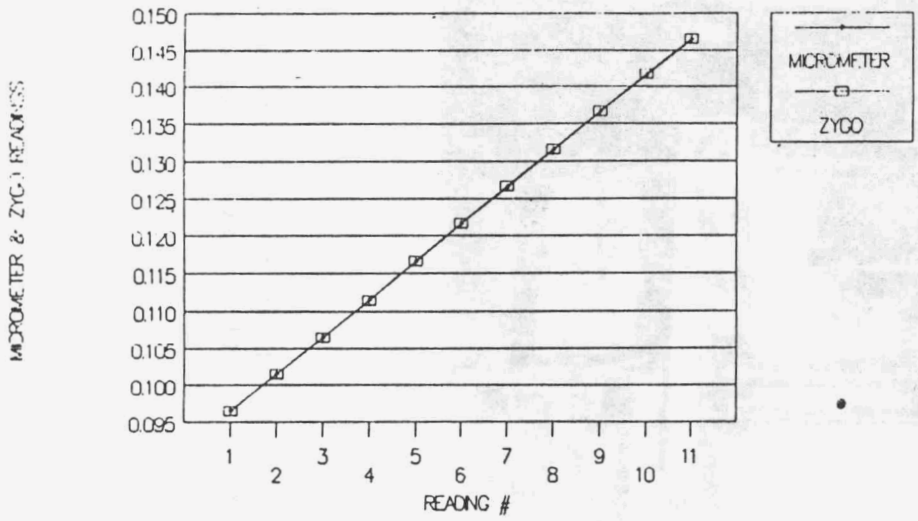

Figure 4. Laser Extensometer characterization, comparison at 1100° C. Same results were obtained at 500,800 and 1000° C

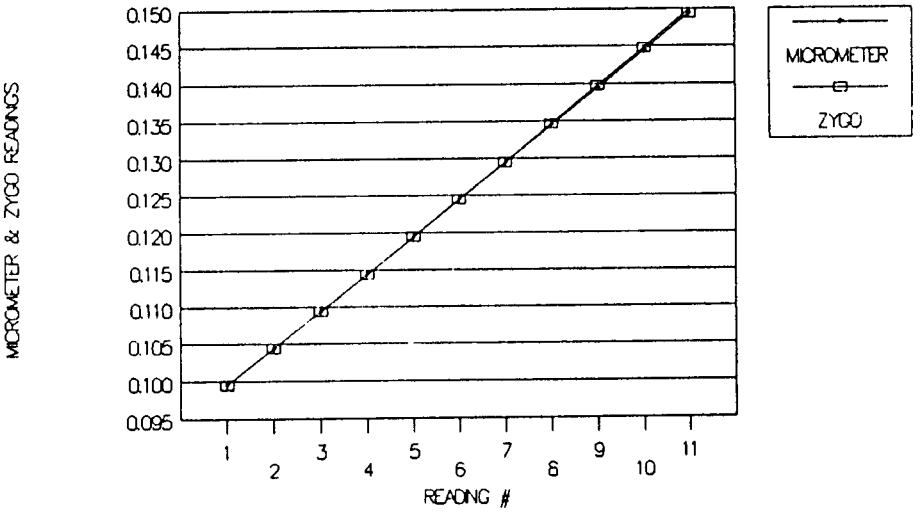

Figure 5.Laser Extensometer characterization comprison at 1200° C

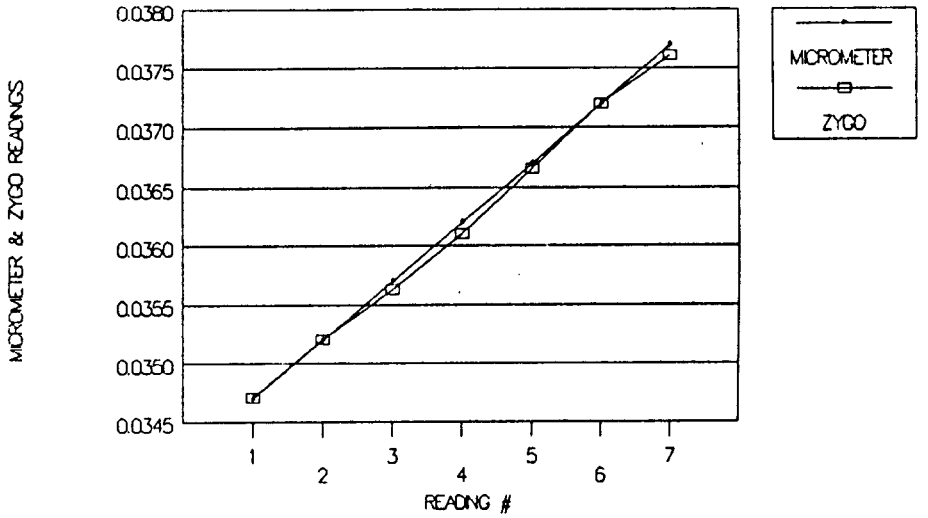

Figure 6. Laser Extensometer characterization comparison at 1300° C

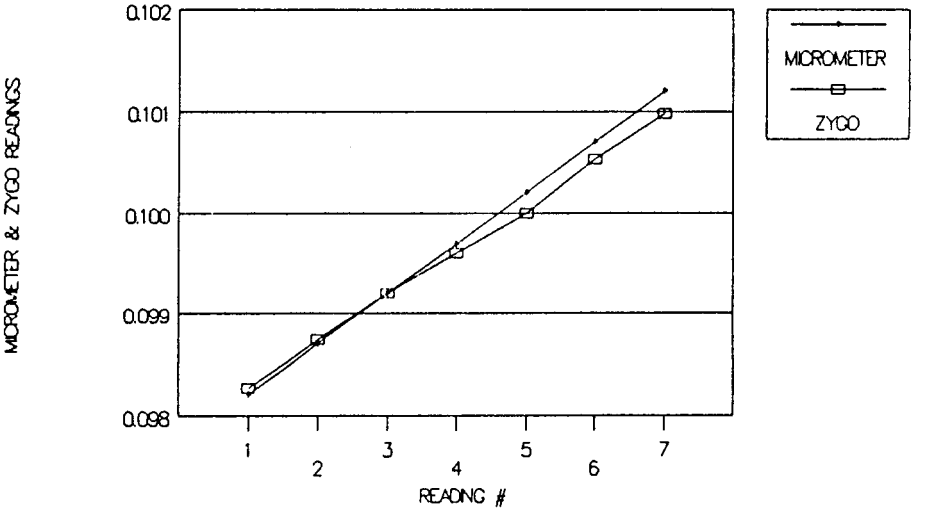

Figure 7. Laser Extensometer characterization comparison at 1400° C

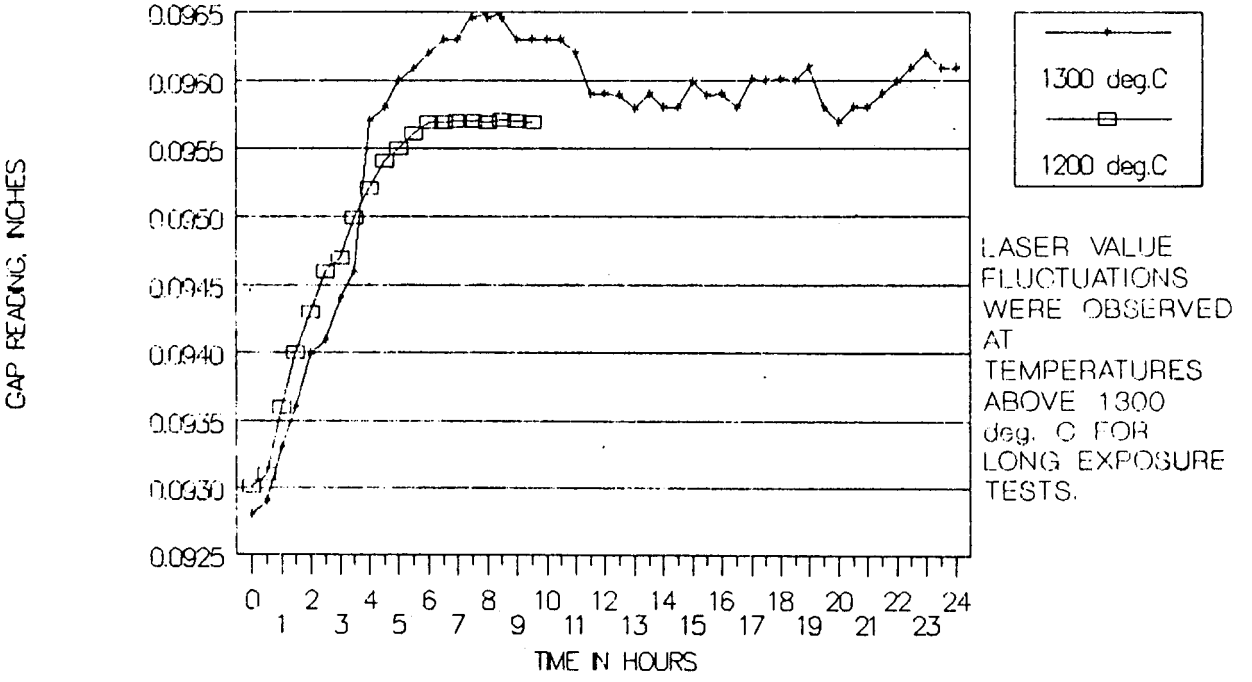

Figure 8. Laser Extensometer characterization, Gap reading vs. Time

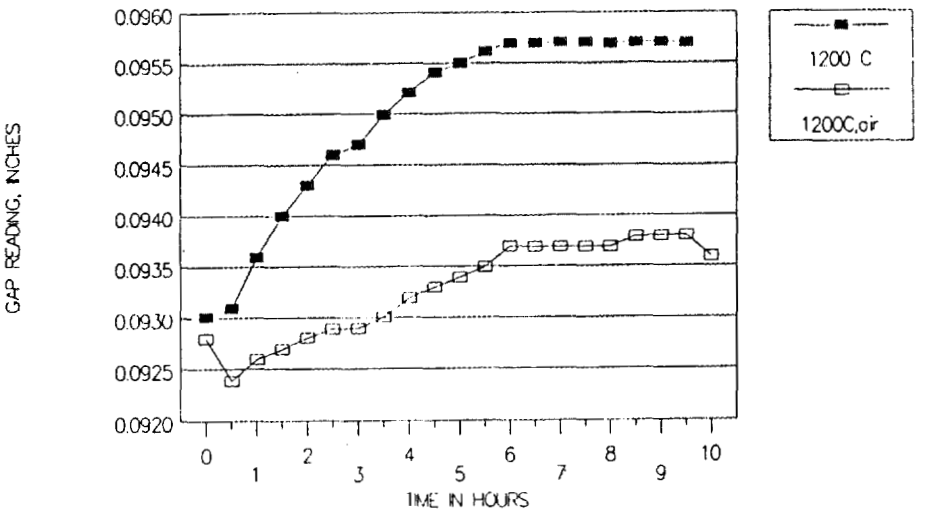

Figure 9. Laser Extensometer characterization, comparison with and without air flow. Same result was obtained at 1300 C

Standard Tensile Test Development

S. M. Wiederhorn, T.-J. Chuang, Weijun Liu and D. E. Roberts
(The National Institute of Standards and Technology)

Objective/Scope:

This project is concerned with the development of test equipment and test procedures for measuring the tensile strength and creep resistance of ceramic materials to tensile stresses at elevated temperatures. Inexpensive techniques of measuring the creep and strength of ceramics at elevated temperatures are being developed and will be used to characterize the mechanical behavior of structural ceramics. The test methods will use self aligning fixtures, and simple grinding techniques for specimen preparation. Creep data obtained with tensile test techniques will be compared with data obtained using flexure and compressive creep techniques. The ultimate goal of the project is to assist in the development of a reliable data base and a methodology that can be used for structural design of heat engines for vehicular applications.

Technical highlights

During the past six months, work continued to characterize the creep and creep rupture behavior of hot-pressed silicon nitride, reinforced with SiC whiskers was studied as a function of applied stress and temperature. This work is being conducted in collaboration with Dr. J.G. Baldoni of the GTE Laboratories in Waltham, MA. The objective of this work is to evaluate the effect of silicon carbide whisker re-enforcement on the creep behavior and the lifetime of these composite materials.

Experimental Technique - The silicon nitride matrix was similar to the AY6 grade sold by GTE. The composite contained approximately 30 volume percent silicon carbide whiskers which were used for reinforcement. Dog-bone specimens, figure 1, developed as part of our tensile creep program were used in this study. The hot pressing direction of the billets used to make the test bars was perpendicular to the tensile axis. To assure failure of the test specimens within the gauge section of the tensile specimens, the gauge section was defined by surface grinding the central portion of the specimen with a 38 mm diameter grinding wheel so as to reduce the total thickness of the gauge section to ≈2mm. This reduction of gauge section represents a minor modification of the specimen geometry discussed in previous reports, figure 1. The width and length of the gauge sections were approximately 2.5mm and 10mm respectively.

Creep tests were conducted using the tensile equipment developed in an earlier phase of the project. The gauge length of the test specimen was monitored by placing small α-SiC flags on the central portion of the test specimen. The position of the flags were monitored as a function of time with a laser extensometer, which was capable of an accuracy of better than ±1μm in the measurement of distance between the two flags. This level of accuracy resulted in an accuracy of ±2μm in the displacement measurements during the evaluation of creep curves for each specimen. Details of the experimental apparatus were published during the current period (D.F. Carroll, S.M. Wiederhorn and D.E. Roberts, "A Technique for Tensile Creep Testing of Ceramics," J. Am. Ceram. Soc. 72[9], 1610-1614 (1989)).

In these studies, the test temperature ranged from 1100°C to 1250°. Tests were conducted in air, with a short ≈24 hour anneal to assure thermal equilibrium within the test furnace prior to application of the stress. Within a 500 hour test period, specimens were permitted

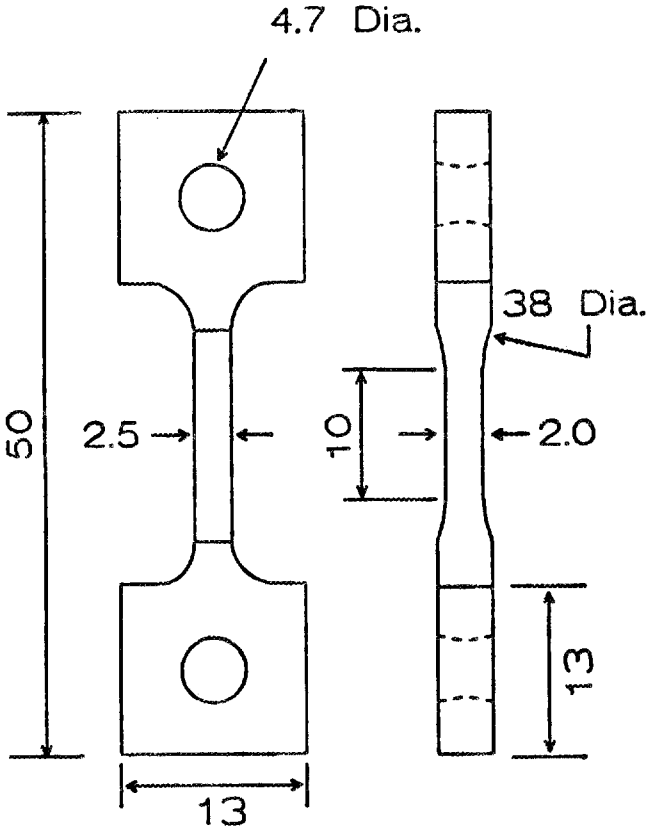

1. The major and minor faces of the flat dogbone-shaped tensile specimen. All dimensions are in millimeters. This figure is not drawn to scale.

to creep to failure so that both the creep and creep rupture behavior as a function of applied stress and temperature could be determined. For test periods exceeding 500 hr runs were terminated and specimens were retested under new experimental conditions. Transient effects were observed for periods exceeding ≈500 hours; hence, some tests were conducted on specimens that were pre-annealed in air for ≈500 hours.

After testing, specimens were examined by optical and transmission electron microscopy to clarify the modes of deformation and fracture of this material. The results of this microstructural analysis is presented in a companion to this report [3.1, Microstructural Analysis of Structural Ceramics (NIST)]] and will not be discussed in detail here.

Results and Discussion - During the past 6 months studies were conducted on both whisker reinforced and whisker free hot-pressed silicon nitride, in both the annealed and unannealed state. Tensile creep results have also been compared with results obtained on material subjected to compressive creep deformation. Characteristic of the deformation of this material is transient creep behavior, especially on specimens that sustained creep loads for times approaching 1000 hr. This behavior is observed on both whisker reinforced and whisker free material. An extreme example of this behavior is shown in figure 2 for a whisker free material that was subjected to a tensile load for ≈1000 hr. As can be seen, there is no steady state region on this curve. For shorter test periods, ≈100 hr., "apparent" steady state creep is achieved before failure, however, microstructural examination of the specimens by transmission electron microscopy suggests that this "steady state creep" is merely a balance between work-hardening, and the cavitation that eventually leads to component failure.

Whisker reinforcement in this material appears to have little effect on the creep resistance of the material. Thus, in figure 3, whisker reinforced materials creep more readily than materials lacking reinforcement. Results for specimens tested in the unannealed state, indicate that the creep rate for both sets of material are almost identical for high creep rates. For low creep rate tests, tests that last ≈1000 hr., annealing occurs in both types of materials. In this case, the creep resistance of the whisker free material is approximately ten times that of the whisker reinforced material. Similar results are obtained on materials that have been annealed for extended periods before testing; the whisker free material exhibits a higher resistance to creep.

Investigations of these materials by transmission electron microscopy suggest that many of the observations discussed above are due in part to phase transformations that occur during high temperature exposure. In the as-received state, the whisker reinforced material contains glass at the SiC whisker interface. This glass is introduced into the composite as a consequence of an amorphous layer on the silicon carbide whiskers before processing the composite. Glass is also present at Si_3N_4 interfaces. In the unannealed specimens, this glass promotes deformation, by enhancing grain boundary sliding and solution re-precipitation at contact sites between grains. Glass at the interfaces of the silicon carbide whiskers appear to nullify the beneficial effect of the whiskers on the creep rate, so that creep in the as-received composite is no better than that of the whisker free material. GTE is currently changing the composition of the composite to reduce or modify the glass at the whisker interfaces, which hopefully will improve the creep resistance of this material.

Annealing improves the creep resistance of both the whisker free and the whisker reinforced materials, due, in part, to devitrification of the glass within the materials. Oxygen penetration into the material during annealing can also modify the composition of the composite and hence the creep behavior. Crystalline materials tend to be more

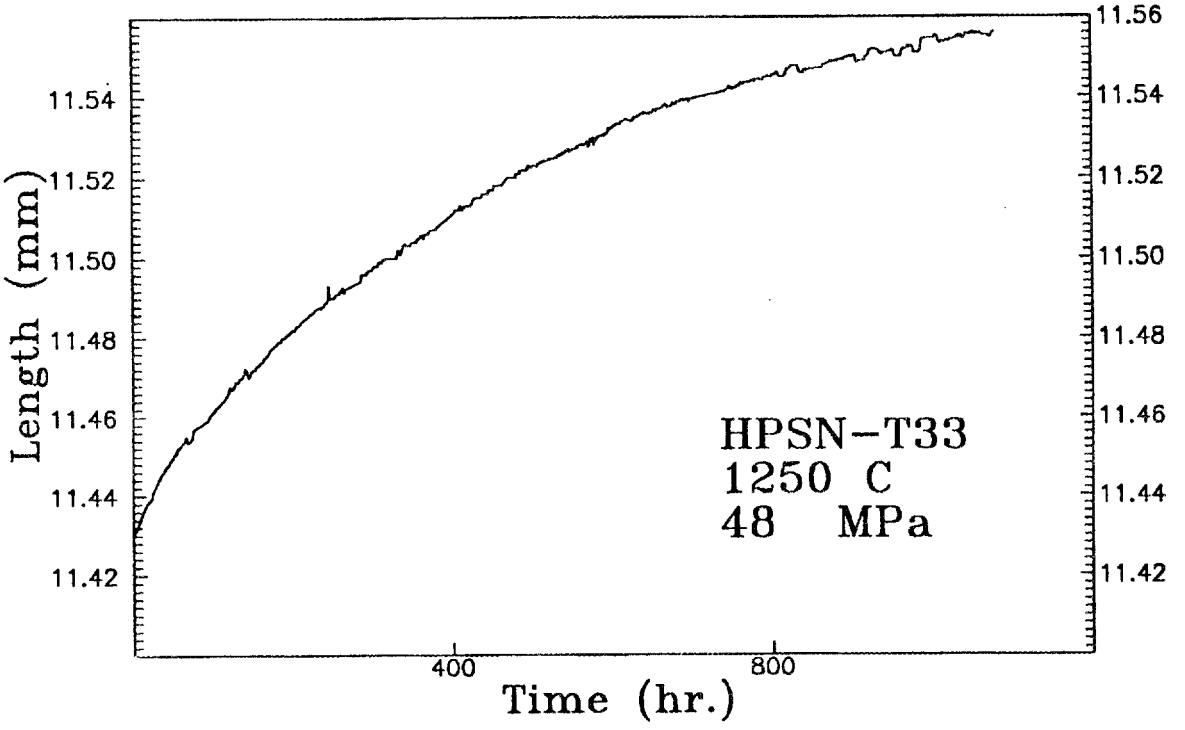

2. Whisker free specimen tested in the as-received state. Extended deformation gives no indication of a steady state region of deformation.

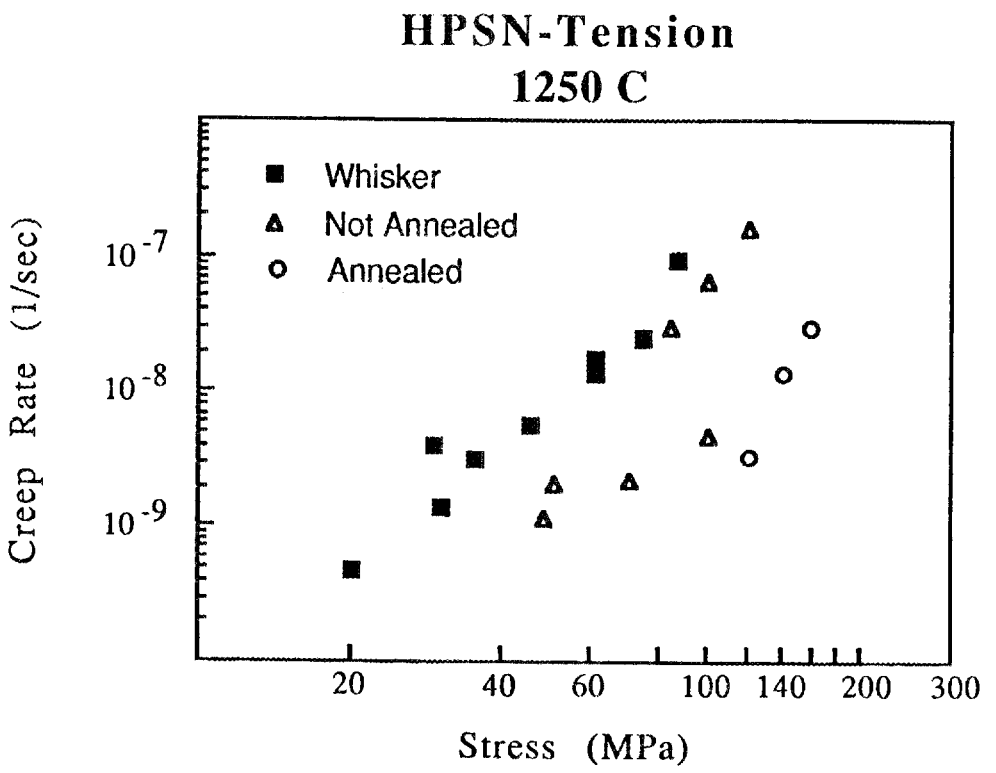

3. Effect of whisker reinforcement on the creep rate of hot-pressed silicon nitride. Annealing improves the creep resistance of the whisker-free material by a factor of ≈10. The open symbols, circles and triangles, are data collected on whisker-free material.

resistant to creep than amorphous materials of the same composition. Therefore, devitrification is used as a method of improving the creep resistance of nitride ceramics. Enhancement of creep resistance is more apparent for the whisker free material, where a factor of 10 reduction in the creep rate is observed for short failure times. Improvement in the creep resistance of the whisker reinforced material occurs primarily at low creep rates, where cavitation does not control the creep behavior. At high creep rates, cavity formation and crack growth dominate the behavior of both the annealed and unannealed, whisker-reinforced specimens, so that devitrification due to annealing had no effect on the creep rate.

A comparison of the creep behavior of whisker reinforced materials in tension and compression indicates a much greater resistance to creep in compression. To achieve the same creep rate, the applied stress must be twice as high in compression as in tension, figure 4. Furthermore, the stress exponent of the creep rate is less in compression, ≈2.5, than in tension, ≈4. This difference in behavior indicates a difference in creep mechanism in the two modes of loading. Based on microstructural analyses of tensile specimens, cavitation cracks form during the creep of this material in tension. Cracks are more prevalent at the higher creep rate. Since crack formation enhances the rate of deformation, the fact that more cracks are formed at the higher creep rates suggests that the higher stress exponent in tension is a consequence of the cavitation process. In compression, the slope and position of the creep curve is almost identical to data obtained by Davis and his colleagues [3] on this material at North Carolina State University. Also made by GTE, their material was identical to our own. Microstructural analyses of the deformed material gave no evidence of significant cavitation or crack formation [3], suggesting that the deformation process did not depend on cavity formation. Based on their observations, Davis and his colleagues identify grain boundary sliding as the primary mechanism of deformation for this material. However, additional experimentation is needed to establish modes of accommodation during compressive creep.

Differences in creep behavior in tension and compression are not only of interest scientifically, but have important practical implications. Normally materials at high temperature are loaded neither in states of pure tension nor pure compression, in which case both states of stress contribute to the rate of deformation. When rates of creep in tension and compression differ substantially, then time dependent shifts in the stress distribution occur, shifts that can lead to a factor of two error in the estimated maximum stress within a component. To assure the reliability of engine components, these creep induced modifications in the stress distribution must be ascertained: hence the need for creep data in both tension and compression.

References:

1. S.M. Wiederhorn, T.-J. Chuang, D.E. Roberts and L. Chuck, "Damage Enhanced Creep in a Siliconized Silicon Carbide: Phenomenology," J. Am. Ceram. Soc. 71, 602-608 (1988).

2. D.F. Carroll and S.M. Wiederhorn, "A technique for Tensile Creep Testing of Ceramics," J. Am. Ceram. Soc. 72[9], 1610-1614 (1989).

3. D.A. Koester, R.D. Nixon, S. Chevacharoenkul and R.F. Davis, Proc. Intern. Conf. on Whisker- and Fiber- Toughened Ceramics, June 7-9, 1988, Oak Ridge National Laboratory, Oak Ridge, TN, in press.

Status of Milestones

All milestones are on schedule.

Publications

1. D.F. Carroll and S.M. Wiederhorn, "A Technique for Tensile Creep Testing of Ceramics," J. Am. Ceram. Soc. 72[9], 1610-1614 (1989).

2. Ching-Fong Chen and Tze-jer Chuang, "Power-Law Creep of SiAlON Ceramics," J. Am. Ceram. Soc., Submitted.

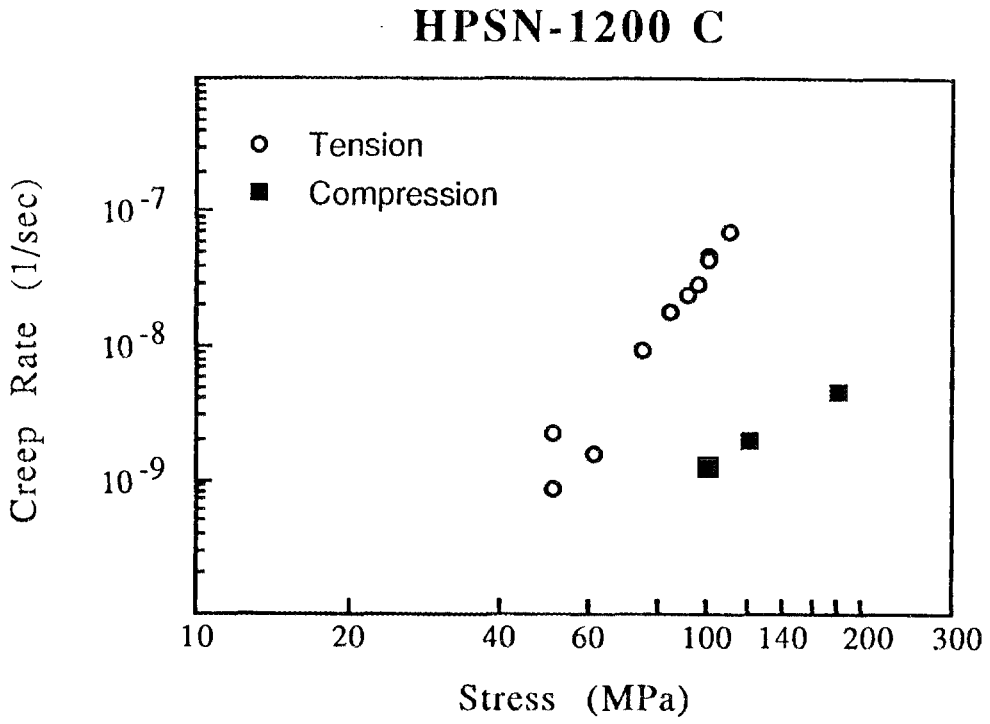

4. Effect of the sign of the applied stress on the creep rate. For a given creep rate, approximately twice as much stress is needed in compression as in tension. This same sort of behavior has been observed on other ceramic materials.

Fracture Toughness of Thin Coatings

J. J. Wert and B. N. Lucas (Vanderbilt University)

Objective/Scope

The goal of this program is to develop the scientific base and technology required to obtain the fracture toughness of thin coatings using displacement measurements obtained from microindentation techniques.

Technical Highlights

The previous six-month period held many unexpected delays for this project, the first coming in the early stages of the reporting period with the departure of the original research assistant. However during this period of transition, most work was at a virtual standstill due to the lengthy delivery time for the machined parts necessary for the assembly of the new equipment. It is estimated that these problems encountered with hardware acquisition set the project back approximately 4 months.

The preliminary tests of the new hardware were conducted during the first week of August with excellent results. Most of the tests conducted during this time were geared at testing the limits of resolution of the hardware and the reproducibility of the data obtained with the new system. After final calibration of the electronics and some hardware redesign, it was possible to acquire meaningful data at loads from 10 g to 1 kg. The ability to obtain data at such low loads was very well received since it allowed overlap with data obtained from the Nanoindenter.

During the last month, strides were made toward characterizing the response of (100) silicon to indentation testing. In past tests conducted with the Nanoindenter, a characteristic "pop" had appeared during the unloading portion of the silicon load-displacement curve. However, with the limited loading capabilities of the instrument, no information had been gathered at loads above 10 grams. In recent tests with the new high load indentation apparatus at ORNL, this "pop" was found to occur at loads up to 20

grams and the load at which the "pop" occurred was found to increase quite linearly with the applied load (Figure 1). Work is ongoing at this time to provide further insight into this materials properties.

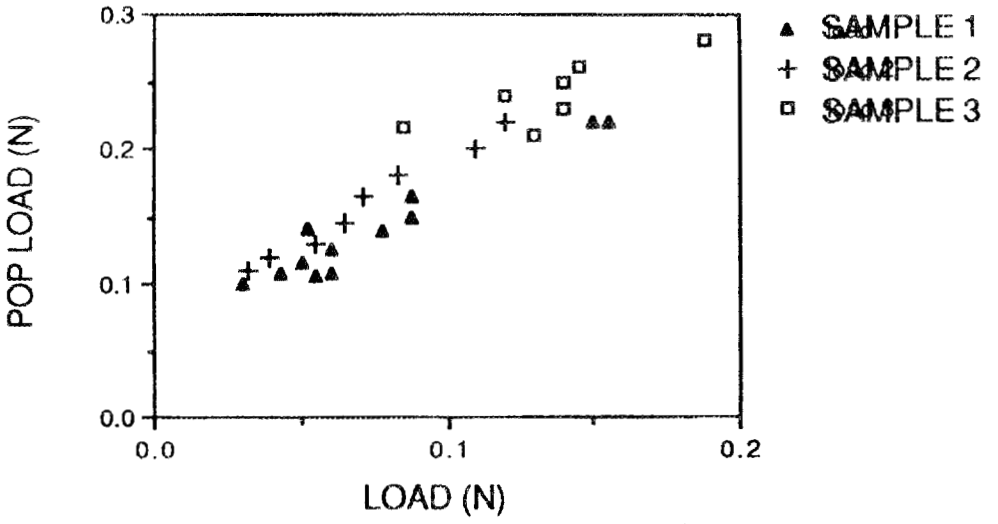

Figure 1. Plot of load versus pop load.

The major disappointment of the project is that insufficient experimental time has not allowed any detailed look at transparent materials and therefore the correlation between visible fracture during indentation and events on the corresponding load displacement curve. The possibility still exists that future work in this area will bring about information that will lead to a new model for fracture toughness of thin films, but there is still much work to be done before this goal is attained.

Effects of Impurities on the Adhesion of Thin Metallic Films to Ceramic Substrates

J. J. Wert, C. J. McHargue, and J. E. Pawel (Vanderbilt University)

Objective/scope

The goal of this program is to study the effects of impurities (placed by ion implantation) on the adhesion of thin metallic films to ceramic substrates and to predict impurities that will increase the adhesion of the systems.

Technical progress

Ion implantation techniques will be used to accurately place impurities at the desired locations for the experiments. During this reporting period, a comprehensive literature review of ion implantation and its effects on the adhesion of thin films to their substrates was completed. Computer simulations of the ion implantation process that include ion range, nuclear damage, and electronic damage information are in progress. This information will be used to choose suitable ion/film/substrate combinations for study.

Preliminary investigations (using chromium metal films and soda lime glass substrates) to determine the optimum sputter deposition parameters for the metal films to be used in this work have been completed. The most important parameters are working gas pressure, working gas flow, target voltage, target-substrate distance, and substrate temperature. The requirements for the experiments are low target voltage, maximum film uniformity, and a reasonable deposition rate (to avoid excessive target heating). The chosen parameters result in good thickness uniformity (small standard deviation of thickness measurements made by surface profilometry) and consistent growth as a function of time. The latter is important because the sputter chamber has no in situ thickness monitor. The target voltage remains under 400 V during the process. Under microscopic examination, the film surfaces appear smooth and generally featureless, showing only a few discontinuities that may be largely superficial.

Adhesion testing was done on these preliminary specimens using both the pull test and the scratch test. In most instances of pull testing, the failure was indicative of high compressive stresses in the surface of the substrate resulting from the film growth. In cases for which the interface did fail, there was large scatter in the adhesion values.

The scratch testing of the chromium/glass system was also inconclusive. Normal loads varying from 20 to 500 g were used but the film was only thinned, not removed, under the stylus. In previous experiments using (evaporated) chromium/sapphire, normal loads of 20 g resulted in film removal. There are several possible explanations for this difference. Because Al_2O_3 is both harder and stiffer (higher elastic modulus) than glass, the stress state under the stylus is different. The coefficients of friction between the moving stylus and the sputter-deposited films were different from those measured previously on the evaporated films and this would also result in a different stress state at the interface. The chromium/glass interface (and its adhesion) may be very different from the chromium/Al_2O_3 interface, both because of the different chemistry involved and because the previous specimens were made by evaporation rather than sputtering. Another explanation is that the sputtered chromium gettered sufficient oxygen during the deposition process to form a chromium oxide, rather than a chromium, film.

Status of milestones

All milestones are proceeding on schedule.

Publications

The paper presented at the Radiation Effects in Insulators-5 Conference will be published in the conference proceedings, a special issue of the *Journal of Nuclear Instruments and Methods in Physics Research, Section B, Beam Interactions with Materials and Atoms.*

3.5 NONDESTRUCTIVE EVALUATION DEVELOPMENT

Nondestructive Characterization
D. J. McGuire (Oak Ridge National Laboratory)

Objective/scope

The purpose of this program is to conduct nondestructive evaluation (NDE) development directed at identifying approaches for quantitative determination of conditions (including both properties and flaws) in ceramics that affect the structural performance. Those materials that have been seriously considered for application in advanced heat engines are all brittle materials whose fracture is affected by structural features whose dimensions are on the order of the dimensions of their microstructure. This work seeks to characterize those features using high-frequency ultrasonics and radiography to detect, size, and locate critical flaws and to measure nondestructively the elastic properties of the host material.

Technical progress

Ultrasonics - W. A. Simpson, Jr., and K. V. Cook. Two sets of commercially fabricated ceramic tiles were received for nondestructive evaluation. The first set consisted of four tiles, designated 89003-6, 89007-13, 890006-11, and 89008-17, which were 10.8 cm square and 8 mm thick and which were to be made into modulus of rupture (MOR) bars following inspection. The tiles were formed by hot isostatic pressing, and thus we anticipated that few flaws exceeding the 20-μm detection limit of our ultrasonic system would be found. All four tiles had been inspected radiographically by the vendor who reported that no flaws were detected in 89003-6, while a very small crack was found in 890006-11. Tiles 89007-13 and 89008-17 supposedly contained a single detectable void and inclusion, respectively. The position of each indication was marked with ink by the vendor.

The tiles were inspected ultrasonically using three procedures. In the first, each tile was examined from both sides using a 75-MHz, 25-mm focal length transducer that was focused about one-third of the way through the thickness. This approach would be expected to find volumetric flaws that did not lie too close to either surface of the sample. The parameters were chosen to provide good coverage throughout the depth of the tile. In the second procedure, both surfaces of each sample were examined with a 50-MHz radially propagating surface wave, that is sensitive to defects lying on or within about one wavelength (~120 μm) of the surface. This procedure has a high sensitivity to surface or near-surface cracks that are perpendicular to the surfaces, regardless of their orientation. In the third procedure, each tile was examined in through-transmission with a 75-MHz transducer. This latter procedure has been effective in detecting cracks that are too deep for surface-wave detection and that are only weakly scattered in a plane parallel to the surfaces.

All of the indications found by the vendor's radiography were easily detected except for the small crack. Visual inspection at 30X magnification of the area around the ink mark designating the location of the crack revealed no discernible flaws. However, on the opposite surface and lying approximately beneath the ink mark, a very shallow, sinuous rille was found. The depth of this rille was about 10 μm, which is probably too small for detection by the surface wave. No evidence of a crack extending down into the tile from the bottom of the rille was seen, but it is possible that residual surface stresses had closed such a crack. Another possibility is that the crack does not extend to within a wavelength of either surface and is very nearly perpendicular to the surfaces. This configuration would be ideal for radiography but very difficult for ultrasonics. If the crack lay at an angle to the surfaces, however, the reverse would be true. This emphasizes the importance of a multidisciplinary attack on the problem of flaw detection in ceramics.

The cracked tile was also examined using a low-frequency ultrasonic angle beam technique, and the crack was easily detected. Since this approach requires *a priori* knowledge of the orientation of the crack, however, it was used only to confirm the presence of the crack and would not be employed during routine evaluation.

The second set of samples consisted of six silicon nitride tiles which were ostensibly similar to the first set of four tiles described above. These tiles were also fabricated by hot isostatic pressing and were designated 89109-1 and -2, 89110-1 and -2, and 89117-1 and -2. Each tile was approximately 110-mm square, and the thicknesses ranged from about 7.5 mm to 10 mm. Following the technique described above, each tile was inspected using two procedures. In the first, the tiles were examined from both sides using a 75-MHz, 25-mm focal length transducer. In this material, the stated focal length is sufficient to allow defects as small as perhaps 25 μm to be detected at depths up to about 3 mm. For the present case, however, the transducer was focused at a depth of about 2 mm, and the two-sided inspection insured that good coverage of the total volume would be maintained. This procedure is not sensitive to flaws lying very near (<200 μm) either surface, but these flaws are normally detected using a high-frequency surface wave inspection, which was omitted because of our findings on the earlier set of four samples.

In the second procedure, all tiles were inspected from one side by monitoring the amplitude of a 75-MHz wave reflected from the opposite surface of the sample. This test is sensitive to cracks which lie at any depth within the sample and is effective regardless of the crack orientation. It has poor sensitivity to small flaws such as voids, but the presence of such defects will be detected by the first procedure.

As expected for hot pressed material, most of the samples appeared to be very clean; that is, there were few ultrasonic flaw indications. No documentation was received with the samples, but one tile, 89110-1, had a small circle which had been inscribed with an ink pen on one surface. No visible marks could be discerned within this circle, but the volumetric flaw test revealed that a very intense scatterer, probably a void, lay within the inscribed area. The flaw was about 2-mm deep, or very nearly at the focal point of the transducer. This defect was sufficiently large that it could be detected from either side of the sample, however.

The only other indications obtained on the volumetric flaw tests were several which occurred very near the edges of two of the samples. These could possibly have been edge effects; however, a thin linear discoloration of the surfaces, which was coincident with the ultrasonic indications, was present in several of the samples. This line extended all the way around the samples and appeared to demarcate the mold in which the samples were pressed.

Following the 75-MHz inspection, an additional flaw test was performed on sample 89110-2 using a 25-MHz, f/6 transducer. Although this unit has less sensitivity than the higher frequency one for flaws smaller than about 50 μm, it produces considerably more energy in the 20- to 50-MHz range and insonifies a much larger volume of the sample. All of the indications obtained in the first inspection were present in the lower frequency test; in addition, a definite pattern of indications, which correlated exactly with a pattern of discoloration of the surface of the sample, emerged near the center of the sample in the latter test. The discoloration was not produced by machining or by slight changes in the elevation of the surface of the sample but appeared to be intrinsic to the sample. Since we could not subject the samples to any type of destructive analysis, the source of these indications is not known. However, the effect appears to extend throughout the sample thickness, and the fact that it is discernible in a backscattering test of this sort would suggest changes in the sample microstructure, chemistry, or density in the affected areas.

The second inspection performed on the samples was that of monitoring the amplitude of the back surface reflectance. No evidence of cracking was detected in any of the samples; however, all of the tiles appeared to be quite inhomogeneous. In samples 89109-2 and 89110-2, the results were particularly striking. A very pronounced pattern of

variation was obtained which correlated with the surface discoloration mentioned earlier. The pattern was much more intense in the reflectance test than in the flaw test, however. Figure 1 shows the results obtained on sample 89110-2. In the other samples, the variation appeared to coincide with machining marks present on the surfaces of each of the specimens. Figure 2 shows this variation obtained on sample 89117-2. For all of the samples, a ring indication running around the periphery of the data image was noted which coincided with the surface discoloration presumably arising from the pressing mold.

The homogeneity of these six samples appeared to be considerably worse than for the four similar tiles examined earlier.

We also received two sets of silicon nitride MOR bars, bearing the designations 2261-66 and 2247EX-68, for inspection. Each set consisted of ten bars which were toughened by the addition of silicon carbide whiskers. Three separate tests were performed on each set. These tests were a volumetric flaw inspection using a 75-MHz, f/3 spherically focused transducer, a simple relative attenuation test in which the back-surface echo using the same transducer was monitored, and a high-frequency surface wave test using a 50 MHz, f/0.2 transducer.

The volumetric flaw test was performed by focusing the transducer at a depth of about 2 mm, or two-thirds of the way through the thickness of a bar. The samples were then scanned from both sides to ensure good coverage of the total volume. From our beam distribution calculations on this transducer, the total depth range over which the flaw response is within -6 dB of the peak value is about 11 wavelengths, or about 1.5 mm. By scanning from both sides, all of the sample thickness (except for a region about 200-μm deep from either surface) can be interrogated. The near-surface region was then evaluated using surface waves.

The volumetric test results showed considerable difference between the two sets of bars. In general, the 2261-66 set exhibited fewer and smaller indications. However, the number 4 bar in this set produced a large indication very near the numbered end. This indication was quite intense, typical of that produced by a large (~250 μm) void, but elongated like the response elicited from a crack. Since it lies very near the end of the bar, however, it likely will be innocuous. Most of the bars in this set yielded 1-2 indications each, which were typical of voids in the 50-100 μm range.

The set designated 2247EX-68 produced many more indications, and the intensity of these indications was characteristic of voids in the 100-200-μm range. The results on these bars were much more typical of those obtained on similar samples which exhibit whisker clumping, that is, inadequate dispersal of the whiskers. One bar, number 6, contained a very intense indication which, if produced by a void, would imply a diameter of >250 μm. This indication was detected from both sides of the bar, but this is not surprising since the ultrasonic A-scan shows that the indication lies near the midplane of the sample. An indication characteristic of cracking occurred very near the end opposite the number in bar number 1. Bars 6 and 10 also produced crack-like indications near the end opposite the number, and bars 4 and 5 yielded similar indications near the center. However, except for bar number 1, which does appear to contain small cracks near the end, these indications are also produced by strings of voids occurring in bars exhibiting whisker clumping.

The back-surface echo test is generally a relatively sensitive method for detecting nonvertical cracks as well as density variations within ceramic samples. The results on both sets of MOR bars were quite similar, with both sets showing considerable variation in the point-to-point amplitude of the back-surface echo. The only clearly identifiable feature detected in either set, however, was an indication very near the end of bar 1 of the 2247EX-68 set which corresponded with the location of the indication detected by the volumetric tests and which was likely caused by one or more small cracks.

The surface wave tests were performed using a high numerical aperture transducer at normal incidence. This configuration produces a radially propagating surface wave which is sensitive to surface and near-surface flaws and to cracks regardless of their orientation.

Since the penetration of a 50-MHz surface wave in silicon nitride is about 120 μm, this test interrogates most of that region not inspected by the preceding examinations. The bars were inspected from both sides, and only a few indications were detected. No indications were found in bar number 1 of the 2247EX-68 set, indicating that, if this bar is cracked near one end, the cracks do not extend to within about 120 μm of either surface. Void-like indications were found in bar number 9 of this set as well as in bar number 1 of the 2261-66 set. In addition, fairly strong crack-like indications were found near the end opposite the number in bar number 9 of the 2247EX-68 set. However, no visible indication of cracking could be seen in this bar.

We continued to study the beam distribution produced inside a ceramic by high-frequency ultrasonic transducers. In particular, we were examining the effect of various aspherical lens designs on the focal distribution produced in cylindrical samples of alumina, silicon nitride, or silicon carbide. Small diameter samples of these materials are extremely difficult to inspect using commercial spherically focused transducers because of the severe astigmatism and spherical aberration introduced by the curvature of the part. We are currently generating beam distributions produced by lenses having both spherical and cylindrical corrections to offset this distortion. We believe that we can ultimately produce a lens design that is capable of stigmatic imaging of internal flaws in a given ceramic of particular diameter with little loss in performance over a relatively wide range of specimen diameters. Since the elastic wave index of refraction is very similar for alumina, silicon nitride, and silicon carbide, such a design would perform equally well in any of these materials. Without such a correction, however, small diameter samples of these materials are currently almost uninspectable ultrasonically at depths exceeding a few hundred microns.

We have completed two aspherical lens designs for a high-frequency transducer to be used for inspection of small-diameter cylindrical specimens. The second design is a marginal improvement over the first, which was estimated to yield at least a 20-dB improvement over a commercial spherical lens. The estimated cost of purchasing this transducer from a commercial vendor remains approximately $10,000, however. We are continuing to negotiate with several vendors in an attempt to lower this cost. We are also examining the possibility of constructing such a transducer in-house.

In order to quantify the signal loss associated with using a commercial spherical transducer to inspect small-diameter cylindrical specimens, we prepared a standard fabricated from a 6-mm diameter silicon nitride rod. A 1270-μm-diam flat-bottomed hole was drilled into the side of the rod to a depth of 4 mm. A second flat-bottomed hole, 250 μm in diameter, was then drilled out of the bottom of the larger hole to an additional depth of 1 mm. This arrangement produced a 250-μm-diam penny-shaped crack standard lying 1 mm deep in the curved specimen and a 1270-μm-diam one lying 2 mm deep. Using a commercial 75-MHz, f/3 transducer, the smaller standard was detected with about a 20-dB loss with respect to the values obtained in flat samples. The larger standard exhibited a loss of almost 30 dB, indicating that the losses attributable to abberation increase with depth.

We have begun examining the possible use of plane-wave insonification of ceramic samples in order to avoid the necessity of focused transducers and the problems attendant to their use. This approach has the great advantage of being applicable in samples of any thickness, whereas focused transducers lose sensitivity rapidly for flaw depths greater than about 3 mm in typical ceramics. However, the signal returned by small flaws (~20 μm) illuminated by plane waves is very much smaller than the system noise for depths greater than a few hundred microns, thus necessitating some form of signal processing if useful information is to be extracted. If this information can be obtained sufficiently rapidly, however, the large volume interrogated by plane waves may more than offset the additional processing time to yield smaller inspection times. We are examining several approaches to achieve this result.

Radiography - B. E. Foster. Four silicon nitride tiles, identified as 89003-6, 89007-13, 890006-11, and 89008-27, were radiographed. These are the same four tiles reported in the Ultrasonics section. All of the indications found by the vendor's radiography were easily detected, including the small crack near one edge. We evaluated this tile using the CT system and detected the crack and a small void.

Six other silicon nitride tiles, identified as 89109-1 and -2, 89110-1 and -2, and 89117-1 and -2 were radiographed. This are the same six tiles reported in the Ultrasonics section. The surfaces of these tiles had a mottled appearance and, in addition, showed a line of discoloration extending all the way around each sample approximately 3 mm in from each edge. The radiographs clearly showed that the mottled appearance seen on the surface was volumetric and throughout the sample. The line was a sharply defined area of apparent reduced density (high radiation transmission) with microcrack-like indications. A section of this line will be evaluated with the CT system in the near future.

The computerized x-ray tomography system that was purchased from Scientific Measurement Systems, Inc., (SMS) in Austin, Texas, has been installed. The purchase agreement includes several progress payment type milestones. Six milestones have been completed. They have included a design review; approval of major item drawings; fabrication of the image processing subsystem; fabrication of the array and back projection processor; receipt of major equipment items; and start of fabrication on the object positioning unit, specimen holder, collimation set, calibration standards, and installation and acceptance testing at ORNL with additional operator training. The x-ray units were malfunctioning intermittently, thus preventing any lengthy scans and obviously preventing accomplishment of acceptance testing. Philips (the x-ray tube manufacturer) replaced the tubes, shortened the high voltage cables, and replaced the EPROM, all to no avail. Then, at our repeated request, they replaced the negative 225-kV generator, which solved the x-ray problem. The x-ray malfunction had delayed checkout of the software. Operation of the system (after solving the x-ray problem) disclosed several bugs in the software, which are being corrected.

A number of ceramic components have been obtained and are being examined for system evaluation and operator training. We are pleased with the high-resolution capability and versatility of the system for inspection of complex ceramic parts and assemblies.

Milestones

Milestone 351103 was completed on schedule.

Publications

Galley proofs for "Applications of Ultrasonics for Advanced Structural Ceramics" by W. A. Simpson, Jr., R. W. McClung, and D. R. Johnson, an invited contribution to the *ASNT Handbook*, have been received and corrected.

A paper describing our work in characterizing whisker-reinforced ceramics has been submitted to *Materials Evaluation*.

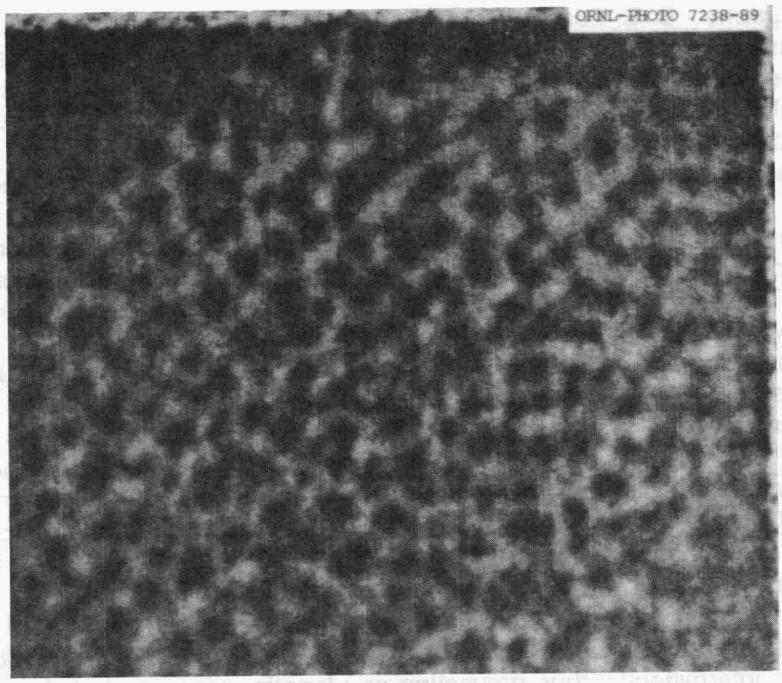

Fig. 1. Ultrasonic transmission results on ceramic tile 89110-2 showing detection of large-scale inhomogeneities.

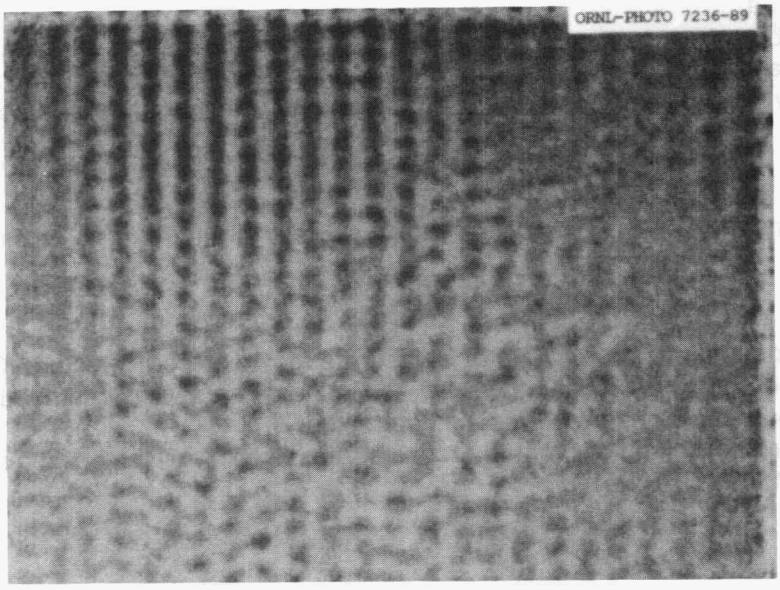

Fig. 2. Ultrasonic transmission results on ceramic tile 89117-2 showing detection of surface grinding marks.

NDE Standards for Advanced Ceramics

R. W. McClung (Oak Ridge National Laboratory)

Objective/scope

The development of standards is important for the establishment of reliability and acceptance of advanced structural materials. A new committee, C-28 on Advanced Ceramics, has been organized in the American Society for Testing and Materials (ASTM) to address this issue. One of the activities of the C-28 is nondestructive examination (NDE). This initial report is to introduce and report the past activities, bringing it up to date. The Task Group on NDE, as one of its first actions, reviewed existing standards on NDE (primarily developed for metals) to determine potential applicability for ceramics. Use of existing or modified standards will be much more efficient than generation of new documents and will ensure the input of a larger body of NDE expertise.

Technical progress

Over 90 NDE standards [most developed by ASTM Committee E-7 on nondestructive testing (NDT)] on all NDE methods were screened. Approximately 38 were identified as having potential applicability to ceramics. Twenty of these, related to liquid penetrant, radiographic, and ultrasonic examination, were given initial review by several task group members, and comments were developed about probable needs for modification. An advisory ballot (within the task group) on eight selected documents developed detailed recommendations for change to the documents for application to ceramics. These recommendations were submitted to Committee E-7 through R. W. McClung, a member of both committees and official liaison between the committees. The comments were accepted by E-7, and ballots of document revisions began (January 1989). A second advisory ballot of the C-28 Task Group on NDE on eight additional E-7 documents resulted in more detailed recommendations for changes. These were provided to the E-7 Committee, and revisions were begun in June 1989 for ballots in Committee E-7.

In addition to the review of E-7 documents (which has helped identify additional standards problems), work has begun on approaches for fabrication of reference flaws in ceramic specimens. These are used for technique development and calibration. Data is also being generated on densities and ultrasonic velocities for potential recommendation for insertion in existing E-7 documents.

Computed Tomography

W. A. Ellingson, T. Hentea, K. Gopalan (Argonne National laboratory), and
H. C. Yeh, J. P. Pollinger (Garrett Ceramic Components Division of Allied-Signal Corp.)

Objective/scope

The objective of this program is to develop X–ray computed tomographic (CT) imaging technology for application to structural ceramic materials. This technique has the potential for mapping short–range (<5 mm) and long–range (>5 mm) density variations (to perhaps 0.5–1%), detecting and sizing high– and low–density inclusions, and detecting and sizing (within limits) cracks in green–state and densified ceramics. CT imaging is capable of interrogating the full volume of a component, and is non–contacting. It is also relatively insensitive to part shape and thus can be used to inspect components with complex shapes, such as turbocharger rotors, rotor shrouds, and large individual turbine blades.

Technical progress

During the current reporting period, we established a new set of test phantoms (turbocharger rotors) with varying organic-binder content and ran a series of microfocus X–ray CT tests on these and other test phantoms.

New test phantom

To better obtain an idea of X–ray CT sensitivity to density variations within the critical hub-blade region of a turbocharger rotor, we have developed a set of rotors that will be produced by Garrett Ceramic Components Division (GCC) of Allied-Signal Aerospace Corporation. Figure 1 shows the drawing from which the rotors will be made. These T–25 turbocharger rotors will be produced by injection molding of Garrett's GN–10 Si_3N_4. Three insert slugs at the critical hub–blade region will have 2, 4, and 6 wt.% binder differences, which should result in approximately 0.08 g/cc mass density difference per 2 wt.% binder from a nominal 2.28 g/cc base material. The slugs will be inserted into the shaft–blade region so that part of the shaft–blade region will have these known variations and part will not. We will report on the fabrication and test results of these new phantoms in the next period.

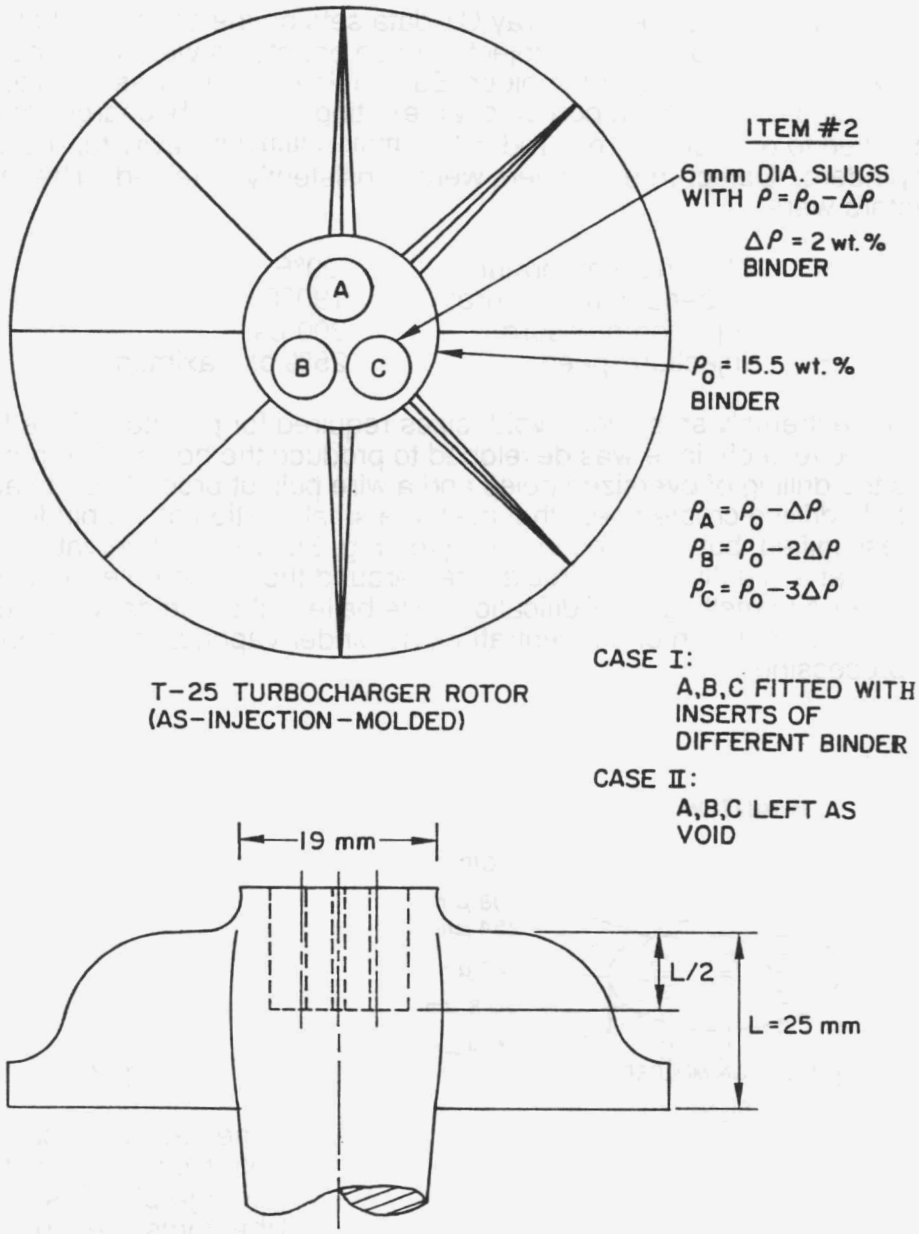

Fig. 1. Schematic Diagram of New Turbo Rotor (or Turbocharger Rotor) X-Ray Computed Tomography Test Phantoms for Density Sensitivity Tests

We conducted a number of X–ray CT data sets on the second set of test phantoms (Fig. 2) made for this project. These phantoms were produced as follows: A screw–type injection molder (Battenfeld 650/300) was used to mold the base cylinder. The shaft portion of an existing T–25 turbocharger rotor die was modified to provide the required $\approx 26-\mathrm{mm}-\mathrm{diameter}$ cavity for molding the base cylinders. Defect-free cylinders were consistently obtained. The molding parameters were:

- Molding temperature: 90°F
- Material temperature: 190°F
- Injection pressure: 200 psi
- Injection speed: 25% of maximum

Due to the extremely small hole (void) sizes required for phantom Type II (Fig. 2), a novel technique was developed to produce the holes. The process involves the drilling of oversized holes and a wire pullout procedure. In all cases, hole drilling created heat that melted a small portion of the binder. The binder resolidified, but changed in color (see Fig. 3). Visual observation indicates that a slightly larger circular area around the drilled hole exhibits a dark color due to melting/resolidification. We believe that the dark area does not change composition or concentration; no binder vaporization was observed during processing.

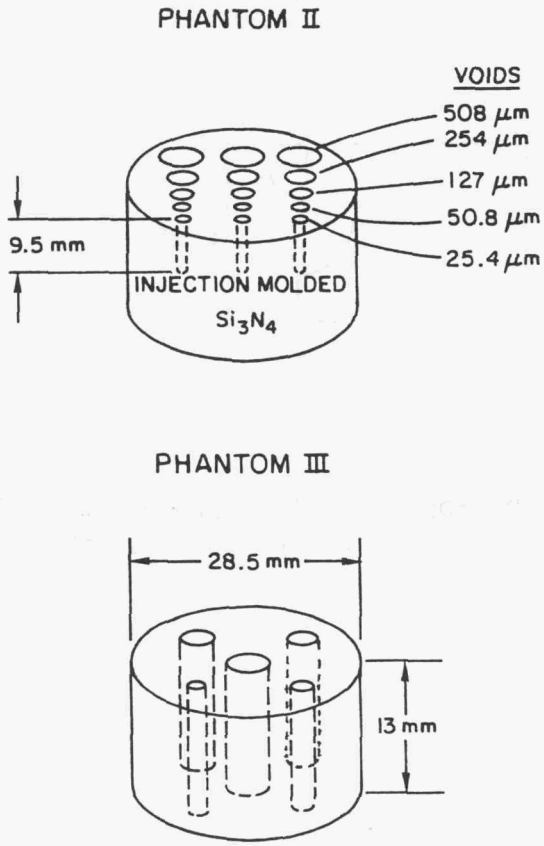

Fig. 2.

Schematic of Second Set of X-ray Computed Tomography Test Phantoms (Test phantoms II and III)

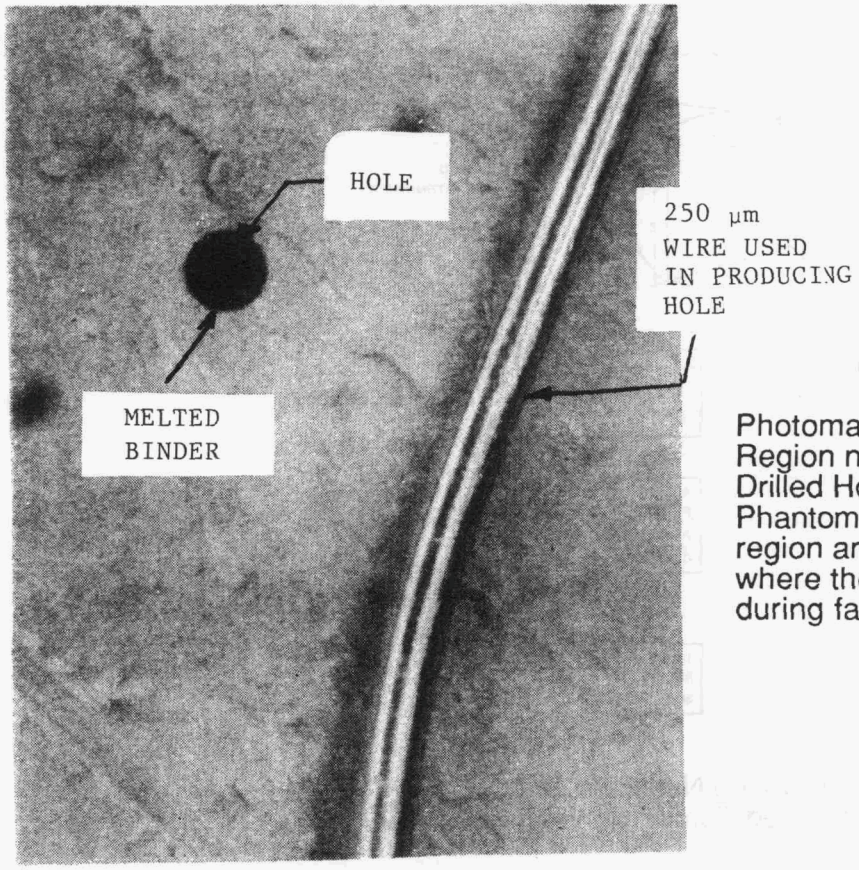

Fig. 3.

Photomacrograph of Region near the 254-mm Drilled Hole in Test Phantom IIB. Note the dark region around the hole where the binder melted during fabrication

To quantify hole diameters, samples were made with the various diameter holes drilled in them and then sectioned. The corresponding-diameter wire was laid next to the hole and optical micrographs were taken. Figure 3, which shows the melted binder, also is one of the micrographs used to confirm hole size. In this case, a 254-mm-diameter hole was compared with the 254-mm-diameter wire lying near the hole.

The holes are laid out in the test phantoms as shown in Fig. 2. The center 25.4-mm hole, in Phantom II that could not be removed. This wire inclusion may allow some interesting characterizations by nondestructive evaluation techniques.

Microfocus X–ray CT images were first obtained on test phantom III. This phantom contains larger drilled holeswith diameters of 5, 4, 3, 2, and 1 mm. The test facility used to obtain the data, shown schematically in Fig. 4, is a 3-D microfocus X–ray CT system that uses an image intensifier and CCD array camera as the detector.

For test phantom III, we used 115-kVp and 0.2-mA X–ray head conditions with a 10-mm focal spot size. Geometric magnification was 2.55, and image reconstructions were done in a 256 x 256 format. The rho filter (also called convolution kernel) for the data was a RAM–LAK filter, although in the next reporting period we will show results from the use of other filters. We used 120 projections, which we know will yield some aliasing in a 256^2 reconstruction.

Figure 5 is a typical reconstructed image of test phantom III. All holes are clearly seen, as would be expected. This is only one transaxial slice, but with the 3-D microfocus X–ray CT system we have generated a full-volume image of this test phantom.

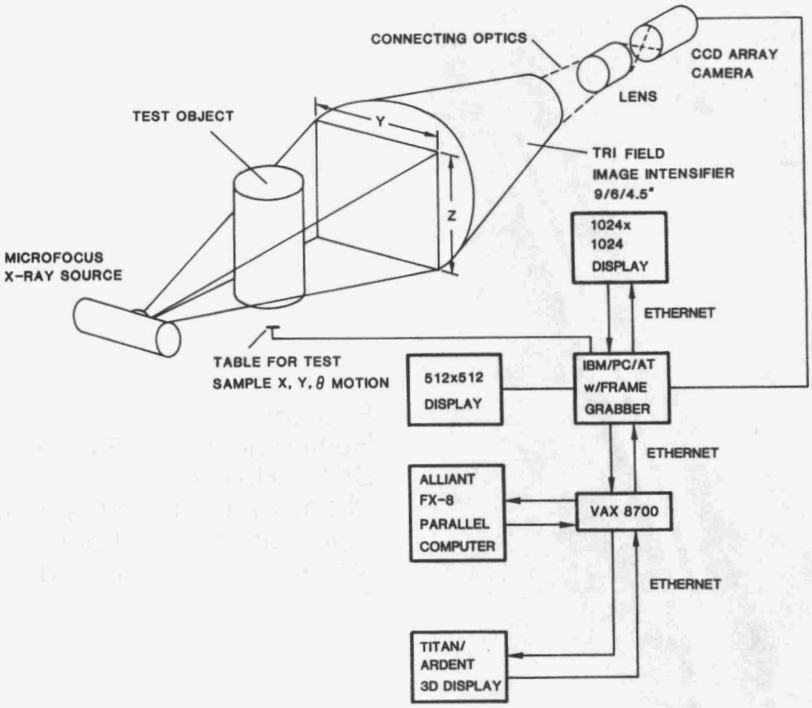

Fig. 4. Schematic of Argonne National Laboratory's 3-D Microfocus X–Ray Computed Tomographic Imaging Facility

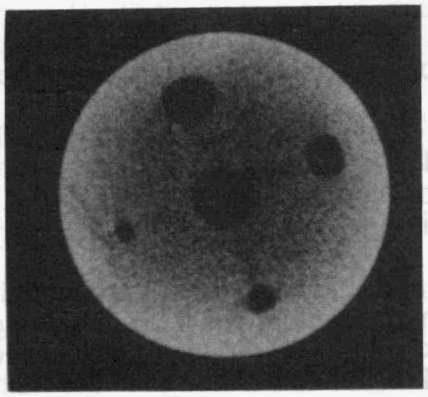

Fig. 5.

Microfocus X-ray Computed Tomographic Image of Test Phantom III

X–Ray computed tomographic imaging of West German rotor

We were fortunate this period to obtain a densified Si_3N_4 rotor from BAM of West Germany. The rotor was about 31 mm in diameter (blade tip to blade tip) and had a tapered shaft nominally of 12 mm diameter. For these studies, also done on the ANL 3-D microtomograph, we used a 140-kV, 0.3-mA, 10-mm focal spot X–ray head setting; 180 projections; 256 x 256 reconstruction; a RAM–LAK rho filter; and a geometric magnification of 2.65. On one end of the shaft was a drilled hole about 2 mm in diameter plus a suggested knit line from injection molding. We observed the drilled hole, but with 180 projections obtained only a "hint" of the knit line.

Figure 6 is a microfocus X–ray CT image of the BAM rotor. The drilled hole is clearly observed, but the knit line (thought to be present) is only suggested.

Figure 7 is a transaxial microfocus X–ray CT image of this same rotor, but taken through the blade–shaft region.

Status of Milestones

On schedule

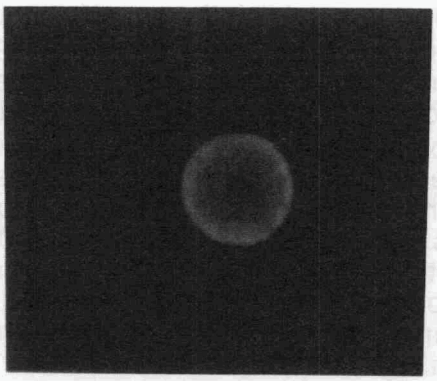

Fig. 6.

Microfocus X–Ray Computed Tomographic Image of Upstream Shaft Region of BAM Dense Si_3N_4 Rotor. Note the 2-mm-diameter drilled hole

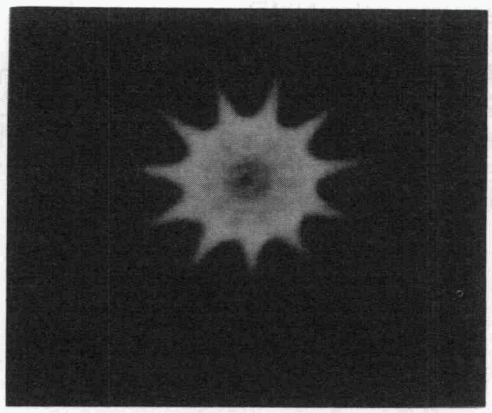

Fig. 7.

Transaxial Microfocus X–Ray Computed Tomographic Image through Blade–Shaft Region of BAM Dense Si_3N_4 Rotor

Nuclear Magnetic Resonance Imaging -

N. Gopalsami, S. L. Dieckman, W. A. Ellingson, R. E. Botto (Argonne National Laboratory), and H. Yeh, and J. P. Pollinger (Garrett Ceramic Components Division of Allied-Signal Aerospace Corp.)

Objectives/scope

The objectives of this program are to (1) investigate the feasibility of nuclear magnetic resonance (NMR) imaging techniques in mapping organic additive distributions in green injection–molded ceramics (experimental emphasis placed on commercial Si_3N_4 materials); (2) investigate the potential for NMR spectroscopic techniques in determining chemical variations within or between organic additive batches that may affect process reliability; (3) investigate the sensitivity of the NMR imaging methods to mixing and injection-molding process variables, as manifested in organic additive distribution homogeneity; and (4) investigate the use of NMR imaging in conjunction with slip cast ceramic processing technology.

Technical progress

Imaging of standard-concentration phantoms

In an effort to establish the sensitivity of NMR imaging techniques to organic additive concentration differences within Si_3N_4 samples, images were acquired of standard-concentration phantoms. The phantoms consisted of 4-8 mm diameter, 3-mm-thick cylindrical, cold-pressed, organic additive/Si_3N_4 pellets placed in a Teflon sample holder. To enable correlation of intensity information between different images, an intensity phantom consisting of a small modulus-of-rupture (MOR) bar fragment was built into the sample holder. Organic additive weight percentages in the various pellets were 10.0, 14.5, 15.5, 18.0, 19.0, and 20.0. Back-projection images of the pellets were acquired on the Bruker Instruments CXP–100 spectrometer at ANL utilizing ANL's homebuilt NMR imaging accessory. The nonnormalized XZ images, acquired with 90 projections and 128 averages, are presented in Fig. 1.

While the intensity variations within the images are due mainly to differences in organic content, additional factors contributing to intensity variations arise from a combination of variations in sample pellet thickness, variations in RF coil tuning due to sample loading, and RF coil inhomogeneities within the NMR imaging probe. Image intensity variations due to these additional factors can be easily removed through standard normalization procedures. A plot of the normalized image intensity vs. organic concentration is presented in Fig. 2. The image intensity for the 20-wt.% phantom is lower than expected due to sample placement outside the RF coil. While sample organic additive percentage correlates well with image intensity, we plan to repeat the experiment with more accurately prepared concentration standards.

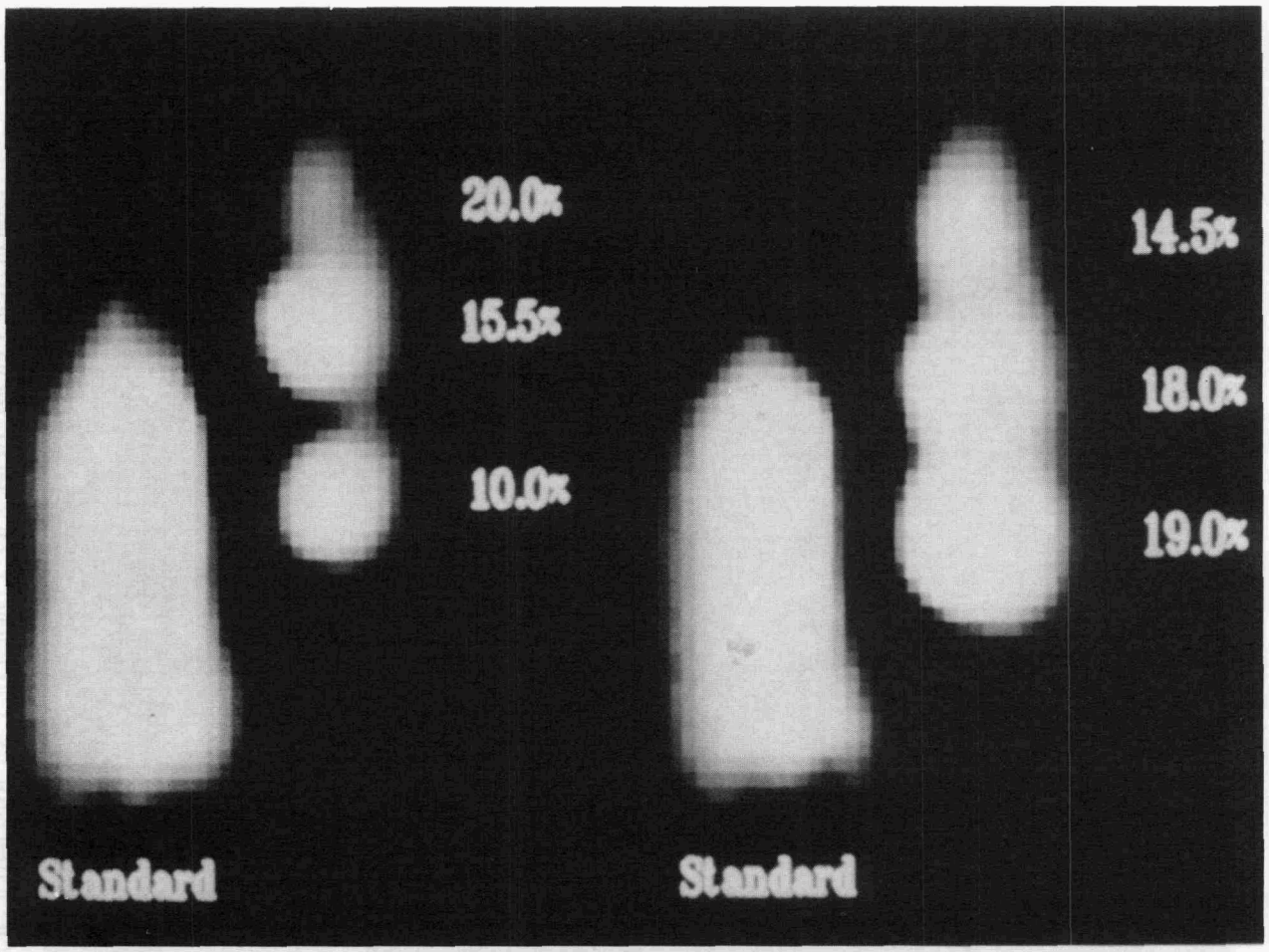

Fig. 1. Nonnormalized Back-Projection Proton NMR Images of Standard Organic Concentration Green–State Si_3N_4 Phantoms

Imaging of MOR bars

To establish NMR imaging sensitivity to processing variables as manifested in organic additive distribution, images were acquired of four specially prepared Si_3N_4 MOR bars. The bars were produced by Garrett Ceramics Component Division of Allied-Signal Aerospace Corporation and differed in mixing and injection-molding processing conditions. Back-projection images of the bars were acquired on the Bruker Instruments CXP–100 spectrometer at ANL utilizing ANL's homebuilt NMR imaging accessory. The samples were oriented vertically in the probe, and XZ images were acquired of each of the bar's two ends. Each image was acquired with 90 projections and 128 averages by applying a 3.6-gauss/cm gradient field.

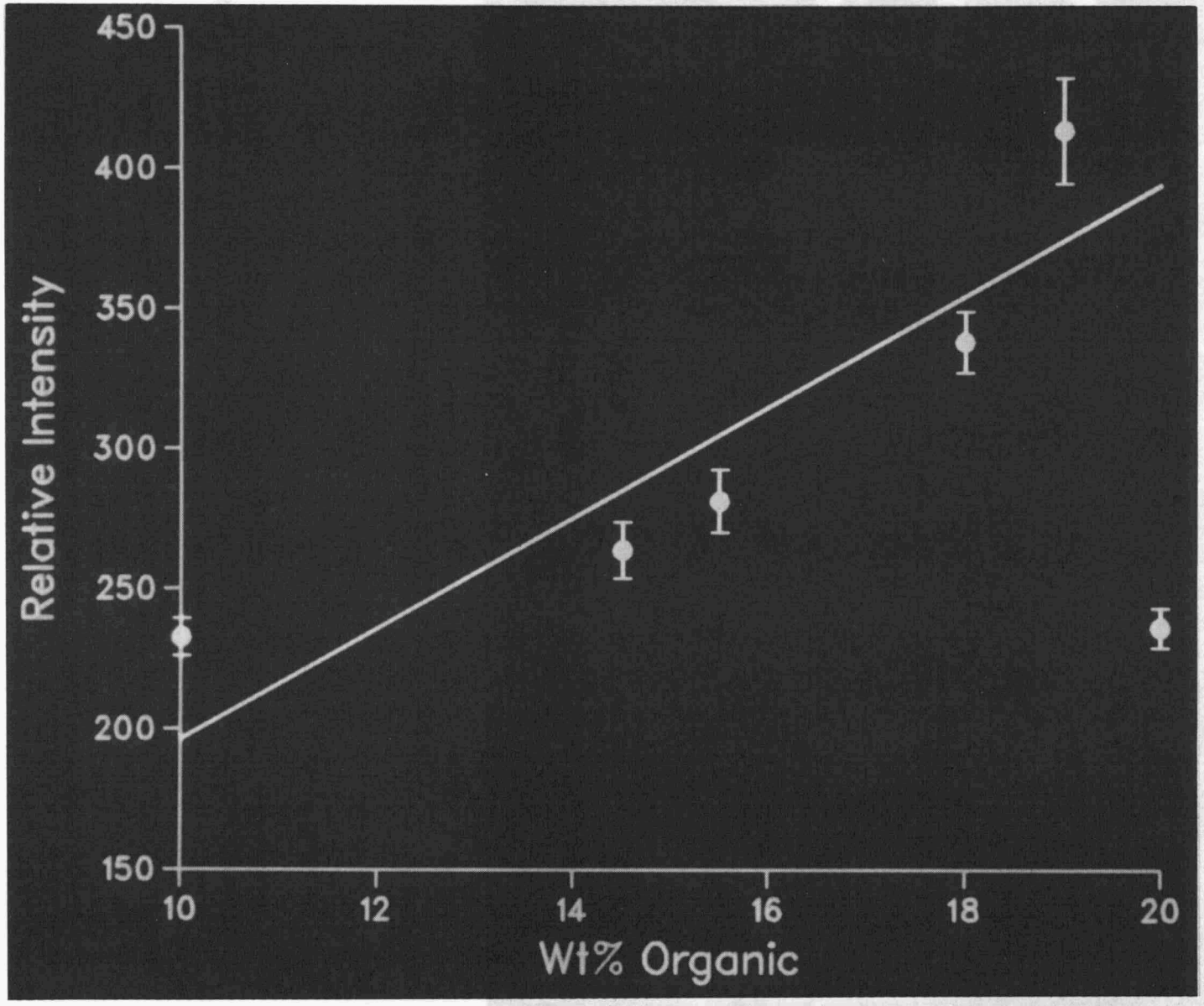

Fig. 2. Plot of Normalized Image Intensity vs. Organic Concentration Obtained From Proton NMR Images Obtained of Green-State Si_3N_4 Ceramics

Representative images of the MOR bars along with the intensity standards are presented in Fig. 3. Image intensity differences apparent within bar #1 suggest an inhomogeneous distribution of organic additives. Differences in intensity apparent in bar #2 are due to RF coil inhomogeneity. The MOR bars have been returned to Garrett for chemical analysis. Image intensities will be correlated with the organic additive concentrations.

Multipulse NMR imaging of Si_3N_4 MOR bars

In an effort to increase the resolution of the NMR images obtained on the green ceramic MOR bars, multipulse NMR spectroscopic and imaging pulse sequences were investigated. These pulse sequences narrow the spectral features (peaks) by decoupling strong homonuclear dipole–dipole interactions. Additionally, because

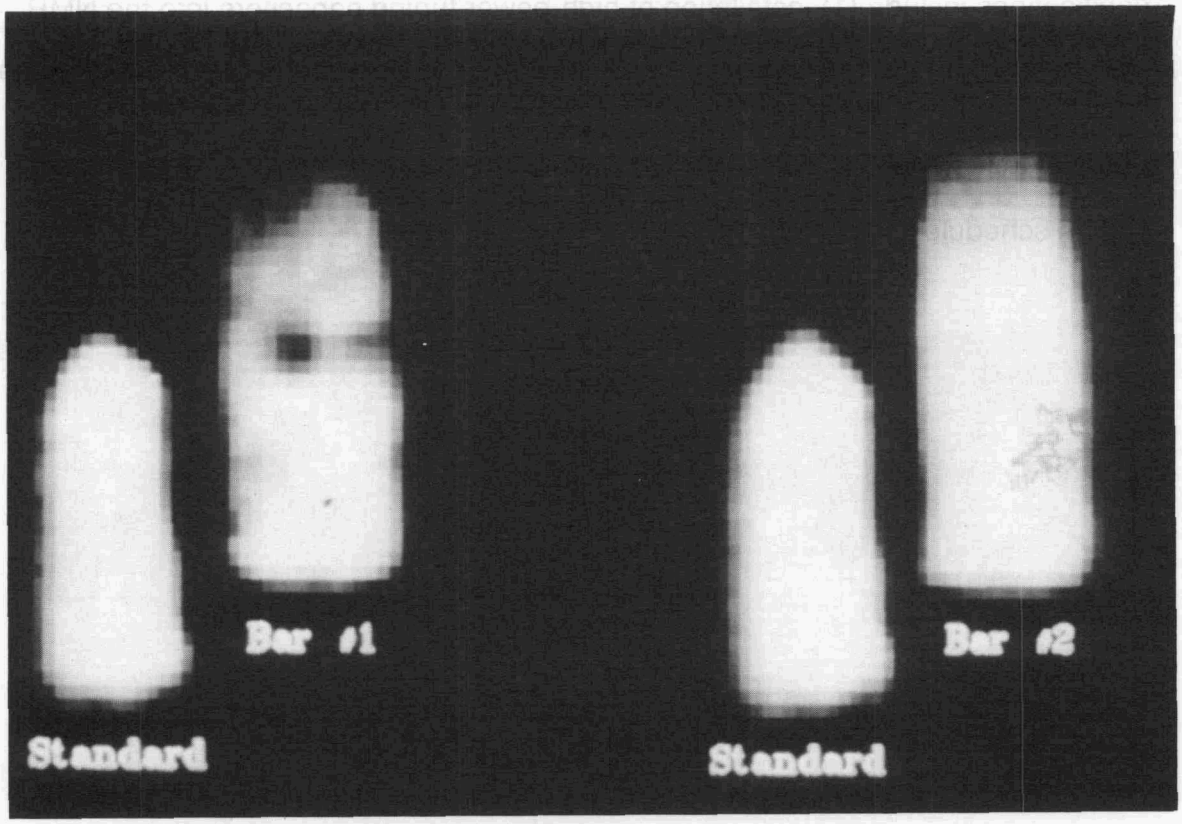

Fig. 3. Back-Projection Proton NMR Images of MOR Bars Obtained Using 90 Projections and 128 Averages. Image intensity differences suggest a sensitivity to injection molding process variables

the total integrated intensity remains constant, there is typically a significant increase in signal-to-noise ratio with the multipulse technique compared to that of conventional one-pulse techniques. Application of multipulse sequences for solid state ^1H NMR spectroscopy can yield drastically narrowed line widths because dipole interactions often dominate the system, yielding line widths in excess of 50 kHz. Application of these pulse sequences, combined with conventional back-projection NMR imaging techniques, will significantly improve resolution in these systems. However, the results obtained from application of multipulse sequences on the soft, solid, green ceramic MOR bars showed little narrowing. These results indicate that the line broadening mechanisms for these systems are not dominated by dipolar broadening, but rather by chemical shift anisotropy.

Real-Time NMR imaging of ceramic slip casting

NMR imaging system modifications for application of spin-echo or echo-recalled NMR imaging pulse sequences are nearing completion. These modifications will allow near-real-time imaging of the ceramic slip casting process. The main system modifications include (1) installation of high-power tuning capacitors into the NMR probe, allowing more accurate RF pulses (2) software development for echo-recalled image reconstruction,: (3) software development for spin-echo image acquisition: and (4) development and installation of RF shaping components.

Status of Milestones

On schedule.

Powder Characterization

O. O. Omatete and A. C. Young (Oak Ridge National Laboratory)

Objective/scope

The objective of this research element is threefold: (1) to identify and characterize those aspects of the chemistry and physics of a ceramic powder-solvent interface that control processing, (2) to develop standard methods of analysis for item 1, and (3) to develop procedures for writing specifications for ceramic powders to include any methods of analysis developed in the project.

Technical progress

Subcontracts. The kick-off meeting between the three university subcontractors and the ORNL representatives was successfully held at ORNL on May 15-16, 1989. The University of Wisconsin was represented by Drs. M. A. Anderson, M. I. Tejedor, and W. A. Zeltner; Rutgers University, by Drs. R. E. Riman and D. J. Shanefield; Pennsylvania State University, by Dr. J. H. Adair; and ORNL by Drs. M. A. Janney, O. O. Omatete, and A. C. Young.

Dr. D. R. Johnson, the program manager, presented an overview of the Ceramic Technology for Advanced Heat Engines project; then, each group gave a review of its special task on silicon nitride: inverse gas-solid chromatography at ORNL, infrared characterization at Wisconsin, nonaqueous interaction at Penn State, and controlled doping at Rutgers.

The group discussed and made decisions on the procedures to be adopted in the round-robin measurements of the electrophoretic mobility of Si_3N_4 in aqueous suspensions. For instance, based on the works at ORNL on the behavior of polystyrene latexes reported earlier and the simultaneous mobility measurements on the same sulfate latex at ORNL and two of the participating universities, the latexes were discarded as "benchmark" materials. Instead, the use of red blood cells and/or phosphated goethite (α–FeOOH) was recommended.

The group decided to meet once every six months to review the progress made within that period. The next meeting was scheduled for the first week of November 1989 at Pennsylvania State University.

The 50-kg Si_3N_4 powder UBE E-10 for the round robin has been bought. This needs to be riffled and distributed to the participants.

In-house. The investigation of the effects of the processing aids (acrylamide monomer, Darvan C, and magnesium nitrate) on alumina suspensions for gelcasting continued during this period. Acid-base titrations, sedimentation, electrophoretic mobility, and specific conductivity measurements of 2 vol % alumina suspensions were examined. Some of the results are shown in Figs. 1 through 3.

Figures 1(*a*) and (*b*) show that the presence of either acrylamide or magnesium nitrate in the suspension has negligible effect on the variation of the pH with molarity compared with the suspension alone (solid circle); on the other hand, Fig. 1(*c*) shows a strong Darvan C influence. Figures 2(*a*) through (*c*) show a similar trend for electrophoretic mobility measurements. Figures 3(*a*) through (*c*) show the variation of the conductivity of the suspension with pH for the addition of two each [Fig. 3(*a*) and (*b*)] and all three [Fig. 3(*c*)] of the processing aids at concentration levels comparable to those in the gelcast slurry. The dominating influence of Darvan C is evidenced by the similarity of the conductivity of the suspensions at 0.1 vol % Darvan C concentration in all three figures, independent of the concentration of the other species. All these show, not unexpectedly, that Darvan C adsorbs strongly on the alumina and is, therefore, a very effective dispersant for the slurry.

The new Hewlett Packard 5890A Series II gas chromatograph (GC) was received during this period. It has been installed in the powder characterization laboratory. The new GC has been used in the inverse gas-solid chromatography (i-GSC) study of two powders: Si_3N_4 and Al_2O_3. The GC column was packed with the as-received powder or the powder oxidized in air at 800°C for 6 h.

Various probe reagents were injected into the column, and its temperature was raised from 60°C to 300°C at 8°C/min.

The straight aliphatics (C_9-C_{12}) and the aromatics (benzene, toluene, and xylenes) all eluted from both Al_2O_3 columns. The probes came out faster from the calcined, cleaner surface; the xylenes separated into two peaks. All the other probes--alcohols (ethanol, propanol, isopropanol, and n-butanol), ketones [acetone, methyl ethyl ketone (MEK), and methyl isobutyl ketone (MIBK)], chloromethanes (chloroform and dichloromethane), ether, and pyridine--did not elute from both columns at 300°C. These results indicate the amphoteric nature of alumina containing both basic and acidic adsorption sites.

The aliphatics and the aromatics eluted from both Si_3N_4 columns; the elution was faster from the cleaner, oxidized powder. Here, there were also two clear peaks for the xylene isomers. Alcohols and pyridine did not elute from both columns. However, for the chloromethanes and the ketones, there were mixed indications. All the ketones and dichloromethane eluted from the as-received column. Both chloroform and dichloromethane, MEK and MIBK, eluted from the oxidized column, but not acetone. Thus, the Si_3N_4 surface adsorbed Lewis bases but not Lewis acids, unlike Al_2O_3.

It is hoped that by the careful observation and quantification of these differences, this i-GSC technique will be used to characterize and differentiate between the same powder, if any differences exist, from separate suppliers or different batches from the same supplier.

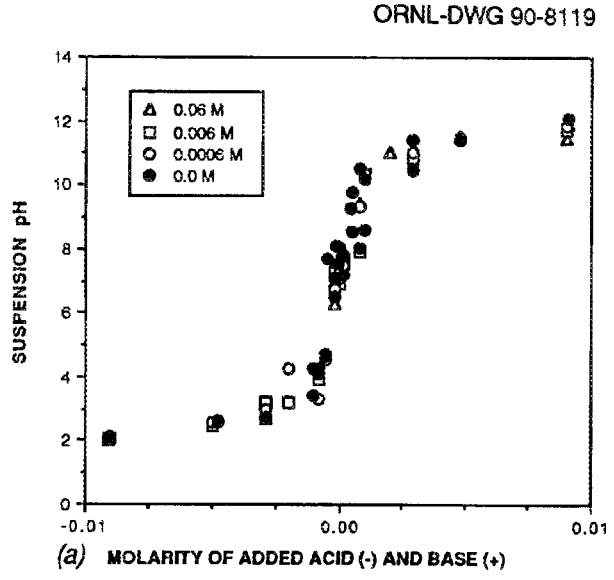

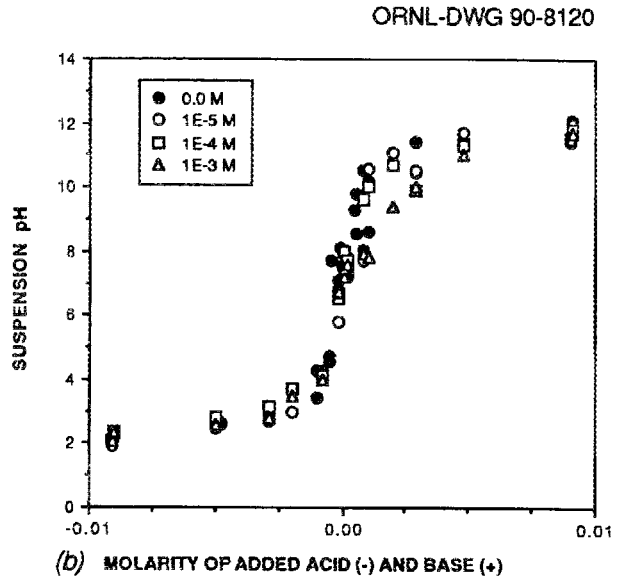

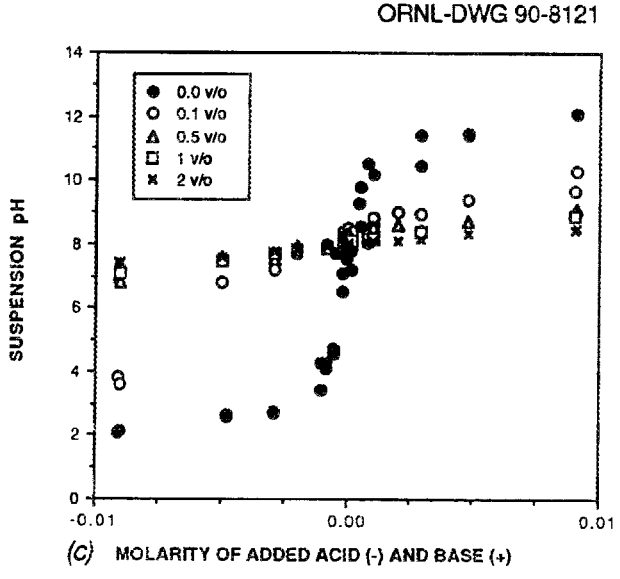

Fig. 1. Molarity of added acid and base vs suspension of aqueous alumina suspension of 2 vol % with (*a*) acrylamide monomer, (*b*) magnesium nitrate, and (*c*) dispersant Darvan C.

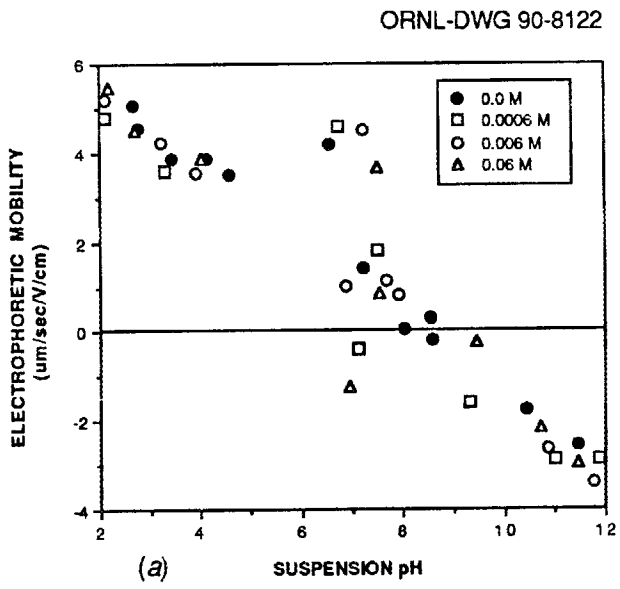

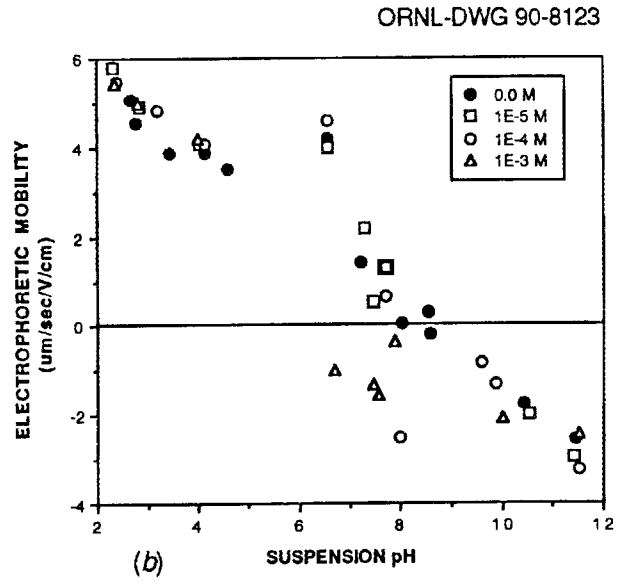

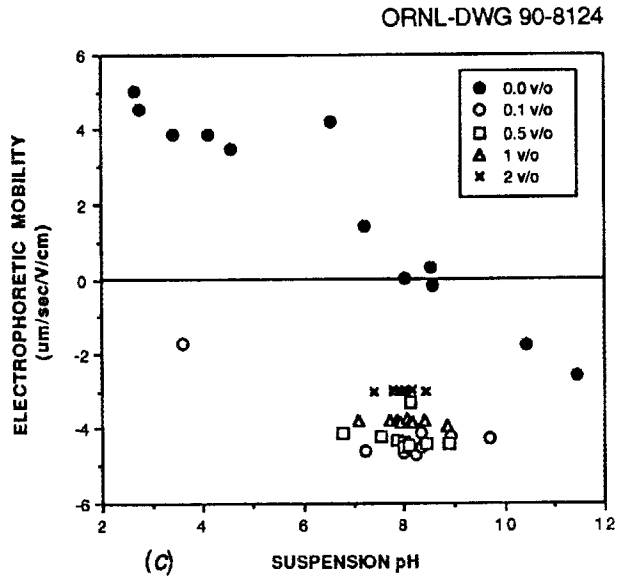

Fig. 2. Suspension vs electrophoretic mobility of aqueous alumina suspension of 2 vol % with (*a*) acrylamide monomer, (*b*) magnesium nitrate, and (*c*) dispersant Darvan C.

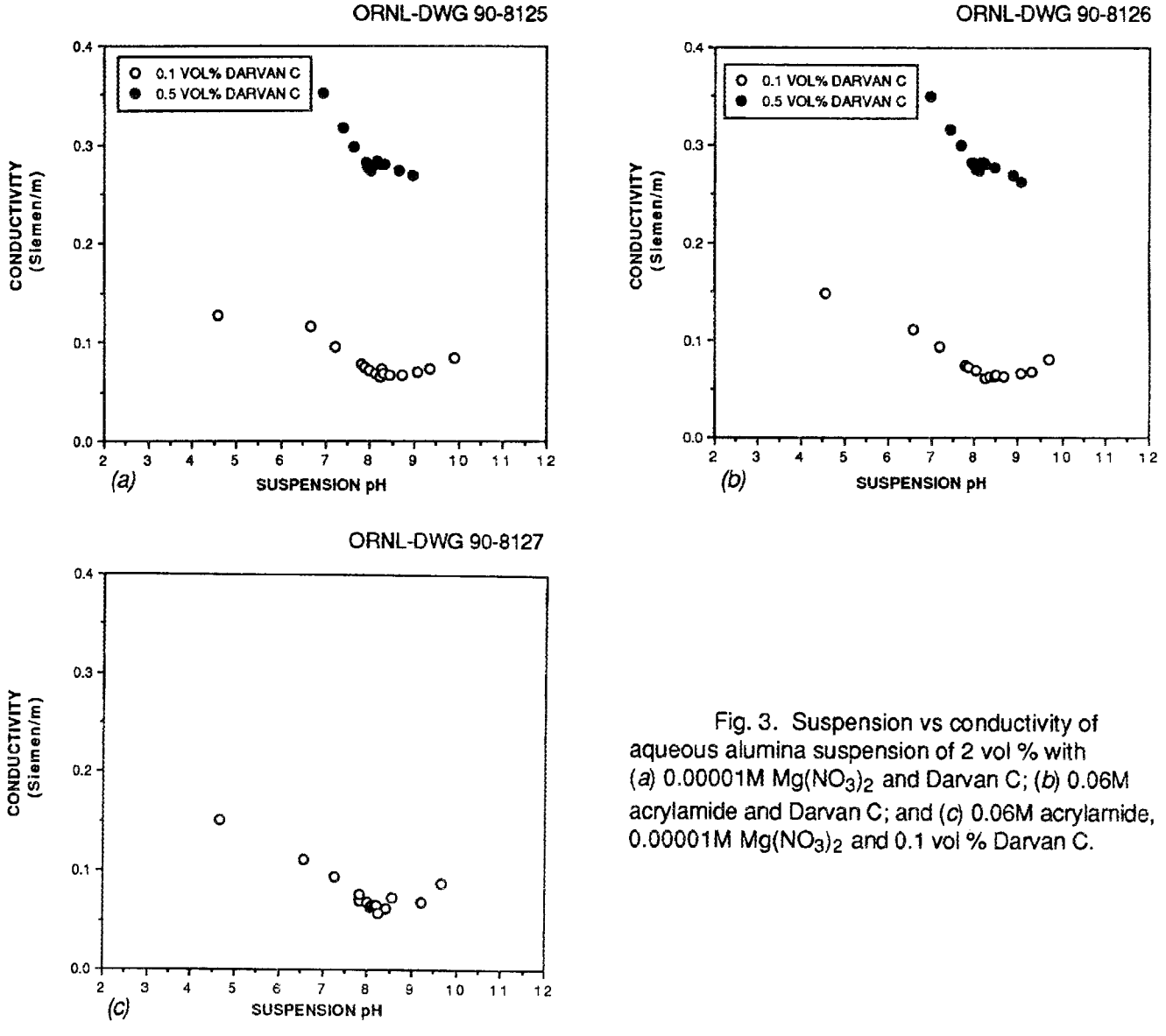

Fig. 3. Suspension vs conductivity of aqueous alumina suspension of 2 vol % with (*a*) 0.00001M $Mg(NO_3)_2$ and Darvan C; (*b*) 0.06M acrylamide and Darvan C; and (*c*) 0.06M acrylamide, 0.00001M $Mg(NO_3)_2$ and 0.1 vol % Darvan C.

Powder Characterization

R. E. Riman, D. J. Shanefield, and J.-F. Wang (Rutgers University)

Abstract

A polystyrene latex was investigated as a possible standard for electrophoretic characterization studies. This powder, recommended by Dr. F. J. Micale of the Sinclair Surface Center of Lehigh University, is Polybead 7307, from Polysciences Inc., of Warrington, PA. It is a monodisperse 0.5 ± 0.02 micron polystyrene powder in water (2.5wt%), with no surfactant and no biocide present. Based on our experimental results, this powder is not suitable for serving as a standard material.

Experimental

The latex was diluted to 0.01 v/o in deionized distilled water, in Falcon polypropylene containers, and either potassium nitrate or potassium perchlorate was added as a supporting electrolyte. Three solution concentrations for each electrolyte were prepared, 0.001, 0.01, and 0.05M. Electrolyte solutions were de-aired for 20 minutes before sample preparations by flushing with nitrogen gas. The pH was adjusted with either HCl or KOH. the sol was equilibrated by shaking for 24 hours. The pH was measured at the same time as the electrophoresis measurement using a Brinkman 686 Titroprocessor with metrohm separate electrodes. Before the pH measurement, the pH meter was calibrated using the Aldrich buffer solutions with pH values 4.00, 7.01, and 10.00. The specific conductance was determined from the sol directly using a Brinkman Metrohm 660 conductometer. The electrophoretic mobility was measured at 25°C by using a modified Malvern Zetasizer II.

Results

The mobility of the powder was measured in two different supporting electrolytes, potassium nitrate and potassium perchlorate, at three different concentrations, 0.001, 0.01, and 0.05M (Fig. 1). The absolute value of the mobility increased with time regardless of the supporting electrolyte or its concentration level (Fig. 2). The change in mobility was strong within the first couple of minutes after injecting the dispersion into the sample cell. Measurement of mobility was taken following the first immediate measurement as rapidly as possible. These two points, separated by 1 minute intervals, are depicted by the solid and dotted lines (Fig. 1). The difference between these two points regardless of pH is almost constant (Fig. 1). The average mobility difference was computed and plotted as a function of supporting electrolyte concentration (Fig. 3). The specific conductance of the dispersions as function of pH valve and electrolyte concentration was measured (Fig. 4). The cell mobility profiles were determined by making the measurements at different positions in the capillary sample cell (Fig. 5). Measurements were made at intervals of 40 clock divisions (0.40mm) starting 0.1mm from one wall of the cell. The nominal diameter of the capillary used was 2.42mm as measured with the laser beams crossing in a medium of refractive index 1.33.

Discussion

The mobility measurements of polystyrene latices in two electrolyte solutions, potassium nitrate and potassium perchlorate, shared several common features. First, they did not obey the DLVO theory --- at higher electrolyte concentration, a more depressed mobility is expected. Second, there were no isoelectric points visible at all three different concentration levels. Last, the latices drifted relatively fast in 0.01M and slow in 0.001M electrolyte concentration (Fig. 1). The above features (as in Fig. 1B, solid lines) were also observed by Dr. Omatete (Fig. 6).

At low electrolyte concentration, 0.001M, an increase in mobility was found either at pH<4 or pH>10 (Fig. 1). This might be due to the increase in conductivity of the solution, and hence an increase in the surface charge of the latices in the same pH regions (Fig. 4). This phenomenon was not found in 0.01 and 0.05 M electrolyte concentrations. However, in 0.05M electrolyte concentration, a probable charge reversal happened either at pH$\cong$4 or pH$\cong$9. No experiments were carried out at pH<3 or >11 and at concentrations greater than 0.05M; beyond these regions the instability of the instrument reading was observed. The leaking to the electrode compartment from the sample cell through a membrane sealing with a teflon spacer and the bubbles either in the sample cell or in the electrode compartment also generated the instability of Zetasizer. The leaking problem may be overcome by polishing the surface of Teflon spacer. All the air bubbles in the electrode and sample cells should be carefully removed before making the measurement.

The conditioning of the sample cell by using the same sample solution is also important. The measurement was taken only after the steady reading of the cell current was reached, because the change of the cell current also leads to the change of the applied electric field of the cell. Usually the conditioning procedure took about 5 minutes.

The first measurement of the sample was started as quickly as possible; usually within 2 seconds after injecting the dispersion into the sample cell. The length of the measurement is 20 seconds. Due to the limitation of the computer software, the second measurement can only be started about 1 minute after the starting of the first measurement. The following measurements can be repeated in 40 second intervals up to 15 cycles. We found that the change in mobility was strong within the first couple of minutes after injecting the dispersion into the sample cell (Fig. 2). Mobility measurements made in low electrolyte concentration, e.g., 0.001M, appear to be less sensitive to time effects in the first minute (Fig. 3). The magnitude of mobility increase measured at potassium perchlorate concentration of 0.05M was almost 10 times of that at 0.001M concentration. The increase of the mobility may be affected by the sedimentation of the big particles or agglomerates and/or by the charging of the silica surface of the sample cell. The readings of the first measurements were consistent. The differences between them were in the range of ± 0.1 m^2/Vs. The cell mobility profiles as function of pH at a fixed electrolyte concentration were also determined (Fig. 5). The two intersection points of the three profiles with different pH values were very close to the stationary positions of the cell, 0.239 R from the wall of the capillary cell. If this finding is true, the real stationary positions of the cell can be obtained by measuring the cell mobility profiles of the dispersion with three arbitrary pH values. However, this needs more work to fully support this conclusion.

The mobility of submicron goethite obtained from The University of Wisconsin was measured at three pH values using a modified Zetasizer II. The results obtained were similar to those from a Pem Kem 3000 run at U. Wisc. (Table 1).

Conclusion

The polystyrene latex is not be recommended as a standard for electrophoretic characterization studies because (1) it does not obey the DLVO theory; (2) it does not have an isoelectric point; and (3) it has a relatively broad mobility distribution (standard deviation $\cong$ 10%).

The mobility of the particle will be measured only in the pH range 4 to 10 if possible. Beyond this range the conductivity of the solution may plan an important role at the mobility measurement, especially at low electrolyte concentrations.

To void the time effect on mobility measurement, the use of low electrolyte concentration, e.g. <0.005m, and fast measurement, e.g. <2 seconds, on samples are recommended.

According to the narrow mobility distribution (standard deviation $\cong$ 6 %) and good agreement between the mobility measurements on geothite particles by using Pem Kem 3000 and Zetasizer II, the U. Wisc. geothite particles may be chosen as a standard for electrophoretic characterization studies.

Mobility of Polystyrene Latex in Potassium Nitrate Solution

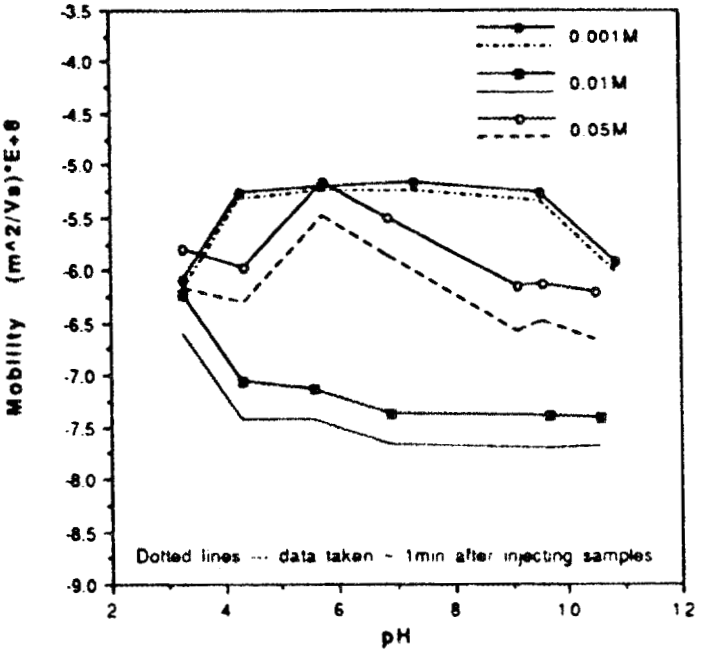

Mobility of Polystyrene Latex in Potassium Perchlorate Solution

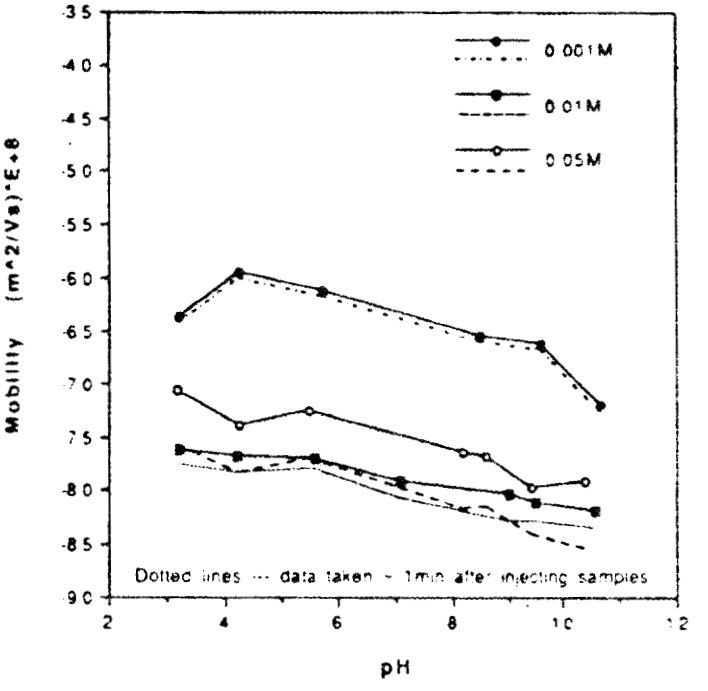

Figure 1

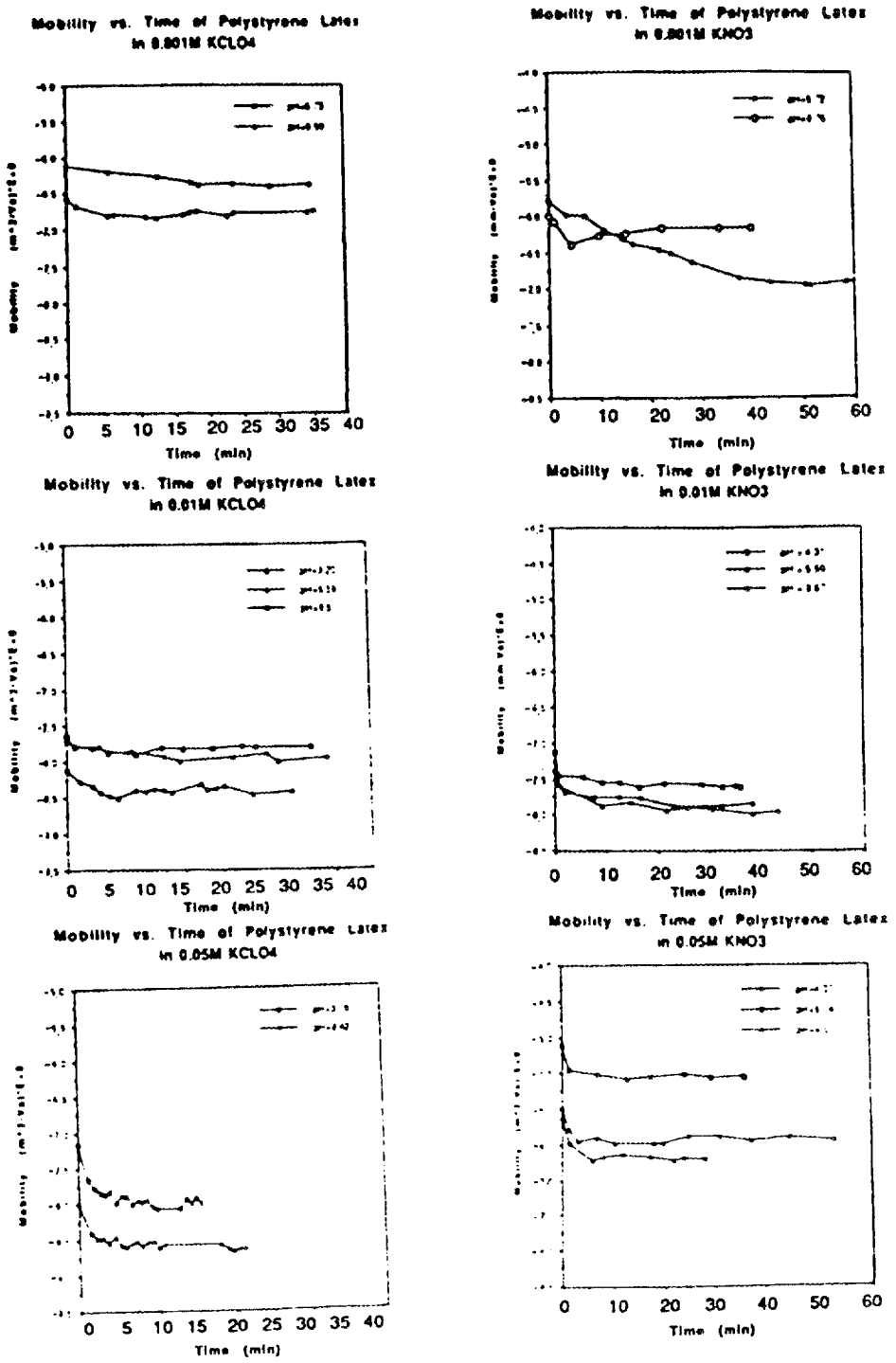
Mobility vs. Time of Polystyrene Latex in 0.001M KCLO4
Mobility vs. Time of Polystyrene Latex in 0.001M KNO3
Mobility vs. Time of Polystyrene Latex in 0.01M KCLO4
Mobility vs. Time of Polystyrene Latex in 0.01M KNO3
Mobility vs. Time of Polystyrene Latex in 0.05M KCLO4
Mobility vs. Time of Polystyrene Latex in 0.05M KNO3
Time (min)
0 5 10 15 20 25 30 35 40
0 10 20 30 40 50 60

Figure 2

Polystyrene Latex in Electrolyte Solutions

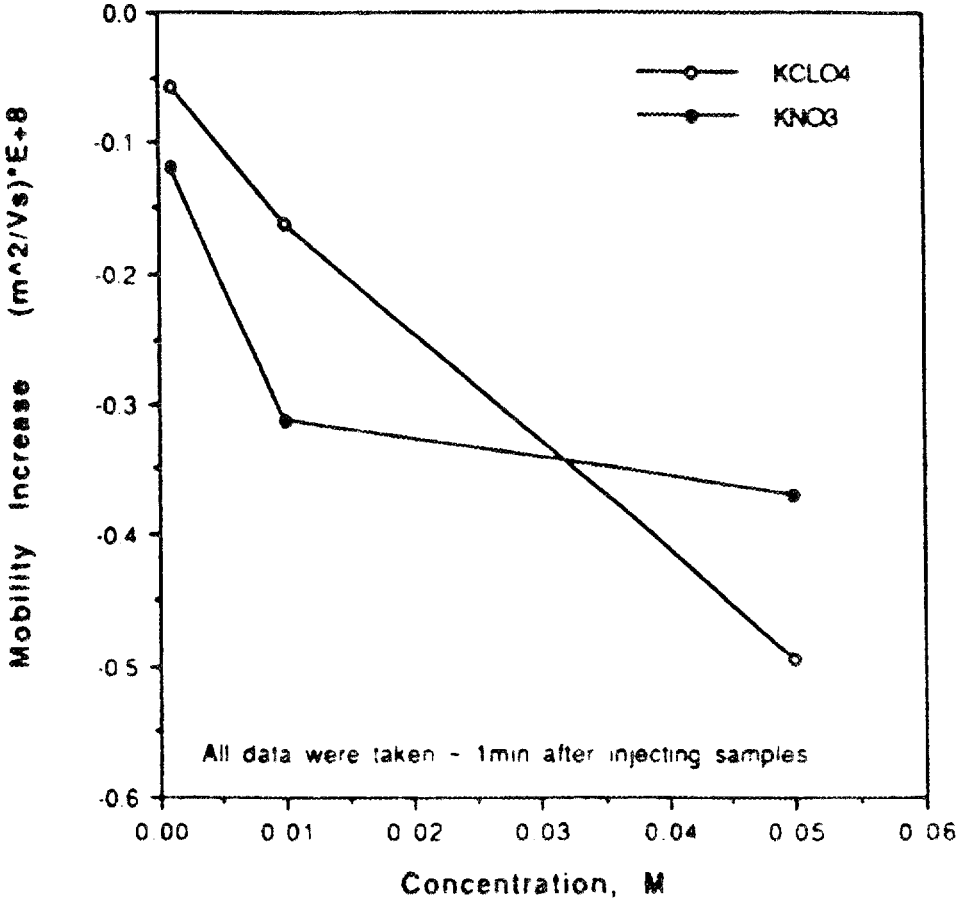

Figure 3

Specific Conductance of Polystyrene Latex in Potassium Nitrate Solution

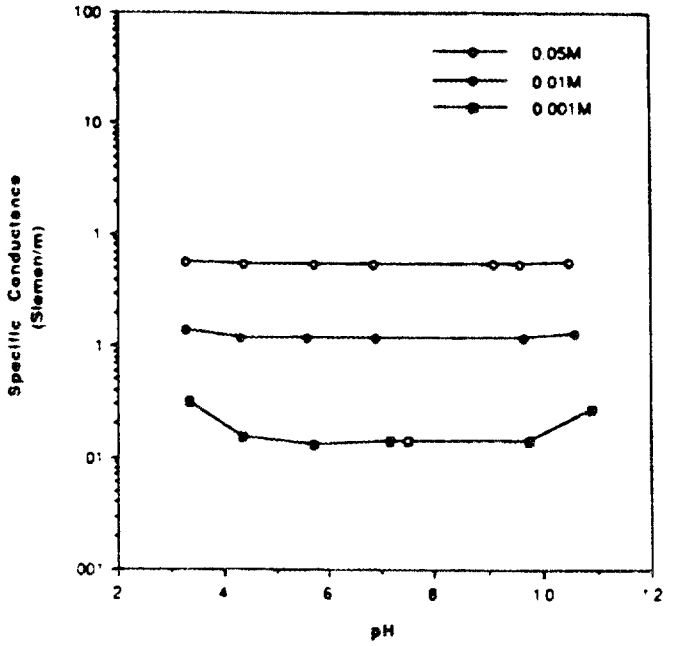

Sp. Conductance of PS Latex Suspension in Potassium Perchlorate Solution

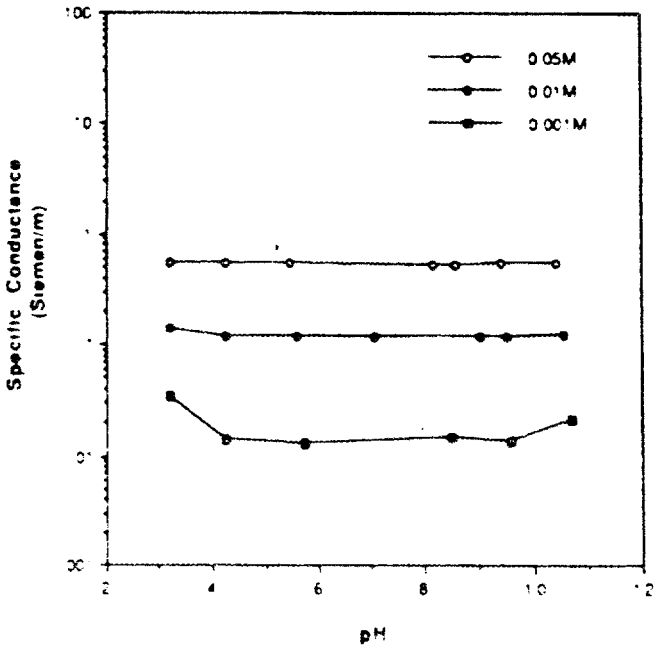

Figure 4

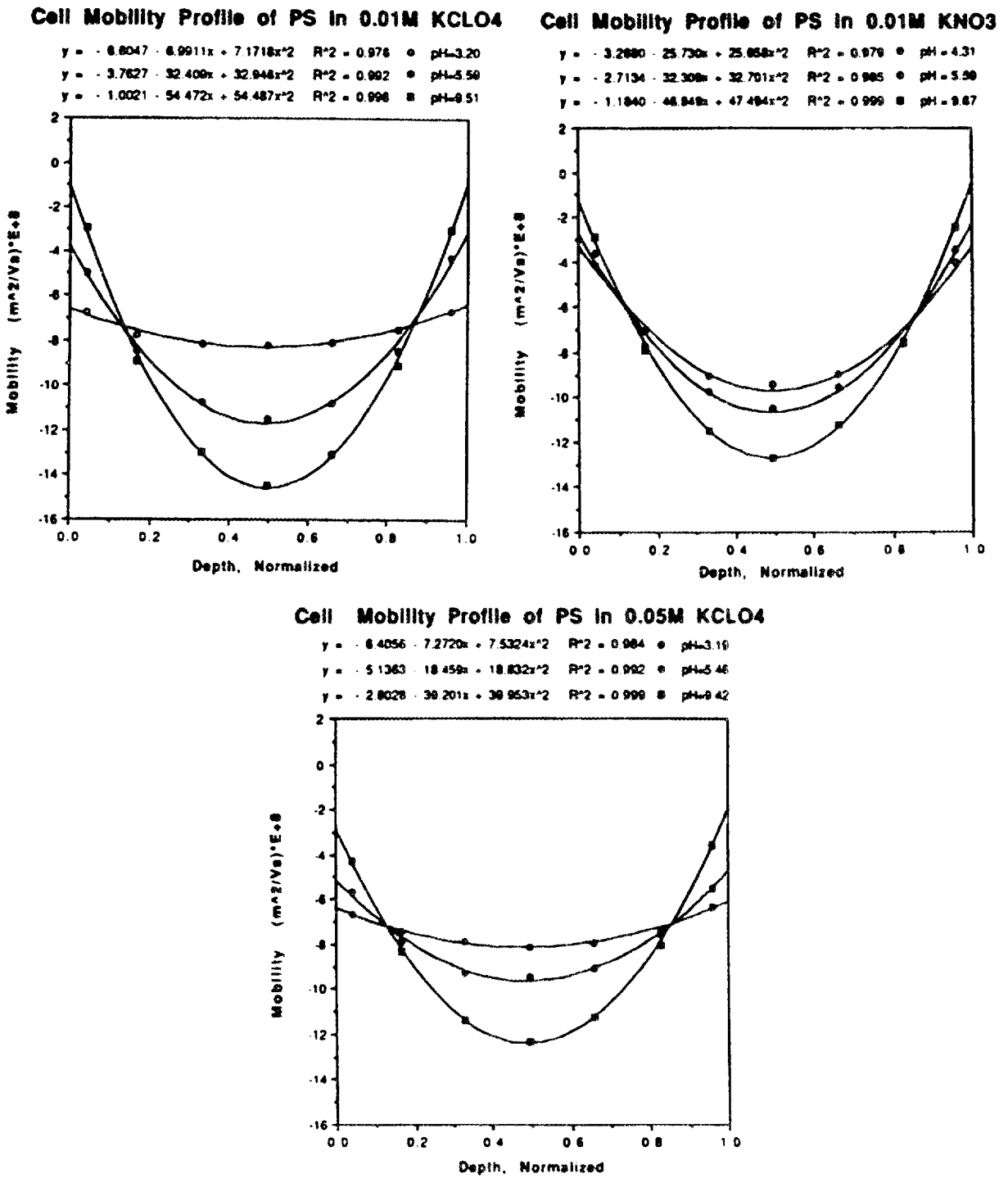
Cell Mobility Profile of PS in 0.01M KCLO4
y = - 6.6047 - 6.9911x + 7.1718x^2 R^2 = 0.976 pH=3.20
y = - 3.7627 - 32.409x + 32.948x^2 R^2 = 0.992 pH=5.59
y = - 1.0021 - 54.472x + 54.487x^2 R^2 = 0.998 pH=9.51
Mobility (m^2/Vs)*E+8
Depth, Normalized
Cell Mobility Profile of PS in 0.01M KNO3
y = - 3.2680 - 25.730x + 25.658x^2 R^2 = 0.979 pH = 4.31
y = - 2.7134 - 32.309x + 32.701x^2 R^2 = 0.985 pH = 5.59
y = - 1.1840 - 46.849x + 47.494x^2 R^2 = 0.999 pH = 9.67
Mobility (m^2/Vs)*E+8
Depth, Normalized
Cell Mobility Profile of PS in 0.05M KCLO4
y = - 6.4056 - 7.2720x + 7.5324x^2 R^2 = 0.984 pH=3.19
y = - 5.1363 - 18.459x + 18.832x^2 R^2 = 0.992 pH=5.46
y = - 2.8028 - 39.201x + 39.953x^2 R^2 = 0.999 pH=9.42
Mobility (m^2/Vs)*E+8
Depth, Normalized

Figure 5

Mobility of 2-112-19 Latex in KNO_3

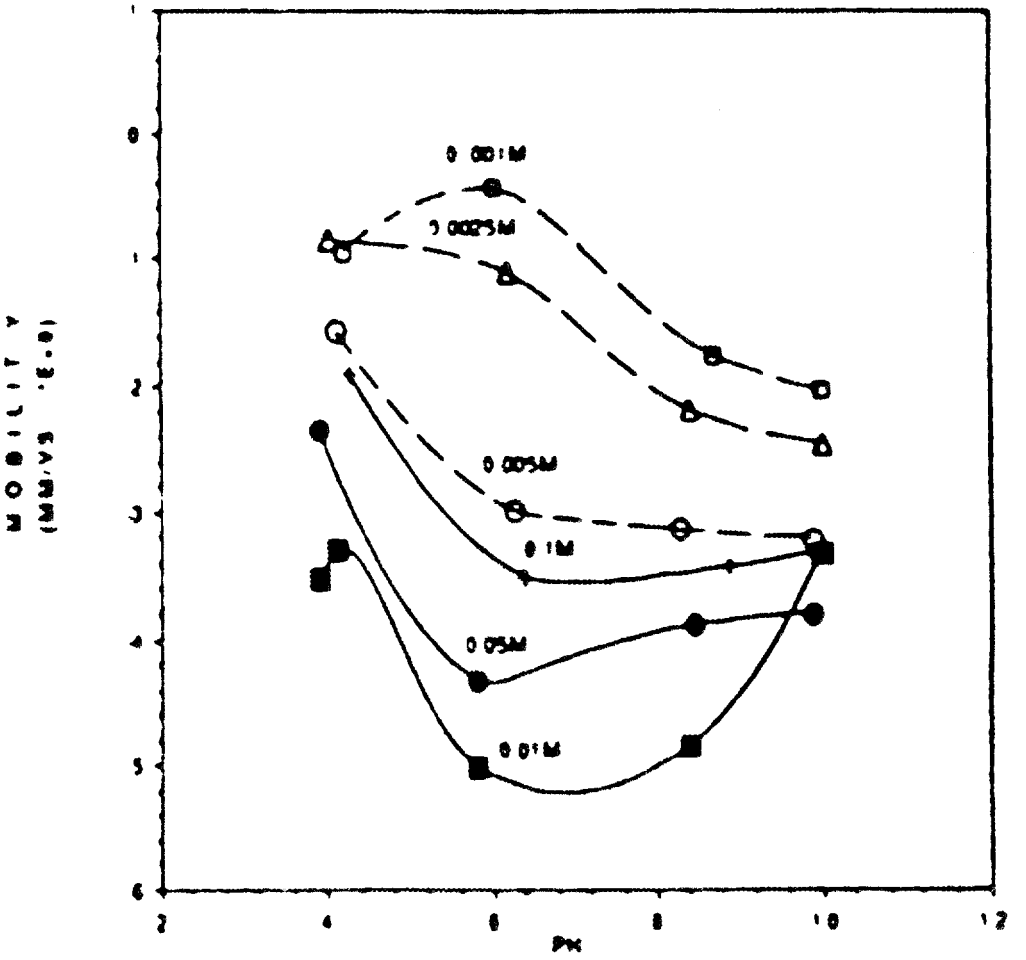

Figure 6

4.0 TECHNOLOGY TRANSFER

4.1 TECHNOLOGY TRANSFER

4.1.1 Technology Transfer

Technology Transfer
D. R. Johnson (Oak Ridge National Laboratory)

Technology transfer in the Ceramic Technology Project is accomplished by a number of mechanisms including the following:

Trade Shows - A portable display describing the program has been built and has been used at numerous national and international trade shows and technical meetings.

Newsletter - A Ceramic Technology Newsletter is published regularly and sent to a large distribution.

Reports - Semiannual technical reports, which include contributions by all participants in the program, are published and sent to a large distribution. Informal bimonthly management and technical reports are distributed to the participants in the program. Open-literature reports are required of all research and development participants.

Direct Assistance - Direct assistance is provided to subcontractors in the program via access to unique characterization and testing facilities at the Oak Ridge National Laboratory.

Workshops - Topical workshops are held on subjects of vital concern to the ceramics community.

International Cooperation - This program is actively involved in and supportive of the cooperative work being done by researchers in West Germany, Sweden, and the United States under an agreement with the International Energy Agency. That work, ultimately aimed at development of international standards includes physical, morphological, and microstructural characterization of ceramic powders and dense ceramic bodies, and mechanical characterization of dense ceramics. Detailed planning and procurement of ceramic powders and flexural test bars have been accomplished. Exchange of preliminary data on ceramic and powder characterization results has been started by those laboratories participating.

IEA Annex II Management
V. J. Tennery (Oak Ridge National Laboratory)

Objective/scope

The IEA Annex II agreement between the United States, the Federal Republic of Germany, and Sweden on structural ceramics is directed to cooperative research and development oriented to the identification and adoption of standardized methods for characterizing these materials. The original Annex II agreement included four subtasks: (1) information exchange, (2) ceramic powder characterization, (3) ceramic chemistry and structural characterization, and (4) ceramic mechanical property characterization. Each country provided selected ceramic powders and sintered structural ceramics for use in the research work in Subtasks 2, 3, and 4 in all three participating countries. Participating laboratories in all three countries agreed to share all resulting data with the purpose of using the knowledge gained from the work for developing standard measurement methods for characterizing ceramic powders and sintered structural ceramics.

The lack of such standard measurement methods has been an impediment to the evolution and development of structural ceramics, both from the point of view of the manufacturer and the user. This Annex II agreement was conceived to accelerate the development of standard methods for determining important properties of these evolving materials.

In the United States, many companies and their research staffs have contributed significant resources in performing the required measurements. In the United States, for example, in Subtask 2, twelve laboratories participated; in Subtask 3, seven laboratories participated; and in Subtask 4, eight laboratories participated.

The research in Subtask 2 included the study of five ceramic powders. For Subtasks 3 and 4, three sintered ceramics were studied, including one from each of the three countries. The ceramic from the United States was a silicon nitride, SNW-1000 from GTE-Wesgo; that from Germany was a hipped silicon carbide from ESK Kempton; and that from Sweden was a silicon nitride from ASEA Cerama.

With the approaching conclusion of Annex II research, considerable discussion has been held in the United States, Germany, and Sweden relative to possible content of continued cooperative international research similar to that conducted under the four subtasks of the original Annex II agreement. Due to the different rates at which the research in Subtasks 2, 3, and 4 has progressed, the status of these discussions differs for each subtask. The research on mechanical properties in Subtask 4 was completed first. Research on powder characterization was completed second, with the work in Subtask 3 being completed last. Research plans in the area of mechanical properties as an extension of the Annex II agreement were reviewed at the Executive Committee meeting held on November 30, 1988, in the United States. Similarly, potential plans for continued research on ceramic powders were discussed at this meeting. Results from Subtask 3 were available last, and it is not clear at this time if further research in this area will be supported as an extension of the Annex II agreement. During the past six months, the research in Subtasks 2, 3, and 4 has essentially been completed, with reports written and published from Subtasks 2 and 4. The final report for Subtask 3 has recently been received at ORNL from Sweden, and it is now scheduled for publication on October 18. The status of the research in the three subtasks, powder characterization, sintered ceramic characterization, and mechanical properties within the United States, is discussed later in this report. In addition, plans for new research on mechanical properties under a new Subtask 5 will also be discussed.

Technical progress

Subtask 2. Ceramic Powder Characterization. A U.S. Working Group Meeting was held at the National Institute of Science and Technology (NIST) on March 30. A report on the technical leader's meeting at Cocoa Beach in January was discussed along with a discussion on preparation of revised data compilation, results of statistical analysis, and technical analysis of chemical data. Various topics were discussed and will be presented to the IEA Annex II Executive Committee scheduled for June. Formulation of further guidelines for recommendations for future work, along with methods to be studied and technical plans for future collaboration, was the basis of this discussion.

At the 91st Annual Meeting of the American Ceramic Society, on April 25, the three national coordinators met to review their national positions on the state of ceramic powder characterization, and the conclusions from the meeting were used to form the basis of the report and recommendation for possible future research due to the Executive Committee from S. Hsu by June 1, 1989. This recommendation was made to the Executive Meeting in Maastricht in June. The U.S. Subtask 2 Working Group also met at Indianapolis on April 24 to review final results of the research and to discuss the status of the position of candidate industrial participants in follow-on research.

The "Conclusions and Recommendations" for Subtask 2, Powder Characterization, as prepared by the technical coordinators at this meeting, were sent out for review May 10, with comments to be returned by the end of May. These "Conclusions and Recommendations" were incorporated into a report presented by S. Hsu at the IEA Annex II Executive Committee Meeting held in Maastricht, The Netherlands, on June 21.

The photomasters for the first report from this subtask, *Characterization of Ceramic Powders: Data*, prepared by NIST, were received on June 13. The report was delivered for final printing on June 16. The completed report was received on July 26. Fifty copies of the report were shipped to Dr. Neumann in Germany and fifty copies to Dr. Pompe in Sweden on July 27. In addition, one copy was sent to each of the Subtask 2 participants in the United States. The second report in this series, which will include an analysis of the data in the first report, is scheduled for publication by the end of December 1989. On June 21, the Executive Committee voted to approve a continuation of the powder research within a new Subtask 6, following a presentation by S. Hsu of NIST of the research plan outline. The detailed plan is to be presented to the Committee at the next meeting scheduled for Dearborn, Michigan, on October 24.

The United States requested approval from Germany and Sweden in late August for permission to release the powder characterization data in the Subtask 2 report to ASTM for consideration in devising ceramic powder characterization standards. Permission was received from representatives of both Germany and Sweden, and S. Hsu of NIST will provide the data to ASTM-C-28.05.04 committee members for restricted use. Progress is continuing on the data analysis report on ceramic powders.

Subtask 3. Chemical Characterization of Sintered Ceramics. Camera-ready mats of the Subtask 3 report were received at ORNL from Mr. Michael Hatcher of KemaNord in Sweden on September 11, and following reformatting, were delivered to ORNL reproduction on September 20. Publication of this report is scheduled for October 18 and will conclude the activity under this subtask.

Subtask 4. Mechanical Properties of Ceramics. The IEA Annex II archives consisting of the three different bar types were distributed on May 23 to each of the three countries. Each set was a random sample of the total population of each bar type.

There have been discussions between the United States and Japan concerning Japanese interest in participating in Subtask 5. Representatives of Ministry of International

Trade and Industry (MITI) in Japan visited ORNL on June 12 to discuss possible cooperative research under the Annex II agreement.

Technical results from this subtask were reported in two papers given at the first meeting of the European Ceramic Society in Maastricht, The Netherlands, in June. The papers were by the author and M. K. Ferber on fractography results and by authors from Germany on statistical analysis of fracture strengths.

The two reports for this subtask were received from the Technical Publications Department. They are entitled, *Statistical Analysis of Flexure Strength Data*, and *Fractography Analysis of Silicon Nitride and Silicon Carbide Structural Ceramics*. On June 28, fifty copies each were sent to Dr. Neumann in Germany and Dr. Pompe in Sweden for distribution to their participants in this subtask. In addition, copies of these reports were sent to all U.S. participants in this subtask. The distribution of these reports essentially completes the planned activities for this subtask. Activity under this subtask is completed with publication of two reports.

Subtask 5. Tensile and Flexural Properties of Ceramics. Discussion concerning work to be done in Subtask 5 has been continuing between the United States, Germany, and Sweden. A meeting was held in Germany on May 2 to discuss German participation in future work. It was decided at that meeting that the research in Germany will include flexure testing, tensile testing, biaxial testing, and prototype component spin testing. It was decided that the research in Germany for Subtask 5 will not be of the round-robin type as before, but rather that there will be certain measurements done in some laboratories, while other laboratories will do other measurements. Here in the United States a more internal uniformity will be used, where each laboratory will do much the same mechanical property measurements as the other U.S. laboratories. A meeting in Sweden was held May 25 to discuss their final agreement with the United States and Germany on future research. Sweden is planning to participate in tensile strength research along with flexure strength measurement research. Their proposal was presented to the IEA Executive Committee in Maastricht. On June 21, the Executive Committee voted to approve new research plans on mechanical properties from Germany, Sweden, and the United States. The research proposals were presented by Dr. Vierkorn-Rudolph (Germany), Mr. Michael Hatcher (Sweden), and Dr. Victor Tennery (United States). This research will henceforth be identified as part of a new Subtask 5. It was also agreed by representatives of the three countries that Japan would be formally invited to participate in both Subtask 5 on mechanical properties and Subtask 6 on ceramic powders. It was agreed at the meeting in Europe on June 21 that Mr. A. A. Chesnes of the DOE would send a formal letter of invitation to MITI in Japan for participation in the new subtasks in Annex II.

A common theme for this research will be flexure and tensile strength measurements on a structural ceramic selected and studied by each participating country. Relative to U.S. participation, the DOE has authorized procurement of room-temperature flexure fixtures and alignment jigs, along with flexure specimens and the blanks for the tensile specimens from a U.S. manufacturer. Garrett GN-10 silicon nitride has been selected for all U.S. research included in Subtask 5. A specification for 160 GN-10 silicon nitride rods was completed by the author, and the procurement process started. Delivery of the rods will start in December and be completed by early spring. Plates of GN-10 have been ordered and will be machined into flexure specimens. Grinding of the tensile specimens will be done at ORNL.

A request was received from Germany to determine if a U.S. laboratory would be willing to determine the tensile strength of about 10 tensile specimens of the silicon nitride, selected by Germany for Subtask 5, if the specimens were ground to our desired dimensions. This was agreed to by letter on August 10, and ORNL will measure the German specimens with strain gauges applied to all specimens. On August 23, a letter was received from Dr. A. Moreno of ENEA in Italy regarding the possibility of Italy joining the present Annex II agreement. A letter was returned explaining the agreements reached by

the Executive Committee relative to new member countries at the June meeting in Maastricht. On September 27, DOE received a formal reply from Japan, stating that Japan will join Subtask 5. The Japanese research proposal was included, which is essentially identical to the United States research plan, and includes both flexural and tensile strength measurements. Notification of these later developments were sent by letter to the nine U.S. laboratories besides ORNL who will be participating in Subtask 5.

It is anticipated that the flexure specimens of GN-10 will be ready for starting the room-temperature strength measurements sometime in December.

Publications

1. *Statistical Analysis of Flexure Strength Data, IEA Annex II, Subtask 4*, by A. Brückner Foit and D. Munz, Institut für Zuverlässigkeit und Schadenskunde im Maschinenbau, University of Karlsruhe, Karlsruhe, West Germany, published by ORNL in June 1989.

2. *Fractography Analysis of Silicon Nitride and Silicon Carbide Structural Ceramics, IEA Annex II, Subtask 4*, by M. K. Ferber, High Temperature Materials Laboratory, Oak Ridge National Laboratory, June 1989.

3. *Characterization of Ceramic Powders: Data, IEA Annex II, Subtask 2*, by A. L. Dragoo, S. G. Malghan, L. -S. H. Lum, S. M. Hsu, and R. Munro, Ceramics Division, National Institute of Standards and Technology, published by ORNL in July 1989.

References

None.

Standard Reference Materials

S. G. Malghan, A. L. Dragoo, L. S. Lum, D. B. Minor, J. F. Kelly, and J. P. Cline (National Institute of Standards and Technology)

Objective/Scope

Ceramics have been successfully employed in engines on a demonstration basis. The successful manufacture and use of ceramics in advanced engines depends on the development of reliable materials that will withstand high, rapidly varying thermal stress loads. Improvement in the characterization of ceramic starting powders is a critical factor in achieving reliable ceramic materials for engine applications. The production and utilization of such powders require characterization methods and property standards for quality assurance.

The objectives of the NBS program are (1) to assist with the division and distribution of five ceramic starting powders for an international round-robin on powder characterization; (2) to provide reliable data on physical (dimensional), chemical and phase characteristics of two silicon nitride powders: a reference and a test powder; and (3) to conduct statistical assessment and modeling of round-robin data. This program is directed toward a critical assessment of powder characterization methodology and toward establishment of a basis for the evaluation of fine powder precursors for ceramic processing. This work will examine and compare by a variety of statistical means the various measurement methodologies employed in the round-robin and the correlations among the various parameters and characteristics evaluated. The results of the round-robin are expected to provide the basis for identifying measurements for which Standard Reference Materials are needed and to provide property and statistical data which will serve the development of internationally accepted standards.

Technical Progress

The technical progress covered in this report includes descriptions of work on the preparation of powder samples for the IEA/ANNEX II, Subtask 2, powder characterization round-robin and of the compilation and analysis of round-robin data.

Division, Distribution and Certification of Ceramic Starting Powders. This phase of the work is completed.

Powder Characterization. Characterization of powders for the Subtask 2 round-robin was completed during the previous reporting period. A statistically designed study on the influence of sample preparation parameters on particle size distribution measurements by x-ray sedimentation (Sedigraph by Micromeritics) has been in progress. This study is conducted in order to provide assistance in the interpretation of the interlaboratory-comparison data and to

the design of experiments of the proposed Subtask 6 (continuation of Subtask 2) intended to test the Sedigraph measurements.

Particle Size Distribution Measurement Parameters. Of the numerous variables, three major parameters -- types of dispersant, ultrasonication power, and ultrasonication time; were examined. Ube's SNE-10 silicon nitride powder was used as a model system, though the results will be applicable to similar silicon nitride powders. Based on the current data available, the following observations are appropriate:

- Quantity of ultrasonication energy (power x time) plays an important role, as long as suitable dispersant is utilized. An appropriate quantity of ultrasonication energy has to be utilized to obtain reproducible particle size distribution. In Figure 1, data on two samples of the Ube's SNE-10 powder are presented in which two levels of ultrasonication energy (3 watts for 3 min and 15 watts for 9 min) were applied using a probe device. Though the range of energy application in this example is fairly large, it is within the range of laboratory practice. These data show a significant change in particle size distribution as a function of sample preparation parameters. An overall difference of 0.2 micron in d_{50} was observed in this example. This difference is not considered to be insignificant, when examined in terms of ball milling time to achieve a d_{50} of 0.75 vs 0.55 micron or sintering time-temperature schedule for two powders of this type of difference in size distribution.

Experiments are in progress to define an optimum set of parameters for particle size distribution measurement by the use of Sedigraph.

Data Analysis. At the IEA meeting in Maastricht, Netherlands, in June 1989, progress of the data analysis task was described. Subsequent to that meeting, in July 1989, the first report on Subtask 2, "Ceramic Powders Characterization-Data" was released. This report covers only the data and simple statistical treatment of the data. Several examples of variation of measurement parameters of powder characteristics are presented. This report has been sent to all 25 participants of the Subtask 2 in Germany, Sweden and U.S.A.

Second report on Subtask 2 is in preparation, ready for publication in December 1989. This report contains technical analysis of the data, procedures used in obtaining the data, data and recommendations. Alan Dragoo has been the primary editor of this report, with assistance from other technical leaders: H. Hausner, FRG; R. Pompe, Sweden. All the sections have been written and reviewed by the technical leaders. Currently, several chapters are being edited to incorporate inputs of the technical leaders.

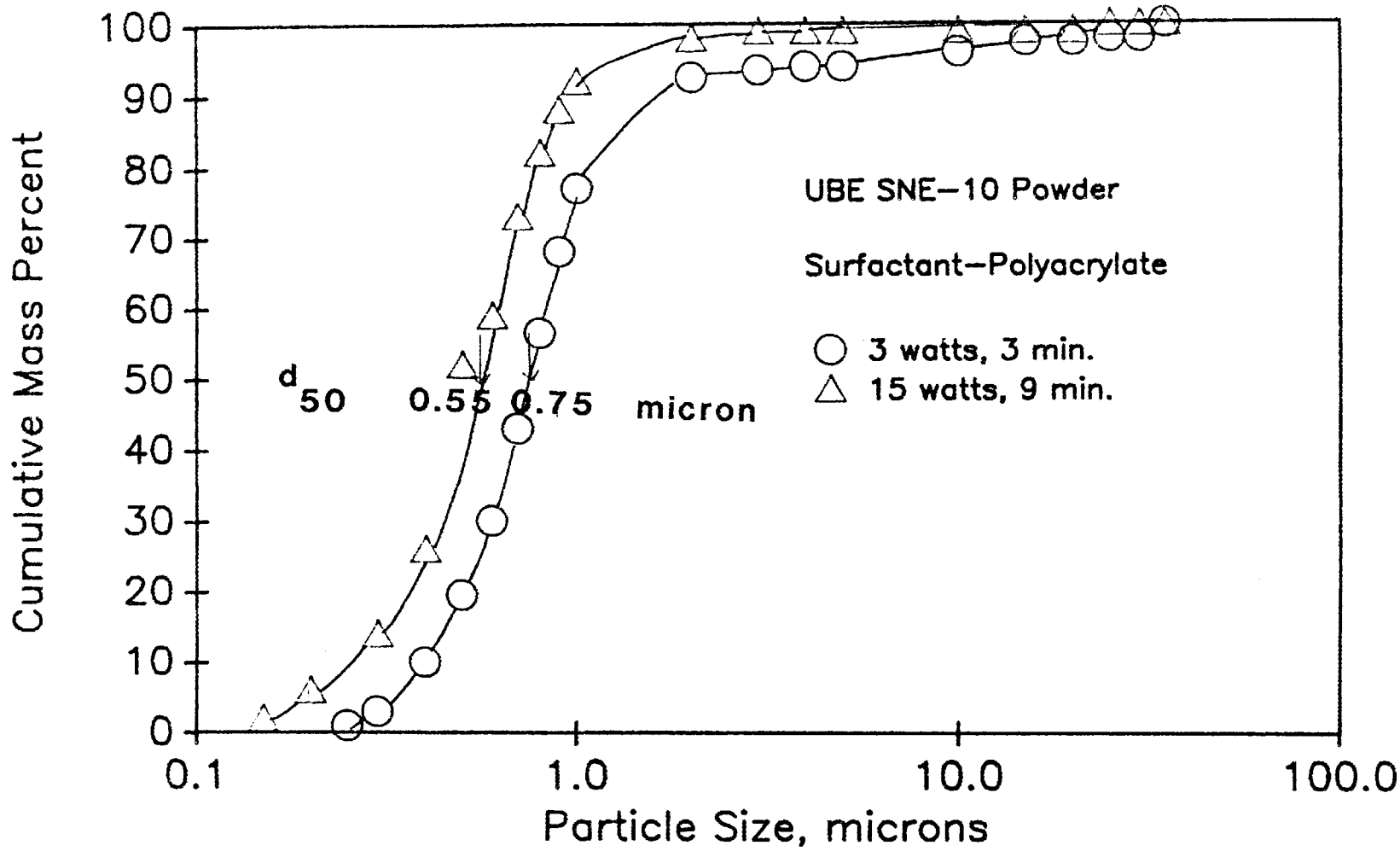

Figure 1. Effect of sample preparation parameters on the measurement of particle size distribution of silicon nitride powder by x-ray sedigraph.

Status of Milestone

Task 1. Subtask A and B are completed. Subtask C, intermediate milestones 411603 and 411604 have shown slippage due to larger than anticipated quantity of revisions and analysis.

Certain commercial equipment, instruments and materials may be identified in this report in order to adequately specify the experimental procedure. Such identification does not imply recommendation or endorsement by the National Institute of Standards and Technology, nor does it imply that the materials or equipment identifies are necessarily the best available for the purpose.

INTERNAL DISTRIBUTION

1-2. Central Research Library
3. Document Reference Section
4-5. Laboratory Records Department
6. Laboratory Records, ORNL RC
7. ORNL Patent Section
8-10. M&C Records Office
11. L. F. Allard, Jr.
12. B. R. Appleton
13. R. L. Beatty
14. P. F. Becher
15. T. M. Besmann
16. P. J. Blau
17. A. Bleier
18. E. E. Bloom
19. K. W. Boling
20. R. A. Bradley
21. C. R. Brinkman
22. V. R. Bullington
23. R. S. Carlsmith
24. P. T. Carlson
25. G. M. Caton
26. R. H. Cooper, Jr.
27. S. A. David
28. J. H. DeVan
29. J. I. Federer
30. M. K. Ferber
31. W. Fulkerson
32. R. L. Graves
33. D. L. Greene
34. M. A. Janney
35-39. D. R. Johnson
40. R. R. Judkins
41. M. A. Karnitz
42. H. D. Kimrey, Jr.
43. T. G. Kollie
44. T. B. Lindemer
45. K. C. Liu
46. E. L. Long, Jr.
47. W. D. Manly
48. R. W. McClung
49. D. L. McElroy
50. J. R. Merriman
51. A. J. Moorhead
52. T. A. Nolan
53. J. L. Rich
54. C. R. Richmond
55. J M Robbins
56. M. Rohr
57. M. W. Rosenthal
58. M. L. Santella
59. A. C. Schaffhauser
60. G. M. Slaughter
61. W. B. Snyder, Jr.
62. E. J. Soderstrom
63. D. P. Stinton
64. R. W. Swindeman
65. V. J. Tennery
66. T. N. Tiegs
67. J. R. Weir, Jr.
68. F. W. Wiffen
69. R. K. Williams
70. S. G. Winslow
71. C. S. Yust

EXTERNAL DISTRIBUTION

72. Donald F. Adams
University of Wyoming
Mechanical Engineering
Department
Laramie, WY 82071

73. Jane W. Adams
Corning Glass Works
SP-DV-21
Corning, NY 14831

74. J. Ahmad
Battelle Columbus Laboratories
Engineering Mechanics Department
505 King Avenue
Columbus, OH 43201-2693

75. Richard L. Allor
Ford Motor Company
Material Systems
Reliability Division
20000 Rotunda Drive
Post Office Box 2053
Dearborn, MI 48121-2053

76. Richard T. Alpaugh
U.S. Department of Energy
Office of Transportation
Technologies
1000 Independence Avenue, S.W.
Forrestal Building CE-322
Washington, DC 20585

77. Norman C. Anderson
Ceradyne, Inc.
Ceramic-to-Metal Division
3169 Redhill Avenue
Costa Mesa, CA 92626

78. H. Arbabi
Brunel University
Department of Materials
Technology
Uxbridge Middlesex UB8 3PH
UNITED KINGDOM

79. V. S. Avva
NC A&T State University
Department of Mechanical
Engineering
Greensboro, NC 27411

80. Michel Badia
Embassy of France
4101 Reservoir Road, S.W.
Washington, DC 20007-2176

81. Kirit J. Bahnsali
U.S. Army Materials
Technology Laboratory
SLCMT-EMM
405 Arsenal Street
Watertown, MA 02172

82. John M. Bailey
Caterpillar Inc.
Research Department
Technical Center
Building L
Post Office Box 1875
Peoria, IL 61656-1875

83. Murray Bailey
NASA Lewis Research Center
21000 Brookpark Road
MS:77-6
Cleveland, OH 44135

84. R. R. Baker
Ceradyne, Inc.
3169 Red Hill Avenue
Costa Mesa, CA 92626

85. J. Gary Baldoni
GTE Laboratories Inc.
40 Sylvan Road
Waltham, MA 02254

86. P. M. Barnard
Ruston Gas Turbines Limited
New Products Division
Firth Road
Lincoln LN6 7AA
ENGLAND

87. A. L. Bement, Jr.
TRW, Inc.
23555 Euclid Avenue
Cleveland, OH 44117

88. M. Bentele
Xamag, Inc.
259 Melville Avenue
Fairfield, CT 06430

89. Clifton G. Bergeron
University of Illinois
Department of Ceramic Engineering
105 South Goodwin Avenue
204 Ceramic Building
Urbana, IL 61801

90. Deane I. Biehler
Caterpillar Inc.
Engineering and Research Materials
Technical Center, Building E
Post Office Box 1875
Peoria, IL 61656-1875

91. William D. Bjorndahl
TRW, Inc.
Materials Characterization and Chemical Analysis Department
One Space Park
Building 01, Room 2060
Redondo Beach, CA 90278

92. Dan Blake
Solar Energy Research Institute
1617 Cole Boulevard
Golden, CO 80401

93. Keith Blandford
Boride Products, Inc.
2879 Aero Park Drive
Traverse City, MI 49684

94. Paul N. Blumberg
Ricardo-ITI
415 East Plaza Drive
Westmont, IL 60559

95. Tibor Bornemisza
Sundstrand Turbomach
Division of Sundstrand Corporation
4400 Ruffin Road
Post Office Box 85757
San Diego, CA 92138-5757

96. Han Juergen Bossmeyer
BMW Technologies, Inc.
Watermill Center
800 South Street
Waltham, MA 02154

97. J. A. M. Boulet
University of Tennessee
310 Perkins Hall
Knoxville, TN 37996

98. Les J. Bowen
GTE Laboratories, Inc.
40 Sylvan Road
Waltham, MA 02254

99. Steve Bradley
Signal UOP Research Center
50 UOP Plaza
Des Plaines, IL 60016-6187

100. Raymond J. Bratton
Westinghouse Electric Corporation
R&D Center
1310 Beulah Road
Pittsburgh, PA 15235

101. Catherine E. Brown
E. I. DuPont de Nemours & Company, Inc.
Experimental Station Information Center
E302/301
Wilmington, DE 19898

102. J. J. Brown
Virginia Polytechnic Institute and State University
Department of Materials Engineering
Blacksburg, VA 24061

103. S. L. Bruner
Ceramatec, Inc.
2425 South 900 West
Salt Lake City, UT 84119

104. W. Bryzik
U.S. Army Tank Automotive Command
R&D Center
Propulsion Systems Division
Warren, MI 48090

105. S. T. Buljan
GTE Laboratories Inc.
40 Sylvan Road
Waltham, MA 02254

106. John M. Byrne, Jr.
PPG Industries, Inc.
Corporate Development Department
One PPG Place
Pittsburgh, PA 15272

107. Donald J. Campbell
Air Force Wright Aeronautical Laboratory
AFWAL/POX
Wright-Patterson AFB, OH 45433

108. Roger Cannon
Rutgers University
Department of Ceramics
Bowser Road
Post Office Box 909
Piscataway, NJ 08855-0909

109. Harry W. Carpenter
19945 Acre Street
Northridge, CA 91324

110. David Carruthers
Allied-Signal Aerospace Company
Garrett Auxiliary Power Division
2739 East Washington Street
Post Office Box 5227
Phoenix, AZ 85010

111. Jere G. Castor
J. C. Enterprise
5078 North 83rd Street
Scottsdale, AZ 85253

112. En-sheng Chen
B&C Engineering Research
13906 Dentwood Drive
Houston, TX 77014

113. Albert A. Chesnes
U.S. Department of Energy
Office of Transportation Technologies
1000 Independence Avenue, S.W.
Forrestal Building CE-30, 5G-048
Washington, DC 20585

114. Frank Childs
EG&G, Inc.
Idaho National Engineering Laboratory
Post Office Box 1625
Idaho Falls, ID 83415

115. Gilbert Y. Chin
Bell Telephone Laboratories
R&D
Murray Hill, NJ 07974

116. Melvin H. Chiogioji
U.S. Department of Energy
Office of Transportation Technologies
1000 Independence Avenue, S.W.
Forrestal Building CE-22
Washington, DC 20585

117. William J. Chmura
Torrington Company
Corporate Research
59 Field Street
Torrington, CT 06790

118. Eugene V. Clark
Turbine Metal Technology, Inc.
7327 Elmo Street
Tujunga, CA 91042-2204

119. William L. Cleary
ORI, Inc.
1375 Piccard Drive
Rockville, MD 20850

120. W. J. Clegg
ICI Advanced Materials
Post Office Box 11
The Heath, Runcorn Chesire
WA7 4QE
ENGLAND

121. Jack L. Clem
J. M. Huber Corporation
Carbon Black Division
Post Office Box 2831
Borger, TX 79008-2831

122. Harry E. Cook
Chrysler Motors Corporation
Automotive Research
and Technical Planning
1200 Chrysler Drive
Highland Park, MI 48288-1118

123. Stephen Copley
University of Southern California
Materials Science Department
Los Angeles, CA 90089-0241

124. John A. Coppola
Carborundum Company
Post Office Box 1054
Niagara Falls, NY 14302

125. Normand D. Corbin
Norton Company
Advanced Ceramics
Goddard Road
Northboro, MA 01532-1545

126. Charles H. Craig
Defense Technology Security
400 Army-Navy Drive, Suite 300
Arlington, VA 22202

127. William J. Croft
U.S. Army Materials
Technology Laboratory
405 Arsenal Street
Watertown, MA 02172

128. Gary M. Crosbie
1430 Culver Avenue
Dearborn, MI 48121

129. Floyd W. Crouse, Jr.
U.S. Department of Energy
Morgantown Energy
Technology Center
Collins Ferry Road
Post Office Box 880
Morgantown, WV 26505

130. Raymond Cutler
Ceramatec, Inc.
2425 South 900 West
Salt Lake City, UT 84119

131. David A. Dalman
Dow Chemical Company
Central Research, Organic Specialties
1776 Building
Midland, MI 48674

132. James I. Dalton
Reynolds Metals Company
Metallurgy Laboratory
Fourth and Canal Streets
Post Office Box 27003
Richmond, VA 23219

133. Stephen C. Danforth
Rutgers University
Bowser Road
Post Office Box 909
Piscataway, NJ 08854

134. Robert F. Davis
North Carolina State University
Materials Engineering Department
232 Riddick Laboratory
Post Office Box 7907
Raleigh, NC 27695

135. Evelyn M. DeLiso
Corning Glass Works
Corning, NY 14831

136. J. Franklyn DeRidder
Omni Electro Motive, Inc.
12 Seely Hill Road
Newfield, NY 14867

137. Keith F. Dufrane
Battelle Columbus Laboratories
505 King Avenue
Columbus, OH 43201

138. Edmund M. Dunn
Texel Company
21 Eire Street
Cambridge, MA 02139

139. Jeremy D. Dunning
Indiana University
Industrial Research
Liaison Program
Bloomington, IN 47405

140. Sunil Dutta
NASA Lewis Research Center
21000 Brookpark Road
MS:49-3
Cleveland, OH 44135

141. Paul N. Dyer
Air Products and Chemicals, Inc.
Post Office Box 538
Allentown, PA 18105

142. Robert J. Eagan
Sandia National Laboratories
Department 1840
Post Office Box 5800
Albuquerque, NM 87185

143. Christopher A. Ebel
Norton Company
Advanced Ceramics
Goddard Road
Northboro, MA 01532-1545

144. J. J. Eberhardt
U.S. Department of Energy
Office of Advanced Transportation
Materials
1000 Independence Avenue, S.W.
Forrestal Building CE-12
Washington, DC 20585

145. William A. Ellingson
Argonne National Laboratory
9700 South Cass Avenue
Argonne, IL 60439

146. Charles D. Estes
U.S. Senate
Committee on Appropriations
SD-152 Dirksen Senate
Office Building
Washington, DC 20510

147. John N. Eustis
U.S. Department of Energy
Office of Industrial Technologies
1000 Independence Avenue, S.W.
Forrestal Building CE-221
Washington, DC 20585

148. Peggy Evanich
National Aeronautics
and Space Administration
Energy Systems Office
Washington, DC 20546

149. Anthony G. Evans
University of California
College of Engineering
Santa Barbara, CA 93106

150. Robert C. Evans
NASA Lewis Research Center
Vehicular Gas Turbine and
Diesel Project Office
21000 Brookpark Road
MS:77-6
Cleveland, OH 44135

151. Katherine T. Faber
Ohio State University
Ceramic Engineering
Department
2041 College Road
Columbus, OH 43210

152. John W. Fairbanks
U.S. Department of Energy
Office of Transportation
Technologies
1000 Independence Avenue, S.W.
Forrestal Building CE-151, 5G-042
Washington, DC 20585

153. Larry Farrell
Babcock and Wilcox
Old Forrest Road
Lynchburg, VA 24505

154. Rolf Fasth
Chem Systems, Inc.
303 South Broadway
Tarrytown, NY 10591

155. H. W. Foglesong
Dow Corning Corporation
3901 South Saginaw Road
Midland, MI 48686

156. Thomas F. Foltz
Avco Corporation
Special Materials Division
Two Industrial Avenue
Lowell, MA 01851

157. Robert G. Frank
Technology Assessment Group
10793 Bentley Pass Lane
Cincinnati, OH 45140

158. Douglas W. Freitag
LVT Missiles and Electronics
Group
Post Office Box 650003
Dallas, TX 75265-0003

159. P. A. Gaydos
Battelle Columbus Laboratories
505 King Avenue
Columbus, OH 43201

160. George E. Gazza
U.S. Army Materials
Technology Laboratory
Ceramics Research Division
405 Arsenal Street
Watertown, MA 02172-0001

161. Bruce W. Gerhold
Phillips Petroleum Company
Engineering Materials, R&D
91-G, PRC
Bartlesville, OK 74004

162. Charles M. Gilmore
George Washington University
Civil, Mechanical, and Environmental
Engineering
Washington, DC 20052

163. Paul Glance
Concept Analysis
R&D
950 Stephenson Highway
Dupont Automotive Development
Building
Troy, MI 48007-7013

164. Fred M. Glaser
U.S. Department of Energy
Office of Fossil Energy
FE-14 GTN
Germantown, MD 20545

165. Joseph W. Glatz
Naval Air Propulsion Test Center
Systems Technology Division
Post Office Box 7176, PE 34
Trenton, NJ 08628

166. W. M. Goldberger
Superior Graphite Company
R&D
2175 East Broad Street
Columbus, OH 43209

167. Stephen T. Gonczy
Signal UOP Research Center
Materials Science Department
50 UOP Plaza
Des Plaines, IL 60016-6187

168. Robert J. Gottschall
U.S. Department of Energy
Office of Material Sciences
ER-131 GTN, MS:G-256
Germantown, MD 20545

169. Earl Graham
Cleveland State University
Department of Chemical Engineering
Euclid Avenue at East 24th Street
Cleveland, OH 44115

170. Kenneth Green
Coors Ceramics Company
17750 West 32nd Street
Golden, CO 80401

171. Robert E. Green, Jr.
Johns Hopkins University
Center for Nondestructive Evaluation
Maryland Hall 107
Baltimore, MD 21218

172. Lance E. Groseclose
General Motors Corporation
Allison Gas Turbine Division
Post Office Box 420
Indianapolis, IN 46206-0420

173. P. Ulf Gummeson
Hoeganaes
R&D
River Road and Taylors Lane
Riverton, NJ 08077

174. Bimleshwar P. Gupta
Solar Energy Research Institute
Solar Heat Research Division
1617 Cole Boulevard
Golden, CO 80401

175. M. D. Gurney
NIPER
Post Office Box 2128
Bartlesville, OK 74005

176. John P. Gyekenyesi
NASA Lewis Research Center
21000 Brookpark Road
MS:49-7
Cleveland, OH 44135

177. J. J. Habeeb
Esso Petroleum Canada
Research Division
Post Office Box 3022
Sarina Ontario N7T 7MI
CANADA

178. H. T. Hahn
Pennsylvania State University
ESM Department
227 Hammond Building
University Park, PA 16802

179. Nabil S. Hakim
Detroit Diesel Corporation
13400 West Outer Drive West
Detroit, MI 48239

180. Friedrich Harbach
Asea Brown Boveri AG
Department of Functional Ceramics
Eppelheimer Strasse 82
D-6900 Heidelberg 1
WEST GERMANY

181. Kay Hardman-Rhyne
DARPA
1400 Wilson Boulevard
Arlington, VA 22209

182. R. A. Harmon
25 Schalren Drive
Latham, NY 12110

183. Stephen D. Hartline
Norton Company
Advanced Ceramics
Goddard Road
Northboro, MA 01532-1545

184. Michael H. Haselkorn
Caterpillar Inc.
Engineering Research Materials
Technical Center, Building E
Post Office Box 1875
Peoria, IL 61656-1875

185. Willard E. Hauth
Dow Corning Corporation
Composite Development Ceramics Program
3901 South Saginaw Road
Midland, MI 48640

186. Kevin L. Haynes
McDonnell Douglas Astronautics Company
Post Office Box 516, MS:107/1
St. Louis, MO 63166

187. Norman L. Hecht
University of Dayton Research Institute
300 College Park
Dayton, OH 45469-0001

188. S. S. Hecker
Los Alamos National Laboratory
Material Science and Technology Division, G-756
Post Office Box 1663
Los Alamos, NM 87545

189. Peter W. Heitman
General Motors Corporation
Allison Gas Turbine Division
Post Office Box 420, W-5
Indianapolis, IN 46206-0420

190. Richard L. Helferich
The Duriron Company, Inc.
Post Office Box 1145
Dayton, OH 45401

191. H. E. Helms
General Motors Corporation
Allison Gas Turbine Division
Post Office Box 420
Indianapolis, IN 46206-0420

192. Thomas L. Henson
GTE Products Corporation
Chemical & Metallurgical Division
Hawes Street
Towanda, PA 18848-0504

193. Thomas P. Herbell
NASA Lewis Research Center
21000 Brookpark Road
MS:49-3
Cleveland, OH 44135

194. Hendrik Heystek
Bureau of Mines
Tuscaloosa Research Center
Post Office Box L
University, AL 35486

195. Robert V. Hillery
General Electric Company
One Neumann Way
Post Office Box 156301
Cincinnati, OH 45215

196. Jonathan W. Hinton
Carborundum Company
Structural Ceramics Division
Post Office Box 1054
Niagara Falls, NY 14302

197. Joe Homeny
University of Illinois
Department of Materials Science and Engineering
105 South Goodwin Avenue
Ceramics Building
Urbana, IL 61801

198. A. T. Hopper
Battelle Columbus Laboratories
Engineering Mechanics Department
505 King Avenue
Columbus, OH 43201-2693

199. George Hsu
Jet Propulsion Laboratory
4800 Oak Grove Drive
MS:512-103
Pasadena, CA 91109

200. Shih Hsu
Digital Equipment Corporation
77 Reed Road
MS:HL02-1/L8
Hudson, MA 01749-2895

201. Stephen M. Hsu
National Institute of Standards and Technology
Institute for Materials Science and Engineering
Gaithersburg, MD 20899

202. Harold A. Huckins
Princeton Advanced Technology, Inc.
56 Finley Road
Princeton, NJ 08540

203. Fred Huettic
Advanced Ceramic Technology, Inc.
17 Deerfield Road
East Brunswick, NJ 08816

204. O. Richard Hughes
Celanese Research Company
86 Morris Avenue
Summit, NJ 07901

205. Joseph E. Hunter, Jr.
General Motors Corporation
Research Labs
Metallurgy Department
12 Mile and Mound Roads
Warren, MI 48090-9055

206. Louis C. Ianniello
U.S. Department of Energy
Office of Material Sciences
ER-13 GTN
Germantown, MD 20545

207. Robert H. Insley
Champion Spark Plug Company
Ceramic Division
20000 Conner Avenue
Detroit, MI 48234

208. Curtis A. Johnson
General Electric Company
Ceramics Branch, Physical Chemistry
Post Office Box 8, K1/3C7
Schenectady, NY 12301

209. Larry Johnson
Argonne National Laboratory
Center for Transportation Research
9700 South Cass Avenue, Bldg. 362
Argonne, IL 60439

210. L. A. Joo
Great Lakes Research Corporation
Post Office Box 1031
Elizabethton, TN 37643

211. A. David Joseph
Sealed Power Corporation
R&D
100 Terrace Plaza
Muskegon, MI 49443

212. Debra Joslin
University of Tennessee
Metallurgical Engineering Department
Knoxville, TN 37996

213. Adam Jostsons
Australian Nuclear Science & Technology Organisation
Lucas Heights Research Laboratories
New Illawarra Road
Lucas Heights, New South Wales
AUSTRALIA

214. Roy Kamo
Adiabatics, Inc.
630 South Mapleton
Columbus, IN 47201

215. Allan Katz
Air Force Wright Aeronautical Laboratory
Metals and Ceramics Division
Materials Laboratory
AFWAL/MLLM
Wright-Patterson AFB, OH 45433

216. R. N. Katz
U.S. Army Materials Technology Laboratory
405 Arsenal Street
Watertown, MA 02172

217. Ted Kawaguchi
Tokai Carbon
375 Park Avenue, Suite 3802
New York, NY 10152

218. Frederick L. Kennard, III
General Motors Corporation
AC Spark Plug Division
Department 32-24
1300 North Dort Highway
Flint, MI 48556

219. J. R. Kidwell
Allied-Signal Aerospace Company
Garrett Auxiliary Power Division
2739 East Washington Street
Post Office Box 5227
Phoenix, AZ 85010

220. Max Klein
Gas Research Institute
8600 West Bryn Mawr Avenue
Chicago, IL 60631

221. C. E. Knapp
Norton Research Corporation
8001 Daly Street
Niagara Falls, Ontario L2G 6S2
CANADA

222. A. S. Kobayashi
University of Washington
Department of Mechanical Engineering
MS:FU10
Seattle, WA 98195

223. Wolfgang Kollenberg
Projektleitung Material-Rohstofforschung - PLR
Kernforschungsanlage Juelich GmbH
Postfach 1913
D-5170 Juelich
WEST GERMANY

224. David M. Kotchick
Allied-Signal Aerospace Company
AiResearch Los Angeles Division
2525 West 190th Street
Torrance, CA 90509

225. Joseph A. Kovach
Eaton Corporation
Manufacturing Technologies Center
32500 Charvon Road
Willoughby Hills, OH 44094

226. Saunders B. Kramer
U.S. Department of Energy
Office of Transportation Systems
1000 Independence Avenue, S.W.
Forrestal Building CE-151
Washington, DC 20585

227. Dan M. Kreiner
Allied-Signal Aerospace Company
Garrett Auxillary Power Division
Post Office Box 5227
Phoenix, AZ 85010

228. A. S. Krieger
Radiation Science, Inc.
Post Office Box 293
Belmont, MA 02178

229. Pieter Krijgsman
Ceramic Design Int. Hold., Ltd.
Post Office Box 68
8050 AB Hattem
THE NETHERLANDS

230. Jack H. L'Amoreux
11346 Gates Mill Drive
Knoxville, TN 37922

231. W. J. Lackey
Georgia Tech Research Institute
Energy and Materials Sciences
Georgia Institute of Technology
Atlanta, GA 30332

232. Everett A. Lake
Air Force Wright Aeronautical Laboratory
AFWAL/POSL
Wright-Patterson AFB, OH 45433-6563

233. Hari S. Lamba
General Motors Corporation
Electro-Motive Division
LaGrange, IL 60525

234. Manfred Langer
Volkswagen AG
Forschung-Neue Technologien Werkstofftechnologie
D-3180 Wolfsburg 1
WEST GERMANY

235. James Lankford
Southwest Research Institute
Department of Materials Sciences
6220 Culebra Road
Post Office Drawer 28510
San Antonio, TX 78284

236. David C. Larsen
Corning Glass Works
Materials Research Department
Sullivan Park, FR-51
Corning, NY 14831

237. S. K. Lau
Carborundum Company
Technology Division
Post Office Box 832
Niagara Falls, NY 14302

238. Harry A. Lawler
Carborundum Company
Niagara Falls R&D Center
Post Office Box 832
Niagara Falls, NY 14302

239. Alan Lawley
Drexel University
Materials Engineering
Philadelphia, PA 19104

240. Daniel Lee
Temescon
2850 7th Street
Berkeley, CA 94710

241. June-Gunn Lee
Korea Advanced Institute of Science and Technology
Post Office Box 131
Dong Dac Mun Seoul
KOREA

242. E. M. Lenoe
Air Force Office of Scientific Research
Office of Naval Research
Liaison Office, Far East
APO San Francisco, CA 96503-0110

243. Stanley R. Levine
NASA Lewis Research Center
21000 Brookpark Road
Cleveland, OH 44135

244. David Lewis
Naval Research Laboratory
Materials Science and Technology
4555 Overlook Avenue, S.W.
Code 63-70
Washington, DC 20375

245. Bill Long
Babcock and Wilcox
Post Office Box 1260
Lynchburg, VA 24505

246. L. A. Lott
EG&G, Inc.
Idaho National Engineering Laboratory
Post Office Box 1625
Idaho Falls, ID 83415

247. Raouf O. Loutfy
Materials and Electrochemical Research Corporation
7960 South Kolb Road
Tucson, AZ 85706

248. Bryan K. Luftglass
Chem Systems, Inc.
303 South Broadway
Tarrytown, NY 10591

249. Robert Lundberg
Swedish Institute for Silicate Research
Box 5403
S-402 29 Gothenburg
SWEDEN

250. Michael J. Lynch
General Electric Company
Medical Systems Group
Post Office Box 414, 7B-36
Milwaukee, WI 53201

251. Vincent L. Magnotta
Air Products and Chemicals, Inc.
Technical Diversification R&D
Post Office Box 538
Allentown, PA 18105

252. Tai-il Mah
Universal Energy Systems
Ceramics and Composites Research
4401 Dayton-Xenia Road
Dayton, OH 45432

253. L. Manes
Commission of the European Communities
Joint Research Centre
Ispra Establishment
1-21020 Ispra (Varese)
ITALY

254. Giel Marijnissen
Interturbine R&D
R&D
Post Office Box 4339
5944 ZG Arcen
THE NETHERLANDS

255. Gerald R. Martin
Fleetguard, Inc.
Cookeville, TN 38501

256. J. W. McCauley
U.S. Army Materials Technology Laboratory
SLCMT-OMM
405 Arsenal Street
Watertown, MA 02172-0001

257. Bryan J. McEntire
Norton Company, TRW Ceramics
Goddard Road
Northboro, MA 01532-1545

258. Thomas D. McGee
Iowa State University
Department of Materials Science and Engineering
Ames, IA 50011

259. H. Christopher McGowan
Advanced Ceramic Technology, Inc.
17 Deerfield Road
East Brunswick, NJ 08816

260. Malcolm G. McLaren
Rutgers University
Department of Ceramics
Bowser Road
Busch Campus
Post Office Box 909
Piscataway, NJ 08854

261. Arthur F. McLean
6225 North Camino Almonte
Tucson, AZ 85718

262. Brian L. Mehosky
British Petroleum
440 Warrensville, Center Rd.
Cleveland, OH 44128

263. Joseph J. Meindl
Reynolds International, Inc.
6603 West Broad Street
Post Office Box 27002
Richmond, VA 23230

264. D. Messier
U.S. Army Materials Technology Laboratory
DRXMR-MC
405 Arsenal Street
Watertown, MA 02172

265. Brad Miller
Norton Company
Advanced Ceramics
Goddard Road
Northboro, MA 01532-1545

266. Amar Mishra
Engelhard Corporation
R&D
Menlo Park, CN-28
Edison, NJ 08818

267. Bill Moehle
Ethyl Corporation
R&D Laboratories
Post Office Box 341
Baton Rouge, LA 70821

268. Helen Moeller
Babcock and Wilcox
Post Office Box 11165
Lynchburg, VA 24506-1165

269. Peter E. D. Morgan
Rockwell International
Science Center
1049 Camino Dos Rios
Post Office Box 1085
Thousand Oaks, CA 91360

270. Lawrence M. Murphy
Manager
Solar Energy Research Institute
Thermal Systems Research Branch
1617 Cole Boulevard
Golden, CO 80401

271. Solomon Musikant
General Electric Company
Space Systems Division
Post Office Box 8555, MS:U-1219
Philadelphia, PA 19101

272. Pero Nannelli
Pennwalt Corporation
900 First Avenue
Post Office Box C
King of Prussia, PA 19406-0018

273. William D. Nix
Stanford University
Department of Materials Science and Engineering
Stanford, CA 94305

274. Richard D. Nixdorf
ReMaxCo Technologies, Inc.
231 Sherway Rd
Knoxville, TN 37922

275. S. D. Nunn
University of Michigan
Materials Science and Engineering
Ann Arbor, MI 48109-2136

276. Brian M. O'Connor
Lubrizol Corporation
Tribology Section
29400 Lakeland Boulevard
Wickliffe, OH 44092

277. W. Richard Ott
Alfred University
Center for Advanced Ceramic Technology
Alfred, NY 14802

278. William C. Owen
Sundstrand Turbomach
Division of Sundstrand Corporation
4400 Ruffin Road
Post Office Box 85757
San Diego, CA 92138-5757

279. Muktesh Paliwal
GTE Products Corporation
Hawes Street
Towanda, PA 18848-0504

280. Joseph E. Palko
General Electric Company
Gas Turbine Division
TTD Building, 55-113
Schenectady, NY 12345

281. Hayne Palmour, III
North Carolina State University
Engineering Research Services Division
2158 Burlington Engineering Labs
Post Office Box 5995
Raleigh, NC 27607

282. Joseph N. Panzarino
Norton Company
Advanced Ceramics
Goddard Road
Northboro, MA 01532-1545

283. Pellegrino Papa
Corning Glass Works
Corning Technical Products Division
Corning, NY 14831

284. R. H. Parrish
Vanderbilt University
Post Office Box 1621, Station B
Nashville, TN 37235

285. James G. Paschal
Reynolds Metals Company
Post Office Box 76154
Atlanta, GA 30358

286. Arvid E. Pasto
GTE Laboratories Inc.
40 Sylvan Road
Waltham, MA 02254

287. James W. Patten
Cummins Engine Company, Inc.
Box 3005, Mail Code 50183
Columbus, IN 47202-3005

288. Robert A. Penty
Eastman Kodak Company
Manufacturing Technology Department
Apparatus Division
901 Elmgrove Road
Rochester, NY 14650

289. Gary R. Peterson
U.S. Department of Energy
Idaho Operations Office
785 D.O.E. Place
Idaho Falls, ID 83402

290. R. Byron Pipes
University of Delaware
Center for Composite Materials
2001 Spencer Laboratory
Newark, DE 19716

291. Bruce J. Pletka
Michigan Technological University
Department of Metallurgical Engineering
Houghton, MI 49931

292. Robert C. Pohanka
Office of Naval Research
800 North Quincy Street
Code 431
Arlington, VA 22217

293. J. P. Pollinger
Allied-Signal Aerospace Company
Garrett Ceramic Components Division
19800 South Van Ness Avenue
Torrance, CA 90509

294. Stephen C. Pred
ICD Group, Inc.
1100 Valley Brook Avenue
Lyndhurst, NJ 07071

295. Karl M. Prewo
United Technologies Corporation
Research Center
Silver Lane , MS:24
East Hartford, CT 06108

296. Hubert B. Probst
NASA Lewis Research Center
Materials Division
21000 Brookpark Road
MS:49-1
Cleveland, OH 44135

297. Joseph M. Proud
GTE Laboratories Inc.
Materials Science Laboratory
40 Sylvan Road
Waltham, MA 02254

298. D. W. Prouse
Ceramatec, Inc.
2425 South 900 West
Salt Lake City, UT 84119

299. Carr Lane Quackenbush
Norton Company
Advanced Ceramics
Goddard Road
Northboro, MA 01532-1545

300. Brian Quigy
National Aeronautics and Space Administration
Energy Systems Office
Washington, DC 20546

301. George Quinn
U.S. Army Materials Technology Laboratory
405 Arsenal Street
Watertown, MA 02172

302. Dennis T. Quinto
Kennametal, Inc.
Phillip M. McKenna Laboratory
Post Office Box 639
Greensburg, PA 15601

303. Dennis W. Readey
Ohio State University
2041 College Road
Columbus, OG 43210

304. Michael J. Readey
Coors Ceramics Company
R&D
17750 West 32nd Street
Golden, CO 80401

305. Robert R. Reeber
U.S. Army Research Office
Post Office Box 12211
Research Triangle Park, NC 27709

306. K. L. Reifsnider
Virginia Polytechnic Institute and State University
Department of Engineering Science and Mechanics
Blacksburg, VA 24061

307. Paul E. Rempes
McDonald Douglass Missle Systems Company
Department E-467
Building 107, Level 1
Post Office Box 516
Mail Code 1066086
St. Louis, MO 63166-0516

308. Theresa M. Resetar
U.S. Army Materials Technology Laboratory
Materials Characterization Center
405 Arsenal Street
SLCMT-OMM
Watertown, MA 02172

309. K. T. Rhee
Rutgers University
College of Engineering
Bowser Road
Post Office Box 909
Piscataway, NJ 08854

310. Roy W. Rice
W. R. Grace and Company
7379 Route 32
Columbus, MD 21044

311. David W. Richerson
Ceramatec, Inc.
2425 South 900 West
Salt Lake City, UT 84119

312. Scott L. Richlen
U.S. Department of Energy
Office of Industrial Programs
1000 Independence Avenue, S.W.
Forrestal Building CE-141
Washington, DC 20585

313. Paul Rieth
Ferro Corporation
661 Willet Road
Buffalo, NY 14218-9990

314. Michael A. Rigdon
Institute for Defense Analyses
1801 Beauregard Street
Alexandria, VA 22311

315. John E. Ritter, Jr.
University of Massachusetts
Mechanical Engineering Department
Amherst, MA 01003

316. Giulio A. Rossi
Norton Company
Advanced Ceramics
Goddard Road
Northboro, MA 01532-1545

317. Barry R. Rossing
Lanxide Corporation
Tralee Industrial Park
Newark, DE 19711

318. Bruce Rubinger
Gobal
50 Milk Street, 15th Floor
Boston, MA 02109

319. Robert Ruh
Air Force Wright Aeronautical Laboratory
Metals and Ceramics Division
AFWAL/MLLM
Wright-Patterson AFB, OH 45433

320. Robert J. Russell, Sr.
Norton Company
Advanced Ceramics
Goddard Road
Northboro, MA 015332-1545

321. George P. Safol
Westinghose Electric Corporation
R&D Center
1310 Beulah Road
Pittsburgh, PA 15235

322. J. A. Salem
NASA Lewis Research Center
21000 Brookpark Center
Cleveland, OH 44135

323. J. Sankar
North Carolina A&T State University
Mechanical Engineering Department
Greensboro, NC 27411

324. Vin K. Sarin
Boston University
Department of Manufacturing Engineering
44 Cummington Street
Boston, MA 02215

325. Maxine L. Savitz
Allied-Signal Aerospace Company
Garrett Ceramic Components Division
19800 South Van Ness Avenue
Torrance, CA 90509

326. Ashok Saxena
Georgia Institute of Technology
Materials Engineering
Atlanta, GA 30332-0245

327. Richard Schapery
Texas A&M University
Civil Engineering Department
College Station, TX 77843

328. Jim Schienle
Allied-Signal Aerospace Company
Garrett Auxiliary Power Division
2739 East Washington Street
Post Office Box 5227, MS:1302-2P
Phoenix, AZ 85010

329. Liselotte J. Schioler
Air Force Office of Scientific Research
Bolling AFB
Washington, DC 20332-6448

330. Richard A. Schmidt
Battelle Columbus Laboratories
Mechanics Section
505 King Avenue
Columbus, OH 43201-2693

331. Arnie Schneck
Deere & Company Technical Center
Post Office Box 128
Wood-Ridge, NJ 07075

332. Matthew Schreiner
ALANX Products L.P.
101 Lake Drive
Newark, DE 19702

333. John Schuldies
Industrial Ceramic Technology, Inc.
37 Enterprise Drive
Ann Arbor, MI 48103

334. R. B. Schulz
U.S. Department of Energy
Office of Transportation Systems
1000 Independence Avenue, S.W.
Forrestal Building CE-34, 5G-046
Washington, DC 20585

335. Wesley J. C. Schuster
Thermo Electron Corporation
Metals Division
115 Eames Street
Post Office Box 340
Wilmington, MA 01887

336. Murray A. Schwartz
Bureau of Mines
30 Orchard Way, North
Potomac, MD 20854

337. Douglas B. Schwarz
Dow Chemical Company
52 Building
Midland, MI 48674

338. Thomas M. Sebestyen
U.S. Army Tank Automotive Command
AMSTA-RGRT
Warren, MI 48397-5000

339. Brian Seegmiller
Coors Ceramics Company
17750 West 32nd Street
Golden, CO 80401

340. Peter T. B. Shaffer
Advanced Refractory Technologies, Inc.
699 Hertel Avenue
Buffalo, NY 14207

341. Laurel M. Sheppard
Advanced Materials and Processes
Route 87
Metals Park, OH 44073

342. Dinesh K. Shetty
University of Utah
Department of Materials Science and Engineering
Salt Lake City, UT 84112

343. Jack D. Sibold
Coors Ceramics Company
17750 West 32nd Street
Golden, CO 80401

344. Neal Sigmon
U.S. House of Representatives
Subcommittee on Interior and Related Events
Rayburn Building, Room B308
Washington, DC 20515

345. Richard Silberglitt
Quest Research Corporation
7600 Leesburg Pike #A
Falls Church, VA 22043

346. A. Sinha
North Carolina A&T State University
Department of Mechanical Engineering
Greensboro, NC 27411

347. Maurice J. Sinnott
University of Michigan
Chemical and Metallurgical Engineering
438 West Engineering Building
Ann Arbor, MI 48109-2136

348. S. R. Skaggs
Los Alamos National Laboratory
Program Office
Post Office Box 1663, MS:F-682
Los Alamos, NM 87545

349. Jay R. Smyth
Allied-Signal Aerospace Company
Garrett Auxillary Power Division
Post Office Box 5227
MS:93-172/1302-2K
Phoenix, AX 85010

350. Rafal Sobotowski
British Petroleum
R&D
3092 Broadway Avenue
Cleveland, OH 44115

351. E. Solidum
Allied-Signal Aerospace Company
Garrett Ceramic Components Division
19800 South Van Ness Avenue
Torrance, CA 90509

352. Thomas M. Sopko
Lubrizol Enterprises, Inc.
29400 Lakeland Boulevard
Wickliffe, OH 44092

353. Richard M. Spriggs
Alfred University
Center for Advanced Ceramic Technology
Alfred, NY 14802

354. Charles Spuckler
NASA Lewis Research Center
2100 Brookpard Road
Cleveland, OH 44135

355. M. Srinivasan
Materials Solutions
Post Office Box 663
Grand Island, NY 14702-0663

356. Gordon L. Starr
Cummins Engine Company, Inc.
Metallic/Cereamic Materials Department
Post Office Box 3005
Mail Code 50183
Columbus, IN 47202-3005

357. L. Brian Starling
ICI Advanced Ceramics
2055 East Technology Circle
Tempe, AZ 85284

358. Harold L. Stocker
General Motors Corporation
Allison Gas Turbine Division
2001 South Tibbs Avenue
Post Office Box 420, T-23
Indianapolis, IN 46206-0420

359. Paul D. Stone
Dow Chemical Company
1801 Building
Midland, MI 48674

360. Roger Storm
Carborundum Company
Niagara Falls R&D Center
Post Office Box 337
Niagara Falls, NY 14302

361. E. E. Strain
Allied-Signal Aerospace Company
Garrett Auxiliary Power Division
Department 76-50
2739 East Washington Street
Building 1302-1N
Post Office Box 5227, MS:301-2N
Phoenix, AZ 85010

362. Thomas N. Strom
NASA Lewis Research Center
21000 Brookpark Road, 77-6
Cleveland, OH 44135

363. Jerry Strong
Albright & Wilson
Post Office Box 26229
Richmond, VA 23260

364. Richard Suddeth
Boeing Motor Airplane Company
Post Office Box 7730, MS:K-76-67
Wichita, KS 67277

365. Paul Sutor
Midwest Research Institute
425 Volker Boulevard
Kansas City, MO 64116

366. P. L. Sutton
U.S. Department of Energy
Office of Transportation Systems
1000 Independence Avenue, S.W.
Forrestal Building CE-322
Washington, DC 20585

367. J. J. Swab
U.S. Army Materials Technology Laboratory
Ceramics Research Division
SLCMT-EMC
405 Arsenal Street
Watertown, MA 02172

368. John W. Swain, Jr.
Kollmorgen Corporation
PCK Technology Division
15424 Garrison Lane
Southgate, MI 48195

369. Lewis Swank
Ford Motor Company
Material Systems Reliability Department
20000 Rotunda Drive
Building SRL, Room S-2023
Post Office Box 2053
Dearborn, MI 48121-2053

370. Chris Tarry
GTE Products Corporation
Hawes Street
Towanda, PA 18848

371. Anthony C. Taylor
U.S. House of Representatives
Committee on Science and Technology
Rayburn Building, Room 2321
Washington, DC 20515

372. Monika O. Ten Eyck
Carborundum Company
Technology Division
Post Office Box 337
Niagara Falls, NY 14302

373. John K. Tien
Columbia University
Center for Strategic Materials
1137 S.W. Mudd Building
New York, NY 10027

374. T. Y. Tien
University of Michigan
Materials and Metallurgical Engineering
Dow Building
Ann Arbor, MI 48109-2136

375. Julian M. Tishkoff
Air Force Office of Scientific Research
(AFOSR/WC) Bolling AFB
Washington, DC 20332

376. Louis E. Toth
National Science Foundation
Division of Materials Research
1800 "G" Street, N.W.
Washington, DC 20550

377. Richard E. Tressler
Pennsylvania State University
Ceramic Science and Engineering
201 Steidle Building
University Park, PA 16802

378. W. T. Tucker
General Electric Company
Research Laboratory
Post Office Box 8
Schenectady, NY 12301

379. Donald L. Vaccari
General Motors Corporation
Allison Gas Turbine Division
2001 South Tibbs Avenue
Post Office Box 420
Speed Code T10B
Indianapolis, IN 46241

380. O. Van Der Biest
Katholieke Universiteit Leuven
Departement Metaalkunde en Toegepaste
de Croylaan 2
B-3030 Leuven
BELGIUM

381. Edward C. Van Reuth
Technology Strategies, Inc.
10722 Shingle Oak Court
Burke, VA 22015

382. Mark Van Roode
Solar Turbines, Inc.
2200 Pacific Highway
Mail Zone R-1
San Diego, CA 92138

383. V. Venkateswaran
Carborundum Company
Niagara Falls R&D Center
Post Office Box 832
Niagara Falls, NY 14302

384. Ted Vojnovich
U.S. Department of Energy
Office of Transportation Systems
1000 Independence Avenue, S.W.
Forrestal Building CE-151
Washington, DC 20585

385. K. E. Voss
Engelhard Corporation
Research Department
Menlo Park, CN-28
Edison, NJ 08818

386. John B. Wachtman, Jr.
Rutgers University
College of Engineering
Bowser Road
Post Office Box 909
Piscataway, NJ 08855-0909

387. Harlan L. Watson
U.S. House of Representatives
Committee on Science and Technology
Rayburn Building, Suite 2321
Washington, DC 20515

388. John D. Watson
Broken Hill Proprietary Co., Ltd.
Melbourne Research Laboratories
245 Wellington Road
Mulgrave 3170 Victoria
AUSTRALIA

389. Karen E. Weber
Detroit Diesel Corporation
13400 West Outer Drive
Detroit, MI 48239

390. C. David Weiss
Caterpillar Inc.
Technical Center, Building E
Post Office Box 1875
Peoria, IL 61656-1875

391. Albert R. C. Westwood
Martin Marietta Laboratories
R&D
1450 South Rolling Road
Baltimore, MD 21227

392. Thomas J. Whalen
Ford Motor Company
Material Systems Reliability Department
20000 Rotunda Drive
Building SRL, Room S-2023
Post Office Box 2053
Dearborn, MI 48121-2053

393. Sheldon M. Wiederhorn
National Institute of Standards and Technology
Inorganic Materials Division
Gaithersburg, MD 20899

394. James C. Williams
General Electric Company
Engineering Materials Technology Labs
One Neumann Way
Cincinnati, OH 45215-6301

395. Janette R. Williams
Kollmorgen Corporation
PCK Technology Division
322 L.I.E. South Service Road
Melville, NY 11747

396. Craig A. Willkens
Norton Company
Advanced Ceramics
Goddard Road
Northboro, MA 01532-1545

397. Roger R. Wills
TRW, Inc.
Valve Division
1455 East 185th Street
Cleveland, OH 44110

398. J. M. Wimmer
Allied-Signal Aerospace Company
Garrett Auxiliary Power Division
2739 East Washington Street
Post Office Box 5227, MS:1302-2P
Phoenix, AZ 85010

399. David Wirth
Coors Ceramics Company
Technical Operations and Engineering
17750 West 32nd Street
Golden, CO 80401

400. Thomas J. Wissing
Eaton Corporation
Engineering & Research Center
26201 Northwestern Highway
Post Office Box 766
Southfield, MI 48037

401. Dale Wittmer
Southern Illinois University at Carbondale
Department of Mechanical Engineering
Carbondale, IL 62901

402. Stanley M. Wolf
U.S. Department of Energy
Office of Industrial Technologies
1000 Independence Avenue, S.W.
Forrestal Building CE-232
Washington, DC 20585

403. George W. Wolter
Howmet Turbine Components Corporation
Technical Center
699 Benston Road
Whitehall, MI 49461

404. James C. Wood
NASA Lewis Research Center
21000 Brookpark Road
MS:500-210
Cleveland, OH 44135

405. Roger P. Worthen
Eaton Corporation
Engineering and Research Center
26201 Northwestern Highway
Post Office Box 766
Southfield, MI 48076

406. J. C. Wurm
Commission of the European Communities
Advanced Materials Research Programme
Rue de la Loi 200
B-1049 Brussels
BELGIUM

407. John Yamanias
Allied-Signal, Inc.
Metals and Ceramics Lab
Post Office Box 1021R
Morristown, NJ 07960-1021

408. Harry C. Yeh
Allied-Signal Aerospace Company
Garrett Ceramic Components Division
19800 South Van Ness Avenue
Torrance, CA 90509

409. Thomas M. Yonushonis
Cummins Engine Company, Inc.
Post Office Box 3005
Mail Code 50183
Columbus, IN 47202-3005

410. Don Zabierek
Air Force Wright Aeronautical Laboratory
AFWAL/POTC
Wright-Patterson AFB, OH 45433

411. Charles Zeh
U.S. Department of Energy
Morgantown Energy Technology Center
Post Office Box 880
Morgantown, WV 26505

412. Anne Marie Zerega
U.S. Department of Energy
Office of Transportation Systems
1000 Independence Avenue, S.W.
Forrestal Building CE-30
Washington, DC 20585

413. Martin Zlotnick
Nichols Research Corporation
8618 Westwood Center Drive
Suite 200
Vienna, VA 22180-2222

414. Klaus M. Zwilsky
National Research Council
National Materials Advisory Board
2101 Constitution Avenue
Washington, DC 20418

415. Department of Energy
Oak Ridge Operations Office
Assistant Manager for Energy Research and Development
Post Office Box 2001
Oak Ridge, TN 37831-8600

416–425. Department of Energy
Office of Scientific and Technical Information
Office of Information Services
Post Office 62
Oak Ridge, TN 37831

For distribution by microfiche as shown in DOE/OSTI-4500, Distribution Category UC-332 (Ceramics/Advanced Materials).

*U.S. GOVERNMENT PRINTING OFFICE: 1990--748-114/20048